INSIGHTS IN CARDIOVASCULAR IMAGING: 2021

EDITED BY: Christos Bourantas, Sebastian Kelle and Steffen Erhard Petersen

PUBLISHED IN: Frontiers in Cardiovascular Medicine

frontiers Research Topics

ISSN 1664-8714
ISBN 978-2-83250-209-9
DOI 10.3389/978-2-83250-209-9

About Frontiers

Frontiers is more than just an open-access publisher of scholarly articles: it is a pioneering approach to the world of academia, radically improving the way scholarly research is managed. The grand vision of Frontiers is a world where all people have an equal opportunity to seek, share and generate knowledge. Frontiers provides immediate and permanent online open access to all its publications, but this alone is not enough to realize our grand goals.

Frontiers Journal Series

The Frontiers Journal Series is a multi-tier and interdisciplinary set of open-access, online journals, promising a paradigm shift from the current review, selection and dissemination processes in academic publishing. All Frontiers journals are driven by researchers for researchers; therefore, they constitute a service to the scholarly community. At the same time, the Frontiers Journal Series operates on a revolutionary invention, the tiered publishing system, initially addressing specific communities of scholars, and gradually climbing up to broader public understanding, thus serving the interests of the lay society, too.

Dedication to Quality

Each Frontiers article is a landmark of the highest quality, thanks to genuinely collaborative interactions between authors and review editors, who include some of the world's best academicians. Research must be certified by peers before entering a stream of knowledge that may eventually reach the public - and shape society; therefore, Frontiers only applies the most rigorous and unbiased reviews.
Frontiers revolutionizes research publishing by freely delivering the most outstanding research, evaluated with no bias from both the academic and social point of view. By applying the most advanced information technologies, Frontiers is catapulting scholarly publishing into a new generation.

What are Frontiers Research Topics?

Frontiers Research Topics are very popular trademarks of the Frontiers Journals Series: they are collections of at least ten articles, all centered on a particular subject. With their unique mix of varied contributions from Original Research to Review Articles, Frontiers Research Topics unify the most influential researchers, the latest key findings and historical advances in a hot research area! Find out more on how to host your own Frontiers Research Topic or contribute to one as an author by contacting the Frontiers Editorial Office: frontiersin.org/about/contact

INSIGHTS IN CARDIOVASCULAR IMAGING: 2021

Topic Editors:
Christos Bourantas, University College London, United Kingdom
Sebastian Kelle, Deutsches Herzzentrum Berlin, Germany
Steffen Erhard Petersen, Queen Mary University of London, United Kingdom

Citation: Bourantas, C., Kelle, S., Petersen, S. E., eds. (2022). Insights in Cardiovascular Imaging: 2021. Lausanne: Frontiers Media SA.
doi: 10.3389/978-2-83250-209-9

Table of Contents

frontiers in Cardiovascular Medicine

BRIEF RESEARCH REPORT
published: 27 September 2021
doi: 10.3389/fcvm.2021.757642

Diagnosis of Cardiac Involvement in Amyloid A Amyloidosis by Cardiovascular Magnetic Resonance Imaging

*Bishwas Chamling[1], Stefanos Drakos[1], Michael Bietenbeck[1], Karin Klingel[2], Claudia Meier[1] and Ali Yilmaz[1]**

[1] Division of Cardiovascular Imaging, Department of Cardiology I, University Hospital Münster, Albert Schweitzer Campus 1, Münster, Germany, [2] Institute for Pathology and Neuropathology, University Hospital Tübingen, Tübingen, Germany

OPEN ACCESS

Edited by:
Fabrizio Ricci,
University of Studies G. d'Annunzio Chieti and Pescara, Italy

Reviewed by:
Andrea Barison,
Gabriele Monasterio Tuscany Foundation (CNR), Italy
Alberto Aimo,
Sant'Anna School of Advanced Studies, Italy

***Correspondence:**
Ali Yilmaz
ali.yilmaz@ukmuenster.de

Specialty section:
This article was submitted to Cardiovascular Imaging, a section of the journal Frontiers in Cardiovascular Medicine

Received: 12 August 2021
Accepted: 01 September 2021
Published: 27 September 2021

Citation:
Chamling B, Drakos S, Bietenbeck M, Klingel K, Meier C and Yilmaz A (2021) Diagnosis of Cardiac Involvement in Amyloid A Amyloidosis by Cardiovascular Magnetic Resonance Imaging. Front. Cardiovasc. Med. 8:757642. doi: 10.3389/fcvm.2021.757642

Background: Diagnosis of cardiac involvement in amyloid A (AA) amyloidosis is challenging since AA amyloidosis is a rare disease and cardiac involvement even less frequent. The diagnostic yield of currently available non-invasive imaging methods is not well-studied and rather limited, and invasive endomyocardial biopsy (EMB) is rarely performed due to the potential risk of this procedure. Cardiovascular magnetic resonance (CMR)-based myocardial tissue characterization by late-gadolinium-enhancement (LGE) imaging and novel-mapping approaches may increase the diagnostic yield in AA amyloidosis.

Methods: Two patients with AA amyloidosis in whom cardiac involvement was suspected based on CMR findings and subsequently proven by biopsy work-up are presented. CMR studies were performed on a 1.5-T system and comprised a cine steady-state free precession pulse sequence for ventricular function and a late-gadolinium-enhancement (LGE) sequence for detection of myocardial pathology. Moreover, a modified Look-Locker inversion recovery (MOLLI) T1-mapping sequence was applied in basal, mid and apical short-axes prior to contrast agent administration and ∼20 min thereafter to determine native T1 and ECV values.

Results: Both patients showed slightly dilated left ventricles (LV) with mild to moderate LV hypertrophy and preserved systolic function. Only a very subtle pattern of LGE was observed in both patients with AA amyloidosis. However, markedly elevated native T1 (max. 1,108 and 1,112 ms, respectively) and extracellular volume fraction (ECV) values (max. 39 and 48%, respectively) were measured in the myocardium suggesting the presence of cardiac involvement - with subsequent EMB-based proof of AA amyloidosis.

Conclusion: We recommend a multi-parametric CMR approach in patients with AA amyloidosis comprising both LGE-based contrast-imaging and T1-mapping-based

ECV measurement of the myocardium for non-invasive work-up of suspected cardiac involvement. The respective CMR findings may be used as gatekeeper for additional invasive procedures (such as EMB) and as a non-invasive monitoring tool regarding assessment and modification of ongoing treatments.

Keywords: AA amyloidosis, cardiac involvement, serum amyloid A (SAA), ECV, cardiovascular magnetic resonance (CMR), mapping—magnetic resonance imaging

INTRODUCTION

Amyloidosis is a family of multifaceted, heterogenous diseases based on abnormally folded proteins characterized by pathological accumulation of insoluble, polymeric protein fibrils in the extracellular space of various tissues and organs—sometimes leading to organ dysfunction, organ failure, and death. So far, there are more than 30 different proteins, which have been identified as amyloidogenic—out of which at least 17 can cause systemic disease (1).

The most common forms of amyloidosis infiltrating the human heart (cardiac amyloidosis, CA) are (i) immunoglobulin light chain (AL) (2) and (ii) transthyretin amyloidosis (ATTR) (3). As a different type, secondary or amyloid A (AA) amyloidosis is caused by overproduction and accumulation of the acute-phase protein "serum amyloid A" (SAA) that can be highly expressed in patients with chronic inflammation, cancers or (auto)inflammatory diseases (4). The incidence of AA amyloidosis, in particular in developed countries, is low since this disorder only occurs as a long-term complication of rather severe chronic inflammatory disorders that in turn are mostly well-managed in developed countries—in case of timely detection.

To identify the underlying inflammatory process in newly diagnosed AA amyloidosis, several factors ranging from genetic variation to ancestral history of patients have to be taken into consideration. For example, SAA1 genotype is one of those predisposing factors supposed to affect amyloidogenesis (e.g., SAA1.1 in Caucasians and SAA1.3 in Japanese homozygotes) (5). Likewise, if amyloidosis is suspected, even in asymptomatic members of certain origins (for e.g., Turkish, Armenian, Greek, Spanish) familial Mediterranean fever (FMF) should be ruled out as a possible underlying cause of AA amyloidosis (6).

Available knowledge indicates that SAA does not affect the human heart directly, and significant clinical cardiac manifestations are rare. However, it has been shown that SAA may be deposited in cardiac tissue (7). If present, it can lead to severe ventricular wall thickening and subsequent stiffness resulting in a restrictive pattern as well as ventricular arrhythmias as major cardiac manifestations (8). Although CA, hypertrophic cardiomyopathy (HCM) and hypertensive heart disease (HHD) can be suspected as underlying disease in case of left ventricular (LV) hypertrophy of unknown origin based on patient history, symptoms, ECG and echocardiography, only myocardial tissue characterization by multi-parametric CMR (comprising late-gadolinium-enhancement imaging and novel mapping-based approaches) allows to safely differentiate between different forms of LV hypertrophy. Recently, Chatzantonis et al. showed a high diagnostic yield of CMR for the non-invasive diagnosis of cardiac ATTR amyloidosis based on the characteristic pattern of LGE in those patients (9). Surprisingly, even an extensive literature search for non-invasive imaging approaches to diagnose cardiac AA amyloidosis did not result in any landmark studies or even case reports illustrating the potential use of CMR imaging.

In the present report, the use of multi-parametric CMR imaging was crucial to diagnose cardiac involvement in case of systemic AA amyloidosis. We present two similar cases of AA amyloidosis in whom cardiac involvement was suspected based on CMR findings and subsequently proven by biopsy work-up. Importantly, both cases showed only a very subtle pattern of LGE—not resembling the well-known characteristic pattern of LGE that can be found in those patients with ATTR and AL amyloidosis. However, additional ECV measurement based on T1-mapping was highly suggestive of an ongoing infiltrative process in the extracellular space of the myocardium.

METHODS AND MATERIALS

Early diagnosis of cardiac involvement in amyloidosis can be challenging due to unspecific or missing clinical manifestations. Although non-invasive imaging modalities such as echocardiography (with speckle-based strain measurement), bone scintigraphy (10) as well as multi-parametric CMR are widely used today and promise both early and specific detection of cardiac amyloidosis (11, 12), invasive EMB still constitutes the gold-standard for the final diagnosis of non-ischemic heart diseases including cardiac amyloidosis (13). Noteworthy, imaging modalities such as bone scintigraphy and multi-parametric CMR were shown to be valuable tools in differentiating cardiac ATTR from AL amyloidosis if additional information on monoclonal protein studies are available and promise early detection of cardiac amyloidosis (9, 14). However, no convincing non-invasive imaging findings have been described so far regarding the detection of cardiac involvement in case of AA amyloidosis.

CMR has been established as a robust diagnostic tool for the work-up of different cardiac diseases including LV hypertrophy of unknown origin and was recently shown to offer a very high diagnostic yield regarding the diagnosis of cardiac ATTR and AL amyloidosis (15, 16). An overview on established diagnostic techniques and staging concepts for patients with CA was summarized recently (17). However, imaging parameters for the detection of cardiac involvement in case of AA amyloidosis are still not established. In the present report, we propose some CMR-based techniques to detect/suspect cardiac AA amyloidosis. The details of patient

characteristics, cardiac imaging as well as EMB work-up are explained in the section separately.

Patient Characteristics

Both subjects were Caucasian males who presented with end stage renal disease (ESRD) requiring dialysis. The first patient was a 44-year-old young male patient with terminal renal insufficiency and was on hemodialysis since 08/2018. A rectal biopsy performed in 11/2019 had revealed SAA depositions. Echocardiography showed a moderate to severe LV hypertrophy with preserved ejection fraction. Additional EMB samples were taken in this patient and confirmed the presence of cardiac AA amyloidosis. Subsequent genetic testing revealed heterozygosity for 2 pathogenic variants of the MEFV-gene and supported the diagnosis of FMF as a plausible cause of AA amyloidosis.

The second subject, a 53-year-old male and tobacco-smoking patient, was initially referred from a regional hospital to our university hospital following clinical deterioration of the general condition during dialysis in addition to new-onset of diffuse abdominal pain. Incidental findings comprised a pericardial effusion with a maximal diameter of 2 cm. Noteworthy, he was treated with colchicine since his childhood due to suspected MFM. This treatment was stopped in 2012 due to onset of terminal renal insufficiency leading to haemodialysis. The suspected diagnosis of FMF was confirmed by molecular genetic analysis as an underlying inflammatory cause after SAA deposits were detected in EMB samples. In addition, liver biopsies were also performed and confirmed the aforementioned results. Details of the respective patient characteristics can be found in **Table 1**. Written informed consent was obtained from all the patients for the publication of any potentially identifiable images or data included in this article and the study protocol conforms to the ethical guidelines of the 1975 Declaration of Helsinki.

Endomyocardial Biopsy Protocol

EMB specimens were obtained from the LV free wall (*via* a femoral artery access site using a 7F long-sheath without angulation following a retrograde approach) as described previously (9). Continuous ECG, blood pressure and pulse oximetry monitoring were performed throughout the whole procedure. Fluoroscopy was used for guidance of the long-sheath and bioptome, and for targeting the region of interest—which was defined in advance by non-invasive CMR. Six EMB samples were collected from the LV. Post-procedural echocardiography was performed to rule out or detect a pericardial effusion possibly caused by the biopsy procedure.

Histological and Immunohistochemical Analyses

EMB samples were fixed in 4% buffered formaldehyde for histology and immunohistochemical staining, or in RNAlater (Ambion Inc., Foster City, USA). EMBs were considered positive for viral infection if viral genomes were detected by nested PCR/reverse transcription PCR, as published previously (18). EMB specimens were stained with Congo red for the diagnosis of cardiac amyloidosis and examined by light microscopy.

TABLE 1 | Patient characteristics.

Parameter	Patient 1	Patient 2
Age (years)	44	53
Sex	Male	Male
BMI (kg/m²)	21.6	21.1
Inflammatory extracardiac diseases	MFM, recurrent fevers, pleurisy, spontaneous bacterial peritonitis, Hepatitis B	MFM, mild recurrent fevers, abdominal and joint discomforts
Current medication	Ca^{++} channel blocker, beta-blocker, colchicine, dihydralazine, ACE-inhibitor, aspirin, atorvastatin, pregabalin, pramiprexol	Ca^{++} channel blocker, beta-blocker, colchicine, iron substitution, ACE-inhibitor
Heart rate	56	61
Blood pressure (mmHg), sys/dia	145/73	110/65
Temperature (°C)	36.8	36.4
C-reactive protein (mg/dl) [< 0,5]	2.2	8
Hematocrit (Pre-Dialysis)	26	31
Leukocyte count [3.9–10.9 × 10^9/L]	5.54	18.84
CK (U/L) [< 174]	143	574
CK-MB (U/L) [< 24]	13	172
eGFR (CKD-EPI) [> 90]	7	8
NT-proBNP (pg/ml) [< 172]	> 35.000	5.740
Major CMR findings		
LV-EF (%)	56	66
LV-EDVi (ml/m²)	111	102
LV-ESVi (ml/m²)	49	35
LV mass (g/m²)	98	87
Max. thickness of the septal wall (mm)	16	13
RV-EF (%)	56	67
Global native T1 [950–1,050 m]	1.098	1.062
Basal septal native T1 [950–1,050 m]	1.108	1.082
Basal lateral native T1 [950–1,050 m]	1.067	1.112
Global native T2 [50–56 m]	58	56
Basal septal T2 [50–56 m]	56	58
Basal lateral T2 [50–56 m]	54	53
Global ECV [25–31%]	36	44
Septal ECV [25–31%]	39	42

(Continued)

TABLE 1 | Continued

Parameter	Patient 1	Patient 2
Lateral ECV [25–31%]	36	48

All data are from the day (± 3) of CMR examination, if not mentioned otherwise. Units are mentioned in small brackets (). Normal range of values are mentioned in large brackets []. BMI, body mass index; FMF, familial mediterranean fever; CMR, cardiovascular magnetic resonance; CK, creatine kinase; CK-MB, creatine kinase myocardial band; eGFR (CKD-EPI), estimated glomerular filtration rate according to chronic kidney disease epidemiology collaboration; NT-proBNP, N-terminal pro brain natriuretic peptides; ECV, extracellular volume fraction.

In addition, Congo red staining was demonstrated by typical green birefringence under cross-polarized light as described earlier (19).

CMR Acquisition, T1/T2 and ECV Measurements

CMR studies were performed on a 1.5-T system (Ambition, Philips Healthcare, Best, The Netherlands). CMR data acquisition was performed according to the standardized protocol suggested by the Society for Cardiovascular Magnetic Resonance (SCMR) (20). Our CMR protocol comprised a cine steady-state free precession pulse sequence for ventricular function and a two-dimensional (2D) inversion recovery fast spoiled gradient-echo sequence 10 to 15 min after administration of a gadolinium-based contrast agent (Gadobutrol 0.10 mmol/kg) for detection of myocardial pathology. Moreover, a modified Look-Locker inversion recovery (MOLLI) T1-mapping sequence was applied in basal, mid and apical short-axes prior to contrast agent administration and ∼20 min thereafter to determine native T1 and ECV values as described previously (21). Motion corrected native and post-contrast T1 maps were generated from the pre- and post-contrast T1 sequences. In each short-axis T1 map the endo- and epicardial contours were manually drawn. For T2-mapping, similar to T1, motion corrected but only native pre-contrast sequences were used. Additionally, for ECV calculation, a region of interest was drawn in the blood pool (avoiding the papillary muscles) in all analyzed T1 maps. Motion corrected and segmented ECV maps were generated from the native and post-contrast segmented T1 maps, using the patient's hematocrit level as described by us elsewhere (21). "Global" T1, T2 and ECV values were calculated by averaging all 16 segments from three short-axis slices.

RESULTS

CMR Findings

Both patients showed similar results regarding cine-imaging: LVs were slightly dilated, mild to moderately hypertrophied with preserved systolic function. Right ventricles (RV) showed no abnormalities with regard to size and function. Regarding myocardial tissue characterization, a subtle and rather diffuse pattern of LGE was detected in the basal segments of the LV lateral wall. Moreover, a little pericardial effusion was observed (**Figure 1A**). Patient 2 showed a slightly more pronounced non-ischemic pattern of LGE in the basal to midventricular inferior/inferolateral segments of the LV wall (**Figure 2**). In addition, some pericardial enhancement suggestive of pericarditis as well as pleural effusion suggestive of polyserositis, most likely in the setting of the underlying disease, were present. Importantly, myocardial mapping measurements resulted in a marked elevation of ECV-values as well as slight elevation of native T1-values predominantly in the basal septal and lateral LV walls, and rather normal T2-values in both patients—indicating a rather chronic, non-inflammatory and most likely infiltrative process (**Figures 1A**, **2**). Detailed mapping results are illustrated in **Table 1**.

Histological and Immunohistochemical Findings

Based on histopathology, there was no evidence of active lymphocytic myocarditis. Using Congo-red staining and immunohistochemistry, the presence of cardiac AA amyloidosis was confirmed with a very subtle and diffuse amyloid pattern in the extracellular space and a marked vascular involvement (**Figure 1B**). In addition, other possible diagnoses such as hypertensive heart disease, hematochromatosis, classic HCM, glycogenosis, Fabry disease or dilated cardiomyopathy were ruled out. Amyloid subtyping was achieved with immunohistochemical staining and showed a pronounced positive reaction for amyloid A (**Figure 1B**). The amyloid deposits were negative regarding lambda and kappa light chain antibodies. Moreover, there was no immunohistological evidence for the presence of ATTR amyloidosis.

DISCUSSION

Cardiac involvement in case of AA amyloidosis is not common and rather challenging to diagnose. An extensive literature search regarding the diagnostic value of non-invasive imaging modalities to diagnose cardiac AA amyloidosis did not result in any landmark studies nor in convincing case reports. Obviously, echocardiography is a widely available tool that has improved significantly the diagnosis of CA after the introduction of speckle-tracking-based strain analysis, however, is still lacking high sensitivity as well as specificity (21–23). In contrast, bone scintigraphy and targeted PET studies offer higher sensitivity and specificity regarding the detection of CA, and even allow to differentiate between AL and ATTR amyloidosis if additional monoclonal protein studies are available. However, convincing reports showing detection of AA amyloidosis by bone scintigraphy or PET are still missing.

Another modality, non-invasive multi-parametric CMR imaging, has gained wide acceptance within the last years and allows (amongst others) sophisticated work-up of non-ischemic cardiomyopathies, and in this context to differentiate between CA and HCM based on the pattern of LGE. While the LGE pattern in case of CA is rather diffuse, starts mostly from the subendocardial layer of the basal segments and eventually spreads to all myocardial layers and segments (16, 24), classic

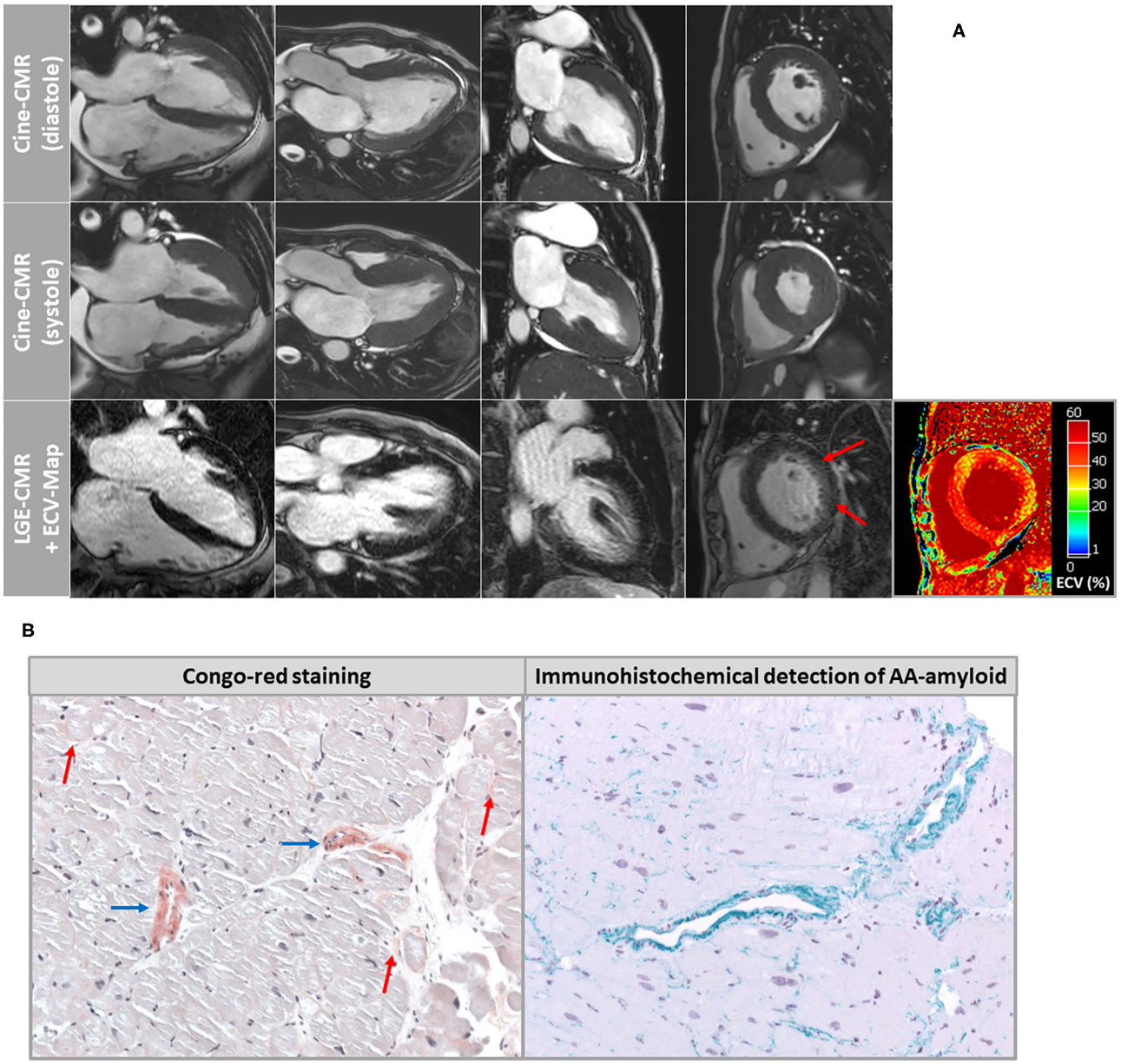

FIGURE 1 | (A) Cardiovascular magnetic resonance (CMR) images of patient-1 showing cine images in diastole and systole as well as corresponding late-gadolinium-enhancement (LGE) and extracellular volume fraction (ECV) maps of the myocardium. A very subtle and rather diffuse pattern of LGE was detected in the basal segments of the LV lateral wall. However, ECV maps illustrated highly elevated myocardial ECV values in the septal and lateral wall segments. **(B)** Histopathological images of endomyocardial biopsy (EMB) samples that were taken in patient-1 from the left ventricular free wall. Congo-red staining showed a diffuse pattern of interstitial amyloidosis (red arrows) in addition to marked accumulation of amyloid deposits within the vessel walls (blue arrows). The subtype AA amyloidosis was proven by specific immunohistochemistry.

HCM is characterized by a patchy and more focally accentuated LGE pattern predominantly occurring in the most hypertrophic septal segments of the left ventricular myocardium (25, 26). Additionally, pre- and post-contrast T1-mapping applied for tissue characterization by measurement of the intrinsic T1-relaxation time of the myocardium allows to determine the ECV value of the myocardium (27). Similarly, T2-mapping is a promising technique for both visualization and *in vivo* quantification of myocardial edema suggestive of myocardial inflammation (28). Myocardial edema is characterized by an increase in myocardial water content (per voxel myocardium) and thereby causes longer T2-relaxation times (29).

Several previous studies have shown that measurement of native T1 and ECV values are useful tools for the work-up of hypertrophic cardiac phenotypes of unknown origin (30). The degree of increase in global native T1 and ECV values

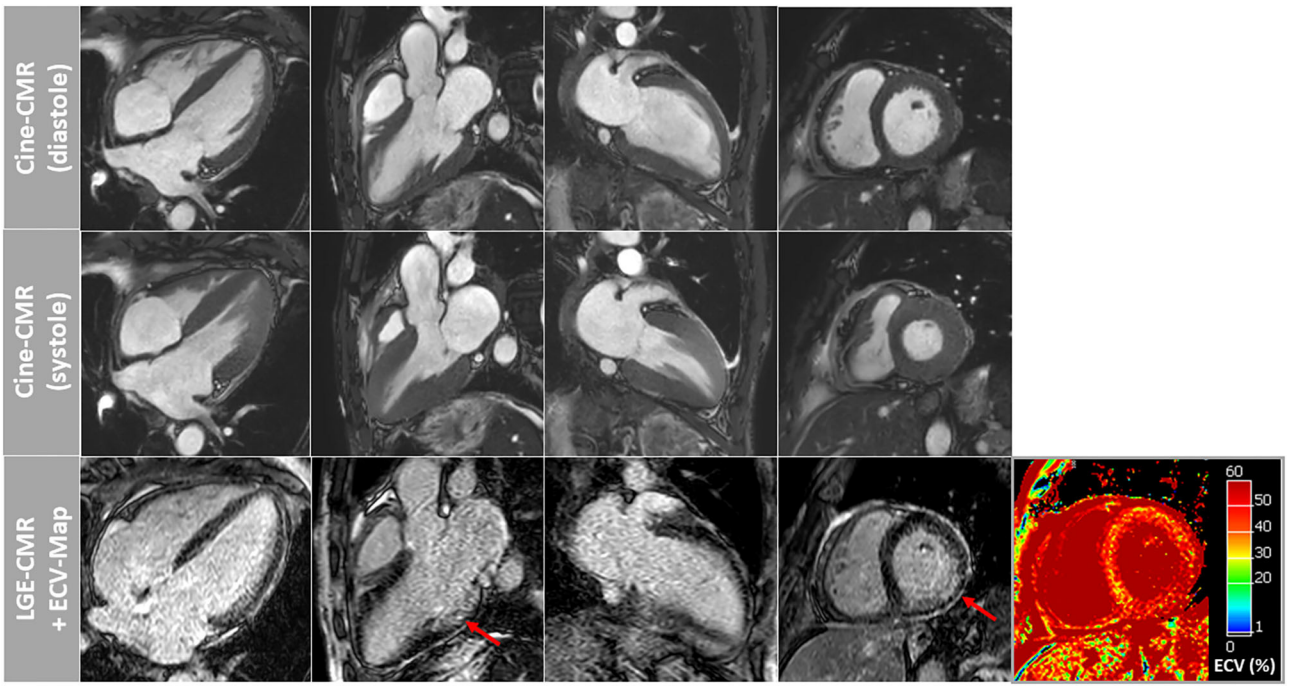

FIGURE 2 | Cardiovascular magnetic resonance (CMR) images of patient-2 showing cine images in diastole and systole as well as corresponding late-gadolinium-enhancement (LGE) and extracellular volume fraction (ECV) maps of the myocardium. A slightly more pronounced non-ischemic pattern of LGE was observed in this patient in the basal to midventricular inferior/inferolateral segments of the LV wall (red arrows). Again, ECV maps illustrated highly elevated myocardial ECV values in the septal and lateral wall segments.

is consistently lower in HCM as compared to CA as there is an extensive, diffuse amyloid infiltration of the extracellular space in case of CA (31) while HCM mostly shows focally accentuated interstitial fibrosis in hypertrophied septal segments (32). Noteworthy, our present report clearly illustrates that only a very subtle pattern of LGE—not resembling the well-known characteristic pattern of LGE that can be found in those patients with ATTR and AL amyloidosis (!)—is seen in case of AA amyloidosis. However, additional ECV measurements based on pre- and post-contrast T1-mapping resulted in surprisingly high myocardial ECV values—suggesting an ongoing infiltrative process in the extracellular space of the myocardium.

Obviously, both patients were on hemodialysis and in principle, "uremic" cardiomyopathy may manifest with LV hypertrophy as well as diffuse (interstitial) myocardial fibrosis that in turn may lead to increased myocardial native T1 and ECV values. In this context, Hayer et al. recently studied $N = 134$ non-diabetic patients with chronic kidney disease (CKD) stages 2 to 5 without myocardial ischemia at 1.5-Tesla and found native T1 values of 966 ± 21 ms in stage 2 patients vs. 994 ± 33 ms in stage five patients ($p < 0.001$) (33). In addition, Hayer et al. studied $N = 24$ patients with end-stage renal disease (ESRD)—again at 1.5-Tesla—and documented septal native T1-values of 1002 ± 30 ms and a myocardial ECV value of 28 ± 2% (34). Unfortunately, comprehensive data regarding myocardial ECV are limited in ESRD patients since gadolinium-based contrast agents are rarely used in those patients. Of course, we cannot exclude an "additional" effect of ESRD on LV hypertrophy, native T1 and ECV values in our patients. However, we believe that such an "additional" or "confounding" effect—apart from cardiac manifestation of AA amyloidosis—was limited due to the following simple reason: The native T1- and ECV-values that were measured in the myocardium of our patients (at 1.5-Tesla) were substantially higher (!) compared to the aforementioned reference values in ESRD patients published recently.

In summary, unlike other well-known subtypes of amyloidosis (such as ATTR and AL), a characteristic pattern of diffuse LGE is not observed in case of AA amyloidosis based on CMR. However, measurement of myocardial ECV—in addition to myocardial T1-/T2-mapping—may be of paramount diagnostic value to detect cardiac involvement in case of AA amyloidosis—despite a missing characteristic LGE pattern. Therefore, we recommend a comprehensive multi-parametric CMR approach comprising the combined analysis of T1-/T2-mapping, measurement of ECV and careful assessment of LGE-images in patients with AA amyloidosis and suspected cardiac involvement.

DATA AVAILABILITY STATEMENT

The original contributions presented in the study are included in the article/supplementary material, further inquiries can be directed to the corresponding author.

ETHICS STATEMENT

Ethical review and approval was not required for the study on human participants in accordance with the local legislation and institutional requirements. Written informed consent for participation was not required for this study in accordance with the national legislation and the institutional requirements. Written informed consent was obtained from the individual(s) for the publication of any potentially identifiable images or data included in this article.

AUTHOR CONTRIBUTIONS

BC devised the project and the main conceptual idea, and wrote the manuscript. SD contributed to sample and data collection. MB and CM provided critical feedback and helped shape the research and analysis. KK performed the histological and immunohistochemical analyses. AY supervised the work, contributed to the interpretation of results, provided critical feedback and helped shape the research, analysis, and manuscript. All authors contributed to the article and approved the submitted version.

REFERENCES

1. Benson MD, Buxbaum JN, Eisenberg DS, Merlini G, Saraiva MJM, Sekijima Y, et al. Amyloid nomenclature 2018: recommendations by the International Society of Amyloidosis (ISA) nomenclature committee. *Amyloid.* (2018) 25:215–9. doi: 10.1080/13506129.2018.1549825
2. Palladini G, Merlini G. What is new in diagnosis and management of light chain amyloidosis? *Blood.* (2016) 128:159–68. doi: 10.1182/blood-2016-01-629790
3. Grogan M, Scott CG, Kyle RA, Zeldenrust SR, Gertz MA, Lin G, et al. Natural history of wild-type transthyretin cardiac amyloidosis and risk stratification using a novel staging system. *J Am Coll Cardiol.* (2016) 68:1014–20. doi: 10.1016/j.jacc.2016.06.033
4. Westermark GT, Fändrich M, Westermark P. AA amyloidosis: pathogenesis and targeted therapy. *Annu Rev Pathol.* (2015) 10:321–44. doi: 10.1146/annurev-pathol-020712-163913
5. Yamada T, Okuda Y, Takasugi K, Wang L, Marks D, Benson MD, et al. An allele of serum amyloid A1 associated with amyloidosis in both Japanese and Caucasians. *Amyloid.* (2003) 10:7–11. doi: 10.3109/13506120308995250
6. Peces R, Afonso S, Peces C, Nevado J, Selgas R. Living kidney transplantation between brothers with unrecognized renal amyloidosis as the first manifestation of familial Mediterranean fever: a case report. *BMC Med Genet.* (2017) 18:97. doi: 10.1186/s12881-017-0457-9
7. Dubrey SW, Cha K, Simms RW, Skinner M, Falk RH. Electrocardiography and Doppler echocardiography in secondary (AA) amyloidosis. *Am J Cardiol.* (1996) 77:313–5. doi: 10.1016/S0002-9149(97)89403-9
8. Hassan W, Al-Sergani H, Mourad W, Tabbaa R. Amyloid heart disease. New frontiers and insights in pathophysiology, diagnosis, and management. *Tex Heart Inst J.* (2005) 32:178–84.
9. Chatzantonis G, Bietenbeck M, Elsanhoury A, Tschöpe C, Pieske B, Tauscher G, et al. Diagnostic value of cardiovascular magnetic resonance in comparison to endomyocardial biopsy in cardiac amyloidosis: a multi-centre study. *Clin Res Cardiol.* (2021) 110:555–68. doi: 10.1007/s00392-020-01771-1
10. Costache II, Buburuz AM, Crisu D, Statescu AM, Ungureanu C, Aursulesei V. The role of echocardiography and 99mTc-HDP scintigraphy in non-invasive diagnosis of cardiac amyloidosis: a case series and literature review. *Medicine.* (2019) 98:e17256. doi: 10.1097/MD.0000000000017256
11. Chen W, Ton V-K, Dilsizian V. Clinical phenotyping of transthyretin cardiac amyloidosis with bone-seeking radiotracers in heart failure with preserved ejection fraction. *Curr Cardiol Rep.* (2018) 20:23. doi: 10.1007/s11886-018-0970-2
12. Andrikopoulou E. Nuclear imaging of cardiac amyloidosis. *J Nucl Cardiol.* (2017) 26:1–4. doi: 10.1007/s12350-017-1028-3
13. From AM, Maleszewski JJ, Rihal CS. Current status of endomyocardial biopsy. *Mayo Clin Proc.* (2011) 86:1095–102. doi: 10.4065/mcp.2011.0296
14. Gillmore JD, Maurer MS, Falk RH, Merlini G, Damy T, Dispenzieri A, et al. Nonbiopsy diagnosis of cardiac transthyretin amyloidosis. *Circulation.* (2016) 133:2404–12. doi: 10.1161/CIRCULATIONAHA.116.021612
15. Maurer MS, Ruberg FL, Weinsaft JW. More than meets the eye: time for a new imaging paradigm to test for cardiac amyloidosis. *J Card Fail.* (2018) 24:87–9. doi: 10.1016/j.cardfail.2017.12.006
16. Maceira AM, Joshi J, Prasad SK, Moon JC, Perugini E, Harding I, et al. Cardiovascular magnetic resonance in cardiac amyloidosis. *Circulation.* (2005) 111:186–93. doi: 10.1161/01.CIR.0000152819.97857.9D
17. Yilmaz A, Bauersachs J, Bengel F, Büchel R, Kindermann I, Klingel K, et al. Diagnosis and treatment of cardiac amyloidosis: position statement of the German Cardiac Society (DGK). *Clin Res Cardiol.* (2021) 110:479–506. doi: 10.1007/s00392-020-01799-3
18. Klingel K, Sauter M, Bock CT, Szalay G, Schnorr J-J, Kandolf R. Molecular pathology of inflammatory cardiomyopathy. *Med Microbiol Immunol.* (2004) 193:101–7. doi: 10.1007/s00430-003-0190-1
19. Vogelsberg H, Mahrholdt H, Deluigi CC, Yilmaz A, Kispert EM, Greulich S, et al. Cardiovascular magnetic resonance in clinically suspected cardiac amyloidosis: noninvasive imaging compared to endomyocardial biopsy. *J Am Coll Cardiol.* (2008) 51:1022–30. doi: 10.1016/j.jacc.2007.10.049
20. Kramer CM, Barkhausen J, Flamm SD, Kim RJ, Nagel E. Standardized cardiovascular magnetic resonance (CMR) protocols 2013 update. *J Cardiovasc Magn Reson.* (2013) 15:91. doi: 10.1186/1532-429X-15-91
21. Korthals D, Chatzantonis G, Bietenbeck M, Meier C, Stalling P, Yilmaz A. CMR-based T1-mapping offers superior diagnostic value compared to longitudinal strain-based assessment of relative apical sparing in cardiac amyloidosis. *Sci Rep.* (2021) 11:15521. doi: 10.1038/s41598-021-94650-2
22. Phelan D, Collier P, Thavendiranathan P, Popović ZB, Hanna M, Plana JC, et al. Relative apical sparing of longitudinal strain using two-dimensional speckle-tracking echocardiography is both sensitive and specific for the diagnosis of cardiac amyloidosis. *Heart.* (2012) 98:1442–8. doi: 10.1136/heartjnl-2012-302353
23. Liu D, Hu K, Niemann M, Herrmann S, Cikes M, Störk S, et al. Effect of combined systolic and diastolic functional parameter assessment for differentiation of cardiac amyloidosis from other causes of concentric left ventricular hypertrophy. *Circ Cardiovasc Imaging.* (2013) 6:1066–72. doi: 10.1161/CIRCIMAGING.113.000683
24. Austin BA, Tang WHW, Rodriguez ER, Tan C, Flamm SD, Taylor DO, et al. Delayed hyper-enhancement magnetic resonance imaging provides incremental diagnostic and prognostic utility in suspected cardiac amyloidosis. *JACC Cardiovasc Imaging.* (2009) 2:1369–77. doi: 10.1016/j.jcmg.2009.08.008
25. Axelsson Raja A, Farhad H, Valente AM, Couce J-P, Jefferies JL, Bundgaard H, et al. Prevalence and progression of late gadolinium enhancement in children and adolescents with hypertrophic cardiomyopathy. *Circulation.* (2018) 138:782–92. doi: 10.1161/CIRCULATIONAHA.117.032966
26. Rowin EJ, Maron MS. The role of cardiac MRI in the diagnosis and risk stratification of hypertrophic cardiomyopathy. *Arrhythmia Electrophysiol Rev.* (2016) 5:197. doi: 10.15420/aer.2016:13:3
27. White SK, Sado DM, Fontana M, Banypersad SM, Maestrini V, Flett AS, et al. T1 mapping for myocardial extracellular volume measurement by CMR: bolus only versus primed infusion technique. *JACC Cardiovasc Imaging.* (2013) 6:955–62. doi: 10.1016/j.jcmg.2013.01.011

28. Giri S, Chung Y-C, Merchant A, Mihai G, Rajagopalan S, Raman SV, et al. T2 quantification for improved detection of myocardial edema. *J Cardiovasc Magn Reson.* (2009) 11:56. doi: 10.1186/1532-429X-11-56
29. Kim PK, Hong YJ, Im DJ, Suh YJ, Park CH, Kim JY, et al. Myocardial T1 and T2 Mapping: Techniques and Clinical Applications. *Korean J Radiol.* (2017) 18:113–31. doi: 10.3348/kjr.2017.18.1.113
30. Messroghli DR, Moon JC, Ferreira VM, Grosse-Wortmann L, He T, Kellman P, et al. Clinical recommendations for cardiovascular magnetic resonance mapping of T1, T2, T2* and extracellular volume: a consensus statement by the Society for Cardiovascular Magnetic Resonance (SCMR) endorsed by the European Association for Cardiovascular Imaging (EACVI). *J Cardiovasc Magn Reson.* (2017) 19:75. doi: 10.1186/s12968-017-0389-8
31. Banypersad SM, Sado DM, Flett AS, Gibbs SDJ, Pinney JH, Maestrini V, et al. Quantification of myocardial extracellular volume fraction in systemic AL amyloidosis: an equilibrium contrast cardiovascular magnetic resonance study. *Circ Cardiovasc Imaging.* (2013) 6:34–9. doi: 10.1161/CIRCIMAGING.112.978627
32. Sado DM, Flett AS, Banypersad SM, White SK, Maestrini V, Quarta G, et al. Cardiovascular magnetic resonance measurement of myocardial extracellular volume in health and disease. *Heart.* (2012) 98:1436–41. doi: 10.1136/heartjnl-2012-302346
33. Hayer MK, Radhakrishnan A, Price AM, Liu B, Baig S, Weston CJ, et al. Defining myocardial abnormalities across the stages of chronic kidney disease: a cardiac magnetic resonance imaging study. *JACC Cardiovasc Imaging.* (2020) 13:2357–67. doi: 10.1016/j.jcmg.2020.04.021
34. Hayer MK, Radhakrishnan A, Price AM, Baig S, Liu B, Ferro CJ, et al. Early effects of kidney transplantation on the heart—a cardiac magnetic resonance multi-parametric study. *Int J Cardiol.* (2019) 293:272–7. doi: 10.1016/j.ijcard.2019.06.007

Conflict of Interest: The authors declare that the research was conducted in the absence of any commercial or financial relationships that could be construed as a potential conflict of interest.

Publisher's Note: All claims expressed in this article are solely those of the authors and do not necessarily represent those of their affiliated organizations, or those of the publisher, the editors and the reviewers. Any product that may be evaluated in this article, or claim that may be made by its manufacturer, is not guaranteed or endorsed by the publisher.

frontiers in Cardiovascular Medicine

ORIGINAL RESEARCH
published: 12 October 2021
doi: 10.3389/fcvm.2021.743849

Assessment of Myocardial Function During Blood Pressure Manipulations Using Feature Tracking Cardiovascular Magnetic Resonance

*Kady Fischer[1,2], Mario D. Neuenschwander[1], Christof Jung[1], Samuel Hurni[3], Bernhard M. Winkler[3], Stefan P. Huettenmoser[2], Bernd Jung[2], Andreas P. Vogt[1], Balthasar Eberle[1] and Dominik P. Guensch[1,2]**

[1] Department of Anaesthesiology and Pain Medicine, Inselspital, Bern University Hospital, University of Bern, Bern, Switzerland, [2] Department of Diagnostic, Interventional and Paediatric Radiology, Inselspital, Bern University Hospital, University of Bern, Bern, Switzerland, [3] Department of Cardiovascular Surgery, Inselspital, University Hospital Bern, Bern, Switzerland

OPEN ACCESS

Edited by:
Ali Yilmaz,
University Hospital Münster, Germany

Reviewed by:
Andreas Rolf,
Kerckhoff Klinik, Germany
Michael Nelson,
University of Texas at Arlington, United States

***Correspondence:**
Dominik P. Guensch
dominik.guensch@gmail.com

Specialty section:
This article was submitted to Cardiovascular Imaging, a section of the journal Frontiers in Cardiovascular Medicine

Received: *19 July 2021*
Accepted: *20 September 2021*
Published: *12 October 2021*

Citation:
Fischer K, Neuenschwander MD, Jung C, Hurni S, Winkler BM, Huettenmoser SP, Jung B, Vogt AP, Eberle B and Guensch DP (2021) Assessment of Myocardial Function During Blood Pressure Manipulations Using Feature Tracking Cardiovascular Magnetic Resonance. Front. Cardiovasc. Med. 8:743849. doi: 10.3389/fcvm.2021.743849

Background: Coronary autoregulation is a feedback system, which maintains near-constant myocardial blood flow over a range of mean arterial pressure (MAP). Yet in emergency or peri-operative situations, hypotensive or hypertensive episodes may quickly arise. It is not yet established how rapid blood pressure changes outside of the autoregulation zone (ARZ) impact left (LV) and right ventricular (RV) function. Using cardiovascular magnetic resonance (CMR) imaging, measurements of myocardial tissue oxygenation and ventricular systolic and diastolic function can comprehensively assess the heart throughout a range of changing blood pressures.

Design and methods: In 10 anesthetized swine, MAP was varied in steps of 10–15 mmHg from 29 to 196 mmHg using phenylephrine and urapidil inside a 3-Tesla MRI scanner. At each MAP level, oxygenation-sensitive (OS) cine images along with arterial and coronary sinus blood gas samples were obtained and blood flow was measured from a surgically implanted flow probe on the left anterior descending coronary artery. Using CMR feature tracking-software, LV and RV circumferential systolic and diastolic strain parameters were measured from the myocardial oxygenation cines.

Results: LV and RV peak strain are compromised both below the lower limit (LV: $\Delta 1.2 \pm 0.4\%$, RV: $\Delta 4.4 \pm 1.2\%$, $p < 0.001$) and above the upper limit (LV: $\Delta 2.1 \pm 0.4$, RV: $\Delta 5.4 \pm 1.4$, $p < 0.001$) of the ARZ in comparison to a baseline of 70 mmHg. LV strain demonstrates a non-linear relationship with invasive and non-invasive measures of oxygenation. Specifically for the LV at hypotensive levels below the ARZ, systolic dysfunction is related to myocardial deoxygenation ($\beta = -0.216$, $p = 0.036$) in OS-CMR and both systolic and diastolic dysfunction are linked to reduced coronary blood flow (peak strain: $\beta = -0.028$, $p = 0.047$, early diastolic strain rate: $\beta = 0.026$, $p = 0.002$). These relationships were not observed at hypertensive levels.

Conclusion: In an animal model, biventricular function is compromised outside the coronary autoregulatory zone. Dysfunction at pressures below the lower limit is likely

caused by insufficient blood flow and tissue deoxygenation. Conversely, hypertension-induced systolic and diastolic dysfunction points to high afterload as a cause. These findings from an experimental model are translatable to the clinical peri-operative environment in which myocardial deformation may have the potential to guide blood pressure management, in particular at varying individual autoregulation thresholds.

Keywords: feature tracking (CMR-FT), general anesthesia (GA), blood pressure, coronary autoregulation, myocardial deformation

INTRODUCTION

Coronary autoregulation ensures near constant coronary blood flow (CBF) over a wide range of blood pressure, known as the autoregulatory zone (ARZ). The general relationship of mean arterial pressure (MAP) to CBF has been well-established (1). In healthy individuals, coronary autoregulation is usually effective between MAP levels from 60 to 140 mmHg. Above and below those thresholds of the ARZ, blood flow becomes mostly pressure dependent. Thus, myocardium may be vulnerable to insufficient perfusion with subsequent ischemia at low pressures, while higher aortic pressures may increase myocardial workload and oxygen demand. Peri-operatively, even short periods of hypotension and hypertension, i.e., markedly fluctuating blood pressures, are associated with poor outcome (2, 3). However, the upper and lower limits of this ARZ differs among individuals and setting. Consequently, the exact characteristics of autoregulation in cardiovascular disease during general anesthesia remain a black box for anesthetists. This may contribute to myocardial injury after non-cardiac surgery (MINS) (4), which has been increasingly focused on over the recent years. Techniques such as oxygenation-sensitive cardiovascular magnetic resonance (OS-CMR) can non-invasively interrogate changes in myocardial oxygenation on a tissue level with high spatial resolution based on local deoxyhemoglobin fractions (5, 6). In 2019, we reported that left ventricular myocardial oxygenation measured by OS-CMR had a curvi-linear association with mean arterial pressure (7). However, the impact of blood pressure regulation and these oxygenation changes on biventricular myocardial function defined by strain have not been systematically examined so far.

Myocardial strain analysis allows for a more detailed quantitative analysis of myocardial deformation and performance on a global and segmental level. Diagnostically, deficiencies in resting CMR-FT of both the left and right ventricle has been shown to be linked to outcome in multiple ischemic and non-ischemic cohorts (8–10). In these studies, strain analysis showed more subtle abnormalities in the absence of global systolic dysfunction and is thus interpreted to be an earlier and more sensitive prognostic modality than conventional assessment of global function alone. Although strain analysis has been performed in echocardiography for many years, the use of feature tracking (FT) software on OS-CMR cine images simultaneously with oxygenation assessments is only possible with CMR. Various markers can be derived from strain analysis, of which peak strain is the most known and best validated (11), representing maximal systolic shortening. Systolic strain rate provides another marker for systolic function. Importantly, diastology can be simultaneously assessed using diastolic strain rate during early active relaxation of the myocardium. This multiparametric approach of strain assessments is beneficial as it provides a comprehensive assessment of various components of myocardial function and layers over the cardiac cycle.

The objective of this analysis was to implement advanced assessments of myocardial deformation by CMR-FT to investigate the impact of systemic mean arterial blood pressure changes on left and right ventricular strain in an anesthetized swine model. Additionally, we aimed to establish the relationship of biventricular strain with changes in myocardial oxygenation, invasive measures of blood oxygen and coronary blood flow within and beyond the boundaries of the coronary autoregulation zone.

MATERIALS AND METHODS

Ethical Statement

This study was approved by the Veterinary Services at the Department of Agriculture and Nature of the Canton Bern, Switzerland [#BE 103/14] (7). The study was carried out in accordance with national and local animal care regulations and adheres to the ARRIVE guidelines.

Experimental Anesthesia Surgical Protocol

For acclimatization, the animals were housed at the University Veterinary Facilities for 48 h prior to the experiments. Fifteen swine (German Large White) were pre-medicated with 20 mg/kg ketamine and 2 mg/kg intra-muscular xylazine. The animals were induced with 10 mg of midazolam and 1 mg atropine and intubated. The animals were ventilated with a tidal volume of 6–8 ml/kg with a positive end-expiratory pressure of 5 mbar. Normocapnic end-tidal CO_2-partial pressures of 35–40 mmHg were targeted. A venous line was placed in the femoral vein and anesthesia was maintained with continuous intra-venous fentanyl (5–30 μg/kg/h) as well as propofol (4–8 mg/kg/h) as required. 5'000 IU of heparin for prophylaxis of thrombosis as well as 75 mg of amiodarone for antiarrhythmic prophylaxis was administered. The femoral artery was cannulated for continuous invasive blood pressure measurements as well as intermittent blood gas analysis. Via access through the right internal jugular vein, an indwelling catheter was placed in the coronary sinus under surgical control. This was used to take blood gas measurements for determining myocardial oxygen extraction

and derived invasive oxygenation measures. Afterwards a left-sided thoracotomy was performed and a perivascular flow probe (Transonic Systems, Ithica, NY, USA) was surgically attached to the proximal left anterior descending (LAD) coronary artery (**Figure 1A**).

Pharmacological Manipulation of Blood Pressure

Inside of a clinical 3T magnetic resonance imaging scanner (MAGNETOM TRIO, Siemens Healthineers, Erlangen, Germany), MAP was adjusted in steps of 10–15 mmHg from a baseline level of 70 mmHg using urapidil and phenylephrine (**Figure 1B**), as published by our group previously (7). At each MAP-level, blood gas samples from the coronary sinus and the femoral artery were obtained, along with OS-CMR images. Phenylephrine is an α1-receptor agonist, constricting peripheral blood vessels and thereby increasing blood pressure. It has no effect on the β1-receptor and thus no impact on inotropy or chronotropy. Also, in contrast to other vasopressors like norepinephrine, it has minimal effect on vasomotor function of the coronary arteries (12). Phenylephrine was administered by infusion pump at a rate of 16–660 μg/min. Urapidil is a selective α1-receptor antagonist and is used to lower blood pressure by dilating peripheral blood vessels (13). Due to the longer half-life time, repetitive i.v.-doses of 5–10 mg were used. Throughout the study, arterial blood pressure, heart rate and coronary blood flow of the LAD were recorded continuously at a rate of one measurement per second.

Experimental Imaging and Analysis

Oxygenation-sensitive (OS) cines were acquired in two short axis planes at base and mid-ventricle using a triggered balanced steady-state free precession sequence as reported before (7). Images were obtained in short end-expiratory apnea, with an acquisition time of four heartbeats per slice. Assessment of the myocardial oxygenation response was measured in the end-systolic frame of the OS-CMR images for each MAP level as reported before (14, 15). The signal measured in the left myocardium was reported as relative change in comparison to the baseline level of 70 mmHg. By assessors blinded to previous findings of myocardial oxygenation and invasive measurements, myocardial deformation was analyzed on the same OS-CMR cines using feature tracking (FT) software. Epicardial as well as endocardial contours were manually traced for the left ventricle and right ventricular free wall on both short axis slices at end-diastole (**Figure 1C**). Strain was assessed for the circumferential orientation. For systolic parameters, peak global circumferential strain (GCS), time to peak strain (TTP) and systolic strain rate (sSR) were extrapolated from the analysis. Early diastolic strain rate (dSR) was used as a measure of diastolic function. End-diastolic and systolic area of the chamber lumen was measured at the mid-ventricular short-axis plane, and fractional area change was calculated. All image analysis was performed with CVI[42] (CircleCVI Inc., version 5.10, Calgary, Canada).

Statistical Analysis

For every subject the FT data were compared to the individual baseline-values (70 mmHg). The autoregulation zone (ARZ) was determined from the coronary blood flow data, from which a non-linear regression curve accounting for repeated measurements per subject was generated from 55'368 data points. The limits of the autoregulation zone were calculated from the first and second derivative of the flow curve, defined previously by Guensch et al. (7). As shown in **Figure 2**, 52 mmHg (blue) was defined here as the lower limit of the autoregulation zone and 127 mmHg (orange) as the upper limit in this sample of anesthetized swine.

Initially, the linear relationship between continuous CMR-FT variables to different parameters of flow and oxygenation was assessed using R Studio (RStudio Inc., Boston, United States)

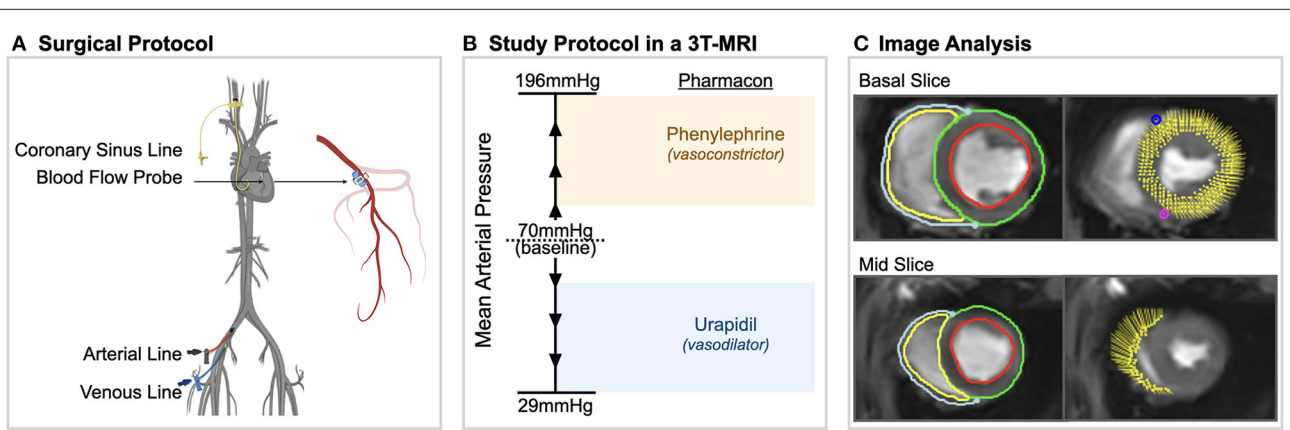

FIGURE 1 | Experimental procedures. **(A)** Surgical procedures included placement of arterial, venous and coronary sinus lines and a blood flow probe on the left anterior descending coronary artery in anesthetized swine. **(B)** In a 3 tesla (T) magnetic resonance imaging (MRI) machine, mean arterial blood pressure was varied in steps of 10–15 mmHg from 29 to 196 mmHg using phenylephrine and urapidil. At each level, oxygenation-sensitive (OS) cine images along with invasive measurements were acquired. **(C)** Using CMR feature tracking-software, left and right ventricular systolic and diastolic strain measurements were obtained from the same cine images in which myocardial oxygenation was measured.

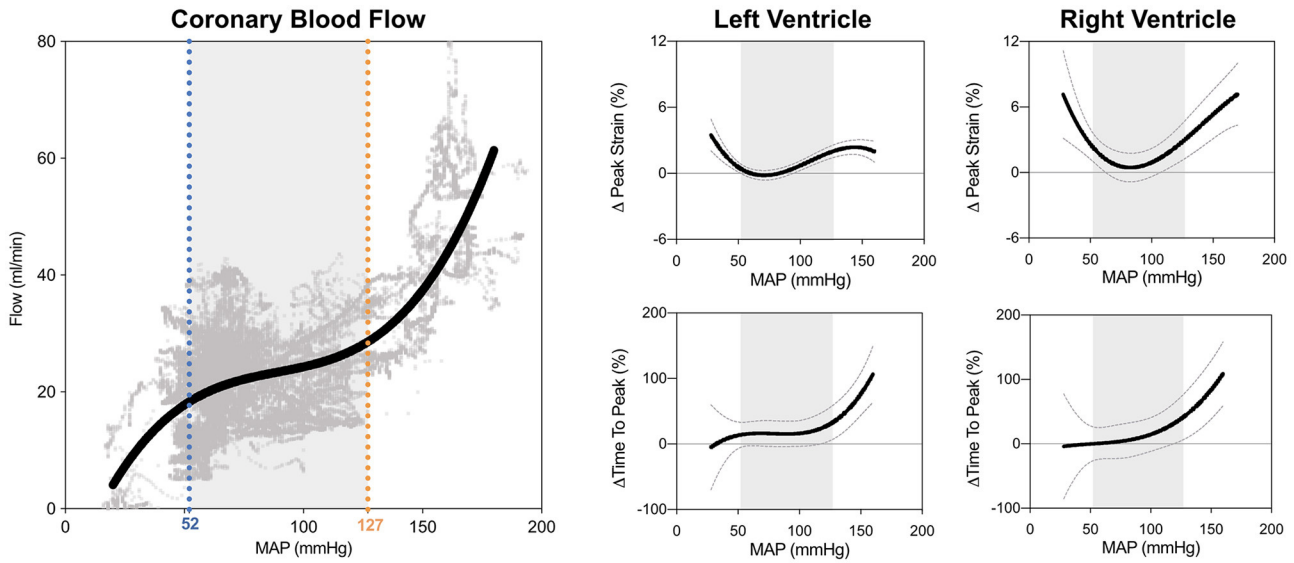

FIGURE 2 | Biventricular systolic strain measures in relation to blood pressure. The limits of the coronary autoregulation zone (ARZ) as calculated from invasive flow measurements are shown on the left. Non-linear relationships and 95% confidence intervals of the fit are shown between mean arterial blood pressure (MAP) and peak circumferential strain and time to peak strain for the left ventricle (middle) and right ventricle (right). Gray shading depicts the ARZ.

with mixed linear models fitted with the *lmer* function in R (*lme4* package) accounting for multiple measurements per animal by including subject identification as a random intercept. To assess the categorical differences in CMR-FT and invasive measures inside and outside of the ARZ, data at each level was categorized into three groups, levels below the ARZ (<52 mmHg), levels within the ARZ (52–127 mmHg), and a third group of levels above the ARZ (>127 mmHg). These groups were compared with a mixed effects model and the *emmeans* package (16) accounting for repeated measures per animal. For visualization purposes, CMR-FT measurements were compared to MAP, and other invasive measures using polynomial non-linear regression. Statistical significance was defined with a two-sided *p*-value of <0.05. GraphPad Prism version 9.0 (GraphPad Software, La Jolla California USA), *R* software (version 3.5.0, R Foundation for Statistical Computing, Vienna, Austria) were used for analysis.

RESULTS

Mean arterial blood (MAP) pressure in anesthetized swine was manipulated through a range of 29–196 mmHg from a baseline blood pressure of 70 mmHg. In total, 105 levels were targeted from 10 different subjects, at which CMR imaging, and invasive measures of CBF and blood oxygenation were acquired. Five of the fifteen animals were excluded prior to analysis: two suffered ventricular fibrillation during surgery; one had underlying peri-myocarditis that was discovered during surgery; there were experimental hardware problems with the remaining two. FT could be performed on 99 of the levels (94%), with 6 levels excluded due to gating issues.

FT-CMR in the Autoregulation Zone

As can be seen in **Figure 2**, GCS of both ventricles was attenuated both above and below the coronary ARZ thresholds. This yielded a u-shaped non-linear relationship ($p < 0.05$) where a more positive value represented poorer strain, which was confirmed with categorical assessments (**Table 1**). In comparison to a baseline MAP of 70 mmHg GCS was compromised by $1.2 \pm 0.4\%$ at hypotensive levels below 52 mmHg ($p = 0.041$ vs. ARZ), and also attenuated by $2.1 \pm 0.4\%$ when MAP was higher than 127 mmHg ($p < 0.001$ vs. ARZ). This was even more pronounced in the RV, with an attenuation in GCS of $4.4 \pm 1.2\%$ below the ARZ ($p = 0.004$ vs. ARZ), and an attenuation of $5.4 \pm 1.4\%$ above the ARZ ($p < 0.001$). On the other hand, time to peak strain (TTP) increased only above the upper limit with a prolongation of 52 ± 21 ms for the LV ($p = 0.008$ vs. ARZ) and 67 ± 30 ms for the RV. This trend was matched by a reduction in systolic strain rate above the upper ARZ limit, whereas diastolic strain rate was not associated to mean arterial blood pressure. When assessing the end-diastolic area of the mid-ventricle, a larger ventricular lumen area was observed for both the LV and the RV above the ARZ in comparison to area at levels within the ARZ, while hypotension below the ARZ only resulted in a small but significant decrease in RV area in the short axis images with no impact on the LV.

Relationship of LV Feature Tracking to Measures of Oxygenation and Blood Flow

As observed in **Figure 3E**, LV-GCS as a marker of systolic function showed a non-linear relationship to myocardial oxygenation measured by OS-CMR. In this non-linear regression analysis, an attenuation in GCS was observed with decreasing oxygenation in OS-CMR (<0%). This is supported with the linear

TABLE 1 | ANOVA comparisons for imaging and invasive measures below and above the autoregulation zone.

	Below ARZ, <52 mmHg	P vs. ARZ	Within ARZ, 52–127 mmHg	Above ARZ, >127 mmHg	P vs. ARZ
LEFT VENTRICLE					
ΔPeak strain, GCS (%)	1.2 (0.4)	0.041*	0.4 (0.2)	2.1 (0.4)	<0.001*
ΔTime to peak, TTP (ms)	20 (21)	0.920	19 (19)	52 (21)	0.008*
ΔSystolic strain rate, sSR (/s)	0.02 (0.14)	0.116	−0.13 (0.12)	0.08 (0.15)	0.042*
ΔDiastolic strain rate, dSR (/s)	−0.02 (0.14)	0.723	−0.08 (0.08)	−0.13 (0.16)	0.183
ΔEnd-diastolic area (mm^2)	−0.04 (3.8)	0.623	1.5 (3.0)	17.8 (4.0)	<0.001*
ΔEnd-systolic area (mm^2)	6.4 (2.9)	0.740	5.4 (2.0)	27.0 (30.7)	<0.001*
ΔFractional area change (%)	−15.4 (6.0)	0.046*	−6.8 (5.1)	−15.9 (6.2)	0.043*
RIGHT VENTRICLE					
ΔPeak strain, GCS (%)	4.4 (1.2)	0.004*	1.0 (0.9)	5.4 (1.4)	<0.001*
ΔTime to peak, TTP (ms)	4 (29)	0.596	14 (25)	67 (30)	0.011*
ΔSystolic strain rate, sSR (/s)	0.13 (0.13)	0.400	0.02 (0.08)	0.70 (0.15)	<0.001*
ΔDiastolic strain rate, dSR (/s)	−0.16 (0.19)	0.903	−0.18 (0.13)	−0.29 (0.21)	0.568
ΔEnd-diastolic area (mm^2)	−5.0 (3.8)	0.022*	2.5 (2.9)	4.6 (4.1)	0.029*
ΔEnd-systolic area (mm^2)	0.1 (4.8)	0.995	0.1 (4.1)	16.3 (5.1)	<0.001*
ΔFractional area change (%)	−6.0 (3.7)	0.219	−2.1 (2.8)	−24.5 (4.0)	<0.001*
OXYGEN MEASURES (LEFT VENTRICLE) AND HEART RATE					
ΔLAD CBF blood flow (ml/min)	−20.8 (8.3)	<0.001*	9.9 (6.7)	45.5 (10.5)	<0.001*
Myocardial oxygenation, OS-CMR (%)	−0.8 (0.9)	0.015*	1.3 (0.6)	2.0 (1.0)	0.431
ΔCoronary sinus saturation, $ScsO_2$ (%)	−6.9 (2.5)	<0.001*	2.8 (2.0)	2.0 (3.1)	0.762
ΔOxygen extraction ratio, O_2er (%)	6.3 (2.0)	<0.001*	−3.6 (1.3)	−4.6 (2.7)	0.731
$\Delta\Omega$, Oxygen excess	−0.17 (0.06)	<0.001*	0.12 (0.04)	0.14 (0.08)	0.750
ΔHeart rate (beats per minute)	−2.4 (3.2)	0.348	0.5 (2.3)	−1.5 (3.9)	0.594

Mean (standard error) change from the baseline level (70 mmHg) acquired from a mixed effects model are shown measurements at levels below, inside and above the autoregulation zone (ARZ) as determined by the invasive measures of coronary blood flow (CBF) in the left anterior descending coronary artery (LAD).
**$p < 0.05$ represents a significant difference in comparison to values inside the autoregulation zone (52–127 mmHg).*

analysis shown in **Table 2** and **Supplementary Figure 1**. When investigating specifically MAP levels below the autoregulation zone where myocardial deoxygenation occurs (**Table 1**), a linear relationship was observed between GCS and OS-CMR ($\beta = 0.216$, $p = 0.036$, **Table 2**), indicating strain dropped by 0.216% with each drop in 1% of myocardial oxygenation. On the other hand, at MAP above the ARZ no linear relationship was observed.

Similar relationships were observed for CBF, where only below the autoregulation zone did a decrease in CBF relate to attenuated FT systolic (GCS: $\beta = -0.028$, $p = 0.047$, sSR: $\beta = -0.004$, $p = 0.017$) and diastolic measures (dSR: $\beta = 0.026$, $p = 0.002$), but no association was observed between strain and CBF at high MAP.

Invasive blood measures of coronary sinus oxygen saturation ($ScsO_2$) and oxygen extraction ratio (O_2er) were linearly correlated to GCS across the entire MAP range (**Figures 3A,C**). This was also observed with systolic strain rate, while there was no link to diastolic strain rate for any MAP range (**Table 2**).

Relationship of RV Feature Tracking to Measures of Oxygenation and Blood Flow

RV strain measurements showed multiple associations with CBF of the LAD and oxygen measures when assessing the entire MAP range (**Figures 3B,D,F**). In particular for OS-CMR, a reduction in left ventricular myocardial oxygenation was associated with a reduction in RV systolic (GCS: $\beta = -0.425$, $p = 0.002$, sSR: $\beta = -0.038$, $p = 0.023$) and diastolic parameters (dSR: 0.048, $p = 0.001$). In line with the LV, RV-GCS and sSR improved with a greater coronary sinus saturation and reduced oxygen extraction ratio (O_2er). These systolic strain measures also improved with enhanced CBF, while none of the invasive measures were correlated with RV diastolic strain rate. In contrast to conditions in the LV, these associations between FT and CBF and oxygen measures were not observed when investigating only MAP levels below the ARZ.

DISCUSSION

We demonstrate in an anesthetized swine model that biventricular systolic function was compromised at blood pressures outside the coronary autoregulation zone. Left ventricular circumferential peak strain (GCS) was attenuated in a non-linear relationship with decreasing myocardial oxygenation in OS-CMR cine images. Specifically, below the autoregulation zone (ARZ), LV-GCS compromise was associated in linear fashion with myocardial deoxygenation, invasive measures of blood deoxygenation and reduced CBF in the LAD.

Advantages of Non-invasive Imaging

Many of the reported markers for investigating adverse effects of blood pressure depressions and elevations do not convey their immediate risk to the patient, nor suggest corrective measures.

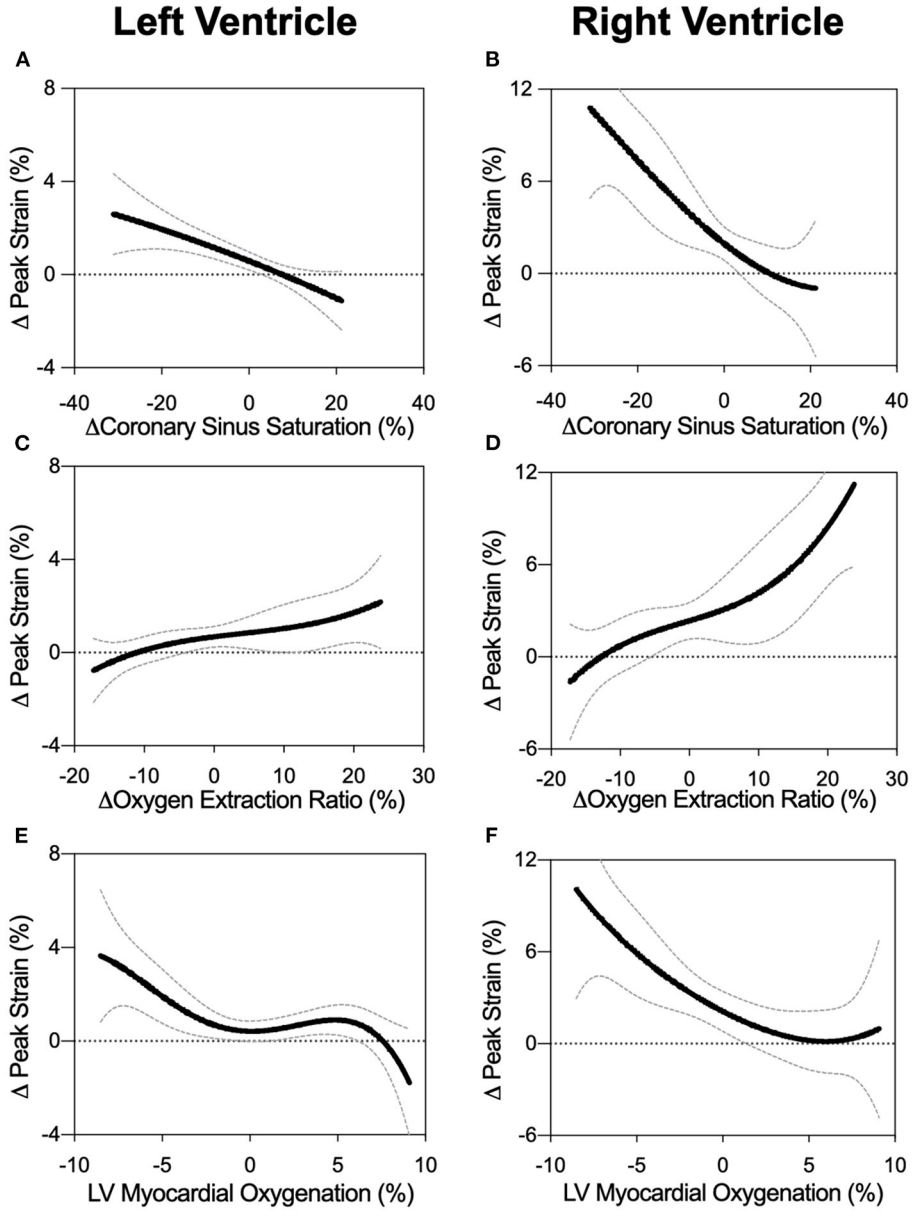

FIGURE 3 | Biventricular GCS in relation to measures of oxygen. Non-linear fits are shown for left and right ventricular peak strain in comparison to changes in coronary sinus oxygen saturation ($ScsO_2$, panels **A** and **B**), oxygen extraction ratio (O_2er, panels **C** and **D**), and the myocardial oxygenation response of the left ventricular myocardium (OS-CMR, panels **E** and **F**).

These include blood biomarkers such as the troponins, which take a few hours to rise, markers of other organ injury, or post-surgical morbidity and mortality. By the time such abnormalities develop, it is usually too late for causative treatment. Functional imaging is advantageous in this regard as it can usually be non-invasively acquired within a short time period in a point-of-care setting. In this study we utilized CMR cine images, as information on myocardial oxygenation and function can be simultaneously investigated and linked. OS-CMR sequences use the blood oxygen level-dependent (BOLD) effect to delineate changes in the myocardial oxygen supply and demand balance, avoiding the requirement of contrast agents.

Multiple studies investigating myocardial oxygenation responses in healthy animal models as well as in various disease models (7, 14, 15, 17–21) have emerged over the last decade. As we use a cine variant, it measures a cardiac phase every 40 ms, thus strain can be analyzed from the same set of images. Other studies were also able to show associations between resting

TABLE 2 | Association of FT and oxygenation measurements outside the autoregulation zone.

	ΔLAD CBF		OS-CMR		$\Delta ScsO_2$		ΔO_2er	
	β	*P*	*β*	*P*	*β*	*P*	*β*	*P*
All MAP LEVELS (29–196 mmHg)								
Left ventricle								
ΔPeak strain, GCS (%)	−0.001	0.869	−0.083	0.109	−0.069	<0.001*	0.058	0.006*
ΔTime to peak, TTP (ms)	−0.077	0.564	2.136	0.143	−0.503	0.156	0.536	0.169
ΔSystolic strain rate, sSR (/s)	−0.001	0.421	−0.009	0.467	−0.006	0.006*	0.005	0.026*
ΔDiastolic strain rate, dSR (/s)	−0.001	0.347	0.015	0.146	−0.004	0.588	0.005	0.548
Right ventricle								
ΔPeak strain, GCS (%)	−0.043	0.008*	−0.425	0.002*	−0.243	<0.001*	0.212	0.001*
ΔTime to peak, TTP (ms)	−0.101	0.647	0.687	0.759	−1.123	0.121	1.362	0.081
ΔSystolic strain rate, sSR (/s)	−0.003	0.012*	−0.038	0.023*	−0.013	0.006*	0.017	0.001*
ΔDiastolic strain rate, dSR (/s)	−0.001	0.856	0.048	<0.001*	−0.006	0.529	0.007	0.511
BELOW ARZ (<52 mmHg)								
Left ventricle								
ΔPeak strain, GCS (%)	−0.028	0.047*	−0.216	0.036*	−0.059	0.258	0.035	0.480
ΔTime to peak, TTP (ms)	0.472	0.204	2.203	0.382	−1.367	0.113	1.116	0.183
ΔSystolic strain rate, sSR (/s)	−0.004	0.017*	−0.019	0.063	−0.007	0.128	0.003	0.436
ΔDiastolic strain rate, dSR (/s)	0.026	0.002*	0.037	0.072	0.004	0.738	0.017	0.106
Right ventricle								
ΔPeak strain, GCS (%)	−0.107	0.071	−0.145	0.662	−0.330	0.156	0.301	0.079
ΔTime to peak, TTP (ms)	0.155	0.719	−1.046	0.589	−1.051	0.355	0.143	0.856
ΔSystolic strain rate, sSR (/s)	−0.010	0.007*	−0.048	0.010*	−0.019	0.122	0.019	0.078
ΔDiastolic strain rate, dSR (/s)	0.004	0.102	0.014	0.350	0.007	0.215	-0.008	0.268
ABOVE ARZ (>127 mmHg)								
Left ventricle								
ΔPeak Strain, GCS (%)	−0.016	0.180	0.018	0.894	−0.046	0.641	0.103	0.345
ΔTime to peak, TTP (ms)	−2.050	0.454	7.601	0.149	3.216	0.011*	-2.630	0.138
ΔSystolic strain rate, sSR (/s)	−0.001	0.936	−0.050	0.360	0.008	0.299	-0.006	0.504
ΔDiastolic strain rate, dSR (/s)	0.001	0.977	0.045	0.163	−0.015	0.551	0.005	0.857
Right ventricle								
ΔPeak strain, GCS(%)	−0.013	0.868	−0.700	0.146	0.969	0.542	1.185	0.230
ΔTime to peak, TTP (ms)	−2.047	0.256	−3.341	0.520	28.36	0.106	10.36	0.521
ΔSystolic strain rate, sSR (/s)	−0.003	0.568	−0.127	0.092	−0.043	0.642	0.162	0.028*
ΔDiastolic strain rate, dSR (/s)	0.010	0.147	0.073	0.104	−0.139	0.114	0.123	0.076

Parameter coefficients (β) and corresponding p-values represent linear associations between strain and measures of oxygenation from all MAP levels below the autoregulation zone (ARZ: <52 mmHg), or independently assessed above the ARZ (>127 mmHg). CBF, coronary blood flow of the left anterior descending coronary artery (LAD); O_2er, oxygen extraction ratio; OS-CMR, oxygenation-sensitive cardiovascular magnetic resonance; $ScsO_2$, coronary sinus oxygen saturation.
*$p < 0.05$.

myocardial oxygenation and strain parameters (14). In order to look at subtle myocardial function changes, intraoperative echocardiography provides an accessible measure to measure strain (22), albeit without the benefit of tissue oxygenation.

Clinical Implications of LV Strain at Hypotensive Periods

A mildly lowered blood pressure can be beneficial as it is easier for the ventricle to unload when there is less systemic resistance. However, afterload reduction, as during anesthesia, is only beneficial to a point where diastolic myocardial or other organ perfusion pressures become critically low. Peri-operative hypotension is a common occurrence, and is associated with a greater risk of peri-operative myocardial infarction (23). Especially elderly high-risk patients are prone to developing hypotension and myocardial ischemia. In humans, analysis from a database of 33,000 non-cardiac surgeries reported that myocardial injury and acute kidney injury are noted after even short periods of intraoperative MAP under 55 mmHg (24), a lower limit similar to that of our anesthetized swine. Monitoring hypotension is important intra- as well as post-operatively. It has been shown that after moderate- to high-risk non-cardiac surgery, eight percent of patients experienced two cumulative hours of MAP-levels below 60 mmHg, and that this hypotension was associated with troponin-defined myocardial injury after non-cardiac surgery (MINS) (25). According to coronary blood

flow data of this study, this lower coronary autoregulatory limit was at a MAP of around 52 mmHg in anesthetized swine. A likely rationale for the reduction in strain at low blood pressure levels is decreased perfusion and subsequent tissue oxygenation below the lower autoregulatory limit (7). At low oxygenation the myocardium suffers lack of substrates and can go into a short-term state of hibernation. It reduces workload to adjust to reduced oxygen supply, which results in attenuated strain (26). This can be observed by the linear association between invasive measurements and function at MAP levels below the ARZ.

We, as well as others, observed that lower autoregulatory limits differ on an individual level as well. Consequently, intraoperative measures of strain, through using intraoperative echocardiography, may guide anesthesiologists along individualized blood pressure management corridors. Beyond cardiac protection, other organs will benefit from adequate perfusion pressure management, too. For instance, ischemic symptoms of the central nervous system can arise at lower MAP limits of 45–55 mmHg in supine subjects (27). Importantly, there is data for cerebrovascular autoregulation that the lower limit of the cortical ARZ may be as high as 90 mmHg in some individuals (28). Thus, it may also be inferred that autoregulation may be compromised in patients with pre-existing coronary pathologies. Since the individual and organ-specific ARZ of every patient are, in effect, a black box, functional measurements would be advantageous to target a MAP that ensures adequate organ function. Therefore, intraoperative patient-side myocardial strain analysis may be a suitable tool. While other vital organs also have their own autoregulation, the resultant perfusion pressure is still driven in part by proper left ventricular function. Therefore, it appears vital to monitor cardiac function when managing blood pressure around a low MAP threshold.

Clinical Implications of LV Strain at Hypertensive Periods

Our animal data indicate that hypertension did not limit myocardial perfusion and oxygenation. Nevertheless, biventricular function was compromised and there was end-diastolic dilation of both ventricles. Not only is systolic function limited, but systolic contraction also becomes prolonged as seen by time to peak strain, although there is no change in heart rate (**Figure 4**). One reason for this might be that the increased workload to counteract high blood pressures compromises function mechanically despite abundant tissue oxygenation. In a clinical context, this may be the case in acute increases during a hypertensive crisis, leading to left-ventricular systolic dysfunction (29). Intraoperative hypertension and tachycardia are associated independently with adverse outcomes after long non-cardiac surgeries, regardless of underlying medical conditions (30). Other studies were inconclusive about associations between intraoperative hypertension and post-surgical morbidity (2). Myocardial oxygenation did not appear compromised by hypertension in our healthy animal model, and since there was even excess oxygen delivery as seen at OS-CMR, blood oximetry and coronary blood flow (7), it may not be immediately clear why these healthy hearts should be vulnerable at hypertension. In fact, we observed a decoupling of myocardial strain from invasive measurements. The non-linear regression graph (**Figure 2**) indicates that systolic function starts to deteriorate at a MAP level, which is lower that the coronary blood flow-defined upper autoregulatory limit. This suggests that with progressive hypertension, myocardial function may be primarily affected by afterload. In particular, hypertensive strain dysfunction was significantly pronounced in the afterload-sensitive right ventricle.

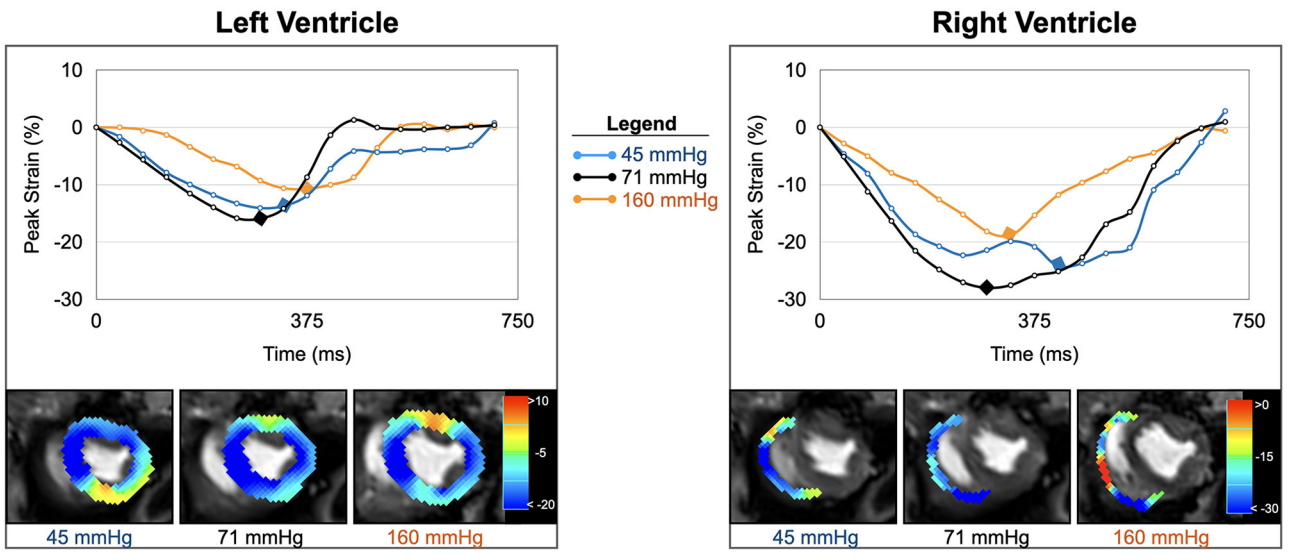

FIGURE 4 | Strain inside and outside the autoregulation zone. Circumferential strain curves and strain overlays at end-systole of one animal are shown for the left and right ventricle. In comparison to baseline (black, 71 mmHg), biventricular strain at low blood pressure (blue, 45 mmHg), and high blood pressure (orange, 161 mmHg) both demonstrate attenuations in peak strain (yellow-red- color in overlay) and prolongations in time to peak strain (marked by diamond in curve).

Clinical Importance of RV Strain

The RV must match the output of the LV. Peri-operative RV dysfunction not only leads to LV underfilling but can also cause upstream problems like venous organ congestion (31, 32). In the presence of chronic high RV afterload, such as in pulmonary hypertension, the RV will progressively adapt with wall hypertrophy (33). However, during short term afterload swings such as those seen in peri-operative situations, rapid adaptation is needed. The RV may dilate to maintain stroke volume (33), and we observed this in our animal model as well. However, concomitant reduction in contractile function can lead to RV failure and low cardiac output (33). A major difference when compared to the LV is the greater sensitivity of the RV to changes in afterload. Our data indicate that a rapid increase in afterload is poorly tolerated, however right ventricular and pulmonary invasive measurements were not acquired in our analysis to confirm this analysis. Also due to the high compliance of the RV in comparison to the LV, greater changes in strain were observed outside the ARZ.

Strain as an Advantageous and Specific Marker for RV Function

Particularly with functional imaging modalities, the RV appears less well-researched than the LV. FT of the RV free wall offers functional monitoring. It signifies already deterioration before RVEF declines and is therefore of prognostic values (34).

While the OS cine modality is suitable for assessing the LV, the myocardial oxygenation response of the RV is not as reliably described with the sequence used. This is due to limitations of spatial resolution defined by the thin RV wall. An advantage of FT and functional analysis is therefore that the RV can be studied even when the target myocardium is thin. Although phenylephrine is reported to increase pulmonary arterial pressure (35), we cannot provide pertinent hemodynamic data in this study, although our RV strain results are highly suggestive in this regard. This study is limited in the fact we did not measure right ventricular or pulmonary hemodynamic measures. However, in a swine model with a surgically constricted pulmonary artery, it was reported that RV GCS measured by echocardiography was linearly correlated with RV systolic pressure, which indicates that free wall strain can aid in detecting acutely increasing RV afterload (36). Our oximetry data, i.e., $ScsO_2$ and O_2er, also reflect global myocardial oxygenation and are not specific to the RV, since the coronary sinus drains venous blood from both ventricles. RV venous drainage both into the coronary sinus and directly into the right atrial and RV cavum precludes any accurate measure of total RV oxygen consumption.

Although changes in RV systolic and diastolic parameters appeared to correlate linearly with many of LV-biased physiological measures it is also known that both RV perfusion and oxygen extraction have key characteristics that differ from the LV (37). The RV is known to have less effective pressure-flow autoregulation (37, 38). This may also explain why we observed closer linear association in the RV of invasive measures across the entire MAP range. This emphasizes the importance of assessing both LV and RV independently with strain analysis, since they react differently to blood pressure changes.

Translating From an Animal Model and Limitations

Our study shows that repetitive assessments of myocardial strain within a single subject across a range of MAP at both hypotension and hypertension demonstrate that alteration of blood pressure is an independent variable driving oxygenation and functional changes. We used an animal model since such a protocol could not be conducted in humans. The advantage of the repetitive measures in an animal model, is that the setting can be highly controlled, however in a clinical setting the changes in myocardial strain are likely a multifactorial process that can also be impacted additional variables such as preload, intracellular calcium dynamics and other factors. This is supported by some of the lower-dependency statistical relationships between strain and invasive measures, indicating further variables may play a role as well. Another advantage of the animal model is that multiple invasive measurements can be obtained to investigate both the impact of blood and oxygen supply represented by CBF vs. and variables depicting the oxygen-supply demand balance. Although there is a physiological link between the two components, a dissociation between perfusion and oxygenation measurements can occur based on the tissue oxygen requirements (39) and consequently oxygenation measurements can be a more sensitive marker of myocardial ischemia. Moreover, as mentioned above, the invasive measures have limitations as well as they do not measure the same regions of the heart, as CBF is measured in the LAD, while coronary sinus oxygen measurements collect blood from a wider region of the heart. Thus, these direct comparisons between the two can be confounded if there is heterogeneity in perfusion and workload across the ventricles. This an advantage of imaging, as a pixelwise approach can be performed of the myocardium.

Although strain values appear consistent with those in human studies (15), further comparisons are needed between the FT analysis of OS-CMR cines and standard cine acquisitions. Due to the difficulty in maintaining stable circulation at extreme MAP levels over longer periods of time, rapid acquisition was needed and thus there were only two short-axis slices were obtained and longitudinal cines were not recorded. The assessment of longitudinal strain, however, would have been advantageous, first because the fiber orientation the RV is mainly in this direction and second in the LV the micro-vessels are located in the subendocardial myocardial layer. Thus, functional subendocardial deficits would represent a very early marker of myocardial ischemia due to increasing wall pressure. While human and porcine cardiac physiology are comparable in many aspects, there are limitations to this animal model as well. Therefore, findings of this study may not necessarily represent human responses under similar conditions, especially not in cardiovascular disease. The used anesthetics might also have influenced myocardial function. While fentanyl has scarce effects on the heart (40), propofol frequently induces hypotension and reduces preload (41). The results are therefore more applicable to

scenarios during general anesthesia, whereas awake subjects may respond differently.

Conclusion

Biventricular function interrogated by cardiovascular magnetic resonance feature-tracking (CMR-FT) is compromised at blood pressures outside of both the upper and lower limit of the coronary autoregulation zone. Ventricular dysfunction at very low blood pressure was shown to be associated both with coronary sinus oximetry data and non-invasive assessment of myocardial tissue oxygenation measured by OS-CMR. During induced hypertension beyond the upper autoregulatory limit, myocardial deformation appears primarily related to the increase in afterload. Further studies are required to understand the effects of acute blood pressure swings on simultaneous myocardial function assessments. Since there are still no consistent definitions of intraoperative hypotension and hypertension (2), myocardial deformation may have the potential to guide blood pressure management. Moreover, these findings are translatable to a clinical peri-operative setting as coronary autoregulation limits differ among individuals. Peri-operative strain assessments could be particularly useful for identifying these individualized thresholds by detecting early signs of myocardial dysfunction prior to the onset of severe clinical sequalae, especially in patients with cardiovascular disease who are more at risk for peri-operative ischemia.

DATA AVAILABILITY STATEMENT

The raw data supporting the conclusions of this article will be made available by the authors, without undue reservation.

ETHICS STATEMENT

The animal study was reviewed and approved by the Veterinary Services at the Department of Agriculture and Nature of the Canton Bern, Switzerland (#BE 103/14). The study was carried out in accordance with national and local animal care regulations and adheres to the ARRIVE guidelines.

AUTHOR CONTRIBUTIONS

This study was conceptualized by DG, KF, AV, and BE. Data was acquired and analyzed by KF, MN, CJ, SH, BW, SPH, BJ, and KF, MN, and DG wrote the first draft. All authors critically reviewed and approved the final manuscript.

FUNDING

This work was funded by institutional funds of the Department of Anaesthesiology and Pain Medicine at the Bern University Hospital, Inselspital, University of Bern and the Foundation for Research in Anaesthesiology and Intensive Care Medicine in Bern Switzerland.

SUPPLEMENTARY MATERIAL

The Supplementary Material for this article can be found online at: https://www.frontiersin.org/articles/10.3389/fcvm.2021.743849/full#supplementary-material

REFERENCES

1. Bayliss WM. On the local reactions of the arterial wall to changes of internal pressure. *J Physiol*. (1902) 28:220–31. doi: 10.1113/jphysiol.1902.sp000911
2. Sessler DI, Bloomstone JA, Aronson S, Berry C, Gan TJ, Kellum JA, et al. Perioperative Quality Initiative consensus statement on intraoperative blood pressure, risk and outcomes for elective surgery. *Br J Anaesth*. (2019) 122:563–74. doi: 10.1016/j.bja.2019.01.013
3. Jinadasa SP, Mueller A, Prasad V, Subramaniam K, Heldt T, Novack V, et al. Blood pressure coefficient of variation and its association with cardiac surgical outcomes. *Anesth Analg*. (2018) 127:832–9. doi: 10.1213/ANE.0000000000003362
4. Abbott TEF, Pearse RM, Archbold RA, Ahmad T, Niebrzegowska E, Wragg A, et al. A prospective International multicentre cohort study of intraoperative heart rate and systolic blood pressure and myocardial injury after noncardiac surgery: results of the VISION study. *Anesth Analg*. (2018);126:1936–45. doi: 10.1213/ANE.0000000000002560
5. Ogawa S, Lee TM, Kay AR, Tank DW. Brain magnetic resonance imaging with contrast dependent on blood oxygenation. *Proc Natl Acad Sci USA*. (1990) 87:9868–72. doi: 10.1073/pnas.87.24.9868
6. Guensch DP, Michel MC, Huettenmoser SP, Jung B, Gulac P, Segiser A, et al. The blood oxygen level dependent (BOLD) effect of *in-vitro* myoglobin and hemoglobin. *Sci Rep*. 2021 11:11464. doi: 10.1038/s41598-021-90908-x
7. Guensch DP, Fischer K, Jung C, Hurni S, Winkler BM, Jung B, et al. Relationship between myocardial oxygenation and blood pressure: experimental validation using oxygenation-sensitive cardiovascular magnetic resonance. *PLoS ONE*. (2019) 14:e0210098. doi: 10.1371/journal.pone.0210098
8. Fischer K, Obrist SJ, Erne SA, Stark AW, Marggraf M, Kaneko K, et al. Feature tracking myocardial strain incrementally improves prognostication in myocarditis beyond traditional CMR imaging features. *JACC Cardiovasc Imaging*. (2020) 13:1891–901. doi: 10.1016/j.jcmg.2020.04.025
9. Eitel I, Stiermaier T, Lange T, Rommel K-P, Koschalka A, Kowallick JT, et al. Cardiac magnetic resonance myocardial feature tracking for optimized prediction of cardiovascular events following myocardial infarction. *JACC Cardiovasc Imaging*. (2018) 11:1433–44. doi: 10.1016/j.jcmg.2017.11.034
10. Romano S, Dell'atti D, Judd RM, Kim RJ, Weinsaft JW, Kim J, et al. Prognostic value of feature-tracking right ventricular longitudinal strain in severe functional tricuspid regurgitation: a multicenter study. *JACC Cardiovasc Imaging*. (2021) 14:1561–8. doi: 10.1016/j.jcmg.2021.02.009
11. Brainin P, Biering-Sørensen SR, Møgelvang R, de Knegt MC, Olsen FJ, Galatius S, et al. Post-systolic shortening: normal values and association with validated echocardiographic and invasive measures of cardiac function. *Int J Cardiovasc Imaging*. (2019) 35:327–37. doi: 10.1007/s10554-018-1474-2
12. Crystal GJ, Kim S-J, Salem MR, Abdel-Latif M. Myocardial oxygen supply/demand relations during phenylephrine infusions in dogs. *Anesth Analg*. (1991) 73:283–8. doi: 10.1213/00000539-199109000-00010
13. Adnot S, Defouilloy C, Brun-Buisson C, Abrouk F, Piquet J, Lemaire F. Hemodynamic effects of urapidil in patients with pulmonary hypertension. A comparative study with hydralazine. *Am Rev Respir Dis*. (1987) 135:288–93.
14. Guensch DP, Kady F, Kyohei Y, Silvia L, Yasushi U, Bernd J, et al. Effect of hyperoxia on myocardial oxygenation and function in patients with stable multivessel coronary artery disease. *J Am Heart Assoc*. (2020) 9:e014739. doi: 10.1161/JAHA.119.014739
15. Fischer K, Yamaji K, Luescher S, Ueki Y, Jung B, von Tengg-Kobligk H, et al. Feasibility of cardiovascular magnetic resonance to detect

oxygenation deficits in patients with multi-vessel coronary artery disease triggered by breathing maneuvers. *J Cardiovasc Magn Reson*. (2018) 20:31. doi: 10.1186/s12968-018-0446-y

16. Lenth RV. *Estimated Marginal Means, aka Least-Squares Means [R package emmeans version 1.6.0]*. Comprehensive R Archive Network (CRAN) (2021). Available online at: https://CRAN.R-project.org/package=emmeans (accessed May 15, 2021).
17. Yang H-J, Oksuz I, Dey D, Sykes J, Klein M, Butler J, et al. Accurate needle-free assessment of myocardial oxygenation for ischemic heart disease in canines using magnetic resonance imaging. *Sci Transl Med*. (2019) 11:eaat4407. doi: 10.1126/scitranslmed.aat4407
18. van den Boomen M, Manhard MK, Snel GJH, Han S, Emblem KE, Slart RHJA, et al. Blood oxygen level–dependent MRI of the myocardium with multiecho gradient-echo spin-echo imaging. *Radiology*. (2020) 294:538–45. doi: 10.1148/radiol.2020191845
19. Manka R, Paetsch I, Schnackenburg B, Gebker R, Fleck E, Jahnke C. BOLD cardiovascular magnetic resonance at 3.0 tesla in myocardial ischemia. *J Cardiovasc Magn Reson*. (2010) 12:54. doi: 10.1186/1532-429X-12-54
20. Jahnke C, Gebker R, Manka R, Schnackenburg B, Fleck E, Paetsch I. Navigator-gated 3D blood oxygen level–dependent CMR at 3.0-T for detection of stress-induced myocardial ischemic reactions. *JACC Cardiovasc Imaging*. (2010) 3:375–84. doi: 10.1016/j.jcmg.2009.12.008
21. Iannino N, Fischer K, Friedrich M, Hafyane T, Mongeon F-P, White M. Myocardial vascular function assessed by dynamic oxygenation-sensitive cardiac magnetic resonance imaging long-term following cardiac transplantation. *Transplantation*. (2021) 105:1347–55. doi: 10.1097/TP.0000000000003419
22. Duncan AE, Alfirevic A, Sessler DI, Popovic ZB, Thomas JD. Perioperative assessment of myocardial deformation. *Anesth Analg*. (2014) 118:525–44. doi: 10.1213/ANE.0000000000000088
23. Hallqvist L, Granath F, Fored M, Bell M. Intraoperative hypotension and myocardial infarction development among high-risk patients undergoing noncardiac surgery: a nested case-control study. *Anesth Analg*. (2021) 133:6–15. doi: 10.1213/ANE.0000000000005391
24. Walsh M, Devereaux PJ, Garg AX, Kurz A, Turan A, Rodseth RN, et al. Relationship between intraoperative mean arterial pressure and clinical outcomes after noncardiac surgery: toward an empirical definition of hypotension. *Anesthesiology*. (2013) 119:507–15. doi: 10.1097/ALN.0b013e3182a10e26
25. Liem VGB, Hoeks SE, Mol KHJM, Potters JW, Grüne F, Stolker RJ, et al. Postoperative hypotension after noncardiac surgery and the association with myocardial injury. *Anesthesiology*. (2020) 133:510–22. doi: 10.1097/ALN.0000000000003368
26. Ross J. Myocardial perfusion-contraction matching. Implications for coronary heart disease and hibernation. *Circulation*. (1991) 83:1076–83. doi: 10.1161/01.CIR.83.3.1076
27. Drummond JC. Blood pressure and the brain: how low can you go? *Anesth Analg*. (2019) 128:759–71. doi: 10.1213/ANE.0000000000004034
28. Joshi B, Ono M, Brown C, Brady K, Easley RB, Yenokyan G, et al. Predicting the limits of cerebral autoregulation during cardiopulmonary bypass. *Anesth Analg*. (2012) 114:503–10. doi: 10.1213/ANE.0b013e31823d292a
29. D'Aloia A, Fiorina C, Vizzardi E, Faggiano P, Dei Cas L. Hypertensive crisis and acute, reversible, left ventricular systolic dysfunction: a case report. *Eur J Heart Fail*. (2002) 4:655–60. doi: 10.1016/S1388-9842(02)00160-5
30. Reich DL, Hossain S, Krol M, Baez B, Patel P, Bernstein A, et al. Predictors of hypotension after induction of general anesthesia. *Anesth Analg*. (2005) 101:622. doi: 10.1213/01.ANE.0000175214.38450.91
31. Silverton N, Djaiani G. Right ventricular function and perioperative risk assessment: the time has come to stop being sinister. *J Cardiothorac Vasc Anesth*. (2019) 33:1287–9. doi: 10.1053/j.jvca.2018.11.027
32. Beaubien-Souligny W, Benkreira A, Robillard P, Bouabdallaoui N, Chassé M, Desjardins G, et al. Alterations in portal vein flow and intrarenal venous flow are associated with acute kidney injury after cardiac surgery: a prospective observational cohort study. *J Am Heart Assoc Cardiovasc Cerebrovasc Dis*. (2018) 7:e009961. doi: 10.1161/JAHA.118.009961
33. Voelkel NF, Quaife RA, Leinwand LA, Barst RJ, McGoon MD, Meldrum DR, et al. Right ventricular function and failure. *Circulation*. (2006) 114:1883–91. doi: 10.1161/CIRCULATIONAHA.106.632208
34. Donauer M, Schneider J, Jander N, Beyersdorf F, Keyl C. Perioperative changes of right ventricular function in cardiac surgical patients assessed by myocardial deformation analysis and 3-dimensional echocardiography. *J Cardiothorac Vasc Anesth*. (2020) 34:708–18. doi: 10.1053/j.jvca.2019.08.026
35. Tanaka M, Dohi S. Effects of phenylephrine and ephedrine on pulmonary arterial pressure in patients with cervical or lumbar epidural anesthesia, or enflurane anesthesia. *J Anesth*. (1994) 8:125–31. doi: 10.1007/BF02514698
36. Cho EJ, Jiamsripong P, Calleja AM, Alharthi MS, McMahon EM, Khandheria BK, et al. Right ventricular free wall circumferential strain reflects graded elevation in acute right ventricular afterload. *Am J Physiol-Heart Circ Physiol*. (2009) 296:H413–20. doi: 10.1152/ajpheart.00923.2008
37. Crystal GJ, Pagel PS. Right ventricular perfusionphysiology and clinical implications. *Anesthesiol J Am Soc Anesthesiol*. (2018) 128:202–18. doi: 10.1097/ALN.0000000000001891
38. Yonekura S, Watanabe N, Caffrey JL, Gaugl JF, Downey HF. Mechanism of attenuated pressure-flow autoregulation in right coronary circulation of dogs. *Circ Res*. (1987) 60:133–41. doi: 10.1161/01.RES.60.1.133
39. Arnold JR, Karamitsos TD, Bhamra-Ariza P, Francis JM, Searle N, Robson MD, et al. Myocardial oxygenation in coronary artery disease: insights from blood oxygen level–dependent magnetic resonance imaging at 3 Tesla. *J Am Coll Cardiol*. (2012) 59:1954–64. doi: 10.1016/j.jacc.2012.01.055
40. Sebel PS, Bovill JG, Boekhorst RAA, Rog N. Cardiovascular effects of high-dose fentanyl anaesthesia. *Acta Anaesthesiol Scand*. (1982) 26:308–15. doi: 10.1111/j.1399-6576.1982.tb01772.x
41. de Wit F, van Vliet AL, de Wilde RB, Jansen JR, Vuyk J, Aarts LP, et al. The effect of propofol on haemodynamics: cardiac output, venous return, mean systemic filling pressure, and vascular resistances †. *BJA Br J Anaesth*. (2016) 116:784–9. doi: 10.1093/bja/aew126

Conflict of Interest: The authors declare that the research was conducted in the absence of any commercial or financial relationships that could be construed as a potential conflict of interest.

Publisher's Note: All claims expressed in this article are solely those of the authors and do not necessarily represent those of their affiliated organizations, or those of the publisher, the editors and the reviewers. Any product that may be evaluated in this article, or claim that may be made by its manufacturer, is not guaranteed or endorsed by the publisher.

frontiers in Cardiovascular Medicine

ORIGINAL RESEARCH
published: 20 October 2021
doi: 10.3389/fcvm.2021.739633

Diagnostic Performance of Fractional Flow Reserve From CT Coronary Angiography With Analytical Method

*Jun-Mei Zhang[1,2], Huan Han[1], Ru-San Tan[1,2], Ping Chai[3,4], Jiang Ming Fam[1], Lynette Teo[4,5], Chee Yang Chin[1], Ching Ching Ong[4,5], Ris Low[1], Gaurav Chandola[1], Shuang Leng[1,2], Weimin Huang[6], John C. Allen[2], Lohendran Baskaran[1,2], Ghassan S. Kassab[7], Adrian Fatt Hoe Low[3], Mark Yan-Yee Chan[3,4], Koo Hui Chan[3,4], Poay Huan Loh[3,4], Aaron Sung Lung Wong[1,2], Swee Yaw Tan[1,2], Terrance Chua[1,2], Soo Teik Lim[1,2] and Liang Zhong[1,2]**

[1] National Heart Centre Singapore, Singapore, Singapore, [2] Duke-NUS Medical School, Singapore, Singapore, [3] Department of Cardiology, National University Heart Centre, Singapore, Singapore, [4] Yong Loo Lin School of Medicine, National University of Singapore, Singapore, Singapore, [5] Department of Diagnostic Imaging, National University Hospital, Singapore, Singapore, [6] Institute for Infocomm Research, Agency for Science, Technology and Research, Singapore, Singapore, [7] California Medical Innovations Institute, San Diego, CA, United States

OPEN ACCESS

Edited by:
Grigorios Korosoglou,
GRN Klinik Weinheim, Germany

Reviewed by:
Matthias Renker,
Kerckhoff Clinic, Germany
Sorin Giusca,
GRN Klinik Weinheim, Germany

***Correspondence:**
Liang Zhong
zhong.liang@nhcs.com.sg

Specialty section:
This article was submitted to Cardiovascular Imaging, a section of the journal Frontiers in Cardiovascular Medicine

Received: 11 July 2021
Accepted: 10 September 2021
Published: 20 October 2021

Citation:
Zhang J-M, Han H, Tan R-S, Chai P, Fam JM, Teo L, Chin CY, Ong CC, Low R, Chandola G, Leng S, Huang W, Allen JC, Baskaran L, Kassab GS, Low AFH, Chan MY-Y, Chan KH, Loh PH, Wong ASL, Tan SY, Chua T, Lim ST and Zhong L (2021) Diagnostic Performance of Fractional Flow Reserve From CT Coronary Angiography With Analytical Method. Front. Cardiovasc. Med. 8:739633. doi: 10.3389/fcvm.2021.739633

The aim of this study was to evaluate a new analytical method for calculating non-invasive fractional flow reserve (FFR_{AM}) to diagnose ischemic coronary lesions. Patients with suspected or known coronary artery disease (CAD) who underwent computed tomography coronary angiography (CTCA) and invasive coronary angiography (ICA) with FFR measurements from two sites were prospectively recruited. Obstructive CAD was defined as diameter stenosis (DS) ≥50% on CTCA or ICA. FFR_{AM} was derived from CTCA images and anatomical features using analytical method and was compared with computational fluid dynamics (CFD)-based FFR (FFR_B) and invasive ICA-based FFR. FFR_{AM}, FFR_B, and invasive FFR ≤0.80 defined ischemia. A total of 108 participants (mean age 60, range: 30–83 years, 75% men) with 169 stenosed coronary arteries were analyzed. The per-vessel accuracy, sensitivity, specificity, and positive predictive and negative predictive values were, respectively, 81, 75, 86, 81, and 82% for FFR_{AM} and 87, 88, 86, 83, and 90% for FFR_B. The area under the receiver operating characteristics curve for FFR_{AM} (0.89 and 0.87) and FFR_B (0.90 and 0.86) were higher than both CTCA- and ICA-derived DS (all $p < 0.0001$) on per-vessel and per-patient bases for discriminating ischemic lesions. The computational time for FFR_{AM} was much shorter than FFR_B (2.2 ± 0.9 min *vs*. 48 ± 36 min, excluding image acquisition and segmentation). FFR_{AM} calculated from a novel and expeditious non-CFD approach possesses a comparable diagnostic performance to CFD-derived FFR_B, with a significantly shorter computational time.

Keywords: coronary artery disease, fractional flow reserve, computed tomography coronary angiography, analytical method, non-invasive

INTRODUCTION

Atherosclerotic plaque deposition in the coronary arterial wall results in anatomical stenosis that may reduce perfusion and induce ischemia in the subtended myocardial territory (1). Fractional flow reserve (FFR), measured during invasive coronary angiography (ICA), is the reference standard for quantifying the functional significance of coronary artery stenoses and discriminating ischemic lesions (2, 3). However, ICA-based FFR measurement incurs additional resource utilization, increases procedural time, and is associated with greater patient discomfort (4). Recently, non-invasive FFR (FFR_{CT}) derived from computed tomography coronary angiography (CTCA) images and computational fluid dynamics (CFD) has demonstrated feasibility for the identification of ischemic coronary lesions (5) with reasonable diagnostic accuracy (6) and prognostication (7).

Mesh generation and iterative solution of numerical equations integral to CFD demand long computational time for the calculation of time-varying instantaneous values of coronary blood flow parameters like velocity, pressure, *etc*. The current CFD-based FFR_{CT} methods take 1 to 4 h per FFR_{CT} analysis (8). Reduced-order (9–11), steady-flow (12) CFD simulations and predictive models using machine learning (13–15) may improve computational efficiency and facilitate shorter turnaround times and/or on-site analysis, which will help garner a wider adoption of non-invasive FFR.

Still an analytical method to calculate FFR non-invasively without the need for computationally demanding CFD modeling would further simplify the derivation of non-invasive FFR from CTCA images. Huo et al. (16) proposed an analytical model that embodied integral equations to be solved based on the dimensions of anatomical stenosis on CTCA and estimates of hyperemic coronary flow derived from *in vitro* and *in vivo* animal experiments. In this study, we developed an original analytical method, FFR_{AM}, that relies on neither CFD nor other inputs other than CTCA images. Flow rate through coronary lesions (Q_{AM}) was estimated from anatomical data reconstructed from CTCA, where anatomical features known to influence the hemodynamics in stenotic arteries, including lesion length, lumen area, flow entrance, and exit angles (17), were explicitly considered. Our aim is to assess the diagnostic performance of FFR_{AM} with reference to our previously developed CFD-based FFR_B and invasive FFR in a cohort of coronary artery disease (CAD) patients.

Abbreviations: AM, analytical method; AUC, area under the receiver operating characteristic curve; CAD, coronary artery disease; CFD, computational fluid dynamics; CTCA, computed tomography coronary angiography; DS, diameter stenosis; FFR, fractional flow reserve; ICA, invasive coronary angiography; L, lesion length; LAD, left anterior descending; LR, likelihood ratio; NPV, negative predictive value; PPV, positive predictive value; Q, flow rate; ROC, receiver operating characteristic; SD, standard deviation; α, flow entrance angle; β, flow exit angle.

MATERIALS AND METHODS

Study Design and Study Population

The current study consecutively enrolled patients from two tertiary centers, with age ≥ 21 years, who had undergone CTCA, and were scheduled to undergo clinically indicated ICA and FFR measurement. The time difference between CTCA and ICA was 32 (19–51) days (median, interquartile range). The exclusion criteria included prior coronary revascularization, acute coronary syndrome occurring between 30 days before CTCA and ICA, angina at rest, left ventricular ejection fraction <30%, hypertrophic cardiomyopathy, significant valve disease including prosthetic heart valve, implanted pacemaker or defibrillator, complex congenital heart disease, estimated glomerular filtration rate <30 ml/min/1.73 m^2, tachycardia or significant arrhythmia, iodinated contrast allergy, contraindication to beta-blocker, nitroglycerin, or adenosine, serious comorbidity with life expectancy <2 years, and pregnancy. The study was approved by the local institutional review boards, and all participants gave written informed consent.

From September 20, 2016 to March 25, 2020, 117 participants were recruited. Nine subjects were excluded: two patients with unsuccessful invasive FFR measurement and seven patients with inadequate CTCA image quality. Among the seven patients, one patient had blooming artifacts due to extreme coronary calcification (Agatston score 3441), and six patients had motion artifacts in the CTCA images. By excluding 10 vessels with missing video recordings of the FFR measurement locations, 108 participants with 169 vessels were included in the analysis (**Figure 1**).

ICA and FFR Measurement

For the recruited patients, invasive FFR measurement was performed according to the institutional protocol. Every participant underwent ICA *via* either the femoral or radial approach using 5F, 6F, or 7F diagnostic or guiding catheters (18). Angiography was performed in standard projections. Diameter stenosis at ICA (DS_{ICA}) was visually assessed (19), and lesions were deemed obstructive if DS_{ICA} ≥50%. The pressure wires/catheters used for the invasive FFR can be found in the **Supplementary Material**. Intra-coronary pressure was measured at the ascending aorta and distal to the coronary lesion in at least one vessel. Hyperemia was induced by either intravenous infusion (140–180 μg/kg/min) or an intracoronary bolus (60–200 μg) of adenosine. A coronary lesion was categorized as ischemic if FFR ≤0.80. Two consultant interventional cardiologists with extensive clinical experience reviewed the ICA images, and the lesions were evaluated based on overall consensus. In case of disagreement, a third independent cardiologist reviewed the films and provided a final diagnosis.

CTCA Acquisition

Every participant underwent CTCA on one of the following scanners with ≥256 detector rows: Toshiba Aquilion One 320 Slice, Canon Aquilion ONE Genesis 640 Slice, Philips Brilliance iCT 256-detector, Siemens Somatom Force dual source 384-detector, GE Revolution single source, and Siemens Somatom

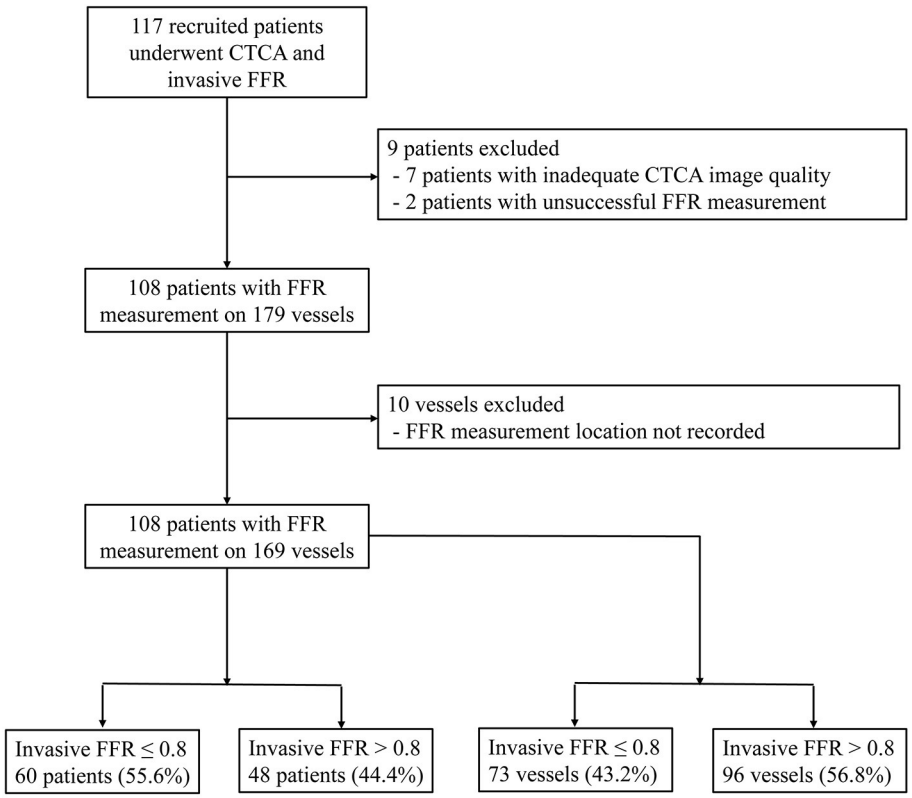

FIGURE 1 | Study inclusion flowchart. CTCA, CT coronary angiography; FFR, fractional flow reserve.

Drive dual source 256-detector. Oral beta-blocker (metoprolol) was administered to the participants with a heart rate >65 beats per min (20). Sublingual glyceryl trinitrate was administered just prior to scanning for optimal coronary vasodilation during image acquisition. Prospective electrocardiogram-triggered protocol was used to acquire image data at pre-specified phases of the heart cycle, and CTCA scan was performed at inspiratory breath-hold. Then, 50 to 75 ml of non-ionic contrast Omnipaque 350 was administered for each scan.

The CTCA studies were read by an accredited reporting radiologist or cardiologist and verified by a second accredited reader. The diameter stenoses of coronary lesions on CTCA images (DS_{CTCA}) were graded according to anatomical severity: normal, absent plaque, and no luminal stenosis; minimal, DS_{CTCA} <25%; mild, 25% $\leq$ DS_{CTCA} $\leq$ 49%; moderate, 50% $\leq$ DS_{CTCA} $\leq$ 69%; severe, 70% $\leq$ DS_{CTCA} $\leq$99%; and occluded, DS_{CTCA} = 100% (20). A coronary lesion was deemed obstructive if DS_{CTCA} $\geq$50%.

CTCA Image Segmentation and 3D Model Reconstruction

Dedicated QAngio CT software (21) (version 3.0, Medis) was used for segmentation and 3D reconstruction of coronary artery. Additional details are found in the **Supplementary Material**. The surface meshes of the 3D coronary artery tree model were generated using 3D Workbench (version 0.8, Medis). **Figure 2** illustrates the workflow for non-invasive FFR calculation in a participant. **Figure 3** depicts the detailed coronary anatomy in another participant with pertinent anatomical parameter inputs for calculating the FFR_{AM}.

Total coronary flow under resting conditions, a required input parameter for non-invasive FFR estimation, is linearly related to left ventricular mass (LVM) (22). The latter was measured using validated Segment CT software (version 2.2, Medviso) (23) that semi-automatically delineated left ventricular (LV) endocardial and epicardial contours on contiguous 2D LV short-axis slices reformatted from the CTCA-reconstructed 3D whole-heart model (**Figure 3**).

Computation of Non-invasive FFR_{AM} With Analytical Model

In our analytical model, $FFR_{AM} = 1 - \frac{P_1+P_2}{P_a}$, where P_a is patient-specific mean aortic pressure estimated as mean cuff pressure minus 6.8 mmHg to account for pressure drop during hyperemia (24), and ΔP_1 and ΔP_2 are pressure drops across the coronary lesion and from the coronary orifice to the proximal end of the coronary lesion, respectively. The latter is calculated from the Hagen–Poiseuille equation according to the viscosity of the blood, lumen area, length, and flow rate of each coronary branch (from the coronary orifice to the proximal end of the coronary lesion), respectively.

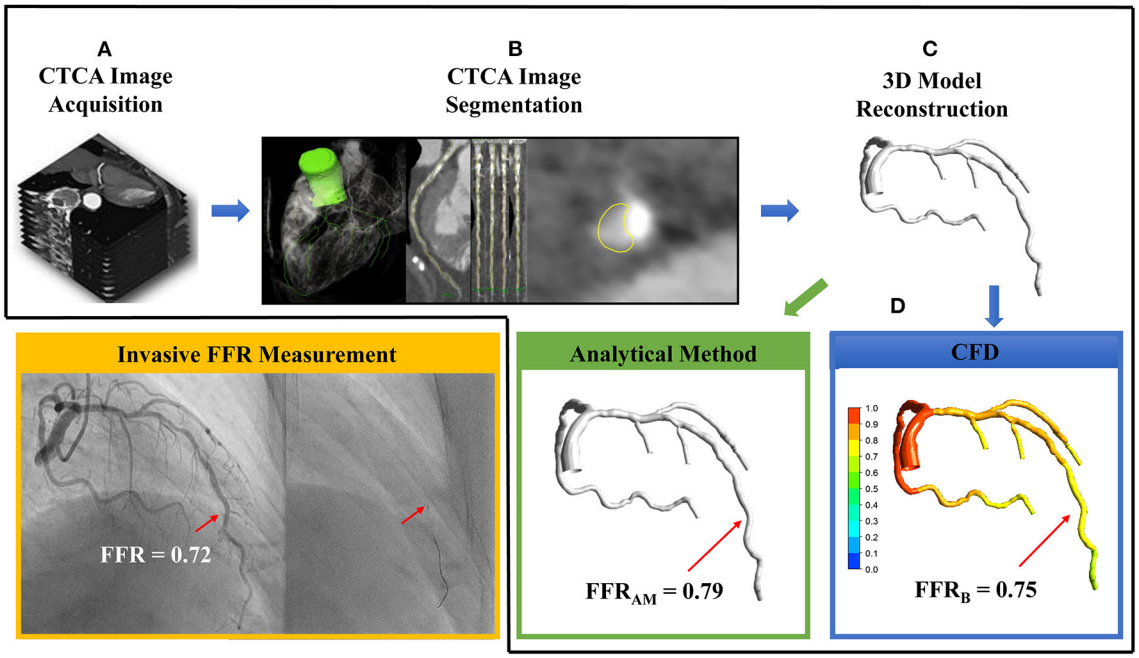

FIGURE 2 | The sequential steps involved in the calculation of non-invasive fractional flow reserve (FFR) include **(A)** computed tomography coronary angiography (CTCA) image acquisition, **(B)** CTCA image segmentation *via* extracting centerlines and delineating lumen contours in the transversal and cross-sectional images, **(C)** 3D reconstruction of subject-specific coronary artery tree, and **(D)** using either analytical method to calculate FFR_{AM} (green box) or computational fluid dynamics simulation to compute FFR_B (blue box). In this case, FFR_{AM} and FFR_B were 0.79 and 0.75, respectively, at the site of invasive FFR 0.72 measured with a pressure catheter (right, inset) during invasive coronary angiography (yellow box).

By law of energy conservation, ΔP_1 entails convective and diffusive energy losses as well as energy loss attributable to sudden constriction and expansion (16). Flow separation and swirling that exacerbate energy losses and pressure drops are related to features such as lesion length, lumen area, flow entrance, exit angles, *etc.* (25). We applied these considerations in series to a coronary lesion model of total length L decomposed schematically into three components: a proximal contracting segment of length L_{ps} and distal expanding segment of length L_{sd}, which bookend a middle maximally stenosed segment of finite length L–L_{ps}-L_{sd} (**Supplementary Figure 1**). The respective pressure drops across the three segments ΔP_{ps}, ΔP_{sd}, and ΔP_{ss} sum up to ΔP_1 and are, from a mechanical engineering perspective, analogous to pressure drops across contracting, expanding, and straight pipes, respectively (**Supplementary Material**). **Figure 3F** illustrates how we measured the anatomical parameters L, L_{ps}, and L_{sd} as well as A_P, A_d, and A_s, the lumen areas at the proximal and distal ends of the coronary lesion, and the maximally stenosed segment, respectively. From these parameters, flow entrance (α) and exit (β) angles were derived to facilitate the calculation of ΔP_{ps} and ΔP_{sd} (**Supplementary Material**).

To calculate the hyperemic flow rate of each coronary branch, we first calculated the total coronary flow rate at resting from CTCA-assessed LVM (22) and then estimated the resting flow rate through the i-th coronary branch using the scaling law (26). Finally, hyperemic flow rate through a coronary lesion located at the i-th branch of the coronary artery tree was computed as k times of its value at resting state (24). The coefficient k reflects the magnitude of flow increase at hyperemia and is dependent on the diameter stenosis of the lesion (DS). Inputting Q_{AM} to the analytical model, ΔP_1 and then FFR_{AM} could be calculated without a need for CFD simulation (**Supplementary Material**).

Computation of Non-invasive FFR_B Based on Reduced-Order CFD Simulation

Reduced-order CFD simulation was performed on the reconstructed 3D coronary artery tree model in deriving non-invasive FFR_B measurement. Additional details can be found in our prior studies (9, 11, 27) and in the **Supplementary Material**. The FFR_B value was extracted at the location on the 3D coronary tree model that best corresponded to the site of the FFR measurement at ICA as judged by cardiologists (JMF and CYC).

Statistical Analysis

Continuous variables were summarized as mean ± standard deviation (SD) or median (interquartile range), and the categorical variables were summarized as frequencies and percentages. Two-sample t-test, Wilcoxon rank-sum test, and Fisher's exact test were used to compare the ischemic and non-ischemic groups on continuous normally distributed variables, continuous parameters with non-normal distribution, and binary variables, respectively. For vessels with multiple lesions, the pressure drops over individual lesions were compared,

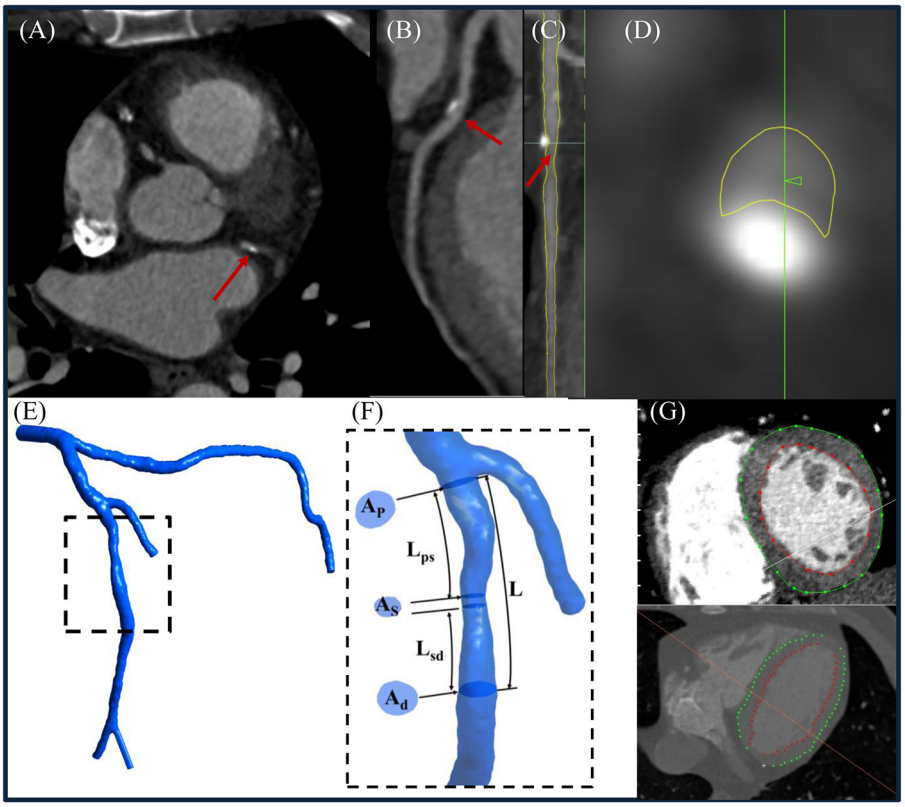

FIGURE 3 | (A) Representative computed tomography coronary angiography (CTCA) cross-sectional slice, **(B)** curved multiplanar reconstructed images of a left anterior descending (LAD) coronary artery, **(C)** straightened LAD with segmented lumen lines (yellow color) in transversal and **(D)** cross-sectional views, **(E)** reconstructed 3D left coronary tree, and **(F)** enlarged view to illustrate how to measure A_p, A_s , A_d, L_{ps}, L_{sd}, and L from the model. **(G)** Left ventricular (LV) endocardial and epicardial contours were delineated from CTCA images to calculate the LV mass. (Note: A_p, A_s, and A_d represented the lumen area at proximal, maximally stenosed, and distal segments, respectively; L_{ps}, L_{sd}, and L were the length measured from the proximal end of the coronary lesion to the proximal end of the maximally stenosed segment, the distal end of the maximally stenosed segment to the distal end of the coronary lesion, and the proximal to the distal ends of the whole coronary lesion, respectively. Flow entrance and exit angles (α and β) were then calculated using Eqs. (A-1) and (A-6) in the **Supplementary Material**, respectively.

and the anatomical parameters associated with the lesion contributing to the largest pressure drop were selected for statistical analysis. The DeLong test (28) was used to compare receiver operating characteristic (ROC) areas under the curve (AUCs). Accuracy, sensitivity, specificity, positive prediction value, negative predictive value (NPV), and likelihood ratios corresponding to the diagnostic threshold were calculated to enable a comparison of the discrimination capability among DS_{CTCA}, DS_{ICA}, and non-invasive FFR indexes. SPSS (version 22, IBM, New York, USA) was used to perform the statistical analyses. Statistical significance was set at $p < 0.05$.

RESULTS

Patient Characteristics

Detailed demographics of the 108 participants (mean age 60 ± 9 years; 81 males) is presented in **Table 1**. Ethnicities included Chinese (80%), Indian/Malay (15%), and other Asians (5%) which closely reflect the ethnic percentages of the Singapore population. The majority of the participants had hypertension (64%) and hyperlipidemia (70%).

Characteristics of Flow Rate and Morphological Parameters

Among 169 vessels, 73 (43%) were ischemic (**Table 2**). A_s and A_d were significantly smaller, and α and β were significantly greater among ischemic vs. non-ischemic lesions, which contribute to the significantly greater ΔP_{ps} and ΔP_{sd} along the contracting and expanding segments, respectively, in the ischemic lesions. There was excellent correlation between flow rates through lesions derived using empirical equations and CFD simulation (mean Q_{AM} 3.38 ± 1.93 ml/s vs. mean Q_{CFD} 3.30 ± 1.97 ml/s; $r = 0.95$, $p < 0.0001$) (**Figure 4**).

Diagnostic Performance of FFR_{AM} for Discriminating Ischemic Lesions

Compared with invasive FFR (mean 0.81 ± 0.13), FFR_{AM} (mean 0.80 ± 0.20) exhibited fair correlation ($r = 0.57$, $p < 0.0001$)

TABLE 1 | Patient characteristics.

	Mean ± SD, median (interquartile), or *n* (%)
Age, years	60 ± 9
Male	81 (75)
BMI, kg/m^2	26.1 ± 4.8
Heart rate at CTCA, bpm	57 ± 6
Race/ethnics	
Chinese, *n* (%)	86 (80)
Indian/Malay, *n* (%)	16 (15)
Other Asians, *n* (%)	6 (5)
Risk factors	
Hypertension, *n* (%)	69 (64)
Hyperlipidemia, *n* (%)	76 (70)
Diabetes, *n* (%)	30 (28)
Current smoker, *n* (%)	16 (15)
Ex-smoker, *n* (%)	9 (8)
Vital signs	
SBP, mmHg	134 ± 17
DBP, mmHg	77 ± 11
Laboratory measures	
Hemoglobin, g/dl	13.9 ± 1.3
Hematocrit, %	41.9 ± 3.4
Creatinine, mmol/L	0.076 ± 0.019
Medications	
Aspirin, *n* (%)	94 (87)
Beta-blocker, *n* (%)	54 (50)
Nitrate, *n* (%)	72 (67)
Statins, *n* (%)	91 (84)
ACEI/ARB, *n* (%)	31 (29)
Clopidogrel, *n* (%)	93 (86)
Calcium channel blockers, *n* (%)	23 (21)
Other medications, *n* (%)	52 (48)
Left ventricular mass, g	115 ± 31
Agatston score	275 (108, 502)

BMI, body mass index; CTCA, computed tomography coronary angiography; SBP, systolic blood pressure; DBP, diastolic blood pressure; ACEI, angiotensin-converting enzyme injection; ARB, angiotensin receptor blocker.

TABLE 2 | Characteristics of flow rate, anatomical parameters, and pressure drop over various coronary lesion segments to calculate the non-invasive FFR_{AM} overall and by study group (ischemic group: FFR ≤ 0.8; non-ischemic group: FFR > 0.8).

Parameter	Overall (*n* = 169)	FFR > 0.80 (*n* = 96)	FFR ≤ 0.8 (*n* = 73)	*p*-value
Q_{CFD} (ml/s)	3.30 ± 1.97	3.27 ± 2.23	3.33 ± 1.67	0.855
Q_{AM} (ml/s)	3.38 ± 1.93	3.21 ± 2.17	3.55 ± 1.67	0.295
A_p (mm^2)	6.80 ± 3.66	7.58 ± 3.79	6.03 ± 3.38	0.012
A_s (mm^2)	3.80 ± 2.16	4.56 ± 2.41	3.05 ± 1.56	<0.0001
A_d (mm^2)	6.62 ± 3.22	7.35 ± 3.47	5.90 ± 2.79	0.008
L (mm)	10.77 ± 6.74	10.07 ± 5.97	11.46 ± 7.40	0.223
L_{ps} (mm)	3.71 ± 3.24	3.64 ± 3.44	3.78 ± 3.06	0.800
L_{sd} (mm)	3.51 ± 2.79	3.31 ± 2.56	3.70 ± 3.01	0.420
α (°)	9.35 ± 9.16	7.15 ± 8.49	12.28 ± 9.25	<0.0001
β (°)	10.06 ± 9.23	7.54 ± 8.07	13.39 ± 9.66	<0.0001
P_{ps} (*mmHg*)	3.37 ± 4.08	1.76 ± 2.71	4.95 ± 4.57	<0.0001
P_{sd} (mmHg)	7.10 ± 11.09	2.92 ± 4.63	11.23 ± 13.79	<0.0001
P_{ss} (mmHg)	1.03±1.64	0.48 ± 0.60	1.59 ± 2.11	<0.0001

Q_{CFD}, flow rate derived from computational fluid dynamics (CFD); Q_{AM}, flow rate estimated from analytical model (AM); A_p, lumen area at the proximal end of the coronary lesions; A_s, lumen area at the maximally stenosed segment; A_d, lumen area at the distal end of the coronary lesions; L, lesion length; L_{ps}, length of the segment from the proximal end of the coronary lesion to the proximal end of the maximally stenosed segment; L_{sd}, length of the segment from the distal end of the maximally stenosed segment to the distal end of the coronary lesion; α, flow entrance angle at the distal end of the proximal contracting segment; β, flow exit angle at the proximal end of the distal expanding segment; P_{ps}, pressure drop due to the contraction of the lumen area at the proximal contracting segment; P_{sd}, pressure drop due to the expansion of lumen area at the distal expanding segment; P_{ss}, pressure drop along the straight maximally stenosed segment.

and agreement with small systematic biases (-0.0027 ± 0.163) (**Figure 4**). Performance metrics using DS_{CTCA} ≥50%, DS_{ICA} ≥50%, FFR_{AM} ≤0.8, and FFR_B ≤0.8 to discriminate ischemic lesions are compared in **Table 3** and **Figure 5**. On a per-vessel level, the ROC AUCs (95% CI) for FFR_{AM} [0.89 (0.84, 0.94)] and FFR_B [0.90 (0.85, 0.94)] were significantly higher than those for DS_{CTCA} [0.61 (0.54, 0.69)] and DS_{ICA} [0.73 (0.65, 0.79)]. On a per-patient level, the ROC AUCs (95% CI) for FFR_{AM} [0.87 (0.79, 0.93)] and FFR_B [0.86 (0.78, 0.92)] were significantly higher than those for DS_{CTCA} [0.52 (0.42, 0.62)] and DS_{ICA} [0.73 (0.64, 0.81)]. DS_{ICA} had a higher AUC than DS_{CTCA} (both p <0.05 on per-vessel and per-patient analyses). There was no significant difference between FFR_{AM} and FFR_B in AUCs on both per-vessel and per-patient analyses (**Figure 5).**

The performance metrics using DS_{CTCA} ≥70%, DS_{ICA} ≥70%, FFR_{AM} ≤0.8, and FFR_B ≤0.8 to discriminate ischemic lesions are compared in **Table 3** and **Figure 6.** On a per-vessel level, the ROC AUCs for FFR_{AM} and FFR_B were significantly higher than those for DS_{CTCA} [0.64 (0.56, 0.71)] and DS_{ICA} [0.74 (0.67, 0.81)]. On a per-patient level, the ROC AUCs for FFR_{AM} and FFR_B were significantly higher than those for DS_{CTCA} [0.61 (0.51, 0.70)] and DS_{ICA} [0.70 (0.60, 0.78)].

With invasive FFR as a reference standard, 32 lesions in 27 patients were wrongly classified with FFR_{AM} and 22 lesions in 19 patients were wrongly classified with FFR_B. At both per-vessel and per-patient levels, FFR_{AM} and FFR_B achieved a significantly improved accuracy compared with DS_{CTCA} ≥50%, DS_{ICA} ≥50%, DS_{CTCA} ≥70%, and DS_{ICA} ≥70% (**Table 3**).

Computational Time FFR_{AM} vs. FFR_B

Excluding image acquisition and segmentation, the computational time for FFR_B was 48 ± 36 min (range 0.12 to 3.67 h) using parallel computation on a Dell T7800 workstation. The corresponding computational time for FFR_{AM} was 2.2 ± 0.9 min, using a single CPU of the same workstation.

DISCUSSION

In this study, we have developed a novel analytical method to determine FFR_{AM} non-invasively from patient-specific 3D models reconstructed from CTCA images. The FFR_{AM} exhibited a good correlation with invasive FFR and had a diagnostic performance close to CFD-based FFR_B. We have

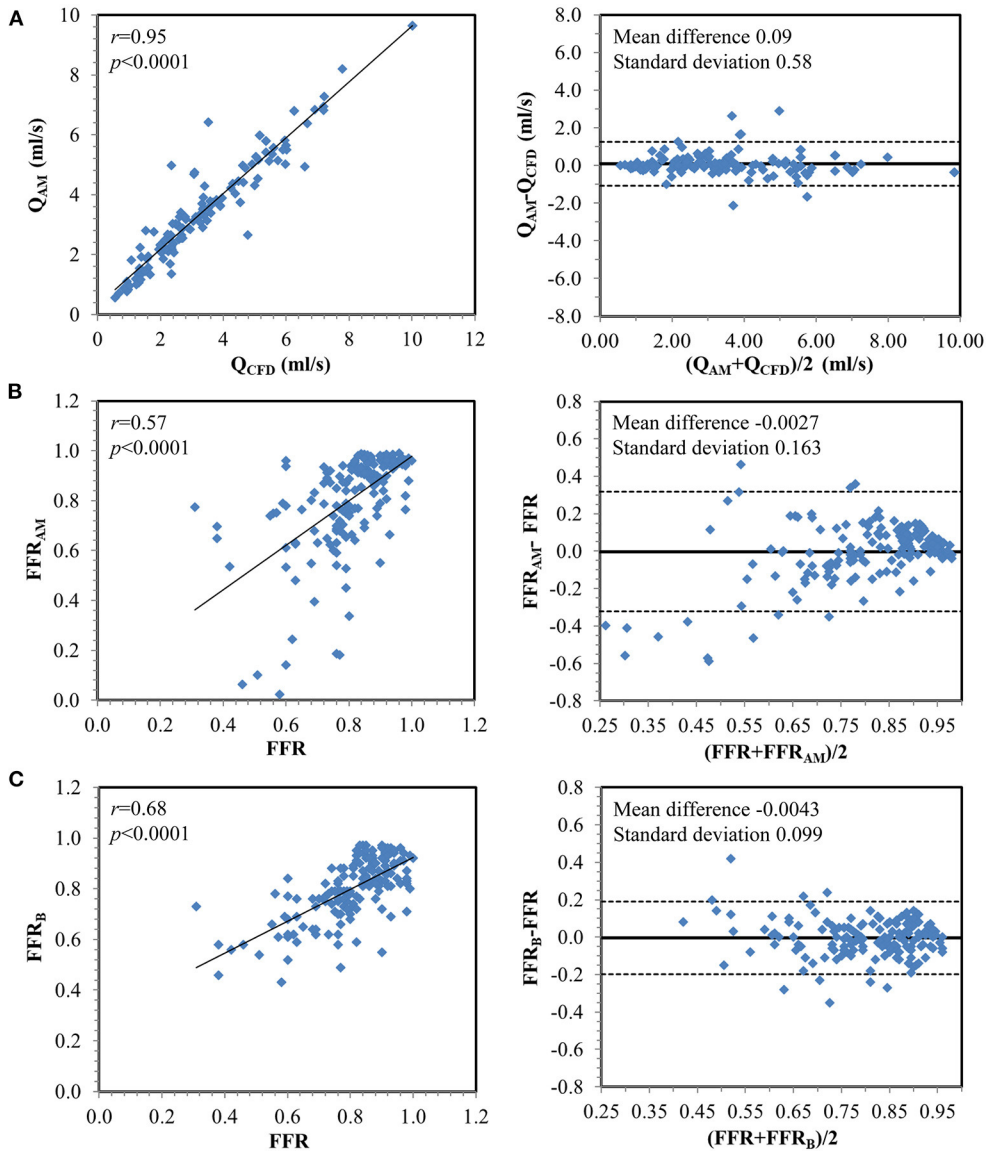

FIGURE 4 | Correlation and Bland–Altman plots **(A)** between flow rates calculated from computational fluid dynamics simulation (Q_{CFD}) and estimated from the analytical model (Q_{AM}) and between invasively measured fractional flow reserve (FFR) with **(B)** FFR_{AM} and **(C)** FFR_B on a per-vessel basis.

also demonstrated the diagnostic performance of FFR_B in a prospective study design. The computational time for FFR_{AM} was much shorter than that for FFR_B.

Our analytical model compartmentalized the stenosed coronary vessel into segments with distinct geometry to simplify the calculation of the corresponding pressure drops. We used anatomical information and LVM to calculate the flow rate through lesions and then input them into empirical equations with anatomical parameters measured on 3D coronary models to calculate energy loss due to the expansion and constriction of the lumen cross-section, which facilitates non-invasive FFR_{AM} calculation. A major advantage of estimating FFR_{AM} non-invasively using the analytical model is computational speed since the computational cost of CFD is eliminated. The analysis took slightly more than 2 min on a single CPU. This speed was achieved with little compromise in diagnostic accuracy. The flow rates through the lesions calculated in our analytical method using only anatomical information had a good correlation with that obtained by CFD simulation ($r = 0.95$), and the derived FFR_{AM} demonstrated a fair correlation and good agreement with invasive FFR and was close to FFR_B. For the diagnosis of ischemia, FFR_{AM} had similar AUC (0.89 *vs.* 0.90, $p = 0.57$ and 0.87 vs. 0.86, $p = 0.78$ on per-vessel and per-patient bases, respectively) and specificity (86 *vs.* 86% and 79 vs. 77% on per-vessel and per-patient bases, respectively) but with slightly lower sensitivity (75 vs. 88% and 73 vs. 86% on per-vessel and per-patient bases, respectively) and NPV (82 vs. 90% and 70 vs. 82% on per-vessel and per-patient bases, respectively) compared

TABLE 3 | (A) Diameter stenoses (DS_{CTCA} and DS_{ICA}) and non-invasive FFR (FFR_{AM} and FFR_B) in study groups (FFR > 0.8 and FFR ≤ 0.8; **(B)** Comparison of diagnostic performance of different parameters for predicting myocardial ischemia at per-vessel level; **(C)** Comparison of diagnostic performance of different parameters for predicting myocardial ischemia at per-patient level.

Parameter	Overall (n = 169)	FFR > 0.80 (n = 96)	FFR ≤ 0.8 (n = 73)	p-value
(A)				
$DS_{CTCA} \geq 50\%$	129 (76%)	64 (67%)	65 (89%)	0.001
$DS_{ICA} \geq 50\%$	119 (70%)	49 (51%)	70 (96%)	<0.0001
$DS_{CTCA} \geq 70\%$	54 (32%)	35 (36%)	19 (26%)	<0.0001
$DS_{ICA} \geq 70\%$	59 (35%)	44 (46%)	15 (21%)	<0.0001
FFR_{AM}	0.80 ± 0.20	0.91 ± 0.09	0.67 ± 0.22	<0.0001
FFR_B	0.80 ± 0.12	0.87 ± 0.08	0.71 ± 0.10	<0.0001

Threshold	Accuracy	Sens	Spec	LR+	LR-	PPV	NPV
(B)							
$DS_{CTCA} \geq 50\%$	0.57	0.89	0.33	1.33	0.33	0.50	0.80
$DS_{ICA} \geq 50\%$	0.69	0.96	0.49	1.88	0.09	0.59	0.94
$DS_{CTCA} \geq 70\%$	0.66	0.47	0.81	2.49	0.65	0.65	0.67
$DS_{ICA} \geq 70\%$	0.76	0.63	0.86	4.57	0.43	0.78	0.75
$FFR_{AM} \leq 0.8$	0.81	0.75	0.86	5.48	0.29	0.81	0.82
$FFR_B \leq 0.8$	0.87	0.88	0.86	6.39	0.14	0.83	0.90
(C)							
$DS_{CTCA} \geq 50\%$	0.57	0.93	0.11	1.04	0.63	0.57	0.56
$DS_{ICA} \geq 50\%$	0.75	0.95	0.51	1.94	0.10	0.71	0.89
$DS_{CTCA} \geq 70\%$	0.59	0.49	0.72	1.78	0.70	0.69	0.53
$DS_{ICA} \geq 70\%$	0.69	0.63	0.77	2.68	0.49	0.77	0.62
$FFR_{AM} \leq 0.8$	0.75	0.73	0.79	3.42	0.34	0.81	0.70
$FFR_B \leq 0.8$	0.82	0.86	0.77	3.69	0.18	0.82	0.82

Sen, sensitivity; Spec, specificity; LR+, positive likelihood ratio; LR-, negative likelihood ratio; PPV, positivity predictive value; NPV, negative predictive value.

with FFR_B. Notably, both methods had superior diagnostic performance to routine methods, including DS_{CTCA} and DS_{ICA}.

The FFR_{AM} derived from the lesion lumen area, length, flow entry and exit angles, and flow rate with fluid equations is different from diameter stenosis and other measurements of coronary morphologic information. It is related more to coronary hemodynamics and physiology. The lesion length and diameter have been employed by other investigators as indirect measures of fractional flow reserve (29). Our current study showed a greater mean value of lesion length (11.46 ± 7.40 vs. 10.07 ± 5.97 mm, $p = 0.223$) and a smaller lesion area (3.05 ± 1.56 vs. 4.56 ± 2.41 mm^2, $p < 0.0001$) in the group with FFR ≤0.8 vs. the group with FFR >0.8. As a result, the estimated coronary morphologic index [eg., lesion length/minimal lesion diameter (29)] from our study is significant greater (12.3 vs. 4.8, $p < 0.0001$) in the group with FFR ≤0.8 vs. the group with FFR >0.8, which is in agreement with the findings from the study of Li (29). In addition to the aforementioned coronary morphologic index, other lesion geometric parameters, like flow entry and exit angles to lesions, have been associated with fluid convective and diffusive energy loss and pressure drop (3, 4). We have incorporated these additional elements in formulating the expressions for FFR_{AM} calculation. By decomposing a coronary lesion model of finite length into a spatial series of a proximal contracting segment, middle stenotic segment, and distal expanding segment to derive the model equations, FFR_{AM} presents an integrated assessment of coronary hemodynamics that provides a more accurate assessment of coronary physiology than morphologic stenosis index.

CTCA-Based Non-invasive FFR to Discriminate Ischemic Lesions

Recent developments in CFD and CTCA imaging have made the calculation of non-invasive FFR feasible. NXT (6) and Discover-flow trials (5) employed standard transient CFD simulation and reported accuracy, sensitivity, specificity of 86, 84, and 86% (6) and 84.3, 87.9, and 82.2% (5), respectively, on a per-vessel basis and 80, 85, and 79% (6) and 87, 93, and 82% (5) on a per-patient basis. In the current study, our previously developed reduced-order CFD-based FFR_B (9) yielded commensurate accuracy, sensitivity, and specificity of 87, 88, and 86% on a per-vessel basis and 82, 86, and 77% on a per-patient basis. While there are limitations to cross-trial comparisons, the AUCs of FFR_B [0.90 (0.85, 0.94) and 0.86 (0.78, 0.92) on per-vessel and per-patient bases, respectively] and FFR_{AM} [0.89 (0.84, 0.94) and 0.87 (0.79, 0.93) on per-vessel and per-patient bases respectively] were in the similar range of and were intermediate between the AUCs reported for FFR_{CT} in the DeFACTO [0.79 (0.72, 0.87) on a per-patient basis] (30) and NXT trials [0.93 (0.91, 0.95) and 0.90 (95% CI: 0.87 to 0.94) on per-vessel and per-patient bases,

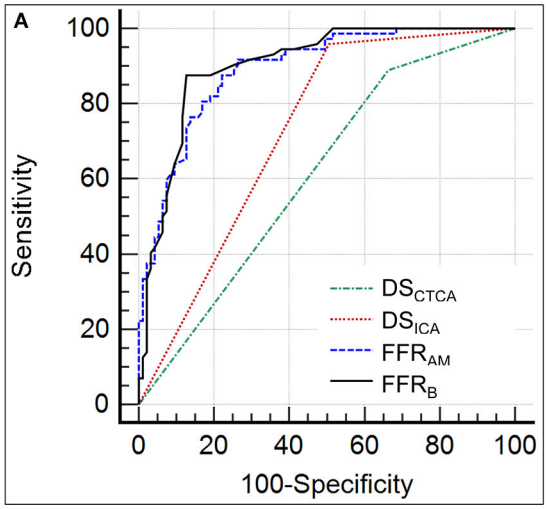

Parameter	AUC (95% CI)
DS_{CTCA}	0.61 (0.54, 0.69)
DS_{ICA}	0.73 (0.65, 0.79)
FFR_{AM}	0.89 (0.84, 0.94)
FFR_{B}	0.90 (0.85, 0.94)

Compare AUCs of the Parameters	*p*-value
DS_{CTCA} vs. DS_{ICA}	0.0053
DS_{CTCA} vs. FFR_{AM}	<0.0001
DS_{ICA} vs. FFR_{AM}	<0.0001
DS_{CTCA} vs. FFR_{B}	<0.0001
DS_{ICA} vs. FFR_{B}	<0.0001
FFR_{AM} vs. FFR_{B}	0.57

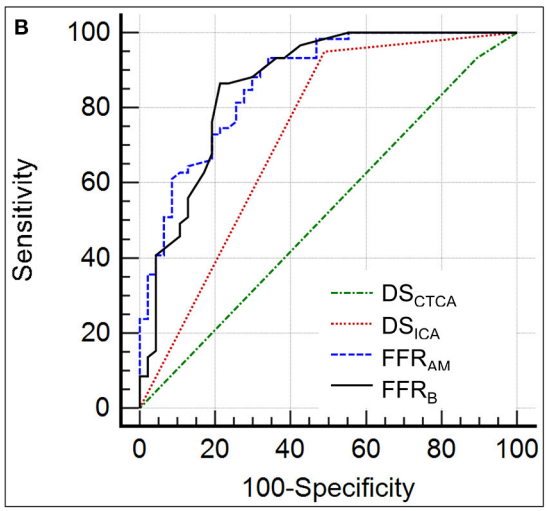

Parameter	AUC (95% CI)
DS_{CTCA}	0.52 (0.42, 0.62)
DS_{ICA}	0.73 (0.64, 0.81)
FFR_{AM}	0.87 (0.79, 0.93)
FFR_{B}	0.86 (0.78, 0.92)

Compare AUCs of the Parameters	*p*-value
DS_{CTCA} vs. DS_{ICA}	<0.0001
DS_{CTCA} vs. FFR_{AM}	<0.0001
DS_{ICA} vs. FFR_{AM}	0.0036
DS_{CTCA} vs. FFR_{B}	<0.0001
DS_{ICA} vs. FFR_{B}	0.0082
FFR_{AM} vs. FFR_{B}	0.78

FIGURE 5 | Comparison of the receiver operating characteristic curves for the discrimination of myocardial ischemia (fractional flow reserve, FFR $\leq$ 0.8) using diameter stenosis (DS; DS_{CTCA} and DS_{ICA}, with a threshold of 50%) and non-invasive FFR (FFR_{AM} and FFR_{B}) on **(A)** per-vessel and **(B)** per-patient levels.

respectively) (6), suggesting that both compared favorably with standard transient CFD-based approaches.

While CFD-based non-invasive FFR can improve the diagnostic performance of DS_{CTCA} alone, it is provided as a remote service with a long turnaround time due to the significant computational costs incurred for mesh generation and iterative solutions to solve numerical equations, which are procedures intrinsic to flow simulation (5, 6). To facilitate on-site non-invasive FFR computation, Coenen *et al.* (31) modeled the coronary vessel as a 1D segment for simulation and mapped the calculated cFFR onto the 3D model reconstructed from CTCA images. The computational time was reduced to 5–10 min per patient, but the accuracy was only 74.6% with invasive FFR as reference (31). Machine-learning based artificial intelligence (AI) algorithms were introduced to reduce the calculation time of non-invasive FFR in some studies that were mainly based on retrospective investigations (13–15). These required ample synthetic datasets for training before the AI algorithms could be applied. Another option to reduce computational time entails the use of analytical models. Huo *et al.* (16) reported an analytical method to estimate FFR from the dimensions of stenosis and hyperemic coronary flow. The method relied on *in vitro* or animal experiments to obtain hyperemic coronary flow, which hindered its applicability outside the laboratory. In contrast, our new analytical model uses only anatomical information and does not require *in vitro* or *in vivo* experiments. With relatively similar diagnostic performance as and lower computational demand than CFD-based approaches, the application of FFR_{AM} for on-site non-invasive FFR analysis may become feasible.

Linkage of Parameters in the Analytical Model to Features in AI Algorithms

AI algorithms can facilitate non-invasive FFR estimation (13). The judicious selection of input parameters plays an important

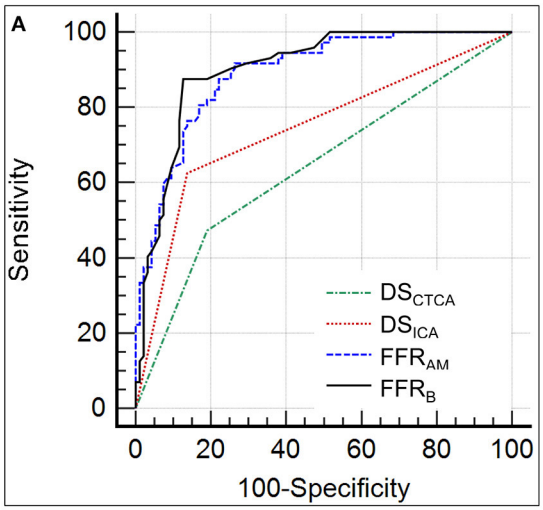

Parameter	AUC (95% CI)
DS_{CTCA}	0.64 (0.56, 0.71)
DS_{ICA}	0.74 (0.67, 0.81)
FFR_{AM}	0.89 (0.84, 0.94)
FFR_B	0.90 (0.85, 0.94)

Compare AUCs of the Parameters	*p*-value
DS_{CTCA} vs. DS_{ICA}	0.02
DS_{CTCA} vs. FFR_{AM}	<0.0001
DS_{ICA} vs. FFR_{AM}	0.0004
DS_{CTCA} vs. FFR_B	<0.0001
DS_{ICA} vs. FFR_B	<0.0001
FFR_{AM} vs. FFR_B	0.57

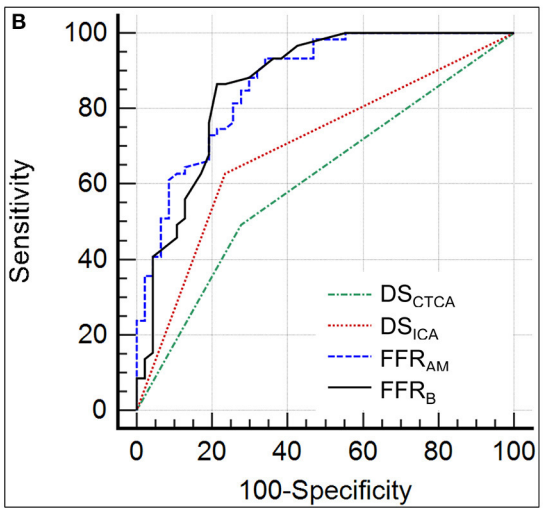

Parameter	AUC (95% CI)
DS_{CTCA}	0.61 (0.51, 0.70)
DS_{ICA}	0.70 (0.60, 0.78)
FFR_{AM}	0.87 (0.79, 0.93)
FFR_B	0.86 (0.78, 0.92)

Compare AUCs of the Parameters	*p*-value
DS_{CTCA} vs. DS_{ICA}	0.11
DS_{CTCA} vs. FFR_{AM}	<0.0001
DS_{ICA} vs. FFR_{AM}	0.0008
DS_{CTCA} vs. FFR_B	<0.0001
DS_{ICA} vs. FFR_B	0.0024
FFR_{AM} vs. FFR_B	0.78

FIGURE 6 | Comparison of the receiver operating characteristic curves for the discrimination of myocardial ischemia (fractional flow reserve, FFR ≤0.8) using diameter stenosis (DS; DS_{CTCA} and DS_{ICA}, with a threshold of 70%) and non-invasive FFR (FFR_{AM} and FFR_B) on **(A)** per-vessel and **(B)** per-patient levels.

role in the accuracy of machine learning. **Table 2** shows the list of anatomical features measured on or derived from CTCA-derived 3D coronary models and their discriminative capability for ischemic lesions. These parameters can aid in the feature selection of diagnostic AI algorithms. Flow quantitation by machine learning can also be facilitated using anatomical features since the coronary flow rates in the lesions that were derived from anatomical information showed a strong correlation with the CFD simulation results in our study ($r = 0.95$, $p < 0.0001$).

Minimal lumen area measured on intravascular ultrasound has been correlated with FFR-ascertained ischemia (32), and a minimal lumen area ≤3.0 mm (2) indicates a high likelihood of significant obstruction in a normal-sized coronary vessel (32). Accordingly, minimal lumen area has been adopted as one of the features for angiography-based machine learning algorithms (33). In our study, the lumen area at the site of maximum stenosis (A_s) was significant smaller in ischemic *vs.* non-ischemic lesions (3.05 ± 1.56 vs. 4.56 ± 2.41 mm^2, $p < 0.0001$), and we believe that it is a prime candidate for feature selection in machine learning. Due to curvature changes in the stenotic region, the flow entrance and exit angles α and β were significantly different between the ischemic and non-ischemic lesions in this study. As such, their effects on FFR prediction can be explored in future machine learning, together with other anatomical parameters, such as lumen areas, lesion lengths, *etc.*

Despite the potential of AI to non-invasive FFR, its clinical application remains challenging. The problem in AI lies in training data paucity, clinical interpretation, commercial deployment, and safety. Our method is based on coronary morphologic parameters and fluid dynamic principles and does not need training data. Importantly, the calculation can be completed with a much shorter computational time than full computational fluid dynamics. Lastly, we have developed a visualization system for physicians to view the computational results from both anatomic modeling and calculated FFR_{AM} and FFR_B. This holds a potential application for the further

personalized management of CAD patients like virtual stent simulation in our recent publication (34).

Limitations of the Study

There are limitations in this study. First, a high calcium score may preclude accurate segmentation, which is a problem common to all CTCA-based analysis. The lumen segmentations were carefully examined by two experienced radiologists in the current study to ensure the accuracy of the results. Second, hyperemia was induced by either an intravenous infusion or intracoronary bolus of adenosine; nonetheless, prior studies have reported that the intravenous infusion of adenosine yielded an identical FFR result compared with intracoronary bolus (35). Lastly, this study did not use recently developed instantaneous wave-free ratio and resting full-cycle ratio non-hyperemic indexes of coronary artery stenosis severity as a reference method.

CONCLUSIONS

In this prospective multicenter study, an analytical method that calculates non-invasive FFR_{AM} from CTCA and anatomical features offers a novel and expeditious non-CFD approach that demonstrated good diagnostic performance for detecting ischemic coronary lesions as ascertained by invasive FFR.

DATA AVAILABILITY STATEMENT

The original contributions presented in the study are included in the article/**Supplementary Material**, further inquiries can be directed to the corresponding authors.

ETHICS STATEMENT

The studies involving human participants were reviewed and approved by SingHealth Centralised Institutional Review Board. The patients/participants provided their written informed consent to participate in this study.

AUTHOR CONTRIBUTIONS

STL and LZ conceived the study design. J-MZ and HH analyzed the data. R-ST, PC, JF, LT, CC, CO, WH, LB, GK, AL, MC, KC, PL, AW, SYT, TC, STL, and LZ interpreted the results. JA performed the statistical analysis. J-MZ drafted the manuscript. R-ST, PC, JF, LT, CC, CO, RL, GC, SL, WH, JA, LB, GK, AL, MC, KC, PL, AW, SYT, TC, STL, and LZ edited and revised the manuscript. All authors read and approved the final manuscript.

FUNDING

This study has received funding from the National Medical Research Council Singapore (NMRC/BnB/0017/2015 and MOH-000358). The funder had no role in the design and conduct of the study; collection, management, analysis, and interpretation of the data; and preparation, review, or approval of the manuscript.

SUPPLEMENTARY MATERIAL

The Supplementary Material for this article can be found online at: https://www.frontiersin.org/articles/10.3389/fcvm.2021.739633/full#supplementary-material

REFERENCES

1. Min JK, Chandrashekhar Y. Atherosclerosis, stenosis, and ischemia: one primary, one secondary, and one tertiary. *JACC Cardiovasc Imaging.* (2018) 11:531–3. doi: 10.1016/j.jcmg.2017.12.006
2. De Bruyne B, Pijls NH, Kalesan B, Barbato E, Tonino PA, Piroth Z, et al. Fractional flow reserve-guided PCI versus medical therapy in stable coronary disease. *N Engl J Med.* (2012) 367:991–1001. doi: 10.1056/NEJMoa1205361
3. Xaplanteris P, Fournier S, Pijls NHJ, Fearon WF, Barbato E, Tonino PAL, et al. Five-year outcomes with PCI guided by fractional flow reserve. *N Engl J Med.* (2018) 379:250–9. doi: 10.1056/NEJMoa1803538
4. Benz DC, Giannopoulos AA. Fractional flow reserve as the standard of reference: all that glistens is not gold. *J Nucl Cardiol.* (2019) 27:1314–6. doi: 10.1007/s12350-019-01771-3
5. Koo BK, Erglis A, Doh JH, Daniels DV, Jegere S, Kim HS, et al. Diagnosis of ischemia-causing coronary stenoses by noninvasive fractional flow reserve computed from coronary computed tomographic angiograms: results from the prospective multicenter DISCOVER-FLOW (diagnosis of ischemia-causing stenoses obtained via noninvasive fractional flow reserve) study. *J Am Coll Cardiol.* (2011) 58:1989–97. doi: 10.1016/j.jacc.2011.06.066
6. Nørgaard BL, Leipsic J, Gaur S, Seneviratne S, Ko BS, Ito H, et al. Diagnostic performance of noninvasive fractional flow reserve derived from coronary computed tomography angiography in suspected coronary artery disease: the NXT trial (analysis of coronary blood flow using CT angiography: next steps). *J Am Coll Cardiol.* (2014) 63:1145–55. doi: 10.1016/j.jacc.2013.11.043
7. Ihdayhid AR, Norgaard BL, Gaur S, Leipsic J, Nerlekar N, Osawa K, et al. Prognostic value and risk continuum of noninvasive fractional flow reserve derived from coronary CT angiography. *Radiology.* (2019) 292:343–51. doi: 10.1148/radiol.2019182264
8. Nørgaard BL, Hjort J, Gaur S, Hansson N, Bøtker HE, Leipsic J, et al. Clinical use of coronary CTA–derived FFR for decision-making in stable CAD. *JACC Cardiovasc Imaging.* (2017) 10:541–50. doi: 10.1016/j.jcmg.2015.11.025
9. Zhang JM, Zhong L, Luo T, Lomarda AM, Huo Y, Yap J, et al. Simplified models of non-invasive fractional flow reserve based on CT images. *PLoS ONE.* (2016) 11:e0153070. doi: 10.1371/journal.pone.0153070
10. Ko BS, Cameron JD, Munnur RK, Wong DTL, Fujisawa Y, Sakaguchi T, et al. Noninvasive CT-derived FFR based on structural and fluid analysis: a comparison with invasive FFR for detection of functionally significant stenosis. *JACC Cardiovasc Imaging.* (2017) 10:663–73. doi: 10.1016/j.jcmg.2016.07.005
11. Zhang JM, Shuang D, Baskaran L, Wu W, Teo SK, Huang W, et al. Advanced analyses of computed tomography coronary angiography can help discriminate ischemic lesions. *Int J Cardiol.* (2018) 267:208–14. doi: 10.1016/j.ijcard.2018.04.020
12. Siogkas PK, Anagnostopoulos CD, Liga R, Exarchos TP, Sakellarios AI, Rigas G, et al. Noninvasive CT-based hemodynamic assessment of coronary lesions derived from fast computational analysis: a comparison against fractional flow reserve. *Eur Radiol.* (2019) 29:2117–26. doi: 10.1007/s00330-018-5781-8
13. Itu L, Rapaka S, Passerini T, Georgescu B, Schwemmer C, Schoebinger M, et al. A machine-learning approach for computation of fractional flow reserve from coronary computed tomography. *J Appl Physiol.* (2016) 121:42–52. doi: 10.1152/japplphysiol.00752.2015
14. Tang CX, Liu CY, Lu MJ, Schoepf UJ, Tesche C, Bayer RR, et al. CT FFR for ischemia-specific CAD with a new computational fluid dynamics

algorithm: a Chinese multicenter study. *JACC Cardiovasc Imaging.* (2020) 13:980–90. doi: 10.1016/j.jcmg.2019.06.018
15. Tesche C, De Cecco CN, Baumann S, Renker M, McLaurin TW, Duguay TM, et al. Coronary CT angiography–derived fractional flow reserve: Machine learning algorithm versus computational fluid dynamics modeling. *Radiology.* (2018) 288:64–72. doi: 10.1148/radiol.2018171291
16. Huo Y, Svendsen M, Choy JS, Zhang Z-D, Kassab GS. A validated predictive model of coronary fractional flow reserve. *J R Soc Interface.* (2012) 9:1325–38. doi: 10.1098/rsif.2011.0605
17. Ahmadi A, Stone GW, Leipsic J, Serruys PW, Shaw L, Hecht H, et al. Association of coronary stenosis and plaque morphology with fractional flow reserve and outcomes. *JAMA Cardiol.* (2016) 1:350–7. doi: 10.1001/jamacardio.2016.0263
18. Bashore TM, Balter S, Barac A, Byrne JG, Cavendish JJ, Chambers CE, et al. 2012 American college of cardiology foundation/society for cardiovascular angiography and interventions expert consensus document on cardiac catheterization laboratory standards update. *J Am Coll Cardiol.* (2012) 59:2221–305. doi: 10.1016/j.jacc.2012.02.010
19. Adjedj J, Xaplanteris P, Toth G, Ferrara A, Pellicano M, Ciccarelli G, et al. Visual and quantitative assessment of coronary stenoses at angiography versus fractional flow reserve: the impact of risk factors. *Circ Cardiovasc Imaging.* (2017) 10:e006243. doi: 10.1161/CIRCIMAGING.117.006243
20. Abbara S, Blanke P, Maroules CD, Cheezum M, Choi AD, Han BK, et al. SCCT guidelines for performance of coronary computed tomographic angiography: a report of the Society of Cardiovascular Computed Tomography Guidelines Committee. *J Cardiovasc Comput Tomogr.* (2009) 3:190–204. doi: 10.1016/j.jcct.2009.03.004
21. Heo R, Park H-B, Lee BK, Shin S, Arsanjani R, Min JK, et al. Optimal boundary detection method and window settings for coronary atherosclerotic plaque volume analysis in coronary computed tomography angiography: comparison with intravascular ultrasound. *Eur Radiol.* (2016) 26:3190–8. doi: 10.1007/s00330-015-4121-5
22. Wieneke H, von Birgelen C, Haude M, Eggebrecht H, Möhlenkamp S, Schmermund A, et al. Determinants of coronary blood flow in humans: quantification by intracoronary doppler and ultrasound. *J Appl Physiol.* (2005) 98:1076–82. doi: 10.1152/japplphysiol.00724.2004
23. Zhang JM, Chandola G, Tan RS, Chai P, Teo LLS, Low R, et al. Quantification of effects of mean blood pressure and left ventricular mass on noninvasive fast fractional flow reserve. *Am J Physiol Heart Circ Physiol.* (2020) 319:H360–9. doi: 10.1152/ajpheart.00135.2020
24. Wilson RF, Wyche K, Christensen BV, Zimmer S, Laxson DD. Effects of adenosine on human coronary arterial circulation. *Circulation.* (1990) 82:1595–606. doi: 10.1161/01.CIR.82.5.1595
25. Rennels DC, Hudson HM. *Pipe Flow: A Practical and Comprehensive Guide*. John Wiley & Sons, Inc. Hoboken, New Jersey (2012). doi: 10.1002/9781118275276
26. Huo Y, Kassab GS. Intraspecific scaling laws of vascular trees. *J R Soc Interface.* (2012) 9:190–200. doi: 10.1098/rsif.2011.0270
27. Zhong L, Zhang JM, Su B, Tan RS, Allen JC, Kassab GS. Application of patient-specific computational fluid dynamics in coronary and intra-cardiac flow simulations: challenges and opportunities. *Front Physiol.* (2018) 9:742. doi: 10.3389/fphys.2018.00742
28. DeLong ER, DeLong D, Clarke-Pearson D. Comparing the areas under two or more correlated receiver operating characteristic curves: a nonparametric approach. *Biometrics.* (1988) 44:837–45. doi: 10.2307/2531595
29. Li M, Zhang J, Pan J, Lu Z. Coronary stenosis: morphologic index characterized by using CT angiography correlates with fractional flow reserve and is associated with hemodynamic status. *Radiology.* (2013) 269:713–21. doi: 10.1148/radiol.13122550
30. Nakazato R, Park HB, Berman DS, Gransar H, Koo BK, Erglis A, et al. Noninvasive fractional flow reserve derived from computed tomography angiography for coronary lesions of intermediate stenosis severity results from the DeFACTO study. *Circ Cardiovasc Imaging.* (2013) 6:881–9. doi: 10.1161/CIRCIMAGING.113.000297
31. Coenen A, Lubbers MM, Kurata A, Kono A, Dedic A, Chelu RG, et al. Fractional flow reserve computed from noninvasive CT angiography data: diagnostic performance of an on-site clinician-operated computational fluid dynamics algorithm. *Radiology.* (2015) 274:674–83. doi: 10.1148/radiol.14140992
32. Kang J, Koo BK, Hu X, Lee JM, Hahn JY, Yang HM, et al. Comparison of fractional flow reserve and intravascular ultrasound-guided intervention strategy for clinical outcomes in patients with intermediate stenosis (FLAVOUR): rationale and design of a randomized clinical trial. *Am Heart J.* (2018) 199:7–12. doi: 10.1016/j.ahj.2017.11.001
33. Cho H, Lee JG, Kang SJ, Kim WJ, Choi SY, Ko J, et al. Angiography-based machine learning for predicting fractional flow reserve in intermediate coronary artery lesions. *J Am Heart Assoc.* (2019) 8:e011685. doi: 10.1161/JAHA.118.011685
34. Chandola G, Zhang JM, Tan RS, Chai P, Teo L, Allen JC, et al. Computed tomography coronary angiography and computational fluid dynamics based on fractional flow reserve before and after percutaneous coronary intervention. *Front Bioeng Biotechnol.* (2021) 9:739667. doi: 10.3389/fbioe.2021.739667
35. Schlunt C, Bietau C, Klinghammer L, Wiedemann R, Rittger H, Ludwig J, et al. Comparison of intracoronary versus intravenous administration of adenosine for measurement of coronary fractional flow reserve. *Circ Cardiovasc Interv.* (2015) 8:e001781. doi: 10.1161/CIRCINTERVENTIONS.114.001781

Conflict of Interest: The authors declare that the research was conducted in the absence of any commercial or financial relationships that could be construed as a potential conflict of interest.

Publisher's Note: All claims expressed in this article are solely those of the authors and do not necessarily represent those of their affiliated organizations, or those of the publisher, the editors and the reviewers. Any product that may be evaluated in this article, or claim that may be made by its manufacturer, is not guaranteed or endorsed by the publisher.

frontiers in Cardiovascular Medicine

ORIGINAL RESEARCH
published: 17 November 2021
doi: 10.3389/fcvm.2021.765961

Fast-Strain Encoded Cardiac Magnetic Resonance During Vasodilator Perfusion Stress Testing

Henning Steen[1], *Moritz Montenbruck*[2], *Sebastian Kelle*[3,4,5], *Sebastian Esch*[2], *Arne Kristian Schwarz*[2], *Sorin Giusca*[6,7] *and Grigorios Korosoglou*[6,7]*

[1] Medneo, Hamburg, Germany, [2] Cardiology/Cardiac Imaging, Marien Hospital, Hamburg, Germany, [3] Department of Internal Medicine/Cardiology, Deutsches Herzzentrum Berlin, Berlin, Germany, [4] Department of Internal Medicine and Cardiology, Charité—Universitätsmedizin Berlin, Campus Virchow-Klinikum, Berlin, Germany, [5] Deutsches Zentrum für Herz-Kreislauf-Forschung (DZHK) (German Centre for Cardiovascular Research), Berlin, Germany, [6] Department of Cardiology, Vascular Medicine and Pneumology, Gesundheitszentren Rhein-Neckar (GRN) Hospital Weinheim, Weinheim, Germany, [7] Cardiac Imaging Center Weinheim, Hector Foundation, Weinheim, Germany

OPEN ACCESS

Edited by:
Fabrizio Ricci,
University of Studies G. d'Annunzio Chieti and Pescara, Italy

Reviewed by:
Theo Pezel,
Hôpital Lariboisière, France
Jérôme Garot,
Institut Cardiovasculaire Paris Sud, France
Dominik Buckert,
Ulm University Medical Center, Germany

***Correspondence:**
Grigorios Korosoglou
gkorosoglou@hotmail.com

Specialty section:
This article was submitted to Cardiovascular Imaging, a section of the journal Frontiers in Cardiovascular Medicine

Received: 27 August 2021
Accepted: 11 October 2021
Published: 17 November 2021

Citation:
Steen H, Montenbruck M, Kelle S, Esch S, Schwarz AK, Giusca S and Korosoglou G (2021) Fast-Strain Encoded Cardiac Magnetic Resonance During Vasodilator Perfusion Stress Testing. Front. Cardiovasc. Med. 8:765961. doi: 10.3389/fcvm.2021.765961

Background: Cardiac magnetic resonance perfusion imaging during vasodilator stress is an established modality in patients with suspected and known coronary artery disease (CAD).

Aim: This study aimed to evaluate the performance of fast-Strain-Encoded-MRI (fast-SENC) for the diagnostic classification and risk stratification of patients with ischemic heart disease.

Methods: Perfusion and fast-SENC cardiac magnetic resonance (CMR) images were retrospectively analyzed in 111 patients who underwent stress CMR. The average myocardial perfusion score index, global and segmental longitudinal and circumferential strain (GLS and GCS and SLS and SCS, respectively), were measured at rest and during stress. The combination of SLS and SCS was referred to as segmental aggregate strain (SAS). Segments exhibiting perfusion defects or SAS impairment during stress were defined as "ischemic." All-cause mortality, non-fatal infarction, and urgent revascularization were deemed as our combined clinical endpoint.

Results: During adenosine stress testing, 44 of 111 (39.6%) patients exhibited inducible perfusion abnormalities. During a mean follow-up of 1.94 ± 0.65 years, 25 (22.5%) patients reached the combined endpoint (death in $n = 2$, infarction in $n = 3$ and urgent revascularization in $n = 20$). Inducible perfusion defects were associated with higher number of segments with inducible SAS reduction ≥6.5% ($\chi^2 = 37.8$, AUC = 0.79, 95% CI = 0.71–0.87, $p < 0.001$). In addition, patients with inducible perfusion defects or SAS impairment exhibited poorer outcomes ($AUC_{Perf} = 0.81$ vs. $AUC_{SAS} = 0.74$, p = NS vs. each other, and $\chi^2 = 30.8$, HR = 10.3 and $\chi^2 = 9.5$, HR = 3.5, respectively, $p < 0.01$ for both).

Conclusion: Purely quantitative strain analysis by fast-SENC during vasodilator stress was related to the diagnosis of ischemia by first-pass perfusion and is non-inferior for the risk stratification of patients with ischemic heart disease. This may bear clinical implications, especially in patients with contraindications for contrast agent administration.

Keywords: fast strain-encoded CMR (fast-SENC), average perfusion score index, adenosine, late gadolinium enhancement, cardiac outcomes

INTRODUCTION

Cardiovascular diseases are the main cause of morbidity and death in the world, annually claiming more lives than all forms of cancer together (1). Non-invasive anatomical imaging of coronary arteries by cardiac computed tomography and functional stress testing like cardiac magnetic resonance (CMR) is currently recommended as first-line diagnostic techniques in patients with suspected or known coronary artery disease (CAD) (2, 3). In this regard, stress CMR is a well-established method for the diagnostic classification and risk stratification of such patients (4–8). Especially vasodilator stress CMR is widely used due to its excellent safety profile and superior accuracy compared with scintigraphy (5, 8, 9).

Currently, the detection of inducible ischemia during vasodilator stress CMR is mostly based on the visual assessment of perfusion defects (5–8), which is subjective and depends on the experience of the readers. In this regard, fast-Strain-Encoded-MRI (fast-SENC) has been utilized for the objective assessment of longitudinal and circumferential myocardial strain (LS and CS) in previous studies [summarized in (10)]. The ability of this technique to diagnose relevant CAD during inotropic stress and predict future adverse events has been previously demonstrated (11, 12). However, limited data are available on the value of fast-SENC to accurately identify perfusion defects and to provide risk stratification in patients who undergo vasodilator stress CMR.

Therefore, we sought to determine the diagnostic and prognostic value of SENC during vasodilator stress in patients with known or suspected CAD. Global LS (GLS) and CS (GCS) and average global strain (GS), as well as segmental LS (SLS) and CS (SCS) and combined information from SLS or SCS, referred to as segmental aggregate strain (SAS) were compared with perfusion data.

Abbreviations: AUC, area under the curve; BMI, body mass index; CABG, coronary artery bypass graft; CMR, cardiovascular magnetic resonance; CAD, coronary artery disease; CCS, chronic coronary syndromes; CS, circumferential strain; Fast-SENC, fast strain encoded sequence; GCS, global circumferential strain; GFR, glomerular filtration rate; GLS, global longitudinal strain; GS, global strain; LGE, late gadolinium enhancement; LS, longitudinal strain; LV, left ventricle; PCI, percutaneous coronary intervention; RV, right ventricle; SCS, segmental circumferential strain; SCS, segmental circumferential strain; SAS, segmental aggregate strain.

METHODS

Study Population

Our patient cohort consisted of patients who underwent adenosine stress CMR between September 2017 and July 2019 in the Marien Hospital Hamburg, Hamburg, Germany and had verified follow-up outcomes. Patients were referred for stress CMR due to known or suspected CAD based on current guidelines (2). CMR was performed as part of standard institutional protocols. All patients were above 18 years old and gave written informed consent. The study was conducted in concordance with the Declaration of Helsinki. Patients were excluded from the study in case of claustrophobia, contraindications to adenosine, such as the history of asthma, low blood pressure, clinical instability, advanced atrioventricular block, or sinus bradycardia, known allergy to gadolinium-based contrast agents, renal failure with a glomerular filtration rate (GFR) $<$ 30 ml/kg/min or inability to give informed consent. All patients were deferred from consuming caffeine-containing beverages and food for 24 h before the examination. If this was not the case the examination was postponed to a later timepoint. Prior to the examination, demographic data, including the presence of arterial hypertension, hyperlipidemia, diabetes mellitus, and previous CAD were acquired.

Cardiac Magnetic Resonance Examination

Examinations were performed using a 1.5 T MR system (Achieva, Philips Healthcare, Best, The Netherlands) equipped with cardiac phased-array receiver coils. Data acquisition was triggered on the R-wave using a 4-lead vector ECG. Cine images were obtained using a breath-hold segmented-k-space balanced fast-field echo sequence (SSFP), employing retrospective ECG gating in long-axis planes (2-, 4-, and 3-chamber views) and contiguous short-axis slices covering the whole ventricles, with typically reconstructed 30 phases per cardiac cycle with 50 and 67% acquired heart phases, respectively, for short and long-axis images.

Adenosine Stress CMR Protocol and Image Acquisitions

A standard protocol for adenosine stress CMR was used, which is described in detail elsewhere (13). In short, patients received a continuous infusion of adenosine. The dose was varied between 140 and 210 μg/kg/min depending on heart rate change and clinical symptoms. During the infusion, patients were

continuously monitored for heart rate and oxygen saturation, and blood pressure was measured every minute. The stress perfusion acquisition was started after at least 3–4 min of the adenosine infusion and when two criteria were met: increase in heart rate of at least 10–15 beats per minute and/or the blood pressure fall of at least 10 mmHg or both and the occurrence of symptoms related to the adenosine infusion. In case of no heart rate or blood pressure response, the dose of the adenosine infusion was increased to 175 or 210 μg/kg body weight/min until a response was observed. In addition, the presence of splenic switch-off was verified according to current recommendations (14). Stress acquisitions were performed using a gadolinium-based contrast agent (Dotarem®- gadoterate meglumine in a dosage of 0.05 mmol/kg). Three short-axis slices were acquired using a single-shot saturation recovery gradient echo sequence (FOV 320 mm, slice thickness = 8 mm, TE = 1.02 ms, TR = 226 ms, TI = 140 ms, Flip angle = 50°). Fast-SENC acquisitions were performed at baseline, and repeated acquisitions were performed in identical planes during infusion of adenosine after meeting the criteria mentioned above and before the administration of gadolinium for the acquisitions of first-pass perfusion scans. The rest perfusion was performed after 10 min using identical planes and the same dosage of the contrast agent. Afterward, late gadolinium enhancement (LGE) acquisitions were performed in three long-axis and multiple short axes, covering the entire left ventricle.

Evaluation of Myocardial Perfusion

All analyses were performed on a commercially available workstation (CVI 42, Circle Cardiovascular Imaging Inc., Calgary, Canada). Results for ventricular volumes, left- and right-ventricular (LV and RV) ejection fraction (%), and myocardial mass were derived from short-axis slices. The presence of myocardial perfusion defects was performed visually in three short-axis images. A perfusion defect was defined as a region in the myocardium exhibiting hypo-enhancement by visual criteria that persists after peak myocardium enhancement for at least 4 RR intervals and corresponds to a coronary territory (15). In addition, semiquantitative perfusion analysis was performed by using a 3-point grading scale (16):

1 = Normal Perfusion,
2 = Perfusion Deficits With <50% Transmurality and
3 = Perfusion Deficits With ≥50% Transmurality During Adenosine Stress

Corresponding images in a patient with normal perfusion during stress, with a subendocardial and with a transmural perfusion defect during vasodilator stress are provided in our **Supplementary Figure 1**. Based on this grading system, an average perfusion score index was built for analysis by patients, by calculating the mean score in 17 myocardial segments, as recommended by the AHA (17). Images were analyzed by experienced operators with more than 10 years of experience in cardiovascular imaging and acquired level 3 certification by the German Society of Cardiology (HS & MM).

Single Heartbeat Fast-SENC Acquisitions

As described previously, fast-SENC is based on the acquisition of high- and low-tuning image sequences with different frequency modulation. Fast-SENC image sequences were analyzed using the MyoStrain software (Myocardial Solutions, Inc., Morrisville, North Carolina, USA), as described previously (18).

With fast-SENC, bright regions in the two frequency modulation images represented static and fully contracted tissues, respectively. Circumferential and longitudinal strain within a range from 5 to −30% were encoded, with negative values translating into active myocardial contraction. In our study, a single heartbeat, a fast-SENC variant with single-shot spiral readouts was employed. Typical imaging parameters were as follows: field-of-view = 256 × 256 mm, slice thickness = 10 mm, voxel size = 4 × 4 × 10 mm, reconstructed resolution = 1 × 1 × 10 mm, single-shot spiral readout with acquisition time TA = 10 ms, flip angle = 30°, effective echo time (TE) = 0.7 ms, repetition time (TR) = 12 ms, temporal resolution = 36 ms, the typical number of acquired heart phases = 22, spectrally selective fat suppression (SPIR), and total acquisition time per slice < 1 s. Data were acquired in three long-axis (four-, three-, and two-chamber) views, and three short-axis views of the LV (basal, mid-ventricular, and apical).

Global circumferential strain by fast-SENC is extracted from 3 long-axis views, whereas GLS is extracted from the 3 short-axis images. The endocardial and epicardial borders were drawn at the end-systolic cardiac phase and are traced throughout the cardiac cycle, using an automatic tissue tracking algorithm. Tracking is then verified and manually corrected if necessary. A 16-segment model was used for the GLS and a 21-segment model for the GCS. For the analysis, GLS and GCS were expressed as the average value of all 16 and 21 segments, respectively. In addition, a GS was calculated by averaging LS and CS in all available segments (19, 20).

Global circumferential strain, GLS, and GS were measured both at baseline and during adenosine stress. In addition, segments with relevant segmental LS and/or CS strain (SAS) impairment during stress were defined as ischemic. The number of such "ischemic" segments was calculated for SLS, SCS, and SLS or SCS which was referred to as SAS in each patient.

Because myocardial shortening occurred in both longitudinal and circumferential directions during systole, the strain values were consequently negative and were so reported. However, throughout the text, and in keeping with most of the literature on the subject, we refer to the absolute values, i.e., higher strain values meaning more deformation and consequently more "negative" values.

Definition of Study Endpoints

Personnel unaware of the CMR results contacted all patients or relatives of patients who underwent stress CMR studies during follow-up. All-cause mortality, the occurrence of non-fatal myocardial infarction, and urgent coronary revascularization by PCI or CABG were selected as the combined primary endpoint of our study. We used all-cause and not only cardiovascular mortality as an endpoint since the prior is free of potential subjectivity, clinically compelling, and therefore most relevant

to the patients (21). In addition, urgent revascularization was fulfilled only if patients were hospitalized unexpectedly because of persisting or increasing chest pain and revascularization was performed urgently within the same hospitalization (22).

Statistical Analysis

Data were presented as $M \pm SD$ for continuous variables and as absolute values and percentages for categorical values. A paired *t*-test was used to compare two groups of normally distributed values. The ANOVA test was used for comparing three or more normally distributed groups with the Scheffé test for *post-hoc* analysis (23). The Mann-Whitney test was used to compare ordinal variables and the Fisher test to compare nominal variables. A Pearson correlation test was employed to test the relation between strain and perfusion variables. A receiver operator characteristics (ROC) analysis was used to identify the best parameter that identifies the presence of perfusion abnormalities or cardiac endpoints. Comparison of the areas under the curve (AUC) of paired data ROC curves was performed using the DeLong method (24). Survival curves were estimated by the Kaplan-Meier method and compared by log-rank tests. In addition, a hierarchic logistic regression model was used to assess the incremental value of myocardial perfusion and strain to clinical variables (age, diabetes mellitus, and history of CAD) for the prediction of the combined endpoint by calculating the corresponding total χ^2 values. Inter- and intra-observer variabilities for strain values were assessed by repeated analysis of 40 randomly selected patients and were calculated as the ratio of the standard deviation to the mean. Based on a statistical power of 90%, a two-sided type I error of 0.05, and the expected *SD* of the results, as well as the expected margins of error (pre-specified non-inferiority margin), we calculated that a minimum of 70 patients would be necessary for our study for a comparison between strain and conventional first-pass perfusion imaging. The MedCalc software version 20.009 (MedCalc, Ostend, Belgium, 2019) was used throughout. All $p < 0.05$ were considered statistically significant.

RESULTS

Demographic, CMR, and Outcome Data

Complete CMR and follow-up data were available in 111 individuals who underwent vasodilator stress perfusion CMR for clinical reasons. Demographic, clinical, and CMR data are

TABLE 1 | Demographic, clinical, and CMR data from our patient cohort.

	All patients ($n = 111$)	Patients w/o inducible perfusion defects ($n = 67$)	Patients with inducible perfusion defects ($n = 44$)	*P*-values	Patients w/o cardiac endpoints (Death/MI/PCI) ($n = 86$)	Patients with cardiac endpoints (Death/MI/PCI) ($n = 25$)	*P*-values
Demographic data							
Age (years)	62.6 ± 11.8	61.4 ± 12.5	64.4 ± 10.4	0.19	62.2 ± 12.6	63.8 ± 8.7	0.56
Male gender	76 (68%)	47 (70%)	29 (66%)	0.64	62 (72%)	14 (56%)	0.13
Arterial hypertension	88 (79%)	53 (79%)	35 (80%)	0.96	69 (80%)	19 (76%)	0.65
Type 2 diabetes mellitus	28 (25%)	20 (30%)	8 (18%)	0.17	20 (23%)	8 (32%)	0.38
Hyperlipidemia	84 (76%)	51 (76%)	33 (75%)	0.89	63 (73%)	21 (84%)	0.28
Past myocardial infarction	16 (14%)	10 (15%)	6 (14%)	0.85	11 (13%)	5 (20%)	0.37
Known CAD	74 (67%)	41 (61%)	33 (75%)	0.13	54 (63%)	20 (80%)	0.11
Body-mass-index (kg/m^2)	27.0 ± 3.8	26.7 ± 4.0	27.4 ± 3.5	0.34	26.9 ± 4.0	27.2 ± 3.3	0.73
Baseline CMR data							
LV ejection fraction (%)	57.1 ± 7.2	57.1 ± 6.8	57.0 ± 7.9	0.96	56.7 ± 7.5	58.6 ± 6.1	0.25
IVS (mm)	11.0 ± 2.1	10.9 ± 2.1	11.2 ± 2.1	0.37	11.2 ± 2.1	10.4 ± 1.7	0.12
Lateral wall (mm)	7.3 ± 2.0	7.3 ± 1.8	7.3 ± 2.3	0.94	7.3 ± 2.0	7.4 ± 2.0	0.74
LV mass (g)	109.2 ± 25.2	104.7 ± 22.0	116.0 ± 28.4	0.02	109.2 ± 24.7	109.0 ± 27.6	0.97
LV mass index (g/m^2)	56.2 ± 10.9	54.4 ± 8.9	59.0 ± 13.1	0.03	56.1 ± 11.0	56.6 ± 11.0	0.82
Native T1 values	1,042 ± 3,446	1,047 ± 32	1,037 ± 35	0.22	1,044 ± 32	1,037 ± 41	0.53
RV ejection fraction (%)	55.8 ± 6.2	56.5 ± 6.4	54.7 ± 5.6	0.12	55.8 ± 6.4	55.9 ± 5.5	0.98
Wall motion score index	1.16 ± 0.33	1.19 ± 0.38	1.11 ± 0.25	0.19	1.19 ± 0.37	1.05 ± 0.14	0.07
CAD related LGE score	1.13 ± 0.28	1.12 ± 0.30	1.13 ± 0.22	0.93	1.13 ± 0.30	1.12 ± 0.19	0.91
Perfusion and strain CMR data							
Perfusion defect (yes/no)	44 (40%)	67 (0%)	44 (100%)	N.A.	22 (26%)	22 (88%)	<0.001
Average perfusion score index	1.12 ± 0.19	1.0 ± 0.0	1.3 ± 0.18	<0.001	1.09 ± 0.15	1.28 ± 0.22	<0.001
GS (%) at baseline	−18.7 ± 2.0	−18.9 ± 1.96	−18.4 ± 2.0	0.18	−18.7 ± 1.9	−18.5 ± 2.1	0.57
GS (%) during stress	−19.4 ± 3.3	−19.8 ± 1.7	−18.9 ± 1.9	0.005	−19.5 ± 1.9	−19.2 ± 1.5	0.54

CAD, coronary artery disease; IVS, intraventricular septum; LGE, late gadolinium enhancement; MI, myocardial infarction; PCI, percutaneous coronary intervention; LV, left ventricular; RV, right ventricular; GS, global strain; w/o, without; CMR, cardiac magnetic resonance.

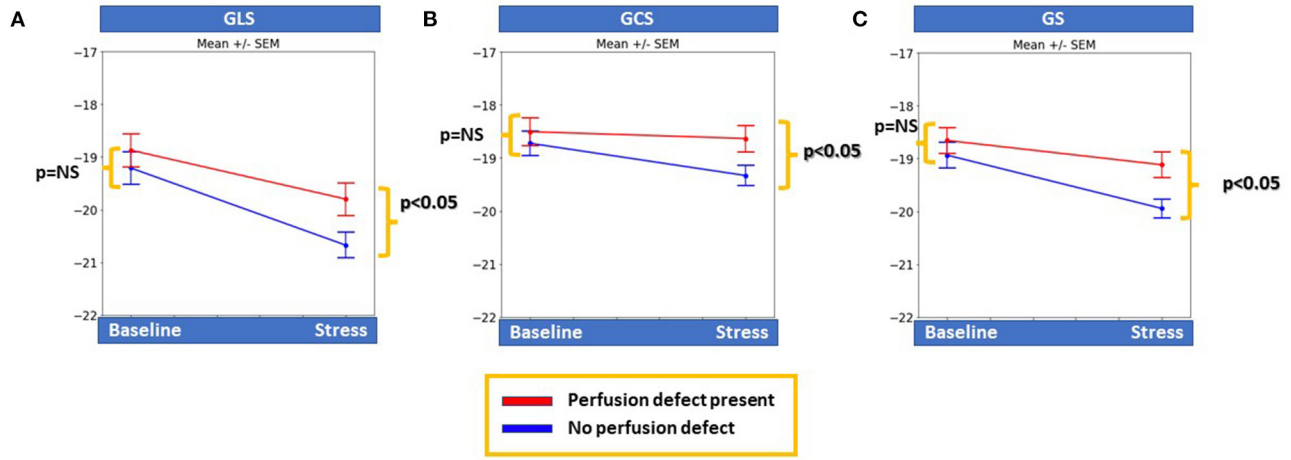

FIGURE 1 | Patients with inducible perfusion abnormalities had significantly lower global longitudinal and circumferential myocardial strain (GLS and GCS, respectively), as well as global strain (GS) during stress compared to patients with negative stress results ($p < 0.05$ for all), whereas baseline strain values were similar for all markers between the two groups **(A–C)**.

provided in **Table 1**. Mean age was 62.6 ± 11.8 years old whereas 28 (25%), 84 (76%), and 16 (14%) patients had diabetes mellitus, hyperlipidemia, and previous infarction, respectively.

During the adenosine stress test, 44 of 111 (39.6%) patients exhibited inducible perfusion abnormalities. Patients with inducible perfusion abnormalities had similar demographic and baseline CMR data to those with negative stress results, except for LV-mass, which was increased in patients with inducible perfusion abnormalities. However, significant differences were observed with the average perfusion score index and for global strain parameters during stress in patients with vs. without perfusion abnormalities (**Table 1**).

Association Between Myocardial Strain and Perfusion

Patients with inducible perfusion defects had significantly lower GLS, GCS, and GS during stress ($p < 0.05$ for all) compared with patients without perfusion defects, whereas all baseline strain values were similar between the 2 groups (**Figures 1A–C**).

Based on *a priori* ROC analysis, a cut-off value of 6.5% for absolute segmental strain (SLS, SCS, and SAS) reduction during vasodilator stress was selected as best indicative for the presence of segmental myocardial ischemia by perfusion analysis. Thus, the number of ischemic segments with inducible SLS, SCS, or SAS decrease ≥6.5% were all indicative for the presence of inducible perfusion defects, with SAS exhibiting the highest accuracy, followed by SCS and SLS ($AUC_{SCS} = 0.78$, 95% CI = 0.69–0.84, $AUC_{SAS} = 0.79$, 95% CI = 0.71–0.87 and $AUC_{SLS} = 0.58$, 95% CI = 0.49–0.68; $p < 0.05$ for SLS vs. SAS and SCS, **Figure 2A**). Therefore, SAS values deriving information both from longitudinal and circumferential deformation were used for further analysis. Corresponding sensitivities and specificities are provided in **Table 2A**.

Patients with inducible perfusion defects exhibited a higher number of segments with inducible SAS decrease ≥6.5% ($\chi^2 = 37.8$, $p < 0.001$) and significantly higher absolute SAS decrease during adenosine stress ($p < 0.001$) (**Figures 2B,C**). In addition, a weak inverse correlation was observed between the average perfusion score and the SAS decrease during stress ($r = -0.34$, $p < 0.01$; **Figure 2D**). On a segmental level, a slight absolute SLS decrease and a blunted SLS increase were noticed in segments with subendocardial and transmural perfusion defects, respectively, compared with segments with normal perfusion during stress, exhibiting a slight SLS increase (**Supplementary Figure 2A**). The same patterns were observed after the exclusion of segments with LGE (**Supplementary Figure 2B**). Additional correlations between perfusion and strain parameters are provided in **Table 3**.

Association With Perfusion and SAS With Clinical Endpoints

During a mean follow-up duration of 1.94 ± 0.65 years, 2 patients died, 3 had a non-fatal myocardial infarction and 20 underwent urgent coronary revascularization by PCI ($n = 15$) or CABG ($n = 5$).

A significant association was observed between inducible perfusion abnormalities and the combined endpoint ($\chi^2 = 31.7$, contingency coefficient = 0.47, $p < 0.001$). The perfusion score index was significantly higher in patients with vs. without cardiac endpoints (**Figure 3A**).

In addition, patients with cardiac endpoints exhibited higher SAS decrease and higher number of ischemic segments by SAS during stress compared with those without cardiac endpoints ($p < 0.001$ for both; **Figures 3B,C**). A strong association also was present between the presence of ischemic segments by SAS and future events ($\chi^2 = 15.2$, $p < 0.001$; **Figure 3D**).

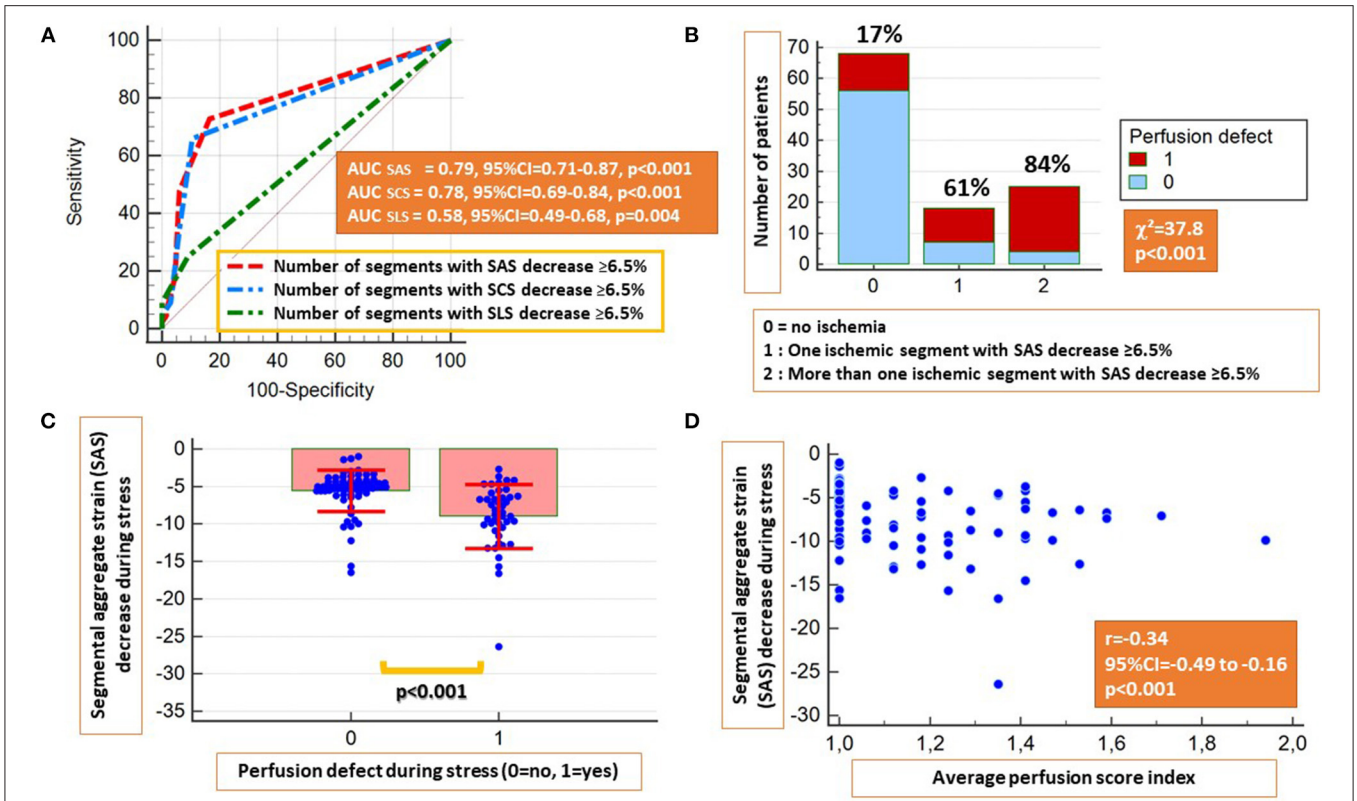

FIGURE 2 | The presence of inducible strain decrease ≥6.5% by segmental LS (SLS), segmental CS (SCS), and segmental aggregate strain (SAS) during stress were all indicative for the presence of inducible perfusion abnormalities, with SCS and SAS exhibiting higher accuracies **(A)**. Patients with inducible perfusion abnormalities exhibited a higher number of ischemic segments by SAS **(B)** and higher absolute SAS decrease during stress **(C)**. A moderate inverse correlation was observed between the perfusion score index and inducible SAS decrease **(D)**.

TABLE 2 | Sensitivities, specificities, and accuracy values for **(A)** detection of inducible perfusion abnormalities by strain and **(B)** Prediction of outcomes using perfusion and strain parameters.

	Parameters	Criterion	Sensitivity	Specificity	AUC	*p*-values
A. Presence of inducible perfusion abnormalities						
Presence of perfusion defects	GS during stress (%)	> −19.8%	71%	64%	0.65	0.004
	SAS strain reduction ≥6.5%	≥6.5%	77%	81%	0.78	0.05 vs. SLS and p = NS vs. SCS
	Number of segments with SAS reduction≥6.5%	≥1 segment	73%	84%	0.79	
B. Cardiac outcomes during follow-up						
Prediction of cardiac endpoint during follow-up	Average perfusion score index	>1.06	82%	77%	0.82	P = NS for perfusion abnormalities or index vs. SAS
	Perfusion abnormality present	≥1	86%	76%	0.81	
	Number of segments with SAS reduction ≥6.5%	≥1	75%	74%	0.74	
	At least one segment with SAS reduction ≥6.5%	≥1	75%	74%	0.74	

AUC, area under the curve; GS, global strain; SAS, segmental aggregate strain; SLS, segmental longitudinal strain; SCS, segmental circumferential strain.

Prediction of Endpoints by Perfusion and Segmental Strain

Both visual perfusion and quantitative SAS analysis predicted the combined cardiac endpoint with similar accuracy rates (AUC = 0.81, 95% CI = 0.72–0.88 vs. 0.74, 95% CI = 0.65–0.82; ΔAUC =0.065, p = NS). Similarly, the perfusion score index performed as well as the number of ischemic segments by SAS, predicting the combined endpoint (AUC = 0.82, 95% CI = 0.73–0.88 vs.0.74, 95% CI = 0.65–0.82; ΔAUC = 0.075, p = NS; **Figures 4A,B**). The corresponding sensitivity and specificity values and Kaplan-Maier curves are provided in **Table 2B** and **Figures 4C,D**, respectively.

The independent association of perfusion and SAS with cardiac outcomes were confirmed by multivariable regression

analysis (**Table 4**). In addition, the presence of impaired SAS during stress exhibited incremental value to perfusion imaging and clinical data for the prediction of the combined endpoint, as shown by the acquired χ^2 values (**Figure 5**).

Intra and Interobserver Variabilities

Intra- and interobserver variabilities for LS, CS were 1.5 and 1.6% and 2.1 and 2.3%, respectively. Total acquisition time was <15 s per patient, whereas the time spent required for quantitative analysis of LS, CS, and SAS was 304 ± 125 s (5.1 ± 2.1 min) per patient.

TABLE 3 | Correlations between the average perfusion score index and strain parameters during stress.

Parameters	GS during stress	Minimum SAS difference during stress	Number of segments with inducible SAS decrease ≥6.5%
Average perfusion score	−0.20 $P = 0.03$	−0.34 $P < 0.001$	0.35 $P < 0.001$

GS, global strain; SAS, segmental aggregate strain.

Patient Case Example

A 58-year-old female patient with arterial hypertension, hyperlipidemia and suspected CAD due to atypical angina underwent adenosine stress CMR, which did not show abnormal findings (not shown). Normal strain response was seen by fast-SENC in the short axis views (**Figures 6A–F**). However, abnormal strain response was detected in the corresponding 3 chamber view fast-SENC images (**Figures 6G,H**) with a significant inducible strain decrease in the apical cap (red arrow in **Figure 6H** and the corresponding bull's eye maps in **Figure 6I**). Due to the absence of a perfusion defect cardiac catheterization was deferred. However, after 1 year the patient underwent urgent revascularization by PCI and stent placement in the LAD.

DISCUSSION

In this analysis of 111 patients with complete perfusion, segmental strain analysis, and follow-up outcomes, we found that:

I. Myocardial perfusion abnormalities during vasodilator administration were associated with clinical outcomes.

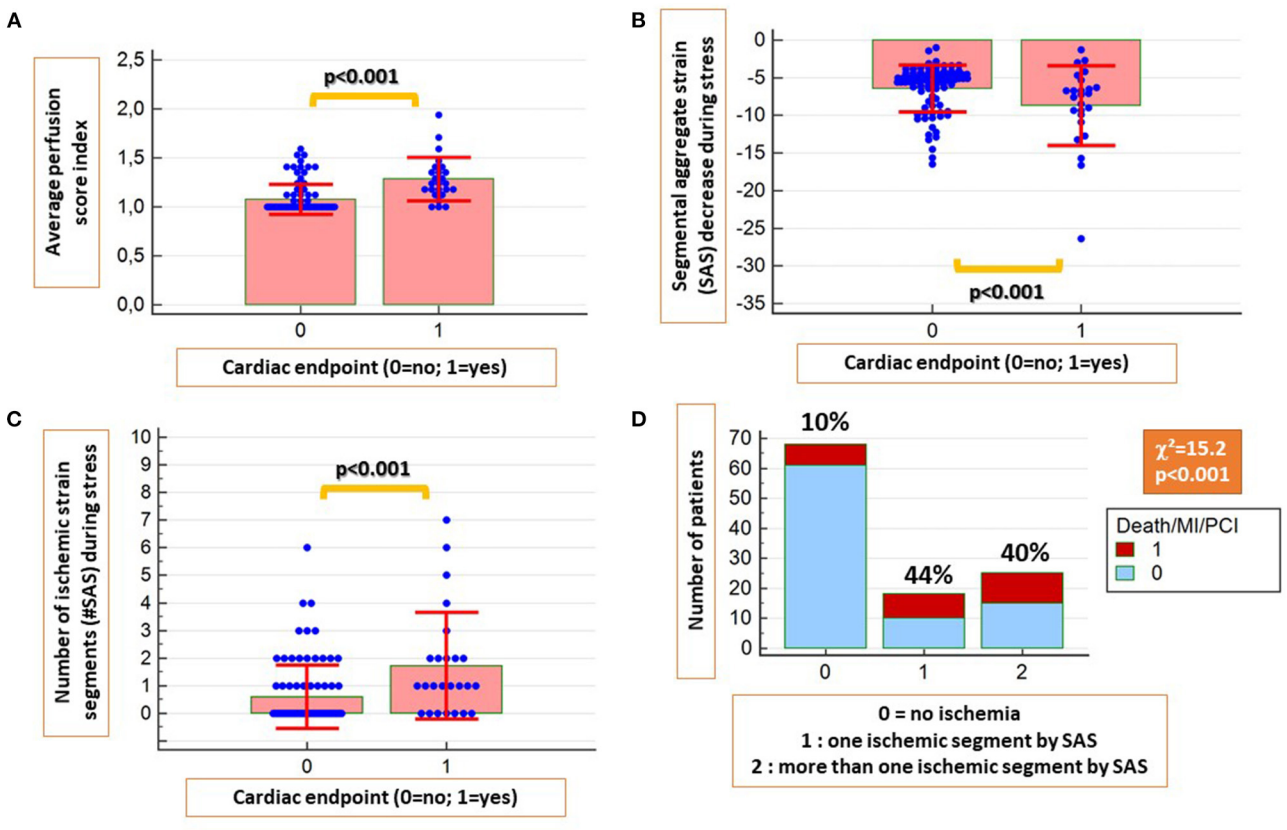

FIGURE 3 | The average perfusion score index was significantly higher in patients with future cardiac endpoints **(A)**. Similarly, patients with cardiac endpoints had significantly higher absolute SAS decrease during stress **(B)** and a higher number of ischemic segments by SAS **(C)**. In addition, a strong association was present between ischemic segments by SAS and future cardiac events **(D)**.

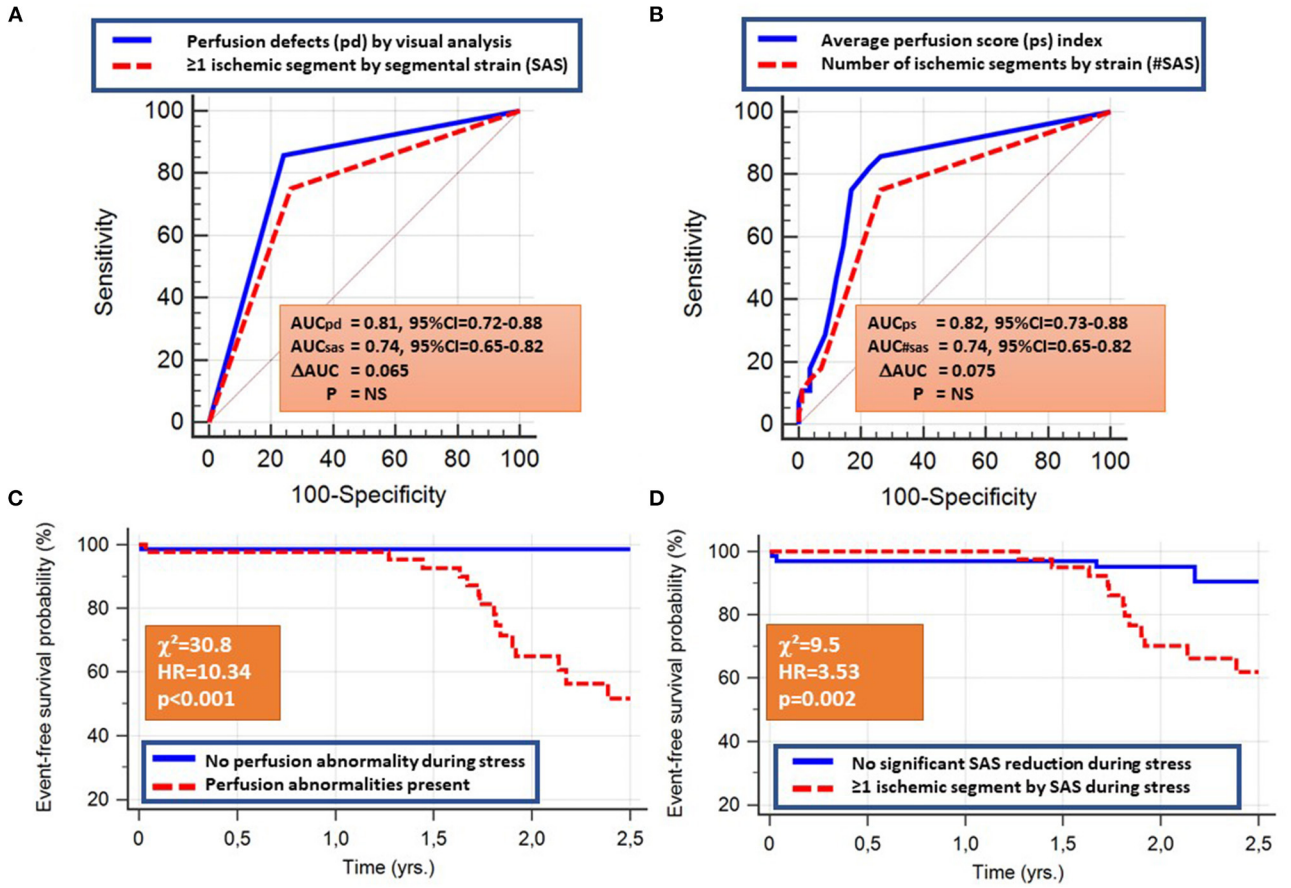

FIGURE 4 | The presence of perfusion abnormalities or at least one ischemic segment by SAS, the average perfusion score, and the number of ischemic segments by SAS all predicted the combined cardiac endpoint with similar accuracy rates **(A,B)**. The corresponding Kaplan-Maier curves are provided in **(C,D)**.

TABLE 4 | Multiple regression analysis for the prediction of the combined endpoint death, non-fatal myocardial infarction, and urgent coronary revascularization during follow-up.

	Coefficients	$r_{partial}$	*p*-values
Age (yrs)	0.00035	0.01	0.91
LVEF (%)	0.0046	0.08	0.40
CAD related LGE score	−0.02	−0.013	0.88
Average perfusion score	0.82	0.36	0.0002
Ischemic segments by SAS	0.23	0.26	0.006

LVEF, left ventricular ejection fraction; SAS, segmental aggregate strain; LGE, late gadolinium enhancement; CAD, coronary artery disease.

II. Evaluation of segmental myocardial strain during baseline and vasodilator stress using fast-SENC was feasible with high reproducibility and within reasonable time-spent.
III. An inducible absolute SAS decrease ≥6.5% during adenosine stress in one or more myocardial segments was associated with inducible perfusion abnormalities during first-pass perfusion imaging.
IV. Perfusion and strain abnormalities during vasodilator stress predicted future cardiac outcomes in patients with ischemic heart disease. Overall, perfusion defects showed numerically higher predictive values for future events, which was an expected finding since perfusion is a well-established marker for the prediction of future events (4, 7). However, segmental strain measures exhibited independent and incremental value for the prediction of outcomes.

Previous Studies

We and others had previously described the incremental value of SENC both for the diagnostic classification and for the risk stratification of patients with suspected and known CAD (11, 12). Quantitative strain analysis enabled the identification of myocardial ischemia already during intermediate stages of inotropic stress, thus exhibiting enhanced sensitivity for the detection of CAD (12). In addition, the incremental value of SENC was demonstrated for the prediction of clinical outcomes during inotropic stress (11). Despite the presence of wide evidence for the diagnostic and prognostic value of inotropic strain in patients with ischemic heart disease, most

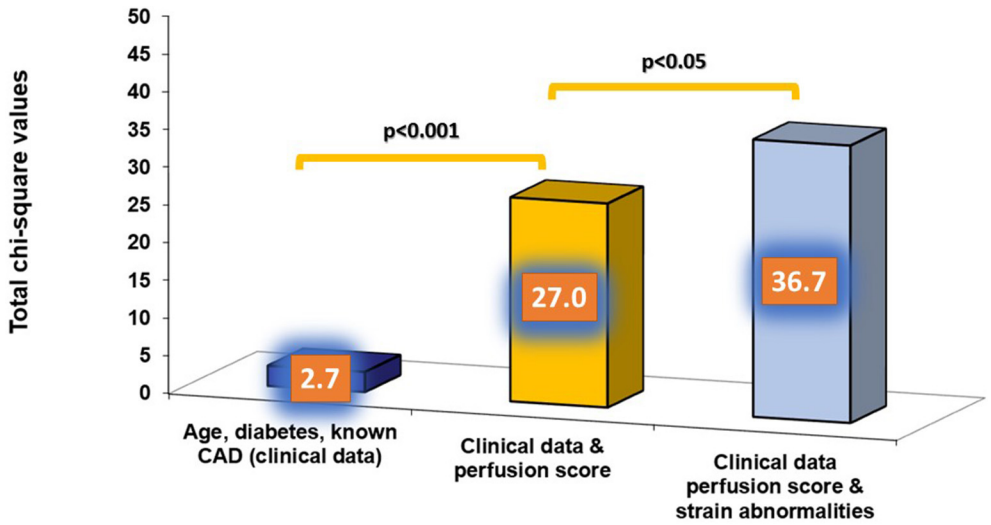

FIGURE 5 | The presence of strain abnormalities added incremental value to perfusion imaging and clinical data for the prediction of the combined endpoint.

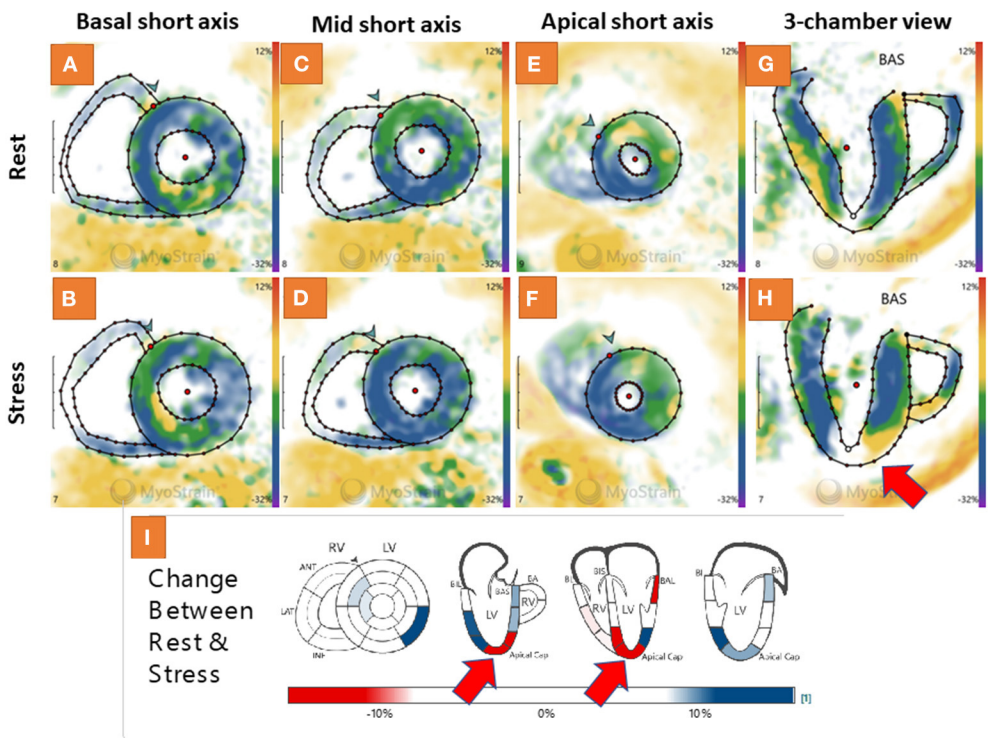

FIGURE 6 | Adenosine stress cardiovascular magnetic resonance (CMR) showed normal findings in a 58-year-old female patient with suspected coronary artery disease (CAD) due to atypical angina (not shown). A normal strain response was also seen by fast-SENC in the short axis views **(A–F)**. However, abnormal strain response was detected in the corresponding 3 chamber view fast-SENC images **(G,H)** with a significant inducible strain decrease in the apical cap [red arrow in **(H)** and the corresponding bull's eye maps in **(I)**].

of the clinical stress CMR studies are currently performed using vasodilator stress with adenosine or regadenoson. In this direction, the study of Romano et al. recently demonstrated the incremental value of longitudinal strain during vasodilator stress for the risk stratification of patients with CAD (25). Thus, using regadenoson perfusion stress CMR, GLS was measured at baseline and during stress in the 2-chamber long-axis cine view. GLS ≥ -19 during vasodilator stress was independently

associated with worse cardiac outcomes, independent of clinical variables, perfusion abnormalities, and LGE data. This study reinforced the incremental value of strain assessment during vasodilator stress CMR. However, the strain was assessed by feature tracking imaging in this study, which was shown to have limitations, such as low reproducibility especially on a regional level and with less experienced operators (26–28). This, along with the fact that analysis was performed only in the 2-chamber long-axis view limits the interpretation of the obtained results (29). In this regard, fast-SENC provides an alternative to FTI and allows for a very quick, single heartbeat and comprehensive evaluation of regional and global myocardial strain with high reproducibility (18). In our study, SENC enabled the comprehensive assessment of myocardial strain with single heartbeat acquisitions with high reproducibility. Worsening myocardial strain during vasodilator stress CMR offered the precise detection of perfusion defects and was also associated with worse ischemic outcomes during follow-up. This may be a particular advantage in patients with contraindications for gadolinium-based contrast agents. Changes in SAS were much more sensitive than global strain (GLS, GCS, and GS) both for the detection of regional ischemia by perfusion analysis and for the prediction of outcomes. This is not striking since ischemia usually occurs regionally in one or two of three perfusion territories and not in all three simultaneously. In contrast to the study by Romano et al. (25) SCS and SAS were more strongly associated with perfusion abnormalities and predictive of outcomes compared with SLS. This may be attributed to methodological differences between FTI and SENC, the latter allowing for more comprehensive and reproducible measures of strain, especially on a regional level, which is decisive for the detection of ischemic heart disease (18, 26–31). Generally, CS is believed to be a more sensitive marker for subtle myocardial dysfunction in asymptomatic patients without any history of cardiovascular disease (32) and a more accurate marker of regional ischemic myocardial dysfunction, which is supported by the results of our study (33).

Implementation of Our Findings Into the Current Clinical Context

Functional stress testing has been the non-invasive gold standard for the diagnostic work-up of patients with suspected and known CAD within the last decades, whereas its role in the diagnostic classification and risk stratification is widely accepted in patients with chronic coronary syndromes (CCS) based on current guidelines (2). Particularly CMR is currently acknowledged by clinicians as the clinical gold standard technique for the assessment of myocardial function, ischemia, and viability, if required all within a single examination, non-invasively and without radiation exposure for the patients. The amount of evidence for the applicability of dobutamine and vasodilator stress CMR for the detection of ischemia and the risk stratification of patients with CAD is large and has been highlighted in previous meta-analyses (6, 7). Based on the recent ISCHEMIA study, however, the role of coronary revascularization guided by the presence of myocardial ischemia has been questioned, since patients with stable coronary disease and moderate or severe ischemia, may not always profit in terms of outcomes from a primary revascularization strategy (34). However, patients with angina at baseline due to obstructive CAD improved in terms of limiting symptoms such as angina and exertional dyspnea from invasive strategies, which is an important cornerstone in the treatment of CAD (35). Furthermore, a recent meta-analysis demonstrated that patients with CCS randomized to elective revascularization vs. optimal medical treatment exhibited benefits in terms of cardiac survival, which improved with longer follow-up durations and were associated with fewer spontaneous myocardial infarctions (36). In addition, the MR-Inform study reinforced the role of vasodilator stress CMR in patients with stable angina and risk factors for CAD, being non-inferior to a primary invasive approach with X-Ray angiography and fractional flow reserve (FFR) measures with respect to clinical outcomes in patients with CCS (37).

From a pathophysiologic point of view, myocardial strain is more sensitive to disturbances of the myocardial metabolism or perfusion, which may be seen in the early stages of many cardiovascular disorders, including CAD and heart failure (38). In this regard, we recently demonstrated that even in patients at risk for heart failure and without coronary or structural heart disease, the impaired myocardial strain may be present as an early sign of subclinical cardiac dysfunction (19). In the present study, reduced strain response was seen in patients with myocardial ischemia during vasodilator stress, compared with those without perfusion abnormalities. Since hyperemic stress leads to redistribution of myocardial blood flow between the endocardium and epicardium (39), it is conceivable that endocardial strain is reduced due to impaired oxygen supply of the endocardium in regions with inducible ischemia, resulting in lower strain values in such regions. Thus, such individuals may have early damage of the sub-endocardial or mid-myocardial layers and therefore experience worse outcomes during follow-up. However, at present, it is not clear whether impaired strain during hyperemic stress requires a specific treatment, which merits further investigation in future studies.

Limitations

Our cohort was relatively small and heterogeneous with a high percentage of patients with known CAD. This limits the extrapolation of our findings to lower risk cohorts. In addition, the follow-up duration was quite short and only 25 endpoints were recorded. Especially the small number of hard endpoints such as death and non-fatal myocardial infarction and the inclusion of only patients with CMR and complete follow-up data are limitations, that need to be accounted for when interpreting our results. In addition, patients who underwent elective revascularization within the first 90 days after abnormal stress perfusion by CMR were excluded from analysis, and

no repeated CMR was performed after the revascularization procedures, which would have helped define the impact of residual ischemia on clinical outcomes. Furthermore, the cut-off value of SS decrease ≥6.5% during vasodilator stress was selected by *a priori* ROC analysis, as best indicative for the presence of myocardial ischemia by perfusion analysis, which may overestimate the association between perfusion defects and strain. However, the same cut-off was then independently applied for the prediction of cardiac events, exhibiting significant prognostic value. In addition, a certain overlap was observed for strain values in patients with and without perfusion abnormalities, so that average strain values may not be useful on an individual scale. However, by a selection of a cut-off value for the strain on a segmental level, clinically acceptable accuracy rates could be achieved for the estimation of perfusion abnormalities and clinical endpoints on a patient-by-patient level. Furthermore, we cannot evaluate the accuracy of strain or perfusion abnormalities for CAD detection by comparing these variables to invasive data in conjunction with FFR measures. However, most of our patients had negative stress test results, which helped defer invasive angiography, and this is clinically meaningful.

Conclusions

Fast-SENC during vasodilator stress was non-inferior compared with standard visual perfusion analysis for the diagnosis of ischemia and the risk stratification of patients with ischemic heart disease. This may bear clinical implications since fast-SENC relies on purely quantitative analysis, which is reproducible and can be performed within reasonable time-spent. Thus, fast-SENC can obviate the need for contrast agent injections in this regard, in the interest of time and costs and potentially patient safety. Now prospective larger-scale trials are warranted to test the ability of fast-SENC to predict hard cardiac outcomes.

DATA AVAILABILITY STATEMENT

The raw data supporting the conclusions of this article will be made available by the authors, without undue reservation.

ETHICS STATEMENT

The studies involving human participants were reviewed and approved by Ethics Committee of the General Medical Council Hamburg. The patients/participants provided their written informed consent to participate in this study.

AUTHOR CONTRIBUTIONS

GK and HS designed the study, performed the analysis, wrote and reviewed the manuscript, and provided important intellectual input. MM performed the acquisitions, reviewed the manuscript, and provided important intellectual input. SK, SE, AS, and SG reviewed the manuscript and provided important intellectual input. All authors contributed to the article and approved the submitted version.

ACKNOWLEDGMENTS

We thank Birgit Hoerig, Kirsten Falk, Ute Pfeiffer, and Silke Morgenstern for their excellent technical assistance with the acquisitions of all CMR scans.

SUPPLEMENTARY MATERIAL

The Supplementary Material for this article can be found online at: https://www.frontiersin.org/articles/10.3389/fcvm.2021.765961/full#supplementary-material

Supplementary Figure 1 | Corresponding mid short axis images in (i) a patient with normal perfusion during stress [**(A,B)**, note the asterisk, pointing to a dark rim artifact during resting perfusion], (ii) a patient with a subendocardial defect [**(C,D)**, red arrow in **(D)**, pointing to an inducible subendocardial perfusion defect of the septal wall] and (iii) a patient with a transmural perfusion defect [**(E,F)**, red arrow in **(F)**, pointing to an inducible transmural perfusion defect of the inferior-septal wall] during vasodilator stress are provided in this figure.

Supplementary Figure 2 | On a segmental level, a slight absolute SLS decrease and a blunted SLS increase was observed in segments with subendocardial and transmural perfusion defects, respectively, vs. segments with normal perfusion during stress, which showed a slight SLS increase **(A)**. The same patterns were observed after exclusion of segments with LGE **(B)**.

Supplementary Table 1 | Hemodynamic data during vasodilator stress.

REFERENCES

1. Virani SS, Alonso A, Aparicio HJ, Benjamin EJ, Bittencourt MS, Callaway CW, et al. Heart disease and stroke statistics-2021 update: a report from the American heart association. *Circulation.* (2021) 143:e254–743. doi: 10.1161/CIR.0000000000000950
2. Knuuti J, Wijns W, Saraste A, Capodanno D, Barbato E, Funck-Brentano C, et al. 2019 ESC guidelines for the diagnosis and management of chronic coronary syndromes. *Eur Heart J.* (2020) 41:407–77. doi: 10.1093/eurheartj/ehz425
3. Patel MR, Calhoon JH, Dehmer GJ, Grantham JA, Maddox TM, Maron DJ, et al. ACC/AATS/AHA/ASE/ASNC/SCAI/SCCT/STS 2017 appropriate use criteria for coronary revascularization in patients with stable ischemic heart disease : a report of the American college of cardiology appropriate use criteria task force, American association for thoracic surgery, American heart association, American society of echocardiography, American society of nuclear cardiology, society for cardiovascular angiography and interventions, society of cardiovascular computed tomography, and society of thoracic surgeons. *J Nucl Cardiol Off Publ Am Soc Nucl Cardiol.* (2017) 24:1759–92. doi: 10.1007/s12350-017-0917-9
4. Korosoglou G, Elhmidi Y, Steen H, Schellberg D, Riedle N, Ahrens J, et al. Prognostic value of high-dose dobutamine stress magnetic resonance imaging in 1,493 consecutive patients: assessment of myocardial wall motion and perfusion. *J Am Coll Cardiol.* (2010) 56:1225–34. doi: 10.1016/j.jacc.2010.06.020
5. Greenwood JP, Maredia N, Younger JF, Brown JM, Nixon J, Everett CC, et al. Cardiovascular magnetic resonance and single-photon emission computed tomography for diagnosis of coronary heart disease (CE-MARC): a prospective trial. *Lancet Lond Engl.* (2012) 379:453–60. doi: 10.1016/S0140-6736(11)61335-4
6. Lipinski MJ, McVey CM, Berger JS, Kramer CM, Salerno M. Prognostic value of stress cardiac magnetic resonance imaging in patients with known or suspected coronary artery disease: a systematic review and meta-analysis. *J Am Coll Cardiol.* (2013) 62:826–38. doi: 10.1016/S0735-1097(13)60809-8

7. Nandalur KR, Dwamena BA, Choudhri AF, Nandalur MR, Carlos RC. Diagnostic performance of stress cardiac magnetic resonance imaging in the detection of coronary artery disease: a meta-analysis. *J Am Coll Cardiol.* (2007) 50:1343–53. doi: 10.1016/j.jacc.2007.06.030
8. Kwong RY, Ge Y, Steel K, Bingham S, Abdullah S, Fujikura K, et al. Cardiac magnetic resonance stress perfusion imaging for evaluation of patients with chest pain. *J Am Coll Cardiol.* (2019) 74:1741–55. doi: 10.1016/j.jacc.2019.07.074
9. Luu JM, Filipchuk NG, Friedrich MG. Indications, safety and image quality of cardiovascular magnetic resonance: experience in >5,000 North American patients. *Int J Cardiol.* (2013) 168:3807–11. doi: 10.1016/j.ijcard.2013.06.032
10. Korosoglou G, Giusca S, Hofmann NP, Patel AR, Lapinskas T, Pieske B, et al. Strain-encoded magnetic resonance: a method for the assessment of myocardial deformation. *ESC Heart Fail.* (2019) 6:584–602. doi: 10.1002/ehf2.12442
11. Korosoglou G, Gitsioudis G, Voss A, Lehrke S, Riedle N, Buss SJ, et al. Strain-encoded cardiac magnetic resonance during high-dose dobutamine stress testing for the estimation of cardiac outcomes: comparison to clinical parameters and conventional wall motion readings. *J Am Coll Cardiol.* (2011) 58:1140–9. doi: 10.1016/j.jacc.2011.03.063
12. Korosoglou G, Lehrke S, Wochele A, Hoerig B, Lossnitzer D, Steen H, et al. Strain-encoded CMR for the detection of inducible ischemia during intermediate stress. *JACC Cardiovasc Imaging.* (2010) 3:361–71. doi: 10.1016/j.jcmg.2009.11.015
13. Kramer CM, Barkhausen J, Flamm SD, Kim RJ, Nagel E. Society for Cardiovascular Magnetic Resonance Board of Trustees Task Force on Standardized Protocols. Standardized cardiovascular magnetic resonance (CMR) protocols 2013 update. *J Cardiovasc Magn Reson.* (2013) 15:91. doi: 10.1186/1532-429X-15-91
14. Kramer CM, Barkhausen J, Bucciarelli-Ducci C, Flamm SD, Kim RJ, Nagel E. Standardized cardiovascular magnetic resonance imaging (CMR) protocols: 2020 update. *J Cardiovasc Magn Reson.* (2020) 22:17. doi: 10.1186/s12968-020-00607-1
15. Schulz-Menger J, Bluemke DA, Bremerich J, Flamm SD, Fogel MA, Friedrich MG, et al. Standardized image interpretation and post processing in cardiovascular magnetic resonance: society for cardiovascular magnetic resonance (SCMR) board of trustees task force on standardized post processing. *J Cardiovasc Magn Reson.* (2013) 15:35. doi: 10.1186/1532-429X-15-35
16. Motwani M, Maredia N, Fairbairn TA, Kozerke S, Radjenovic A, Greenwood JP, et al. High-resolution versus standard-resolution cardiovascular MR myocardial perfusion imaging for the detection of coronary artery disease. *Circ Cardiovasc Imaging.* (2012) 5:306–13. doi: 10.1161/CIRCIMAGING.111.971796
17. Cerqueira MD, Weissman NJ, Dilsizian V, Jacobs AK, Kaul S, Laskey WK, et al. Standardized myocardial segmentation and nomenclature for tomographic imaging of the heart. A statement for healthcare professionals from the cardiac imaging committee of the council on clinical cardiology of the American heart association. *Circulation.* (2002) 105:539–42. doi: 10.1161/hc0402.102975
18. Giusca S, Korosoglou G, Zieschang V, Stoiber L, Schnackenburg B, Stehning C, et al. Reproducibility study on myocardial strain assessment using fast-SENC cardiac magnetic resonance imaging. *Sci Rep.* (2018) 8:14100. doi: 10.1038/s41598-018-32226-3
19. Korosoglou G, Giusca S, Montenbruck M, Patel AR, Lapinskas T, Götze C, et al. Fast strain-encoded cardiac magnetic resonance for diagnostic classification and risk stratification of heart failure patients. *JACC Cardiovasc Imaging.* (2021) 14:1177–8. doi: 10.1016/j.jcmg.2020.10.024
20. Steen H, Giusca S, Montenbruck M, Patel A, Pieske B, Florian A, et al. Left and right ventricular strain using fast strain-encoded cardiac magnetic resonance for the diagnostic classification of patients with chronic non-ischemic heart failure due dilated or hypertrophic cardiomyopathies and cardiac amyloidosis. *J Cardiovasc Magn Reson.* (2021) 23:45. doi: 10.1186/s12968-021-00711-w
21. Morrow DA, Wiviott SD. Classification of deaths in cardiovascular outcomes trials. *Circulation.* (2019) 139:874–6. doi: 10.1161/CIRCULATIONAHA.118.038359
22. Xaplanteris P, Fournier S, Pijls NHJ, Fearon WF, Barbato E, Tonino PAL, et al. Five-Year outcomes with pci guided by fractional flow reserve. *N Engl J Med.* (2018) 379:250–9. doi: 10.1056/NEJMoa1803538
23. Mi J, Sampson AR. A comparison of the bonferroni and scheffé bounds. *J Stat Plan Inference.* (1993) 36:101–5. doi: 10.1016/0378-3758(93)90105-F
24. DeLong ER, DeLong DM, Clarke-Pearson DL. Comparing the areas under two or more correlated receiver operating characteristic curves: a nonparametric approach. *Biometrics.* (1988) 44:837–45. doi: 10.2307/2531595
25. Romano S, Romer B, Evans K, Trybula M, Shenoy C, Kwong RY, et al. Prognostic implications of blunted feature-tracking global longitudinal strain during vasodilator cardiovascular magnetic resonance stress imaging. *JACC Cardiovasc Imaging.* (2020) 13 (1 Pt. 1):58–65. doi: 10.1016/j.jcmg.2019.03.002
26. Feisst A, Kuetting DLR, Dabir D, Luetkens J, Homsi R, Schild HH, et al. Influence of observer experience on cardiac magnetic resonance strain measurements using feature tracking and conventional tagging. *IJC Heart Vasc.* (2018) 18:46–51. doi: 10.1016/j.ijcha.2018.02.007
27. Mangion K, Burke NMM, McComb C, Carrick D, Woodward R, Berry C. Feature-tracking myocardial strain in healthy adults- a magnetic resonance study at 3.0 tesla. *Sci Rep.* (2019) 9:3239. doi: 10.1038/s41598-019-39807-w
28. Almutairi HM, Boubertakh R, Miquel ME, Petersen SE. Myocardial deformation assessment using cardiovascular magnetic resonance-feature tracking technique. *Br J Radiol.* (2017) 90:20170072. doi: 10.1259/bjr.20170072
29. Korosoglou G, Giusca S. Strain for Stress Testing: Is it a Featuring or Supporting Role in Cardiac Magnetic Resonance? *JACC Cardiovasc Imaging.* (2020) 13 (1 Pt 1):66–8. doi: 10.1016/j.jcmg.2019.04.006
30. Bucius P, Erley J, Tanacli R, Zieschang V, Giusca S, Korosoglou G, et al. Comparison of feature tracking, fast-SENC, and myocardial tagging for global and segmental left ventricular strain. *ESC Heart Fail.* (2020) 7:523–32. doi: 10.1002/ehf2.12576
31. Wu L, Germans T, Güçlü A, Heymans MW, Allaart CP, van Rossum AC. Feature tracking compared with tissue tagging measurements of segmental strain by cardiovascular magnetic resonance. *J Cardiovasc Magn Reson.* (2014) 16:10. doi: 10.1186/1532-429X-16-10
32. Choi E-Y, Rosen BD, Fernandes VRS, Yan RT, Yoneyama K, Donekal S, et al. Prognostic value of myocardial circumferential strain for incident heart failure and cardiovascular events in asymptomatic individuals: the multi-ethnic study of atherosclerosis. *Eur Heart J.* (2013) 34:2354–61. doi: 10.1093/eurheartj/eht133
33. Buss SJ, Krautz B, Hofmann N, Sander Y, Rust L, Giusca S, et al. Prediction of functional recovery by cardiac magnetic resonance feature tracking imaging in first time ST-elevation myocardial infarction. Comparison to infarct size and transmurality by late gadolinium enhancement. *Int J Cardiol.* (2015) 183:162–70. doi: 10.1016/j.ijcard.2015.01.022
34. Maron DJ, Hochman JS, Reynolds HR, Bangalore S, O'Brien SM, Boden WE, et al. Initial invasive or conservative strategy for stable coronary disease. *N Engl J Med.* (2020) 382:1395–407. doi: 10.1056/NEJMoa1915922
35. Spertus JA, Jones PG, Maron DJ, O'Brien SM, Reynolds HR, Rosenberg Y, et al. Health-Status outcomes with invasive or conservative care in coronary disease. *N Engl J Med.* (2020) 382:1408–19. doi: 10.1056/NEJMoa1916370
36. Navarese EP, Lansky AJ, Kereiakes DJ, Kubica J, Gurbel PA, Gorog DA, et al. Cardiac mortality in patients randomised to elective coronary revascularisation plus medical therapy or medical therapy alone: a systematic review and meta-analysis. *Eur Heart J.* (2021) ehab246. doi: 10.1093/eurheartj/ehab246
37. Nagel E, Greenwood JP, McCann GP, Bettencourt N, Shah AM, Hussain ST, et al. Magnetic resonance perfusion or fractional flow reserve in coronary disease. *N Engl J Med.* (2019) 380:2418–28. doi: 10.1056/NEJMoa1716734
38. Voigt J-U, Exner B, Schmiedehausen K, Huchzermeyer C, Reulbach U, Nixdorff U, et al. Strain-rate imaging during dobutamine stress echocardiography provides objective evidence of inducible ischemia. *Circulation.* (2003) 107:2120–6. doi: 10.1161/01.CIR.0000065249.69988.AA
39. Larghat A, Biglands J, Maredia N, Greenwood JP, Ball SG, Jerosch-Herold M, et al. Endocardial and epicardial myocardial perfusion determined by semi-quantitative and quantitative myocardial perfusion magnetic resonance. *Int J Cardiovasc Imaging.* (2012) 28:1499–511. doi: 10.1007/s10554-011-9982-3

Conflict of Interest: HS, SK, and GK received research grants from Myocardial Solutions. SK owns stock options of Myocardial Solutions.

The remaining authors declare that the research was conducted in the absence of any commercial or financial relationships that could be construed as a potential conflict of interest.

Publisher's Note: All claims expressed in this article are solely those of the authors and do not necessarily represent those of their affiliated organizations, or those of the publisher, the editors and the reviewers. Any product that may be evaluated in this article, or claim that may be made by its manufacturer, is not guaranteed or endorsed by the publisher.

frontiers in Cardiovascular Medicine

ORIGINAL RESEARCH
published: 07 December 2021
doi: 10.3389/fcvm.2021.775039

Clinical Relevance of Right Atrial Functional Response to Treatment in Pulmonary Arterial Hypertension

Manuel J. Richter[1], Daniel Zedler[1], Dominik Berliner[2], Philipp Douschan[1,3], Henning Gall[1], Hossein A. Ghofrani[1,4,5], Lucas Kimmig[1], Nils Kremer[1], Karen M. Olsson[6], Bruno Brita da Rocha[1], Stephan Rosenkranz[7], Werner Seeger[1], Athiththan Yogeswaran[1], Zvonimir Rako[1†] and Khodr Tello[1†]*

[1] Department of Internal Medicine, Justus-Liebig-University Giessen, Universities of Giessen and Marburg Lung Center (UGMLC), Member of the German Center for Lung Research (DZL), Giessen, Germany, [2] Department of Cardiology, Hannover Medical School, Hannover, Germany, [3] Division of Pulmonology, Department of Internal Medicine and Ludwig Boltzmann Institute for Lung Vascular Research, Medical University of Graz, Graz, Austria, [4] Department of Pneumology, Kerckhoff Heart, Rheuma and Thoracic Center, Bad Nauheim, Germany, [5] Department of Medicine, Imperial College London, London, United Kingdom, [6] Department of Respiratory Medicine, German Center for Lung Research Biomedical Research in Endstage and Obstructive Lung Disease Hannover (DZL/BREATH), Hannover Medical School, Hannover, Germany, [7] Klinik III für Innere Medizin and Cologne Cardiovascular Research Center (CCRC), Herzzentrum der Universität zu Köln, Köln, Germany

OPEN ACCESS

Edited by:
Matteo Cameli, University of Siena, Italy

Reviewed by:
Mark L. Ormiston, Queen's University, Canada
Christoph Sinning, University Heart and Vascular Center Hamburg (UHZ), Germany

***Correspondence:**
Manuel J. Richter
manuel.richter@innere.med.uni-giessen.de

† These authors have contributed equally to this work

Specialty section:
This article was submitted to Cardiovascular Imaging, a section of the journal Frontiers in Cardiovascular Medicine

Received: *13 September 2021*
Accepted: *05 November 2021*
Published: *07 December 2021*

Citation:
Richter MJ, Zedler D, Berliner D, Douschan P, Gall H, Ghofrani HA, Kimmig L, Kremer N, Olsson KM, Brita da Rocha B, Rosenkranz S, Seeger W, Yogeswaran A, Rako Z and Tello K (2021) Clinical Relevance of Right Atrial Functional Response to Treatment in Pulmonary Arterial Hypertension. Front. Cardiovasc. Med. 8:775039. doi: 10.3389/fcvm.2021.775039

Background: Right atrial (RA) function has emerged as an important determinant of outcome in pulmonary arterial hypertension (PAH). However, studies exploring RA function after initiation of specific pulmonary vascular treatment and its association with outcome in patients with incident PAH are lacking.

Methods: RA peak longitudinal strain (PLS), passive strain (PS), and peak active contraction strain (PACS) were retrospectively assessed in 56 treatment-naïve patients with PAH at baseline and during follow-up after initiation of specific monotherapy or combination therapy. Patients were grouped according to their individual RA functional response to treatment, based on change from baseline (Δ): worsened (first Δ-tertile), stable (second Δ-tertile), and improved (third Δ-tertile). The Spearman's rho correlation and linear regression analysis were used to determine associations. Time to clinical worsening (defined as deterioration of functional class or 6-min walking distance, disease-related hospital admission, or death) was measured from the follow-up assessment. The association of RA functional treatment response with time to clinical worsening was assessed using the Kaplan–Meier and the Cox regression analyses.

Results: Median (interquartile range) time to echocardiographic follow-up was 11 (9–12) months. Of the 56 patients, 37 patients (66%) received specific dual or triple combination therapy. Δ RA PLS during follow-up was significantly associated with changes in key hemodynamic and echocardiographic parameters. The change of pulmonary vascular resistance, right ventricular (RV) end-systolic area, and global longitudinal strain were independently associated with Δ RA PLS. The median time to clinical worsening after echocardiographic follow-up was 6 (2–14) months [17 events (30%)]. In the multivariate Cox regression analysis, worsening of RA PLS was significantly associated with clinical deterioration (hazard ratio: 4.87; 95% CI: 1.26–18.76; $p = 0.022$). Patients with worsened RA PLS had a significantly poorer prognosis than those with stable or improved

RA PLS (log-rank $p = 0.012$). By contrast, PS and PACS did not yield significant prognostic information.

Conclusion: Treatment-naïve patients with PAH may show different RA functional response patterns to PAH therapy. These functional patterns are significantly associated with clinically relevant outcome measures. Improvements of RA function are driven by reductions of afterload, RV remodeling, and RV dysfunction.

Keywords: pulmonary hypertension, echocardiography, speckle tracking, outcome, right atrium

INTRODUCTION

Pulmonary arterial hypertension (PAH) is a severe multifactorial disease characterized by increased total pulmonary resistance with subsequent right ventricular (RV) pressure overload (1). Increased RV afterload results in adaptive and maladaptive RV remodeling (hypertrophy and dilatation, respectively), eventually leading to RV failure (2). In addition to the right ventricle, remodeling of the right atrium has come into focus in pulmonary hypertension (PH) in the recent years. Alterations of right atrial (RA) function are relevant prognostic markers of adverse outcomes (3, 4). RA function is characterized by three phases: a reservoir phase during atrial filling when the tricuspid valve is closed, a conduit phase during passive emptying of the right atrium into the right ventricle when the tricuspid valve is open, and an active "contractile" phase during atrial systole (contraction) (5). Initially, chronic RV pressure overload causes an increase in RA contractility and RA dilation due to elevated RV diastolic pressure and tricuspid regurgitation (6). RV remodeling leads to impaired RA function, which results in worsening of reservoir (4), conduit (7), and contractile functions (8). The interaction of the right atrium and right ventricle may play a crucial role in PH. A loss of that interaction in the sense of RA-RV "uncoupling" results in alterations of RA function to a failing reservoir phase and an impaired conduit component that are inevitably associated with a reduction of cardiac output and RV filling (6). Most recently, it was shown that longitudinal assessment of RA function after treatment initiation may serve as an additional predictive marker in children with PH (9). However, the clinical relevance of RA functional response to specific vasoactive treatment in adult patients with PAH is currently unknown. Therefore, we aimed to longitudinally assess and characterize RA function in treatment-naïve adult patients with PAH.

MATERIALS AND METHODS

Study Design and Patients

Data from consecutive, treatment-naïve adult patients referred to our PH clinic between December 2017 and April 2020 and enrolled in the prospectively recruiting the Giessen PH Registry (10) were retrospectively analyzed. The diagnosis of PAH was made by the multidisciplinary PH board at the University Hospital Giessen according to the updated recommendations (11). Patients with pacemakers ($n = 1$) or atrial fibrillation or atrial flutter ($n = 2$) at the time of evaluation were excluded. All the patients received individual targeted PAH therapy based on current guidelines and best standard of care (12). Prior to treatment initiation, patients underwent baseline evaluation. Median time between baseline right heart catheterization and echocardiography was 16.5 (2–46.3) days. Invasive pulmonary hemodynamics and pulmonary arterial capacitance (PAC) were measured as previously defined (13). All the participants gave a written informed consent for the enrollment into the Giessen PH Registry. The investigation conforms to the Declaration of Helsinki and was approved by the Ethics Committee of the Faculty of Medicine at the University of Giessen (approval #266/11).

Echocardiography

All the measurements were performed as recommended by current echocardiographic guidelines (14, 15) and obtained using a Vivid E9 device (GE Healthcare, Wauwatosa, Wisconsin, USA). Tricuspid annular plane systolic excursion (TAPSE) and RV fractional area change (FAC) were quantified. RA area was measured at end-systole. RA pressure (RAP) was estimated by evaluation of inferior vena cava diameters (expiratory and inspiratory) and percent collapse during inspiration. Pulmonary arterial systolic pressure (PASP) was calculated as the transtricuspid gradient + RAP (16). Tricuspid valve regurgitation was graded as mild, moderate, or severe as recommended (17). RV global longitudinal strain was measured as previously described (18).

Echocardiographic images were analyzed by an independent investigator who was not directly involved in the image acquisition and who was blinded to the clinical data. Measurements were made using EchoPac software (version 201, GE Healthcare, Wauwatosa, Wisconsin, USA).

Tracing of the right atrium was performed as shown in **Figure 1** according to the current recommendations (7, 19, 20). Using a right ventricle-focused apical four-chamber view, the region of interest was manually placed on the RA endocardial border. After automatic tracing of the six segments, every segment was manually adjusted to the thickness of the RA wall. The zero reference was set at the R wave and all the strains were positive. RA peak longitudinal strain (PLS) and peak active contraction strain (PACS) were assessed as measures of the reservoir phase and contraction phase, respectively. RA passive strain (PS), indicative of conduit function, was calculated from the difference between RA peak longitudinal and active strain as shown in **Figure 1**. Intra- and interobserver variability for PLS were assessed in a random subset (20%) of the cohort.

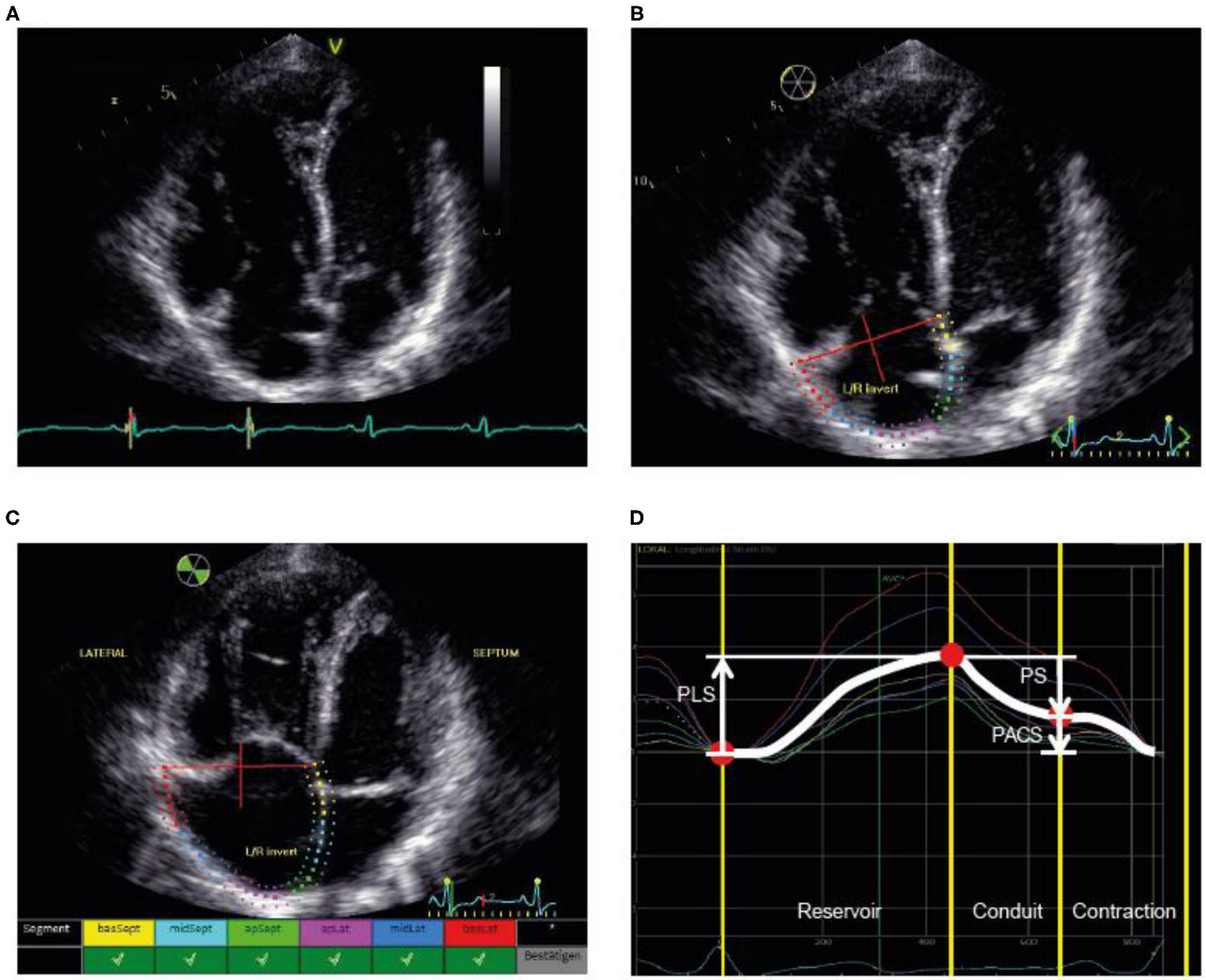

FIGURE 1 | Illustration of the assessment of RA strain. **(A)** First, the RV-focused apical four-chamber view was used with selection of the cardiac cycle and adjustment of the electrocardiogram (to R-wave). **(B)** Second, the RA endocardial border was traced as the region of interest, covering the RA lateral wall, roof, and septal wall. **(C)** Third, processing provided an overview wherever speckle tracking was feasible for the selected regions. **(D)** Fourth, the different phases were identified and the strain values determined. PACS, peak active contraction strain; PLS, peak longitudinal strain; PS, passive strain; RA, right atrial; RV, right ventricular.

Outcome

Clinical worsening was assessed after follow-up echocardiography and was defined as any of the following: reduction in exercise capacity (−15% compared with the baseline 6-min walk test), worsening in the WHO functional class, clinical deterioration requiring hospital admission (need for new PAH therapies or intravenous diuretics), or death (21). Follow-up was assessed until July 2021.

Statistical Analysis

The Kolmogorov–Smirnov test was used for assessment of normal distribution. The Pearson's chi-squared test, related-samples Wilcoxon signed-rank test, the paired samples *t*-test, the independent samples Kruskal–Wallis test, or the one-way ANOVA was used to analyze differences between groups, as appropriate. The Spearman's rank correlation was used to measure association between variables. Inter- and intraobserver variability were assessed using intraclass correlation coefficients and coefficient of variation.

A backward (based on likelihood ratio) multivariate linear regression model was built to determine the parameter most strongly related to the change of RA function. Variable selection was limited to three variables to avoid overfitting and was based on clinical relevance. Model 1 included the absolute change of mean pulmonary arterial pressure (mPAP), PAC, and pulmonary vascular resistance (PVR). Model 2 included the absolute change of TAPSE/PASP, FAC, and RV end-systolic area. Model 3 incorporated the absolute change of TAPSE/PASP, FAC, and RV global longitudinal strain. Multicollinearity was assessed using the variance inflation factor.

The uni- and multivariate Cox proportional hazards models were built to assess the relationship between RA function and the clinical outcome, with RA function included either as a continuous variable or as a categorical variable based on tertiles (with tertile III, "improved," set as the reference category). Owing to the limited number of events, adjusted covariates were limited to age and sex. For further evaluation, the Kaplan–Meier analyses with log-rank tests were used, with all the events or censoring times measured from the date of follow-up echocardiography.

For all the analyses, $p < 0.05$ was considered as statistically significant.

The SPSS version 26.0 and 27.0 (IBM, Armonk, New York, USA) and GraphPad Prism version 8.4.3 (GraphPad Software, San Diego, USA) were used for statistical analyses.

RESULTS

Patients

The majority of the patients with incident PAH presented with an advanced WHO functional class (**Table 1**). Baseline pulmonary hemodynamics demonstrated a precapillary pattern of PH with substantially elevated pulmonary pressures and resistance. As shown in **Table 2**, patients presented with substantial RV and RA enlargement, depressed RV systolic function measured by FAC, and impaired RA function compared with values previously reported in healthy controls (19). Baseline PLS and PACS were associated with the severity of tricuspid regurgitation. We observed significantly higher PLS and PACS values in patients with mild-to-moderate tricuspid regurgitation compared with patients with severe regurgitation (**Supplementary Figure S1**).

Median (interquartile range) time to echocardiographic follow-up was 11 (9–12) months. The majority of patients (66%) received specific dual or triple combination therapy as maximal treatment. Under specific treatment, pulmonary hemodynamic indices and RV remodeling showed substantial improvement (**Tables 1**, **2**). However, RA PLS, PS, and PACS remained unchanged despite significantly decreased RA size during follow-up.

Intraclass correlation coefficients and coefficients of variation showed good inter- and intraobserver agreement for RA PLS (**Supplementary Table S1**).

TABLE 1 | Characteristics of the patient.

Characteristics	Patients with PAH ($n = 56$)		
	Baseline	Follow-up	*p* value
Male/female, *n/n*	21/35		
Age, years	62 ± 15		
PAH subtype, *n* (%)			
Idiopathic PAH	55 (98.2)		
PAH with overt features of venous/capillary involvement	1 (1.8)		
WHO FC, *n* (%)			
I		4 (7.1)	<0.001
II	11 (19.6)	16 (28.6)	
III	40 (71.4)	29 (51.8)	
IV	5 (8.9)	7 (12.5)	
BNP (pg/ml)	133 [65–307]*	89 [29–249]*	0.003
Right heart catheterization		†	
Mean pulmonary arterial pressure, mm Hg	42 ± 10	40 ± 10	0.003
Right atrial pressure, mm Hg	8 [6–10]	8 [6–11]	0.127
Pulmonary vascular resistance, Wood Units	7.6 ± 3.1	6.0 ± 3.0	0.066
Cardiac index, l/min/m^2	2.4 ± 0.5	2.8 ± 0.7	0.147
Pulmonary arterial wedge pressure, mm Hg	11 [8–13]	10 [9–13]	0.547
Pulmonary arterial capacitance, ml/mm Hg	1.5 [1.0–2.0]	1.7 [1.2–2.7]	0.003
Maximal treatment, *n* (%)			
Monotherapy		19 (33.9)	
Dual therapy		25 (44.6)	
Triple therapy		12 (21.4)	

PH, pulmonary hypertension; FC, functional class; BNP, B-type natriuretic peptide. Values represent mean ± SD, unless otherwise specified.

**Available in 55 patients.*

† Follow-up right heart catheter data were available in 38 patients.

Clinical Relevance of Longitudinal RA Function

We observed significant associations of baseline RA PLS, PS, and PACS with key baseline parameters (**Supplementary Table S2**). Among various associations, we observed a strong correlation of baseline RA PLS with baseline RV global longitudinal strain (*rho*: −0.639; $p < 0.001$) and B-type natriuretic peptide (BNP) (*rho*: −0.569; $p < 0.001$).

The difference of RA PLS (Δ RA PLS) from baseline to follow-up was significantly associated with a change of the following parameters during follow-up: Δ TAPSE/PASP, Δ BNP, Δ PVR, Δ PAC, Δ mPAP (*rho*: −0.428; $p = 0.008$; plot not shown) and Δ RV end-systolic area. Of note, we observed the strongest association of Δ RA PLS with Δ RV global longitudinal strain (**Figure 2**). Δ RA PACS was significantly associated with Δ BNP (*rho*: −0.400; $p = 0.003$), Δ PVR (*rho*: −0.341; $p = 0.036$) and Δ PAC (*rho*: −0.349; $p = 0.032$), while Δ PS was only associated with Δ RV end-diastolic area (*rho*: −0.323; $p = 0.017$; plots not shown). Of note, no association was observed between Δ PS and Δ RV global longitudinal strain ($p = 0.204$; plot not shown).

In the multivariate linear regression analysis model 1 (including Δ PVR, Δ PAC, and Δ mPAP), we found that Δ PVR was independently associated with Δ RA PLS [multivariate B-coefficient (95% CI): −1.59 (−2.44 to −0.73); $p < 0.001$]. In the corresponding multivariate model 2 (including Δ TAPSE/PASP, Δ FAC, and Δ RV end-systolic area), we found that Δ RV end-systolic area was independently associated with Δ RA PLS [multivariate B-coefficient (95% CI): −1.09 (−1.74 to −0.45); $p < 0.001$]. Model 3 (including Δ TAPSE/PASP, Δ FAC, and Δ RV global longitudinal strain) showed that Δ RV global longitudinal change was independently associated with Δ RA PLS [multivariate B-coefficient (95% CI): 1.16 (0.60–1.72); $p < 0.001$]. In addition, model 2 showed that Δ TAPSE/PASP was

TABLE 2 | Echocardiographic measurements.

	Patients with PAH ($n = 56$)		
	Baseline	**Follow-up**	***P*-value**
Right ventricle			
RV end-diastolic area, cm^2	27 [22–32]	23 [18–29]*	< 0.001
RV end-systolic area, cm^2	20 [16–24]	15 [12–19]*	< 0.001
Fractional area change, %	25 ± 11	29 ± 11*	0.010
TAPSE, mm	20 [18–22]	21 [19–23]	0.105
PASP, mmHg	67 ± 23†	61 ± 21‡	0.089
TAPSE/PASP, mm/mmHg	0.29 [0.21–0.40]†	0.35 [0.27–0.44]‡	0.109
RV global longitudinal strain, %	−15.1 ± 4.7	−16.8 ± 4.8‡	0.007
Tricuspid valve regurgitation			< 0.001
None/mild	23 (41.1)	26 (46.4)	
Moderate	29 (51.8)	21 (37.5)	
Severe	4 (7.1)	9 (16.1)	
Right atrium			
RA area, cm^2	17 [15–20]	15 [12–20]	0.014
Peak longitudinal strain, %	31 [23–36]	29 [22–39]	0.864
Passive strain, %	8 ± 5	10 ± 8*	0.0117
Peak active contraction strain, %	21 ± 7	20 ± 10*	0.704
Inferior vena cava diameter, mm	18 [15–20]†	18 [14–21]§	0.928

PAH, pulmonary arterial hypertension; PASP, pulmonary arterial systolic pressure; RA, right atrial; RV, right ventricular; TAPSE, tricuspid annular plane systolic excursion.
Values represent mean ± SD or median (interquartile range) (for normally or non-normally distributed parameters, respectively), unless otherwise specified.
**Available in 55 patients.*
†Available in 52 patients.
‡Available in 54 patients.
§Available in 49 patients.

significantly associated with Δ RA PS [multivariate B-coefficient (95% CI): 14.43 (4.82–24.05); $p < 0.001$]. Of note, the models could not identify a significant predictor for Δ RA PACS (data not shown).

For further analysis, the patients were grouped into tertiles according to their Δ RA PLS: worsened (Δ −17.8 to −4.2%), stable (Δ −4.2% to 4.0%), and improved (Δ 4.0% to 44.6%) longitudinal RA function (**Figures 3A,B**). Δ RA PS and PACS were grouped in an analogous manner (**Supplementary Figure S2**). As shown in **Table 3**, no significant differences in baseline hemodynamic or echocardiographic parameters were observed when stratifying by tertile of Δ RA PLS. However, during follow-up, patients with improved RA PLS showed a significantly greater reduction of mPAP and PVR and improvement of PAC, RV strain, TAPSE/PASP, and BNP compared with patients with stable or worsened RA PLS (**Table 3**). Finally, we grouped Δ RA PLS, Δ RA PS, and Δ RA PACS according to the number of specific vasoactive treatments used (mono, dual, or triple therapy; **Supplementary Figure S3**). Δ RA PLS and Δ RA PACS showed no significant differences dependent on the treatment regimen used, while Δ RA PS was highest in patients receiving monotherapy. Of note, we observed a reduction of RV end-systolic area in both treatment groups (monotherapy and combination therapy). However, an improvement in FAC was only observed in those patients receiving combination therapy (**Supplementary Figure S4**).

Prognostic Impact of RA Functional Response to Treatment

In total, 17 clinical worsening events [12 hospitalizations (including four escalations of specific PAH therapy and five deaths) were observed during a median follow-up period of 6 (2–14) months (mean 9 ± 8 months) after the echocardiographic follow-up. First, we explored the prognostic relevance of Δ RA function as a continuous variable in the univariate Cox regression analysis. Δ RA PLS (per one unit increase) was significantly associated with the composite endpoint with a hazard ratio of 0.925 (95% CI: 0.873–0.981; $p = 0.009$), while Δ PS ($p = 0.085$) and Δ PACS ($p = 0.167$) were not.

Second, we performed the univariate Cox regression analysis with the RA PLS treatment response patterns stratified by tertile. The pattern was significantly associated with clinical worsening. Patients with worsening of RA PLS during follow-up (tertile I) showed a hazard ratio of 4.16 (95% CI: 1.15–14.96; $p = 0.029$) for the composite endpoint. Similarly, worsening of RA PS during follow-up (tertile I) was significantly associated with the composite endpoint with a hazard ratio of 4.93 (95% CI: 1.08–22.54; $p = 0.040$). Patients with stable RA PS or stable PLS (tertile II) showed non-significantly increased hazard ratios of 2.76 (95% CI: 0.53–14.32; $p = 0.226$) and 1.10 (95% CI: 0.22–5.47; $p = 0.907$), respectively. In the multivariate Cox regression analysis, adjusting for age and sex, worsening of RA PLS during follow-up was significantly associated with clinical deterioration (multivariate hazard ratio: 4.87; 95% CI: 1.26–18.76; $p = 0.022$). This was supported by the Kaplan–Meier analysis which showed a significantly higher clinical worsening event rate in patients with worsened RA PLS compared with patients who had stable or improved RA PLS during follow-up (log-rank $p = 0.012$; **Figure 3C**). In addition, worsening RA PS remained significantly associated with the composite endpoint within the multivariate model (multivariate hazard ratio: 5.18; 95% CI: 1.13–23.83; $p = 0.035$). However, in the Kaplan–Meier analysis, Δ RA PS stratified by tertile was not able to predict outcome (log-rank $p = 0.063$; plot not shown). Of note, Δ RA PACS was not able to predict outcome in the Cox regression analysis (tertile 1: $p = 0.319$; tertile 2: $p = 0.972$) or the Kaplan–Meier analysis (log-rank $p = 0.491$; plot not shown).

DISCUSSION

In this study, we have demonstrated that therapy-naïve PAH may show different responses to treatment with respect to RA functional parameters. Moreover, these response patterns are associated with clinically relevant outcome parameters.

Within the last decade, the prognostic and clinical importance of RA function in patients with PH has increasingly come into focus (5, 22). Measurements of altered RA function (reservoir, conduit, or active contractile function) are helpful tools for the evaluation of the severity of RV dysfunction and prognosis

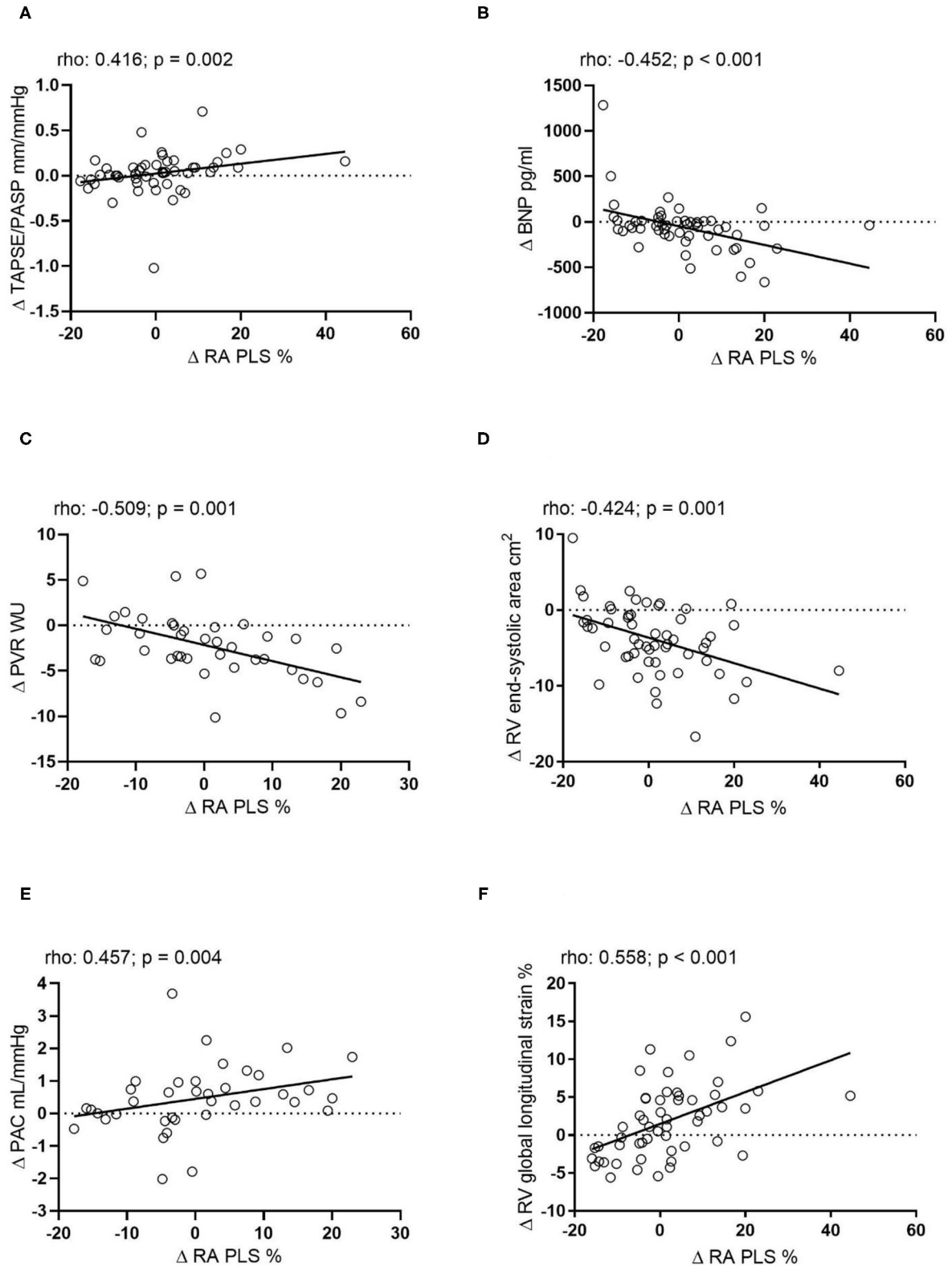

FIGURE 2 | Correlation of the absolute change of RA PLS during echocardiographic follow-up with the absolute change of **(A)** TAPSE/PASP ($n = 44$), **(B)** BNP ($n = 54$), **(C)** PVR ($n = 38$), **(D)** RV end-systolic area ($n = 55$), **(E)** PAC ($n = 38$), and **(F)** RV global longitudinal strain ($n = 54$). Δ, change; BNP, B-type natriuretic peptide; mPAP, mean pulmonary arterial pressure; PAC, pulmonary arterial capacitance; PASP, pulmonary arterial systolic pressure; PVR, pulmonary vascular resistance; RA PLS, right atrial peak longitudinal strain; RV, right ventricular; TAPSE, tricuspid annular plane systolic excursion; WU, Wood Units.

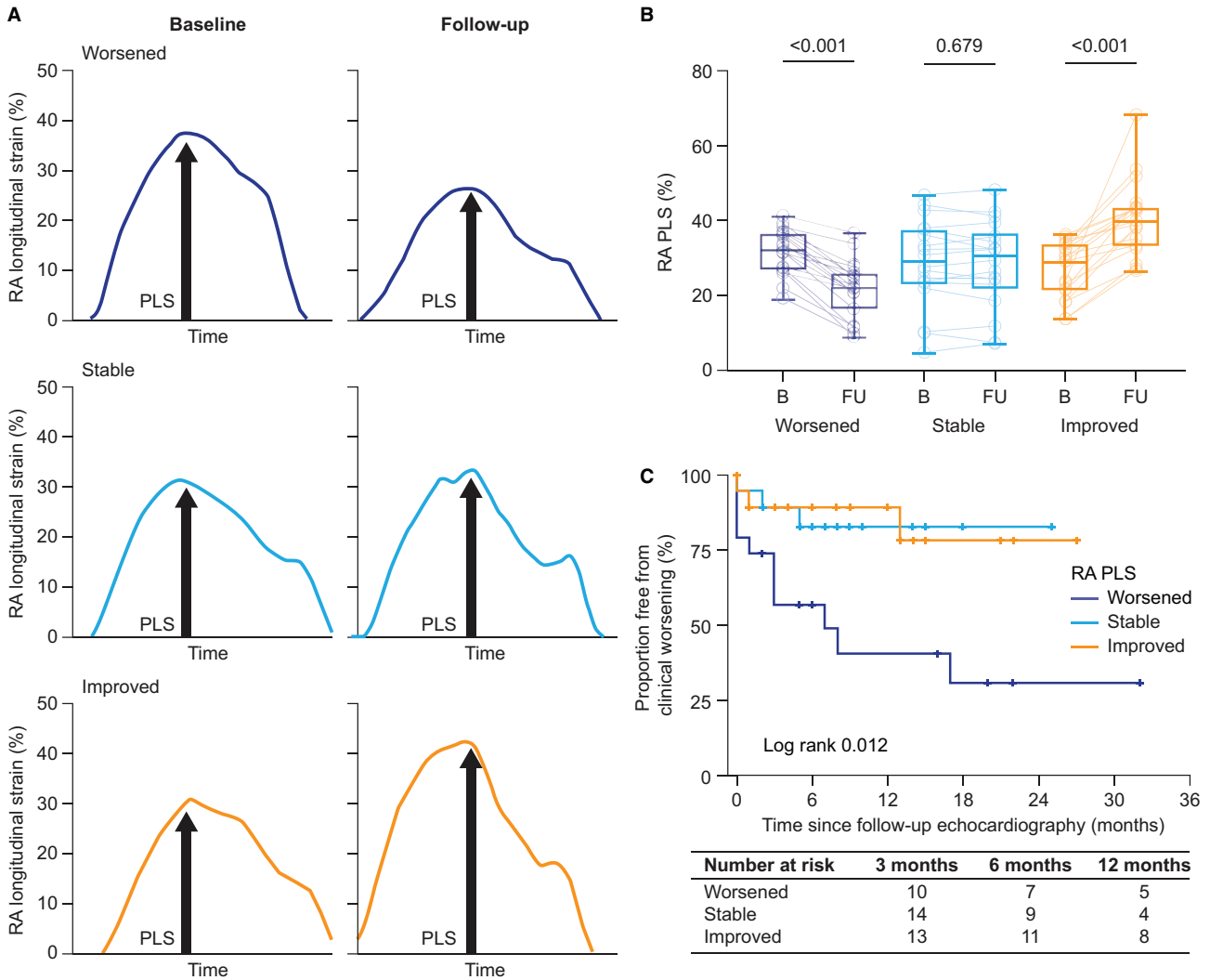

FIGURE 3 | Longitudinal RA function. **(A)** Illustration of the assessment of RA phases at baseline and during follow-up according to the change in RA function (worsened, stable, and improved). Stratification was based on tertile of absolute change of RA PLS and RA PACS. **(B)** RA PLS stratified by tertile of absolute change [tertile I (worsened): Δ −17.8% to −4.2%; tertile II (stable): Δ −4.2% to 4.0%; and tertile III (improved): Δ 4.0% to 44.6%]. Box-plots show median, interquartile range, and minimum to maximum values. **(C)** The Kaplan–Meier plots of time to clinical worsening since follow-up echocardiography stratified by RA function based on RA PLS. RA, right atrial; PACS, peak active contraction strain; PLS, peak longitudinal strain.

in PH (4, 9). Furthermore, RA phasic performance is altered in relation to impaired diastolic function of the chronically overloaded right ventricle, leading to backward venous flow and systemic congestion through RA functional impairment (23). In addition, alterations of RV systolic function accompanied by maladaptive RV remodeling and secondary tricuspid valve regurgitation directly result in loss of phasic RA function, leading to RA remodeling (6, 22). Recently, the longitudinal assessment of RA function after initiation of PAH treatment has been shown to serve as an additional parameter to predict outcome in children with PH (9). It is as of yet unknown whether RA function and its response to PAH treatment during follow-up would also serve as clinically relevant marker in adults.

Δ RA PLS emerged as a clinically relevant parameter in our study. This is consistent with data from Alenezi and coworkers, who identified PLS as the RA parameter of major clinical relevance (4). The relevance of RA PLS may underline the importance of the reservoir function itself and the early impact of RV maladaptation on this specific phase (24). Of note, we observed no prognostic relevance of Δ RA PS (as a measure of the conduit phase) using the Kaplan–Meier analysis, although RA conduit fraction percent (defined as the percentage of total RA area change happening prior to the electrical p wave) was previously associated with risk of adverse events in pediatric PAH (9, 25). Although both parameters mirror RA conduit function, they might not be directly comparable. Furthermore, pediatric

TABLE 3 | Key baseline parameters and changes during follow-up stratified by tertile of longitudinal RA function.

Characteristics	RA peak longitudinal strain tertile			
	Worsened ($n = 19$)	Stable ($n = 18$)	Improved ($n = 19$)	*p* value
Baseline				
BNP, pg/ml	106 [88–220]	182 [44–559]*	160 [62–429]	0.797
Mean pulmonary arterial pressure, mm Hg	41 ± 10	40 ± 9	46 ± 11	0.187
Right atrial pressure, mm Hg	8 [5–9]	8 [6–13]	8 [6–10]	0.508
Pulmonary vascular resistance, Wood Units	7 ± 3	7 ± 3	9 ± 3	0.178
Cardiac index, l/min/m^2	2.4 ± 0.4	2.5 ± 0.6	2.3 ± 0.5	0.399
Pulmonary arterial capacitance, ml/mmHg	1.4 [1.1–2.3]	1.6 [1.1–1.9]	1.4 [0.9–1.9]	0.624
RV end-diastolic area, cm^2	23 [18–29]	28 [23–35]	28 [25–32]	0.095
RV end-systolic area, cm^2	18 [12–22]	18 [17–20]	22 [17–27]	0.131
Fractional area change, %	27 ± 8	24 ± 14	24 ± 10	0.655
TAPSE/PASP, mm/mmHg	0.29 [0.22–0.40]	0.31 [0.21–0.46]	0.28 [0.18–0.41]	0.668
RV global longitudinal strain, %	−17.2 ± 3.7	−13.1 ± 5.5	−14.7 ± 4.3	0.050
RA area, cm^2	17 [14–20]	18 [17–20]	18 [14–22]	0.288
Δ During follow-up				
Δ Mean pulmonary arterial pressure, mm Hg	2 ± 10†	−7 ± 11‡	−8 ± 8†	0.039
Δ Pulmonary arterial capacitance, ml/mm Hg	−0.02 [−0.53–0.27]†	0.63 [−0.11–1.00]‡	0.88 [0.36–1.4]†	0.006
Δ Pulmonary vascular resistance, Wood Units	−0.1 ± 3.0†	−2.4 ± 3.7‡	−4.2 ± 2.8†	0.009
Δ BNP, pg/ml	0 [−71–68]	−61 [−154–6]§	−83 [−305 to −21]	0.015
Δ TAPSE/PASP	−0.02 [−0.08–0.02]	0.04 [−0.04–0.14]*	0.09 [0.03–0.17]	0.018
Δ RA area, cm^2	1 ± 7	−3 ± 4	−3 ± 5	0.083
Δ RV end-diastolic area, cm^2	−2 ± 6*	−4 ± 3	−5 ± 5	0.103
Δ RV end-systolic area, cm^2	−1 ± 4	−5 ± 4	−6 ± 5	0.005
Δ Fractional area change, %	1 ± 11¶	6 ± 13	7.1 ± 15	0.271
Δ RV global longitudinal strain, %	−1.7 [−3.7 to −0.7]*	1.2 [−0.9–4.8]	4.6 [2.6–5.8]	<0.001

Δ, change; BNP, B-type natriuretic peptide; PASP, pulmonary arterial systolic pressure; RA, right atrial; RV, right ventricular; TAPSE, tricuspid annular plane systolic excursion.
Values represent mean ± SD or median (interquartile range) (for normally or non-normally distributed parameters, respectively), unless otherwise specified.
**Available in 17 patients.*
†Available in 13 patients.
‡Available in 12 patients.
§Available in 16 patients.
¶Available in 18 patients.

PAH might differ significantly from PAH in adults; limited data exist on comparison of these two populations.

Although we observed no general normalization or restoration of RA function in the overall study population after starting PAH treatment, subanalysis revealed different individual patterns of RA functional response by means of changes in PLS. We were able to identify three different patterns of RA function, with either improved, stable, or worsened reservoir function (as mirrored by RA PLS). Moreover, our data indicate that improvement or deterioration of RA function is directly associated with the extent of RV reverse remodeling. Substantial improvement of RA function was associated with a relevant reduction of afterload, pressure, and RV volume under specific therapy. In turn, impairment of RV function during follow-up was directly related to worsening of RA PLS with a subsequent higher probability for a clinical worsening event, highlighting the importance of RA-RV interplay. Improvement of RV function (strain, FAC, and RV volume) after starting PAH treatment was therefore associated with improved RA function. Moreover, our data indicate that RA strain is a dependent variable whose improvements are secondary to improvements in pulmonary arterial and RV parameters. Patients who failed to improve under specific therapy, with no RV reverse remodeling or reduction of afterload, eventually showed worsened RA mechanics as measured by peak RA strain. Of note, RA PLS mirrors RA reservoir function during RV contraction (26). Therefore, the observed association of RV global longitudinal strain with RA PLS indicates that improved RV systolic function also translates into improved RA reservoir function. Again, this highlights the interplay and importance of the RA-RV axis (6).

Decreased afterload leads to better RV function and obviously to better RA filling, presumably through less RV filling at end-diastole and improved venous return. As there is a continuum of elevated PVR, reduced RV function and consecutive impairment of RA function in PH, a failure of the RA-RV axis eventually enhances consecutive dyspnea and congestion (23). Thus, the key target of PH medication is afterload reduction which indirectly improves downstream RV and RA function through improved

hemodynamic interplay. Our data emphasize that the RA-RV axis is a unit rather than two separate entities and that RV and RA function are inextricably linked to each other. Therapies directly supporting RA function (27) may play an important role in this context and studies are warranted.

Limitations

This study has some limitations. First of all, this is a retrospective single-center study and our results may need to be validated in larger prospective cohorts. The sample size and event rate limited the multivariate models and prevented further in-depth analysis. However, to the best of our knowledge, this is the largest study conducted so far focusing on the clinical relevance of RA function in treatment-naïve patients with PAH. Moreover, we were able to provide follow-up data on RA function after treatment initiation, providing additional important information regarding the adaptation of RA function during treatment. The relatively short follow-up period of the study cohort may be an additional limitation.

Conclusion

After initiation of specific pulmonary vascular therapy, patients with PAH may show different patterns of RA functional response. Recovery of RA functional parameters is significantly related to improvement of RV function. Patients with improvement of RA function in response to PAH therapy have better outcomes than those with stable or worsening RA function. RA functional improvement may thus serve as an additional predictor of treatment response.

DATA AVAILABILITY STATEMENT

The raw data supporting the conclusions of this article will be made available by the authors, without undue reservation.

ETHICS STATEMENT

All participants gave written informed consent for the enrollment into the University of Giessen PH Registry. The investigation conforms to the Declaration of Helsinki and was approved by the Ethics Committee of the Faculty of Medicine at the University of Giessen (approval #266/11). The patients/participants provided their written informed consent to participate in this study.

AUTHOR CONTRIBUTIONS

KT, HAG, WS, HG, and MR contribute to the study design and patient recruitment. KT, HAG, DZ, ZR, WS, HG, and MR contribute to the data collection and analysis. HG and MR contribute to the statistical analyses. KT, HAG, AY, LK, DZ, PD, WS, HG, and MR contribute to the drafting of the manuscript. KT, HAG, AY, DZ, WS, SR, DZ, PD, DB, KO, HG, BB, AY, and MR contribute to the critical revision of the manuscript for important intellectual content. All authors contributed to the article and approved the submitted version.

FUNDING

MR and LK received funding from the JLU-CAREER program (German Research Foundation, DFG, 413584448). KT received funding from the Collaborative Research Center (SFB) 1213—Pulmonary Hypertension and Cor Pulmonale, Grant Number SFB1213/1, project B08 (German Research Foundation, Bonn, Germany). PD was funded by the European Respiratory Society—ERS Clinical Training Research Fellowship (CTF202004-00806).

ACKNOWLEDGMENTS

The manuscript is part of the doctoral thesis of DZ. We thank Claire Mulligan, PhD (Beacon Medical Communications Ltd., Brighton, UK) for editorial support, funded by the University of Giessen.

SUPPLEMENTARY MATERIAL

The Supplementary Material for this article can be found online at: https://www.frontiersin.org/articles/10.3389/fcvm.2021.775039/full#supplementary-material

REFERENCES

1. Ren X, Johns RA, Gao WD. EXPRESS: right heart in pulmonary hypertension: from adaptation to failure. *Pulm Circ*. (2019) 9:2045894019845611. doi: 10.1177/2045894019845611
2. Vonk Noordegraaf A, Chin KM, Haddad F, Hassoun PM, Hemnes AR, Hopkins SR, et al. Pathophysiology of the right ventricle and of the pulmonary circulation in pulmonary hypertension: an update. *Eur Respir J*. (2019) 53:1801900. doi: 10.1183/13993003.01900-2018
3. D'Alto M, D'Andrea A, Di Salvo G, Scognamiglio G, Argiento P, Romeo E, et al. Right atrial function and prognosis in idiopathic pulmonary arterial hypertension. *Int J Cardiol*. (2017) 248:320–5. doi: 10.1016/j.ijcard.2017.08.047
4. Alenezi F, Mandawat A, Il'Giovine ZJ, Shaw LK, Siddiqui I, Tapson VF, et al. Clinical utility and prognostic value of right atrial function in pulmonary hypertension. *Circ Cardiovasc Imaging*. (2018) 11:e006984. doi: 10.1161/CIRCIMAGING.117.006984
5. Alenezi F, Rajagopal S. The right atrium, more than a storehouse. *Int J Cardiol*. (2021) 331:329–30. doi: 10.1016/j.ijcard.2021.01.069
6. Gaynor SL, Maniar HS, Bloch JB, Steendijk P, Moon MR. Right atrial and ventricular adaptation to chronic right ventricular pressure overload. *Circulation*. (2005) 112(9 Suppl.):I212–8. doi: 10.1161/CIRCULATIONAHA.104.517789
7. Richter MJ, Fortuni F, Wiegand MA, Dalmer A, Vanderpool R, Ghofrani HA, et al. Association of right atrial conduit phase with right ventricular lusitropic function in pulmonary hypertension. *Int J Cardiovasc Imaging*. (2020) 36:633–42. doi: 10.1007/s10554-019-01763-x
8. Bening C, Leyh R. Right atrial contractile dynamics are impaired in patients with postcapillary pulmonary hypertension. *Exp Ther Med*. (2016) 12:792–8. doi: 10.3892/etm.2016.3399

9. Frank BS, Schafer M, Thomas TM, Ivy DD, Jone PN. Longitudinal assessment of right atrial conduit fraction provides additional insight to predict adverse events in pediatric pulmonary hypertension. *Int J Cardiol*. (2021) 329:242–5. doi: 10.1016/j.ijcard.2020.12.073
10. Gall H, Felix JF, Schneck FK, Milger K, Sommer N, Voswinckel R, et al. The Giessen Pulmonary Hypertension Registry: survival in pulmonary hypertension subgroups. *J Heart Lung Transplant*. (2017) 36:957–67. doi: 10.1016/j.healun.2017.02.016
11. Simonneau G, Montani D, Celermajer DS, Denton CP, Gatzoulis MA, Krowka M, et al. Haemodynamic definitions and updated clinical classification of pulmonary hypertension. *Eur Respir J*. (2019) 53:1801913. doi: 10.1183/13993003.01913-2018
12. Galie N, Channick RN, Frantz RP, Grunig E, Jing ZC, Moiseeva O, et al. Risk stratification and medical therapy of pulmonary arterial hypertension. *Eur Respir J*. (2019) 53:1801889. doi: 10.1183/13993003.01889-2018
13. Oakland HT, Joseph P, Elassal A, Cullinan M, Heerdt PM, Singh I. Diagnostic utility of sub-maximum cardiopulmonary exercise testing in the ambulatory setting for heart failure with preserved ejection fraction. *Pulm Circ*. (2020) 10:2045894020972273. doi: 10.1177/2045894020972273
14. Rudski LG, Lai WW, Afilalo J, Hua L, Handschumacher MD, Chandrasekaran K, et al. Guidelines for the echocardiographic assessment of the right heart in adults: a report from the American Society of Echocardiography endorsed by the European Association of Echocardiography, a registered branch of the European Society of Cardiology, and the Canadian Society of Echocardiography. *J Am Soc Echocardiogr*. (2010) 23:685–713. doi: 10.1016/j.echo.2010.05.010
15. Kiely DG, Levin D, Hassoun P, Ivy DD, Jone PN, Bwika J, et al. EXPRESS: statement on imaging and pulmonary hypertension from the Pulmonary Vascular Research Institute (PVRI). *Pulm Circ*. (2019) 9:2045894019841990. doi: 10.1177/2045894019841990
16. Gall H, Yogeswaran A, Fuge J, Sommer N, Grimminger F, Seeger W, et al. Validity of echocardiographic tricuspid regurgitation gradient to screen for new definition of pulmonary hypertension. *EClinicalMedicine*. (2021) 34:100822. doi: 10.1016/j.eclinm.2021.100822
17. Hahn RT, Thomas JD, Khalique OK, Cavalcante JL, Praz F, Zoghbi WA. Imaging assessment of tricuspid regurgitation severity. *JACC Cardiovasc Imaging*. (2019) 12:469–90. doi: 10.1016/j.jcmg.2018.07.033
18. Richter MJ, Badagliacca R, Wan J, Vanderpool R, Dalmer A, Ghofrani HA, et al. Right ventricular dyssynchrony: from load-independent right ventricular function to wall stress in severe pulmonary arterial hypertension. *Pulm Circ*. (2020) 10:2045894020925759. doi: 10.1177/2045894020925759
19. Padeletti M, Cameli M, Lisi M, Malandrino A, Zaca V, Mondillo S. Reference values of right atrial longitudinal strain imaging by two-dimensional speckle tracking. *Echocardiography*. (2012) 29:147–52. doi: 10.1111/j.1540-8175.2011.01564.x
20. Badano LP, Kolias TJ, Muraru D, Abraham TP, Aurigemma G, Edvardsen T, et al. Standardization of left atrial, right ventricular, and right atrial deformation imaging using two-dimensional speckle tracking echocardiography: a consensus document of the EACVI/ASE/Industry Task Force to standardize deformation imaging. *Eur Heart J Cardiovasc Imaging*. (2018) 19:591–600. doi: 10.1093/ehjci/jey042
21. McLaughlin VV, Badesch DB, Delcroix M, Fleming TR, Gaine SP, Galie N, et al. End points and clinical trial design in pulmonary arterial hypertension. *J Am Coll Cardiol*. (2009) 54(1 Suppl.):S97–107. doi: 10.1016/j.jacc.2009.04.007
22. Alenezi F, Rajagopal S, Kutty S. Assessing right atrial function in pulmonary hypertension: window to the soul of the right heart? *Am J Physiol Heart Circ Physiol*. (2020) 318:H154–5. doi: 10.1152/ajpheart.00739.2019
23. Marcus JT, Westerhof BE, Groeneveldt JA, Bogaard HJ, de Man FS, Vonk Noordegraaf A. Vena cava backflow and right ventricular stiffness in pulmonary arterial hypertension. *Eur Respir J*. (2019) 54:1900625. doi: 10.1183/13993003.00625-2019
24. Gaynor SL, Maniar HS, Prasad SM, Steendijk P, Moon MR. Reservoir and conduit function of right atrium: impact on right ventricular filling and cardiac output. *Am J Physiol Heart Circ Physiol*. (2005) 288:H2140–5. doi: 10.1152/ajpheart.00566.2004
25. Frank BS, Schafer M, Thomas TM, Haxel C, Ivy DD, Jone PN. Right atrial conduit phase emptying predicts risk of adverse events in pediatric pulmonary arterial hypertension. *J Am Soc Echocardiogr*. (2020) 33:1006–13. doi: 10.1016/j.echo.2020.02.015
26. Hasselberg NE, Kagiyama N, Soyama Y, Sugahara M, Goda A, Ryo-Koriyama K, et al. The prognostic value of right atrial strain imaging in patients with precapillary pulmonary hypertension. *J Am Soc Echocardiogr*. (2021) 34:851–61.e1. doi: 10.1016/j.echo.2021.03.007
27. Khural JS, Houston BA, Leary PJ, Mathai SC, Kolb TM, Damico R, et al. Right atrial pacing to improve acute hemodynamics in pulmonary arterial hypertension. *Am J Respir Crit Care Med*. (2021) 203:508–11. doi: 10.1164/rccm.202006-2278LE

Conflict of Interest: MR has received support from Bayer; speaker fees from Bayer, Janssen-Cilag GmbH, and OMT and consultancy fees from Bayer and Janssen-Cilag GmbH. PD reports personal fees and non-financial support from Actelion, non-financial support from Astra Zeneca, non-financial support from Bayer, non-financial support from GSK, personal fees and non-financial support from MSD, non-financial support from Novartis, non-financial support from Teva, non-financial support from Boehringer Ingelheim, non-financial support from Vifor, non-financial support from Menarini outside the submitted work. HG has received consultancy fees from Bayer, Actelion, Pfizer, Merck, GSK, and Novartis; fees for participation in advisory boards from Bayer, Pfizer, GSK, Actelion, and Takeda; lecture fees from Bayer HealthCare, GSK, Actelion, and Encysive/Pfizer; industry-sponsored grants from Bayer HealthCare, Aires, Encysive/Pfizer, and Novartis; and sponsored grants from the German Research Foundation, Excellence Cluster Cardiopulmonary Research, and the German Ministry for Education and Research. WS has received speaker/consultancy fees from Abivax, Bayer AG, Liquidia Technologies, Pieris Pharmaceuticals, United Therapeutics and Vectura. HG has received fees from Actelion, AstraZeneca, Bayer, BMS, GSK, Janssen-Cilag, Lilly, MSD, Novartis, OMT, Pfizer, and United Therapeutics. KT has received speaking fees from Actelion and Bayer.

The remaining authors declare that the research was conducted in the absence of any commercial or financial relationships that could be construed as a potential conflict of interest.

Publisher's Note: All claims expressed in this article are solely those of the authors and do not necessarily represent those of their affiliated organizations, or those of the publisher, the editors and the reviewers. Any product that may be evaluated in this article, or claim that may be made by its manufacturer, is not guaranteed or endorsed by the publisher.

frontiers in Cardiovascular Medicine

ORIGINAL RESEARCH
published: 07 December 2021
doi: 10.3389/fcvm.2021.771363

Myocardial Extracellular Volume Fraction and T1 Mapping by Cardiac Magnetic Resonance Compared Between Patients With and Without Type 2 Diabetes, and the Effect of ECV and T2D on Cardiovascular Outcomes

Issarayus Laohabut[1], *Thammarak Songsangjinda*[1], *Yodying Kaolawanich*[1], *Ahthit Yindeengam*[2] *and Rungroj Krittayaphong*[1]*

[1] Division of Cardiology, Department of Medicine, Faculty of Medicine Siriraj Hospital, Mahidol University, Bangkok, Thailand, [2] Faculty of Medicine Siriraj Hospital, Her Majesty Cardiac Center, Mahidol University, Bangkok, Thailand

OPEN ACCESS

Edited by:
Grigorios Korosoglou,
GRN Klinik Weinheim, Germany

Reviewed by:
Sorin Giusca,
GRN Klinik Weinheim, Germany
Alexandros Kallifatidis,
St.Luke's Hospital, Greece

***Correspondence:**
Rungroj Krittayaphong
rungroj.kri@mahidol.ac.th

Specialty section:
This article was submitted to Cardiovascular Imaging, a section of the journal Frontiers in Cardiovascular Medicine

Received: 06 September 2021
Accepted: 01 November 2021
Published: 07 December 2021

Citation:
Laohabut I, Songsangjinda T, Kaolawanich Y, Yindeengam A and Krittayaphong R (2021) Myocardial Extracellular Volume Fraction and T1 Mapping by Cardiac Magnetic Resonance Compared Between Patients With and Without Type 2 Diabetes, and the Effect of ECV and T2D on Cardiovascular Outcomes. Front. Cardiovasc. Med. 8:771363. doi: 10.3389/fcvm.2021.771363

Background: To investigate the difference in myocardial extracellular volume fraction (ECV) by cardiac magnetic resonance (CMR) T1 mapping between patients with and without type 2 diabetes (T2D), and the effect of ECV and T2D on cardiovascular (CV) outcomes.

Methods: All patients aged > 18 years with known or suspected coronary artery disease who underwent CMR for assessment of myocardial ischemia or myocardial viability at the Department of Cardiology of the Faculty of Medicine Siriraj Hospital, Mahidol University, Bangkok, Thailand from September 2017 to December 2018 were screened for inclusion eligibility. Left ventricular ejection fraction (LVEF), late gadolinium enhancement, and T1 mapping were performed. ECV values were derived from myocardial native T1 and contrast-enhanced T1 values that were obtained using modified Look-Locker inversion recovery at the septum of the mid-cavity short-axis map. Demographic data, clinical characteristics, and CV outcomes were collected by retrospective chart review. Composite CV outcomes included CV death, acute coronary syndrome, heart failure hospitalization, or ventricular tachycardia (VT)/ventricular fibrillation.

Results: A total of 739 subjects (mean age: 69.5 ± 14.0 years, 49.3% men) were included. Of those, 188 subjects had T2D (25.4%). ECV was significantly higher in T2D than in non-T2D (30.0 ± 5.9% vs. 28.8 ± 4.7%, $p = 0.004$). During the mean follow-up duration of 26.2 ± 8.5 months, 43 patients (5.8%) had a clinical composite outcome, as follows: three CV death (0.4%), seven acute coronary syndrome (0.9%), 33 heart failure hospitalization (4.5%), and one VT (0.1%). T2D, low LVEF, and high ECV were all identified as independent predictors of CV events. Patients with T2D and high ECV had the highest risk of CV events.

Conclusion: Among patients with known or suspected coronary artery disease, patients with T2D had a higher ECV. T2D and high ECV were both found to be independent risk factors for adverse CV outcomes.

Keywords: myocardial extracellular volume fraction, type 2 diabetes, cardiovascular outcomes, cardiac magnetic resonance, T1 mapping

INTRODUCTION

Type 2 diabetes mellitus (T2D), which is a common chronic disease, is a well-recognized risk factor for heart failure (HF) independent of age, hypertension (HT), obesity, hypercholesterolemia, and coronary artery disease (CAD) (1). Patients with T2D have worse outcomes once HF has developed (2). The direct effect of hyperglycemia and insulin resistance on myocardial cellular metabolism may contribute to cardiac dysfunction by alteration of energy-substrate supply and impairment of metabolic-substrate switching under stress conditions. T2D also causes various morphologic changes of myocytes, extracellular matrix (ECM), and microvasculature. In addition, the accumulation of advanced glycation end products (AGEs) in the myocardium may contribute to HF events. AGEs increase both cardiac stiffening and collagen cross-linking in the myocardial ECM, both of which adversely affect systolic and diastolic cardiac function (3, 4). Since ECM expansion in humans is reversible, such as by inhibition of the renin-angiotensin-aldosterone system, quantification of ECM expansion may be a useful therapeutic marker for early cardiac involvement in patients with T2D.

Advanced cardiac magnetic resonance (CMR) imaging facilitates detailed, non-invasive characterization of the myocardium, including T1-mapping, and the derived parameter is extracellular volume fraction (ECV) (5). Some previous studies investigated the role of ECV in patients with diabetes and pre-diabetes compared to normal controls. Both of those studies reported increased ECV to be associated with a longer duration of diabetes, and that increased ECV may be associated with elevated glycated hemoglobin (HbA_1c) level (6, 7). Another study found a significant association between diabetes and increased ECV, and that elevated ECV was significantly associated with an increased risk of adverse clinical outcomes, including HF and death (8).

This study aimed to investigate myocardial ECV by CMR T1 mapping compared between patients with and without T2D among patients with known or suspected CAD who were referred for CMR, and the effect of ECV and T2D on cardiovascular (CV) outcomes, including CV death, acute coronary syndrome (ACS), HF hospitalization, or ventricular tachycardia (VT)/ventricular fibrillation (VF).

METHODS

Study Population

The study design was a retrospective cohort study. All patients aged >18 years with known or suspected CAD who underwent CMR for assessment of myocardial ischemia or myocardial viability at the Department of Cardiology of the Faculty of Medicine Siriraj Hospital, Mahidol University, Bangkok, Thailand during September 2017 to December 2018 were screened for inclusion eligibility. Native and post-contrast T1 maps were routinely performed in every clinical CMR study. All included patients were followed-up at our center for at least 6 months after the date of CMR. Patients diagnosed with cardiac amyloidosis or hypertrophic cardiomyopathy were excluded. Study patients were then allocated to either the T2D group or the non-T2D group. Patients included in the T2D group were either previously diagnosed as T2D at another center, had a documented diagnosis in their Siriraj Hospital medical record, were receiving anti-diabetic medications, or had a documented laboratory test of either fasting plasma glucose $\geq$126 mg/dl or $HbA_{1C} \geq 6.5\%$ at least two times. The protocol for this study was approved by the Siriraj Institutional Review Board. Written informed consent was not obtained from study patients due to the retrospective confidentiality preserving nature of our study.

CMR Image Acquisition

Cardiac magnetic resonance (CMR) was performed on an Ingenia 3.0T MR system (Phillips Healthcare, Best, The Netherlands) using ECG gating. The default CMR protocol includes a steady-state pre-precession sequence using the balanced-fast-field-echo technique of left ventricular (LV) short-axis, four-chamber, two-chamber, and three-chamber views, late gadolinium enhancement (LGE), and native and contrast-enhanced T1 mapping. LGE was performed by the three-dimensional segmented-gradient-echo inversion-recovery sequence.

T1 mapping was performed using modified Look-Locker inversion recovery (MOLLI) in a 5-(3)-3 scheme (5, 9). MOLLI was performed with breath-holding technique in mid-diastole in a single mid-ventricular short-axis slice (TR 2.2 ms, TE 1.8 ms, eight different TIs, matrix 152 × 150, field of view 300 × 300 mm^2, flip angle 20°, SENSE 2, and 10-mm slice thickness).

CMR Analysis

The basic analysis was performed using IntelliSpace Portal (ISP) software version 11.1 (Phillips Healthcare, Best, The Netherlands) by well-trained radiographers (10-year experience) and cardiologist fellows (3–5 year experience). Cine images were analyzed and LV volumetric data were obtained to derive left ventricular ejection fraction (LVEF). LGE images were analyzed by visual assessment based on the consensus of two readers and were interpreted as ischemic or non-ischemic (10). For ischemic LGE, the transmural extent of LGE was graded as a subendocardial or transmural scar for each myocardial segment according to the recommendation of the American

Heart Association (AHA) (11). The analysis was blinded to the patient's name and functional images.

Native and contrast-enhanced T1 mapping was performed using CVI42 software version 5.12 (Circle Cardiovascular Imaging, Calgary, Alberta, Canada). The region of interest (ROI) was selected manually at the entire interventricular septum of the mid-cavity short-axis map while taking care to avoid imaging artifacts. According to the recommendation by the Society of Cardiovascular Magnetic Resonance (5), ROI for T1 mapping that was used to calculate ECV can be drawn at the septal segments or a complete single short-axis slice (usually a mid-ventricular slice). However, a single ROI drawn in the septum on mid-cavity short-axis maps is preferred to avoid lung, liver, and veins as sources of susceptibility artifacts. In another review article (12), the authors summarized that septal sampling has been shown to yield the greatest precision and minimize the effect of considerable variations of regional T1 values caused by the artifact-prone LV free wall myocardium. ECV was calculated using the following formula (13):

$$\text{ECV}\ (\%) = (1 - \text{Hematocrit}) \times \left(\frac{\frac{1}{\text{Post contrast T1}_{\text{Myocardium}}} - \frac{1}{\text{Native T1}_{\text{Myocardium}}}}{\frac{1}{\text{Post contrast T1}_{\text{Blood}}} - \frac{1}{\text{Native T1}_{\text{Blood}}}} \right) \times 100$$

According to a previous study that validated synthetic hematocrit (Hct) values derived from blood T1 obtained using a 3.0-T Philips MR system (Phillips Healthcare, Best, The Netherlands), we used the following formula to analyze the synthetic hematocrit (values between 0 and 1) for ECV (14):

$$\text{Synthetic Hct MOLLI} = (869.7 \times [1/\text{T1}_{\text{blood}}]) - 0.071$$

Data Collection

The following data were collected: age, gender, anthropometric data, underlying disease of HT, CAD, CKD, T2D, and the medications being used by the patient at the time of CMR. Collected laboratory data included hematocrit, serum creatinine, LDL, and HbA_{1c}, and those data were collected as close to the date of CMR as possible.

Outcome

The main outcome was a composite CV outcome consisting of CV death, ACS, HF hospitalization, or VT/VF. Data were collected from a medical record review. Events were collected from the time of CMR until the last follow-up visit by identifying the documented diagnosis of events by primary physicians and/or consulting cardiologists.

Statistical Analysis

Continuous data are presented as mean plus/minus SD, and means between two groups were compared using the Student's *t*-test for unpaired data. Categorical data are presented as the number and percentage of patients, and differences between groups were analyzed using the chi-squared test. Baseline characteristics, laboratory data, and CMR data were compared between patients with and without the composite outcome. Univariate and multivariate analyses were performed to identify variables that predict the composite outcome. We used all data (demographic data, CV risk factors, laboratory data, and CMR data) except medications for the univariate model and then selected variables with a $p < 0.05$ from univariate analysis to run a multivariate model. Time-to-event analysis was performed using Cox regression, and the results are presented as Kaplan–Meier curves. The incremental prognostic value of variables in the final multivariate model was assessed using a Cox regression model based on clinical data, investigational data, and ECV values. The incremental value was assessed by considering these variables in hierarchical order, and by comparing the global chi-squared value derived from each hierarchical model. All analyses were performed using SPSS version 18 (SPSS, Inc., Chicago, IL, USA). A $p < 0.05$ indicates statistical significance.

RESULTS

During the study period, 1,217 subjects underwent contrast-enhanced CMR for assessment of myocardial ischemia or viability. After the exclusion of patients with unavailable follow-up data and/or poor image quality, 739 patients remained for the final analysis. Of those eligible patients, 188 (25.4%) were allocated to the T2D group. A flow diagram of the patient enrollment process is shown in **Figure 1**.

Baseline Clinical and CMR Data of Patients With T2D and Non-T2D

Table 1 shows baseline patient characteristics compared between those with and without T2D. T2D subjects were significantly

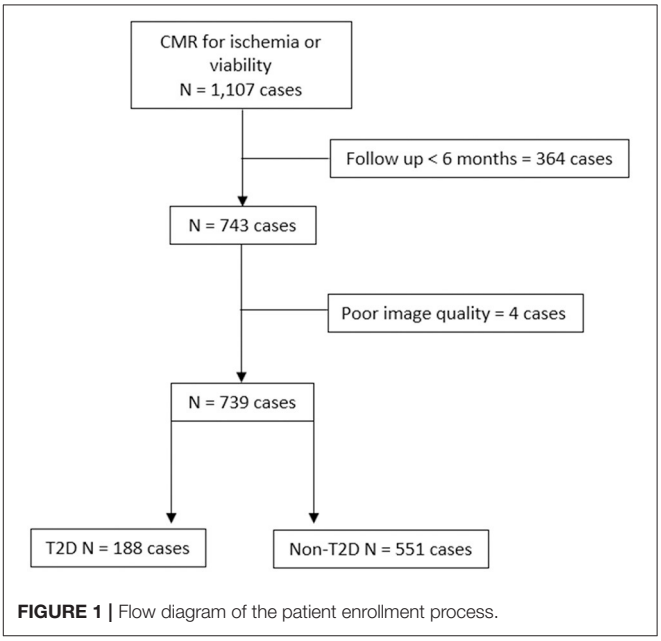

FIGURE 1 | Flow diagram of the patient enrollment process.

TABLE 1 | Baseline demographic and clinical data of all patients, and compared between those with and without type 2 diabetes.

Data	All ($N = 739$)	T2D ($n = 188$)	Non-T2D ($n = 551$)	*p*
Age (years)	69.5 ± 14.0	72.4 ± 10.5	68.5 ± 14.8	***<0.001***
Male gender	364 (49.3%)	93 (49.5%)	271 (49.2%)	0.946
BMI (kg/m^2)	25.4 ± 4.7	26.9 ± 5.6	24.8 ± 4.2	***<0.001***
Hypertension	418 (56.6%)	142 (75.5%)	276 (50.1%)	***<0.001***
Smoking	47 (6.4%)	17 (9.0%)	30 (5.4%)	0.081
Family history of CAD	7 (0.9%)	1 (0.5%)	6 (1.1%)	0.685
DLP	432 (58.5%)	143 (76.1%)	289 (52.5%)	***<0.001***
History of MI	57 (7.7%)	13 (6.9%)	44 (8.0%)	0.635
CKD	185 (25.0%)	88 (46.8%)	97 (17.6%)	***<0.001***
Cardiovascular medication:				
Beta-blockers	315 (42.6%)	93 (49.5%)	222 (40.3%)	***0.028***
CCB	216 (29.2%)	89 (47.3%)	127 (23.0%)	***<0.001***
Nitrates	138 (18.7%)	49 (26.1%)	89 (16.2%)	***0.003***
ACEI	83 (11.2%)	21 (11.2%)	62 (11.3%)	0.975
ARB	123 (16.6%)	39 (20.7%)	84 (15.2%)	0.080
Aldosterone antagonist	30 (4.1%)	5 (2.7%)	25 (4.5%)	0.260
Aspirin	317 (42.9%)	115 (61.2%)	202 (63.7%)	***<0.001***
P_2Y_{12} inhibitors	114 (15.4%)	40 (21.3%)	74 (13.4%)	***0.010***
Statins	409 (55.3%)	152 (80.9%)	257 (46.6%)	***<0.001***
Laboratory data				
Hct (%)	38.8 ± 5.2	38.0 ± 5.2	39.2 ± 5.1	***0.010***
GFR (ml/min/1.73 m^2)	56.2 ± 24.0	53.5 ± 24.5	60.0 ± 22.8	***0.018***
LDL (mg/dl)	83.7 ± 36.6	79.8 ± 38.8	89.2 ± 32.6	***0.026***
HbA1C (%)	6.2 ± 2.2	6.8 ± 2.0	5.1 ± 2.4	***<0.001***
CMR findings				
LVEF (%)	64.2 ± 17.8	64.7 ± 18.9	64.0 ± 17.4	0.599
LVEF < 50%	134 (18.1%)	38 (20.2%)	96 (17.4%)	0.391
LGE present (%)	236 (31.9%)	73 (38.8%)	163 (29.6%)	***0.019***
T1 native (ms)	1,332 ± 63	1,335 ± 75	1,331 ± 58	0.516
ECV (%)	29.1 ± 5.0	30.0 ± 5.9	28.8 ± 4.7	***0.004***

Data presented as number and percentage of patients or mean ± SD.

A $p < 0.05$ indicates statistical significance (bold-italic).

T2D, type 2 diabetes; BMI, body mass index; CKD, chronic kidney disease; CAD, coronary artery disease; CCB, calcium channel blockers; ACEI, angiotensin converting enzyme inhibitors; ARB, angiotensin-receptor blockers; Hct, hematocrit; GFR, glomerular filtration rate; LDL, low-density lipoprotein-cholesterol; LVEF, left ventricular ejection fraction; ECV, extracellular volume fraction.

older (72.4 ± 10.5 vs. 68.5 ± 14.8 years, $p = 0.024$), had more comorbidities, and used more CV medications. In T2D group, the anti-diabetic medications used were metformin in 97 (51.6%), sulfonylurea in 78 (40.4%), thiazolidinediones in 21 (10.6%), DPP-4 inhibitors in 52 (27.7%), SGLT-2 inhibitors in 17 (9.0%), GLP-1 agonists in six (3.2%), and insulin in 14 (6.9%) patients. History of coronary disease confirmed by coronary angiogram before CMR was demonstrated in 92 patients (12.4%); 27 (29.4%), 28 (30.4%), and 37 (40.2%) had single, double, and triple vessel disease, respectively. Among patients with a coronary angiogram, 87 (94.6%) had coronary revascularization before CMR.

Results of CMR demonstrated an average LVEF of 64.2 ± 17.8%. There were no significant differences in LVEF and native T1 between T2D and non-T2D; however, T2D had a greater proportion of LGE and significantly higher ECV compared to non-T2D. LV hypertrophy as defined by LV mass index more than 95% of healthy volunteers was demonstrated in 65 cases (8.8%). LGE was present in 236 patients (31.9%). The mean number of segments with the scar was 5.2 ± 3.7 (from the 16-segment model). Among those who had LGE, it was CAD pattern (subendocardial or transmural scar) in 78.8%, non-CAD pattern in 19.1%, and combined in 2.1%. Sixty-five out of 191 patients (34.0%) with CAD pattern LGE were asymptomatic. Subsequent management of patients with asymptomatic CAD was restricted to the adjustment of cardiac medications in 23 (35.4%) cases, whereas 15 (23.1%) underwent invasive angiography due to ischemia or other clinical indications. For those who underwent coronary angiography, 14 out of 15 (94%) had significant stenosis in at least one coronary artery. With patients exhibiting non-ischemic LGE, mid-wall scar, patchy scar, right ventricular insertion scar, and the subepicardial

TABLE 2 | Baseline demographic and clinical data of all patients, and compared between those with and without cardiovascular composite outcome.

Variables	Composite outcome ($n = 43$)	No composite outcome ($n = 696$)	*p*
Age (years)	72.2 ± 14.1	69.3 ± 13.9	0.190
Male gender	24 (55.8%)	340 (48.9%)	0.375
BMI (kg/m^2)	25.0 ± 5.0	25.4 ± 5.0	0.564
T2D	24 (55.8%)	164 (23.6%)	***<0.001***
Hypertension	25 (58.1%)	393 (56.5%)	0.830
Smoking	3 (7.0%)	44 (6.3%)	0.749
Family history of CAD	1 (2.3%)	6 (0.9%)	0.344
DLP	24 (55.8%)	408 (58.6%)	0.717
History of MI	8 (18.6%)	49 (7.0%)	***0.013***
CKD	21 (48.8%)	164 (23.6%)	***<0.001***
Laboratory data			
Hct (%)	37.2 ± 5.1	38.9 ± 5.2	***0.042***
GFR (ml/min/1.73 m^2)	45.1 ± 24.7	57.5 ± 23.6	***0.006***
LDL (mg/dl)	83.8 ± 49.5	83.7 ± 34.8	0.991
HbA_{1c} (%) ($n = 265$)	6.8 ± 2.0	5.1 ± 2.4	***<0.001***
CMR findings			
LVEF (%)	49.1 ± 22.8	65.1 ± 17.0	***<0.001***
LGE present (%)	23 (53.5%)	213 (30.6%)	***0.002***
T1 native (ms)	1371 ± 93	1330 ± 60	***0.006***
ECV (%)	32.0 ± 7.0	29.0 ± 4.8	***0.008***

Data presented as number and percentage of patients or mean ± SD.
A $p < 0.05$ indicates statistical significance (bold-italic).
BMI, body mass index; T2D, type 2 diabetes; CKD, chronic kidney disease; CAD, coronary artery disease; CCB, calcium channel blockers; ACEI, angiotensin-converting enzyme inhibitors; ARB, angiotensin-receptor blockers; Hct, hematocrit; GFR, glomerular filtration rate; LDL, low-density lipoprotein-cholesterol; HbA_{1C}, glycated hemoglobin; LVEF, left ventricular ejection fraction; ECV, extracellular volume fraction.

scar was detected in 18 (36%), 12 (24%), 10 (20%), and 18 (36%) cases, respectively. Eight patients had two patterns of nonischemic LGE.

Myocardial ischemia was observed in 229 (31.0%) cases. The mean number of ischemic segments was 3.4 ± 3.7. With patients exhibiting inducible ischemia, 104 (45.4%) had just adjustment of their cardiac medications, whereas 96 (41.9%) underwent invasive angiography. For those who had a coronary angiogram, significant stenosis of at least one major coronary artery was demonstrated in 91 (95.8%). Indirect evidence of diastolic dysfunction such as LV hypertrophy and left atrial enlargement was observed in 65 (8.8%) and 148 (20.0%) patients, respectively.

CV Outcomes

The overall mean follow-up duration was 26.2 ± 8.5 months. Fifty-seven patients (7.7%) experienced death ($n = 20$), ACS ($n = 7$), HF hospitalization ($n = 33$), or VT/VF ($n = 1$) during follow-up. The composite outcomes (CV death, ACS, HF hospitalization, or VT/VF) occurred in 43 patients (5.8%). Comparisons of baseline clinical data and CMR data between patients with and without composite outcomes are shown in **Table 2**. Patients with a composite outcome had a higher proportion of T2D, CKD, CV drugs, LGE and lower Hct, GFR, and LVEF compared to those without the composite outcomes. Native T1 and ECV were higher in patients with composite outcomes.

TABLE 3 | Univariate and multivariate analysis for independent predictors of cardiovascular composite outcome.

Variables	Univariate analysis		Multivariate analysis	
	HR (95% CI)	*P*	aHR (95% CI)	*p*
Age ≥ 65	1.22 (0.60–2.48)	0.583		
Male gender	1.32 (0.72–2.40)	0.373		
BMI ≥ 25	1.04 (0.57–1.90)	0.900		
T2D	2.78 (1.52–5.10)	***0.001***	2.76 (1.51–5.06)	***0.001***
Hypertension	1.07 (0.58–0.96)	0.830		
Smoking	1.08 (0.34–3.50)	0.894		
Family history of CAD	4.31 (0.59–31.49)	0.150		
DLP	0.83 (0.45–1.51)	0.530		
History of MI	3.10 (1.44–6.6.9)	***0.004***		
CKD	2.57 (1.41–4.69)	***0.002***		
GFR	2.72 (1.18–6.29)	***0.019***		
LVEF < 50%	3.57 (1.93–6.59)	***<0.001***	3.11 (1.67–5.80)	***<0.001***
LGE present	2.58 (1.42–4.69)	***0.002***		
T1 native ≥ 1,367 ms	2.21 (1.17–4.16)	***0.014***		
ECV ≥ 30.95%	2.14 (1.14–4.04)	**0.019**	2.06 (1.12–3.79)	***0.020***

A $p < 0.05$ indicates statistical significance (bold-italic).
HR, hazard ratio; aHR, adjusted hazard ratio; T2D, type 2 diabetes; CKD, chronic kidney disease; ARB, angiotensin-receptor blockers; GFR, glomerular filtration rate; LVEF, left ventricular ejection fraction; ECV, extracellular volume fraction.

Univariate and Multivariate Analysis

All variables from **Table 2** were used for both univariate and multivariate analyses to identify predictors of the composite outcome. ECV was classified as high when the ECV was in the top quartile. The cut-off for the top quartile of ECV was 30.95%. From multivariate analysis, T2D [hazard ratio (HR): 2.41, 95% CI: 1.17–4.98], high ECV (HR: 2.01, 95% CI: 1.03–3.93), and LVEF <50% (HR: 2.31, 95% CI: 1.10–4.88) were identified as independent predictors of CV events (**Table 3**). The addition of ECV data significantly improved the prognostic power of a model, namely, CV risk factors, T2D status, and LVEF data, with a significant increase in global chi-squared values from 1.7 with CV risk factors without T2D to 17.6 for CV risk factors with T2D, to 36.1 for CV risk factors with T2D and LVEF <50%, and to 41.2 for CV risk factors with T2D, LVEF < 50%, and ECV ≥ 30.95% (**Figure 2**).

Survival Analysis

Figure 3 shows adjusted and unadjusted hazard graphs of the cumulative event rate compared between patients with and without T2D, and between patients with ECV above and below the 30.95% cut-off value. Patients with T2D and patients with high ECV both had an increased incidence of CV composite outcomes over time.

Figure 4 shows adjusted and unadjusted hazard graphs of the cumulative event rate compared among four groups, namely, (1)

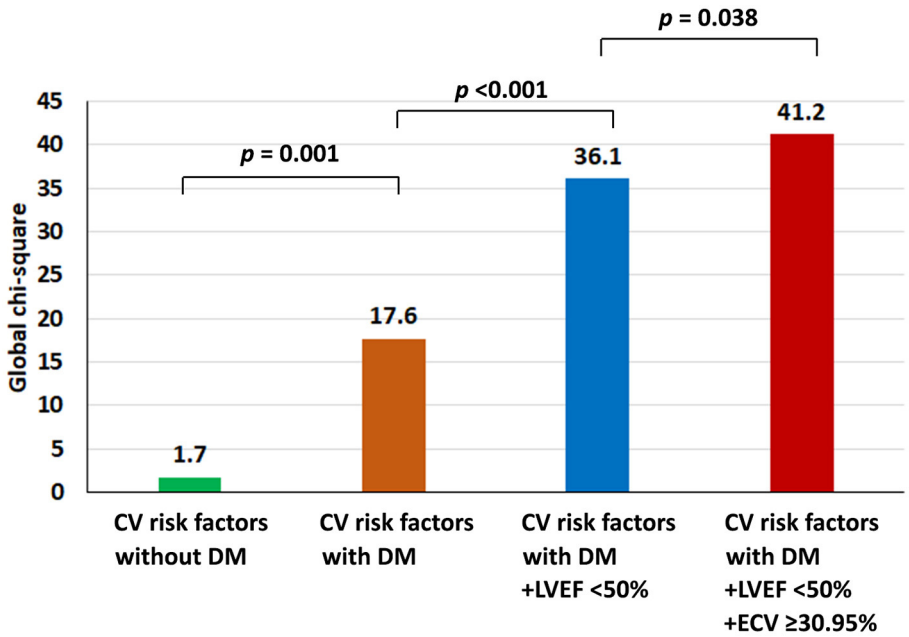

FIGURE 2 | Incremental prognostic value shown as global chi-squared value compared among patients with type 2 diabetes (T2D); patients with T2D and left ventricular ejection fraction (LVEF) < 50%; and patients with T2D, LVEF < 50%, and extracellular volume fraction ≥30.95%.

T2D and ECV ≥ 30.95%, (2) T2D and ECV < 30.95%, (3) non-T2D and ECV ≥ 30.95%, and (4) non-T2D and ECV < 30.95%. Both graphs demonstrate that the highest event rate was among patients with T2D and high ECV, and the lowest event rate was among patients with non-T2D and lower ECV. Patients with only one of these two factors had a prognosis in between the two aforementioned groups. **Figure 5** shows ECV mapping of patients with T2D and high ECV, T2D and lower ECV, high ECV without T2D, and lower ECV without T2D.

Sensitivity Analysis for ECV Data

To explore whether the significant finding of the predictive value of ECV remains significant when comparing ECV by methods other than the fourth quartile compared to the other three quartiles, we performed a sensitivity analysis of ECV for predicting clinical outcomes, including a hazard graph of patients with ECV above and below the cut-off value derived from receiver operating characteristic curve analysis (**Figure 6A**), and a hazard graph of each quartile of ECV (**Figure 6B**). Both of those sensitivity analyses showed a higher ECV to be significantly associated with an increased risk of adverse clinical outcomes. This finding reflects the predictive ability of ECV in this clinical setting.

We also performed a sensitivity analysis using ECV based on the results of actual Hct with 6 months before CMR which was available in 358 (48.4%) patients. ECV derived from the actual Hct had an HR and 95% CI for clinical outcomes of 3.37 (1.62–6.98). Multivariate analysis using ECV derived from actual Hct demonstrated that T2D, LVEF < 50%, high ECV (the fourth quartile of ECV and history of myocardial infarction were in the final model. The HR and 95% CI of ECV in the multivariate model were 2.50 (1.18–5.28).

DISCUSSION

This retrospective cohort study focused on the relationship between T2D and ECV, and the influence of these two factors on the clinical outcomes of patients who were referred for CMR for assessment of myocardial ischemia or viability. Our results showed ECV to be significantly higher in T2D than in non-T2D. Regarding CV outcome, T2D and high ECV were both found to be independent predictors of composite CV outcome. Patients with coexisting T2D and high ECV were shown to be at significantly higher risk of experiencing an adverse CV outcome.

T2D was previously reported to be significantly associated with an increased risk of CV outcomes, namely, HF (1), sudden cardiac death (15), and myocardial infarction (16). Our results also showed T2D to be significantly associated with composite CV outcome (HR: 2.95, 95% CI: 1.24–7.01), which is consistent with the results of previous studies.

A previous study reported that T2D was associated with higher ECV compared to non-T2D [30.2%, interquartile range (IQR): 26.9–32.7% vs. 28.1%, IQR: 25.9–31.0, respectively; $p < 0.001$] (8), and that higher ECV was significantly associated with the combined endpoints of death or incident HF admission for both patients with T2D (HR: 1.52, 95% CI: 1.21–1.89) and patients with non-T2D (HR: 1.46, 95% CI: 1.25–1.71). Our study showed that patients with T2D had higher ECV. T2D, high ECV, and LVEF < 50% were all found to be independent predictors of an increased risk for adverse CV outcomes. The impact

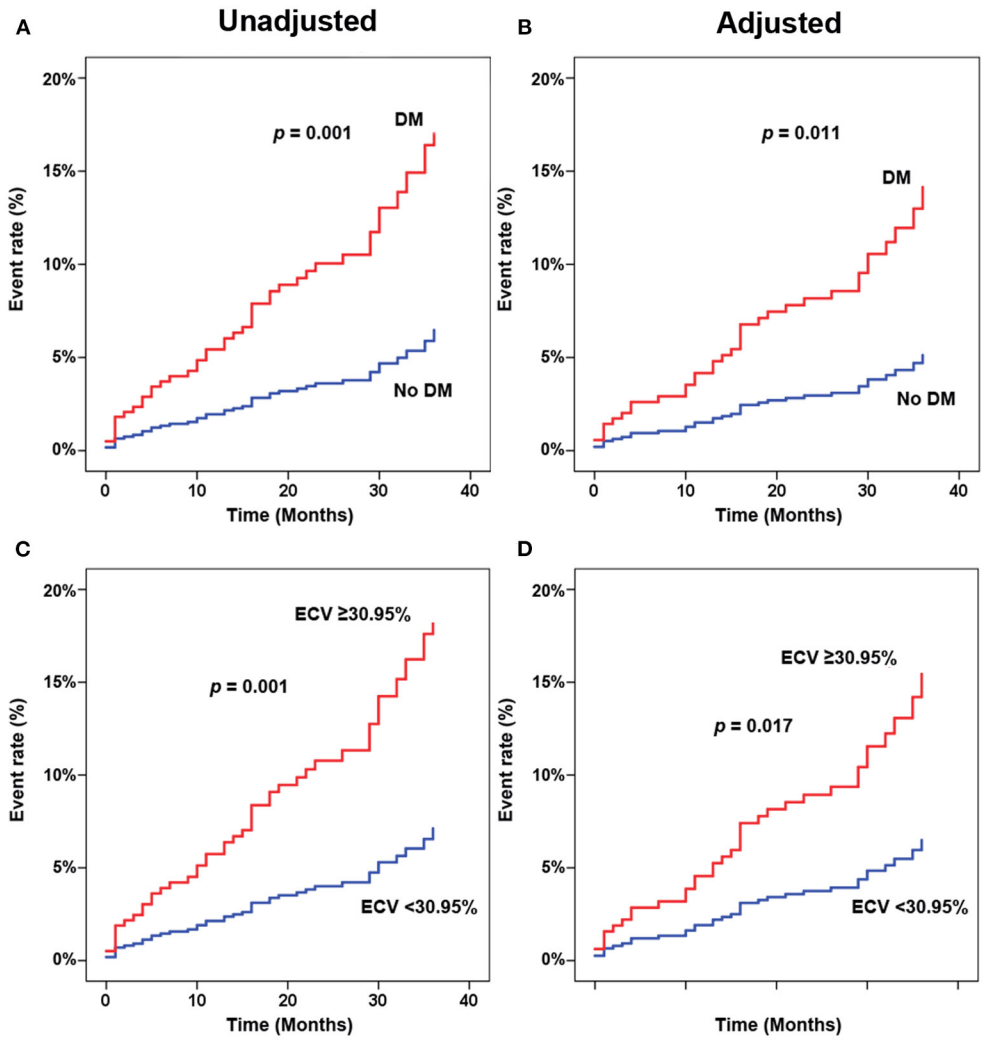

FIGURE 3 | Adjusted **(A,C)** and unadjusted **(B,D)** hazard graphs of the cumulative event rate compared between patients with and without type 2 diabetes (T2D) **(A,B)**, and between patients with extracellular volume fraction (ECV) above and below the cut-off value.

of T2D and high ECV on CV outcomes was independent of LVEF. ECV was associated with worse composite CV outcomes (HR: 2.01, 95% CI: 1.03–3.93). We also showed the incremental prognostic value of the factors that independently predict composite outcomes that were derived from the final multivariate model, including T2D, LVEF < 50%, and high ECV. In addition, we demonstrated that patients with coexisting T2D and high ECV were associated with a higher risk of adverse CV outcomes.

Although LGE was a significant predictor for clinical outcome in the univariate analysis, it was removed from the final multivariate model. LGE, LVEF < 50%, and high ECV are variables derived from CMR and the three variables may have different impacts on the incremental prognostic value. We tested this hypothesis by running an analysis on the incremental prognostic value three times with the simulation of the presence of the data on two components and adding the third component. We found that with the presence of data of LVEF < 50%, and high ECV, adding LGE data did not significantly increase the prognostic value. However, LVEF < 50% or high ECV significantly increase the prognostic value when they were added as the third variable. This finding means that LVEF < 50% and high ECV were more significant predictors than LGE.

Late gadolinium enhancement (LGE) is a good predictor of clinical outcomes in patients with T2D (17). Stress CMR images had an add-on predictive value on top of LGE in patients with and without T2D (18, 19). It helps reclassify risk in patients with T2D who were referred for stress CMR. LGE is a hallmark for poor outcomes in patients with T2D whereas myocardial ischemia was a good predictor both in patients with and without T2D (19). Our study explores the predictive value of ECV which is another aspect of CMR in patients with T2D.

As mentioned earlier, T2D is associated with various morphologic changes to myocytes, ECM, and microvasculature, which individually and in combination exert an adverse

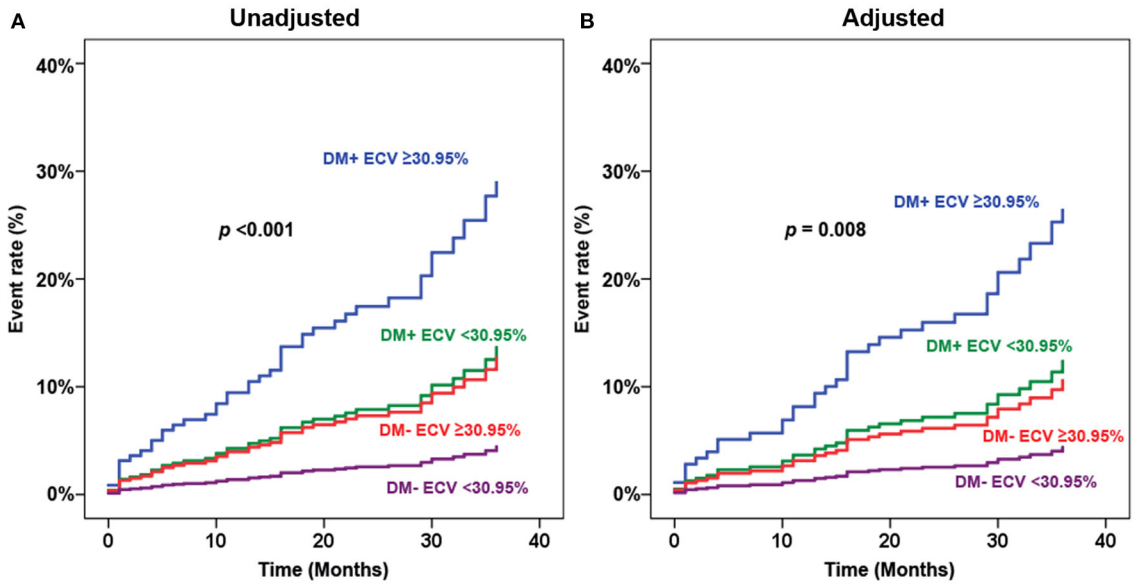

FIGURE 4 | Adjusted **(A)** and unadjusted **(B)** hazard graphs of the cumulative event rate compared among four groups, namely, (1) type 2 diabetes (T2D) and extracellular volume fraction (ECV) ≥30.95%, (2) T2D and ECV < 30.95%, (3) non-T2D and ECV ≥ 30.95%, and (4) non-T2D and ECV < 30.95%.

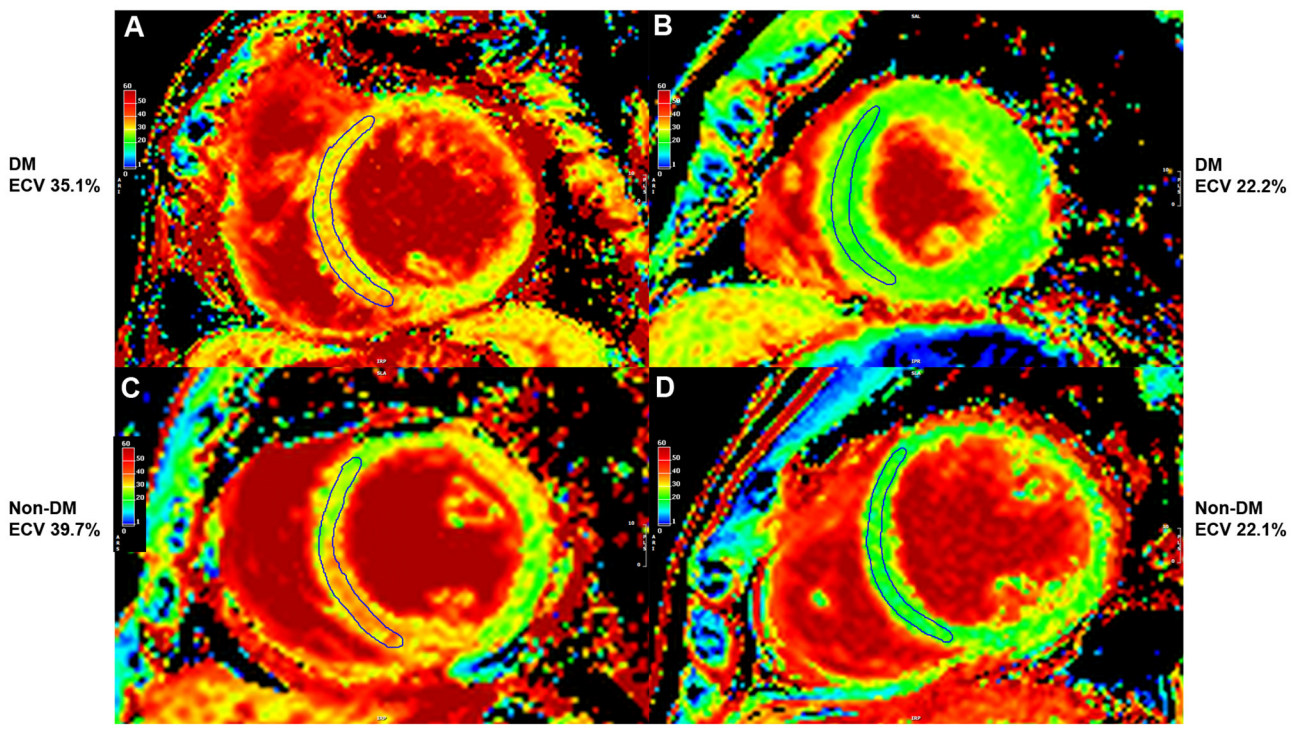

FIGURE 5 | Extracellular volume fraction (ECV) mapping of patients with type 2 diabetes (T2D) and high ECV **(A)**, T2D and lower ECV **(B)**, high ECV without T2D **(C)**, and lower ECV without T2D **(D)**.

influence on CV outcomes. T2D effectuates myocardial ECM expansion *via* the accumulation of AGEs, with reported resulting myocardial fibrosis, systolic and diastolic dysfunction (20), vasomotor dysfunction (21), arrhythmia (22), and mortality (8). The results of this study prove that patients with T2D have higher ECV, which has a strong negative impact on worse CV outcomes when compared to patients with non-T2D.

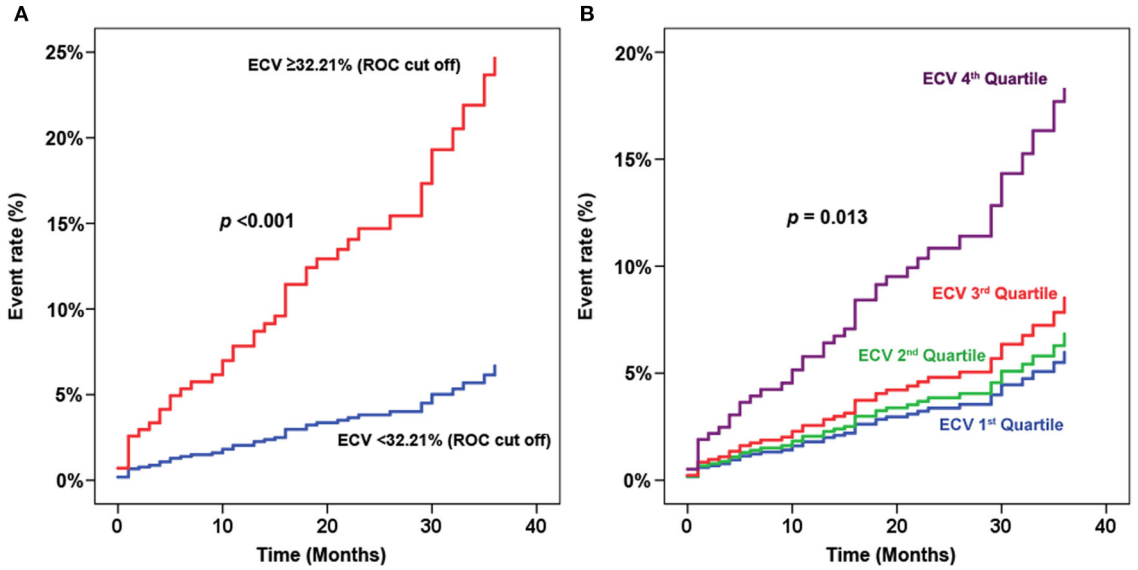

FIGURE 6 | Sensitivity analysis of extracellular volume fraction (ECV) for predicting clinical outcomes. **(A)** Hazard graph of patients with ECV above and below the cut-off value derived from receiver operating characteristic (ROC) curve analysis. **(B)** Hazard graph of each quartile of ECV.

We demonstrated that high ECV is an independent predictor for the adverse CV outcomes in patients with T2D. High ECV added prognostic value on top of CV risk factors, T2D status, and low LVEF. Although LGE data is an independent prognostic factor in patients with T2D (17), it was not an independent predictor in the presence of T2D, low LVEF, and ECV data.

Limitations

This study has some limitations. First, our study had a retrospective design. Given that our data were retrospectively collected and hematocrit level was not routinely required before CMR, we did not have available hematocrit data for all patients. To compensate, we used a synthetic hematocrit formula to derive ECV in this study. Second, the data included in this study was from a single center. Third, this is a retrospective cohort study based on the existing CMR data to answer the research question. Therefore, we did not have healthy normal as a control group. However, our study aimed to determine, among patients with known or suspected CAD who were referred for CMR, the difference in ECV between T2D and non-T2D and to determine the influence of T2D and ECV on composite clinical outcome. A multicenter study in a much larger study population and longer follow-up duration may yield greater insight into the relationship between T2D and ECV, and may identify additional risk factors for adverse CV outcomes. Furthermore, the effect of medication changes on CMR variables, including ECV merits further investigation in future studies.

CONCLUSION

Among patients with known or suspected CAD, ECV was higher in patients with T2D than in patients with non-T2D. T2D, low LVEF, and high ECV were both identified as independent predictors of adverse CV outcomes. Patients with T2D with coexisting high ECV were strongly associated with adverse CV outcomes.

DATA AVAILABILITY STATEMENT

The original contributions presented in the study are included in the article/supplementary material, further inquiries can be directed to the corresponding author.

ETHICS STATEMENT

The protocol for this study was approved by the Siriraj Institutional Review Board. The Ethics Committee waived the requirement of written informed consent for participation.

AUTHOR CONTRIBUTIONS

Concept and design, data acquisition, interpretation of data, manuscript preparation, manuscript revision, and manuscript review by IL and RK. Data acquisition, data analysis, manuscript revision, and manuscript review by TS, YK, and AY. All authors read, approved the final manuscript, and approved the submission of this manuscript for journal publication.

ACKNOWLEDGMENTS

The authors gratefully acknowledge Prajak Tanapibunpon, for data management.

REFERENCES

1. Kannel WB, Hjortland M, Castelli WP. Role of diabetes in congestive heart failure: the Framingham study. *Am J Cardiol.* (1974) 34:29–34. doi: 10.1016/0002-9149(74)90089-7
2. Standl E, Schnell O, McGuire DK. Heart Failure Considerations of Antihyperglycemic Medications for Type 2 Diabetes. *Circ Res.* (2016) 118:1830–43. doi: 10.1161/CIRCRESAHA.116.306924
3. MacDonald MR, Petrie MC, Hawkins NM, Petrie JR, Fisher M, McKelvie R, et al. Diabetes, left ventricular systolic dysfunction, and chronic heart failure. *Eur Heart J.* (2008) 29:1224–40. doi: 10.1093/eurheartj/ehn156
4. Russell ND, Cooper ME. 50 years forward: mechanisms of hyperglycaemia-driven diabetic complications. *Diabetologia.* (2015) 58:1708–14. doi: 10.1007/s00125-015-3600-1
5. Messroghli DR, Moon JC, Ferreira VM, Grosse-Wortmann L, He T, Kellman P, et al. Clinical recommendations for cardiovascular magnetic resonance mapping of T1, T2, T2* and extracellular volume: A consensus statement by the Society for Cardiovascular Magnetic Resonance (SCMR) endorsed by the European Association for Cardiovascular Imaging (EACVI). *J Cardiovasc Magn Reson.* (2017) 19:75. doi: 10.1186/s12968-017-0389-8
6. Shang Y, Zhang X, Leng W, Chen L, Lei X, Zhang T, et al. Assessment of diabetic cardiomyopathy by cardiovascular magnetic resonance T1 mapping: correlation with left-ventricular diastolic dysfunction and diabetic duration. *J Diabetes Res.* (2017) 2017:9584278. doi: 10.1155/2017/9584278
7. Storz C, Hetterich H, Lorbeer R, Heber SD, Schafnitzel A, Patscheider H, et al. Myocardial tissue characterization by contrast-enhanced cardiac magnetic resonance imaging in subjects with prediabetes, diabetes, and normal controls with preserved ejection fraction from the general population. *Eur Heart J Cardiovasc Imaging.* (2018) 19:701–8. doi: 10.1093/ehjci/jex190
8. Wong TC, Piehler KM, Kang IA, Kadakkal A, Kellman P, Schwartzman DS, et al. Myocardial extracellular volume fraction quantified by cardiovascular magnetic resonance is increased in diabetes and associated with mortality and incident heart failure admission. *Eur Heart J.* (2014) 35:657–64. doi: 10.1093/eurheartj/eht193
9. Higgins DM, Moon JC. Review of T1 mapping methods: comparative effectiveness including reproducibility issues. *Curr Cardiovasc Imaging Rep.* (2014) 7:9252. doi: 10.1007/s12410-013-9252-y
10. Lee E, Ibrahim EH, Parwani P, Bhave N, Stojanovska J. Practical guide to evaluating myocardial disease by cardiac MRI. *AJR Am J Roentgenol.* (2020) 214:546–56. doi: 10.2214/AJR.19.22076
11. Cerqueira MD, Weissman NJ, Dilsizian V, Jacobs AK, Kaul S, Laskey WK, et al. Standardized myocardial segmentation and nomenclature for tomographic imaging of the heart. A statement for healthcare professionals from the Cardiac Imaging Committee of the Council on Clinical Cardiology of the American Heart Association. *Int J Cardiovasc Imaging.* (2002) 18:539–42. doi: 10.1161/hc0402.102975
12. Puntmann VO, Peker E, Chandrashekhar Y, Nagel E. T1 Mapping in characterizing myocardial disease: a comprehensive review. *Circ Res.* (2016) 119:277–99. doi: 10.1161/CIRCRESAHA.116.307974
13. Haaf P, Garg P, Messroghli DR, Broadbent DA, Greenwood JP, Plein S. Cardiac T1 Mapping and Extracellular Volume (ECV) in clinical practice: a comprehensive review. *J Cardiovasc Magn Reson.* (2016) 18:89. doi: 10.1186/s12968-016-0308-4
14. Fent GJ, Garg P, Foley JRJ, Swoboda PP, Dobson LE, Erhayiem B, et al. Synthetic myocardial extracellular volume fraction. *JACC Cardiovasc Imaging.* (2017) 10:1402–4. doi: 10.1016/j.jcmg.2016.12.007
15. Jouven X, Lemaitre RN, Rea TD, Sotoodehnia N, Empana JP, Siscovick DS. Diabetes, glucose level, and risk of sudden cardiac death. *Eur Heart J.* (2005) 26:2142–7. doi: 10.1093/eurheartj/ehi376
16. Schelbert EB, Cao JJ, Sigurdsson S, Aspelund T, Kellman P, Aletras AH, et al. Prevalence and prognosis of unrecognized myocardial infarction determined by cardiac magnetic resonance in older adults. *JAMA.* (2012) 308:890–6. doi: 10.1001/2012.jama.11089
17. Kwong RY, Sattar H, Wu H, Vorobiof G, Gandla V, Steel K, et al. Incidence and prognostic implication of unrecognized myocardial scar characterized by cardiac magnetic resonance in diabetic patients without clinical evidence of myocardial infarction. *Circulation.* (2008) 118:1011–20. doi: 10.1161/CIRCULATIONAHA.107.727826
18. Heydari B, Juan YH, Liu H, Abbasi S, Shah R, Blankstein R, et al. Stress perfusion cardiac magnetic resonance imaging effectively risk stratifies diabetic patients with suspected myocardial ischemia. *Circ Cardiovasc Imaging.* (2016) 9:e004136. doi: 10.1161/CIRCIMAGING.115.004136
19. Giusca S, Kelle S, Nagel E, Buss SJ, Voss A, Puntmann V, et al. Differences in the prognostic relevance of myocardial ischaemia and scar by cardiac magnetic resonance in patients with and without diabetes mellitus. *Eur Heart J Cardiovasc Imaging.* (2016) 17:812–20. doi: 10.1093/ehjci/jev220
20. Weber KT, Brilla CG. Pathological hypertrophy and cardiac interstitium. Fibrosis and renin-angiotensin-aldosterone system. *Circulation.* (1991) 83:1849–65. doi: 10.1161/01.CIR.83.6.1849
21. Schwartzkopff B, Brehm M, Mundhenke M, Strauer BE. Repair of coronary arterioles after treatment with perindopril in hypertensive heart disease. *Hypertension.* (2000) 36:220–5. doi: 10.1161/01.HYP.36.2.220
22. Tamarappoo BK, John BT, Reinier K, Teodorescu C, Uy-Evanado A, Gunson K, et al. Vulnerable myocardial interstitium in patients with isolated left ventricular hypertrophy and sudden cardiac death: a postmortem histological evaluation. *J Am Heart Assoc.* (2012) 1:e001511. doi: 10.1161/JAHA.112.001511

Conflict of Interest: The authors declare that the research was conducted in the absence of any commercial or financial relationships that could be construed as a potential conflict of interest.

frontiers in Cardiovascular Medicine

SYSTEMATIC REVIEW
published: 17 December 2021
doi: 10.3389/fcvm.2021.771647

Normal Ranges of Right Atrial Strain and Strain Rate by Two-Dimensional Speckle-Tracking Echocardiography: A Systematic Review and Meta-Analysis

Ali Hosseinsabet[1]*, *Roshanak Mahmoudian*[1], *Arash Jalali*[2], *Reza Mohseni-Badalabadi*[1] *and Tahereh Davarpasand*[1]

[1] Department of Cardiology, Tehran Heart Center, Tehran University of Medical Sciences, Tehran, Iran, [2] Department of Research, Tehran Heart Center, Tehran University of Medical Sciences, Tehran, Iran

Background: Normal range values of right atrial (RA) phasic function markers are essential for the identification of normal and abnormal values, comparison with reference values, and the clinical meaning of obtained values. Accordingly, we aimed to define the normal range values of RA phasic function markers obtained by 2D speckle-tracking echocardiography through a meta-analysis and determine the main sources of heterogeneity among reported values.

Methods: PUBMED, SCOPUS, and EMBASE databases were searched for the following keywords: "right atrial/right atrium" and "strain/speckle/deformation" and "echocardiography." Studies were selected that included a human healthy adult group without any cardiovascular diseases or risk factors and that were written in the English language. For the calculation of each marker of RA phasic functions, a random-effect model was used. Meta-regression was employed to define the major sources of variabilities among reported values.

Results: Fifteen studies that included 2,469 healthy subjects were selected for analysis. The normal range values for RA strain and strain rate were 42.7% (95% CI, 39.4 to 45.9%) and 2.1 s^{-1} (95% CI, 2.0 to 2.1 s^{-1}) during the reservoir phase, respectively, 23.6% (95% CI, 20.7 to 26.6%) and −1.9 s^{-1} (95% CI, −2.2 to −1.7 s^{-1}) during the conduit phase, correspondingly, and 16.1% (95% CI, 13.6 to 18.6%) and −1.8 s^{-1} (95% CI, −2.0 to −1.5 s^{-1}) during the contraction phase, respectively. The sources of heterogeneity for the normal range of these markers were the number of participants, the type of software, the method of global value calculation, the right ventricular fractional area change, the left ventricular (LV) ejection fraction, the RA volume index, sex, the heart rate, the diastolic blood pressure, the body mass index, and the body surface area.

Conclusions: Using 2D speckle-tracking echocardiography, we defined normal values for RA phasic function markers and identified the sources of heterogeneity as demographic, anthropometric, hemodynamic, and echocardiography factors.

Systematic Review Registration: https://www.crd.york.ac.uk/prospero/display_record.php?ID=CRD42021236578, identifier: CRD42021236578.

Keywords: right atrium, speckle-tracking echocardiography, strain, normal range, meta-analysis

OPEN ACCESS

Edited by:
Luigi P. Badano,
University of Milano Bicocca, Italy

Reviewed by:
Matteo Cameli,
University of Siena, Italy
Christoph Sinning,
University Heart and Vascular Center Hamburg (UHZ), Germany

***Correspondence:**
Ali Hosseinsabet
Ali_hosseinsabet@yahoo.com

Specialty section:
This article was submitted to Cardiovascular Imaging, a section of the journal Frontiers in Cardiovascular Medicine

Received: *06 September 2021*
Accepted: *24 November 2021*
Published: *17 December 2021*

Citation:
Hosseinsabet A, Mahmoudian R, Jalali A, Mohseni-Badalabadi R and Davarpasand T (2021) Normal Ranges of Right Atrial Strain and Strain Rate by Two-Dimensional Speckle-Tracking Echocardiography: A Systematic Review and Meta-Analysis. Front. Cardiovasc. Med. 8:771647. doi: 10.3389/fcvm.2021.771647

INTRODUCTION

The right atrium (RA) is pivotal for blood entrance to the heart. It manages not only right ventricular (RV) filling during diastole by reserving the blood during systole but also the delivery of the stored blood during early diastole and further RV filling by contraction in late diastole. Unlike the left atrium (LA), the RA interacts with a lower pressure chamber, the RV, which has less myocardial mass than the LV (1).

RA phasic functions can be evaluated by several methods such as echocardiography and cardiac magnetic resonance (2, 3). Nonetheless, echocardiography has been the main method for the assessment of RA phasic functions because of its availability and low cost. Consequently, the recent decades have witnessed the advent of several echocardiographic modalities for the evaluation of RA phasic functions (4, 5). Among these modalities, 2D speckle-tracking echocardiography (2DSTE) is prominent because of its angle independence when compared with tissue Doppler imaging, low load dependency when compared with volumetric methods in normal subjects, and relative resistance against translational motion (6–8). The 2DSTE modality can evaluate RA phasic functions in healthy subjects and demonstrate impairment in various disorders such as diabetes and pulmonary hypertension (4, 9–23). This echocardiographic modality also has a prognostic role in pulmonary hypertension and post-myocardial infarction events (24–26). Comparison between feature-tracking magnetic resonance imaging and 2DSTE demonstrates a good agreement between these two methods in the assessment of the deformation parameters of RA phasic functions (27). Although there is a consensus regarding how to measure the deformation indices of RA phasic functions by 2DSTE (28), the lack of a normal reference range for comparison impedes more clinical usage of this method.

In this study, we drew upon a systematic review and a meta-analysis to obtain the normal ranges of various 2DSTE-derived markers of RA phasic functions and to clarify the main sources of heterogeneity in their reported values.

METHODS

Search Profile

On April 29, 2021, we searched PUBMED, SCOPUS, and EMBASE databases *via* the following keywords: "right atrial/right atrium" and "strain/speckle/deformation" and "echocardiography". The search was limited to studies in the English language (**Supplementary Material 1**). References were also searched to find other related studies. We applied the Preferred Reporting Items for Systematic Reviews and Meta-Analyses (PRISMA) guidelines (29). On March 13, 2021, our study was recorded in the Prospero database (CRD42021236578).

Study Selection

The inclusion criteria were composed of the evaluation of the RA by 2DSTE or velocity vector imaging and the inclusion of a normal healthy control group without any cardiovascular diseases or risk factors. The exclusion criteria consisted of animal studies, conference articles, case reports, editorials, letters to the editor, review articles, articles without abstracts, the inclusion of subjects below 18 years of age, and RA evaluation by tissue Doppler imaging. Also excluded were studies that used the same data set. (The exception was one article featuring a large study population). If articles had the same number of subjects, the article citing the gating for measurements was selected. Additionally, studies that presented the values separately for sex subgroups were excluded. The titles and abstracts of the studies selected from the aforementioned databases were reviewed by three independent researchers (R.M., R.M.B., and A.H.). Discordances among the reviewers were resolved by discussion between A.H. and T.D.

Data Collection

R.M., R.M.B., and A.H. independently reviewed the full text of the eligible studies. The demographic characteristics, clinical information, and echocardiography data (including the deformation markers of RA phasic functions) of the control group were recorded. Discordances between the three aforementioned researchers were resolved through discussion between A.H. and T.D. The studies that seemed to have used the same or overlap data sets were excluded. (The exception was one article, the control group of which had the highest number of subjects of all the studies).

Statistical Analysis

Stata software, Release 16 (College Station, TX: StataCorp LLC), was used for statistical analysis. A random-effects model was employed to calculate the mean and the 95% confidence interval (CI) for each phasic strain and strain rate. Heterogeneity and inconsistency among the selected studies were assessed by Cochrane's Q test ($P < 0.1$) and I2 statistic, respectively. The results pertaining to each phasic strain and strain rate were demonstrated as forest plots. Reported demographic characteristics, clinical findings, and echocardiography data were considered sources of heterogeneity concerning each phasic strain and strain rate, and the effects of these variables on the variation of the normal range of each phasic strain and strain rate were assessed by meta-regression. Through a comparison between the results of the random-effects model and a fixed-effects model, the stability of the estimated normal range for each phasic strain and strain rate was checked. Egger's test ($P < 0.1$) and funnel plots were utilized to evaluate publication bias.

The criteria recommended by Downs and Black for the evaluation of the quality (internal and external validity) of studies were drawn upon (30). Well-defined methods were used in the reporting of inter and intraobserver variabilities, the heart rate, systolic and diastolic blood pressures, the phasic strain, and the phasic strain rate. The blindness of the operator who obtained images and the echocardiographer who analyzed videos was considered an additional criterion for quality in keeping with previously published systematic reviews and meta-analyses in this context. R.M., R.M.B., and A.H. independently checked the quality of the studies selected, and the differences in their assessments were resolved through an agreement between A.H. and T.D.

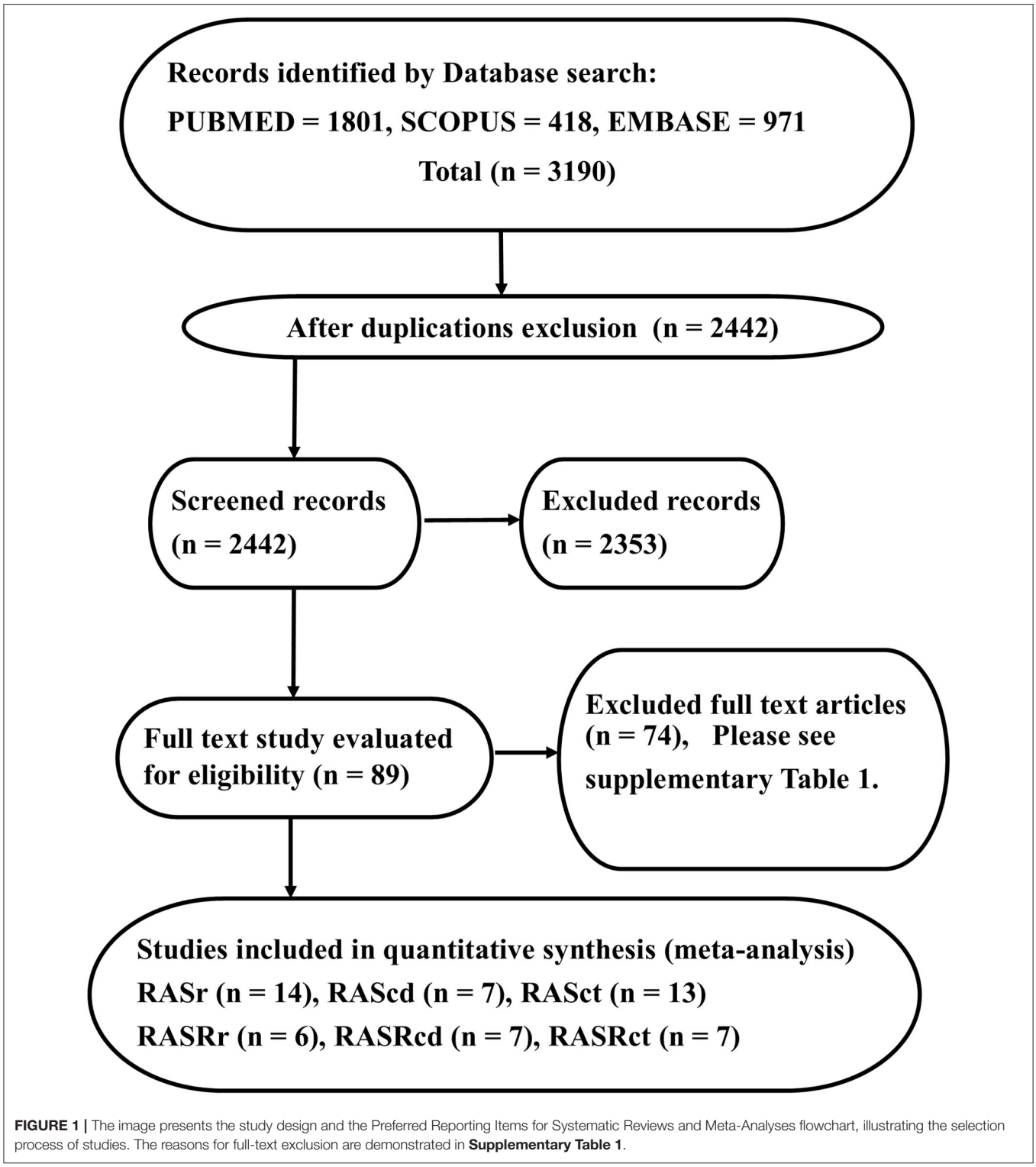

FIGURE 1 | The image presents the study design and the Preferred Reporting Items for Systematic Reviews and Meta-Analyses flowchart, illustrating the selection process of studies. The reasons for full-text exclusion are demonstrated in **Supplementary Table 1**.

RESULTS

Study Selection

The PRISMA diagram of our study is presented in **Figure 1**. Our database search yielded 3,190 studies. Following the exclusion of duplicate studies, 2,442 studies were selected for title and abstract review. Eighty-nine studies were identified as suitable for full-text review. Our reference search failed to identify any other studies.

Next, 74 studies were excluded (**Supplementary Table 1**), and 15 studies were considered eligible for further analysis. Fourteen

studies (2,469 subjects) featured RA strain assessment during the reservoir phase (RASr), seven studies (2,112 subjects) assessed RA strain during the conduit phase (RAScd), 13 studies (2,409 subjects) offered RA strain assessment during the contraction phase (RASct), six studies (269 subjects) evaluated the peak RA strain rate during the reservoir phase (pRASRr) and the peak RA strain rate during the conduit phase (pRASRcd), and seven studies (299 subjects) presented peak RA strain rate assessment during the contraction phase (pRASRct) (**Table 1**). The mean age of the participants in these studies ranged between 25 and 51 years, and male subjects comprised a range from 0 to 100%.

The Normal Ranges of RA Phasic Strain and Strain Rate

Reservoir Function Markers

The reported mean normal value for RASr was 42.7% (95% CI, 39.4 to 45.9%), which ranged from 32.0 to 56.9%. Inter-study heterogeneity ($Q = 289$; $P < 0.01$) and inconsistency ($I^2 = 97.7\%$) were significant. The fixed-effects model demonstrated a mean RASr value of 43.7% (95% CI, 43.2 to 44.1%) (**Figure 2**).

The reported mean normal value for pRASRr was 2.1 s^{-1} (95% CI, 2.0 to 2.1 s^{-1}). The normal range of RASRr varied between 2.0 and 2.2 s^{-1}. Inter-study heterogeneity ($Q = 5$; $P = 0.44$) and inconsistency ($I^2 = 6.9\%$) were non-significant. The fixed-effects model demonstrated a mean value pRASRr value of 2.1 s^{-1} (95% CI, 2.0 to 2.1 s^{-1}) (**Figure 3**).

Conduit Function Markers

The reported mean normal value for RAScd was 23.6% (95% CI, 20.7 to 26.6%). The normal range of RAScd varied between 18.0 and 27.1%. Inter-study heterogeneity ($Q = 431$; $P < 0.01$), and inconsistency ($I^2 = 98.0\%$) were significant. The fixed-effects model showed a mean RAScd value of 20.3% (95% CI, 19.9 to 20.6%) (**Figure 4**).

The reported mean normal value for pRASRcd was -1.9 s^{-1} (95% CI, -2.2 to -1.7 s^{-1}), which ranged from -2.2 to -1.5 s^{-1}. Inter-study heterogeneity ($Q = 37$; $P < 0.01$) and inconsistency ($I^2 = 88.8\%$) were significant. The fixed-effects model demonstrated a mean pRASRcd value of -2.0 s^{-1} (95% CI, -2.1 to -1.9 s^{-1}) (**Figure 5**).

Contraction Function Markers

The reported mean normal value for RASct was 16.1% (95% CI, 13.6 to 18.6%), which ranged from 11.7 to 27.6%. Inter-study heterogeneity ($Q = 2{,}150$; $P < 0.01$) and inconsistency ($I^2 = 99.0\%$) were significant. The fixed-effects model showed a mean RASct value of 18.1 % (95% CI, 17.9 to 18.4%) (**Figure 6**).

The reported mean normal value for pRASRct was -1.8 s^{-1} (95% CI, -2.0 to -1.5 s^{-1}). The normal range of pRASRct varied between -2.2 s^{-1} and -1.5 s^{-1}. Inter-study heterogeneity ($Q = 48$; $P < 0.01$) and inconsistency ($I^2 = 92.3\%$) were significant. The fixed-effects model demonstrated a mean pRASRct value of -1.7 s^{-1} (95% CI, -1.7 to -1.6 s^{-1}) (**Figure 7**).

Meta-Regression

Reservoir Function Markers

In the case of RASr, sex (male) ($\beta = -0.12$; $P = 0.028$) and diastolic blood pressure ($\beta = -1.13$; $P = 0.036$) were sources of between-study heterogeneity. Apropos of pRASRs, between-study heterogeneity was not statistically significant (**Table 2**).

Conduit Function Markers

The LV ejection fraction ($\beta = 0.87$; $P = 0.014$), the RA volume index ($\beta = 2.09$; $P = 0.010$), the software used for analysis ($\beta = 5.13$; $P = 0.032$), and the method of global value calculation ($\beta = 2.10$; $P = 0.004$) were the sources of inter-study heterogeneity for RAScd. In regard to pRASRcd, the RV fractional area change ($\beta = 0.04$; $P = 0.031$) and the method of global value calculation ($\beta = 0.17$; $P = 0.018$) were the sources of between-study heterogeneity (**Table 2**).

Contraction Function Markers

With respect to RASct, the number of study participants ($\beta = 0.01$; $P < 0.001$), the heart rate ($\beta = 0.46$; $P = 0.007$), the body mass index ($\beta = -1.44$; $P = 0.030$), the body surface area ($\beta = -27.23$; $P = 0.018$), the RV fractional area change ($\beta = -0.40$; $P = 0.007$), and the method of global value calculation ($\beta = 3.89$; $P < 0.001$) were the sources of between-study heterogeneity. The RV fractional area change ($\beta = 0.03$; $P = 0.003$) was the source of heterogeneity for pRASRct (**Table 2**).

Publication Bias

Publication bias was non-significant for RASr (P for Egger's test = 0.744), RAScd (P for Egger's test = 0.580), RASct (P for Egger's test = 0.400), RASRr (P for Egger's test = 0.290), RASRcd (P for Egger's test = 0.856), and RASRct (P for Egger's test = 0.118).

Study Quality Assessment

The studies incorporated in the present meta-analysis fulfilled six to nine criteria among the 11 proposed quality criteria. All the studies fulfilled more than 50% of the proposed quality criteria. One study fulfilled nine criteria (82%), five studies fulfilled eight (73%), four studies fulfilled seven (64%), and five studies fulfilled six (55%). All the studies defined their objectives, outcomes, confounders, main findings, and strain imaging protocols (**Supplementary Table 2**).

DISCUSSION

To the best of our knowledge, we are the first to present the normal ranges of all RA phasic functions (strain and strain rate) through a meta-analysis. A cardiac cycle includes interactions between the RA and the RV. In the RV systolic time, the tricuspid annulus is pulled toward the cardiac apex concurrently with the entrance of the flow from the cava veins into the RA. In this phase (the reservoir phase), the RA myocardium is stretched. In the early RV diastolic time, which is concurrent with the RA conduit phase, the tricuspid valve opens and the tricuspid annulus returns to its original place due to RV relaxation (reduced RA stretching).

TABLE 1 | Study characteristics.

Study	Year	N	Age (y)	Male (%)	HR (bpm)	BMI (kg/m^2)	BSA (m^2)	SBP (mmHg)	DBP (mmHg)	LVEF (%)	RAVI (2D) (ml/m^2)	RV FAC (%)	TAPSE (mm)	RVSm (cm/s)	SPAP mmHg	RV E/e′ ratio	FR (Hz)	Platform	Software	Probe	Gating	Model	Track ability (%)	Method of calculation	Measured deformation index	Disease studied
Padeletti et al.	2012	103	34.1 ± 15.1	40.8	74.8 ± 14.6	22.4 ± 3.5	NR	118 ± 14.1	76.4 ± 9.1	61.87 ± 3.67	NR	NR	23±3	14±3	NR	NR	60–80	Vivid I,GE	EchoPac	NR	RR	6	93	Global	RASr, RASct, RASRr, RASRcd, RASRct	Healthy subjects for normal reference range
D'Ascenzi et al.	2013	78	25.20 ± 3.92	64	72.16 ± 13.11	NR	1.82 ± 0.18	NR	NR	NR	19.89 ± 4.99	NR	23.18 ± 3.27	14±3	NR	4.11 ± 1.05	60–80	Vivid 7, GE	EchoPac	NR	RR	6	NR	Average	RASr, RASct	Athletics
Peluso et al.	2013	195	43 ± 15	44	68 ± 11	23 ± 3	1.78 ± 0.19	122 ± 14	74 ± 8	NR	23 ± 7	NR	NR	NR	NR	NR	73	Vivid E9,GE	EchoPAC v110.1.3	M5S	PP	NR	93	Global	RASr, RAScd, RASct	Healthy subjects for normal reference range
Pagourelias et al.	2013	26	26.6 ± 5.6	100	65 ± 9	22.4 ± 2.4	2.01 ± 0.16	120.6 ± 8	75 ± 9	NR	NR	42.7 ± 7.2	NR	14.8 ± 1.7	18.3 ± 8.6	4 ± 0.85	<90	Vivid S5, GE	EchoPAC	M3S	RR	6	NR	Average	RASr, RASct, RASRr, RASRcd, RASRct	Athletics
Gabrielli et al.	2014	20	27 ± 4	100	76 ± 12	23 ± 2.7	1.80 ± 0.12	NR	NR	60 ± 6	19.0 ± 5.1	40 ± 5	28 ± 3	NR	NR	NR	>50	Vivid Q,GE	EchoPac version 108.1.6	M4S	PP	6	NR	Average	RASr, RASct, RASRr, RASRcd, RASRct	Athletics
Durmus et al.	2015	40	45.9 ± 7.6	48	NR	NR	NR	NR	NR	64.5 ± 4.9	NR	33.8 ± 3.7	24.3±3.4	12.9±2.0	19.8±6.2	NR	>40	Vivid 7,GE	EchoPAC 6.1	NR	RR	NR	NR	NR	RASr, RASct	Scleroderma
McClean et al.	2015	20	27 ± 8	100	63 ± 9	NR	1.96 ± 0.13	129 ± 18	81 ± 14	NR	23 ± 5	NR	NR	NR	NR	NR	40–90	Vivid Q,GE	EchoPAC 6.0	NR	RR	6	NR	Average	RASr, RAScd, RASct	Athletics
Querejeta Roca et al.	2015	30	49.2 ± 12.3	33	69 ± 11	23.9 ± 3.9	NR	124 ± 12	71 ± 9	61 ± 5	NR	54 ± 6	21.5 ± 1.1	14.2 ± 2.3	NR	NR	NR		Tomtec system	NR	NR	NR	NR	NR	RASr, RASRr, RASRcd, RASRct	Pulmonary arterial pressure
Tadic et al.	2015	60	51 ± 8	49	73 ± 7	24.4 ± 2.6	1.92 ± 0.15	121 ± 10	72 ± 8	64 ± 4	20.8 ± 4.6	NR	22 ±3	NR	21 ±4	4.5 ± 1.5	NR	Vivid 7,GE	EchoPAC 110.1.2	NR	RR	6	NR	Average	RASr, RAScd, RASct, RASRr, RASRcd, RASRct	Diabetes and prediabetes
Gabrielli et al.	2016	30	35 ± 4	100	69 ± 12	NR	1.9 ± 0.2	119 ± 6	77 ± 4	61 ± 5	22.6 ± 4.7	49 ± 7	NR	NR	NR	NR	>60	Vivid– Q; GE	EchoPac version 108.1.6	M4S	PP	6	97.5	Average	RASct, RASRct	Athletics
Brand et al.	2018	123	42.4 ± 10.9	0	71 ± 11	22.4 ± 2.8	NR	117 ± 14	71 ± 10	61 ± 5	NR	41.1 ± 10.5	24.4 ± 3.8	14.2 ± 1.9	20.0 ± 4.2	NR	NR	Vivid E9,GE	EchoPAC PC	M5S	RR	NR	92.7	Global	RASr, RAScd, RASct	Healthy subjects
Li et al.	2018	30	46.82 ± 5.45	57	71.55 ± 15.35	27.06 ± 4.38	NR	122.19 ± 6.69	73.51 ± 7.19	NR	24.9 ± 4.17	NR	NR	NR	24.31 ± 5.63	NR	70–90	Acuson SC2000 Ultrasound system; Siemens Medical Solutions	NR	NR	RR	NR	NR	Average	RASr, RASRr, RASRcd, RASRct	Sleep apnea
Can Bostan et al.	2020	70	33.9 ± 9.5	63	76 ± 11	NR	1.58 ± 0.30	123 ± 7	74 ± 7	54.6 ± 4.3	19.8 ± 6.8	41.3 ± 7.5	23.6 ± 3.2	14.6 ± 1.7	19.8 ± 8.0	NR	>50	Epiq 7, Philips	NR	S5-1	RR	6	NR	NR	RASr, RAScd, RASct	Smokers
Palmer et al.	2020	101	41 (30–52)	44	68 ± 11	25.27 ± 2.82	1.89 ± 0.21	123.38 ± 15.46	74.02 ± 11.21	62 ± 6	21 ± 6	52 ± 8	21 ± 4	NR	NR	NR	40– 80	EPIQ7, Philips	2D Cardiac Performance Analysis; TomTec Imaging Systems	X5-1	RR	3	NR	NR	RASr, RAScd, RASct	Healthy subjects
Soulat-Dufour et al.	2020	1543	47 ± 17	51	NR	NR	1.77 ± 0.22	120 ± 13	74 ± 9	NR	19.4 ± 6.0	NR	NR	NR	NR	NR	NR	NR	Image Arena; TOMTEC	NR	RR	NR	79	NR	RASr, RAScd, RASct	Healthy subjects

BMI, Body mass index; BSA, Body surface area; DBP, Diastolic blood pressure; FR, Frame rate; HR, Heart rate; LVEF, Left ventricular ejection fraction; NR, Not reported; pRASRr, peak Right atrial strain rate during the reservoir phase; pRASRcd, peak Right atrial strain rate during the conduit phase; pRASRct, peak Right atrial strain rate during the contraction phase; RASr, Right atrial strain during the reservoir phase; RAScd, Right atrial strain during the conduit phase; RASct, Right atrial strain during the contraction phase; RAVI, Right atrial volume index; RV, Right ventricle; RVFAC, Right ventricular fractional area change; RVSm, Right ventricular systolic velocity; SBP, Systolic blood pressure; SPAP, Systolic pulmonary artery pressure; TAPSE, Tricuspid annular plane systolic excursion.

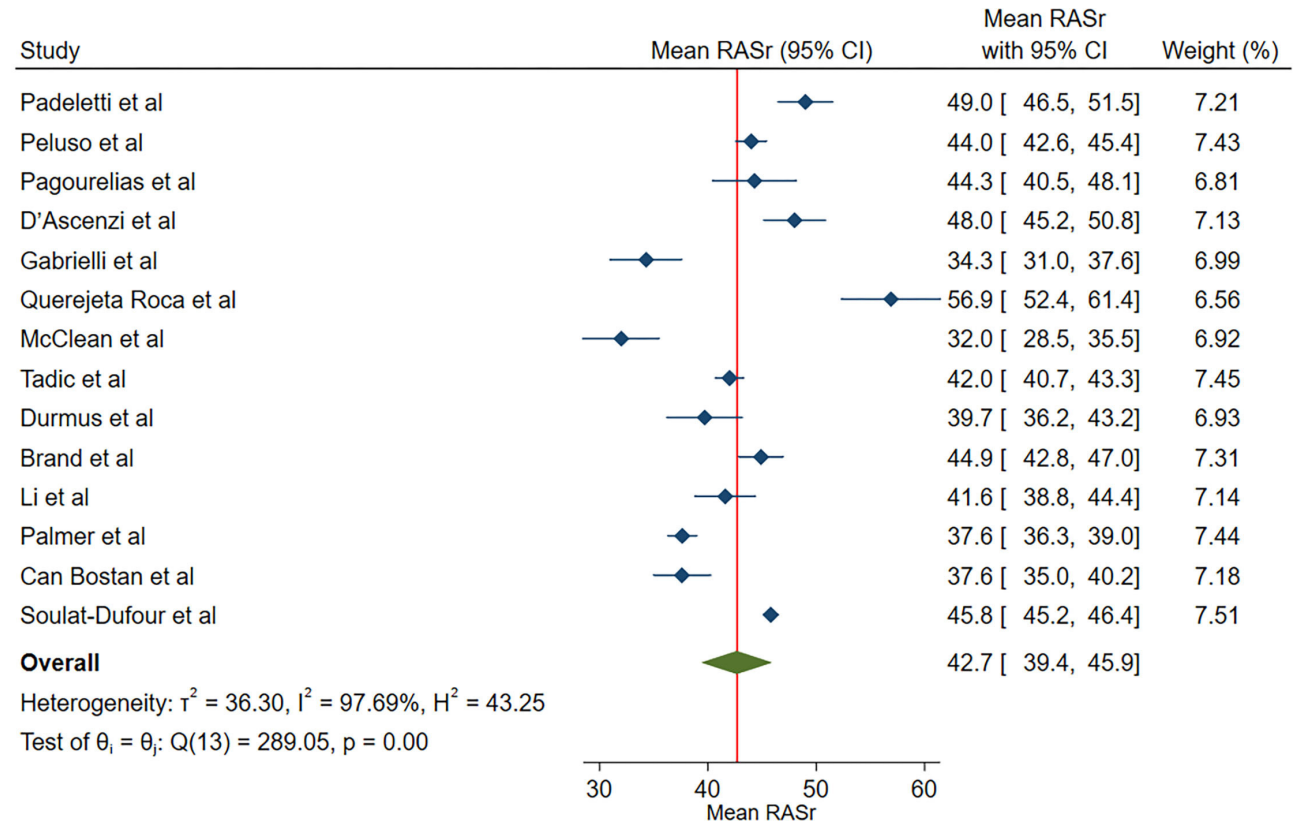

FIGURE 2 | The image demonstrates the normal range of the longitudinal 2D speckle-tracking echocardiography-derived right atrial strain during the reservoir phase.

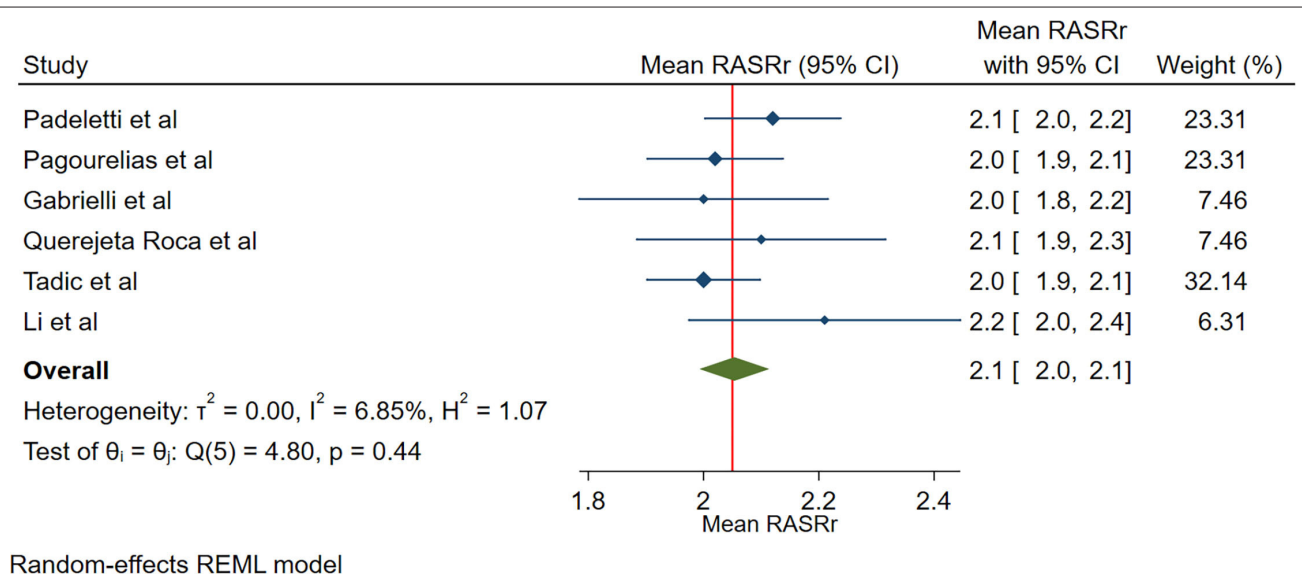

FIGURE 3 | The image demonstrates the normal range of the longitudinal 2D speckle-tracking echocardiography-derived peak right atrial strain rate during the reservoir phase.

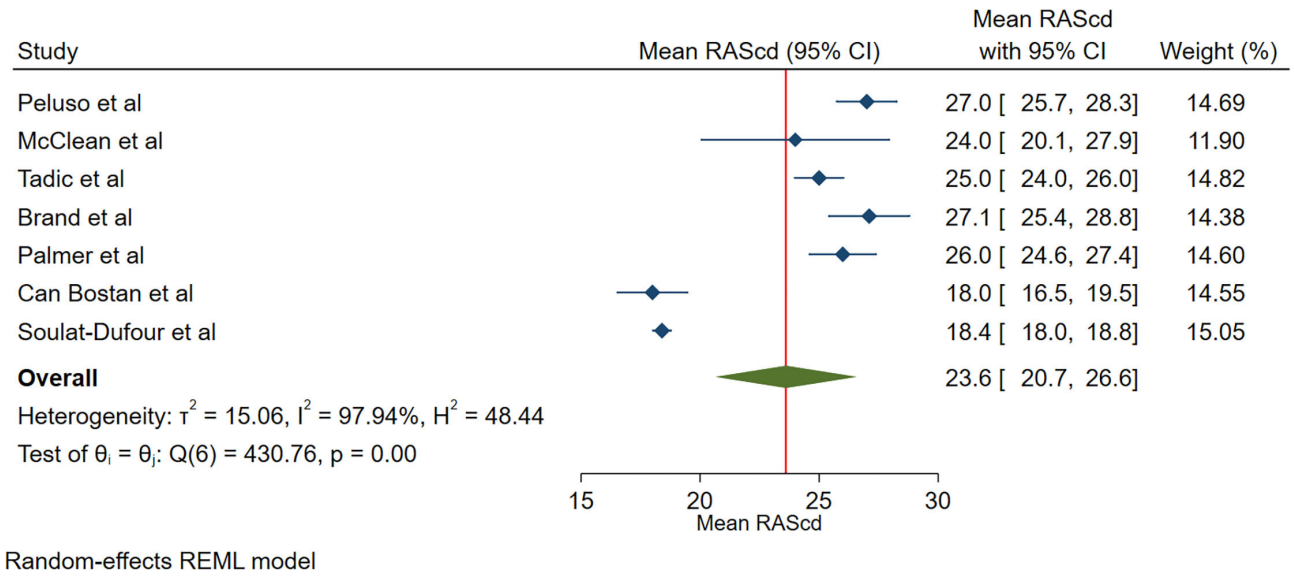

FIGURE 4 | The image demonstrates the normal range of the longitudinal 2D speckle-tracking echocardiography-derived right atrial strain during the conduit phase.

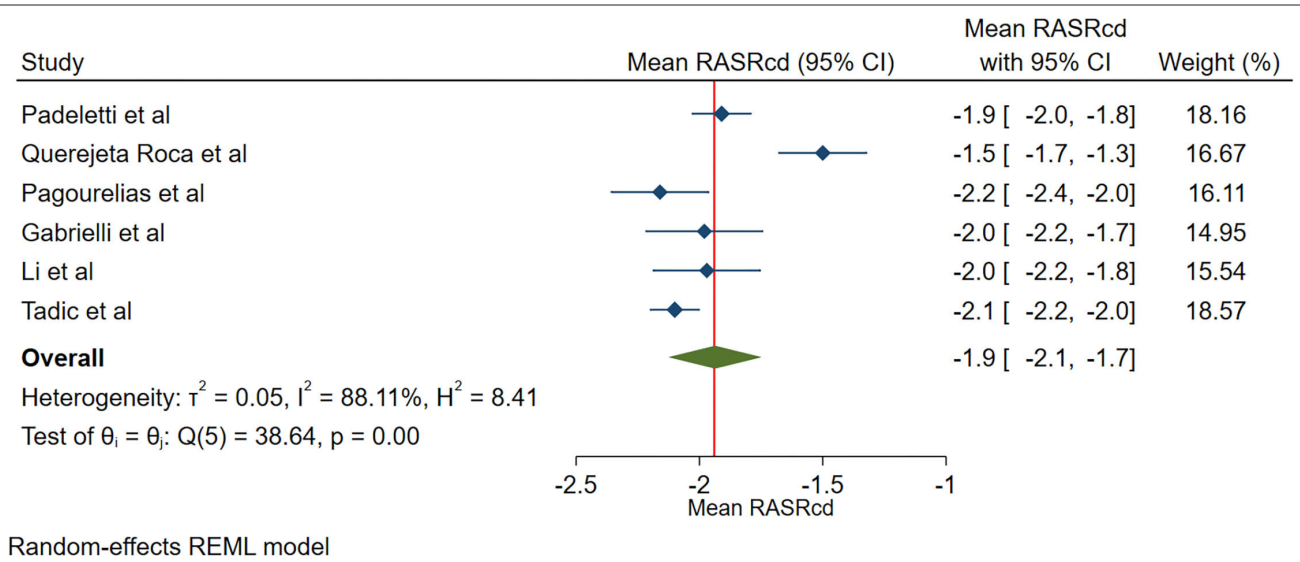

FIGURE 5 | The image demonstrates the normal range of the longitudinal 2D speckle-tracking echocardiography-derived peak right atrial strain rate during the conduit phase.

In the late RV diastolic time, which coincides with the RA contraction phase, the RA contracts, and the length of the RA myocardial fibers decreases (1).

The markers of the 3 RA phasic functions are predictive of prognosis in patients with pulmonary hypertension, while the markers of the RA reservoir and conduit functions are correlated with functional capacity in patients with systemic sclerosis and idiopathic pulmonary hypertension (25, 31–34). In addition, RASr correlates with the RA pressure and the occurrence of postoperative atrial fibrillation (35, 36).

Sources of Heterogeneity

The Reservoir Function

According to some studies, RASr increases in women in comparison with men (4, 11). We found that sex was a source of inter-study variation (37).

In a previous investigation, RASr was decreased in patients with high normal blood pressure, defined as a diastolic blood pressure of about 9 mm Hg higher than the normal diastolic blood pressure in the control group (79 vs. 70 mm Hg), during a 24-h blood pressure monitoring (38). Our findings are in line

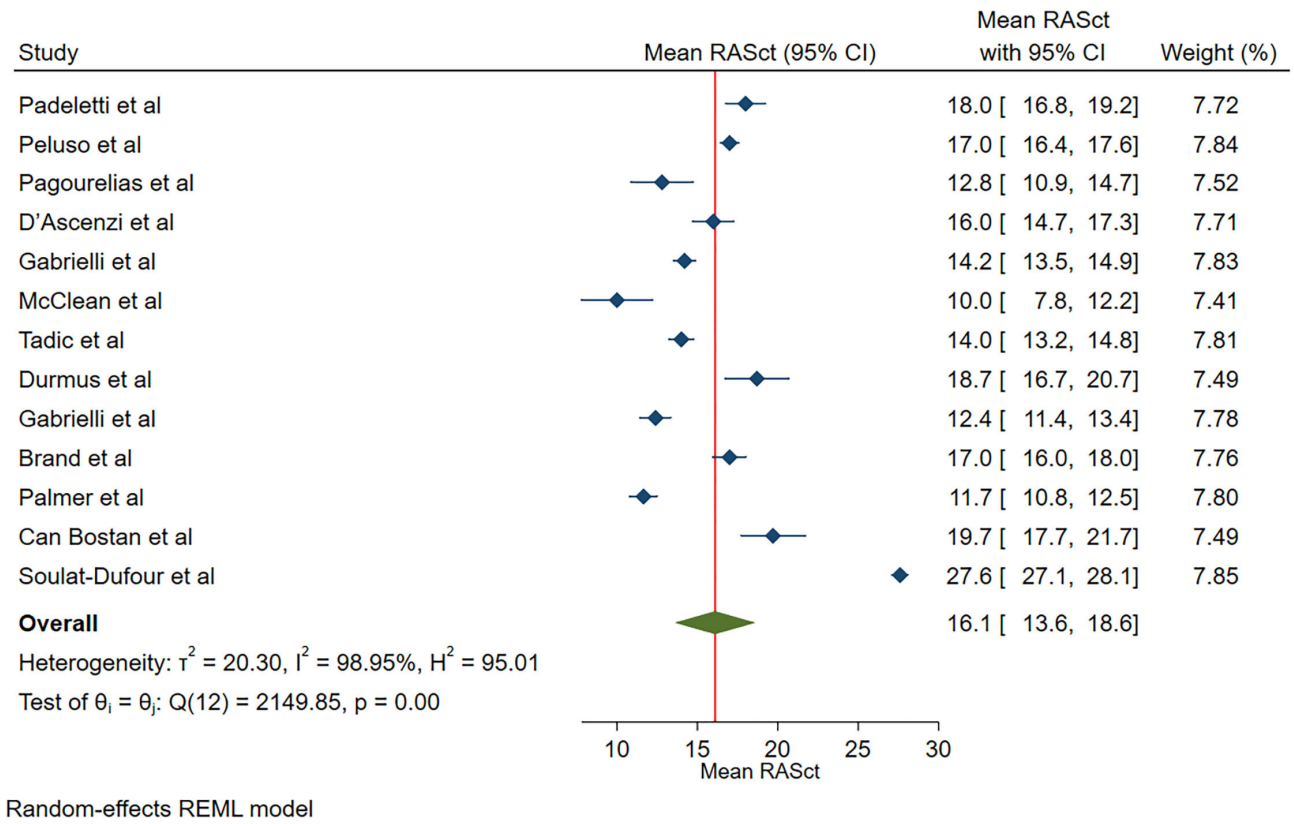

FIGURE 6 | The image demonstrates the normal range of the longitudinal 2D speckle-tracking echocardiography-derived right atrial strain during the contraction phase.

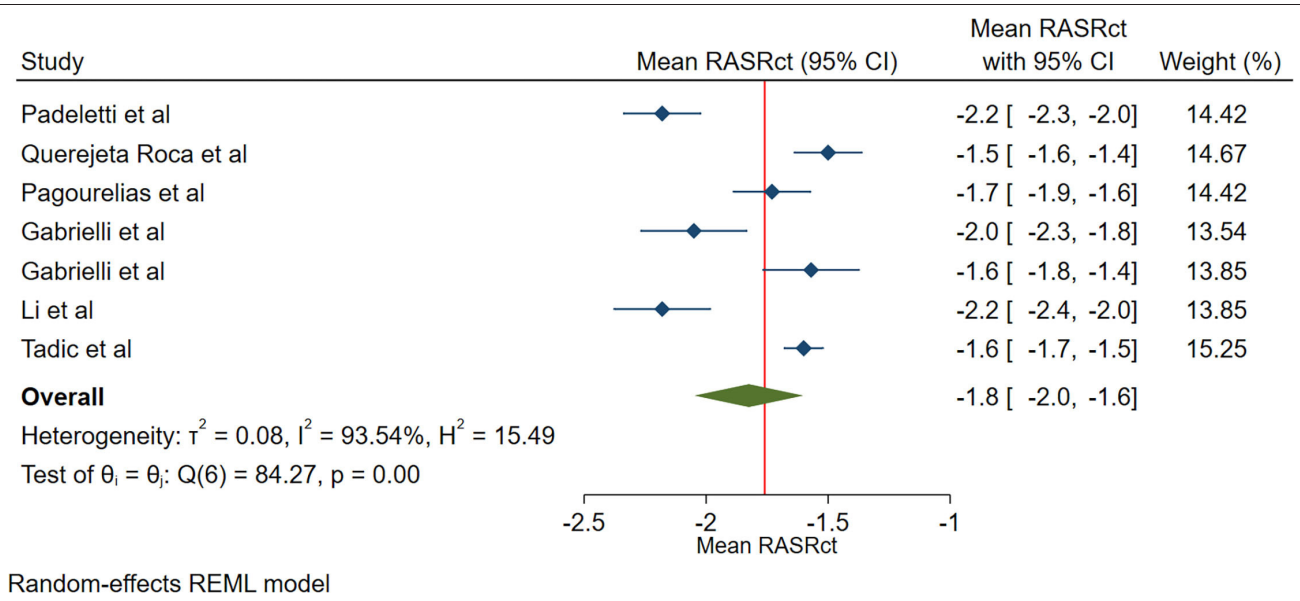

FIGURE 7 | The image demonstrates the normal range of the longitudinal 2D speckle-tracking echocardiography-derived peak right atrial strain rate during the contraction phase.

TABLE 2 | Meta-regression analysis for longitudinal two-dimensional speckle tracking echocardiography derived right atrial strains and strain rates.

Variables	RASr			RAScd			RASct			pRASRr			pRASRcd			pRASRct		
	n	β (95% CI)	*p*-value	n	β (95% CI)	*p*-value	n	β (95% CI)	*p*-value	n	β (95% CI)	*p*-value	n	β (95% CI)	*p*-value	n	β (95% CI)	*p*-value
Year of publication	14	−0.54 (−1.72, 0.63)	0.364	7	−0.78 (−1.75, 0.19)	0.114	13	0.53 (−0.34, 1.41)	0.233	6	0.01 (−0.04, 0.05)	0.805	6	0.01 (−0.10, 0.12)	0.806	7	0.01 (−0.12, 0.15)	0.844
Number of participants	14	0.00 (−0.01,0.01)	0.539	7	0.00 (−0.01,0.00)	0.134	13	0.01 (0.01,0.01)	<0.001	6	0.00 (0.00,0.00)	0.464	6	0.00 (−0.01,0.01)	0.917	7	0.00 (−0.01,0.01)	0.440
Age	14	0.22 (−0.13, 0.58)	0.221	7	0.08 (−0.36, 0.52)	0.719	13	0.22 (−0.05, 0.50)	0.115	6	0.00 (−0.01, 0.01)	0.920	6	0.01 (−0.01, 0.03)	0.406	7	0.01 (−0.01, 0.03)	0.469
Sex (Male)	14	−0.12 (−0.23, −0.01)	0.028	7	−0.06 (−0.17, 0.05)	0.310	13	−0.06 (−0.14, 0.01)	0.111	6	0.00 (0.00, 0.00)	0.387	6	0.00 (−0.01, 0.00)	0.140	7	0.00 (−0.01, 0.01)	0.950
Heart rate, bpm	12	0.11 (−0.89, 1.1)	0.830	6	−0.45 (−1.08, 0.19)	0.166	11	0.46 (0.13, 0.80)	0.007	6	0.00 (−0.01, 0.02)	0.722	6	0.00 (−0.06, 0.06)	0.989	7	−0.04 (−0.10, 0.01)	0.126
BMI, kg/m^2	9	−0.92 (−3.73, 1.89)	0.520	4	−0.61 (−1.43, 0.21)	0.146	7	−1.44 (−2.74, −0.14)	0.030	6	0.01 (−0.04, 0.07)	0.592	6	0.01 (−0.12, 0.14)	0.897	6	−0.03 (−0.19, 0.14)	0.760
BSA, m^2	9	−1.16 (−32.67, 30.35)	0.942	6	19.72 (−1.59, 41.02)	0.070	10	−27.23 (−49.83, −4.64)	0.018	3	0.12 (−0.98, 1.23)	0.826	3	−0.85 (−2.31, 0.60)	0.251	4	1.49 (−1.29, 4.26)	0.295
SBP, mmHg	11	−1.01 (−2.08, 0.07)	0.067	7	−0.11 (−1.08, 0.86)	0.828	10	−0.61 (−1.58, 0.36)	0.220	5	0.00 (−0.05, 0.04)	0.855	5	0.06 (0.05, 0.17)	0.264	6	0.05 (−0.08, 0.18)	0.453
DBP, mmHg	11	−1.31 (−2.54, −0.09)	0.036	7	−0.20 (−1.33, 0.92)	0.725	10	−0.71 (−1.89, 0.48)	0.242	5	0.01 (−0.02, 0.05)	0.416	5	−0.05 (−0.17, 0.06)	0.370	6	−0.05 (−0.16, 0.07)	0.433
LVEF, %	8	0.44 (−1.39, 2.28)	0.636	4	0.87 (0.18, 1.56)	0.014	8	−0.32 (−1.09, 0.44)	0.409	4	−0.02 (−0.07, 0.03)	0.450	4	−0.07 (−0.26, 0.11)	0.419	5	0.05 (−0.17, 0.27)	0.663
RAVI, mL/m^2	9	−0.21 (−2.14, 1.73)	0.835	6	2.09 (0.50, 3.68)	0.010	9	−1.75 (−3.89, 0.40)	0.111	3	0.04 (−0.01, 0.09)	0.133	3	0.01 (−0.04, 0.07)	0.677	4	−0.03 (−0.19, 0.14)	0.751
RVFAC, %	7	0.54 (−0.26, 1.33)	0.185	3	0.31 (−1.13, 1.75)	0.675	7	−0.40 (−0.70, −0.11)	0.007	3	0.01 (−0.01, 0.03)	0.477	3	0.04 (0.00, 0.08)	0.031	4	0.03 (0.01, 0.05)	0.003
TAPSE, mm	9	−1.60 (−3.78, 0.59)	0.153	4	−0.60 (−4.20, 3.00)	0.742	8	0.26 (−0.75, 1.26)	0.616	4	−0.01 (−0.05, 0.04)	0.784	4	−0.03 (−0.15, 0.08)	0.591	4	−0.07 (−0.07, −0.19)	0.272
RVSm, cm/s	7	1.11 (−7.89, 10.12)	0.808	2	–	–	6	−1.65 (−4.79, 1.48)	0.302	3	−0.13 (−0.33, 0.08)	0.228	3	−0.49 (−1.73, 0.75)	0.442	3	0.34 (−1.14, 1.83)	0.651

(Continued)

TABLE 2 | Continued

Variables		RASr		RAScd			RASct			pRASRr			pRASRcd			pRASRct	
	n	β (95% CI)	*p*-value	n	β (95% CI)	*p*-value	n	β (95% CI)	*p*-value	n	β (95% CI)	*p*-value	n	β (95% CI)	*p*-value	n	β (95% CI)	*p*-value
SPAP, mmHg	6	−0.13 (−1.47, 1.21)	0.851	3	3.28 (−9.71, 16.26)	0.621	5	0.63 (−2.74, 4.00)	0.713	3	0.03 (−0.02, 0.07)	0.317	3	0.03 (−0.02, 0.08)	0.201	3	−0.08 (−0.21, 0.05)	0.235
Gating	13	2.74 (−5.07, 10.55)	0.492	7	−3.97 (−12.41, 4.46)	0.356	13	2.03 (−3.95, 8.02)	0.505	5	0.06 (−0.18, 0.30)	0.638	5	−0.05 (−0.37, 0.26)	0.748	6	−0.11 (−0.65, 0.43)	0.692
Software	12	−1.59 (−8.60, 5.43)	0.658	6	5.13 (0.44, 9.82)	0.032	12	−4.64 (−10.13, 0.85)	0.097	5	−0.11 (−0.28, 0.06)	0.195	5	−0.31 (−0.64, 0.01)	0.056	6	0.01 (−0.53, 0.54)	0.975
Method of calculation	9	5.50 (−1.64,12.65)	0.131	4	2.10 (0.69, 3.50)	0.004	9	3.89 (1.83, 5.95)	<0.001	5	0.10 (−0.04, 0.23)	0.167	5	0.17 (0.03, 0.31)	0.018	6	−0.36 (−0.94,0.22)	0.220

BMI, Body mass index; BSA, Body surface area; DBP; Diastolic blood pressure; FR, Frame rate; HR, Heart rate; LVEF, Left ventricular ejection fraction; NR, Not reported; pRASRr, peak Right atrial strain rate during the reservoir phase; pRASRcd, peak Right atrial strain rate during the conduit phase; pRASRct, peak Right atrial strain rate during the contraction phase; RASr, Right atrial strain during the reservoir phase; RAScd, Right atrial strain during the conduit phase; RASct, Right atrial strain during the contraction phase; RAVI, Right atrial volume index; RV, Right ventricle; RVFAC, Right ventricular fractional area change; RVSm, Right ventricular systolic velocity; SBP, Systolic blood pressure; SPAP, Systolic pulmonary artery pressure; TAPSE, Tricuspid annular plane systolic excursion.

with that study insofar as the range of the diastolic blood pressure in our study was between 71 and 81 mm Hg.

The Conduit Function

The RA conduit function is correlated with the LV ejection fraction in patients with a reduced ejection fraction (2). In our meta-analysis, we assessed studies that enrolled patients with normal cardiac function. Still, the LV ejection fraction in these studies ranged from 55 to 65%.

A previous investigation demonstrated that during the head-up title test with increased inclination, the LA volume and conduit function decreased (7). Stated otherwise, a decrease in the LA volume is in tandem with a reduction in the LA conduit function. Concerning the RA, in patients with end-stage renal disease, the RA volume and conduit function decrease after hemodialysis, which is compatible with the aforementioned study regarding the LA (39). It can, therefore, be explained why the inter-study difference vis-a-vis the RA volume index may lead to an inter-study difference in terms of the RA conduit function.

The LV systolic function is a determinant of the LA conduit function (40), and the RV fractional area change is a marker of the RV systolic function (41). Hence, it is reasonable that the RV systolic function is a determinant of the RA conduit function and that the difference regarding the RV fractional area change between studies is a source of between-study heterogeneity.

The global strain can be calculated by two methods, one of which uses the entire myocardial line length while computing the global strain, whereas the other one averages the values computed at the segmental level. These methods are mathematically the same. Nevertheless, in practice, the presence of a bad track or noisy signal segment can be a source of difference between these two methods. This segment is included in the calculation in the first method and excluded in the second method. More differences manifest themselves when the segments are not equal in size and the weight of small and large segments is similar (42). Indeed, such differences in the methodology of global strain calculation can be a source of between-study heterogeneity.

The software used by researchers was another source of heterogeneity. Intervendor variability is mainly due to post-processing factors such as differences in algorithms and the calculation methods of deformation markers, as well as the control of outliers and the order in which deformation markers are calculated (43).

The Contraction Function

Some studies have reported that a rise in the body mass index is accompanied by a decline in the LA contraction function (44, 45), which can be used as a rationale to assume that a decrease in the RA contraction function is allied to an increase in the body mass index. This may explain why the body mass index was a source of inter-study heterogeneity in our meta-analysis. The correlation between the body mass index and the body surface area may render the latter a source of between-study variabilities. In addition, with an increase in body size, the initial length of the RA myocardium increases, leading to a decrease in strain since strain is the ratio of length change to the initial length.

The number of participants can be deemed a measure of researchers' expertise in the measurement of strain and strain rates (14). The level of expertise may, thus, affect the results of studies. Studies do not tend to mention the level of their researchers' expertise, and a consensus has yet to emerge regarding the objective criteria of expertise in this field.

Whereas some studies claim that there is a correlation between the heart rate and aggravation in atrial contraction, some other studies refute this notion (27, 46). According to our results, an increase in age was correlated with an increase in the RA contraction function; be that as it may, this association cannot be considered etiologic because what we sought to determine was the source of heterogeneity between studies. The range of the reported heart rate in our study was between 63 and 76 beats per minute, which is acceptable for the normal population.

As was mentioned above, based on our findings, the RV fractional area change was a source of between-study heterogeneity inasmuch as an increase in the RV fractional area change was correlated with an increase in the RA conduit function. While the RV fractional area change was a source of heterogeneity concerning the RA conduit function, an increased RV fractional area change was associated with a decrease in the RA contraction function. This finding can be explained by the fact that with an increase in the conduit phase for RV filling, the RA contraction function decreases and vice versa. This issue is seen in the case of grade I LV diastolic dysfunction, in which a decrease in LV diastolic filling in the early diastole is in tandem with an increase in LV diastolic filling in the late diastole due to the contraction of the LA.

Publication Bias

We found no publication bias. However, the low number of studies, especially in the case of the RA phasic strain rate, undermines the accuracy of our results.

Our study selection was done independently. All the stages of study selection were checked by three researchers, and any discrepancy was ultimately removed through an agreement between two researchers. We think that this adopted method minimized the possibility of missing available studies.

Our study yielded normal ranges for the longitudinal markers of the RA phasic functions obtained by 2DSTE. Although we analyzed a limited number of studies, our study proved preliminary data regarding the normal ranges of these markers. Further research is needed to obtain more robust data on the normal ranges of these markers in different populations. Our study can be helpful for clinicians interested in right heart disease in that it defines what constitutes normal ranges for RA phasic functions. Additionally, information on the normal ranges of the deformation markers of the RA phasic functions may be helpful in patient follow-up since it could identify the time of RA involvement in the disease process. Another salient point raised by our study is the need for further well-designed studies in this field.

Study Limitations

Fifteen studies that included 2,469 healthy subjects were selected for our meta-analysis concerning various markers of the RA phasic functions (strain and strain rate). Despite the low sample size of our investigation, we hope that until larger meta-analyses are undertaken, clinicians will find our results useful. In contrast with previous meta-analyses that included randomized clinical trials, our meta-analysis evaluated observational and case-control studies. Accordingly, the fact that we encountered a high rate of heterogeneity by comparison with the meta-analyses that evaluated randomized clinical trials can be deemed expectable (47).

The expertise level of researchers is another matter that is obscure in studies in this field and should be considered in future studies. The majority of the studies included in the meta-analysis had small patient populations, which further underscores the need for large-scale investigations in this context. What should also be borne in mind in the interpretation of our findings is that we analyzed merely the data of studies and not the data of patients who participated in the studies. Moreover, the quality of the studies subjected to analysis was evaluated through checklists (14, 48). Such checklists offer an insight into the quality of studies, but they lack objectivity in some items (49). Notably, we did not consider the quality of a study an exclusion criterion. The overall quality of the studies meta-analyzed herein was acceptable because they fulfilled six to nine criteria among the 11 proposed quality criteria. In addition, we did not consider the quality of study in our analysis and did not a stratified meta-analysis.

CONCLUSIONS

According to the results of the present study, the mean global value was 42.7% for RASr (95% CI, 39.4 to 45.9%), 23.6% for RAScd (95% CI, 20.7 to 26.6%), 16.1% for RASct (95% CI, 13.6 to 18.6%), 2.1 s^{-1} for pRASRr (95% CI, 2.0 to 2.1 s^{-1}), −1.9 s^{-1} for pRASRcd (95% CI, −2.2 to −1.7 s^{-1}), and −1.8 s^{-1} for pRASRct (95% CI, −2.0 to −1.5 s^{-1}). The sources of heterogeneity in terms of the normal ranges of these markers were the number of participants, the type of software, the method of global value calculation, the RV fractional area, the LV ejection fraction, the RA volume index, sex, the heart rate, the diastolic blood pressure, the body mass index, and the body surface area.

AUTHOR CONTRIBUTIONS

AH, TD, and RM-B: concept/design. AH, TD, RM-B, RM, and AJ: data analysis/interpretation and approval of article. AH: drafting article. TD, RM-B, RM, and AJ: critical revision of article. AJ: statistics. AH, RM, and RM-B: data collection. All authors contributed to the article and approved the submitted version.

SUPPLEMENTARY MATERIAL

The Supplementary Material for this article can be found online at: https://www.frontiersin.org/articles/10.3389/fcvm.2021.771647/full#supplementary-material

REFERENCES

1. Tadic M. The right atrium, a forgotten cardiac chamber: An updated review of multimodality imaging. *J Clin Ultrasound.* (2015) 43:335–45. doi: 10.1002/jcu.22261
2. Jain S, Kuriakose D, Edelstein I, Ansari B, Oldland G, Gaddam S, et al. Right atrial phasic function in heart failure with preserved and reduced ejection fraction. *JACC Cardiovasc Imaging.* (2019) 12:1460–70. doi: 10.1016/j.jcmg.2018.08.020
3. Huang J, Yang C, Ni CF, Yan ZN, Fan L, Song XT. Right atrial function assessed by volume-derived values and speckle tracking echocardiography in patients with hypertrophic cardiomyopathy. *BMC Cardiovasc Disord.* (2020) 20:335. doi: 10.1186/s12872-020-01610-1
4. Soulat-Dufour L, Addetia K, Miyoshi T, Citro R, Daimon M, Fajardo PG, et al. Normal values of right atrial size and function according to age, sex, and ethnicity: results of the world alliance societies of echocardiography study. *J Am Soc Echocardiogr.* (2021) 34:286–300. doi: 10.1016/j.echo.2020.11.004
5. Nemes A, Kormányos Á, Domsik P, Kalapos A, Ambrus N, Lengyel C, et al. Normal reference values of right atrial strain parameters using three-dimensional speckle-tracking echocardiography (results from the MAGYAR-Healthy Study). *Int J Cardiovasc Imaging.* (2019) 35:2009–18. doi: 10.1007/s10554-019-01655-0
6. Mor-Avi V, Lang RM, Badano LP, Belohlavek M, Cardim NM, Derumeaux G, et al. Current and evolving echocardiographic techniques for the quantitative evaluation of cardiac mechanics: ASE/EAE consensus statement on methodology and indications endorsed by the Japanese Society of Echocardiography. *J Am Soc Echocardiogr.* (2011) 24:277–313. doi: 10.1093/ejechocard/jer021
7. Genovese D, Singh A, Volpato V, Kruse E, Weinert L, Yamat M, et al. Load dependency of left atrial strain in normal subjects. *J Am Soc Echocardiogr.* (2018) 31:1221–8. doi: 10.1016/j.echo.2018.07.016
8. Thomas L, Muraru D, Popescu BA, Sitges M, Rosca M, Pedrizzetti G, et al. Evaluation of left atrial size and function: relevance for clinical practice. *J Am Soc Echocardiogr.* (2020) 33:934–52. doi: 10.1016/j.echo.2020.03.021
9. Padeletti M, Cameli M, Lisi M, Malandrino A, Zacà V, Mondillo S. Reference values of right atrial longitudinal strain imaging by two-dimensional speckle tracking. *Echocardiography.* (2012) 29:147–52. doi: 10.1111/j.1540-8175.2011.01564.x
10. D'Ascenzi F, Cameli M, Padeletti M, Lisi M, Zacà V, Natali B, et al. Characterization of right atrial function and dimension in top-level athletes: a speckle tracking study. *Int J Cardiovasc Imaging.* (2013) 29:87–94. doi: 10.1007/s10554-012-0063-z
11. Peluso D, Badano LP, Muraru D, Dal Bianco L, Cucchini U, Kocabay G, et al. Right atrial size and function assessed with three-dimensional and speckle-tracking echocardiography in 200 healthy volunteers. *Eur Heart J Cardiovasc Imaging.* (2013) 14:1106–14. doi: 10.1093/ehjci/jet024
12. Pagourelias ED, Kouidi E, Efthimiadis GK, Deligiannis A, Geleris P, Vassilikos V. Right atrial and ventricular adaptations to training in male Caucasian athletes: an echocardiographic study. *J Am Soc Echocardiogr.* (2013) 26:1344–52. doi: 10.1016/j.echo.2013.07.019
13. Gabrielli L, Bijnens BH, Butakoff C, Duchateau N, Montserrat S, Merino B, et al. Atrial functional and geometrical remodeling in highly trained male athletes: for better or worse? *Eur J Appl Physiol.* (2014) 114:1143–52. doi: 10.1007/s00421-014-2845-6
14. Durmus E, Sunbul M, Tigen K, Kivrak T, Ozen G, Sari I, et al. Right ventricular and atrial functions in systemic sclerosis patients without pulmonary hypertension. Speckle-tracking echocardiographic study. *Herz.* (2015) 40:709–15. doi: 10.1007/s00059-014-4113-2
15. McClean G, George K, Lord R, Utomi V, Jones N, Somauroo J, et al. Chronic adaptation of atrial structure and function in elite male athletes. *Eur Heart J Cardiovasc Imaging.* (2015) 16:417–22. doi: 10.1093/ehjci/jeu215
16. Querejeta Roca G, Campbell P, Claggett B, Solomon SD, Shah AM. Right atrial function in pulmonary arterial hypertension. *Circ Cardiovasc Imaging.* (2015) 8:e003521. doi: 10.1161/CIRCIMAGING.115.003521
17. Tadic M, Ilic S, Cuspidi C, Ivanovic B, Bukarica L, Kostic N, et al. Left and right atrial phasic function and deformation in untreated patients with prediabetes and type 2 diabetes mellitus. *Int J Cardiovasc Imaging.* (2015) 31:65–76. doi: 10.1007/s10554-014-0536-3
18. Gabrielli L, Bijnens BH, Brambila C, Duchateau N, Marin J, Sitges-Serra I, et al. Differential atrial performance at rest and exercise in athletes: Potential trigger for developing atrial dysfunction? *Scand J Med Sci Sports.* (2016) 26:1444–54. doi: 10.1111/sms.12610
19. Sanchis L. Sanz-de La Garza M, Bijnens B, Giraldeau G, Grazioli G, Marin J, et al. Gender influence on the adaptation of atrial performance to training. *Eur J Sport Sci.* (2017) 17:720–6. doi: 10.1080/17461391.2017.1294620
20. Brand A, Bathe M, Hübscher A, Baldenhofer G, Hättasch R, Seeland U, et al. Normative reference data, determinants, and clinical implications of right atrial reservoir function in women assessed by 2D speckle-tracking echocardiography. *Echocardiography.* (2018) 35:1542–9. doi: 10.1111/echo.14092
21. Li J, Lu C, Wang W, Gong K, Zhao L, Wang Z. Assessment of right atrium dysfunction in patients with obstructive sleep apnea syndrome using velocity vector imaging. *Cardiovasc Ultrasound.* (2018) 16:32. doi: 10.1186/s12947-018-0150-y
22. Can Bostan O, Ozben B, Bayram T, Sayar N, Eryuksel E. The effect of smoking on atrial and ventricular functions in healthy subjects: A speckle tracking echocardiography study. *J Clin Ultrasound.* (2020) 48:462–9. doi: 10.1002/jcu.22854
23. Palmer C, Truong VT, Klas B, Wolking S, Ornella A, Young M, et al. Left and right atrial speckle tracking: Comparison of three methods of time reference gating. *Echocardiography.* (2020) 37:1021–9. doi: 10.1111/echo.14770
24. Bai Y, Yang J, Liu J, Ning H, Zhang R. Right atrial function for the prediction of prognosis in connective tissue disease-associated pulmonary arterial hypertension: a study with two-dimensional speckle tracking. *Int J Cardiovasc Imaging.* (2019) 35:1637–49. doi: 10.1007/s10554-019-01613-w
25. Alenezi F, Mandawat A. Il'Giovine ZJ, Shaw LK, Siddiqui I, Tapson VF, et al. Clinical utility and prognostic value of right atrial function in pulmonary hypertension. *Circ Cardiovasc Imaging.* (2018) 11:e006984. doi: 10.1161/CIRCIMAGING.117.006984
26. Schuster A, Backhaus SJ, Stiermaier T, Navarra JL, Uhlig J, Rommel KP, et al. Impact of right atrial physiology on heart failure and adverse events after myocardial infarction. *J Clin Med.* (2020) 9:210. doi: 10.3390/jcm9010210
27. Truong VT, Palmer C, Young M, Wolking S, Ngo TNM, Sheets B, et al. Right atrial deformation using cardiovascular magnetic resonance myocardial feature tracking compared with two-dimensional speckle tracking echocardiography in healthy volunteers. *Sci Rep.* (2020) 10:5237. doi: 10.1038/s41598-020-62105-9
28. Badano LP, Kolias TJ, Muraru D, Abraham TP, Aurigemma G, Edvardsen T, et al. Standardization of left atrial, right ventricular, and right atrial deformation imaging using two-dimensional speckle tracking echocardiography: a consensus document of the EACVI/ASE/Industry Task Force to standardize deformation imaging. *Eur Heart J Cardiovasc Imaging.* (2018) 19:591–600. doi: 10.1093/ehjci/jey042
29. Moher D, Liberati A, Tetzlaff J, Altman DG. PRISMA Group. Preferred reporting items for systematic reviews and meta-analyses: the PRISMA statement. *PLoS Med.* (2009) 6:e1000097. doi: 10.1371/journal.pmed.1000097
30. Downs SH, Black N. The feasibility of creating a checklist for the assessment of the methodological quality both of randomised and non-randomised studies of health care interventions. *J Epidemiol Community Health.* (1998) 52:377–84. doi: 10.1136/jech.52.6.377
31. Hasselberg NE, Kagiyama N, Soyama Y, Sugahara M, Goda A, Ryo-Koriyama K, et al. The prognostic value of right atrial strain imaging in patients with precapillary pulmonary hypertension. *J Am Soc Echocardiogr.* (2021) 34:851–61.e1. doi: 10.1016/j.echo.2021.03.007
32. Nógrádi Á, Porpáczy A, Porcsa L, Minier T, Czirják L, Komócsi A, et al. Relation of right atrial mechanics to functional capacity in patients with systemic sclerosis. *Am J Cardiol.* (2018) 122:1249–54. doi: 10.1016/j.amjcard.2018.06.021
33. Saha SK, Söderberg S, Lindqvist P. Association of right atrial mechanics with hemodynamics and physical capacity in patients with idiopathic pulmonary arterial hypertension: insight from a single-center cohort in northern Sweden. *Echocardiography.* (2016) 33:46–56. doi: 10.1111/echo.12993
34. Liu W, Wang Y, Zhou J, Bai H, Wang F, Wang J. The association of functional capacity with right atrial deformation in patients with pulmonary arterial hypertension: a study with two-dimensional speckle tracking. *Heart Lung Circ.* (2018) 27:350–8. doi: 10.1016/j.hlc.2017.02.029

35. Miah N, Faxén UL, Lund LH, Venkateshvaran A. Diagnostic utility of right atrial reservoir strain to identify elevated right atrial pressure in heart failure. *Int J Cardiol.* (2021) 324:227–32. doi: 10.1016/j.ijcard.2020.09.008
36. Aksu U, Kalkan K, Gulcu O, Aksakal E, Öztürk M, Topcu S. The role of the right atrium in development of postoperative atrial fibrillation: a speckle tracking echocardiography study. *J Clin Ultrasound.* (2019) 47:470–6. doi: 10.1002/jcu.22736
37. Moustafa S, Zuhairy H, Youssef MA, Alvarez N, Connelly MS, Prieur T, et al. Right and left atrial dissimilarities in normal subjects explored by speckle tracking echocardiography. *Echocardiography.* (2015) 32:1392–9. doi: 10.1111/echo.12880
38. Tadic M, Cuspidi C, Pencic B, Sljivic A, Ivanovic B, Neskovic A, et al. High-normal blood pressure impacts the right heart mechanics: a three-dimensional echocardiography and two-dimensional speckle tracking imaging study. *Blood Press Monit.* (2014) 19:145–52. doi: 10.1097/MBP.0000000000000043
39. Ünlü S, Sahinarslan A, Gökalp G, Seçkin Ö, Arinsoy ST, Boyaci NB, et al. The impact of volume overload on right heart function in end-stage renal disease patients on hemodialysis. *Echocardiography.* (2018) 35:314–21. doi: 10.1111/echo.13768
40. Ramkumar S, Yang H, Wang Y, Nolan M, Negishi T, Negishi K, et al. Association of the active and passive components of left atrial deformation with left ventricular function. *J Am Soc Echocardiogr.* (2017) 30:659–66. doi: 10.1016/j.echo.2017.03.014
41. Lang RM, Badano LP, Mor-Avi V, Afilalo J, Armstrong A, Ernande L, et al. Recommendations for cardiac chamber quantification by echocardiography in adults: an update from the American Society of Echocardiography and the European Association of Cardiovascular Imaging. *J Am Soc Echocardiogr.* (2015) 28:1–39.e14. doi: 10.1016/j.echo.2014.10.003
42. Voigt JU, Pedrizzetti G, Lysyansky P, Marwick TH, Houle H, Baumann R, et al. Definitions for a common standard for 2D speckle tracking echocardiography: consensus document of the EACVI/ASE/Industry Task Force to standardize deformation imaging. *Eur Heart J Cardiovasc Imaging.* (2015) 16:1–11. doi: 10.1093/ehjci/jeu184
43. Negishi K, Lucas S, Negishi T, Hamilton J, Marwick TH. What is the primary source of discordance in strain measurement between vendors: imaging or analysis? *Ultrasound Med Biol.* (2013) 39:714–20. doi: 10.1016/j.ultrasmedbio.2012.11.021
44. Mohseni-Badalabadi R, Mehrabi-Pari S, Hosseinsabet A. Evaluation of the left atrial function by two-dimensional speckle-tracking echocardiography in diabetic patients with obesity. *Int J Cardiovasc Imaging.* (2020) 36:643–52. doi: 10.1007/s10554-020-01768-x
45. Tadic M, Cuspidi C, Ilic I, Suzic-Lazić J, Zivanovic V, Jozika L, et al. The relationship between blood pressure variability, obesity and left atrial phasic function in hypertensive population. *Int J Cardiovasc Imaging.* (2016) 32:603–12. doi: 10.1007/s10554-015-0822-8
46. Qu YY, Buckert D, Ma GS, Rasche V. Quantitative assessment of left and right atrial strains using cardiovascular magnetic resonance based tissue tracking. *Front Cardiovasc Med.* (2021) 8:690240. doi: 10.3389/fcvm.2021.690240
47. Delgado-Rodríguez M. Systematic reviews of meta-analyses: applications and limitations. *J Epidemiol Community Health.* (2006) 60:90–2. doi: 10.1136/jech.2005.035253
48. Truong VT, Phan HT, Pham KNP, Duong HNH, Ngo TNM, Palmer C, et al. Normal ranges of left ventricular strain by three-dimensional speckle-tracking echocardiography in adults: a systematic review and meta-analysis. *J Am Soc Echocardiogr.* (2019) 32:1586–97.e5. doi: 10.1016/j.echo.2019.07.012
49. Levy PT, Machefsky A, Sanchez AA, Patel MD, Rogal S, Fowler S, et al. Reference ranges of left ventricular strain measures by two-dimensional speckle-tracking echocardiography in children: a systematic review and meta-analysis. *J Am Soc Echocardiogr.* (2016) 29:209–25.e6. doi: 10.1016/j.echo.2015.11.016

Conflict of Interest: The authors declare that the research was conducted in the absence of any commercial or financial relationships that could be construed as a potential conflict of interest.

Publisher's Note: All claims expressed in this article are solely those of the authors and do not necessarily represent those of their affiliated organizations, or those of the publisher, the editors and the reviewers. Any product that may be evaluated in this article, or claim that may be made by its manufacturer, is not guaranteed or endorsed by the publisher.

frontiers in Cardiovascular Medicine

SYSTEMATIC REVIEW
published: 17 December 2021
doi: 10.3389/fcvm.2021.772803

Electrocardiographic Features of Left Ventricular Diastolic Dysfunction and Heart Failure With Preserved Ejection Fraction: A Systematic Review

Anne-Mar Van Ommen[1†], Elise Laura Kessler[1†], Gideon Valstar[1], N. Charlotte Onland-Moret[2], Maarten Jan Cramer[3], Frans Rutten[2], Ruben Coronel[4,5] and Hester Den Ruijter[1]*

[1] Laboratory of Experimental Cardiology, University Medical Center Utrecht, Utrecht, Netherlands, [2] Julius Center for Health Sciences and Primary Care, University Medical Center Utrecht, Utrecht, Netherlands, [3] Department of Cardiology, University Medical Center Utrecht, Utrecht, Netherlands, [4] Department of Experimental Cardiology, Amsterdam University Medical Center, Amsterdam, Netherlands, [5] Institut de rythmologie et modélisation cardiaque (IHU-Liryc), Pessac, France

OPEN ACCESS

Edited by:
Nay Aung,
Queen Mary University of London,
United Kingdom

Reviewed by:
Stefan van Duijvenboden,
University College London,
United Kingdom
Laura Stefani,
University of Florence, Italy

***Correspondence:**
Hester Den Ruijter
h.m.denRuijter-2@umcutrecht.nl

[†] These authors have contributed equally to this work

Specialty section:
This article was submitted to Cardiovascular Imaging, a section of the journal Frontiers in Cardiovascular Medicine

Received: 09 September 2021
Accepted: 16 November 2021
Published: 17 December 2021

Citation:
Van Ommen A-M, Kessler EL, Valstar G, Onland-Moret NC, Cramer MJ, Rutten F, Coronel R and Den Ruijter H (2021) Electrocardiographic Features of Left Ventricular Diastolic Dysfunction and Heart Failure With Preserved Ejection Fraction: A Systematic Review. Front. Cardiovasc. Med. 8:772803. doi: 10.3389/fcvm.2021.772803

Background: Electrocardiographic features are well-known for heart failure with reduced ejection fraction (HFrEF), but not for left ventricular diastolic dysfunction (LVDD) and heart failure with preserved ejection fraction (HFpEF). As ECG features could help to identify high-risk individuals in primary care, we systematically reviewed the literature for ECG features diagnosing women and men suspected of LVDD and HFpEF.

Methods and Results: Among the 7,127 records identified, only 10 studies reported diagnostic measures, of which 9 studied LVDD. For LVDD, the most promising features were T-end-P/(PQ*age), which is the electrocardiographic equivalent of the passive-to-active filling (AUC: 0.91–0.96), and repolarization times (QTc interval ≥ 350 ms, AUC: 0.85). For HFpEF, the Cornell product ≥ 1,800 mm*ms showed poor sensitivity of 40% (AUC: 0.62). No studies presented results stratified by sex.

Conclusion: Electrocardiographic features are not widely evaluated in diagnostic studies for LVDD and HFpEF. Only for LVDD, two ECG features related to the diastolic interval, and repolarization measures showed diagnostic potential. To improve diagnosis and care for women and men suspected of heart failure, reporting of sex-specific data on ECG features is encouraged.

Keywords: sex-differences, diagnosis, HFpEF-heart failure with preserved ejection fraction, LVDD-left ventricular diastolic dysfunction, primary care, electrocardiography (ECG)

INTRODUCTION

The prevalence of heart failure with preserved ejection fraction is increasing relative to heart failure with reduced ejection fraction (HFrEF) (1), and affects women more than men in a 2:1 ratio (2). Left ventricular diastolic dysfunction (LVDD) is considered the pre-stage of heart failure with preserved ejection fraction (HFpEF). LVDD is marked by elevated filling pressures, abnormal relaxation, and decreased compliance of the left ventricle (LV), often accompanied by increased atrial volumes and left ventricular mass (3, 4). The lack of reliable diagnostic tools for the detection of HFpEF likely contributes to the underdiagnosis in primary care (5). Thus, direct referral for

echocardiography follows when heart failure is suspected (6). Currently, echocardiography is not implemented in primary care, while ECG is. For HFrEF, certain ECG features are clearly linked, i.e., prolonged PR interval (7), low voltages (8), QRS prolongation (9), and QT prolongation, dispersion, and variability (10). Also, several ECG features were shown to be too help to identify HFrEF in primary care populations (11, 12). Similarly, ECG features could help in selecting patients needing echocardiography for HFpEF, but ECG features associated with HFpEF are less established. Recently, a meta-analysis reported a higher incidence of right bundle branch block (RBBB) or atrial fibrillation (AF) in HFpEF compared to HFrEF (13). This suggests that ECG changes associated with HFrEF cannot be directly extrapolated to HFpEF. However, in this meta-analysis, ECG features for LVDD were not studied and there was no comparison made with healthy individuals, or between women and men. Therefore, we performed a systematic review to identify ECG features in patients with LVDD or HFpEF. As the prevalence of HFpEF differs between men and women (2) and several ECG features are marked by sex-specific cut-offs (14), we also documented sex-specific reporting of diagnostic performance for LVDD and HFpEF.

METHODS

Data Sources and Searches

We searched PubMed and EMBASE for articles on April 18, 2019 and updated our search up to October 26, 2021. Our search terms included electrocardiogram, diagnosis, heart failure, diastolic dysfunction, and variants of these terms and comprised only human studies. The full search string can be found in **Supplementary Method I**. After the removal of duplicates, all records were screened by title and abstract by two of three independent researchers (A.v.O., E.K., and G.V.). A further selection was made after reading full-texts and application of the in- and exclusion criteria. Disagreements were resolved by discussion. Among the studies retrieved for full-text assessment, reference lists were screened, and a citation search was performed for additional relevant studies by two researchers (A.v.O and E.K.).

Study Selection

Eligible studies were cross-sectional in patients suspected of LVDD or heart failure (domain), questioning whether ECG features (determinant) were diagnostic for LVDD or HFpEF (outcome). A 12-lead resting surface ECG should be part of the assessment. Participants should not have a history of the disease of interest, and the healthy controls were the non-diseased individuals as defined by the authors of the original articles. We excluded animal studies, *in vitro* studies, reviews, conference papers/abstracts, case studies, and editorials. For studies that were not full-text available, we contacted the corresponding author. If we did not receive a response, the study was excluded. Studies that were written in a language other than English, Dutch, or German were also excluded. Detailed information on well-defined ECG features had to be reported (e.g., exact values, cut-off values, or absence or presence of pre-defined criteria). Studies only reporting whether an ECG was normal or abnormal, without specifications, were not considered eligible. Diagnosis of LVDD or HFpEF had to be established according to existing guidelines (3, 4, 6, 15, 16). Studies on LVDD were only included if the diagnosis was based on multiple echocardiographic parameters to prevent misclassification (3, 16). The search and selection processes are visualized in the PRISMA flow diagram presented in **Figure 1**.

Data Extraction

Study characteristics are reported in **Supplementary Table I**, including the name of the first author, year of publication, country, age and number of participants, percentage of women participating, study in- and exclusion criteria, mean left ventricular ejection fraction [LVEF (%)], ECG features studied, prevalence and definition of LVDD/HFpEF, and association measure between ECG feature and the diagnosis of LVDD or HFpEF. Additionally, we recorded if sex-stratified outcomes were given and whether sex was included in a multivariable model (if applicable). Data-extraction was performed by a single researcher (A.v.O.) and checked by another researcher (E.K.). We used the PRISMA reporting guidelines (17) and registered the protocol of this systematic review in PROSPERO (https://www.crd.york.ac.uk/prospero/) with the registration number: CRD42020212907.

Critical Appraisal

For all studies selected, a critical appraisal was performed independently by two researchers (A.v.O, E.K.) in accordance with the QUADAS-2 criteria (18). Four domains i.e., patient selection, index test, reference test, and flow and timing were scored (**Table 1**). Additionally, the level of evidence in terms of the association measure provided for diagnosis of LVDD/HFpEF was rated. Studies presenting sensitivity/specificity/negative predictive value (NPV)/positive predictive value (PPV) and area under the curve (AUC) values were classified as the highest level of evidence. Odds ratio (OR), relative risk (RR), or correlation coefficient were classified as intermediate levels of evidence. Studies reporting numbers/percentages and between-group differences were judged as low level of evidence. As ECG parameters and association measures were highly heterogeneous, we only assessed publication bias when $\geq$5 studies reported the same ECG parameter and association measure. Based on the reported outcomes of the high level of evidence studies we judged ECG features as promising or not.

RESULTS

In total, 7,127 articles were screened, and 22 met the predefined in- and exclusion criteria (**Figure 1**, **Supplementary Table I**). All 22 studies were published between 2003 and 2021. In total, 25 ECG parameters were investigated. Moreover, 16 parameters were studied only once. LVDD was the outcome in 18 studies and HFpEF in 4 studies. All 25 parameters were grouped by phase in the cardiac cycle: the atrial activation, ventricular

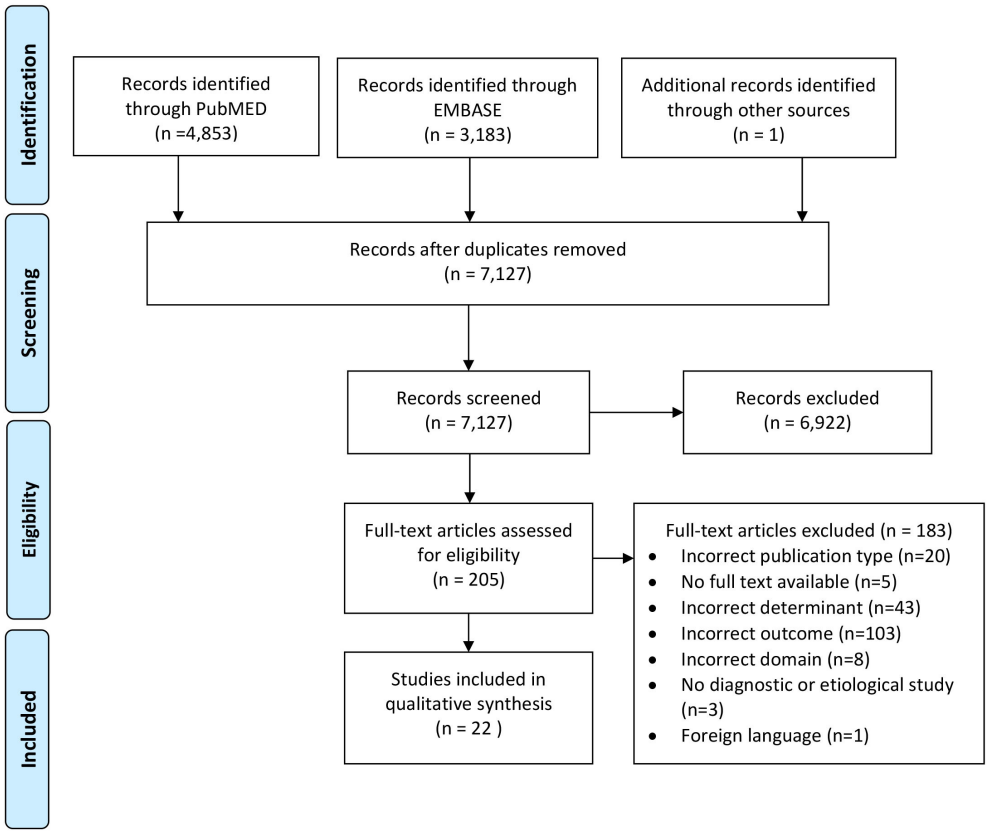

FIGURE 1 | PRISMA flow diagram summarizing the search and selection process applying pre-defined in- and exclusion criteria.

depolarization, ventricular repolarization, and the full diastole (**Figure 2**, **Supplementary Table II**). All parameters from the 10 diagnostic studies are discussed in the text and summarized in **Table 2**.

Critical Appraisal

The overall quality of the studies was acceptable, all studies met the applicability criteria, and six studies had an overall low risk of bias on all domains (**Table 1**). We did not exclude studies because of a high risk of bias. The major reason for the high risk of bias in the study selection domain was a case-control design. Secondly, many studies applied extensive exclusion criteria that led to the exclusion of difficult to diagnose patients affecting the diagnostic accuracy of ECG features and reducing the generalizability of the findings. Information on blinded interpretation of the index test and reference was often lacking resulting in an unclear risk of bias in these domains. The interval between performing the ECG and the echocardiogram (assessed in the flow and timing domain) was often not reported, but no stringent concerns were raised in this period was longer than 6 weeks. The majority of studies had a low or intermediate level of evidence. A total of nine studies reported appropriate association measures for the diagnosis of LVDD or HFpEF and were thus classified as a high level of evidence.

Atrial Contraction Related Features

Electrocardiographic (ECG) features derived from atrial contraction up to the ventricular depolarization were described in 11 articles (20–25, 29–33).

PTFV1 and Morris Index

In 417 individuals considered at risk for heart failure (e.g., history of hypertension, diabetes, obesity, or having received potential cardiotoxic chemotherapy) enrolled through local media advertising, the P-wave terminal force in lead V1 (PTFV1) $\leq -4{,}000$ μV*ms showed a PPV of 67% and a sensitivity of 36% for LVDD (prevalence LVDD = 65%) (21). In another study with individuals undergoing echocardiography as part of routine cardiac care (20), the sensitivity, specificity, PPV, and NPV of a PTFV1 $\geq$0.04 mm*s were 27, 100, 100, and 38%, respectively, for a diagnosis of LVDD [present in 62 of 117 participants (53%)]. In 8 among the 117 participants (6.8%), the Morris index was present resulting in a sensitivity, specificity, and PPV and NPV for LVDD of 13, 100, 100, and 34%, respectively (20).

P-Wave Area, Dispersion, and Duration

In 140 individuals in whom coronary artery disease (CAD) was ruled out with a negative exercise test or coronary angiography (CAG), *P*-wave dispersion (>0.045 s) showed a sensitivity

TABLE 1 | Critical appraisal, evaluation of the level of evidence, and applicability for the selected studies in accordance with the QUADAS-2 criteria.

Year of publication	1st author	Country/Population	Critical appraisal				Level of evidence	Applicability		
			Patient selection	Index test (ECG)	Reference test (Diagnosis)	Flow and timing		Domain	Determinant	Outcome
2010	Boles	Ireland	Unclear	Low	Low	Low	Intermediate	No concerns	No concerns	No concerns
2003	Dogan	Turkey	Low	Low	Unclear	Low	Low	No concerns	No concerns	No concerns
2012	Eicher	France	Low	Unclear	Unclear	Low	Low	No concerns	No concerns	No concerns
2005	Gunduz	Turkey	High	Unclear	Unclear	High	Low	No concerns	No concerns	No concerns
2021	Hayiroglu	Turkey	Low	Unclear	Low	Low	High	No concerns	No concerns	No concerns
2012	Hsu	Taiwan	Low	Low	Low	Low	Intermediate	No concerns	No concerns	No concerns
2015	Kadi	Turkey	High	Low	Low	High	Intermediate	No concerns	No concerns	No concerns
2016	Khan	Pakistan	Unclear	Low	Unclear	Unclear	High	No concerns	No concerns	No concerns
2014	Krepp	USA	High	Low	Low	High	High	No concerns	No concerns	No concerns
2008	Miwa	Japan	High	Unclear	Unclear	Unclear	Low	No concerns	No concerns	No concerns
2013	Namdar	Switzerland	High	Low	Low	Unclear	High	No concerns	No concerns	No concerns
2018	Nikolaidou	UK	Low	Low	Low	Low	Low	No concerns	No concerns	No concerns
2012	Ofman	USA	High	Low	Unclear	High	Intermediate	No concerns	No concerns	No concerns
2016	Onoune	Japan	Unclear	Low	Low	Low	Intermediate	No concerns	No concerns	No concerns
2006	Palmieri	Europe/USA	Low	Low	Low	Low	Low	No concerns	No concerns	No concerns
2012	Sauer	USA	Low	Low	Low	Low	Intermediate	No concerns	No concerns	No concerns
2019	Sumita	Japan	Low	Unclear	Unclear	Low	High	No concerns	No concerns	No concerns
2014	Taha	Egypt	High	Low	Low	Low	High	No concerns	No concerns	No concerns
2019	Tan	Singapore	High	Unclear	Unclear	High	High	No concerns	No concerns	No concerns
2013	Tsai	Taiwan	Low	Low	Low	Low	High	No concerns	No concerns	No concerns
2011	Wilcox	USA	Low	Low	Low	Low	High	No concerns	No concerns	No concerns
2017	Yang	Australia	Low	Unclear	Unclear	Low	High	No concerns	No concerns	No concerns

Green boxes represent either a low risk of bias, a high level of evidence, and no concerns with respect to applicability. Grey boxes represent an unclear risk of bias. Yellow boxes represent an intermediate level of evidence. Red boxes represent either a high risk of bias or a low level of evidence.

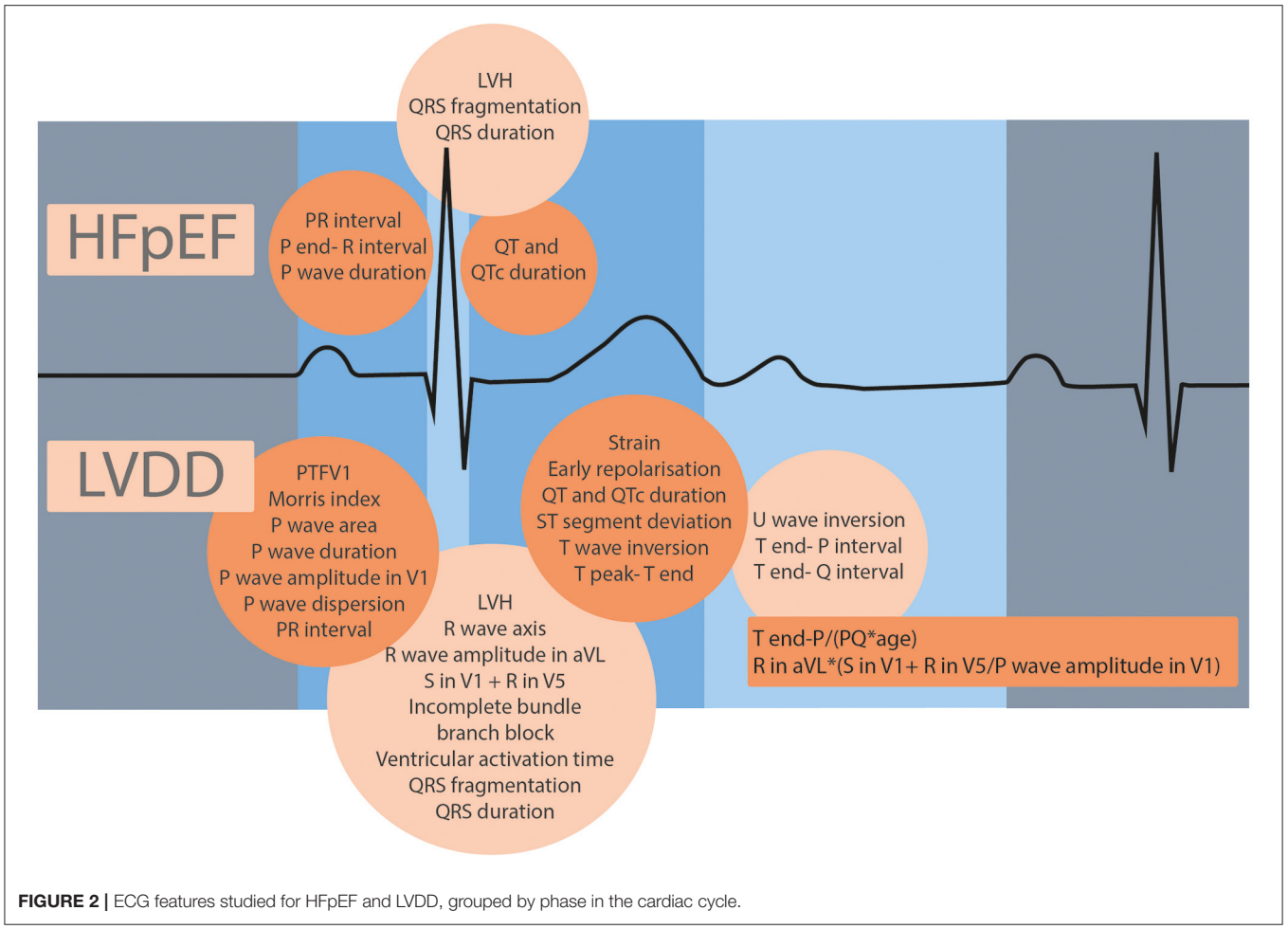

FIGURE 2 | ECG features studied for HFpEF and LVDD, grouped by phase in the cardiac cycle.

and specificity of 98 and 64% for LVDD (prevalence LVDD = 60%) (23). In another study in 270 patients undergoing echocardiography for clinical indications (e.g., abnormal physical examination, hypertension, or suspicion of CAD or heart failure), *P*-wave duration, *P*-wave area, and dispersion were measured (22). Measurements were corrected for heart rate using Bazett's formula, and for all features, significantly higher values were found in individuals with LVDD compared to those without LVDD (prevalence LVDD = 33%). For the corrected *P*-wave area, the AUC for diagnosing LVDD was 0.6 (22). The AUC for both corrected *P*-wave duration, and *P*-wave dispersion was 0.62. In a similar population (prevalence LVDD = 53%), *P*-wave duration > 110 ms was more sensitive for LVDD (sensitivity 86%, specificity 86%), and a *P*-wave duration > 120 ms was more specific for LVDD (sensitivity 34% and specificity 100%) (20).

P-Wave Amplitude

The amplitude of *P*-wave was measured in one study with LVDD as an outcome in 204 individuals without CAD or other major cardiac pathologies visiting the outpatient cardiology clinic (19). At a cut-off value ≥ 0.102 mV, this parameter showed a sensitivity of 67% and specificity of 60% with an AUC of 0.69 in this population with a prevalence of LVDD of 42%.

PQ Interval

One study reported the diagnostic performance of a PQ interval of ≥ 150 ms for LVDD, in individuals with diastolic function classification based on echocardiography (24). AUC, sensitivity, specificity, PPV and NPV were 0.65, 78, 46, 58, and 68%. In this study, LVDD was present in 81 of the 164 participants (prevalence = 49%).

Ventricular Depolarization

In total, 9 studies reported ECG parameters representing ventricular depolarization and their relationship to LVDD (21, 24, 25, 28, 29, 33–36). Of note, many studies (19, 20, 23, 25, 28, 35, 37) used a QRS duration of above 120 or 130 ms, or the presence of complete bundle branch block (BBB), as exclusion criteria.

Left Ventricular Hypertrophy

The Cornell product with a cut-off value ≥ 1,595 mm*ms based on the 3rd quartile Cornell product was used to determine LVDD (prevalence = 57%) in a group of 185 individuals, undergoing both echocardiography and coronary computed tomography angiography (CCTA) for clinical indications (25). For the detection of LVDD, the sensitivity and specificity were 36 and 90% and PPV and NPV were 83 and 52%, respectively. Another study used 3rd quartile sex-specific cut-off values of the

TABLE 2 | Summary of diagnostic association measures of ECG features for LVDD and HFpEF when compared to non-diseased individuals.

LVDD/HFpEF	Phase	ECG feature	Definition	Study	Cut-off value	Findings
	Atrial activation	P wave amplitude in V1	Peak of P wave to the iso-electric line of TP interval in lead V1	Hayiroglu et al. (19)	≥ 0.102 mV	AUC = 0.69, sensitivity = 67%, specificity = 60%
LVDD		PTFV1	P-wave terminal force in lead V1 is the multiplication of the amplitude by duration of the terminal part of the P-wave in lead V1.	Sumita et al. (20)	PTFV1 ≥0.04 mm*s	Sens = 27%, spec = 100%, PPV = 100%, NPV = 38%
				Yang et al. (21)	PTFV1 ≤-4,000 μV*ms	Sens = 36%, PPV = 67%
		Morris Index	Present when P wave negative phase' width and amplitude are both > 1 mm.	Sumita et al. (20)		Sens = 13%, spec = 100%, PPV = 100%, NPV = 34%
		P wave area	P wave area is the multiplication of the P wave amplitude (mV) by 0.5 P wave duration (ms) in lead II.	Tsai et al. (22)	corrected P wave area > 60 ms*mV	AUC = 0.60, sens = 58%, spec = 56%
		P wave duration	Duration of P wave.	Tsai et al. (22)	corrected P wave duration > 85 ms	AUC = 0.62, sens = 65%, spec = 46%
				Sumita et al. (20)	P wave duration > 110 ms	Sens = 86%, spec = 86%
				Sumita et al. (20)	P wave duration > 120 ms	Sens = 34%, spec = 100%
		P wave dispersion	Difference between longest and shortest P wave recorded from multiple ECG leads.	Taha et al. (23)	P wave dispersion > 45 ms	Sens = 98%, spec = 64%
				Tsai et al. (22)	P wave dispersion > 65 ms	AUC = 0.62, sens = 62%, spec = 57%
		PQ- and PR interval	Beginning of P wave until onset of Q or R wave.	Namdar et al. (24)	PQ ≥ 150 ms	AUC = 0.65, sens = 78%, spec = 46%, PPV = 58%, NPV = 68%
	Ventricular depolarization	LVH	Most common criteria for left ventricular hypertrophy include: (1) Cornell voltage criteria: S in V3 + R in aVL > 28 mm (men), S in V3 + R in aVL > 20 mm (women). (2) Cornell product: (amplitude S in V3+R in aVL)*QRS duration. (3) Sokolow Lyon criteria: S wave in V1 and tallest R wave in V5 or V6 are ≥35 mm, or R wave in aVL ≥11 mm.	Krepp et al. (25)	Cornell product ≥ 1,595 mm*ms	Sens = 36%, spec = 90%, PPV = 83%, NPV = 52%
		Sum of S wave amplitude in V1 and R wave amplitude in V5		Hayiroglu et al. (19)	≥ 1.85 mV	AUC = 0.68, sensitivity and specificity = 65%
		R wave amplitude in aVL	R wave amplitude in aVL	Hayiroglu et al. (19)	≥0.517 mV	AUC = 0.68, sensitivity = 62%, specificity = 61%,
	Ventricular repolarization	QT interval	Interval between Q wave onset and end of T wave.	Taha et al. (23)	QT > 330 ms	Sens = 69%, spec = 64%
		QTc interval	As QT interval decreases when heart rate increases, QT interval is often corrected for heart rate (QTc) by Bazett's formula.	Taha et al. (23)	QTc ≥ 395 ms	Sens = 81%, spec = 79%
				Khan et al. (26)	QTc ≥ 435 ms	AUC = 0.82, sens = 71%, spec = 81%, PPV = 65%, NPV = 85%
				Wilcox et al. (27)	QTc ≥ 435 ms	Sens = 73%, spec = 74%
		ST segment deviation	ST segment deviation from J point of at least 20 mV.	Yang et al. (21)		Sens = 28%, PPV = 67%
		T peak—T end	Interval between peak and end of T wave.	Taha et al. (23)	T peak—T end > 95 ms	Sens = 76%, spec = 29%
	Full diastolic period	T end—P interval	End of T wave to P wave onset.	Namdar et al. (24)	T end—P ≤311 ms	AUC = 0.82, sens = 79%, spec = 72%, PPV = 74%, NPV = 78%

(Continued)

TABLE 2 | Continued

LVDD/HFpEFPhase	ECG feature	Definition	Study	Cut-off value	Findings
	T end−Q interval	End of T wave to Q wave onset.	Namdar et al. (24)	T end−Q ≤ 455 ms	AUC = 0.77, sens = 73%, spec = 73%, PPV = 73%, NPV = 73%
Indexes	T end-P/(PQ*age)		Namdar et al. (24)	(T end-P/(PQ*age) ≥ 0.0333	AUC = 0.96, sens = 90%, spec = 92%, PPV = 91%, NPV = 90%
	T end-Q/(PQ*age)		Namdar et al. (24)	(T end-Q/(PQ*age) ≥ 0.0489	AUC = 0.95, sens = 89%, spec = 94%, PPV = 94%, NPV = 90%
	R in aVL * (S in V1 + R in V5)/P wave amplitude in V1)		Hayiroglu et al. (19)	≥ 8.53 mV	AUC = 0.78, sensitivity and specificity = 70%
HFpEF	Ventricular depolarization	LVH	See LVDD	Tan et al. (28)	Cornell product ≥ 1,800 mm*ms	AUC = 0.62, sens = 40%, spec = 80%

AUC, area under the receiver operating characteristics curve; BBB, bundle branch block; HFpEF, heart failure with preserved ejection fraction; LVDD, left ventricular diastolic dysfunction; NPV, negative predictive value; PPV, positive predictive value; PTFV1, P-wave terminal force in lead V1; LVH, left ventricular hypertrophy; sens, sensitivity; spec, specificity.

Cornell product (1,442 mm*ms for men and 1,515 mm*ms for women) and found a PPV and sensitivity of 77 and 29% for LVDD (prevalence LVDD = 65%) (21).

In the only study reporting diagnostic association measures for HFpEF, a Cornell product ≥ 1,800 mm*ms showed a sensitivity, specificity, and AUC of 40, 80, and 0.62 for the detection of HFpEF (prevalence HFPEF = 52%) when compared to controls with hypertension (28).

Another group used the sum of the amplitude in S wave in V1 and R wave in V5 (derived from the Sokolow-Lyon criteria) as a diagnostic measure for LVDD in individuals without CAD or other major cardiac pathologies (19). This ECG feature showed a sensitivity of 62%, specificity of 61%, and AUC of 0.68 at a cut-off value of ≥ 1.85 mV. The same authors also studied R wave amplitude in lead aVL. For this feature, lower sensitivity and specificity of 60%, and AUC of 0.65 were found at a cut-off of ≥0.517 mV.

Ventricular Repolarization

Features of ventricular repolarization, defined as the period between the end of the QRS complex and the end of the *T*-wave, were reported by 12 studies (21, 23–27, 33, 37–39).

QTc and QT Interval

In 140 individuals without signs of CAD (based on stress ECG or CAG), QT and QTc intervals were significantly longer in individuals with LVDD compared to individuals without LVDD (prevalence LVDD = 60%) (23). A QTc interval ≥ 395 ms could diagnose LVDD with a sensitivity and specificity of 81 and 79%, whereas a QT interval > 330 ms showed lower sensitivity and specificity of 69 and 64%, respectively. Wilcox et al. measured QTc interval, QT interval, and J point- T interval corrected for heart rate (JTc) is firstly a derivation group referred for the suspicion of heart failure, and secondly, a validation group referred for stress echocardiography (prevalence LVDD = 64% in the derivation group) (27). For the detection of grade II or higher LVDD in the derivation group, a QTc interval ≥ 435 ms had a sensitivity and specificity of 73 and 74%. A QTc interval ≥435 ms in the validation cohort was associated with lower e' velocities, but diagnostic association measures for LVDD categories were not reported. For both the derivation and validation groups QT intervals were higher in individuals with LVDD, but diagnostic association measures were not reported. A significant interaction between JTc interval and QRS duration was observed, however, there was no significant association between JTc and a reduced septal e' velocity in individuals with prolonged QRS duration. One other study, with LVDD as the outcome (prevalence LVDD = 60%), used the same cut-off value for QTc duration and found sensitivity, specificity, NPV, PPV, and AUC value of 71, 81, 85, 65%, and 0.82, respectively, in 300 individuals with the suspicion of heart failure (26).

ST-Segment Deviation

In a group of patients at risk for heart failure, ST-segment deviation in lead V5 and V6 was present in 29% compared to 25% of the participants with and without LVDD (prevalence LVDD = 65%). PPV and sensitivity for LVDD were 67 and 28%,

respectively (21). Individuals with known CAD were excluded in this study, but the presence of CAD in the study population was not stated.

T-Peak-T-End Interval

In 140 individuals where CAD was ruled out, there was no significant difference for T-peak-T-end interval comparing individuals with and without LVDD. Sensitivity and specificity were 76% and 29%, respectively (23).

Diastolic Period and Indexes

The diastolic period, defined as the end of the T-wave until the onset of the QRS complex, comprised two studies (24, 40).

Indexes Related to Diastolic Period: T-End-P/(PQ*age) and T-End-Q/(PQ*age)

A study in 164 individuals with echocardiography data available on LVDD classification (24) found that T-end-P-interval and T-end-Q-interval were significantly shorter in individuals with LVDD compared to without LVDD. Two diagnostic indexes consisting of several ECG features and age were tested in the derivation group of this study, the first index being T-end-P/(PQ*age), the second being T-end-Q/(PQ*age). The first index showed an AUC value of 0.96 and sensitivity, specificity, PPV, NPV, and accuracy of above 0.9 for LVDD at a cut-off value of 0.0333. As a reference, the value of this index was 0.06 ± 0.026 for individuals $\leq$ 60 years without LVDD, compared to 0.0269 ± 0.005 for individuals in this age category with grade II LVDD ($p < 0.005$). For individuals, $>$ 60 years old without LVDD a value of 0.042 ± 0.011 was found, compared to 0.021 ± 0.01 in grade II LVDD. Similarly, the AUC for the second index was high at 0.95 with high sensitivity, specificity, PPV, NPV, and accuracy for LVDD at a cut-off value of 0.0489. The index T-end-P/(PQ*age) was also validated reporting an AUC value of 0.91 and high values for sensitivity, specificity, PPV, NPV, and accuracy (82, 93, 93, 82, and 88%, respectively).

Electrocardiographic Diastolic Index (EDI)

In a study of 204 patients without CAD, or other major cardiac pathologies the validity of an ECG index involving *P*-wave amplitude in lead V1, components of the Sokolow-Lyon criteria, and Cornell product was tested. The index being aVL R wave amplitude * (V1 S amplitude + V5 R amplitude)/P wave amplitude in V1) showed the highest diagnostic value for LVDD when the index was $\geq$ 8.53 mV with an AUC of 0.78, the sensitivity of 70%, and specificity of 70%.

ECG Cut-Off Values and Outcomes in Women and Men

None of the studies reported diagnostic properties of ECG features separately for women or men. However, Yang et al. used sex-specific cut-off values for the Cornell product (21). Although sex-specific outcomes were not reported, many intermediate levels evidence studies performing multivariate regression analysis used biological sex as a covariate (21, 22, 27, 28, 37, 38).

DISCUSSION

Electrocardiographic (ECG) features of LVDD and HFpEF were not frequently studied, and we identified 8 studies that showed diagnostic performance of ECG features in LVDD. Only one study reported the diagnostic value of ECG features in HFpEF. No studies reported data for women and men separately despite known differences between men and women in prevalence of HFpEF, and in normal electrocardiographic times.

Discussion of the Different Identified Features

The index [T-end-P/(PQ*age)], which electrocardiographically reflects the ratio of the early filling phase to the atrial contraction phase of the diastole, showed a reduced ratio with worsening diastolic function. This index, described by Namdar et al. (24) showed the best diagnostic properties (AUC:0.96 and 0.91 in the derivation and validation group) of all ECG features studied. It showed that it was able to identify LVDD in situations, where echocardiography is not directly available. This index has not yet been validated further.

As the early filling phase (T-end-P) shortens when QT and PQ intervals are prolonged and heart rate increases, it is not surprising that many studies reported the association of higher PQ and QTc intervals with LVDD (13, 20, 22–27, 30, 32). PQ time, as well as *P*-wave dispersion and duration, have been established as markers of cardiac degeneration and as risk factors for atrial fibrillation and all-cause mortality (41). Biphasic *P*-waves are typically associated with dilated atria in heart failure and a negative force in lead V1 is mandatory for abnormal PTFV1 and the Morris index. The association of increased atrial conduction times with LVDD and HFpEF underlines the idea that LVDD and HFpEF are outcomes of accelerated cardiac aging (42).

The QTc interval is longer in women compared to men (14, 43), and therefore has sex-specific cut-off values (44). The QTc interval can be influenced by many factors, e.g., genetic disorders, medication usage, electrolyte disorders, obesity, diabetes, and a prolonged QRS duration (44). Although QTc prolongation observed in LVDD is not explained by prolonged QRS duration as shown by Wilcox et al. (27), left ventricular myocardial systolic and diastolic dyssynchrony has been observed in HFpEF patients with narrow QRS complexes when compared to healthy controls (45). Hypothetically, this dyssynchrony could be driven by altered intracellular calcium handling in cardiomyocytes, a condition that also can result in QTc prolongation (46). Alternative explanations for QTc prolongation in LVDD could be an autonomic imbalance (42, 47), or influences of comorbidities and medication usage, although some of the studies in this review excluded individuals using QTc prolongation medication (23, 30).

Although an increased left ventricular mass index is part of the structural domain within the HFA-PEFF algorithm (4) for HFpEF diagnosis, the poor diagnostic performance of electrocardiographic signs of LVH was described, for both LVDD and HFpEF. Hayiroglu et al. (19) tested an index predominantly involving amplitude signals for LVH, and P wave amplitude, as a

measure for LVDD based on the hypothesis that these signals are predictive for LVDD given the high prevalence of LVH and AF in this population. Criteria related to slower ventricular conduction were deliberately left out of the equation because the authors reasoned these are predictive of CAD and HFrEF. However, this index had poorer diagnostic performance compared to the [T-end-P/(PQ*age)] index.

Heterogeneity in Determinants and Association Measures

There is large heterogeneity in the (cut-offs of) ECG features that were reported in the different studies, which resulted in a small number of studies that investigated the same ECG feature. Also, some studies corrected ECG features for heart rate, while others did not. As deconditioning and autonomic imbalance in heart failure generally leads to higher resting heart rates (48), the usefulness of heart rate correction in HFpEF diagnosis is controversial and worth investigating.

We only selected studies that diagnosed LVDD or HFpEF in line with current or prior guidelines, but as the diagnostic criteria considered the gold standard changed frequently over the years, this resulted in the heterogeneity of assessment of LVDD and HFpEF (3, 4, 6, 15, 16).

Many studies did not report the diagnostic properties of the parameters studied, leading to a low level of evidence. However, when diagnostic properties were provided, there was also heterogeneity in the diagnostic properties described. For example, only reporting PPV and sensitivity (21), leaves question marks about the discriminative value of the ECG features studied. Altogether, this resulted in limited comparability of the included studies. Thus, it was not possible to pool studies in a meta-analysis, nor to assess publication bias. Nevertheless, some of the low levels of evidence studies showed neutral results comparing individuals with LVDD and HFpEF to controls (**Supplementary Table I**).

Strengths and Limitations

Strengths: We addressed the value of ECG features in diagnosing LVDD and HFpEF in a systematic manner. In addition, we reported if and how sex is accounted for in the analyses, which is important to identify knowledge gaps that currently still exist in the field of cardiology.

Limitations: We included only studies with a 12-lead resting surface ECG. Hence, we excluded studies that took features from exercise ECGs such as heart rate variability and ST-segment hump sign (23, 47, 49, 50). We recognize that those may be relevant for the diagnosis of LVDD and HFpEF, but interpretation and implementation in primary care would be a limitation.

Recommendations and Directions for Future Research

Both features that showed high diagnostic performance for LVDD, the index reflecting the ratio of passive and active filling and ventricular repolarization times, were not studied in HFpEF. We recommend validation of these features for HFpEF in individuals suspected of heart failure, taking into account specific conditions such as premature ventricular beats or drug regiments. In addition, we recommend that future studies based on implementation reports on the inter-observer performance of ECG features be studied and assess whether measuring ECG features needs training. ECG features for LVDD and HFpEF diagnosis could be very useful in primary care, but the interpretation by healthcare workers with limited experience in reading ECGs could decrease applicability. Although more complex, many efforts are undertaken to produce reliable (screening) methods using deep learning algorithms for LVDD and HFpEF diagnosis (51–54). The largest potential of these models is adding features distilled from raw ECG data that would otherwise not be accessible, thus providing new information. Finally, we recommend disclosing how ECG features for LVDD and HFpEF perform in men and women separately to increase application in clinical practice.

CONCLUSION

Electrocardiographic (ECG) features are not widely evaluated in diagnostic studies for LVDD and HFpEF. Only for LVDD, two ECG features related to the diastolic interval, and repolarization measures showed diagnostic potential. To improve diagnosis and care for women and men suspected of heart failure, reporting of sex-specific data on ECG features is encouraged.

DATA AVAILABILITY STATEMENT

The original contributions presented in the study are included in the article/**Supplementary Material**, further inquiries can be directed to the corresponding author/s.

AUTHOR CONTRIBUTIONS

The literature search, data collection, and analysis were performed by GV, EK, and A-MV. The first draft of the manuscript was written by A-MV and EK. All authors commented on previous versions of the manuscript, contributed to the study conception and design, and read and approved the submitted version.

FUNDING

This research was funded by European Research Council consolidator grant 866478 (UCARE), Dutch Cardiovascular Alliance grant 2020B004 (IMPRESS), Leducq Network of Excellence 16CVD02 (RHYTHM), and Dutch Cardiovascular Alliance grant 2020B008 (RECONNEXT).

SUPPLEMENTARY MATERIAL

The Supplementary Material for this article can be found online at: https://www.frontiersin.org/articles/10.3389/fcvm.2021.772803/full#supplementary-material

REFERENCES

1. Steinberg BA, Zhao X, Heidenreich PA, Peterson ED, Bhatt DL, Cannon CP, et al. Trends in patients hospitalized with heart failure and preserved left ventricular ejection fraction: prevalence, therapies, and outcomes. *Circulation.* (2012) 126:65–75. doi: 10.1161/CIRCULATIONAHA.111.080770
2. Redfield MM, Jacobsen SJ, Burnett JC, Mahoney DW, Bailey KR, Rodeheffer RJ. Burden of systolic and diastolic ventricular dysfunction in the community. *JAMA.* (2003) 289:194. doi: 10.1001/jama.289.2.194
3. Nagueh SF, Smiseth OA, Appleton CP, Byrd BF, Dokainish H, Edvardsen T, et al. Recommendations for the evaluation of left ventricular diastolic function by echocardiography: an update from the american society of echocardiography and the European Association of Cardiovascular Imaging. *J Am Soc Echocardiogr.* (2016) 29:277–314. doi: 10.1016/j.echo.2016.01.011
4. Pieske B, Tschöpe C, De Boer RA, Fraser AG, Anker SD, Donal E, et al. How to diagnose heart failure with preserved ejection fraction: The HFA-PEFF diagnostic algorithm: a consensus recommendation from the Heart Failure Association (HFA) of the European Society of Cardiology (ESC). *Eur Heart J.* (2019) 40:3297–317. doi: 10.1093/eurheartj/ehz641
5. Van Riet EES, Hoes AW, Limburg A, Landman MAJ, Van Der Hoeven H, Rutten FH. Prevalence of unrecognized heart failure in older persons with shortness of breath on exertion. *Eur J Heart Fail.* (2014) 16:772–7. doi: 10.1002/ejhf.110
6. Ponikowski P, Voors AA, Anker SD, Bueno H, Cleland JGF, Coats AJS, et al. 2016 ESC guidelines for the diagnosis and treatment of acute and chronic heart failure. *Eur Heart J.* (2016) 37:2129–200m. doi: 10.1093/eurheartj/ehw128
7. Magnani JW, Wang N, Nelson KP, Connelly S, Deo R, Rodondi N, et al. The electrocardiographic PR interval and adverse outcomes in older adults: the health, aging and body composition study. *Circ Arrhythm Electrophysiol.* (2013) 6:84–90. doi: 10.1161/CIRCEP.112.975342
8. Kataoka H, Madias JE. Changes in the amplitude of electrocardiogram QRS complexes during follow-up of heart failure patients. *J Electrocardiol.* (2011) 44:394.e1-394.e9. doi: 10.1016/j.jelectrocard.2010.12.160
9. Dhingra R, Pencina MJ, Wang TJ, Nam BH, Benjamin EJ, Levy D, et al. Electrocardiographic QRS duration and the risk of congestive heart failure: the framingham heart study. *Hypertension.* (2006) 47:861–7. doi: 10.1161/01.HYP.0000217141.20163.23
10. Coronel R, Wilders R, Verkerk AO, Wiegerinck RF, Benoist D, Bernus O. Electrophysiological changes in heart failure and their implications for arrhythmogenesis. *Biochim Biophys Acta.* (2013) 1832:2432–41. doi: 10.1016/j.bbadis.2013.04.002
11. Houghton AR, Sparrow NJ, Toms E, Cowley AJ. Should general practitioners use the electrocardiogram to select patients with suspected heart failure for echocardiography? *Int J Cardiol.* (1997) 62:31–6. doi: 10.1016/S0167-5273(97)00181-2
12. Daamen MAMJ, Brunner-la Rocca HP, Tan FES, Hamers JPH, Schols JMGA. Clinical diagnosis of heart failure in nursing home residents based on history, physical exam, BNP and ECG: is it reliable? *Eur Geriatr Med.* (2017) 8:59–65. doi: 10.1016/j.eurger.2016.10.003
13. Nikolaidou T, Samuel NA, Marincowitz C, Fox DJ, Cleland JGF, Clark AL. Electrocardiographic characteristics in patients with heart failure and normal ejection fraction: a systematic review and meta-analysis. *Ann Noninvasive Electrocardiol.* (2020) 25:e12710. doi: 10.1111/anec.12710
14. Linde C, Bongiorni MG, Birgersdotter-Green U, Curtis AB, Deisenhofer I, Furokawa T, et al. Sex differences in cardiac arrhythmia: a consensus document of the european heart rhythm association, endorsed by the heart rhythm society and Asia pacific heart rhythm society. *Europace.* (2018) 20:1565–ao. doi: 10.1093/europace/euy067
15. Paulus WJ, Tschöpe C, Sanderson JE, Rusconi C, Flachskampf FA, Rademakers FE, et al. How to diagnose diastolic heart failure: a consensus statement on the diagnosis of heart failure with normal left ventricular ejection fraction by the Heart Failure and Echocardiography Associations of the European Society of Cardiology. *Eur Heart J.* (2007) 28:2539–50. doi: 10.1093/eurheartj/ehm037
16. Nagueh SF, Appleton CP, Gillebert TC, Marino PN, Oh JK, Smiseth OA, et al. Recommendations for the evaluation of left ventricular diastolic function by echocardiography. *J Am Soc Echocardiogr.* (2009) 22:107–33. doi: 10.1016/j.echo.2008.11.023
17. Liberati A, Altman DG, Tetzlaff J, Mulrow C, Gøtzsche PC, Ioannidis JPA, et al. The PRISMA statement for reporting systematic reviews and meta-analyses of studies that evaluate health care interventions: explanation and elaboration. *PLoS Med.* (2009) 6:e1000100. doi: 10.1371/journal.pmed.1000100
18. Whiting PF, Rutjes AW, Westwood ME, Mallett S, Deeks JJ, Reitsma JB, et al. QUADAS-2: a revised tool for the quality assessment of diagnostic accuracy studies. *Ann Intern Med.* (2011) 155:529–36. doi: 10.7326/0003-4819-155-8-201110180-00009
19. Hayiroglu MI, Çinar T, Çiçek V, Asal S, Kiliç S, Keser N, et al. A simple formula to predict echocardiographic diastolic dysfunction—electrocardiographic diastolic index. *Herz.* (2021) 46:159–65. doi: 10.1007/s00059-020-04972-6
20. Sumita Y, Nakatani S, Murakami I, Taniguchi M. Significance of left atrial overload by electrocardiogram in the assessment of left ventricular diastolic dysfunction. *J Echocardiogr.* (2019) 18:105–12. doi: 10.1007/s12574-019-00458-5
21. Yang H, Marwick TH, Wang Y, Nolan M, Negishi K, Khan F, et al. Association between electrocardiographic and echocardiographic markers of stage B heart failure and cardiovascular outcome. *ESC Hear Fail.* (2017) 4:417–31. doi: 10.1002/ehf2.12151
22. Tsai WC, Lee KT, Wu MT, Chu CS, Lin TH, Hsu PC, et al. Significant correlation of p-wave parameters with left atrial volume index and left ventricular diastolic function. *Am J Med Sci.* (2013) 346:45–51. doi: 10.1097/MAJ.0b013e318265d8f7
23. Taha T, Sayed K, Saad M, Samir M. How accurate can electrocardiogram predict left ventricular diastolic dysfunction? *Egypt Hear J.* (2016) 68:117–23. doi: 10.1016/j.ehj.2015.01.002
24. Namdar M, Biaggi P, Stähli B, Bütler B, Casado-Arroyo R, Ricciardi D, et al. A novel electrocardiographic index for the diagnosis of diastolic dysfunction. *PLoS One.* (2013) 8:e79152. doi: 10.1371/journal.pone.0079152
25. Krepp JM, Lin F, Min JK, Devereux RB, Okin PM. Relationship of electrocardiographic left ventricular hypertrophy to the presence of diastolic dysfunction. *Ann Noninvasive Electrocardiol.* (2014) 19:552–60. doi: 10.1111/anec.12166
26. Khan HS, Iftikhar I, Khan Q. Validity of electrocardiographic QT interval in predicting left ventricular diastolic dysfunction in patients with suspected heart failure. *J Coll Physicians Surg Pakistan.* (2016) 26:353–6.
27. Wilcox JE, Rosenberg J, Vallakati A, Gheorghiade M, Shah SJ. Usefulness of electrocardiographic QT interval to predict left ventricular diastolic dysfunction. *Am J Cardiol.* (2011) 108:1760–6. doi: 10.1016/j.amjcard.2011.07.050
28. Tan ESJ, Chan SP, Xu CF, Yap J, Richards AM, Ling LH, et al. Cornell product is an ECG marker of heart failure with preserved ejection fraction. *Heart Asia.* (2019) 11:1–6. doi: 10.1136/heartasia-2018-011108
29. Boles U, Almuntaser I, Brown A, Murphy RRT, Mahmud A, Feely J. Ventricular activation time as a marker for diastolic dysfunction in early hypertension. *Am J Hypertens.* (2010) 23:781–5. doi: 10.1038/ajh.2010.58
30. Dogan A, Ozaydin M, Nazli C, Altinbas A, Gedikli O, Kinay O, et al. Does impaired left ventricular relaxation affect P wave dispersion in patients with hypertension? *Ann Noninvasive Electrocardiol.* (2003) 8:189–93. doi: 10.1046/j.1542-474X.2003.08304.x
31. Eicher JC, Laurent G, Mathé A, Barthez O, Bertaux G, Philip JL, et al. Atrial dyssynchrony syndrome: an overlooked phenomenon and a potential cause of "diastolic" heart failure. *Eur J Heart Fail.* (2012) 14:248–58. doi: 10.1093/eurjhf/hfr169
32. Gunduz H, Binak E, Arinc H, Akdemir R, Ozhan H, Tamer A, et al. The relationship between P wave dispersion and diastolic dysfunction. *Texas Hear Inst J.* (2005) 32:163–7.
33. Nikolaidou T, Pellicori P, Zhang J, Kazmi S, Goode KM, Cleland JG, et al. Prevalence, predictors, and prognostic implications of PR interval prolongation in patients with heart failure. *Clin Res Cardiol.* (2018) 107:108–19. doi: 10.1007/s00392-017-1162-6
34. Hsu PC, Tsai WC, Lin TH, Su HM, Voon WC, Lai W Ter, et al. Association of arterial stiffness and electrocardiography-determined left ventricular hypertrophy with left ventricular diastolic dysfunction. *PLoS One.* (2012) 7:e49100. doi: 10.1371/journal.pone.0049100

35. Kadi H, Demir AK, Ceyhan K, Damar IH, Karaman K, Zorlu Ç. Association of fragmented QRS complexes on ECG with left ventricular diastolic function in hypertensive patients. *Turk Kardiyol Dern Ars.* (2015) 43:149–56. doi: 10.5543/tkda.2015.04495
36. Onoue Y, Izumiya Y, Hanatani S, Kimura Y, Araki S, Sakamoto K, et al. Fragmented QRS complex is a diagnostic tool in patients with left ventricular diastolic dysfunction. *Heart Vessels.* (2016) 31:563–7. doi: 10.1007/s00380-015-0651-7
37. Ofman P, Cook JR, Navaravong L, Levine RA, Peralta A, Gaziano JM, et al. T-wave inversion and diastolic dysfunction in patients with electrocardiographic left ventricular hypertrophy. *J Electrocardiol [Internet].* (2012) 45:764–9. doi: 10.1016/j.jelectrocard.2012.06.001
38. Palmieri V, Okin PM, Bella JN, Wachtell K, Oikarinen L, Gerdts E, et al. Electrocardiographic strain pattern and left ventricular diastolic function in hypertensive patients with left ventricular hypertrophy: the LIFE study. *J Hypertens.* (2006) 24:2079–84. doi: 10.1097/01.hjh.0000244958.85232.06
39. Sauer A, Wilcox JE, Andrei AC, Passman R, Goldberger JJ, Shah SJ. Diastolic electromechanical coupling: association of the ecg t-peak to t-end interval with echocardiographic markers of diastolic dysfunction. *Circ Arrhythmia Electrophysiol.* (2012) 5:537–43. doi: 10.1161/CIRCEP.111.969717
40. Miwa K. Appearance of electrocardiographic initial U-wave inversion dependent on pressure-induced early diastolic impairment in patients with hypertension. *Clin Cardiol.* (2009) 32:593–6. doi: 10.1002/clc.20487
41. Kwok CS, Rashid M, Beynon R, Barker D, Patwala A, Morley-Davies A, et al. Prolonged PR interval, first-degree heart block and adverse cardiovascular outcomes: a systematic review and meta-analysis. *Heart.* (2016) 102:672–80. doi: 10.1136/heartjnl-2015-308956
42. Borlaug BA. The pathophysiology of heart failure with preserved ejection fraction. *Nat Rev Cardiol.* (2014) 11:507–15. doi: 10.1038/nrcardio.2014.83
43. Burke JH, Ehlert FA, Kruse JT, Parker MA, Goldberger JJ, Kadish AH. Gender-specific differences in the QT interval and the effect of autonomic tone and menstrual cycle in healthy adults. *Am J Cardiol.* (1997) 79:178–81. doi: 10.1016/S0002-9149(96)00707-2
44. Rautaharju PM, Surawicz B, Gettes LS. AHA/ACCF/HRS recommendations for the standardization and interpretation of the electrocardiogram: Part IV: the ST segment, t and u waves, and the QT interval: aa scientific statement from the American Heart Association Electrocardiography and Arrhythmias C. *Circulation.* (2009) 119:241–50. doi: 10.1161/CIRCULATIONAHA.108.191096
45. Phan TT, Abozguia K, Shivu GN, Ahmed I, Patel K, Leyva F, et al. Myocardial contractile inefficiency and dyssynchrony in heart failure with preserved ejection fraction and narrow QRS complex. *J Am Soc Echocardiogr.* (2010) 23:201–6. doi: 10.1016/j.echo.2009.11.004
46. Vyas H, O'Leary PW, Earing MG, Cetta F, Ackerman MJ. Mechanical dysfunction in extreme QT prolongation. *J Am Soc Echocardiogr.* (2008) 21:511.e15–511.e17. doi: 10.1016/j.echo.2007.08.001
47. Phan TT, Shivu GN, Abozguia K, Davies C, Nassimizadeh M, Jimenez D, et al. Impaired heart rate recovery and chronotropic incompetence in patients with heart failure with preserved ejection fraction. *Circ Hear Fail.* (2010) 3:29–34. doi: 10.1161/CIRCHEARTFAILURE.109.877720
48. Davey PP, Barlow C, Hart G. Prolongation of the QT interval in heart failure occurs at low but not at high heart rates. *Clin Sci.* (2000) 98:603–10. doi: 10.1042/cs0980603
49. Michaelides AP, Raftopoulos LG, Aggeli C, Liakos C, Antoniades C, Fourlas C, et al. Correlation of ST-segment "hump sign" during exercise testing with impaired diastolic function of the left ventricle. *J Electrocardiol.* (2010) 43:167–72. doi: 10.1016/j.jelectrocard.2009.09.001
50. Blackman AO, Neto JS, Lima ML, Rodrigues TMA, Gomes OM. Assessment and clinical relevance of the dynamic parameters of ventricular repolarization in patients with grade i left ventricular diastolic dysfunction. *Can J Physiol Pharmacol.* (2019) 97:577–80. doi: 10.1139/cjpp-2018-0507
51. Kagiyama N, Piccirilli M, Yanamala N, Shrestha S, Farjo PD, Casaclang-Verzosa G, et al. Machine learning assessment of left ventricular diastolic function based on electrocardiographic features. *J Am Coll Cardiol.* (2020) 76:930–41. doi: 10.1016/j.jacc.2020.06.061
52. Kwon JM, Kim KH, Jeon KH, Kim HM, Kim MJ, Lim SM, et al. Development and validation of deep-learning algorithm for electrocardiography-based heart failure identification. *Korean Circ J.* (2019) 49:629–39. doi: 10.4070/kcj.2018.0446
53. Potter EL, Rodrigues CHM, Ascher DB, Abhayaratna WP, Sengupta PP, Marwick TH. Machine learning of ECG waveforms to improve selection for testing for asymptomatic left ventricular dysfunction. *JACC Cardiovasc Imaging.* (2021) 14:1904–15. doi: 10.1016/j.jcmg.2021.04.020
54. Unterhuber M, Rommel K-P, Kresoja K-P, Lurz J, Kornej J, Hindricks G, et al. Deep learning detects heart failure with preserved ejection fraction using a baseline electrocardiogram. *Eur Hear J Digit Heal.* (2021). doi: 10.1093/ehjdh/ztab081. [Epub ahead of print].

Conflict of Interest: The authors declare that the research was conducted in the absence of any commercial or financial relationships that could be construed as a potential conflict of interest.

Publisher's Note: All claims expressed in this article are solely those of the authors and do not necessarily represent those of their affiliated organizations, or those of the publisher, the editors and the reviewers. Any product that may be evaluated in this article, or claim that may be made by its manufacturer, is not guaranteed or endorsed by the publisher.

frontiers in Cardiovascular Medicine

ORIGINAL RESEARCH
published: 24 December 2021
doi: 10.3389/fcvm.2021.803567

Relationship Between Left Ventricular Ejection Fraction Variation and Systemic Vascular Resistance: A Prospective Cardiovascular Magnetic Resonance Study

Damien Mandry[1,2], *Nicolas Girerd*[3,4,5], *Zohra Lamiral*[5], *Olivier Huttin*[3,4], *Laura Filippetti*[4], *Emilien Micard*[5], *Marine Beaumont*[2,5], *Marie-Paule Bernadette Ncho Mottoh*[4], *Nathalie Pace*[4], *Faïez Zannad*[3,4,5], *Patrick Rossignol*[3,5,6] *and Pierre-Yves Marie*[3,7]*

[1] CHRU-Nancy, Université de Lorraine, Department of Radiology, Nancy, France, [2] Université de Lorraine, INSERM, UMR-1254, Nancy, France, [3] Université de Lorraine, INSERM, UMR-1116, Nancy, France, [4] CHRU-Nancy, Université de Lorraine, Department of Cardiology, Nancy, France, [5] Université de Lorraine, CHRU-Nancy, INSERM, CIC 1433, Nancy, France, [6] FCRIN INI-CRCT, Nancy, France, [7] CHRU-Nancy, Université de Lorraine, Department of Nuclear Medicine and Nancyclotep, Nancy, France

OPEN ACCESS

Edited by:
Fabrizio Ricci,
University of Studies G. d'Annunzio Chieti and Pescara, Italy

Reviewed by:
Vincenzo Cicchitti,
Asl Lanciano Vasto Chieti, Italy
Federico Archilletti,
University of Studies G. d'Annunzio Chieti and Pescara, Italy
Antonio Procopio,
SS. Annunziata University Hospital, Italy

***Correspondence:**
Pierre-Yves Marie
py.marie@chru-nancy.fr

Specialty section:
This article was submitted to Cardiovascular Imaging, a section of the journal Frontiers in Cardiovascular Medicine

Received: 28 October 2021
Accepted: 07 December 2021
Published: 24 December 2021

Citation:
Mandry D, Girerd N, Lamiral Z, Huttin O, Filippetti L, Micard E, Beaumont M, Ncho Mottoh M-PB, Pace N, Zannad F, Rossignol P and Marie P-Y (2021) Relationship Between Left Ventricular Ejection Fraction Variation and Systemic Vascular Resistance: A Prospective Cardiovascular Magnetic Resonance Study. Front. Cardiovasc. Med. 8:803567. doi: 10.3389/fcvm.2021.803567

Introduction: This cardiovascular magnetic resonance (CMR) study aims to determine whether changes in systemic vascular resistance (SVR), obtained from CMR flow sequences, might explain the significant long-term changes in left ventricular (LV) ejection fraction (EF) observed in subjects with no cardiac disease history.

Methods: Cohort subjects without any known cardiac disease but with high rates of hypertension and obesity, underwent CMR with phase-contrast sequences both at baseline and at a median follow-up of 5.2 years. Longitudinal changes in EF were analyzed for any concomitant changes in blood pressure and vascular function, notably the indexed SVR given by the formula: mean brachial blood pressure / cardiac output x body surface area.

Results: A total of 118 subjects (53 ± 12 years, 52% women) were included, 26% had hypertension, and 52% were obese. Eighteen (15%) had significant EF variations between baseline and follow-up (7 increased EF and 11 decreased EF). Longitudinal changes in EF were inversely related to concomitant changes in mean and diastolic blood pressures ($p = 0.030$ and $p = 0.027$, respectively) and much more significantly to SVR ($p < 0.001$). On average, these SVR changes were -8.08 ± 9.21 and $+8.14 \pm 8.28$ mmHg.min.m^2.L^{-1}, respectively, in subjects with significant increases and decreases in EF, and 3.32 ± 7.53 mmHg.min.m^2.L^{-1} in subjects with a stable EF (overall $p < 0.001$).

Conclusions: Significant EF variations are not uncommon during the long-term CMR follow-up of populations with no evident health issues except for uncomplicated hypertension and obesity. However, most of these variations are linked to SVR changes and may therefore be unrelated to any intrinsic change in LV contractility.

This underscores the benefits of specifically assessing LV afterload when EF is monitored in populations at risk of vascular dysfunction.

Clinical Trial Registration: ClinicalTrials.gov, identifier: NCT01716819 and NCT02430805.

Keywords: flow-encoding sequence, ejection fraction, systemic vascular resistance, hypertension, obesity, cardiovascular magnetic resonance

INTRODUCTION

The left ventricular (LV) ejection fraction (EF) remains extensively used to quantify LV systolic performance (1), with cardiovascular magnetic resonance (CMR) imaging being the reference technique for measuring EF and monitoring EF changes (1–4). The major limitation of this type of approach is the EF dependence on loading conditions which is also an issue for most other parameters used to assess LV systolic function (5). An individual's EF measurement is not constant but varies, particularly as a function of the afterload and blood pressure (BP) (6–8). It is therefore generally recommended to record the bracial BP observed during individual EF measurements (9–11).

Nowadays LV afterload is assessed more specifically and non-invasively by combining the information from brachial BP to the stroke volume values provided by CMR flow-velocity sequences (12–14). This approach allows to measure several parameters known to reflect or to greatly impact LV afterload, notably systemic vascular resistance (SVR), effective arterial elastance (Ea), and total arterial compliance (TAC) (12–14).

A previously published CMR study showed that EF and SVR measurements were interdependent in the months following an acute myocardial infarction (MI), with the increase in EF associated with a concomitant decrease in SVR under a post-MI vasodilating medical regimen (13). It is however unclear whether such SVR changes might also explain the significant EF variations observed in subjects with no evident cardiac disease but at increased risk of developing cardiovascular disease, such as hypertensive and/or obese subjects.

The current CMR-based study aims to determine whether longitudinal changes in LV afterload and particularly in SVR, might explain the significant EF changes observed over time in subjects with no evident health issues except for uncomplicated hypertension and obesity.

MATERIALS AND METHODS

Study Populations

Subjects evaluated in the current study did not have any medical history of cardiac disease. Cardiovascular monitoring was performed using the same CMR protocol with subjects pooled from two different cohorts:

(1) The "Role of the Renin-Angiotensin Aldosterone System in the Mechanisms of Transition to Heart Failure in Abdominal Obesity (R2C2-II)" cohort has already been described elsewhere (12, 14, 15). The cohort included middle-aged subjects (40–65 years) with abdominal obesity, no cardiovascular medication and no cardiovascular disease except for stage 1 hypertension. Subjects were invited to participate in a >4-year longitudinal study, which included CMR at baseline and at follow-up (ClinicalTrials.gov NCT01716819).

(2) The "Predisposition and Transition Mechanisms from Arterial Hypertension to Heart Failure (Hypercare)" family-based study included 58 subjects younger than 60 years of age, with uncomplicated hypertension or a history of familial hypertension. This longitudinal study, which included CMR investigations at baseline and at 4 years, has already been described elsewhere (12) (ClinicalTrials.gov NCT02430805).

The main exclusion criteria for both cohorts were: diabetes; inflammatory or infectious disease; renal, hepatic or pulmonary insufficiency; and a history of malignant disease. The local Ethics Committee approved both cohort studies, with all study participants providing their signed informed consent to participate.

CMR Recording and Analysis

CMRs were performed on a 3-T or 1.5-T magnet (GE Medical Systems, Milwaukee, WI, USA) (12–15). An automated sphygmomanometer (Maglife C, Schiller Medical, Wissembourg, France) was used to measure brachial blood pressure (BP) during the CMR examinations. Averaged values were used for the analyses presented below.

A steady-state free precession pulse sequence and dedicated software (MASS^{TM}, Medis, The Netherlands) were used to measure LV end-diastolic volume, end-diastolic mass, and EF in contiguous short-axis. The concentric remodeling (CR) index was defined as LV mass/end-diastolic volume ratio (12–15).

Cardiac output was determined using a velocity-encoded phase-contrast gradient-echo sequence on a slice positioned perpendicularly to the ascending aorta (12–15). Stroke volume (SV) was determined with the "CV flow" software (Medis, The Netherlands), with velocities corrected using an ROI-based method in instances of obvious offset errors.

Values of cardiac output and stroke volume were used to estimate systemic vascular resistance (SVR: mean pressure/cardiac output) (12–19), effective arterial elastance [Ea = 0.9 × systolic BP (mmHg)/stroke volume (mL)] (12, 15–19), and total arterial compliance index [TAC = stroke volume (mmHg)/pulse pressure (mmHg)] (12, 14–17). All these CMR-derived parameters were indexed to body surface area, except for EF and CR. Since none of the study subjects had any medical history of cardiac disease, the central venous pressure was considered normal and thus negligible for the determination of SVR.

As already detailed elsewhere, abnormally high values of SVR, LV mass and concentric remodeling index were defined as the upper limits of the 95% confidence intervals observed in

TABLE 1 | Comparison of the main recorded data between baseline and follow-up.

	Baseline	Follow-up	*P*-value
Age (years)	52.5 ± 12.5	58.5 ± 12.3	____
Female gender	61 (51.7%)	61 (51.7%)	____
Body weight (kg)	83.8 ± 14.7	86.5 ± 15.0	0.0004
Body mass index (kg.m^{-2})	29.6 ± 4.8	30.7 ± 4.9	<0.0001
Obesity	61 (51.7%)	65 (55.1%)	0.80
Heart rate (bpm)	70.3 ± 11.5	65.9 ± 10.7	0.002
Systolic BP (mmHg)	128.7 ± 18.1	128.7 ± 16.3	0.60
Diastolic BP (mmHg)	74.7 ± 12.3	76.3 ± 10.4	0.045
Mean BP (mmHg)	92.4 ± 13.2	93.4 ± 10.8	0.15
Pulse BP (mmHg)	54.0 ± 12.9	52.4 ± 13.4	0.13
Indexed stroke volume (mL.m^{-2})	43.1 ± 8.9	41.9 ± 8.8	0.44
Cardiac index (L.min^{-1}.m^{-2})	3.00 ± 0.66	2.72 ± 0.53	<0.0001
Indexed SVR (mmHg.min.m^2.L^{-1})	32.1 ± 7.9	35.6 ± 7.6	<0.0001
Abnormal (>40 mmHg.min.m^2.L^{-1})	17 (14.4 %)	29 (24.6 %)	0.45
Indexed TAC (mL.mmHg^{-1}.m^{-2})	0.84 ± 0.23	0.85 ± 0.27	0.65
Indexed Ea (mmHg.mL^{-1}.m^2)	2.79 ± 0.67	2.89 ± 0.76	0.40
Indexed ESV (mL.m^{-2})	28.9 ± 7.5	28.3 ± 7.6	0.15
Indexed EDV (mL.m^{-2})	71.8 ± 12.2	69.3 ± 13.0	0.006
EF (%)	60.0 ± 6.3	59.6 ± 5.3	0.46
Abnormal (<50%)	5 (4.2%)	4 (3.4%)	0.56
Indexed LV mass (g.m^{-2})	50.5 ± 10.5	48.2 ± 9.6	<0.0001
CR index (g.mL^{-1})	0.71 ± 0.15	0.71 ± 0.14	0.19

BP, blood pressure; CR, concentric remodeling; Ea, effective arterial elastance; EDV, end-diastolic volume; EF, ejection fraction; LV, left ventricle; TAC, total arterial compliance; SVR, systemic vascular resistance.

TABLE 2 | Association between longitudinal changes in LVEF and baseline and concomitant changes in clinical and hemodynamic variables.

Parameter	r_s (95% CI)	*P*-value
Female gender	−0.60 (−2.05, 0.84)	0.72
Body mass index (kg.m^{-2})	−0.01 (−0.19, 0.17)	0.91
Δ from baseline	−0.09 (−0.27, 0.09)	0.31
Age (years)	−0.13 (−0.30, 0.05)	0.16
Δ from baseline	0.02 (−0.16, 0.20)	0.84
Heart rate (bpm)	0.02 (−0.16, 0.20)	0.84
Δ from baseline	−0.10 (−0.28, 0.08)	0.27
Systolic BP (mmHg)	−0.03 (−0.21, 0.16)	0.78
Δ from baseline	−0.08 (−0.26, 0.10)	0.38
Diastolic BP (mmHg)	0.06 (−0.12, 0.24)	0.52
Δ from baseline	−0.20 (−0.37, −0.02)	0.027
Mean BP (mmHg)	0.06 (−0.12, 0.24)	0.50
Δ from baseline	−0.20 (−0.36, −0.02)	0.031
Pulse BP (mmHg)	−0.10 (−0.27, 0.09)	0.30
Δ from baseline	0.10 (−0.08, 0.27)	0.29
Indexed EDV (mL.m^{-2})	0.07 (−0.06, 0.12)	0.484
Δ from baseline	0.05 (−0.16, 0.05)	0.330
Baseline EF	−0.63 (−0.73, −0.50)	<0.0001
Indexed SVR (mmHg.min.m^2.L^{-1})	0.32 (0.14, 0.47)	0.0005
Δ from baseline	−0.44 (−0.57, −0.28)	<.0001
Indexed TAC (mL.mmHg^{-1}.m^{-2})	−0.13 (−0.30, 0.06)	0.18
Δ from baseline	0.19 (0.01, 0.36)	0.038
Indexed Ea (mmHg.mL^{-1}.m^2)	−0.17 (−0.34, 0.01)	0.059
Δ from baseline	−0.42 (−0.56, −0.26)	<0.0001

a healthy non-obese middle-aged population investigated using the same CMR methodology (12). A significant EF change was additionally defined as an absolute difference > 8% according to a reproducibility study also performed with the same MRI methodology in our center (13).

Statistical Analyses

Analyses were performed using the commercially available SAS software version 9.4 (SAS Institute Inc. Cary, NC, USA). Continuous variables are expressed as mean and standard deviations (SD) and categorical variables as numbers and percentages (**Table 1**). Paired comparisons between baseline and follow-up were evaluated using the Wilcoxon sum rank test for continuous variables and the Mc Nemar test for categorical variables. Spearman correlation coefficients and their 95% CI intervals were computed for the baseline-to-follow-up changes in EF and the selected variables listed in **Table 2**. Univariate and multivariate ascending regression analyses were performed to check Linear model assumptions with p-values < 0.05 to enter variables and >0.10 to remove variables (**Table 3**).

TABLE 3 | Linear regression models obtained through forward selections, with Beta coefficients [standard error (SE)], P and R^2 values, for predicting the follow-up to baseline differences in EF (A). The model was additionally built after excluding the baseline EF value (B).

		Beta (SE)	*P*-value	Global R^2
A	Intercept	30.83 ± 3.66	<0.0001	
	Change in SVR	−0.22 ± 0.05	<0.0001	
	Baseline EF	−0.51 ± 0.06	<0.0001	0.50
B	Intercept	0.51 ± 0.50	0.31	
	Change in SVR	−0.30 ± 0.06	<0.0001	0.19

RESULTS

Baseline Characteristics of the Study Population

The study population consisted of a total of 118 subjects. As detailed in **Table 1**, the mean age was 53 ± 12 years, 62 (52%) were women, and 61 (52%) were mild to moderately obese with body mass indexes ranging from 30 to 40 kg.m^{-2}.

Based on the inclusion criteria, none of these 118 subjects had any history of cardiovascular disease except for uncomplicated hypertension (n = 31, 26%). CMR did not detect any significant cardiac abnormalities, except that 5 subjects had an EF below the 50% level (EF ranging from 43 to 47%), 3 and 17 subjects, respectively, had a higher-than-normal LV mass and CR index.

Evolution at Follow-Up

Follow-up investigations, performed at a median of 5.2 years from baseline (range 3.7–8.4 years), provided evidence of

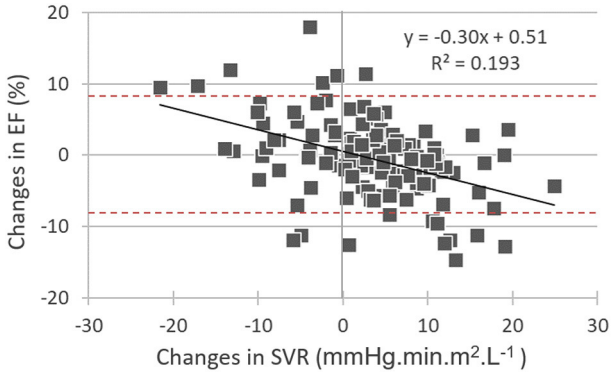

FIGURE 1 | Correlations between baseline-to-follow-up differences in: (i) left ventricular ejection fraction (EF changes) and (ii) systemic vascular resistance (SVR changes). It may additionally be observed that many EF changes are outside of the −8% to +8% interval (red dashed lines) and may thus be considered significant.

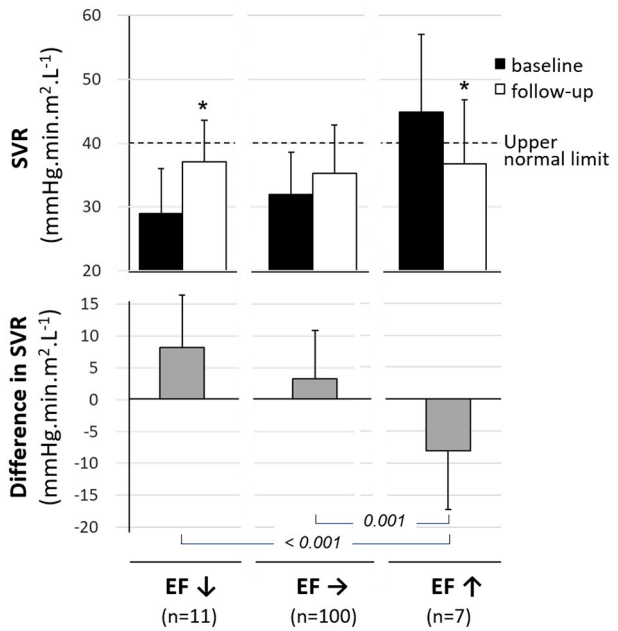

FIGURE 2 | Mean values (±SD) for baseline (black columns) and follow-up (white columns) levels of systemic vascular resistance (SVR, upper panel) and for the mean difference in SVR between baseline and follow-up (gray columns, median panel) in subjects categorized in 3 groups based on baseline-to-follow-up variations in LV ejection fraction -i.e., significant decrease (EF↓), significant increase (EF↑) and stable EF (EF→). *$p < 0.05$ for paired comparisons between baseline and 6 months.

significant increases in body weight, body mass index, diastolic BP and SVR, compared to baseline (**Table 1**).

Only 4 subjects (3%) had <50% EF at follow-up, but 18 (15%) had significant EF variations between baseline and follow-up (7 increased EF and 11 decreased EF). The 4 patients with <50% EF at follow-up exhibited a significant EF deterioration during follow-up (−7.8 ± 6.0%), compared to the other patients (0.35 ± 6.0%, $p = 0.01$). All were male with no specific differences in baseline characteristics compared to other male study subjects.

Among the 5 subjects with <50% EF at baseline, only one still had <50% EF at follow-up, whereas the 4 others had EF increases that exceeded the 50% level at follow-up.

Correlates of Baseline-to-Follow-Up Changes in EF

As detailed in **Table 2**, EF differences between baseline and follow-up were inversely correlated to the corresponding differences in mean BP ($p = 0.03$) and diastolic BP ($p = 0.027$).

This predictive value of BP-changes was however much lower than that provided by the baseline-to-follow-up changes in effective arterial elastance (Ea) and in SVR (both $p < 0.001$; **Table 2**). The baseline levels of EF, Ea and SVR were additional univariate predictors, whereas all other analyzed parameters were not (**Table 2**).

On the multivariate regression analysis, which considered all the significant univariate predictors from **Table 2**, EF changes were significantly and independently related to the baseline-to-follow-up change in SVR together with the baseline EF value (see **Table 3**). Only the follow-up change in SVR was kept in the model after baseline EF had been excluded (**Table 3**). **Figure 1** displays the inverse association between the follow-up changes in EF and SVR.

As illustrated in **Figure 2**, baseline-to-follow-up changes in SVR were markedly different between subjects with a significant increase in EF at follow-up and those with a significant decrease in EF (−8.08 ± 9.21 mmHg.min.m^2.L^{-1} vs. 8.14 ± 8.28 mmHg.min.m^2.L^{-1}, $p < 0.001$). The remaining subjects with stable EFs had no significant baseline-to-follow-up changes in SVR (SVR difference in this group: 3.32 ± 7.53 mmHg.min.m^2.L^{-1}) (**Figure 2**).

Finally, the percentage value of significant EF variations over time (>8%), initially observed in the overall study population (15.3%), was significantly lower after EF-changes had been adjusted for SVR-changes and baseline EF using equations shown in **Table 3** (5.9%, $p = 0.013$).

DISCUSSION

In a population with no history of cardiac disease but including hypertensive and obese subjects, the present CMR study shows that significant long-term EF variations are not uncommon, affecting some 15% of the study population. These variations correlate to SVR changes and may thus be unrelated to any intrinsic changes in LV contractility.

SVR is the main component of the LV afterload and reflects the opposing resistance of the microcirculation that must be overcome by the LV to eject blood. In the current study population, mean SVR increased over time (**Table 1**), consistent with a functional deterioration of the microcirculation. Such a deterioration is often associated with the aging process, together with an increase in the stiffness of large arteries and may be further promoted by hypertension and obesity (20, 21). Our

study population's high rate of hypertension (26%) and obesity (52%) may potentially accelerate the rate of SVR deterioration, consequently impacting the EF. Subjects with isolated obesity have already been shown to exhibit a significant deterioration in large-vessel compliance as well as an increase in the vascular resistance of small resistive vessels, compared to non-obese subjects, using the same CMR protocol (14, 15).

The interdependence of the EF on cardiac loading conditions is well-established. Despite this limitation, EF remains extensively used to quantify LV systolic performance (1). The current recommendation therefore requires brachial BP to be reported for each EF measurement (9–11). The change in BP was a significant predictor of EF change but only for diastolic and mean BP levels. Diastolic BP has already been shown to have a greater impact on EF than systolic BP, particularly in heart failure with preserved EF (6).

We also measured more specific functional arterial parameters from conventional CMR flow sequences. These allowed to determine aortic stroke volume, independently of other CMR sequences used to assess LV function, and more accurately than Doppler-based techniques (22). Combining these stroke volume values with brachial BP measurements allowed to evaluate three functional vascular parameters: (i) total arterial compliance (TAC) index, which is predominantly determined by the great elastic arteries (12, 14–17) (ii) systemic vascular resistance (SVR), which is mainly attributed to the resistive microvessels (12–19), and (iii) global arterial load (Ea), a comprehensive measure of the arterial load that depends on both arterial compliance and arterial resistance (12, 15–19) and is strongly linked to LV remodeling (12, 15). However, Ea-changes were not found to be better predictors of EF variations than SVR-changes in the current study. This is consistent with what was

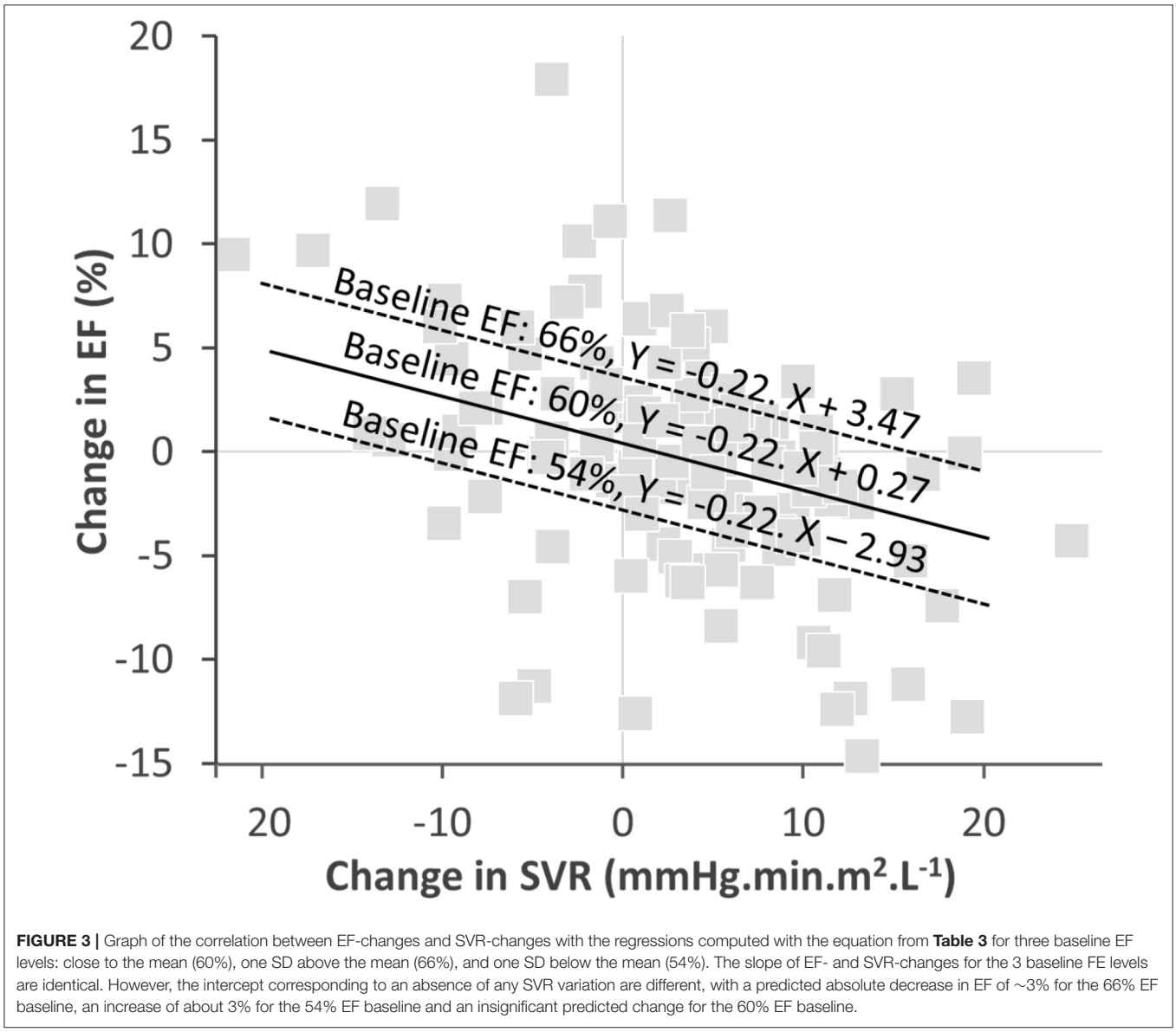

FIGURE 3 | Graph of the correlation between EF-changes and SVR-changes with the regressions computed with the equation from **Table 3** for three baseline EF levels: close to the mean (60%), one SD above the mean (66%), and one SD below the mean (54%). The slope of EF- and SVR-changes for the 3 baseline FE levels are identical. However, the intercept corresponding to an absence of any SVR variation are different, with a predicted absolute decrease in EF of ∼3% for the 66% EF baseline, an increase of about 3% for the 54% EF baseline and an insignificant predicted change for the 60% EF baseline.

previously reported in post-myocardial infarction patients (13). SVR changes presumably impact stroke volume and EF more directly, than Ea changes -i.e., small arteries which contribute to SVR not only constitute a main component of the LV afterload but also the exit door through which the stroke volume needs to pass before leaving the arterial tree.

A significant decrease in SVR has already been shown to be the predominant mechanism by which the EF increases during exercise in heart disease patients (23), and during the months following a myocardial infarction (13). A vasodilator-related decrease in SVR was additionally shown to be associated with proportional increases in stroke volume and cardiac output of heart failure patients (24). Additional data from several individual cases included in our cohort also confirm significant variations in cardiovascular function and remodeling after changes in antihypertensive treatment (results not shown). These changes were unfortunately not systematically recorded during the long-term follow-up of this cohort and therefore constitute one of the limitations of the current study. Another limitation is that intrinsic contractility was not directly assessed in this cohort.

It may additionally be pointed out that the EF variations were unrelated to the concomitant changes in LV end-diastolic volume (**Table 2**), an indicator of the LV preload, contrary to what was documented for SVR, an indicator of LV afterload.

It is also worth mentioning that in addition to the SVR changes, the baseline EF level was an independent predictor of EF variations over time. The impact of baseline EF could at least partly be attributed to a regression to the mean - i.e., a statistic phenomenon that implies that a sample point of a random variable, which is distant from the mean value on a first measurement, has a high probability of being closer to the mean value on a second measurement. This point is further detailed and illustrated in **Figure 3**.

The current study defined a significant EF variation using an absolute threshold of 8% which corresponds to the results of a reproducibility analysis previously reported by our team using the same CMR methodology (13). The threshold may vary depending on the different conditions tested in the reproducibility analysis (25). This does however not modify the consideration that the rate of EF changes over time may be significantly lowered after adjusting for concomitant SVR changes observed with CMR. Such an adjustment would help identify cases where a decrease in EF relates to vascular rather than myocardial deterioration and ultimately identify different therapeutic targets.

CONCLUSION

The current longitudinal CMR study of a cohort including hypertensive and obese subjects shows that significant long-term variations in EF are not uncommon, but that most of these variations are potentially driven by changes in SVR rather than changes in LV contractility. Although a causative relationship is only suggested and remains to be proven, this observation underscores the benefits of specifically assessing LV afterload when EF is monitored in populations at risk of vascular dysfunction.

DATA AVAILABILITY STATEMENT

The raw data supporting the conclusions of this article will be made available by the authors, without undue reservation.

ETHICS STATEMENT

The studies involving human participants were reviewed and approved by Comité de Protection des Personnes se prêtant à la recherche biomédicale (CPP) - Est. The patients/participants provided their written informed consent to participate in this study.

AUTHOR CONTRIBUTIONS

DM, NG, ZL, and P-YM: analysis and interpretation of the data. DM, NG, MB, FZ, PR, and P-YM: writing or revision of the manuscript. OH, LF, EM, M-PN, and NP: study implementation and management of the included subjects. All authors contributed to the article and approved the submitted version.

FUNDING

This study was funded by a National Health Ministry (Programme Hospitalier de Recherche Clinique) and the 6th framework program of the European Commission (Ingenious HyperCare Network of Excellence; contract number LSHM-CT-2006-037093).

ACKNOWLEDGMENTS

The authors wish to thank Dr. Petra Neufing for critical review of the manuscript.

REFERENCES

1. Harbo MB, Nordén ES, Narula J, Sjaastad I, Espe EKS. Quantifying left ventricular function in heart failure: what makes a clinically valuable parameter? *Prog Cardiovasc Dis.* (2020) 63:552–60. doi: 10.1016/j.pcad.2020.05.007
2. Mavrogeni S, Katsi V, Vartela V, Noutsias M, Markousis-Mavrogenis G, Kolovou G, et al. The emerging role of cardiovascular magnetic resonance in the evaluation of hypertensive heart disease. *BMC Cardiovasc Disord.* (2017) 17:132. doi: 10.1186/s12872-017-0556-8
3. Moody WE, Edwards NC, Chue CD, Taylor RJ, Ferro CJ, Townend JN, et al. Variability in cardiac MR measurement of left ventricular ejection fraction, volumes and mass in healthy adults: defining a significant change at 1 year. *Br J Radiol.* (2015) 88:20140831. doi: 10.1259/bjr.20140831
4. Fratz S, Chung T, Greil GF, Samyn MM, Taylor AM, Valsangiacomo Buechel ER, et al. Guidelines and protocols for cardiovascular magnetic resonance in children and adults with congenital heart disease: SCMR expert consensus group on congenital heart disease. *J Cardiovasc Magn Reson.* (2013) 15:51. doi: 10.1186/1532-429X-15-51

5. Dahl JS, Carter-Storch R. First-phase ejection fraction: the FEV1 of the heart? *JACC Cardiovasc Imaging.* (2019) 12:64–6. doi: 10.1016/j.jcmg.2018.10.007
6. Wei FF, Xue R, Thijs L, Liang W, Owusu-Agyeman M, He X, et al. Associations of left ventricular structure and function with blood pressure in heart failure with preserved ejection fraction: analysis of the TOPCAT trial. *J Am Heart Assoc.* (2020) 9:e016009. doi: 10.1161/JAHA.119.016009
7. Wolz DE, Flores AR, Grandis DJ, Orie JE, Schulman DS. Abnormal left ventricular ejection fraction response to mental stress and exercise in cardiomyopathy. *J Nucl Cardiol.* (1995) 2:144–50. doi: 10.1016/S1071-3581(95)80025-5
8. Bairey CN, de Yang L, Berman DS, Rozanski A. Comparison of physiologic ejection fraction responses to activities of daily living: implications for clinical testing. *J Am Coll Cardiol.* (1990) 16:847–54. doi: 10.1016/S0735-1097(10)80332-8
9. Galderisi M, Cosyns B, Edvardsen T, Cardim N, Delgado V, Di Salvo G, et al. Standardization of adult transthoracic echocardiography reporting in agreement with recent chamber quantification, diastolic function, and heart valve disease recommendations: an expert consensus document of the European Association of Cardiovascular Imaging. *Eur Heart J Cardiovasc Imaging.* (2017) 18:1301–10. doi: 10.1093/ehjci/jex244
10. Hesse B, Lindhardt TB, Acampa W, Anagnostopoulos C, Ballinger J, Bax JJ, et al. EANM/ESC guidelines for radionuclide imaging of cardiac function. *Eur J Nucl Med Mol Imaging.* (2008) 35:851–85. doi: 10.1007/s00259-007-0694-9
11. Galderisi M, Henein MY, D'hooge J, Sicari R, Badano LP, Zamorano JL, et al. Recommendations of the European Association of Echocardiography: how to use echo-Doppler in clinical trials: different modalities for different purposes. *Eur J Echocardiogr.* (2011) 12:339–53. doi: 10.1093/ejechocard/jer051
12. Marie PY, Mandry D, Huttin O, Micard E, Bonnemains L, Girerd N, et al. Comprehensive monitoring of cardiac remodeling with aortic stroke volume values provided by a phase-contrast MRI sequence. *J Hypertens.* (2016) 34:967–73. doi: 10.1097/HJH.0000000000000889
13. Huttin O, Mandry D, Eschalier R, Zhang L, Micard E, Odille F, et al. Cardiac remodeling following reperfused acute myocardial infarction is linked to the concomitant evolution of vascular function as assessed by cardiovascular magnetic resonance. *J Cardiovasc Magn Reson.* (2017) 19:2. doi: 10.1186/s12968-016-0314-6
14. Mandry D, Eschalier R, Kearney-Schwartz A, Rossignol P, Joly L, Djaballah W, et al. Comprehensive MRI analysis of early cardiac and vascular remodeling in middle-aged patients with abdominal obesity. *J Hypertens.* (2012) 30:567–73. doi: 10.1097/HJH.0b013e32834f6f3f
15. Mandry D, Girerd N, Lamiral Z, Huttin O, Filippetti L, Micard E, et al. Arterial and cardiac remodeling associated with extra weight gain in an isolated abdominal obesity cohort. *Front Cardiovasc Med.* (2021) 8:771022. doi: 10.3389/fcvm.2021.771022
16. Otsuki T, Maeda S, Iemitsu M, Saito Y, Tanimura Y, Ajisaka R, et al. Contribution of systemic arterial compliance and systemic vascular resistance to effective arterial elastance changes during exercise in humans. *Acta Physiol.* (2006) 188:15–20. doi: 10.1111/j.1748-1716.2006.01596.x
17. Otsuki T, Maeda S, Iemitsu M, Saito Y, Tanimura Y, Ajisaka R, et al. Systemic arterial compliance, systemic vascular resistance, and effective arterial elastance during exercise in endurance-trained men. *Am J Physiol Regul Integr Comp Physiol.* (2008) 295:R228–35. doi: 10.1152/ajpregu.00009.2008
18. Monge García MI, Saludes Orduña P, Cecconi M. Understanding arterial load. *Intensive Care Med.* (2016) 42:1625–7. doi: 10.1007/s00134-016-4212-z
19. Chemla D, Antony I, Lecarpentier Y, Nitenberg A. Contribution of systemic vascular resistance and total arterial compliance to effective arterial elastance in humans. *Am J Physiol Heart Circ Physiol.* (2003) 285:H614–20. doi: 10.1152/ajpheart.00823.2002
20. Savoia C, Battistoni A, Calvez V, Cesario V, Montefusco G, Filippini A. Microvascular alterations in hypertension and vascular aging. *Curr Hypertens Rev.* (2017) 13:16–23. doi: 10.2174/1573402113666170505115010
21. Sorop O, Olver TD, van de Wouw J, Heinonen I, van Duin RW, Duncker DJ, et al. The microcirculation: a key player in obesity-associated cardiovascular disease. *Cardiovasc Res.* (2017) 113:1035–45. doi: 10.1093/cvr/cvx093
22. Srichai MB, Lim RP, Wong S, Lee VS. Cardiovascular applications of phase-contrast MRI. *AJR Am J Roentgenol.* (2009) 192:662–75. doi: 10.2214/AJR.07.3744
23. Akima T, Takase B, Kosuda S, Ohsuzu F, Kawai T, Ishihara M, et al. Systemic peripheral vascular resistance as a determinant of functional cardiac reserve in response to exercise in patients with heart disease. *Angiology.* (2007) 58:463–71. doi: 10.1177/0003319706294558
24. Cole RT, Gheorghiade M, Georgiopoulou VV, Gupta D, Marti CN, Kalogeropoulos AP, et al. Reassessing the use of vasodilators in heart failure. *Expert Rev Cardiovasc Ther.* (2012) 10:1141–51. doi: 10.1586/erc.12.108
25. Gandy SJ, Waugh SA, Nicholas RS, Simpson HJ, Milne W, Houston JG. Comparison of the reproducibility of quantitative cardiac left ventricular assessments in healthy volunteers using different MRI scanners: a multicenter simulation. *J Magn Reson Imaging.* (2008) 28:359–65. doi: 10.1002/jmri.21401

Conflict of Interest: The authors declare that the research was conducted in the absence of any commercial or financial relationships that could be construed as a potential conflict of interest.

Publisher's Note: All claims expressed in this article are solely those of the authors and do not necessarily represent those of their affiliated organizations, or those of the publisher, the editors and the reviewers. Any product that may be evaluated in this article, or claim that may be made by its manufacturer, is not guaranteed or endorsed by the publisher.

frontiers in Cardiovascular Medicine

STUDY PROTOCOL
published: 31 January 2022
doi: 10.3389/fcvm.2021.778010

Prognostic Value of Coronary CT Angiography-Derived Fractional Flow Reserve in Non-obstructive Coronary Artery Disease: A Prospective Multicenter Observational Study

Fan Zhou[1†], Qian Chen[2†], Xiao Luo[3†], Wei Cao[4†], Ziwen Li[5†], Bo Zhang[6†], U. Joseph Schoepf[7], Callum E. Gill[7], Lili Guo[8], Hong Gao[9], Qingyao Li[10], Yibing Shi[11], Tingting Tang[12], Xiaochen Liu[13], Honglin Wu[14], Dongqing Wang[15], Feng Xu[16], Dongsheng Jin[17], Sheng Huang[18], Haige Li[19], Changjie Pan[20], Hongmei Gu[21], Lixiang Xie[22], Ximing Wang[23], Jing Ye[24], Jianwei Jiang[25], Hanqing Zhao[26], Xiangming Fang[27], Yi Xu[28], Wei Xing[29], Xiaohu Li[30], Xindao Yin[2]*, Guang Ming Lu[1]* and Long Jiang Zhang[1]**

[1] Department of Radiology, Jinling Hospital, Medical School of Nanjing University, Nanjing, China, [2] Department of Radiology, Nanjing First Hospital, Nanjing Medical University, Nanjing, China, [3] Department of Radiology, People's Hospital of Maanshan, Maanshan, China, [4] Department of Radiology, The First People's Hospital of Xuzhou, Xuzhou, China, [5] Department of Radiology, Lianyungang Clinical Medical College of Nanjing Medical University, Lianyungang, China, [6] Department of Radiology, Taizhou People's Hospital, Taizhou, China, [7] Division of Cardiovascular Imaging, Department of Radiology and Radiological Science, Medical University of South Carolina, Charleston, SC, United States, [8] Department of Medical Imaging, The Affiliated Huai'an No.1 People's Hospital of Nanjing Medical University, Huai'an, China, [9] Department of Medical Imaging, Qinhuai Medical Region of Jinling Hospital, Nanjing, China, [10] Department of Radiology, Affiliated Hospital of Integrated Traditional Chinese and Western Medicine, Nanjing University of Chinese Medicine, Nanjing, China, [11] Department of Diagnostic Radiology, Xuzhou Central Hospital, Xuzhou, China, [12] Department of Diagnostic Radiology, Yancheng No.1 Hospital, Affiliated Hospital of Nantong University, Yancheng, China, [13] Department of Medical Imaging, Hai'an City People's Hospital, Haian, China, [14] Department of Radiology, The Affiliated Wujin Hospital of Jiangsu University, Changzhou, China, [15] Department of Medical Imaging, Affiliated Hospital of Jiangsu University, Zhenjiang, China, [16] Department of Medical Imaging, The Affiliated Suqian First People's Hospital of Nanjing Medical University, Suqian, China, [17] Department of Radiology, Jiangsu Province Official Hospital, Jiangsu Jiankang Vocational College, Nanjing, China, [18] Department of Radiology, The Second Affiliated Hospital of Nantong University, Nantong, China, [19] Department of Medical Imaging, The Second Affiliated Hospital of Nanjing Medical University, Nanjing, China, [20] Department of Radiology, The Affiliated Changzhou No.2 People's Hospital of Nanjing Medical University, Changzhou, China, [21] Medical Imaging Center, Affiliated Hospital of Nantong University, Nantong, China, [22] Department of Radiology, The Affiliated Hospital of Xuzhou Medical University, Xuzhou, China, [23] Department of Radiology, The First Affiliated Hospital of Soochow University, Suzhou, China, [24] Radiology Department, Subei People's Hospital of Jiangsu Province, Yangzhou, China, [25] Department of Medical Imaging, Affiliated Hospital of Jiangnan University, Wuxi, China, [26] Department of Medical Imaging, The Affiliated Huaihai Hospital of Xuzhou Medical University, Xuzhou, China, [27] Department of Radiology, The Affiliated Wuxi People's Hospital of Nanjing Medical University, Wuxi, China, [28] Department of Radiology, The First Affiliated Hospital of Nanjing Medical University, Nanjing, China, [29] Department of Radiology, Third Affiliated Hospital of Soochow University, Soochow University, Changzhou, China, [30] Department of Radiology, The First Affiliated Hospital of Anhui Medical University, Hefei, China*

Coronary artery disease (CAD) is a major contributor to morbidity and mortality worldwide. Myocardial ischemia may occur in patients with normal or non-obstructive CAD on invasive coronary angiography (ICA). The comprehensive evaluation of coronary CT angiography (CCTA) integrated with fractional flow reserve derived from CCTA (CT-FFR) to CAD may be essential to improve the outcomes of patients with non-obstructive CAD. China CT-FFR Study-2 (ChiCTR2000031410) is a large-scale prospective, observational study in 29 medical centers in China. The primary purpose is to uncover the relationship between the CCTA findings (including CT-FFR) and the

OPEN ACCESS

Edited by:
Andrea Igoren Guaricci, Azienda Ospedaliero Universitaria Consorziale Policlinico di Bari, Italy

Reviewed by:
Nazario Carrabba, Careggi Hospital, Italy
Filippo Cademartiri, Gabriele Monasterio Tuscany Foundation (CNR), Italy

***Correspondence:**
Long Jiang Zhang
kevinzhlj@163.com
Guang Ming Lu
cjr.luguangming@vip.163.com
Xindao Yin
y.163yy@163.com
Xiaohu Li
lixiaohu@ahmu.edu.cn

[†]These authors have contributed equally to this work

Specialty section:
This article was submitted to Cardiovascular Imaging, a section of the journal Frontiers in Cardiovascular Medicine

Received: *16 September 2021*
Accepted: *06 December 2021*
Published: *31 January 2022*

Citation:
Zhou F, Chen Q, Luo X, Cao W, Li Z, Zhang B, Schoepf UJ, Gill CE, Guo L, Gao H, Li Q, Shi Y, Tang T, Liu X, Wu H, Wang D, Xu F, Jin D, Huang S, Li H, Pan C, Gu H, Xie L, Wang X, Ye J, Jiang J, Zhao H, Fang X, Xu Y, Xing W, Li X, Yin X, Lu GM and Zhang LJ (2022) Prognostic Value of Coronary CT Angiography-Derived Fractional Flow Reserve in Non-obstructive Coronary Artery Disease: A Prospective Multicenter Observational Study. Front. Cardiovasc. Med. 8:778010. doi: 10.3389/fcvm.2021.778010

outcome of patients with non-obstructive CAD. At least 10,000 patients with non-obstructive CAD but without previous revascularization will be enrolled. A 5-year follow-up will be performed. The primary endpoint is the occurrence of major adverse cardiovascular events (MACE), including all-cause mortality, non-fatal myocardial infarct, unplanned revascularization, and hospitalization for unstable angina. Clinical characteristics, laboratory and imaging examination results will be collected to analyze their prognostic value.

Keywords: non-obstructive coronary artery disease, coronary computed tomography angiography, fractional flow reserve, major adverse cardiovascular events, coronary plaque assessment

INTRODUCTION

Cardiovascular disease is a worldwide disease, but China is one of the countries with the heaviest disease burden (1). Since the 1980s, the burden of ischemic heart disease (IHD) in China has been increasing and has become more marked in the past 20 years (2). In 2013, IHD was reported to be the leading cause of death in six provinces, accounting for ∼78% of the Chinese population (3). Moreover, IHD was ranked as the second leading cause of premature death in 2010 (2). The assessment and management of patients with coronary artery disease (CAD) have always focused on detecting and treating obstructive coronary artery stenosis (i.e., lumen obstruction of >50% [or >70%] by visual assessment) (4). However, the patients with CAD often are asymptomatic prior to myocardial infarction (MI), and coronary death with culprit lesions that are often non-obstructive before the events (5–7). The risk of cardiovascular events in patients with non-obstructive CAD is significantly higher than in patients without CAD (8, 9). Recently, the value of non-obstructive CAD and high-risk plaque (HRP) has been established (10).

Coronary CT angiography (CCTA) is a widely used non-invasive imaging modality to evaluate CAD and has demonstrated a high diagnostic performance in detecting obstructive and non-obstructive CAD on invasive coronary angiography (ICA) (11). Likewise, CCTA can also identify HRP seen on intravascular ultrasound or optical computed tomography (12). Coronary artery data and reporting system (CAD-RADS) has been reported to provide additional prognostic value beyond a coronary artery calcium score (CACS) and atherosclerotic cardiovascular disease (ASCVD) risk score (13). However, this reporting system does not consider the functional information of CAD, which is more important to determine the physiological nature of coronary stenoses than the anatomy (14). A previous study showed that 35% of non-obstructive CAD (diameter stenosis < 50%) was associated with ischemia (fractional flow reserve [FFR] ≤ 0.80), while 20% of lesions with >50% stenosis had no ischemia (15).

Coronary CT angiography-derived FFR (CT-FFR) has been reported to be a potential alternative to provide a physiological evaluation of the entire coronary artery tree, with high diagnostic accuracy in stable CAD patients compared with invasive FFR, the gold standard (16). Moreover, CCTA combined with selective CT-FFR is shown to be associated with a safety reduction of unnecessary ICA and relevant costs when compared with standard clinical practice (17). According to the ADVANCE (18) trial, patients with a negative CT-FFR have less revascularization and a trend toward lower major adverse cardiovascular events (MACE) and significantly lower MI or cardiovascular death. We hypothesize that integrating CCTA with CT-FFR will improve the recognition of subclinical plaques, optimize the risk stratification, and improve the prognosis of patients with non-obstructive CAD. Therefore, a large prospective study cohort from 29 medical centers in China (China CT-FFR Study-2) is designed to verify this hypothesis through a 5-year long-term follow-up.

The aims of this study are to (1) establish a large cohort of patients with non-obstructive CAD based on the Chinese population and conduct a long-term follow-up observation and (2) explore the predictive value of CT-FFR for MACE in patients with non-obstructive CAD beyond the clinical and anatomical factors.

METHODS AND ANALYSIS

Study Design

This is a prospective, observational, multicenter registry study. The trial protocol and written informed consent forms have been reviewed and approved by the clinical trial ethics committee at Jinling Hospital, Medical School of Nanjing University (General Hospital of Eastern Theater Command), and by each center before the initiation of the investigation. All enrolled patients will provide written informed consent at admission for their data collection and utilization for future anonymous studies. The study has been registered on http://www.chictr.org.cn (ChiCTR2000031410). This study is partially supported by the National Key Research and Development Program of China (no. 2017YFC0113400), Jiangsu Provincial Key Research and Development Program (no. BE2020699), and Key Program of the National Natural Science Foundation of China (no. 81830057) for LJZ.

Selection of Subjects

We aim to include ten thousand patients referred for CCTA examination by physicians for the evaluation of suspected or known CAD and subsequently diagnosed as non-obstructive CAD by CCTA (defined as a coronary artery stenosis [maximal stenosis] greater than or equal to 20% but <50% [for left main coronary artery] or greater than or equal to 20% but <70% [for any other epicardial

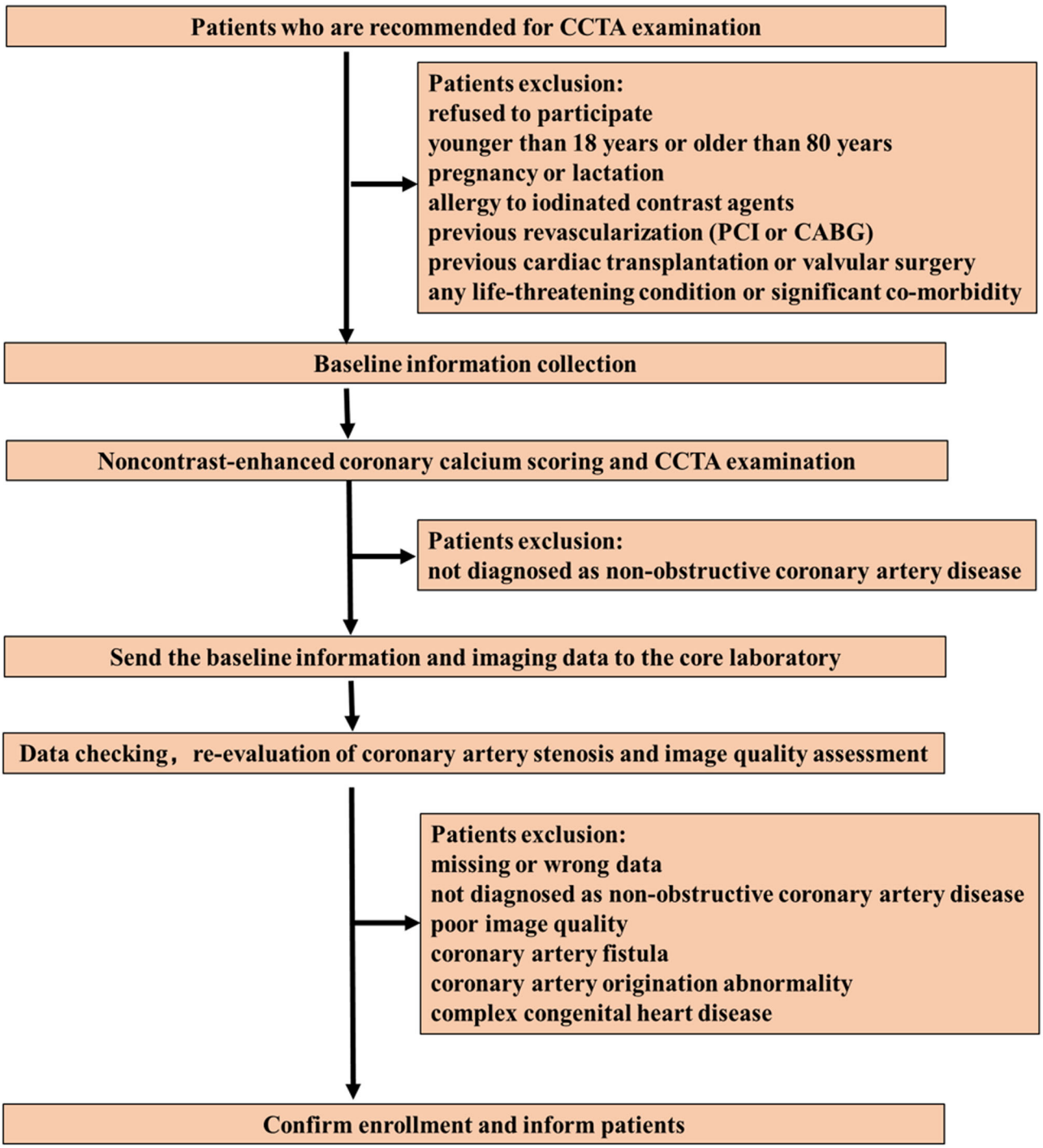

FIGURE 1 | Patient enrollment flow chart. CCTA, coronary computed tomography angiography; PCI, percutaneous coronary intervention; CABG, coronary artery bypass grafting.

coronary artery] in vessel segments ≥1.5 mm diameter) (19) but without previous revascularization (percutaneous coronary intervention [PCI] or coronary artery bypass grafting [CABG]). The enrollment process is shown in **Figure 1**.

Inclusion Criteria

1) The patient must sign a written informed consent before any study procedures.
2) Non-obstructive coronary CAD by CCTA (a coronary artery stenosis [maximal stenosis] ≥20% but <50% [for left main

coronary artery] or ≥20% but <70% [for any other epicardial coronary artery] in vessel segments ≥1.5 mm diameter).

Exclusion Criteria

1) Refusal to participate.
2) <18 years or >80 years.
3) Pregnancy or lactation.
4) Allergy to iodinated contrast agents.
5) Previous revascularization (PCI or CABG).
6) Previous cardiac transplantation or valvular surgery.
7) Any life-threatening condition or severe co-morbidity.
8) Patients with poor image quality studies, unsuitable for further analysis.
9) Coronary artery fistula and anomalous origin.
10) Complex congenital heart disease.
11) Missing data.

During the initial screening stage (conducted by each center), any patients who meet any one of the above 1-7 exclusion criteria will be excluded. The final enrollment will be determined by the core laboratory (Jinling Hospital, Medical School of Nanjing University) after double-checking the data, re-evaluating coronary artery stenosis and image quality.

STUDY PROCEDURES

Clinical Variables

Baseline clinical characteristics will be obtained through an electronic questionnaire for each participating patient at enrollment, including age, sex, height, weight, diabetes mellitus, hypertension, hyperlipidemia, smoking, drinking, positive CAD family history, clinical symptoms, all patient-reported examinations, medications, and surgeries associated with the cardiovascular disease within 6 months (**Tables 1**–**5**). Diabetes mellitus is defined as a history of diabetes mellitus diagnosed or treated by a physician, treated with oral antidiabetic therapy, or an admission fasting blood glucose level ≥126 mg/dl. Hypertension is defined as a history of high blood pressure diagnosed or treated by a physician, treated with antihypertensive therapy, or an admission blood pressure ≥140/90 mmHg. Dyslipidemia is defined as a history of hyperlipidemia diagnosed or treated by a physician, being in treatment with antihyperlipidemic drugs, or admission total cholesterol (TC) ≥200 mg/dl. Smoking/drinking is defined as current smoker/drinker or prior smoker/drinker within the last year. Positive CAD family history is defined as cardiac death or MI in first-degree relatives (<55 years in men or < 65 years in women). Chest pain will be recorded and classified as typical angina, atypical angina and non-anginal chest pain according to the site, characteristics and duration of the chest discomfort and its relationship with exercise, and the inducing and relieving factors (20). Typical angina is considered to meet the following three characteristics: (a) constricting discomfort in the front of the chest or in the neck, jaw, shoulder, or arm; (b) induced by excessive physical activity; and (c) relieved by rest or nitrates within 5 min. Patients presenting with two of the aforementioned typical angina features are considered to have atypical angina.

TABLE 1 | Baseline demographic information.

Name: _____ ID number:_____
Birthday:_____ Sex: ☐Male ☐Female
Height: cm Weight: kg
Telephone number (participant):_____
Telephone number (first relatives):_____
Relationship between relatives and participant:_____

ID, Identity document; cm, centimeter; kg, kilogram.

TABLE 2 | Baseline clinical information.

1. Hypertension: ☐Yes ☐No (meet one of the following three factors)
   ☐systolic blood pressure ≥140 mmHg
   ☐diastolic blood pressure ≥90 mmHg
   ☐being treated with antihypertensive therapy
2. Diabetes mellitus: ☐Yes ☐No (meet one of the following two factors)
   ☐fasting blood glucose level ≥126mg/dl
   ☐being treated with oral antidiabetic therapy
3. Dyslipidemia: ☐Yes ☐No (meet one of the following two factors)
   ☐total cholesterol ≥200mg/dl
   ☐being treated with antihyperlipidemic drugs
4. Smoking: ☐Yes ☐No (meet one of the following two factors)
   ☐current smoker
   ☐previous smoker within the last year
5. Drinking: ☐Yes ☐No (meet one of the following two factors)
   ☐current drinker
   ☐previous drinker within the last year
6. Positive family history: ☐Yes ☐No (meet one of the following two factors)
   ☐cardiac death or MI in first-degree relatives younger than 55 years in men
   ☐cardiac death or MI in first-degree relatives younger than 65 years in women
7. Clinical symptoms:
   ☐chest pain: ☐in the front of the chest or in the neck, jaw, shoulder, or arm
   ☐precipitated by physical exertion
   ☐relieved by rest or nitrates within 5 min
   ☐palpitation ☐dyspnea ☐syncope ☐other

MI, myocardial infarction.

Patients presenting with only one or none of the typical angina characteristics are supposed to have non-anginal chest pain. Relevant medications will be recorded as statin, antiplatelet, beta-blockers, angiotensin-converting enzyme inhibitors (ACEI), angiotensin-receptor blockers (ARB), oral hypoglycemic agent, insulin, oral anticoagulation, calcium channel blocker (CCB), and diuretic. In addition, laboratory test results for C-reactive protein, triglycerides, TC, low-density lipoprotein cholesterol (LDL-C), high-density lipoprotein cholesterol (HDL-C), and cardiac enzyme level will be collected, if possible. The Framingham risk score (FRS) will be calculated for subjects with the complete information of age, sex, TC, HDL-C, systolic blood pressure, diabetes mellitus, antihypertensive medication, and smoking status (21). Meanwhile, the Multi-Ethnic Study of Atherosclerosis (MESA) score will also be calculated using age, gender, race/ethnicity, diabetes mellitus, smoking status, TC, HDL-C, antihyperlipidemic drugs, and MI family history (22).

TABLE 3 | Baseline medications information.

Whether there is a history of cardiovascular disease-related drug use within 6 months before the examination: ☐Yes ☐No (If yes, continue to fill in the content below)
☐statin: dose:_____ duration: from_____to
☐antiplatelet: dose:_____duration: from_____to
☐beta-blocker: dose:_____ duration: from_____to
☐ACEI: dose:_____duration: from_____to
☐ARB: dose:_____ duration: from_____to
☐CCB: dose:_____duration: from_____to
☐diuretic: dose:_____ duration: from_____to
☐oral hypoglycemic agents: dose:_____ duration: from_____to
☐insulin: dose:_____ duration: from_____to
☐oral anticoagulation: dose:_____duration: from_____to
☐other: dose:_____ duration: from_____to

ACEI, angiotensin converting enzyme inhibitor; ARB, angiotensin-receptor blocker; CCB, calcium channel blocker.

TABLE 4 | Baseline surgical information.

Whether there is a history of cardiovascular disease-related surgeries within 6 months before the examination: ☐Yes ☐No (If yes, continue to fill in the content below)
1. Surgical method:
Surgical date:
Postoperative diagnosis:
2. Surgical method:
Surgical time:
Postoperative diagnosis:
3. Surgical method:
Surgical time:
Postoperative diagnosis:
4. Surgical method:
Surgical time:
Postoperative diagnosis:
……

TABLE 5 | Baseline imaging tests information.

Whether there is a history of cardiovascular disease-related imaging examinations before the examination: ☐Yes ☐No (If yes, continue to fill in the content below)
1. Examination method: ☐CT ☐MRI ☐OCT ☐PET ☐SPECT ☐other
time:_____ region:
diagnosis:
2. Examination method: ☐CT ☐MRI ☐OCT ☐PET ☐SPECT ☐other
time:_____ region:
diagnosis:
3. Examination method: ☐CT ☐MRI ☐OCT ☐PET ☐SPECT ☐other
time:_____ region:
diagnosis:
4. Examination method: ☐CT ☐MRI ☐OCT ☐PET ☐SPECT ☐other
time:_____ region:
diagnosis:
5. Examination method: ☐CT ☐MRI ☐OCT ☐PET ☐SPECT ☐other
time:_____ region:
diagnosis:
……

CCTA Scanning Protocols

All CCTA acquisitions will be performed in each medical center using CT scanners with ≥64 detector rows. A non-contrast enhanced coronary calcium scoring study will be obtained before the CCTA examination. The specific scanning protocols are consistent with the routine clinical practice of CCTA in each medical center. Nitroglycerin and beta-blockers will be administered according to the standard practice of each center. Baseline scanning characteristics will be obtained through an electronic questionnaire for each participating patient after CCTA examination, such as scanning equipment, scanning protocols, the name, concentration, dosage and injection rate of iodinated contrast agent, average heart rate during scanning, and the usage of nitroglycerin and beta-blockers. All the Digital Imaging and Communications in Medicine (DICOM) files will be transferred to the core laboratory online or offline for image quality and coronary stenosis assessment after the initial screening in each center. After double-checking the data, subjects who meet the inclusion criteria will be finally enrolled and informed by the core laboratory.

Image Quality Analysis

The CCTA images will be evaluated in consensus by two cardiovascular radiologists (FZ and CXT, with 5 and 8 years of experience in CCTA interpretation) at the core laboratory. Image quality assessment will be performed using a four-point Likert scale as follows: 4 = excellent (clear delineation of the coronary arteries, no motion artifacts, and slight noise); 3 = good (mild blurring and minor motion artifacts); 2 = acceptable (moderate blurring and mild motion artifacts or minor discontinuity); and 1 = non-diagnostic (severe motion artifacts or discontinuity made the coronary artery structures not differentiable). Patients with poor image quality (score = 1) unsuitable for further analysis will be excluded (23).

Coronary Plaque Evaluation

The coronary artery is divided into 17 segments according to the American Heart Association (AHA) classification (24). The right coronary artery (RCA) includes segments 1, 2, 3, 4, and 16. The left main (LM) and left anterior descending (LAD) include segments 5, 6, 7, 8, 9, and 10. The left circumflex (LCX) includes segments 11, 12, 13, 14, and 15. Coronary plaques will be identified in segments with a diameter ≥1.5 mm. Lesions located in the major epicardial coronary arteries will be classified as proximal (segments 1, 6, and 11), middle (segments 2 and 7), and distal (segments 3, 8, and 13).

Evaluation of the Coronary Plaque Calcification

To quantify coronary plaque calcification, the Agatston score (AS) will be calculated for each patient by multiplying the calcified lesion area by the maximum density of a single target

lesion in this area using a semiautomated software (SyngoVia, Siemens Healthineers, Forchheim, Germany) (25). Based on the AS, patients will be divided into four groups: 0, 1–99, 100–299, and ≥300 (26). In addition, we will evaluate the degree of plaque calcification of the most severe lesion using the arc of calcification in the short axis. Accordingly, the degree of target lesion calcification is defined as: (1) no calcification (no calcification present); (2) mild (<90°arc calcification); (3) moderate (90–180°arc calcification); (4) severe (180–270°arc calcification); or (5) very severe (270–360°arc calcification) (27).

Quantitative Evaluation of the Coronary Plaque

Quantitative plaque analysis will be performed by a group of observers using a semiautomated software (QAngioCT, Medics, Leiden, The Netherlands). The following plaque parameters will be assessed: %DS (degree of lumen stenosis calculated at the site of maximal stenosis, defined as 100% × [reference diameter-minimal lumen diameter, MLD]/reference diameter); plaque length; MLD and minimal lumen area (MLA); plaque volume (defined as vessel volume minus lumen volume), such as the total volume, the volume of calcification components (>350 HU), lipid components (<30 HU), fiber-fatty components (30–130 HU) and fibrous components (131–350 HU) (28); plaque burden (PB) (defined as 100% × [plaque volume/vessel volume]); and the remodeling index (RI) (automatically calculated), calculated as the diameter, i.e., both plaque and vessel lumen at the site of maximal stenosis divided by the mean diameter of the proximal and distal reference site. Plaque volume and burden will be summed on a per-segment, per-vessel, and per-patient level. According to the RI, lesions will be categorized into three groups as follows: positive remodeling (PR; RI > 1.0), negative remodeling (RI < 0.88), and intermediate remodeling (0.88 ≤ RI ≤ 1.0).

On a per-lesion basis, CAD-RADS categories are defined as follows: CAD-RADS 1 (1–24% stenosis or present coronary plaque without apparent stenosis), CAD-RADS 2 (25–49% stenosis), and CAD-RADS 3 (50–69% stenosis). On a per-segment/vessel/patient basis, CAD-RADS categories will be evaluated based on the maximal stenosis. According to the AHA classification, the number of segments ≥1.5 mm diameter with any calcified, non-calcified, or mixed plaque will be recorded, regardless of the degree of stenosis, for the calculation of segment involvement score (SIS). The maximum SIS value that can be derived is 17 for each patient. A comprehensive CTA risk score will be calculated using an online calculator (http://18.224.14.19/calcApp/) according to the previous study (29). The CCTA risk score is derived from CONFIRM registry, and the calculated content includes the presence, location, extent, severity, and composition of CAD.

Qualitative Evaluation of the Coronary Plaque

According to previous studies, four signs of coronary artery plaques on CCTA will be recorded as HRP features, namely, low-density plaque (LAP), PR, punctate calcification (SC), and napkin ring sign (NRS) (26). LAP is defined as the plaque component with an attenuation of <30 HU. RI > 1 indicates PR. SC is defined as any discrete calcification less than or equal to 3 mm in length and occupying less than or equal to 90° arc when viewed in the short axis. NRS is recognized as a central low attenuation plaque with a peripheral rim of higher attenuation of the non-calcified plaque.

CT-FFR Measurements

All CT-FFR values will be calculated by using an automated software ("Shukun-FFR" software from Shukun [Beijing] Technology Co., Ltd). The "Shukun-FFR" software consists of two main components, the coronary arteries segmentation model and the computational fluid dynamics (CFD) simulation model. Specifically, a modified V-Net is first used to to segment coronary arteries from the CCTA image firstly (30). Then, we adopt prior knowledge to name vascular branches based on additional anatomical rules, using previous vessel segmentation results as input. The final reduced-order CFD model is applied to compute the flow and pressure of blood and calculate CT-FFR values automatically for all points along coronary arteries. CT-FFR values will be determined for coronary arteries ≥1.5 mm in diameter in the core laboratory by two cardiovascular radiologists (observers A and B). The automatically identified coronary plaques and the degree of lumen stenosis will be verified by another well-experienced observer. Observer A will carry out measurements two times separately (recorded as A1, A2). The time interval between the two measurements is 2 weeks to eliminate the effect of memory; observer B will measure one time (recorded as B). CT-FFR values will be measured at the proximal, distal, and 20 mm distal to the stenosis and the end of the target vessel (at least 1.5 mm diameter). CT-FFR ≤ 0.80 indicates the hemodynamic significance of coronary stenosis. Patients with CT-FFR ≤ 0.80, which is 20 mm distal to the stenosis, are deemed to have lesion-specific ischemia. Patients without lesion-specific ischemia but with CT-FFR ≤ 0.80 at the end of the target vessel are deemed to have distal vessel ischemia.

Endpoints and Definition

Outcomes will be ascertained by phone contact with the patient (or family member if needed), reviewing medical records or consulting with the attending physicians, if possible, and adjudicated blindly by an independent clinical event committee according to ACC/AHA standards and the fourth universal definition of MI by reviewing symptoms, cardiac laboratory biomarker data, electrocardiogram results, and cardiovascular imaging findings (31, 32).

Primary Endpoints

The primary endpoint is the occurrence of MACE at follow-up, defined as a composite of all-cause death, non-fatal MI, unplanned revascularization (at least 60 days after the CCTA examination), and hospitalization for unstable angina. Death cases consist of cardiovascular death, non-cardiovascular death, and undetermined cause of death. Cardiovascular death includes death attributable to sudden cardiac death, acute MI, heart failure, cardiovascular bleeding, stroke, cardiovascular procedure, and other cardiovascular causes, such as pulmonary embolism. When a definite non-cardiovascular

cause is documented, a cardiovascular reason for death could be excluded. Non-fatal MI consists of ST-segment elevation myocardial infarction (STEMI) and non–STEMI. Unstable angina is defined as the symptoms of ischemic chest pain at rest, and the final diagnosis is myocardial ischemia with objective evidence but without elevation of cardiac biomarkers. For the primary endpoints, the first occurrence timepiont of any one of the above events will be recorded. The follow-up duration is recorded as the interval from baseline CCTA examination to the day of follow-up.

Secondary Endpoints

Secondary endpoints include cardiovascular death, atrial fibrillation, non-fatal MI, non-fatal stroke, unplanned revascularization, hospitalization for unstable angina, medication adjustment, invasive or non-invasive cardiovascular tests, cumulative radiation exposure from all cardiovascular tests, and total cardiac costs. Medication adjustment includes the increase or decrease of the drug dose and the new addition or discontinuation of medications. For the secondary endpoints, the time of the occurrence for any one of the above events should be recorded.

Follow-Up

Telephone follow-up will be performed for each enrollee annually by the follow-up team of each medical center until the completion of the 5-year follow-up. The follow-up team in each center includes at least one nurse, one cardiovascular radiologist, and one cardiovascular physician. The follow-up team will first contact the patient via a phone call. If it is unsuccessful, the personal contact will be called for updated information. After documentation of three unsuccessful attempts (on three different days over 1 month) by the follow-up team, a subject will be considered lost to telephone follow-up. If the outcome of this subject cannot be traced through the medical record system, the subject will eventually be deemed to be lost to follow-up. The follow-up team of the core laboratory will randomly select 10% of the subjects from each other medical center for review to confirm the authenticity of the follow-up data.

Data Collection and Management

Data management and coordination will be performed by the core laboratory. Study investigators in each medical center will collect all text data regarding baseline clinical characteristics, laboratory results, medical/interventional treatments and outcomes and enter them into a web-based electronic case report form. All imaging data will be transmitted to the core laboratory in an anonymous form. A reference number will be assigned to every single enrolled patient. The final China CT-FFR Study-2 database, including text and imaging data, will be constructed from the individual and valid databases, which will be provided by each participating center. Centers providing forms with more than 5% of missing values will be excluded from the final China CT-FFR Study-2 database.

Trial Status

The study was started in November 2019, and initially included 24 medical centers from all 13 regions of Jiangsu Province (**Table 6**). Due to the COVID-19 pandemic (from February 2020 to July 2020), study progress was significantly delayed. In August 2020, another three medical centers from Jiangsu Province and two from Anhui Province joined the study, with the agreement of the members of the Data Safety and Monitoring Board and a common end date of December 30, 2021 was defined. The number of target subjects for each center is determined based on the number of daily CCTA examinations and each centers requests.

Data Analysis

According to the Kolmogorov-Smirnov test, continuous data will be categorized as normally or non-normally distributed data. Mean ± SD will be used to express the quantitative variables for uniformity of presentation, regardless of the distribution. Independent sample *t*-tests, paired *t*-tests, or ANOVA tests will be conducted for the comparison of normally distributed continuous data, as appropriate. The difference analysis of non-normally distributed data will be performed by using the non-parametric test. Categorical variables will be expressed as presented as numbers and frequencies or percentages. Pearson's chi-squared test or the likelihood ratio will be used to compare the differences of categorical data between groups, as appropriate. Univariate and multivariate Cox proportional hazard models will be performed to calculate the hazard ratio (HR) with a 95% CI and to estimate the association between variables and the hazards of MACE. Kaplan-Meier plots with the log-rank tests will be generated to estimate cumulative rates of MACE. The receiver operating characteristics (ROC) curve analysis will be performed to determine the optimal cut-off values of quantitative data. The area under the curve (AUC) for each model will be compared. The patient's annual total cardiac cost will be compared using the non-parametric Wilcoxon rank-sum test or a two-sample *t*-test. Intraclass correlation coefficient (ICC) and Spearman correlation coefficient will be used to assess the inter- and intra-observer agreement. Considering the selection bias and potential heterogeneity between 29 centers, a center effect analysis will be performed. If there is a central effect, a stratified analysis and sensitivity analysis will be performed, or it will be adjusted as a random factor. A $p \leq 0.05$ is considered statistically significant.

DISCUSSION

Coronary CT angiography has been recommended as the first-choice imaging modality for patients with stable CAD. In addition to the unique ability for non-invasive qualitative and quantitative evaluation of coronary atherosclerotic plaque, CCTA can provide functional information without the increased burden of radiation exposure and administration of stress agents. Compared with conventional CCTA alone, it has been demonstrated that CT-FFR had improved discrimination of ischemia (33). The Prospective Multicenter Imaging Study for Evaluation of Chest Pain (PROMISE) trial demonstrated that

TABLE 6 | Detail information of the medical centers.

No.	Centers	Principal Investigator (PI)	Target number of subjects
1	Jinling hospital	Long Jiang Zhang	1,000
2	Nanjing first hospital	Xindao Yin	1,000
3	Taizhou people's hospital	Bo Zhang	500
4	The first affiliated hospital of nanjing medical university	Yi Xu	500
5	The affiliated wuxi people's hospital of nanjing medical university	Xiangming Fang	500
6	Affiliated hospital of jiangnan university	Jianwei Jiang	500
7	Subei people's hospital of jiangsu province	Jing Ye	500
8	The first affiliated hospital of soochow university	Ximing Wang	500
9	The affiliated hospital of xuzhou medical university	Lixiang Xie	500
10	The first affiliated hospital of anhui medical university*	Xiaohu Li	500
11	Affiliated hospital of nantong university	Hongmei Gu	300
12	The affiliated huai'an No.1 people's hospital of nanjing medical university	Lili Guo	300
13	Third affiliated hospital of soochow university	Wei Xing	300
14	The affiliated changzhou No.2 people's hospital of nanjing medical university	Changjie Pan	300
15	The second affiliated hospital of nanjing medical university	Haige Li	200
16	The second affiliated hospital of nantong university	Sheng Huang	200
17	The first affiliated hospital of kangda college nanjing medical university	Ying Zhou	200
18	Jiangsu province official hospital	Dongsheng Jin	200
19	Affiliated hospital of jiangsu university	Dongqing Wang	200
20	The affiliated suqian first people's hospital of nanjing medical university	Feng Xu	200
21	The affiliated wujin hospital of jiangsu university	Honglin Wu	200
22	Qinhuai medical region of jinling hospital	Hong Gao	200
23	Hai'an city people's hospital	Ping Wu	200
24	Yancheng No.1 hospital	Dingyou Lu	200
25	The huaihai affiliated hospital of xuzhou medical university	Hanqing Zhao	200
26	Xuzhou central hospital*	Yibing Shi	200
27	The first people's hospital of xuzhou*	Wei Cao	200
28	Affiliated Hospital of Integrated Traditional Chinese and Western Medicine*	Zongjun Zhang	100
29	People' hospital of maanshan*	Xiao Luo	100

**Medical centers joined in August 2020.*

the 9-month costs of patients with stable angina in the CT-FFR group were slightly higher than that in the routine care group, but the difference was not significant ($p = 0.10$) (34). The inconsistent conclusions about the socioeconomic effects of CT-FFR with previous studies may be due to the fact that only 31% of the patients in the CT-FFR group have undergone CT-FFR examinations in this study (35, 36). In addition, all patients have stable angina, but CT-FFR is believed to minimize unnecessary care and resources for patients with mild stenosis and equivocal stenosis, which highlights the significance of CT-FFR for patients with non-obstructive CAD (37). The previous study showed that among symptomatic patients who underwent CCTA, only a few patients were diagnosed with obstructive CAD (8). However, it is reported that about 10% of total MI is caused by non-obstructive CAD (MINOCA), and 18.7% of MINOCA patients will have MACE after 1-year of follow-up (38). Although several CCTA-based scoring systems have been proven to have prognostic value, the functional information was not included in these studies (13, 29, 39). The China CT-FFR Study-2 is designed to investigate the potential ability of CT-FFR to improve the risk stratification of patients with non-obstructive CAD beyond the clinical and morphological information using large-scale data with long-term follow-up. The baseline clinical information can be used to explore its relationship with the CAD. The baseline CCTA findings will provide the data on the morbidity of non-obstructive CAD. The longitudinal follow-up data will uncover the association between CT-FFR and HRP identified on baseline CCTA and downstream risk of MACE. Further, this observational registry will be valuable for the design of future randomized controlled trials.

Despite its strengths, this study has some limitations. First, this is a large observational registry, which has inherent limitations, such as selection bias and potential heterogeneity between centers. Second, most of the medical centers are from the same province, resulting in a lack of external verification. Third, there is no uniform scanning protocol for baseline CCTA, the scanning characteristics should be adjusted during subsequent data analysis. The scanning protocols of each center will be recorded for the central effect analysis. If there is a central effect, a stratified analysis and sensitivity analysis will be performed, or it will be adjusted as a random factor. Fourth, no blood or

other biological samples will be collected at the baseline of this study, which may cause some critical information to be missed.

CONCLUSION

The China CT-FFR Study-2 is a prospective, observational, multicenter registry study. At least 10,000 patients with non-obstructive CAD will be enrolled from 29 medical centers in China. Baseline clinical information and CCTA findings (such as CT-FFR) will be collected. A 5-year follow-up will be performed by phone contact to ascertain the outcomes of patients. To the best of our knowledge, this is the largest prospective observable study to explore the relationship between CT-FFR and prognosis in China. Based on the excellent performance of CT-FFR for diagnosing myocardial ischemia and its predictive value for future risk of MACE, we believe that the China CT-FFR Study-2 will be helpful to provide unique risk stratification of patients with non-obstructive CAD.

ETHICS STATEMENT

The studies involving human participants were reviewed and approved by Clinical Trial Ethics Committee of General Hospital of Eastern Theater Command. The patients/participants provided their written informed consent to participate in this study.

AUTHOR CONTRIBUTIONS

LJZ and GML contributed to conception and design of the study. FZ was a major contributor in writing the manuscript. FZ, QC, XLu, WC, ZL, and BZ made the equal contribution to this study. QC, ZL, QL, TT, and XLiu contributed to data collection. LJZ, GML, XY, XLi, XLu, WC, BZ, LG, HGa, YS, HW, DW, FX, DJ, SH, HL, CP, HGu, LX, XW, JY, JJ, HZ, XF, YX, and WX organized the database. UJS and CEG contributed to the language revisions. All authors contributed to manuscript revision, read, and approved the submitted version.

FUNDING

This study was funded by the National Key Research and Development Program of China (no. 2017YFC0113400), the Jiangsu Provincial Key Research and Development Program (no. BE2020699), and the Key Program of the National Natural Science Foundation of China (no. 81830057) for LJZ. XLi was funded by the National Natural Science Foundation of China (no. 82071897).

REFERENCES

1. Zhao D, Liu J, Wang M, Zhang X, Zhou M. Epidemiology of cardiovascular disease in China: current features and implications. *Nat Rev Cardiol.* (2019) 16:203–12. doi: 10.1038/s41569-018-0119-4
2. Yang G, Wang Y, Zeng Y, Gao GF, Liang X, Zhou M, et al. Rapid health transition in China, 1990-2010: findings from the Global Burden of Disease Study 2010. *Lancet.* (2013) 381:1987–2015. doi: 10.1016/S0140-6736(13)61097-1
3. Zhou M, Wang H, Zhu J, Chen W, Wang L, Liu S, et al. Cause-specific mortality for 240 causes in China during 1990-2013: a systematic subnational analysis for the Global Burden of Disease Study 2013. *Lancet.* (2016) 387:251–72. doi: 10.1016/S0140-6736(15)00551-6
4. Arbab-Zadeh A, Fuster V. From detecting the vulnerable plaque to managing the vulnerable patient: JACC State-of-the-Art Review. *J Am Coll Cardiol.* (2019) 74:1582–93. doi: 10.1016/j.jacc.2019.07.062
5. Muhlestein JB, Lappé DL, Lima JA, Rosen BD, May HT, Knight S, et al. Effect of screening for coronary artery disease using CT angiography on mortality and cardiac events in high-risk patients with diabetes: the FACTOR-64 randomized clinical trial. *JAMA.* (2014) 312:2234–43. doi: 10.1001/jama.2014.15825
6. Fishbein MC. Siegel RJ. How big are coronary atherosclerotic plaques that rupture? *Circulation.* (1996) 94:2662–6. doi: 10.1161/01.CIR.94.10.2662
7. Planer D, Mehran R, Ohman EM, White HD, Newman JD, Xu K, et al. Prognosis of patients with non-ST-segment-elevation myocardial infarction and nonobstructive coronary artery disease: propensity-matched analysis from the Acute Catheterization and Urgent Intervention Triage Strategy trial. *Circ Cardiovasc Interv.* (2014) 7:285–93. doi: 10.1161/CIRCINTERVENTIONS.113.000606
8. Emami H, Takx RAP, Mayrhofer T, Janjua S, Park J, Pursnani A, et al. Nonobstructive coronary artery disease by coronary CT angiography improves risk stratification and allocation of statin therapy. *JACC Cardiovasc Imaging.* (2017) 10:1031–8. doi: 10.1016/j.jcmg.2016.10.022
9. Maddox TM, Stanislawski MA, Grunwald GK, Bradley SM, Ho PM, Tsai TT, et al. Nonobstructive coronary artery disease and risk of myocardial infarction. *JAMA.* (2014) 312:1754–63. doi: 10.1001/jama.2014.14681
10. Ferencik M, Mayrhofer T, Bittner DO, Emami H, Puchner SB, Lu MT, et al. Use of high-risk coronary atherosclerotic plaque detection for risk stratification of patients with stable chest pain: a secondary analysis of the PROMISE randomized clinical trial. *JAMA Cardiol.* (2018) 3:144–52. doi: 10.1001/jamacardio.2017.4973
11. Miller JM, Rochitte CE, Dewey M, Arbab-Zadeh A, Niinuma H, Gottlieb I, et al. Diagnostic performance of coronary angiography by 64-row CT. *N Engl J Med.* (2008) 359:2324–36. doi: 10.1056/NEJMoa0806576
12. Marwan M, Taher MA, El Meniawy K, Awadallah H, Pflederer T, Schuhbäck A, et al. In vivo CT detection of lipid-rich coronary artery atherosclerotic plaques using quantitative histogram analysis: a head to head comparison with IVUS. *Atherosclerosis.* (2011) 215:110–5. doi: 10.1016/j.atherosclerosis.2010.12.006
13. Bittner DO, Mayrhofer T, Budoff M, Szilveszter B, Foldyna B, Hallett TR, et al. Prognostic value of coronary CTA in stable chest pain: CAD-RADS, CAC, and cardiovascular events in PROMISE. *JACC Cardiovasc Imaging.* (2020) 13:1534–45. doi: 10.1016/j.jcmg.2019.09.012
14. Ciccarelli G, Barbato E, Toth GG, Gahl B, Xaplanteris P, Fournier S, et al. Angiography versus hemodynamics to predict the natural history of coronary stenoses: fractional flow reserve versus angiography in multivessel evaluation 2 substudy. *Circulation.* (2018) 137:1475–85. doi: 10.1161/CIRCULATIONAHA.117.028782
15. Imai S, Kondo T, Stone GW, Kawase Y, Ahmadi AA, Narula J, et al. Abnormal fractional flow reserve in nonobstructive coronary artery disease. *Circ Cardiovasc Interv.* (2019) 12:e006961. doi: 10.1161/CIRCINTERVENTIONS.118.006961
16. Driessen RS, Danad I, Stuijfzand WJ, Raijmakers PG, Schumacher SP, van Diemen PA, et al. Comparison of coronary computed tomography angiography, fractional flow reserve, and perfusion imaging for ischemia diagnosis. *J Am Coll Cardiol.* (2019) 73:161–73. doi: 10.1016/j.jacc.2018.10.056

17. Douglas PS, De Bruyne B, Pontone G, Patel MR, Norgaard BL, Byrne RA, et al. 1-year outcomes of FFRCT-guided care in patients with suspected coronary disease: the PLATFORM study. *J Am Coll Cardiol.* (2016) 68:435–45. doi: 10.1016/j.jacc.2016.05.057
18. Patel MR, Nørgaard BL, Fairbairn TA, Nieman K, Akasaka T, Berman DS, et al. 1-Year impact on medical practice and clinical outcomes of FFR_{CT}: the ADVANCE registry. *JACC Cardiovasc Imaging.* (2020) 13:97–105. doi: 10.1016/j.jcmg.2019.03.003
19. Sharaf B, Wood T, Shaw L, Johnson BD, Kelsey S, Anderson RD, et al. Adverse outcomes among women presenting with signs and symptoms of ischemia and no obstructive coronary artery disease: findings from the National Heart, Lung, and Blood Institute-sponsored Women's Ischemia Syndrome Evaluation (WISE) angiographic core laboratory. *Am Heart J.* (2013) 166:134–41. doi: 10.1016/j.ahj.2013.04.002
20. Knuuti J, Wijns W, Saraste A, Capodanno D, Barbato E, Funck-Brentano C, et al. 2019 ESC Guidelines for the diagnosis and management of chronic coronary syndromes. *Eur Heart J.* (2020) 41:407–77. doi: 10.1093/eurheartj/ehz425
21. D'Agostino RB Sr, Vasan RS, Pencina MJ, Wolf PA, Cobain M, Massaro JM, et al. General cardiovascular risk profile for use in primary care: the Framingham Heart Study. *Circulation.* (2008) 117:743–53. doi: 10.1161/CIRCULATIONAHA.107.699579
22. McClelland RL, Jorgensen NW, Budoff M, Blaha MJ, Post WS, Kronmal RA, et al. 10-Year coronary heart disease risk prediction using coronary artery calcium and traditional risk factors: derivation in the MESA (Multi-Ethnic Study of Atherosclerosis) with validation in the HNR (Heinz Nixdorf Recall) study and the DHS (Dallas Heart Study). *J Am Coll Cardiol.* (2015) 66:1643–53. doi: 10.1016/j.jacc.2015.08.035
23. Zhang LJ, Wang Y, Schoepf UJ, Meinel FG, Bayer RR. 2nd, Qi L, et al. Image quality, radiation dose, and diagnostic accuracy of prospectively ECG-triggered high-pitch coronary CT angiography at 70 kVp in a clinical setting: comparison with invasive coronary angiography. *Eur Radiol.* (2016) 26:797–806. doi: 10.1007/s00330-015-3868-z
24. Sand NPR, Veien KT, Nielsen SS, Nørgaard BL, Larsen P, Johansen A, et al. Prospective comparison of FFR derived from coronary CT angiography with SPECT perfusion imaging in stable coronary artery disease: the ReASSESS study. *JACC Cardiovasc Imaging.* (2018) 11:1640–50. doi: 10.1016/j.jcmg.2018.05.004
25. Agatston AS, Janowitz WR, Hildner FJ, Zusmer NR, Viamonte M Jr, Detrano R. Quantification of coronary artery calcium using ultrafast computed tomography. *J Am Coll Cardiol.* (1990) 15:827–32. doi: 10.1016/0735-1097(90)90282-T
26. Hecht HS, Blaha MJ, Kazerooni EA, Cury RC, Budoff M, Leipsic J, et al. CAC-DRS: coronary Artery Calcium Data and Reporting System. An expert consensus document of the Society of Cardiovascular Computed Tomography (SCCT). *J Cardiovasc Comput Tomogr.* (2018) 12:185–91. doi: 10.1016/j.jcct.2018.03.008
27. Sekimoto T, Akutsu Y, Hamazaki Y, Sakai K, Kosaki R, Yokota H, et al. Regional calcified plaque score evaluated by multidetector computed tomography for predicting the addition of rotational atherectomy during percutaneous coronary intervention. *J Cardiovasc Comput Tomogr.* (2016) 10:221–8. doi: 10.1016/j.jcct.2016.01.004
28. van Rosendael AR, Narula J, Lin FY, van den Hoogen IJ, Gianni U, Al Hussein Alawamlh O, et al. Association of high-density calcified 1K plaque with risk of acute coronary syndrome. *JAMA Cardiol.* (2020) 5:282–90. doi: 10.1001/jamacardio.2019.5315
29. van Rosendael AR, Shaw LJ, Xie JX, Dimitriu-Leen AC, Smit JM, Scholte AJ, et al. Superior risk stratification with coronary computed tomography angiography using a comprehensive atherosclerotic risk score. *JACC Cardiovasc Imaging.* (2019) 12:1987–97. doi: 10.1016/j.jcmg.2018.10.024
30. F. Milletari, N. Navab and S. Ahmadi. V-Net: Fully Convolutional Neural Networks for Volumetric Medical Image Segmentation. In: *2016 Fourth International Conference on 3D Vision (3DV)*. Stanford, CA (2016). p. 565–71.
31. Hicks KA, Tcheng JE, Bozkurt B, Chaitman BR, Cutlip DE, Farb A, et al. 2014 ACC/AHA Key data elements and definitions for cardiovascular endpoint events in clinical trials: a report of the American College of Cardiology/American Heart Association task force on clinical data standards (writing committee to develop cardiovascular endpoints data Standards). *J Am Coll Cardiol.* (2015) 66:403–69. doi: 10.1016/j.jacc.2014.12.018
32. Thygesen K, Alpert JS, Jaffe AS, Chaitman BR, Bax JJ, Morrow DA, et al. Fourth universal definition of myocardial infarction (2018). *Circulation.* (2018) 138:e618–51. doi: 10.1161/CIR.0000000000000617
33. Dreyer RP, Tavella R, Curtis JP, Wang Y, Pauspathy S, Messenger J. et al. Myocardial infarction with non-obstructive coronary arteries as compared with myocardial infarction and obstructive coronary disease: outcomes in a Medicare population. *Eur Heart J.* (2020) 41:870–8. doi: 10.1093/eurheartj/ehz403
34. Curzen N, Nicholas Z, Stuart B, Wilding S, Hill K, Shambrook J, et al. Fractional flow reserve derived from computed tomography coronary angiography in the assessment and management of stable chest pain: the FORECAST randomized trial. *Eur Heart J.* (2021) 42:3844–52. doi: 10.1093/eurheartj/ehab444
35. Kimura T, Shiomi H, Kuribayashi S, Takaaki I, Susumu K, Hiroshi I, et al. Cost analysis of non-invasive fractional flow reserve derived from coronary computed tomographic angiography in Japan. *Cardiovasc Interv Ther.* (2015) 30:38–44. doi: 10.1007/s12928-014-0285-1
36. Chinnaiyan KM, Safian RD, Gallagher ML, George J, Dixon SR, Bilolikar AN, et al. Clinical use of CT-derived fractional flow reserve in the emergency department. *JACC Cardiovasc Imaging.* (2020) 13:452–61. doi: 10.1016/j.jcmg.2019.05.025
37. Antoniades C, West HW. Coronary CT angiography as an "one-stop shop" to detect the high-risk plaque and the vulnerable patient. *Eur Heart J.* (2021) 42:3853–5. doi: 10.1093/eurheartj/ehab538
38. Nørgaard BL, Leipsic J, Gaur S, Seneviratne S, Ko BS, Ito H. et al. Diagnostic performance of noninvasive fractional flow reserve derived from coronary computed tomography angiography in suspected coronary artery disease: the NXT trial (Analysis of Coronary Blood Flow Using CT Angiography: Next Steps). *J Am Coll Cardiol.* (2014) 63:1145–55. doi: 10.1016/j.jacc.2013.11.043
39. Finck T, Hardenberg J, Will A, Hendrich E, Haller B, Martinoff S. et al. 10-year follow-up after coronary computed tomography angiography in patients with suspected coronary artery disease. *JACC Cardiovasc Imaging.* (2019) 12:1330–8. doi: 10.1016/j.jcmg.2018.07.020

Conflict of Interest: UJS is a consultant for and/or receives research support from Bayer, Bracco, Elucid Bio, Guerbet, HeartFlow, Keya Medical, and Siemens Healthineers.

The remaining authors declare that the research was conducted in the absence of any commercial or financial relationships that could be construed as a potential conflict of interest.

Publisher's Note: All claims expressed in this article are solely those of the authors and do not necessarily represent those of their affiliated organizations, or those of the publisher, the editors and the reviewers. Any product that may be evaluated in this article, or claim that may be made by its manufacturer, is not guaranteed or endorsed by the publisher.

frontiers in Cardiovascular Medicine

CASE REPORT
published: 02 February 2022
doi: 10.3389/fcvm.2022.812765

Case Report: Biatrial Myxoma With Pulmonary Embolism and Cerebral Embolism: Clinical Experience and Literature Review

Haifeng Ran†, Guiqin Chen†, Jie Hu, Yulun He, Junwei Liu, Fangling Li, Heng Liu and Tijiang Zhang**

Department of Radiology, The Affiliated Hospital of Zunyi Medical University, Medical Imaging Center of Guizhou Province, Zunyi, China

OPEN ACCESS

Edited by:
Navneet Narula, NYU Grossman School of Medicine, United States

Reviewed by:
Barun Bagga, New York University, United States
Francesca Bursi, University Hospital of Modena, Italy
Konstantin V. Zavadovsky, Russian Academy of Sciences (RAS), Russia

***Correspondence:**
Heng Liu
zmcliuh@163.com
Tijiang Zhang
tijzhang@163.com

†These authors have contributed equally to this work and share first authorship

Specialty section:
This article was submitted to Cardiovascular Imaging, a section of the journal Frontiers in Cardiovascular Medicine

Received: *11 November 2021*
Accepted: *10 January 2022*
Published: *02 February 2022*

Citation:
Ran H, Chen G, Hu J, He Y, Liu J, Li F, Liu H and Zhang T (2022) Case Report: Biatrial Myxoma With Pulmonary Embolism and Cerebral Embolism: Clinical Experience and Literature Review. Front. Cardiovasc. Med. 9:812765. doi: 10.3389/fcvm.2022.812765

Cardiac myxoma is a common benign primary intracardiac tumor in the general population, and it is generally characterized as a benign tumor, and the morbidity of biatrial myxoma is low. Cases of biatrial myxoma in young patients are extremely rare. Furthermore, severe complications of cardiac myxoma, such as cerebral embolism, can have fatal consequences. Imaging can effectively assist in making a correct diagnosis and a safe and efficient surgical treatment plan. In this case report, we describe a unique case of a young woman who presented with biatrial myxoma accompanied by pulmonary embolism and cerebral embolism. Computed tomography pulmonary angiography (CTPA) detected multiple filling defects in the bilateral cardiac and bilateral inferior pulmonary artery basal branches. Transthoracic echocardiography (TTE) revealed irregular isoechoic masses in the bilateral atrium. Postoperative histopathology confirmed a biatrial myxoma. The patient was discharged on the ninth day after surgery.

Keywords: biatrial myxoma, pulmonary embolism, cerebral embolism, computed tomography, magnetic resonance imaging, echocardiography

INTRODUCTION

Cardiac myxoma is a common benign primary intracardiac tumor with an incidence rate of 0.0017% (1). Atrial myxoma occurs most commonly in middle-aged and older women, and the most frequent site of cardiac myxoma is the left atrium, followed by the right atrium. However, biatrial myxoma is relatively rare, and contributes to only 2.5% of the total incidence of cardiac myxoma (2, 3). In particular, biatrial myxoma complicating pulmonary embolism and cerebral embolism is extremely rare in young patients. To the best of our knowledge, such cases have not yet been reported in the literature. The awareness of embolic events due to atrial myxoma in young patients is still unsystematic and incomplete. When fragments of biatrial myxoma produce complicating pulmonary embolism and cerebral embolism, patients will be in a critical situation, and it is essential to diagnose and treat the patient as soon as possible to stop the aggravation of the disease and save the patient's life. In this article, we describe a rare biatrial myxoma complicated by pulmonary embolism and cerebral embolism, and review its clinical and imaging characteristics reported in previous cases. These characteristics help clinicians and radiologists pay attention to this disease and can effectively assist in establishing accurate diagnosis and developing a safe and efficient surgical treatment plan.

CASE DESCRIPTION

A 17-year-old girl presented to our hospital on August 22, 2021 with clouding of consciousness for more than 3 days. At 3+days prior, the patient was unable to speak the patient was unable to speak when called softly and unable to open the right eye, combined with involuntary movements of the limbs and incontinence. The patient visited the local hospital immediately, where relevant tests were performed, suggesting intracranial lesions. Since the specific treatment measures were unavailable at the previous hospital, she was transferred to our hospital for further treatment. There was no history of trauma or familial genetic diseases, such as high blood pressure and diabetes. Physical examination revealed a body temperature of 37.0°C, heart rate of 110 bpm, regular heart rhythm, blood pressure of 113/77 mmHg, and no pathological murmurs in the valve region; pulmonary auscultation revealed coarse rales in the entire lung. The pupils were equal, round, and pupillary light reflexes were delayed. Both lower limbs exhibited hypertonia and hyperreflexia of the knee and tendon reflexes. Laboratory examinations revealed the following levels (normal range): coagulation function test showed D-dimer was 0.57 mg/L (<0.5 mg/L) and fibrinogen was 5.82 g/L (2.00–4.00 g/L). Routine blood tests showed that the absolute value of neutrophils was 7.38×10^9/L (1.8×10^9/L–6.3×10^9/L). Infection-related markers showed that the hypersensitive C-reactive protein level was 111.563 mg/L (0.068–8.200 mg/L). Creatine kinase, α-hydroxybutyrate dehydrogenase, and lactate dehydrogenase levels were 148 U/L (26–140 U/L), 218 U/L (90–180 U/L), and 295 U/L (140–271 U/L), respectively. Computed tomography pulmonary angiography (CTPA) detected filling defects in the right atrium, left atrium, and left lower pulmonary basilar artery (**Figure 1**), and a diagnosis of Pulmonary embolism was made. Transthoracic echocardiography (TTE) revealed irregular iso-echoic masses in the bilateral atrium that were likely myxomas, given their location and appearance in a young patient; the myxoma in the left atrium measured approximately 38 × 21 mm, and it was attached to the junction of the lower part of the interatrial septum (IAS) and the root of the anterior mitral leaflet; in the right atrium it measured approximately 51 × 27 mm, and it was attached to the lower part of the IAS (**Figure 2A**). These masses resulted in the acceleration of the tricuspid valve antegrade flow (**Figure 2B**). Craniocerebral computed tomography (CT) showed extensive hypodensity in the bilateral parts of the pons and patchy hypodensity in the left corona radiata area and bilateral basal ganglia areas. Magnetic resonance imaging (MRI) also revealed extensive hypointensity on T_1-weighted imaging and hyperintensity on T_2-weighted imaging in the bilateral parts of the pons, and a patchy hyperintensity on T_2-weighted imaging in the bilateral basal ganglia areas; bilateral centrum semiovale; and right frontoparietal lobe, which presented as high signal on diffusion-weighted imaging (DWI) (**Figure 3**). This confirmed

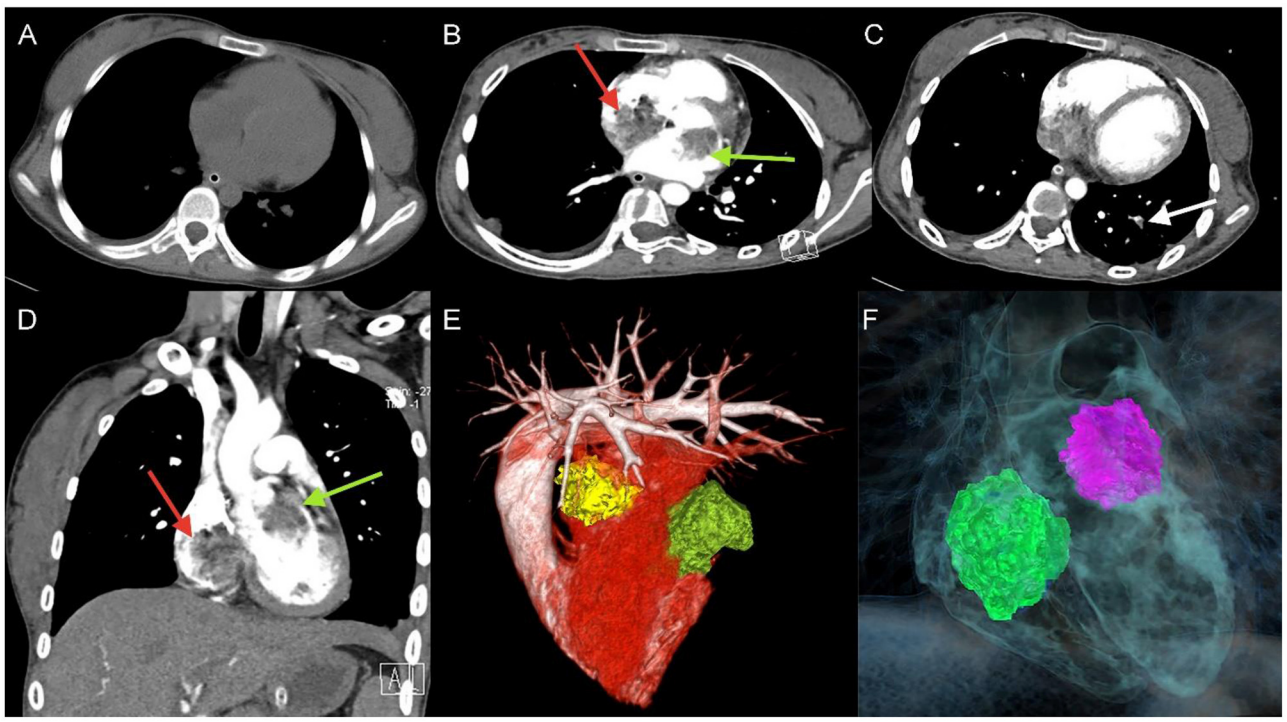

FIGURE 1 | Unenhanced thoracic CT **(A)**, axial and coronal views of Computed tomography pulmonary angiography (CTPA) detected filling defects in right atrium (red arrow), left atrium (green arrow) **(B,D)**, and left lower pulmonary basilar artery (white arrow) **(C)**, three-dimensional reconstruction of heart **(E)** and **(F)** corresponding schematic illustration demonstrating the biatrial myxoma.

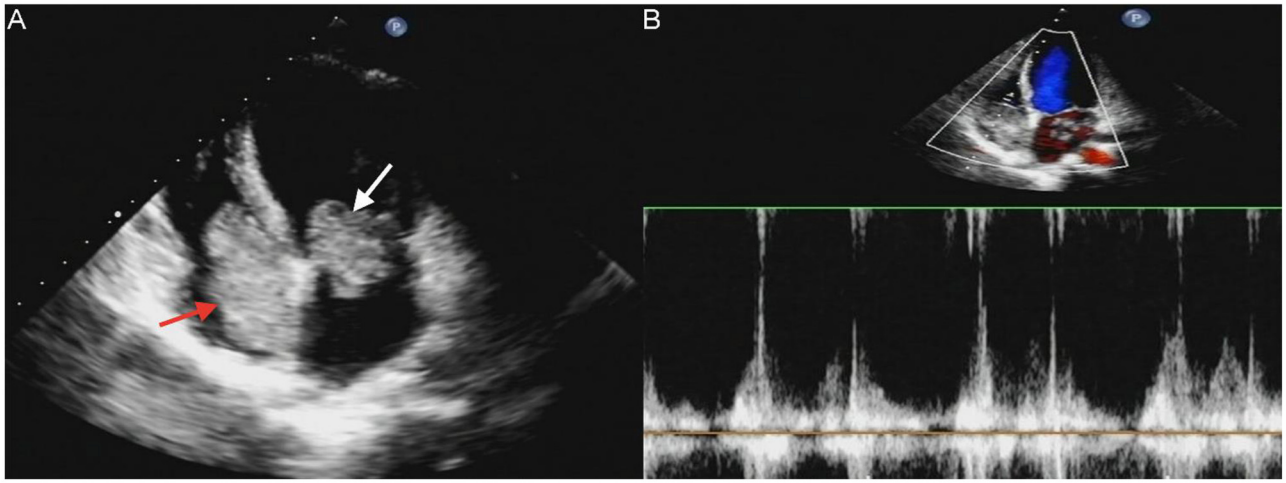

FIGURE 2 | Transthoracic echocardiography (TTE) revealed masses attached to the atrial septum in the left atrial cavity (white arrow) and the right atrial cavity (red arrow) **(A)**. Acceleration of tricuspid valves antegrade flow **(B)**.

the diagnosis of brain ischemia. To prevent thrombosis, low molecular weight heparin calcium (subcutaneous injection, 0.4 ml/12 h) was commenced on the second day of admission and continued until discharge. The patient underwent successful removal surgery for a biatrial myxoma. The masses were sent for histological examination, which confirmed the presence of a myxomatous matrix containing myxoma cells (**Figure 4**). The patient recovered uneventfully and was discharged 9 days after the procedure. The patient has been followed-up postoperatively for over 2.5 months, and limb motor function of the patient has recovered to some degree, but there is intellectual and cognitive decline.

LITERATURE REVIEW

In order to present the literature review, case reports of all biatrial myxoma among child and adolescent patients in the English language were searched from the PubMed, Web of Science, and Ovid databases, dating between January 1, 1980 and August 31, 2021. Key words were used for the search, which included "biatrial myxoma," "bilateral atrial myxoma," "bilateral Atrial myxomas," "pulmonary embolism," and "cerebral embolism." The flow chart of the literature screening process is presented in **Figure 5**. A total of five articles involving five cases were included in the analysis. For each case, we documented the first author, publication year, and the patient's age, sex, presentation, tumor size, image features, operation, outcome, and follow-up results (**Table 1**).

According to the literature, from January 1980 to August 2021, only 44 cases of biatrial myxoma have been reported. Our results revealed a predominance of biatrial myxoma between 40 and 65 years of age (52.2% of the cases), however, only six cases have been reported for patients of 18 years or less (about 13.6%; including of our case) of biatrial myxoma, comprising three girls and three boys, with a female to male ratio of 1:1. Remarkably,

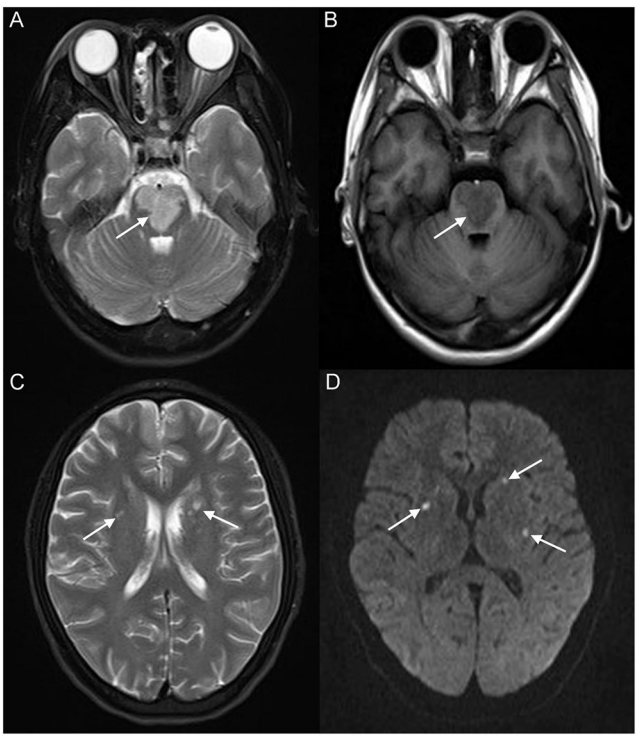

FIGURE 3 | Brain magnetic resonance imaging (MRI) revealed extensive hyperintensity on T_2-weighted imaging and hypointensity on T_1-weighted imaging of the bilateral parts of the pons (white arrow) **(A,B)**; a patchy hyperintensity on T_2-weighted imaging of the bilateral basal ganglia, bilateral centrum semiovale (white arrow) **(C)**, and right frontoparietal lobe, which presented a high signal on diffusion-weighted imaging (DWI) (white arrow) **(D)**.

the presentation of these patients was predominantly associated with embolic events, such as pulmonary embolism and cerebral embolism. However, all patients with pulmonary and cerebral

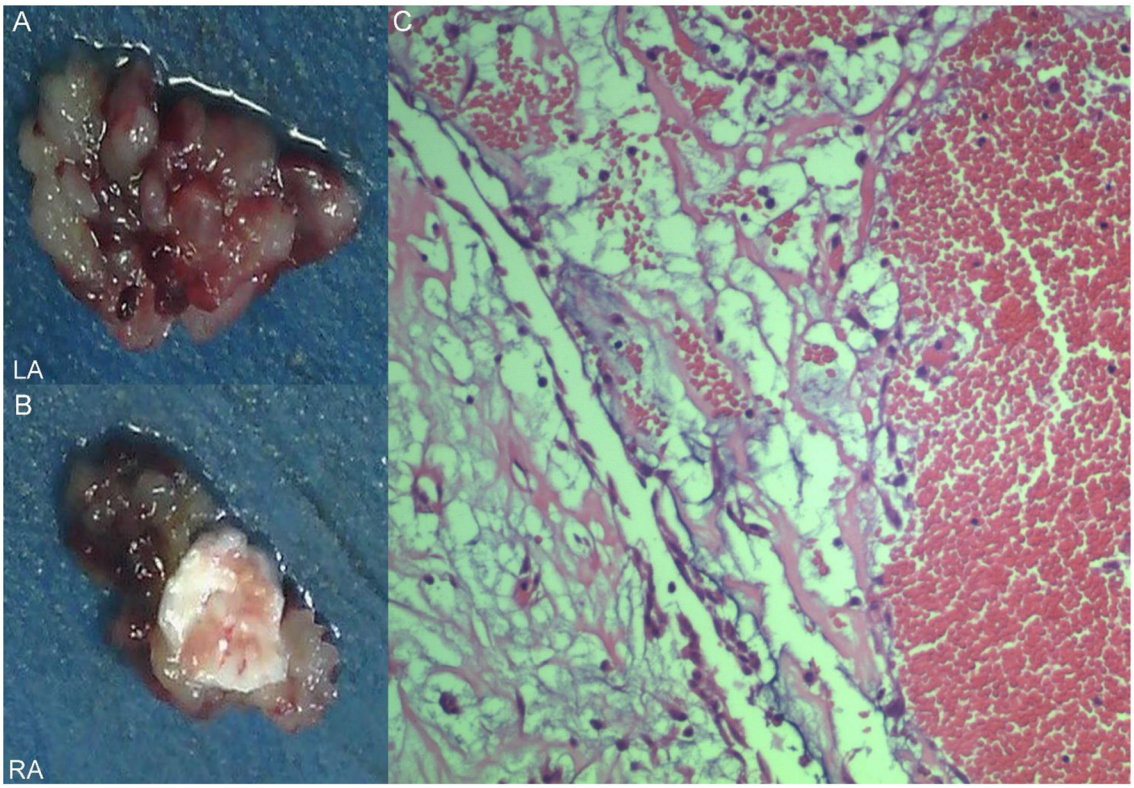

FIGURE 4 | Excised villous biatrial atrial myxoma **(A,B)** and histology of atrial myxoma. Acid-mucopolysaccharide matrix with characteristic astrocytes and spindle cells which have ovoid nuclei and are surrounded by thin-walled capillaries (Hematoxylin and Eosin, ×200) **(C)**.

embolism had only one or the other, and the occurrence of both pulmonary and cerebral embolism simultaneously has not been reported. Fortunately, most patients were discharged after surgical operations, suggesting that biatrial myxoma has a relatively good prognosis.

DISCUSSION AND CONCLUSIONS

In this case report, we present the case of a 17-year-old girl with biatrial myxoma, which is a rare, surgically correctable underlying cause of stroke and acute pulmonary embolism in a young patient. According to the clinical presentations and the results of echocardiography, clinicians suspected that the biatrial mass was a cardiac myxoma. As mentioned in the literature, cardiac myxoma is the most frequent benign tumor of primary cardiac tumors, accounting for more than 50% of primary cardiac tumors in adults, but only 5% occur in adolescents (6) and the incidence of cardiac myxoma is approximately 0.0008–0.015% (9). In addition, approximately 75% of cardiac myxomas involve the left atrium and approximately 20% of them are found in the right atrium, and cases of myxoma arising in the bilateral atrium are extremely rare, accounting for only 2.5% of the total incidence (10, 11). According to the literature review, only six cases of biatrial myxoma have been reported before (including our case) in pediatric patients. Moreover, only our patient had a biatrial myxoma complicated by pulmonary embolism and cerebral embolism.

The clinical manifestations and symptoms of cardiac myxomas vary and are not specific and can be divided into the following three groups: first, obstructive manifestations occur most frequently in approximately 50% of patients with atrial myxoma, including dizziness and dyspnea; second, embolization symptoms of myxoma, which affect more than one-third of patients with cardiac myxoma, and the presentations depend on the location of cardiac myxoma, such as pulmonary hypertension, chest pain, and severe headache; third, systemic symptoms, such as palpitation, fatigue, and fever, occur in approximately 58% of patients with cardiac myxoma (12, 13). However, patients with cardiac myxoma can also be asymptomatic (14). In our review, the most frequent symptom of the patients was dyspnea; subsequently, syncope and palpitations were also common.

Cardiac myxoma may cause embolic events during tumor tissue shedding, and cases of obstruction are relatively common in cardiac myxomas, and the morbidity rate of embolism is approximately 30–40% (14). Neurologic events are the most common embolic events followed by systemic embolic events, typically occurring at a rate of 42 and 29%, respectively. However, pulmonary embolic events are rare (15). Pulmonary embolism and cerebral stroke are uncommon but extremely significant complications of cardiac myxoma, with the risk of embolic

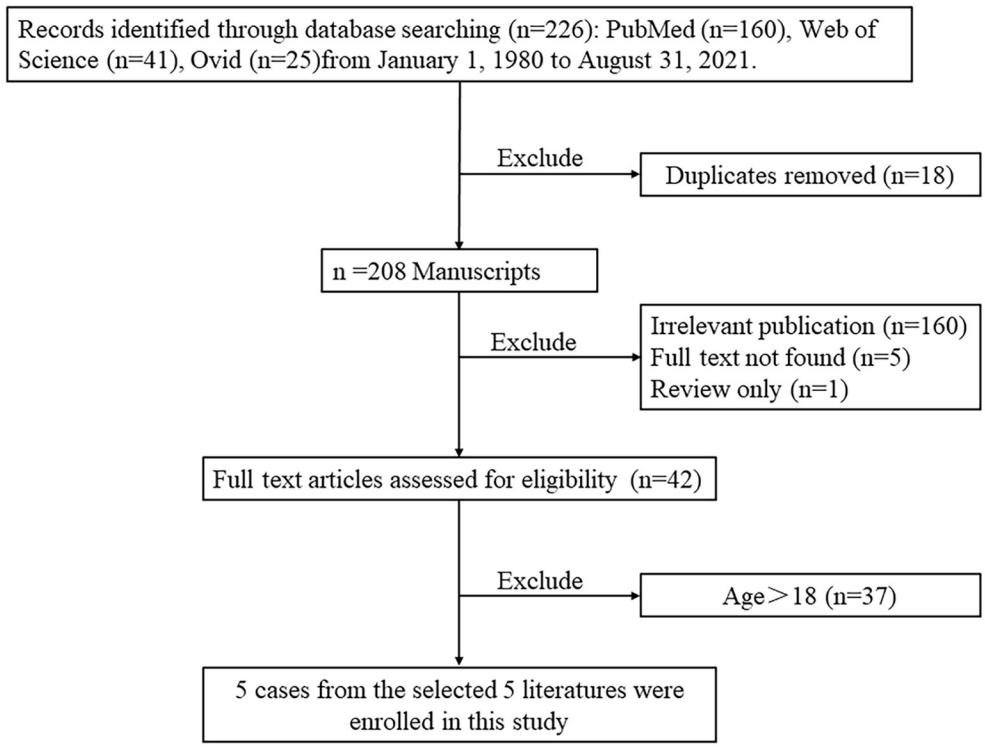

FIGURE 5 | The flow chart of the literature screening process for biatrial myxoma in children and adolescent patients.

events in cases of cardiac myxoma associated with the mass's appearance; typically, villous myxomas are more likely to cause embolism (16). Acute embolic stroke occurs when shedding tumor tissue reaches the cerebrovascular system, and it is often associated with high rates of mortality and disability, which poses a great risk to the life of the patients. Atrial myxomas have become a potential source of emboli; therefore, the primary presentation of many patients with a clinical history of myxomas is stroke (17, 18). In our case, the primary reason for the patient to go to the hospital for treatment was unconsciousness. Brain MRI revealed territorial cerebral infarction in the bilateral parts of the pons and small area cerebral infarction in the bilateral basal ganglia areas, bilateral centrum semiovale, and right frontoparietal lobe.

Pulmonary embolic events are rare, but when they occur, it is important to identify the source of the embolus, and in previous reviews of the literature, the majority of emboli originated from deep venous thrombosis (DVT), accounting for about 50–70%. In addition to DVT, cancer-related emboli are also quite common (19). Clinically significant embolic events are uncommon in patients with atrial myxoma. However, in cases of right atrial or right ventricular myxoma, embolectomy of tumor fragments into the pulmonary vasculature with subsequent pulmonary hypertension has been reported (14). In the early stages of pulmonary embolism, the clinical symptoms and imaging manifestations are atypical, and it is easy to misdiagnose pulmonary embolism as pneumonia; however, the role of non-contrast chest CT scans in the diagnosis of pulmonary embolism is limited; currently, the preferred technique for the diagnosis of pulmonary embolism is CTPA, which can detect filling defects in the pulmonary circulation and help to confirm the diagnosis of pulmonary embolism, and it is clinically important to assess the severity of a patient's pulmonary embolism based on the results of CTPA (20). In our case, infiltrates were seen in the posterior basal segment of the left lower lung lobe on non-contrast chest CT and the patient was diagnosed with pneumonia; subsequent CTPA clearly showed the infiltrates to be filling defects of the pulmonary artery.

Imaging such as CT, MRI, TTE, and CTPA play an important role in the preoperative diagnosis of cardiac myxoma. Transthoracic echocardiography can reveal the location of the tumor attachment and the appearance features of the mass. Computed tomography pulmonary angiography is a useful tool that shows the location, size, and appearance of pulmonary emboli. Imaging approaches can play a key role in the diagnosis of symptomatic or asymptomatic cases. We recommend non-invasive imaging examinations for preoperative diagnosis of patients with cardiac myxoma. According to the results of these examinations, the patients underwent surgery and the mass was totally resected, and their operation was successful.

Once the correct diagnosis has been validated, an effective treatment strategy should be determined. Surgical excision of the cardiac myxoma is the principal treatment modality and should be considered as the preferred option (21). Prompt surgical treatment is indicated to decrease the risk of complications and sudden death. However, our case represents a very

TABLE 1 | The cases of biatrial. myxoma in children and adolescent patients from the literature review.

Case (No.)	References	Sex	Age	Presentation	Tumor size (mm)		Image feature	Operation	Outcome	Follow-up (months)
					LA	RA				
1	Hanly et al., (4)	F	14	Bilateral pleuritic chest pain/loss of energy	NM	NM	A-mode: sonic mass in the left atrium, and right atrium.	Yes	Discharged	16
2	Deshpande et al., (5)	F	18	Congestive heart failure	70 × 45 × 25	55 × 50 × 30	TTE: biatrial cardiac masses.	Yes	Discharged	24
3	Cilliers et'al. (6)	M	8	Sudden onset of shortness of breath	39 × 26	6 × 38	X ray: large globular heart. TTE: large pedunculated biatrial masses.	Yes	Discharged	—
4	Mahilmaran et al., (7)	M	12	Fatigability, swelling of the legs, facial puffiness, abdominal distention, progressive breathlessness	30 × 19	80 × 40	TTE: an 8 × 4 cm myxoma arising from the right atrium, another pedunculated myxoma, 3 × 1.9 cm, was seen in the left atrium.	Yes	Discharged	24
5	Ananthanarayanan et al., (8)	M	14	Transient ischemic attack	60 × 40	40 × 30	TTE: biatrial myxoma attached to the interatrial septum.	Yes	Discharged	—
6	PC	F	17	Loss of consciousness	38 × 21	51 × 27	TTE: irregular iso-echoic masses in bilateral atrium. CTPA: filling defects in right atrium, left atrium, and left lower pulmonary basilar artery. Brain MRI: extensive hyperintensity on T2-weighted imaging and hypointensity on T1-weighted imaging of the bilateral parts of the pons.	Yes	Discharged	2.5

PC, present case; F, female; M, male; LA, left atrium; RA, right atrium; NM, not mention; TTE, Transthoracic echocardiography; CTPA, computed tomography pulmonary angiography; MRI, magnetic resonance imaging.

complex situation of biatrial myxoma complicated by pulmonary embolism and cerebral embolism, and therefore, careful attention should be paid to certain perioperative details to achieve a predictable and successful surgical outcome.

Clinically, cases of cardiac myxoma are common; however, cases of bilateral myxoma combined with pulmonary embolism and cerebral infarction are rare. The clinical symptoms of myxoma are complex and variable, and patients may even be asymptomatic, based on whether valves are obstructed by cardiac myxoma and occurrence of systemic embolism and secondary symptoms. Computed tomography, MRI, TTE, and other imaging methods can effectively assist in making a definitive diagnosis and provide a guarantee for the treatment and prognosis of patients with myxoma. Once a diagnosis is established, surgical management is the primary treatment.

DATA AVAILABILITY STATEMENT

The original contributions presented in the study are included in the article/supplementary material, further inquiries can be directed to the corresponding author/s.

ETHICS STATEMENT

The studies involving human participants were reviewed and approved by the Ethics Committee of The Affiliated Hospital of Zunyi Medical University. Written informed consent to participate in this study was provided by the participants' legal guardian/next of kin. Written informed consent was obtained from the individual(s), and minor(s)' legal guardian/next of kin, for the publication of any potentially identifiable images or data included in this article.

AUTHOR CONTRIBUTIONS

HR and GC: manuscript writing. JH and FL: manuscript revision. YH and JL: collection of data or analysis. HL and TZ: conception and critical review. All authors contributed to the article and approved the submitted version.

ACKNOWLEDGMENTS

The authors thank the members of their research group for useful discussions.

REFERENCES

1. Vijan V, Vupputuri A, Chandrasekharan Nair R. An unusual case of biatrial myxoma in a young female. *Case Rep Cardiol.* (2016) 2016:3545480. doi: 10.1155/2016/3545480
2. Yoon DH, Roberts W. Sex distribution in cardiac myxomas. *Am J Cardiol.* (2002) 90:563–5. doi: 10.1016/s0002-9149(02)02540-7
3. Wen XY, Chen YM Yu LL, Wang SR, Zheng HB, Chen ZB, et al. Neurological manifestations of atrial myxoma: a retrospective analysis. *Oncol Lett.* (2018) 16:4635–9. doi: 10.3892/ol.2018.9218
4. Hanly J, de Buitleir M, Shaw K, Maurer B, FitzGerald MX. Bi-atrial myxomas presenting as recurrent pulmonary emboli in a girl. *Postgrad Med J.* (1984) 60:147–50. doi: 10.1136/pgmj.60.700.147
5. Deshpande A, Kumar S, Chopra P. Recurrent, biatrial, familial cardiac myxomas. *Int J Cardiol.* (1994) 47:71–3. doi: 10.1016/0167-5273(94)90136-8
6. Cilliers AM, van Unen H, Lala S, Vanderdonck KH, Hartman E. Massive biatrial myxomas in a child. *Pediatr Cardiol.* (1999) 20:150–1. doi: 10.1007/s002469900425
7. Mahilmaran A, Seshadri M, Nayar PG, Sudarsana G, Abraham KA. Familial cardiac myxoma: Carney's complex. *Tex Heart Inst J.* (2003) 30:80–2.
8. Ananthanarayanan C, Bishnoi AK, Ramani J, Gandhi H. Dumb-bell in the heart: rare case of biatrial myxoma with mitral regurgitation. *Asian Cardiovasc Thorac Ann.* (2016) 24:796–97. doi: 10.1177/0218492316655640
9. Li Y, Li X, Wang X, Chen L. Biatrial myxoma floating like a butterfly: a case report and review of the literature. *Medicine (Baltimore).* (2018) 97:e9558. doi: 10.1097/MD.0000000000009558
10. Irani AD, Estrera AL, Buja LM, Safi HJ. Biatrial myxoma: a case report and review of the literature. *J Card Surg.* (2008) 23:385–90. doi: 10.1111/j.1540-8191.2007.00545
11. Babs Animashaun I, Akinseye OA, Akinseye LI, Akinboboye OO. Right atrial myxoma and syncope. *Am J Case Rep.* (2015) 16:645–7. doi: 10.12659/AJCR.894513
12. Kesav P, John S, Joshi P, Gaba WH, Hussain SI. Cardiac myxoma embolization causing ischemic stroke and multiple partially thrombosed cerebral aneurysms. *Stroke.* (2021) 52:e10–4. doi: 10.1161/STROKEAHA.120.031679
13. Azari A, Moravvej Z, Chamanian S, Bigdelu L. An unusual biatrial cardiac myxoma in a young patient. *Korean J Thorac Cardiovasc Surg.* (2015) 48:67–9. doi: 10.5090/kjtcs.2015.48.1.67
14. Reynen K. Cardiac myxomas. *N Engl J Med.* (1995) 333:1610–7. doi: 10.1056/NEJM199512143332407
15. Rokadia HK, Heresi GA, Tan CD, Raymond DP, Budd GT, Farver C, et al. A 33-year-old man with multiple bilateral pulmonary pseudoaneurysms. *Chest.* (2015) 148:e112–7. doi: 10.1378/chest.15-0624
16. Aydin C, Taşal A, Ay Y, Vatankulu MA, Inan B, Bacaksiz A, et al. A Giant right atrial villous myxoma with simultaneous pulmonary embolism. *Int J Surg Case Rep.* (2014) 5:206–8. doi: 10.1016/j.ijscr.2013.11.014
17. Waikar HD, Jayakrishnan AG, Bandusena BSN, Priyadarshan P, Kamalaneson PP, Ileperuma A, et al. Left atrial myxoma presenting as cerebral embolism. *J Cardiothorac Vasc Anesth.* (2020) 34:3452–61. doi: 10.1053/j.jvca.2020.06.061
18. Lee VH, Connolly HM, Brown RD Jr. Central nervous system manifestations of cardiac myxoma. *Arch Neurol.* (2007) 64:1115–20. doi: 10.1001/archneur.64.8.1115
19. Ma G, Wang D, He Y, Zhang R, Zhou Y, Ying K. Pulmonary embolism as the initial manifestation of right atrial myxoma: a case report and review of the literature. *Medicine (Baltimore).* (2019) 98:e18386. doi: 10.1097/MD.0000000000018386
20. Howard L. Acute pulmonary embolism. *Clin Med (Lond).* (2019) 19:243–7. doi: 10.7861/clinmedicine.19-3-247
21. Wan Y, Du H, Zhang L, Guo S, Xu L, Li Y, et al. Multiple cerebral metastases and metastatic aneurysms in patients with left atrial Myxoma: a case report. *BMC Neurol.* (2019) 19:249. doi: 10.1186/s12883-019-1474-4

Conflict of Interest: The authors declare that the research was conducted in the absence of any commercial or financial relationships that could be construed as a potential conflict of interest.

frontiers in Cardiovascular Medicine

ORIGINAL RESEARCH
published: 15 February 2022
doi: 10.3389/fcvm.2021.816985

A Systematic Quality Scoring Analysis to Assess Automated Cardiovascular Magnetic Resonance Segmentation Algorithms

*Elisa Rauseo[1,2], Muhammad Omer[3], Alborz Amir-Khalili[3], Alireza Sojoudi[3], Thu-Thao Le[4], Stuart Alexander Cook[4,5], Derek John Hausenloy[4,5,6,7,8], Briana Ang[4], Desiree-Faye Toh[4], Jennifer Bryant[4], Calvin Woon Loong Chin[4], Jose Miguel Paiva[3], Kenneth Fung[1,2], Jackie Cooper[1], Mohammed Yunus Khanji[1,2,9], Nay Aung[1,2] and Steffen Erhard Petersen[1,2,10,11]**

[1] NIHR Barts Biomedical Research Centre, William Harvey Research Institute, Queen Mary University, London, United Kingdom, [2] Barts Heart Centre, St Bartholomew's Hospital, Barts Health NHS Trust, London, United Kingdom, [3] Circle Cardiovascular Imaging, Calgary, AB, Canada, [4] National Heart Centre Singapore, Singapore, Singapore, [5] Cardiovascular and Metabolic Disorders Program, Duke-National University of Singapore, Singapore, Singapore, [6] Yong Loo Lin School of Medicine, National University Singapore, Singapore, Singapore, [7] The Hatter Cardiovascular Institute, University College London, London, United Kingdom, [8] Cardiovascular Research Center, College of Medical and Health Sciences, Asia University, Taichung, Taiwan, [9] Department of Cardiology, Newham University Hospital, Barts Health NHS Trust, London, United Kingdom, [10] Health Data Research UK, London, United Kingdom, [11] Alan Turing Institute, London, United Kingdom

OPEN ACCESS

Edited by:
Salah D. Qanadli,
University of Lausanne, Switzerland

Reviewed by:
Filippo Cademartiri,
Gabriele Monasterio Tuscany Foundation (CNR), Italy
Marcos Martin-Fernandez,
University of Valladolid, Spain

***Correspondence:**
Steffen Erhard Petersen
s.e.petersen@qmul.ac.uk

Specialty section:
This article was submitted to Cardiovascular Imaging, a section of the journal Frontiers in Cardiovascular Medicine

Received: 17 November 2021
Accepted: 22 December 2021
Published: 15 February 2022

Citation:
Rauseo E, Omer M, Amir-Khalili A, Sojoudi A, Le T-T, Cook SA, Hausenloy DJ, Ang B, Toh D-F, Bryant J, Chin CWL, Paiva JM, Fung K, Cooper J, Khanji MY, Aung N and Petersen SE (2022) A Systematic Quality Scoring Analysis to Assess Automated Cardiovascular Magnetic Resonance Segmentation Algorithms. Front. Cardiovasc. Med. 8:816985. doi: 10.3389/fcvm.2021.816985

Background: The quantitative measures used to assess the performance of automated methods often do not reflect the clinical acceptability of contouring. A quality-based assessment of automated cardiac magnetic resonance (CMR) segmentation more relevant to clinical practice is therefore needed.

Objective: We propose a new method for assessing the quality of machine learning (ML) outputs. We evaluate the clinical utility of the proposed method as it is employed to systematically analyse the quality of an automated contouring algorithm.

Methods: A dataset of short-axis (SAX) cine CMR images from a clinically heterogeneous population ($n = 217$) were manually contoured by a team of experienced investigators. On the same images we derived automated contours using a ML algorithm. A contour quality scoring application randomly presented manual and automated contours to four blinded clinicians, who were asked to assign a quality score from a predefined rubric. Firstly, we analyzed the distribution of quality scores between the two contouring methods across all clinicians. Secondly, we analyzed the interobserver reliability between the raters. Finally, we examined whether there was a variation in scores based on the type of contour, SAX slice level, and underlying disease.

Results: The overall distribution of scores between the two methods was significantly different, with automated contours scoring better than the manual (OR (95% CI) = 1.17 (1.07–1.28), $p = 0.001$; $n = 9401$). There was substantial scoring agreement between raters for each contouring method independently, albeit it was significantly better for automated segmentation (automated: AC2 = 0.940, 95% CI, 0.937–0.943 vs manual: AC2 = 0.934, 95% CI, 0.931–0.937; $p = 0.006$). Next, the analysis of quality scores based on different factors was performed. Our approach helped identify trends patterns of lower segmentation quality as observed for left ventricle epicardial and basal contours

with both methods. Similarly, significant differences in quality between the two methods were also found in dilated cardiomyopathy and hypertension.

Conclusions: Our results confirm the ability of our systematic scoring analysis to determine the clinical acceptability of automated contours. This approach focused on the contours' clinical utility could ultimately improve clinicians' confidence in artificial intelligence and its acceptability in the clinical workflow.

Keywords: cardiac magnetic resonance (CMR), cardiac segmentation, machine learning, automated contouring, quality control, assessment

INTRODUCTION

Cardiac magnetic resonance (CMR) is the gold standard non-invasive imaging modality for accurate quantification of cardiac chamber volume, myocardial mass and function (1). Image segmentation is an essential step in deriving such quantitative measures that provide valuable information for early detection and monitorning of a wide range of cardiovascular diseases (CVDs) (2–5). However, manual analysis of CMR images is time-consuming and prone to subjective errors, as the delineation quality strongly depends on the operator's experience (6).

Automated segmentation based on machine learning (ML) algorithms can reduce the inter- and intra-observer variability and speed up the contouring process (7). Additionally, these ML-based methods can expedite the extraction of clinically relevant information from larger image datasets. Although several studies have shown promising results in efficiency and consistency (8–10), important challenges need to be addressed before automatic contouring methods can be robustly and routinely applied in clinical practice.

Automatically generated contours often require manual operator corrections to make the results clinically acceptable (11). An adequate quality-based assessment of the performance of such tools is, therefore, needed. Several quantitative measures have been proposed to assess the quality of automated segmentation against "ground truth" reference, represented by manual contours (12). The most commonly used metrics are based on position, distance and volume overlap (13). However, these measures have a low correlation to clinical contour quality and may not predict clinicians' trust for the contouring method. Therefore, evaluating the performance of automated algorithms in terms of clinical applicability is needed.

In this paper, we describe a new method for assessing the quality of ML outputs by involving clinicians during the algorithm validation process. We evaluate the effectiveness of the proposed method as it is employed to systematically analyse the quality of an automated contouring algorithm.

We used a quality control (QC) scoring system to record the judgments of blinded clinicians on the quality of randomly presented manual and automatic contours. We evaluated the clinical acceptability of automated contouring by analyzing the degree of agreement between two segmentation methods based on the quality scores. We also assessed the scoring system's reliability between the clinicians and whether factors potentially making the segmentation more challenging would have affected the quality judgment.

Abbreviations: AC2, second-order agreement coefficient; CI, confidence interval; CMR, cardiovascular magnetic resonance; CNN, convolutional neural network; CVDs, cardiovascular diseases; DCM, dilated cardiomyopathy; DCS, dice similarity coefficient; ED, end-diastole; ES, end-systole; GUI, graphical user interface; HD, hausdorff distance; HTN, hypertension; HCM, hypertrophic cardiomyopathy; IHD, ischaemic heart disease; LV, left ventricle; LVNC, left ventricular non-compaction; ML, machine learning; NHCS, national health center singapore; OR, odds ratios; QC, quality control; RCA, reverse classification accuracy; RV, right ventricle; SAX, short-axis; SOP, standard operating procedures; UKB, united Kingdom Biobank.

METHODS

Dataset

The dataset included in this study contained short-axis (SAX) cine CMR images from 217 subjects who were participants from the National Heart Center Singapore (NHCS) Biobank. Patients' information on sex and age were not available as data were anonymised before the analysis. The study population was heterogeneous and comprised both healthy subjects (n = 42) and patients with different CVDs: dilated cardiomyopathy (DCM) (n = 33), hypertension (HTN) (n = 107), hypertrophic cardiomyopathy (HCM) (n = 13), ischaemic heart disease (IHD) (n = 15), left ventricular non-compaction (LVNC) (n = 6), and myocarditis (n = 1). It should be noted that our dataset did not include conditions with uncertain diagnosis (e.g. suspected cardiomyopathy) or with non-pathological changes in cardiac morphology (e.g. athlete's heart). Furthermore, only the images deemed of good quality were included and retained for further analysis.

Manual Image Analysis

The manual segmentation was performed by a group of experienced investigators from the National Heart Centre Singapore (NHCS), consisting of CMR consultants, well-trained clinical research fellows and engineers, using a standardized protocol described in detail in a separate publication (14). Two operators with over five years' experience (LTT and CWLC) then checked the contouring quality to select the studies deemed for further analysis.

Specifically, left ventricle (LV) endocardial and epicardial borders and the right ventricle (RV) endocardial borders were manually traced in SAX slices at end-diastole (ED) and end-systole (ES) time frames using the cvi42 post-processing software

(version 5.1.1, Circle Cardiovascular Imaging Inc., Calgary, Alberta, Canada). ED and ES phases were defined, respectively, as the image with the largest and smallest LV blood volume at visual inspection. The manual contours and the corresponding images were saved for later processing.

Automated Image Analysis

A ML algorithm trained at Circle Cardiovascular Imaging Inc. was then applied to the same set of manually annotated SAX images to obtain automated contours. A deep convolutional neural network (CNN) was trained to perform SAX image segmentation. A similar model architecture as that of the standard U-Net was adopted for this purpose, along with various data augmentation techniques to enhance the generalizability of the trained model (15). The model was trained on the UK Biobank (UKB) data, a large-scale population-based imaging study mainly composed of healthy subjects as well as individuals with some pathological conditions including HCM and HTN (16, 17). The output of the model was a pixel level classification of the image, where the classes represented one of the SAX tissues including the LV endocardium, LV epicardium, and RV endocardium. The resulting predicted segmentations of the LV and RV were finally saved to be displayed in the contour quality scoring application.

QC Scoring System

A contour quality scoring application was developed to input clinician's feedback on both manual and automated contours obtained from the same images. The application was composed of a graphical user interface (GUI) to display contoured images and offered user interactivity to rapidly parse through the data and input user's feedback on the quality of the presented contours.

The GUI of the contour quality scoring tool is shown in **Figure 1**. From the dataset constructed with both manual and corresponding automated contours, the application selected a case randomly to present to the user and expected a quality score from a predefined rubric. The left panel of the GUI showed a SAX image with the corresponding index of the image out of the total number of images available in the database. The right panel, instead, showed the same image with an overlaid contour to which the user was asked to assign a quality score. Once the user inputed the score, arrow keys on the keyboard were used to advance to the next available image in the database.

The source of the contour was not shown to the user to avoid causing any unwanted bias in the rating of the contours. In addition, multiple annotations for each image were displayed separately to receive quality rating for each contour type individually. The process continued until the user rated all cases available in the dataset, resulting in ratings received for both source of contours for each image in the dataset.

The UKB SOP for analysis of LV and RV chambers was used as a reference for assessing the quality of the contoured images (18). The quality score was assigned based on how the contour would have affected clinical outcomes or whether it was judged to be clinically plausible or not.

The scoring rubric included scores ranging from one to *four*. A score of one was assigned to significantly inaccurate segmentation and thus considered clinically unacceptable. A score of two was given to bad quality contours, which required significant manual changes to make them clinically acceptable. A score of three was assigned to fair or clinically acceptable contours with minor or negligible inaccuracies in the segmentation considered not clinically relevant. Finally, a score of four was assigned to contours considered of good quality with no changes needed.

Furthermore, as images were presented independent of spatiotemporal context, contour quality assessment was mainly based on how well the area of the delineated structure was approximated. Consequently, small contours and small deviations were rarely assigned a quality score of $\leq$2, as that was considered not clinically relevant. Special attention was given to the RV endocardial contour, especially at SAX basal slices, for which two separate regions may be contoured. In such cases, a score of three was given if the two disjoint contours sufficiently encompassed the underlying anatomy; otherwise, they were scored as two or *one*. An illustration of some contours to which raters assigned different quality scores is shown in **Figure 2**.

Four clinicians (SEP, MK, KF and ER), from a United Kingdom institution (Barts Heart Center) and varying degrees of experience in analyzing CMR were then asked to independently visualize the contours and assign quality scores using our proposed application. The results were recorded in a database for later analysis.

Firstly, we evaluated the distribution of quality scores between the two segmentation methods across all clinicians. Secondly, we analyzed the quality scores assigned by each rater to evaluate the interobserver variability among the four clincians. Finally, we examined whether there was a variation in quality according to the type of contour, SAX slice level and underlying disease.

Statistics

Wilcoxon signed-rank test was used to evaluate the differences in the distribution of quality scores between automated and manual for each physician. Combined results over all physicians, and comparison of contour type, slice level and underlying disease were tested using multi level mixed effects ordered logistic regression fitted using the meologit command in Stata. This model takes account of the clustering of ratings from different clinicians for each image. The image was fitted as a random effect with rater and segmentation method fitted as fixed effects. Odds ratios (OR) were obtained from the above model to assess whether the odds of obtaining a higher quality score differed by the method. Interaction terms were fitted to test whether fixed effects differed between manual and automated scores. A p-value lower than 0.05 was considered statistically significant.

Interobserver reliability was assessed using Gwet's second-order agreement coefficient with ordinal weighting applied (AC2) (19). Details of the calculation are given in the supplementary methods and the ordinal weights used are shown in **Supplementary Table 1**. We chose this statistics method over Cohen's Kappa because it has the advantage to assess reliability between multiple observers, and it can be adjusted for both chance agreement and misclassification errors (19, 20). It has been shown to provide a more stable reliability coefficient than

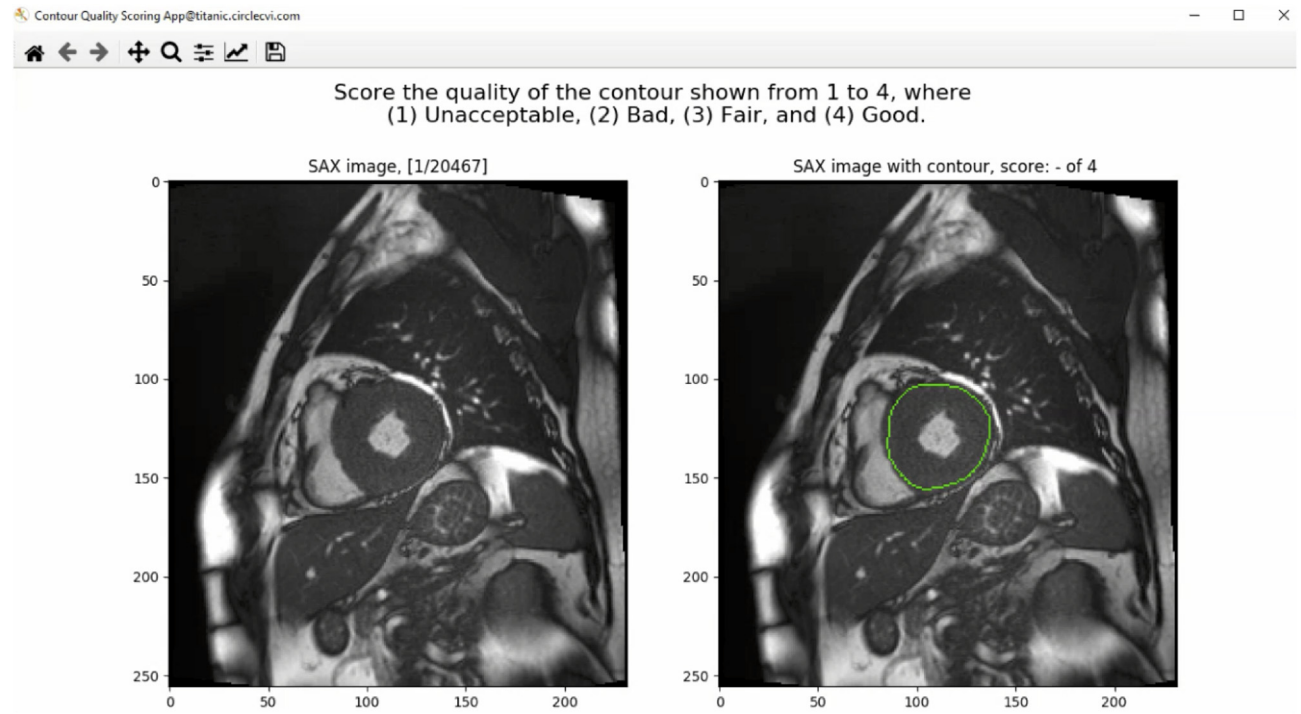

FIGURE 1 | The graphical user interface (GUI) of the contour quality scoring tool. The left panel shows the current SAX image. The right panel shows the same image with overlaid contour to which the rater is asked to assign a quality score. The title above the right panel shows a blank quality score, which will be updated when a value is entered by the user.

Kappa when prevalences differ between the categories as is the case in our data where images were much more likely to be assigned a quality score of four than a score of *one*. The reliability coefficient value and 95% confidence interval (CI) was calculated for both manual and automated contour quality scores. The interpretation of the AC2 coefficient was according to the probabilistic method for benchmarking suggested by Gwet (21). Substantial reliability corresponding to 0.61–0.80 interval was defined acceptable in this study and the benchmark category was selected as the first category with cumulative membership probability exceeding 95%.

Statistical analysis was performed using Python Version 3.6.4 (Python Software Foundation, Delaware USA) and Stata version 17 (StataCorp, Texas).

RESULTS

Four clinicians with different level of expertise generated a total of 38,991 quality scores. The overall mean quality scores assigned for manual and automated contours were 3.78 ± 0.45 (n = 18,516) and 3.78 ± 0.50 (n = 20,475), respectively. However the distribution of quality scores differed between the two segmentation methods and was statistically significant (OR (95% CI) = 1.17 (1.07–1.28), p = 0.001; n = 9401), with automated scoring better than manual on 1,068 occasions compared to 881 occasions where the manual scoring was higher.

We subsequently investigated the distribution of the scores for each rater (**Figure 3**). We observed that the difference between the mean quality scores assigned to each segmentation method was not statistically significant for most evaluators, except for rater B (**Table 1**). The distribution of quality scores after excluding rater B, showed no significant difference between the two methods (OR (95% CI) = 1.05 (0.94–1.17); p = 0.40).

The inter-observer agreement for manual and automated contours was also investigated using Gwet's AC2 agreement coefficient with ordinal weighting.

Overall, there was substantial inter-observer reliability for quality scoring of both manual and automated contours (AC2 = 0.937, 95% CI, (0.935–0.939)). In particular, the score agreement between all raters for automated contours was significantly better than for the manual segmentation (AC2 = 0.940, 95% CI, (0.937–0.943) and AC2 = 0.934, 95% CI, (0.931–0.937), respectively, p = 0.006).

All AC2 values were qualified as very good using the probabilistic benchmark procedure, with 100% membership probability for the interval 0.8–1.0. The inter-observer agreement for each method of contouring is shown in **Figure 4**.

Quality Score Analysis According to the Contour Type, Slice Level and Underlying Disease

Delineating cardiac contours might be a challenging task in some circumstances, and this might negatively impact the clinical acceptability of segmentation. For instance, manual corrections might be needed when contouring areas with increased LV trabeculation, for apical slices or RV walls. Thus, to gain more

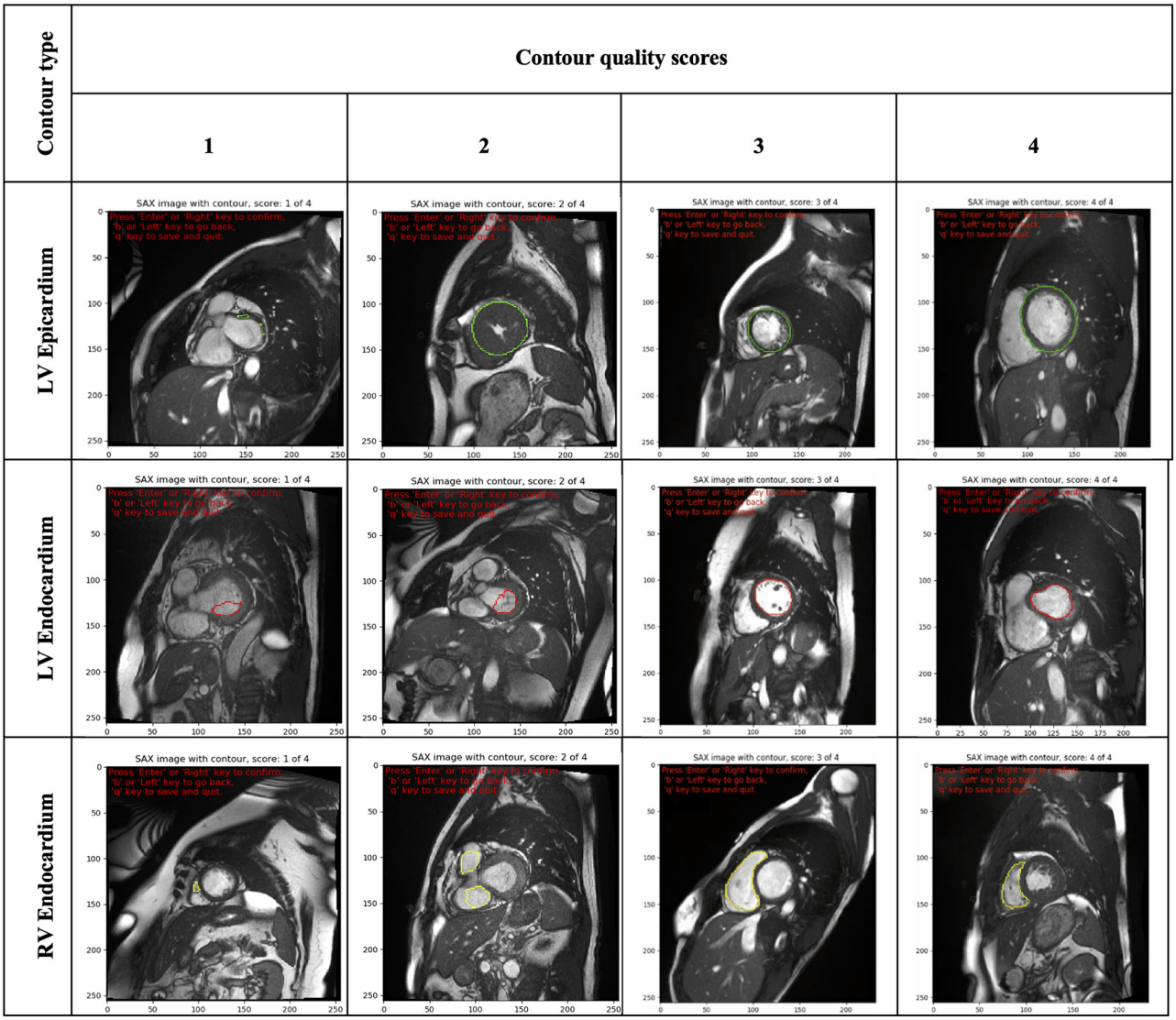

FIGURE 2 | Illustration of some contours (LV epicardial, LV endocardial and RV endocardial) showing the range of quality scores (from 1 to 4). LV, left ventricle; RV, right ventricle.

insight into the variation in quality for both sources of contours, the scores were dichotomized using multiple factors.

Firstly, we analyzed the distribution of quality scores between the two segmentation methods based on the contour type (**Figure 5**).

For manual segmentation, the mean quality scores by contour type were 3.92 ± 0.30 (n = 6,243), 3.61 ± 0.53 (n = 6,339), and 3.82 ± 0.44 (n = 5,934) for LV endocardial, LV epicardial, and RV endocardial contours, respectively. Compared to LV epicardial, both LV endocardial (OR (95% CI) = 22.89 (17.26–30.35) and RV endocardial (OR (95% CI) = 6.00 (4.74–7.58) had significantly higher quality ($p < 0.0001$). For automated segmentation, instead, the mean quality scores were 3.89 ± 0.38 (n = 7,158), 3.73 ± 0.52 (n = 6,879), and 3.73 ± 0.57 (n = 6,438) for LV endocardial, LV epicardial, and RV endocardial contours, respectively. Compared to LV epicardial, both LV endocardial (OR (95% CI) = 9.84 (7.09–13.66) and RV endocardial (OR (95% CI) = 1.68 (1.27–2.22) had significantly higher quality ($p < 0.0001$). A significant interaction was found suggesting that the differences in quality between contour types was more pronounced for the manual scores.

The segmentation complexity depends also on the slice level of the image. For instance, basal and apical images might be more challenging to contour than the mid ventricular images. For that reason, the contours quality scores were also analyzed based on the SAX slice level (**Figure 6**). For manual segmentation, the mean quality scores were 3.65 ± 0.56 (n = 1,667), 3.57 ± 0.62 (n = 1,797), and 3.82 ± 0.40 (n = 15,052), for apical, basal, and mid-ventricular levels, respectively. Compared to mid level, both basal (OR (95% CI) = 0.18 (0.13–0.25) and apical (OR (95% CI)

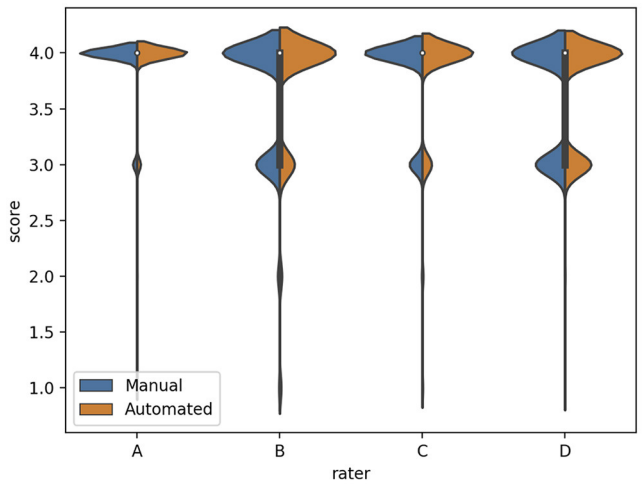

FIGURE 3 | The distribution of quality scores for each rater for both sources of contours: manual (blue) and automated (orange) segmentation.

TABLE 1 | Comparison of the mean quality score for manual and automated contours, and their corresponding Wilcoxon test p-value for statistical significance, for each rater.

Rater	Mean quality score		*P* value (Wilcoxon test)
	Manual	Automated	
A	3.94	3.93	0.29 ($n = 3,283$)
B	3.67	3.71	<0.001 ($n = 2,266$)
C	3.81	3.81	0.87 ($n = 3,281$)
D	3.68	3.69	0.56 ($n = 571$)

$= 0.44$ (0.31–0.63) had significantly lower quality scores ($p < 0.0001$). Whereas the quality scores for the automated contours were 3.63 ± 0.66 ($n = 2,084$), 3.42 ± 0.80 ($n = 1,954$), and 3.85 ± 0.40 ($n = 16,437$), for apical, basal, and mid-ventricular levels, respectively. Compared to mid level, both basal (OR (95% CI) $= 0.06$ (0.04–0.09) and apical (OR (95% CI) $= 0.29$ (0.19–0.44) had significantly lower quality scores ($p < 0.0001$). A significant interaction was found ($p < 0.0001$) suggesting that reductions in quality for basal levels were more pronounced for the automated scores. Instead, the interaction was not significant for the apical levels ($p = 0.17$).

Finally, specific changes in cardiac structures associated with some conditions might also affect the contours quality. Therefore, we analyzed whether there was a variation in manual and automated quality scores based on the underlying pathology (**Figure 7**). In particular, we analyzed the quality score assigned for both manual and automated contours in the following subsets: DCM (manual: 3.83 ± 0.04 vs automated: 3.77 ± 0.54; OR (95% CI) $= 0.59$ (0.45–0.77); $p < 0.0001$), HCM (3.67 ± 0.52 vs 3.61 ± 0.63; OR(95% CI) $= 0.83$ (0.60–1.15); $p = 0.27$), HTN (3.76 ± 0.46 vs 3.82 ± 0.45; OR (95% CI) $= 2.73$ (2.22–3.37); $p < 0.0001$), healthy controls (3.78 ± 0.47 vs 3.80 ± 0.48; OR(95% CI) $= 0.61$ (0.36–1.00); p=0.051), IHD with normal (3.78 ± 0.44 vs 3.79 ± 0.47; OR(95% CI) $= 1.44$ (0.95–2.20); p=0.09) and reduced ejection fraction (EF) (3.77 ± 0.46 vs 3.72 ± 0.63; OR(95% CI_=0.72 (0.40–1.28); $p = 0.26$), LVNC (3.84 ± 0.38 vs 3.73 ± 0.57; OR(95% CI) $= 0.67$ (0.40–1.12); $p = 0.13$), myocarditis (3.91 ± 0.29 vs 3.80 ± 0.53; OR(95% CI)= 6.77 (0.70–65.43); $p = 0.10$). Only in DCM and HTN subgroups, there were significant differences in quality between the two contouring methods. In particular, manual contours received higher quality scores than the automated ones in DCM, while an opposite trend was observed for HTN.

DISCUSSION

Overall, our results showed significant clinical acceptability of automated contours based on quality scores assigned by four clinicians. Furthermore, there was substantial agreement between the evaluators in assessing the quality of both segmentation methods. In particular, the scoring agreement was significantly better for automated segmentation. These findings confirm the accuracy of this automated segmentation method based on its clinical acceptability.

Importantly, our QC approach allowed identification of scenarios where segmentation quality differed. Analysis of the quality scores by contour type and SAX slice level revealed a significantly lower quality of the LV epicardial contours, particularly with manual segmentation. Similar results were observed for the basal and apical contours. Furthermore, the reduction in quality for basal contours was more pronounced with the automated method. The scoring analysis by pathology, instead, did not show significant differences in contour quality between the two methods, except for DCM and HTN. Such patterns of lower segmentation quality would thus be subjected to further manual changes.

Therefore, our results on a small but varied image dataset confirm the ability of this method to rapidly assess the clinical acceptance of automated contours without using quantitative comparative metrics, which rely on the availability of hight quality, thoroughly validated "ground truth" data.

Furthermore, our scoring system has proven to be reliable among clinicians with different level of experience. Finally, we have shown that a systematic scoring analysis allows the identification of the poorly segmented images that may need further manual correction.

This study confirms the importance of a quality-based assessment of automated segmentation that directly relates to the clinical practice and might supplement other comparative metrics, as described below.

In most comparative studies, the automated segmentation performance is typically assessed on labeled validation datasets, distinct from the datasets used to train the ML algorithm. The most common evaluation approach is based on comparing the predicted segmentation against a "ground truth" reference, usually represented by manual expert annotations.

Several quantitative parameters can be used to measure the agreement between manual and automated segmentation, each one presenting different properties and suitability for specific tasks (12). The most used metrics are those based on position, surfaces distance, and volumetric overlap. In particular, the Dice similarity coefficient (DSC) and the Hausdorff distance (HD) are

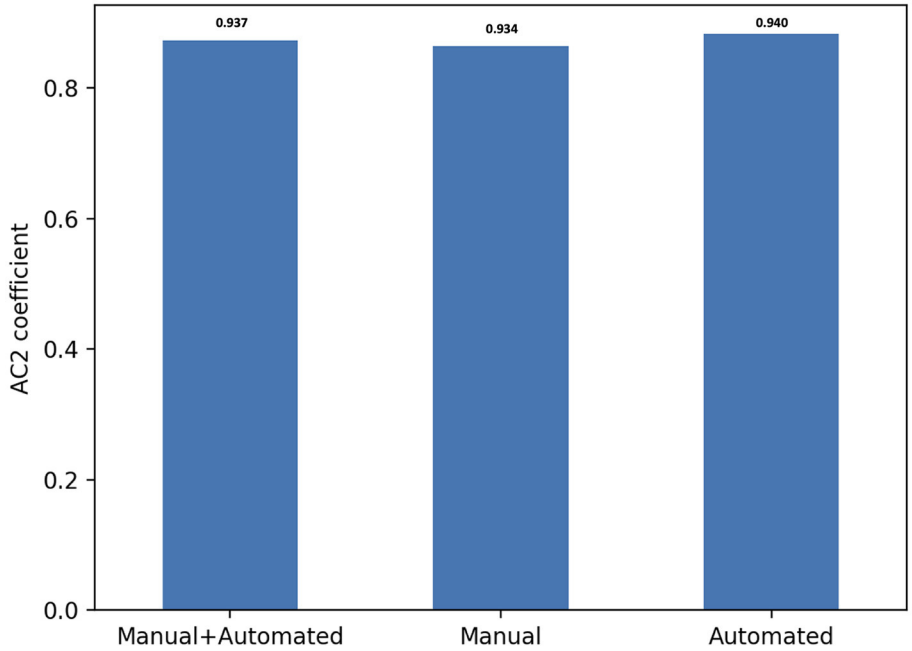

FIGURE 4 | Score agreement between all raters for manual, automated contours and both segmentation methods. The interobserver reliability is expressed using Gwet's second-order agreement coefficient with ordinal weighting applied (AC2) (y axis).

considered the best measures for the geometric quantification of boundary similarities. The DSC is a common measure of region overlap and it is mostly used in validating volume segmentations and measuring repeatability (13, 22). The HD, instead, is a distance-based measure that take into consideration the spatial position of voxels or distance between contours (12). These properties make the HD more suitable to validate algorithm where the boundary of segmented region is important (23).

Although these quantitative measures capture the differences between manual and automated contours, they might not necessarily predict whether they are clinically plausible or not.

A qualitative analysis focused on the clinical utility of contours is therefore essential to ensure the reliability of the automatically computed results and thus their acceptability in the clinical workflow.

The most common way to assess the quality of segmentation is based on expert manual inspection. However, besides being strongly subjective, visual QC is a time-consuming task, and it might be unfeasible to perform on large datasets.

Automated QC techniques can address these issues, and promising results have been already described in the literature (24, 25).

Despite some advantages over visual QC process, most of these methods still require large and fully annotated training datasets to evaluate the ML models. However, this might be challenging in real life, as we can mostly rely on relatively small sets of accurately segmented reference images.

Several ML and deep learning methods that do not require fully annotated datasets have been used to evaluate automated segmentation and estimate quantitative metrics (26, 27).

For instance, Robinson and colleagues used reverse classification accuracy (RCA) to predict the per-case quality of automated segmentations using only a small set of reference images and contouring (28). The RCA method of predicting quality of ML outputs is based on the assumption that a test case that happens to match the distribution of reference training images will result in high quality prediction while out of distribution (OOD) test cases will result in low quality predictions. With this assumption, a classifier is trained on both in-distribution and OOD data to predict the performance of the segmentation algorithm. However, such classifier when used as a discriminator alongside a segmentation network (generator) can improve segmentation quality on OOD cases, which is a basis of generative adversarial networks (GANs). By coupling a generator with a descriminator, the segmentation head of the GAN could then outperform the RCA classifier. In short, if a classification network is trained to accurately predict the performance of a segmentation network – as was done with the RCA approach – it implies that the segmentation algorithm may not have been sufficiently trained or was trained on a limited dataset (compared to the classification network). This approach also does not guarantee the generalizability of the classification network to other OOD test cases that the RCA was not trained on, thus limiting its utility to yet another subset of data.

Unlike Robinson's method, our approach aims to assess the clinical acceptability of automatic contours rather than predicting the segmentation accuracy. Furthermore, our systematic scoring analysis enables identifying cases where the segmentation has failed based on clinicians' judgment. Only these selected images would thus require further manual operator

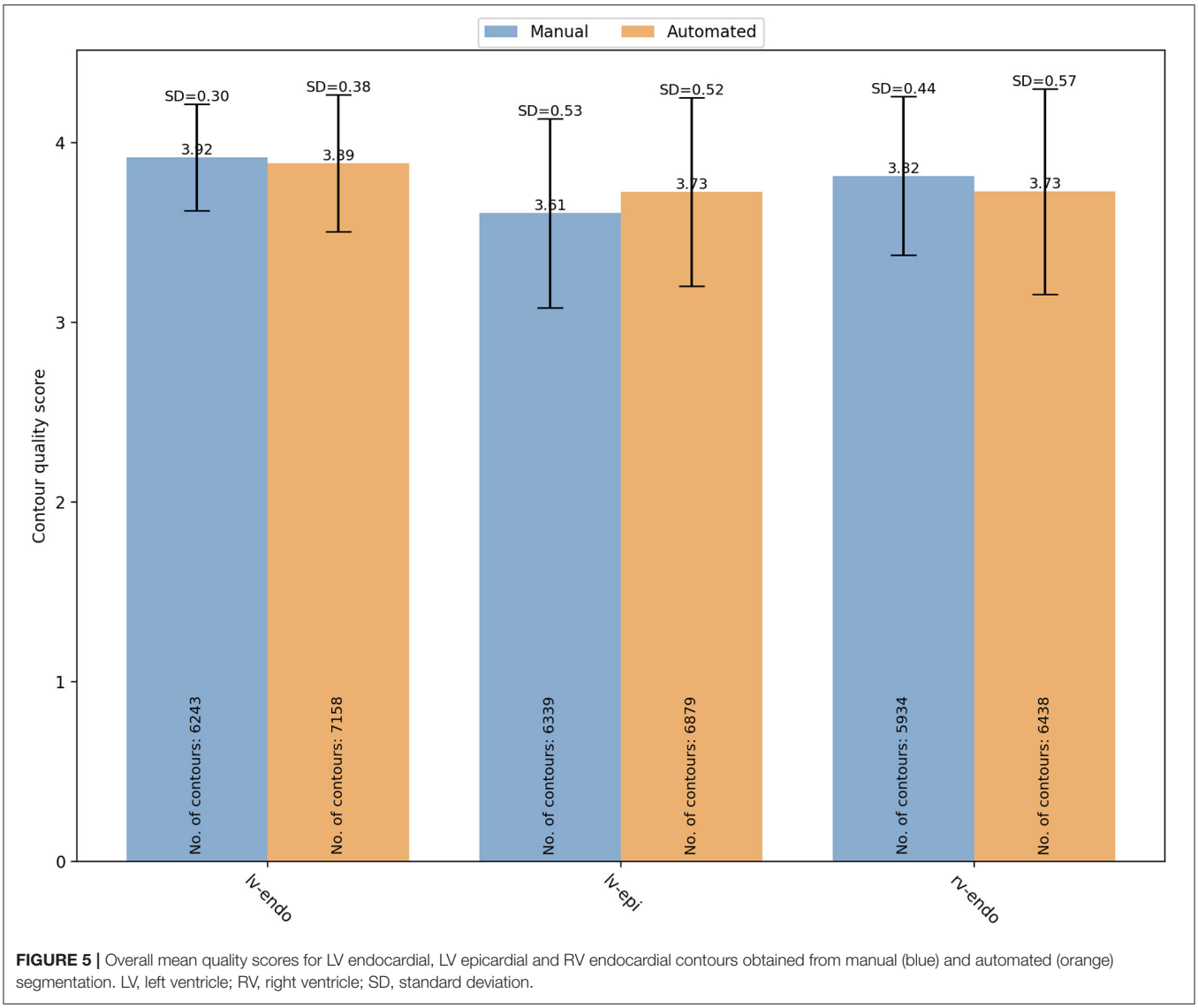

FIGURE 5 | Overall mean quality scores for LV endocardial, LV epicardial and RV endocardial contours obtained from manual (blue) and automated (orange) segmentation. LV, left ventricle; RV, right ventricle; SD, standard deviation.

corrections. This will save time in the review process. Besides, clinical assessment of automated contours can potentially be obtained more efficiently across multiple institutions using our contours quality scoring system.

Furthermore, unlike other QC methods described so far, our approach captures the clinical acceptance of automated segmentation in a blinded manner. The observer clinicians do not know whether the evaluated contours are manual or automated by the algorithm when scoring them. Indeed, knowing the source of segmentation could influence their clinical decision and potentially introduce bias. Having blinded observers can thus minimize the risk of such unintended bias in the qualitative assessment.

A blind manner approach to evaluate the quality of automated contouring was also used by Gooding et al. who proposed a framework based on the Turing Test method, also referred to as the "Imitation Game" (29). This approach assumes that the inability of an interrogator to distinguish the machine behavior from the human behavior may indicate a good machine performance (30). Based on these assumptions, the authors presented contours from different thoracic organs to eight blinded clinical observers, who were asked to determine whether they were automated or manually generated. The inability of observers to correctly identify the source of contours was considered an indicator that the predicted contours were acceptable or at least of the same quality as the human standard, indicating a reduced need for manual editing. Furthermore, they found that the misclassification rate better predicted the time saved for editing auto-contours than other standard quantitative metrics, such as the DSC value.

Although the Turing indistinguishability might be considered a surrogate measure of automated contouring performance (31), it does not necessarily predict their clinical acceptability. Our approach, instead, is based on the assumption that if automated contours are judged of good quality by blinded observer clinicians, then they might be considered clinically acceptable. Therefore, our QC framework allows an evaluation of automated method more relevant to clinical applications and

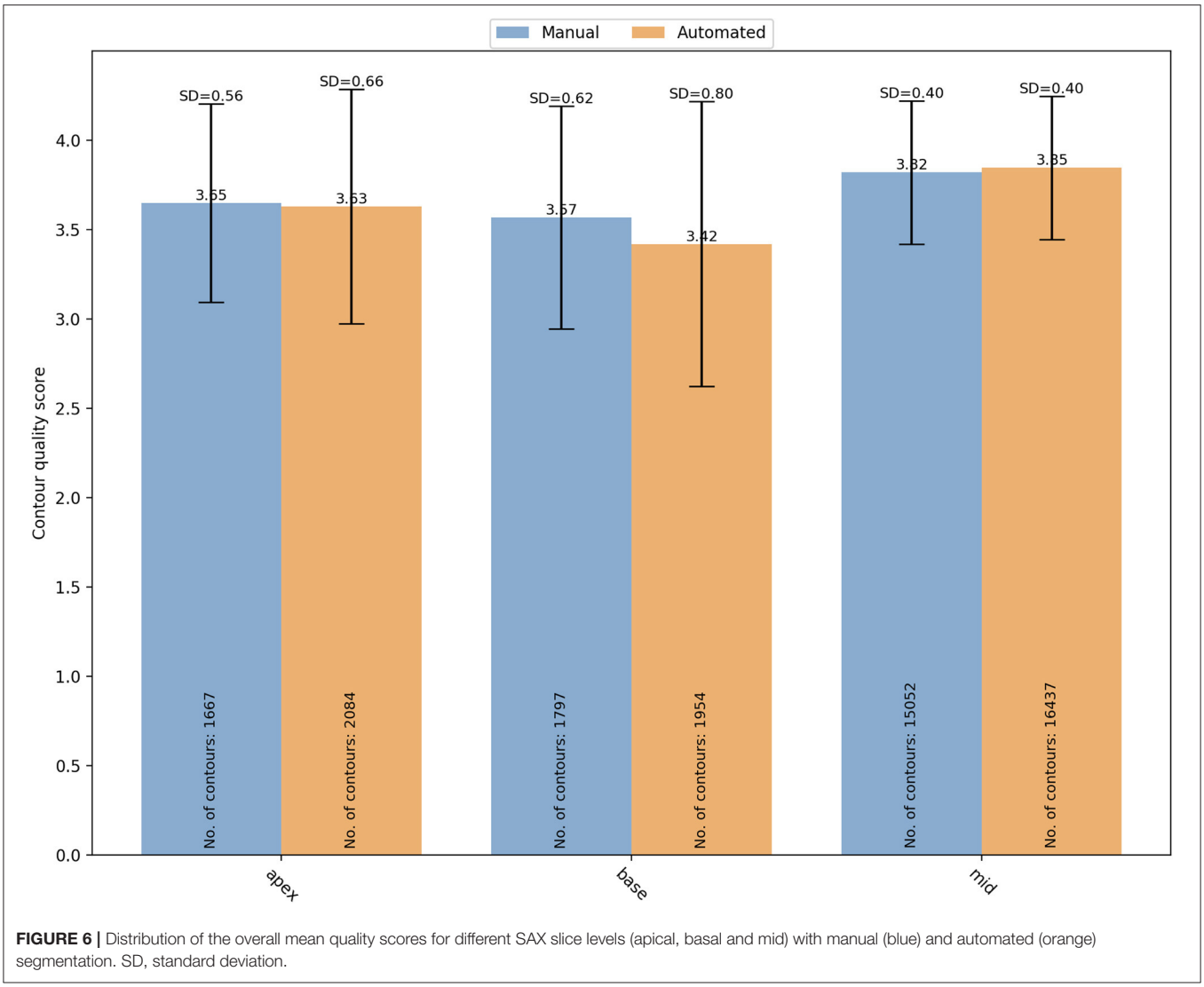

FIGURE 6 | Distribution of the overall mean quality scores for different SAX slice levels (apical, basal and mid) with manual (blue) and automated (orange) segmentation. SD, standard deviation.

independent from how much the ML algorithm can imitate human performance.

Finally, since our method of assessing automated segmentation is not based on extensive manual expert annotations but on contour quality scores easily obtainable from clinicians, it might be used for quality controlling large-scale imaging datasets such as the UKB Imaging Study.

Limitations

The dataset used for the scoring analysis was composed exclusively of good quality images. Therefore, although our method can be applied to real-life datasets with a similar level of image quality, care must be taken when generalizing such results to low-quality image datasets.

The manual segmentation and the quality assessment of all contours were performed by two different teams of clinicians, whose judgment was based on two different SOPs for post-processing analysis. Although this would account for some differences in the image interpretation, the scoring analysis by underlying pathology showed good agreement between the quality of automatic and manual contours in most cases. This suggests that the quality assessment was based on the clinical acceptability rather than the accuracy of the contour drawing and is more in line with a real-world clincal scenario. This indicates that our approach is suitable for QC analysis involving multiple centers with different institutional guidelines and clinicians with varying contour styles.

Although we did not assess the inter-observer variability between the NHCS operators for this specific study, an excellent inter-operator reproducibility of cardiac measurements was reported in a previous publication (14).

We did not evaluate the automated segmentation accuracy using quantitative metrics. Therefore, we could not study whether there was a correlation between quantitative metrics and clinical contour quality. However, that was beyond the scope of this paper. Our purpose was to present a method allowing a more clinically relevant evaluation of automated contouring, thus not based on the quantitative assessment of the ML algorithm.

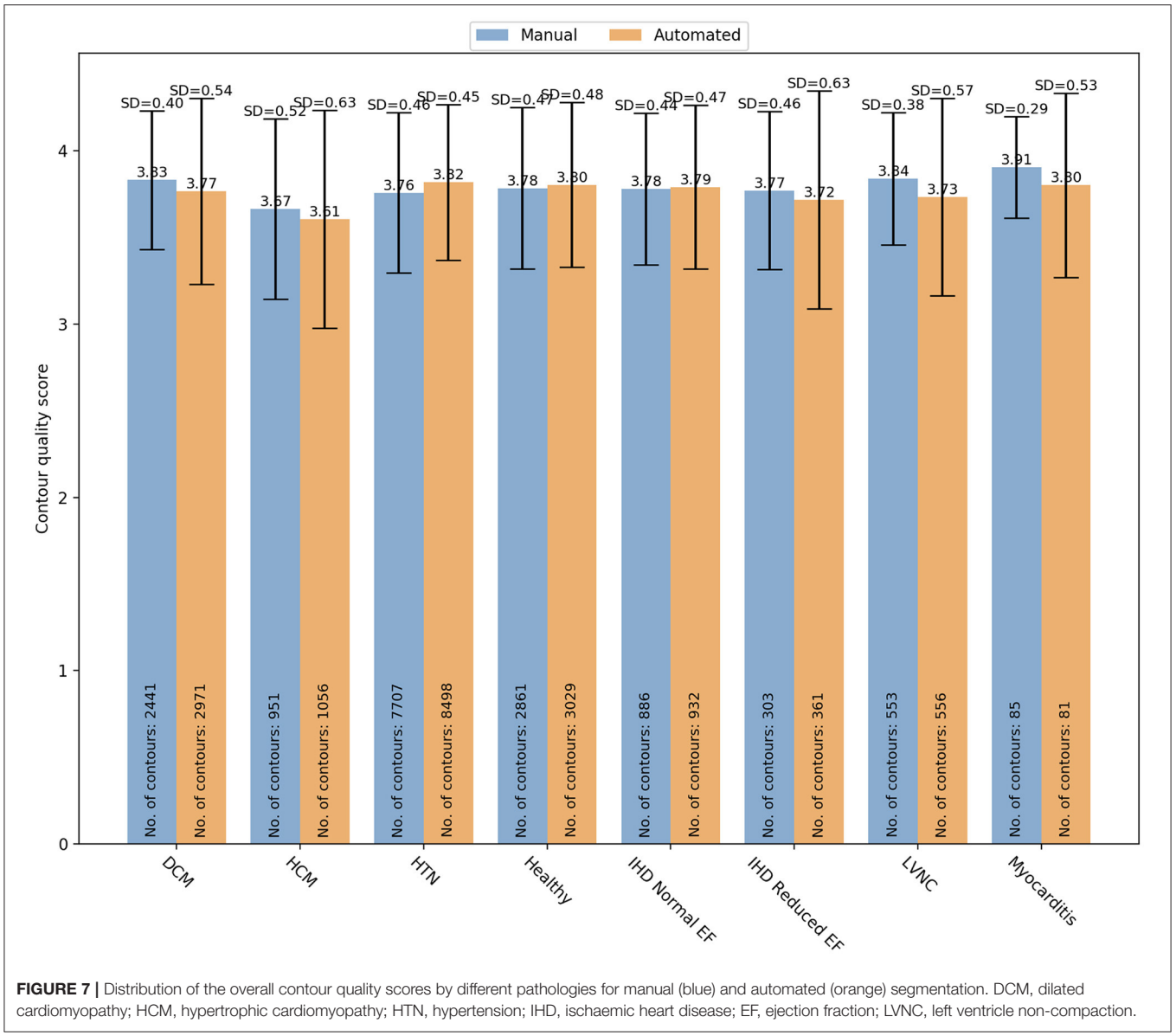

FIGURE 7 | Distribution of the overall contour quality scores by different pathologies for manual (blue) and automated (orange) segmentation. DCM, dilated cardiomyopathy; HCM, hypertrophic cardiomyopathy; HTN, hypertension; IHD, ischaemic heart disease; EF, ejection fraction; LVNC, left ventricle non-compaction.

We could not assess the intra-rater agreement across multiple instances in this study. However, the validated UKB standardized protocol used as a reference to grade contouring has produced good to excellent intra and inter-observer variability, as shown in a previous publication (18).

Finally, we did not assess whether factors like sex, age and patients' ethnicity could influence the contouring quality as data were fully anonymised. Future studies, perhaps on larger datasets integrating clinical and demographic information, might address this question.

CONCLUSION

There is a growing need for a quality-based evaluation of automated segmentation more relevant to clinical practice and supplementing other quantitative measures of ML performance. Our systematic scoring analysis allows assessing automated contouring based on their clinical acceptability by involving clinicians directly during the algorithm validation process. This approach focused on the contours clinical utility could ultimately improve clinicians' confidence in AI and its acceptability in the clinical workflow.

DATA AVAILABILITY STATEMENT

The raw data supporting the conclusions of this article will be made available by the authors, without undue reservation.

ETHICS STATEMENT

The studies involving human participants were reviewed and approved by National Health Center Singapore (NHCS). The

patients/participants provided their written informed consent to participate in this study.

AUTHOR CONTRIBUTIONS

SEP, MO, AA-K, AS, MYK, and JMP conceived and designed the study. MO, JC, and ER performed data analysis. ER wrote the manuscript. T-TL, SAC, DJH, BA, D-FT, JB, and CWLC performed manual contours. The automated segmentation was performed by Circle Cardiovascular Imaging Inc. ER, SEP, MYK, and KF assessed the quality of both manual and automated contours. All authors read and approved the final manuscript.

FUNDING

SEP acknowledges support from the National Institute for Health Research (NIHR) Biomedical Research Center at Barts. SEP acknowledges the British Heart Foundation for funding the manual analysis to create a cardiovascular magnetic resonance imaging reference standard for the UK Biobank imaging resource in 5000 CMR scans (www.bhf.org.uk; PG/14/89/31194). SEP acknowledges support from the SmartHeart EPSRC programme grant (www.nihr.ac.uk; EP/P001009/1). SEP and ER also acknowledge support from the London Medical Imaging and Artificial Intelligence Center for Value Based Healthcare (AI4VBH), which is funded from the Data to Early Diagnosis and Precision Medicine strand of the government's Industrial Strategy Challenge Fund, managed and delivered by Innovate UK on behalf of UK Research and Innovation (UKRI). N.A. recognizes the National Institute for Health Research (NIHR) Integrated Academic Training programme which supports his Academic Clinical Lectureship post. DJH is supported by the Duke-NUS Signature Research Programme funded by the Ministry of Health, Singapore Ministry of Health's National Medical Research Council under its Clinician Scientist-Senior Investigator scheme (NMRC/CSA-SI/0011/2017), Centre Grant (CGAug16M006), and Collaborative Centre Grant scheme (NMRC/CGAug16C006).

SUPPLEMENTARY MATERIAL

The Supplementary Material for this article can be found online at: https://www.frontiersin.org/articles/10.3389/fcvm.2021.816985/full#supplementary-material

REFERENCES

1. Arnold JR, McCann GP. Cardiovascular magnetic resonance: applications and practical considerations for the general cardiologist. *Heart.* (2019) 106:174–81. doi: 10.1136/heartjnl-2019-314856
2. Busse A, Rajagopal R, Yücel S, Beller E, Öner A, Streckenbach F, et al. Cardiac MRI—Update 2020. *Radiologe.* (2020) 60:33–40. doi: 10.1007/s00117-020-00687-1
3. Steel KE, Kwong RY. Application of cardiac magnetic resonance imaging in cardiomyopathy. *Curr Heart Fail Rep.* (2008) 5:128–35. doi: 10.1007/s11897-008-0021-1
4. Baritussio A, Scatteia A, Bucciarelli-Ducci C. Role of cardiovascular magnetic resonance in acute and chronic ischemic heart disease. *Int J Cardiovasc Imaging.* (2018) 34:67–80. doi: 10.1007/s10554-017-1116-0
5. Nguyen KL, Hu P, Finn JP. Cardiac magnetic resonance quantification of structure-function relationships in heart failure. *Heart Fail Clin.* (2021) 17:9–24. doi: 10.1016/j.hfc.2020.08.001
6. Bailly A, Lipiecki J, Chabrot P, Alfidja A, Garcier JM, Ughetto S, et al. Assessment of left ventricular volumes and function by cine-MR imaging depending on the investigator's experience. *Surg Radiol Anat.* (2009) 31:113–20. doi: 10.1007/s00276-008-0415-5
7. Bernard O, Lalande A, Zotti C, Cervenansky F, Yang X, Heng PA, et al. Deep learning techniques for automatic MRI cardiac multi-structures segmentation and diagnosis: is the problem solved? *IEEE Trans Med Imaging.* (2018) 37:2514–25. doi: 10.1109/TMI.2018.2837502
8. Leiner T, Rueckert D, Suinesiaputra A, Baeßler B, Nezafat R, Išgum I, et al. Machine learning in cardiovascular magnetic resonance: Basic concepts and applications. *J Cardiovasc Magn Reson.* (2019) 21:1–14. doi: 10.1186/s12968-019-0575-y
9. Bai W, Sinclair M, Tarroni G, Oktay O, Rajchl M, Vaillant G, et al. Automated cardiovascular magnetic resonance image analysis with fully convolutional networks 08 Information and Computing Sciences 0801 Artificial Intelligence and Image Processing. *J Cardiovasc Magn Reson.* (2018) 20:65. doi: 10.1186/s12968-018-0471-x
10. Attar R, Pereañez M, Gooya A, Albà X, Zhang L, de Vila MH, et al. Quantitative CMR population imaging on 20,000 subjects of the UK biobank imaging study: LV/RV quantification pipeline and its evaluation. *Med Image Anal.* (2019) 56:26–42. doi: 10.1016/j.media.2019.05.006
11. Thrall JH, Li X, Li Q, Cruz C, Do S, Dreyer K, et al. Artificial Intelligence and machine learning in radiology: opportunities, challenges, pitfalls, and criteria for success. *J Am Coll Radiol.* (2018) 15:504–8. doi: 10.1016/j.jacr.2017.12.026
12. Taha AA, Hanbury A. Metrics for evaluating 3D medical image segmentation: analysis, selection, and tool. *BMC Med Imaging.* (2015) 15:29. doi: 10.1186/s12880-015-0068-x
13. Crum WR, Camara O, Hill DLG. Generalized overlap measures for evaluation and validation in medical image analysis. *IEEE Trans Med Imaging.* (2006) 25:1451–61. doi: 10.1109/TMI.2006.880587
14. Le TT, Tan RS, De Deyn M, Goh EPC, Han Y, Leong BR, et al. Cardiovascular magnetic resonance reference ranges for the heart and aorta in Chinese at 3T. *J Cardiovasc Magn Reson.* (2016) 18:1–13. doi: 10.1186/s12968-016-0236-3
15. Ronneberger O, Fischer P, Brox T. U-Net: convolutional networks for biomedical image segmentation. In: Navab N, Hornegger J, Wells W, Frangi A, editors. *Medical Image Computing and Computer-Assisted Intervention – MICCAI 2015. Lecture Notes in Computer Science, Vol 9351.* Cham: Springer (2015). doi: 10.1007/978-3-319-24574-4_28
16. Sudlow C, Gallacher J, Allen N, Beral V, Burton P, Danesh J, et al. UK Biobank: an open access resource for identifying the causes of a wide range of complex diseases of middle and old age. *PLoS Med.* (2015) 12:1001779. doi: 10.1371/journal.pmed.1001779
17. Petersen SE, Matthews PM, Bamberg F, Bluemke DA, Francis JM, Friedrich MG, et al. Imaging in population science: cardiovascular magnetic resonance in 100,000 participants of UK Biobank - rationale, challenges and approaches. *J Cardiovasc Magn Reson.* (2013) 15:46. doi: 10.1186/1532-429X-15-46
18. Petersen SE, Aung N, Sanghvi MM, Zemrak F, Fung K, Paiva JM, et al. Reference ranges for cardiac structure and function using cardiovascular magnetic resonance (CMR) in Caucasians from the UK Biobank population cohort. *J Cardiovasc Magn Reson.* (2017) 19:18. doi: 10.1186/s12968-017-0327-9
19. Gwet LK. *Handbook of Inter-rater Reliability: The Definitive Guide to Measuring the Extent of Agreement Among Raters*. Gaithersburg, MD: Advanced Analytics, LLC (2014).
20. Blood E, Spratt KF. Disagreement on agreement: two alternative agreement coefficients. In: *SAS Global Forum, Orlando, Florida.* (2007) 106: 1–12. Available online at: https://support.sas.com/resources/papers/proceedings/proceedings/forum2007/186-2007.pdf (accessed November 16, 2021).

21. Landis JR, Koch GG. An application of hierarchical kappa-type statistics in the assessment of majority agreement among multiple observers. *Biometrics.* (1977) 33:363–74. doi: 10.2307/2529786
22. Zou KH, Warfield SK, Bharatha A, Tempany CMC, Kaus MR, Haker SJ, et al. Statistical validation of image segmentation quality based on a spatial overlap index. *Acad Radiol.* (2004) 11:178–89. doi: 10.1016/S1076-6332(03)00671-8
23. Fenster A, Chiu B. Evaluation of segmentation algorithms for medical imaging. *Annu Int Conf IEEE Eng Med Biol - Proc.* (2005) 7:7186–9. doi: 10.1109/IEMBS.2005.1616166
24. Fan W, Davidson I. Reverse testing: an efficient framework to select amongst classifiers under sample selection bias. In: *Proceedings of the 12th ACM SIGKDD international conference on Knowledge discovery and data mining - KDD '06*. New York, NY: ACM Press (2006). p.147–56. doi: 10.1145/1150402.1150422
25. Zhong E, Fan W, Yang Q, Verscheure O, Ren J. Cross validation framework to choose amongst models and datasets for transfer learning. In: Balcázar JL, Bonchi F, Gionis A, Sebag M, editors. *Machine Learning and Knowledge Discovery in Databases. ECML PKDD 2010. Lecture Notes in Computer Science, Vol 6323*. Berlin; Heidelberg: Springer (2010). doi: 10.1007/978-3-642-15939-8_35
26. Kohlberger T, Singh V, Alvino C, Bahlmann C, Grady L. Evaluating segmentation error without ground truth. *Med Image Comput Comput Assist Interv*. (2012) 15:528–36. doi: 10.1007/978-3-642-33415-3_65
27. Bhaskaruni D, Moss FP, Lan C. Estimating prediction qualities without ground truth: a revisit of the reverse testing framework. In: *IEEE 24th International Conference on Pattern Recognition (ICPR)* Beijing. (2018). p. 49–54. doi: 10.1109/ICPR.2018.8545706
28. Robinson R, Valindria VV, Bai W, Oktay O, Kainz B, Suzuki H, et al. Automated quality control in image segmentation: application to the UK Biobank cardiovascular magnetic resonance imaging study. *J Cardiovasc Magn Reson.* (2019) 21:18. doi: 10.1186/s12968-019-0523-x
29. Gooding MJ, Smith AJ, Tariq M, Aljabar P, Peressutti D, van der Stoep J, et al. Comparative evaluation of autocontouring in clinical practice: a practical method using the Turing test. *Med Phys.* (2018) 45:5105–15. doi: 10.1002/mp.13200
30. Turing AM. Computing machinery and intelligence. *MIND.* (1950) 59:433–60. doi: 10.1093/mind/LIX.236.433
31. Harnad S. The turing test is not a trick: turing indistinguishability is a scientific criterion. *ACM SIGART Bull.* (1992) 3:9–10. doi: 10.1145/141420.141422

Author Disclaimer: The views expressed are those of the authors and not necessarily those of the AI4VBH Consortium members, the NHS, Innovate UK, or UKRI.

Conflict of Interest: SEP provides consultancy to and owns stock of Cardiovascular Imaging Inc, Calgary, Alberta, Canada.

The remaining authors declare that the research was conducted in the absence of any commercial or financial relationships that could be construed as a potential conflict of interest.

Publisher's Note: All claims expressed in this article are solely those of the authors and do not necessarily represent those of their affiliated organizations, or those of the publisher, the editors and the reviewers. Any product that may be evaluated in this article, or claim that may be made by its manufacturer, is not guaranteed or endorsed by the publisher.

frontiers in Cardiovascular Medicine

ORIGINAL RESEARCH
published: 24 February 2022
doi: 10.3389/fcvm.2022.800720

Combined Analysis of Myocardial Deformation and Oxygenation Detects Inducible Ischemia Unmasked by Breathing Maneuvers in Chronic Coronary Syndrome

Barbara Spicher[1†], Kady Fischer[1†], Zoe A. Zimmerli[1], Kyohei Yamaji[2], Yasushi Ueki[2], Carina N. Bertschinger[3], Bernd Jung[3], Tatsuhiko Otsuka[2], Marius R. Bigler[2], Christoph Gräni[2], Hendrik von Tengg-Kobligk[3], Lorenz Räber[2], Balthasar Eberle[1] and Dominik P. Guensch[1,3]*

[1] Department of Anaesthesiology and Pain Medicine, Inselspital, University Hospital Bern, University of Bern, Bern, Switzerland, [2] Department of Cardiology, Inselspital, University Hospital Bern, University of Bern, Bern, Switzerland, [3] Department of Diagnostic, Interventional and Paediatric Radiology, Inselspital, University Hospital Bern, University of Bern, Bern, Switzerland

OPEN ACCESS

Edited by:
Michael Schär,
Johns Hopkins University,
United States

Reviewed by:
Thorsten Leucker,
Johns Hopkins University,
United States
Bharath Ambale Venkatesh,
Johns Hopkins University,
United States

***Correspondence:**
Dominik P. Guensch
dominik.guensch@gmail.com

[†] These authors share first authorship

Specialty section:
This article was submitted to Cardiovascular Imaging, a section of the journal Frontiers in Cardiovascular Medicine

Received: 23 October 2021
Accepted: 31 January 2022
Published: 24 February 2022

Citation:
Spicher B, Fischer K, Zimmerli ZA, Yamaji K, Ueki Y, Bertschinger CN, Jung B, Otsuka T, Bigler MR, Gräni C, von Tengg-Kobligk H, Räber L, Eberle B and Guensch DP (2022) Combined Analysis of Myocardial Deformation and Oxygenation Detects Inducible Ischemia Unmasked by Breathing Maneuvers in Chronic Coronary Syndrome. Front. Cardiovasc. Med. 9:800720. doi: 10.3389/fcvm.2022.800720

Introduction: In patients with chronic coronary syndromes, hyperventilation followed by apnea has been shown to unmask myocardium susceptible to inducible deoxygenation. The aim of this study was to assess whether such a provoked response is co-localized with myocardial dysfunction.

Methods: A group of twenty-six CAD patients with a defined stenosis (quantitative coronary angiography > 50%) underwent a cardiovascular magnetic resonance (CMR) exam prior to revascularization. Healthy volunteers older than 50 years served as controls ($n = 12$). Participants hyperventilated for 60s followed by brief apnea. Oxygenation-sensitive images were analyzed for changes in myocardial oxygenation and strain.

Results: In healthy subjects, hyperventilation resulted in global myocardial deoxygenation (-10.2 ± 8.2%, $p < 0.001$) and augmented peak circumferential systolic strain (-3.3 ± 1.6%, $p < 0.001$). At the end of apnea, myocardial signal intensity had increased (+9.1 ± 5.3%, $p < 0.001$) and strain had normalized to baseline. CAD patients had a similar global oxygenation response to hyperventilation (−5.8 ± 9.6%, $p = 0.085$) but showed no change in peak strain from their resting state (-1.3 ± 1.6%), which was significantly attenuated in comparison the strain response observed in controls ($p = 0.008$). With apnea, the CAD patients showed an attenuated global oxygenation response to apnea compared to controls (+2.7 ± 6.2%, $p < 0.001$). This was accompanied by a significant depression of peak strain (3.0 ± 1.7%, $p < 0.001$), which also differed from the control response ($p = 0.025$). Regional analysis demonstrated that post-stenotic myocardium was most susceptible to de-oxygenation and systolic strain abnormalities during respiratory maneuvers. CMR measures at rest were unable to discriminate post-stenotic territory ($p > 0.05$), yet this was significant for both myocardial oxygenation [area under the curve (AUC): 0.88, $p > 0.001$] and peak strain (AUC: 0.73, $p = 0.023$) measured with apnea. A combined analysis of myocardial oxygenation

and peak strain resulted in an incrementally higher AUC of 0.91, $p < 0.001$ than strain alone.

Conclusion: In myocardium of patients with chronic coronary syndromes and primarily intermediate coronary stenoses, cine oxygenation-sensitive CMR can identify an impaired vascular and functional response to a vasoactive breathing maneuver stimulus indicative of inducible ischemia.

Keywords: coronary artery disease, oxygenation-sensitive imaging, cardiovascular magnetic resonance, feature tracking (CMR-FT), strain, breathing maneuver

INTRODUCTION

Coronary artery disease (CAD) can be classified into subcategories of acute coronary syndromes (ACS) and chronic coronary syndromes (CCS) (1). CCS encompasses a range of clinical scenarios and can include but are not limited to patients who have stable symptoms following revascularization and patients where an obstructive coronary stenosis was observed during screening. In these patients, symptoms and myocardial abnormalities may not be apparent during resting conditions as there may not be a mismatch of oxygen supply to demand. This may rapidly change when the heart is exposed to stressors or vasoactive stimuli that tips this oxygen supply-demand balance. This can induce a cascade of changes in the myocardium including a reduction in tissue perfusion and oxygenation balance, and subsequent diastolic and systolic dysfunction (2, 3). Multiple non-invasive imaging techniques can assess patients at various stages in this cascade (4), and with new developments in cardiovascular magnetic resonance (CMR) there is potential to investigate the triggered change in both myocardial tissue and functional measures associated with inducible ischemia in CCS.

Oxygenation-Sensitive Cardiovascular Magnetic Resonance

Non-invasive imaging of myocardial ischemia is a rapidly developing field, with a significant expansion in the variety of imaging techniques available to investigate changes in the myocardial tissue perfusion and oxygenation. A concomitant deoxygenation response has been demonstrated using Oxygenation-Sensitive (OS)-CMR (5). OS-CMR does not rely on gadolinium contrast but uses deoxyhemoglobin as an endogenous contrast agent, based on its paramagnetic molecular properties (6). The resulting local magnetic field inhomogeneities cause a loss of regional signal intensity (SI) in CMR images acquired using OS sequences (7–10). In contrast, oxygenated hemoglobin is diamagnetic and leads to weak field stabilization, which does not change SI. Thus, OS-CMR offers an attractive option for non-invasive detection and localization of regional myocardial deoxygenation without the use of exogenous contrast. While OS-CMR can indicate oxygen supply-and-demand mismatch, inducible ischemia is the sequela. Therefore, an additional measure of ventricular dysfunction would be beneficial.

Assessing Regional Myocardial Function With CMR Feature Tracking

Regional analysis of myocardial strain using CMR feature tracking (FT) is a more recent technique to assess myocardial function. Myocardial strain provides insight into contractile and lusitropic function in which feature tracking techniques follow the relative movement of unique features in the image throughout the cardiac cycle in the longitudinal, circumferential and radial axis. Post-processing software allows for quantification of multiple systolic and diastolic deformation parameters, such as peak systolic strain (PS), time to PS (TTP), and myocardial diastolic strain rate (dSR). The association of changes of OS-CMR-derived myocardial oxygenation with regional myocardial function has not been studied so far in cardiovascular patients. In swine, this combined analysis was performed and FT measurements from OS images were shown to be linked with myocardial deoxygenation at low perfusion pressures (11). With the use of FT software, the OS cines used for oxygenation analysis can be simultaneously interrogated to assess strain parameters.

Breathing Maneuvers for Provocation of an Endogenous Coronary Vasomotor Response

Pharmacological agents such as adenosine or regadenoson are often used diagnostically to test coronary vasoreactivity. Yet the heart has natural feedback loops to respond to non-pharmacological stimuli as well as exercise, sympathetic function testing (i.e., cold pressor test), and changes in breathing patterns. The mechanisms of hyperventilation and apnea on myocardial oxygenation balance are not fully understood, but a key regulatory pathway appears to be through local blood carbon dioxide (CO_2) partial pressures. Hyperventilation induces hypocapnia, which is known to be a potent coronary vasoconstrictor. Apnea has an opposing effect increasing CO_2 and this subsequent hypercapnia induces significant vasodilation in healthy coronary vessels (12, 13). This has been demonstrated using inhaled gas mixtures (14, 15) and paced intentional breathing maneuvers (12, 16). Hypercapnic coronary vasodilation has been described since 1970, and it has been hypothesized that hypercapnia could induce inter-coronary flow redistributions that may result in a steal phenomenon in CAD patients (13). Meanwhile, this assumption has been verified by Fischer et al. (12) using OS-CMR in an animal model of acute

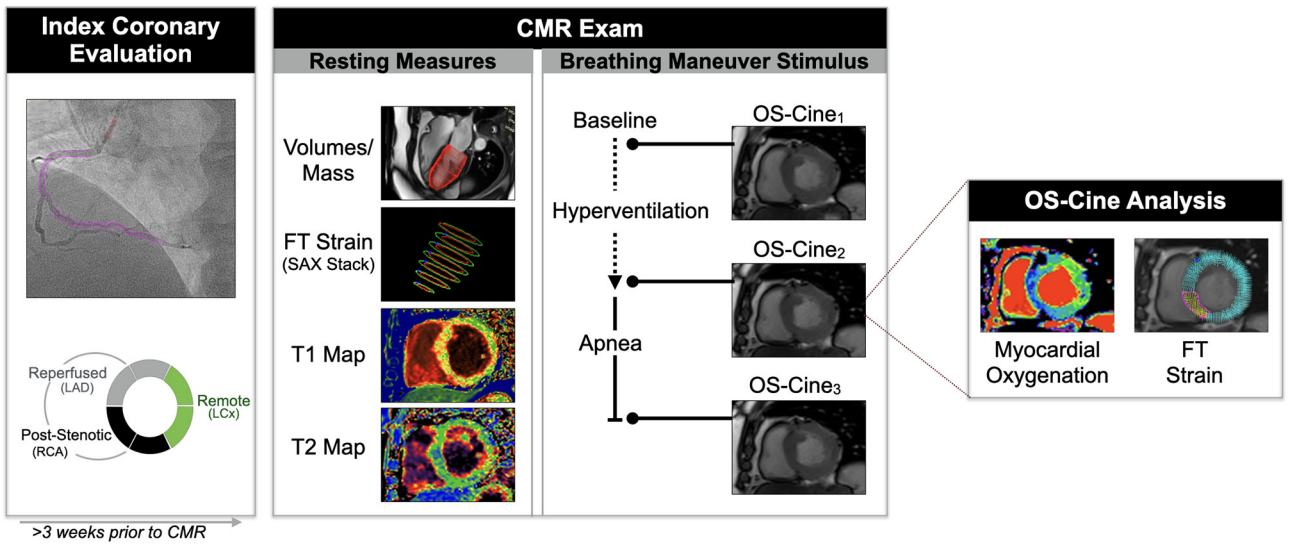

FIGURE 1 | Study methods. From the angiography images, quantitative coronary angiography was used to calculate the diameters stenosis of all coronary territories and the myocardial segments were categorized as post-stenotic, reperfused or remote territory based on the individual coronary anatomy. A contrast-free CMR exam was performed at least 3 weeks after the index angiography. Common functional and tissue characterization sequences were acquired at rest, and an oxygenation-sensitive (OS)-cine was acquired repetitively during a breathing maneuver stimulus. From the OS-cine both signal intensity changes indicating the myocardial oxygenation response and feature tracking (FT) strain parameters were measured for the global myocardium, and per myocardial segment.

coronary stenosis. However, the effect on myocardial contractile function is unknown.

This study aimed to investigate the association of provoked dynamic myocardial oxygenation changes, as measured using OS-CMR, with regional myocardial strain in healthy subjects and patients with well-defined CCS.

MATERIALS AND METHODS

Study Population

The study protocol was approved by the ethics board of the Canton of Bern and complies with the ethical guidelines of the 1975 Declaration of Helsinki. A total of twenty-six patients with a diagnosis of CAD and twelve healthy volunteers in a comparable age-range (50–70 years) were included. Seventeen (45%) of the participants had been included in previous publications (17, 18). All participants had given their written informed consent prior to enrolment into the study. The patients were recruited for their CMR in the time interval between their initial coronary computed tomography or invasive coronary angiography visit (>3 weeks) and their subsequent admission for revascularization. From these diagnostic exams the presence of obstructive CAD was verified and patients were included if at least one untreated major epicardial coronary artery with more than 50% stenosis by quantitative coronary angiography (QCA) was present during the CMR scan, together with at least one patent epicardial vessel. Exclusion criteria included general contraindications to CMR, pregnancy, pre-existing coronary bypass grafts, severe pulmonary disease, and any unstable medical condition. Moreover, patients with a ST-elevation myocardial infarction (STEMI) as reason for the initial angiography were not included in this analysis. Healthy subjects were required to be between the ages of 50–70 years, be non-smokers for the past 6 months and to be without a history of cardiopulmonary disease or pertinent medication. Participants were also asked to abstain from caffeine-rich intake for twelve hours prior to the CMR exam.

CMR Protocol

All participants underwent a contrast-free exam in a 3T MRI scanner (MAGNETOM Skyra^{TM} or Prisma^{TM}, Siemens Healthineers, Erlangen, Germany). A short-axis stack along with two long-axis images were obtained for the analysis of baseline ventricular function parameters. Additionally, native T1 and T2 maps were acquired in a basal and mid-ventricular slice. OS-CMR cines were obtained in these same slice positions. Under resting conditions, a baseline OS cine was acquired during a brief (5–8 s) breath-hold. Participants were then instructed to hyperventilate for 60 s (30 breaths/min paced by a metronome), and immediately following hyperventilation, to maintain apnea at a comfortable exhalation level. Throughout the entire duration of this apneic period, OS-cines were acquired continuously until participants indicated their need to resume breathing (**Figure 1**).

CMR Sequence Parameters

All images were obtained at an end-expiratory breath-hold. OS-CMR images were obtained with an ECG-triggered balanced steady-state free precession sequence (TR/TE 3.4/1.70 ms, temporal resolution 40.7 ms, flip angle 35°, voxel size 2.0 x 2.0 x 10.0 mm, matrix 192 x 120, bandwidth 1302 Hz/Px). Standard cine images were acquired with a standard gated balanced steady-state free precession cine sequence (TR/TE 3.3/1.43 ms, 25

TABLE 1 | Patient characteristics.

Demographics	Healthy volunteers ($n = 12$)	Patients ($n = 25$)
Age (years)	56 ± 5	65 ± 9*
Sex (female)	4 (33%)	3 (12%)
Body mass index (kg/m^2)	24.4 ± 2.1	28.0 ± 4.6*
Body weight (kg)	72.5 ± 10.4	85.3 ± 16.2*
Global left ventricular CMR measures		
Mass index (g/m^2)	75 ± 15	68 ± 10
End-diastolic volume index (ml/m^2)	86 ± 16	72 ± 15
End-systolic volume index (ml/m^2)	32 ± 7	27 ± 11
Stroke volume index (ml/m^2)	54 ± 11	44 ± 11
Ejection fraction (%)	63 ± 5	62 ± 10
Cardiac index (L/min/m^2)	3.1 ± 0.7	2.9 ± 0.8
Peak strain$_{SAXstack}$ (%)	−20.4 ± 3.6	−19.3 ± 1.9
Native T1 mapping (ms)	1,209 ± 41	1,228 ± 51
T2 mapping (ms)	39.2 ± 1.8	39.6 ± 2.4
Coronary risk factors		
Dyslipidemia	–	17 (68%)
Hypertension	–	14 (56%)
Diabetes mellitus	–	8 (32%)
Sleep apnea syndrome	–	3 (12%)
Medication		
Aspirin	–	25 (100%)
Statins	–	22 (88%)
Dual anti-platelet therapy	–	21 (84%)
Beta-blockers	–	18 (72%)
Angiotensin-converting enzyme inhibitors	–	9 (36%)
Angiotensin receptor blocker	–	7 (28%)
Calcium channel blocker	–	4 (16%)

*Baseline characteristics of the study subjects at the time of CMR exam. Data reported as mean ± SD or n (%). *p < 0.05 between groups.*

TABLE 2 | Coronary angiography.

	Patients ($n = 25$)
Maximum diameter stenosis (%)	67 ± 16
>50% diameter stenosis*	
Left anterior descending artery	13 (52%)
Circumflex artery	6 (24%)
Right coronary artery	10 (40%)
Proximal involvement†	
Proximal	17 (68%)
Mid	8 (32%)
Distal	0 (0%)
Post-stenotic AHA myocardial segments	
Whole heart (/16)	5.0 [3.5–6.0]
Basal (/6)	2.0 [0.0–2.0]
Mid (/6)	2.0 [2.0–2.0]
Apex (/4)	1.0 [1.0–2.0]
Prior PCI	
Left anterior descending	8 (32%)
Left circumflex	2 (8%)
Right coronary artery	10 (40%)
None	5 (20%)
Reperfused AHA myocardial segments	
Whole heart (/16)	5.0 [2.5–6.0]
Basal (/6)	2.0 [0.0–2.0]
Mid (/6)	2.0 [0.5–2.0]
Apex (/4)	1.0 [0.5–2.0]

*Coronary status at the time of the cardiovascular magnetic resonance exam. Data is reported as mean ± SD, n (%) or as median [interquartile range]. The number of post-stenotic and reperfused myocardial AHA segments correspond to the classification of myocardial territories derived from the coronary angiography. AHA, American Heart Association; PCI, percutaneous coronary intervention. *A significant stenosis in multiple vessels per patient was possible. †Location of the most proximal significant lesion (>50% diameter stenosis).*

cardiac phases, flip angle 65°, voxel size 1.6 x 1.6 x 6.0 mm, matrix 192 x 120, bandwidth 962 Hz/Px). T2 maps were generated after acquiring three single-shot gradient echo images (TE 1.32 ms, flip angle = 12°; voxel size 1.9 x 1.9 x 8.0 mm, bandwidth 1184 Hz/Px with T2 preparation times of 0, 30, and 55 ms). A 5(3)3-modified Look-Locker sequence was used for T1 mapping, (TR/TE 281/1.12 ms, flip angle 35°, voxel size 1.4 x 1.4 x 8.0 mm, bandwidth 1085 Hz/Px).

CMR Image Analysis

All analysis was blinded and conducted with cmr^{42} (Circle CVI, Calgary, Canada). To analyse clinical CMR measures at rest, T1 and T2 maps were quantified, and left-ventricular function and feature tracking strain analysis at rest was performed on the full short axis (SAX) stack cines. For the analysis of images acquired during the breathing maneuver stimulus, the relative changes of OS signal intensity (SI) in end-systolic frames, and myocardial strain as measured by CMR-FT were acquired from the same OS cines. For CMR-FT analysis, each cardiac cycle was assessed for circumferential peak strain (PS), time to PS (TTP), and peak early diastolic strain rate (dSR). Measurements for the radial orientation are provided in the supplement. All parameters were determined and reported for global measurements and for the American Heart Association segment model.

Coronary Angiography Analysis

Independent readers analyzed the angiography images to quantify the percent diameter of the stenosis. Afterwards to allocate the coronary angiogram findings to the regional CMR analysis, the angiography readers classified each myocardial segment into one of three categories based on the individual coronary anatomy: (1) territories subtended to a current stenosis (QCA > 50%; post-stenotic) that had no previous reperfusion treatment, (2) territories revascularized at the initial angiography by coronary stenting (reperfused), or (3) territories perfused by a patent native coronary artery (remote). This allocation was primarily based on the classical perfusion territories (19), with the impact on basal, mid and apex slices determined by the proximal hierarchy of the lesions. A figure detailing

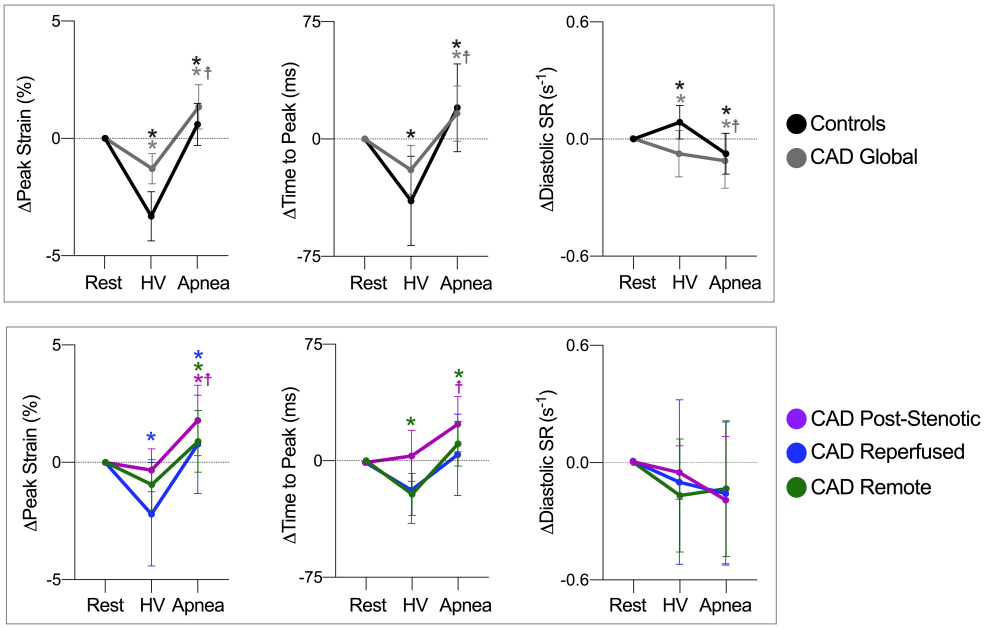

FIGURE 2 | Response of circumferential strain parameters to breathing maneuvers. Data are mean (±95%CI) changes of global peak strain, time to peak strain and early diastolic strain rate (dSR) after hyperventilation (HV) and apnea. Global myocardial changes are shown on the top row for healthy controls (black) and coronary artery disease CAD patients (gray), and for angiography defined myocardial territories on the bottom. *$p < 0.05$ from the previous step, †$p < 0.05$ at rest vs. apnea.

this allocation protocol can be visualized in the publication by Fischer et al. (20). The angiographic readers then adjusted the territory classification based on individual coronary anatomy and dominance (17). The segmental CMR values then were averaged according to the angiography classification.

Statistical Analysis

Continuous data are reported as mean ± standard deviation (SD), categorical data as frequency and percentage. Statistical analysis compared datasets acquired at three time points: at rest, immediately post-hyperventilation, and closest to 30 s of apnea. Myocardial oxygenation response to hyperventilation is given as percent change of OS-SI relative to the image at resting conditions. For the apnea-provoked response at 30 s, the first image acquired during full breath-hold was used as reference. Strain parameters are reported as Δ-change. First, the global myocardial response was compared between participant groups using a linear regression model accounting for sex and age as covariates. Strain data from the three time points were compared within-group only, in order to assess whether strain changed globally, or within the respective territory during the breathing maneuvers. Here, a mixed-effects model was used, accounting for repeated measures and with Tukey's *post-hoc* analysis if applicable. Thereafter, both strain (Δ) and myocardial oxygenation responses (%) were compared for each breathing maneuver step. Pearson's correlation coefficients were used to investigate the association of strain and OS-SI with mapping values.

Receiver operating characteristic curves (ROC) were used to calculate the discriminating ability of imaging parameters for the detection of post-stenotic myocardium defined by angiography. This was performed first for traditional CMR measures acquired at rest including T1 and T2 mapping, ejection fraction, and circumferential peak strain ($PS_{SAXStack}$). ROC curves were then created for both the myocardial oxygenation response and the CMR-FT measured from the OS cine at the end of apnea. A curve combining both features at the end of the stimulus was created using binary logistic regression. Area under the curve (AUC) between correlated curves was compared using the Hanley and McNeil test.

For validation purposes, global and regional strain measurements from all the resting OS cines of the CAD patients ($n = 25$) were compared to strain measurements of the function stack cines using a two-way mixed intra-class correlation (ICC) for absolute agreement. ICC was further calculated for inter-observer agreement with a second blinded reader ($n = 25$). Statistical analyses were performed with GraphPad Prism version 9.0 (GraphPad Software, La Jolla California USA) and *R* software (version 3.5.0, R Foundation for Statistical Computing, Vienna, Austria). Results were considered statistically significant at a two-tailed value $p < 0.05$.

RESULTS

Data Inclusion

One patient was excluded from analysis due to poor triggering in the CMR images. Specifically for the OS cine, FT and OS data was available from all the remaining 25 patients, and regionally 92% of the segments could be analyzed for peak strain and time to peak strain, with all exclusions due to poor plane position and

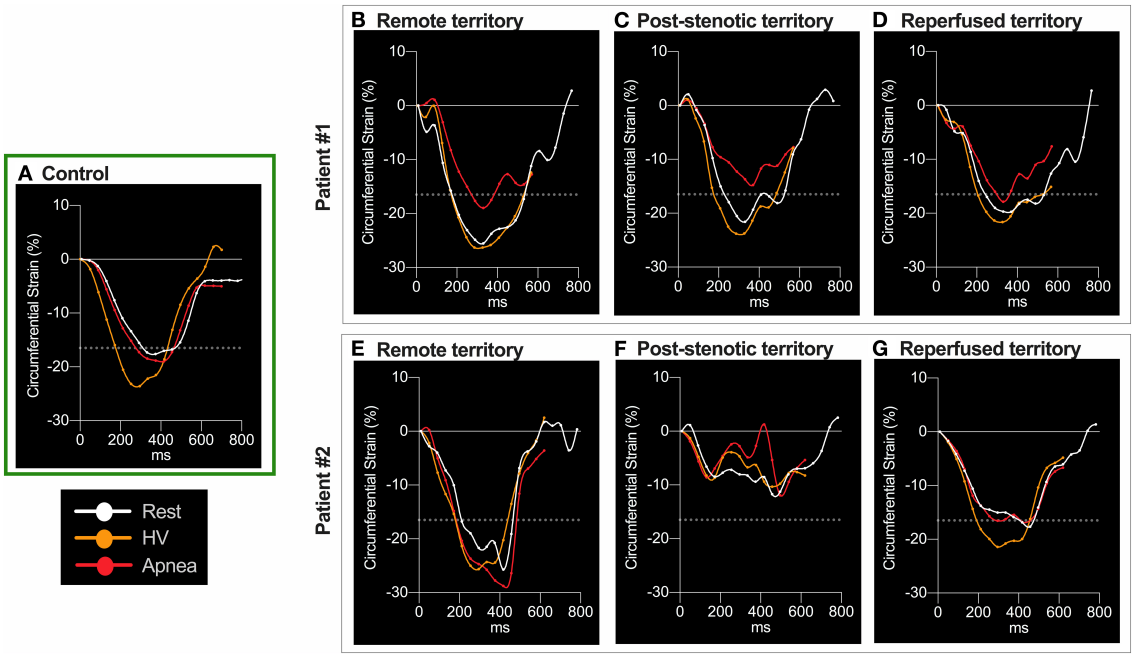

FIGURE 3 | Circumferential strain curve at the different breathing maneuver steps. Circumferential strain during the cardiac cycle for three subjects. In the healthy control participant **(A)**, hyperventilation (HV, orange) improved peak strain (PS), seen by the more negative values, and shortened time to peak strain (TTP) in comparison to resting conditions (white). Both normalized with apnea (red). The dotted line denotes the level of 1 SD below mean PS of control subjects at rest (-16.5%). Values lower than−16.5% were regarded as normal peak circumferential shortening in strain. Patient 1: All three territories had normal PS at rest. HV improved PS without altering TTP. In remote myocardium **(B)** PS was not attenuated beyond−16.5% and TTP remained unchanged during apnea. In post-stenotic territory regional T1 was 1153ms and T2 was elevated at 45.2ms. Here apnea aggravated PS more severely to a subnormal level **(C)** and prolonged TTP. The increase in TTP was representative for post-stenotic myocardium in CAD. Reperfused territory experienced stable TTP and less apnea-induced attenuation of PS, still being in the normal range **(D)**. In the reperfused segments normal native T1 (1120ms) and slightly increased T2 (42.2ms) were found in this patient 33 days after NSTEMI. Patient 2: PS in remote territory remained relatively unaffected by the breathing maneuver **(E)**. In post-stenotic **(F)** territories PS was abnormal already at rest and also during provocation. In contrast to the majority of patients, here apnea even provoked severe systolic function in the post-stenotic segments (T1, 1273 ms; T2, 35.9 ms). In territories reperfused 36 days after an NSTEMI **(G)**, PS was borderline with no attenuation due to the breathing maneuvers (T1, 1252 ms; T2, 36.5 ms).

no individual segments excluded for tracking issues. Diastolic strain rate could be acquired in 81% of segments, and myocardial oxygenation in 92%.

Participant Characteristics

Baseline characteristics are provided in **Table 1**. All patients had at least one stenosed coronary vessel with QCA > 50%, with an average diameter stenosis of 67 ± 16%. In the CAD patients, a significant lesion was either in the proximal (68%) or mid (32%) portion of the relevant coronary artery (**Table 2**). As a result, when translating to the AHA segmentation for the CMR images, all patients had at least one segment in the mid-slice classified as post-stenotic territory, with a median of 5.0 [3.5–6.0] of the 16 myocardial AHA segments defined as post-stenotic when considering the entire ventricle. A PCI procedure was performed during the initial visit in 20 patients (80%).

Standard left ventricular function measures of ejection fraction (63 ± 5 vs. 62 ± 10%, $p = 0.965$) and cardiac index (3.1 ± 0.7 vs. 2.9 ± 0.8 L/min/m^2, $p = 0.745$) acquired at resting conditions did not differ between controls and patients. Nor did global peak circumferential strain acquired from the standard short axis stack differ between the groups ($PS_{SAXStack}$ −19.3 ± 1.9 vs.−20.4 ± 3.6 %, $p = 0.279$). Similarly, there was no difference in the tissue characterization in global native T1 (1209 ± 41 vs. 1228 ± 51 ms, $p = 0.055$) and T2 mapping (39.2 ± 1.8 vs. 39.6 ± 2.4 ms, $p = 0.642$) between groups. Nor were there regional differences between post-stenotic, reperfused and remote territory for either native T1 (1229 ± 53, 1222 ± 66, and 1223 ± 52 ms, $p = 0.857$) or T2 (40.4 ± 3.5, 39.3 ± 1.9, and 39.4 ± 2.9 ms, respectively, $p = 0.654$).

Validation of Strain Analysis From ECG-Triggered OS Cines

For global and post-stenotic myocardium strain results from OS cines there was moderate to good intra-class correlation with results derived from the function stack for both global and territorial measurements ($n = 25$, **Supplementary Table 1**). Global PS showed best agreement (ICC: 0.900, $p < 0.001$) between sequence types. The ICC for inter-observer agreement for PS from the OS cines was excellent at 0.907 ($p < 0.001$, $n = 25$).

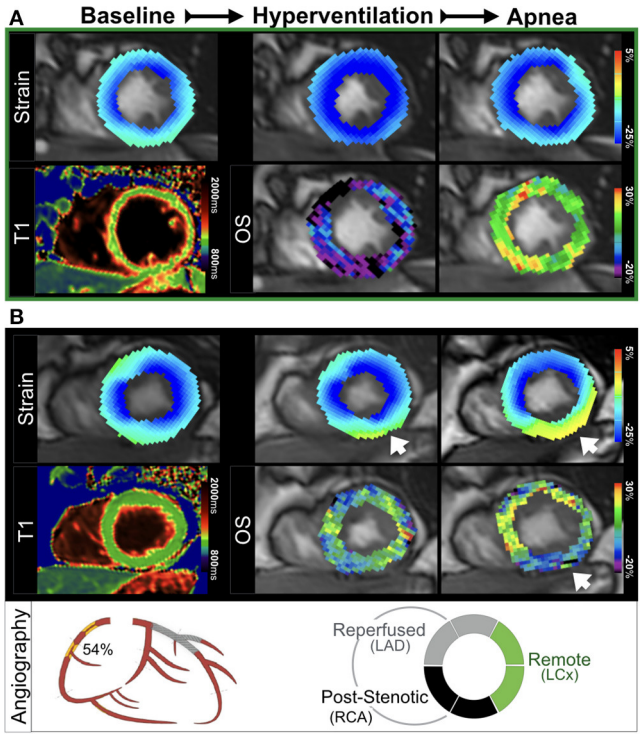

FIGURE 4 | Ventricular dysfunction and myocardial deoxygenation induced by apnea. **(A)** In a healthy control, hyperventilation (HV) augmented peak strain (PS) homogenously to more negative values. This was accompanied by a HV-induced decrease in OS-SI (blue), followed by an increase of oxygenation (green-yellow) with apnea and normalization of (PS), which is the physiologic response to the breathing maneuver sequence. **(B)** In a patient (**Figure 2**, patient 1) with an RCA stenosis (QCA 54%) and a stented LAD, a normal PS was observed in the myocardium at rest. Hyperventilation induced a mild peak strain abnormality in the inferior wall that worsened in apnea (yellow, arrow). This functional reduction was colocalized with apnea-induced regional deoxygenation in post-stenotic myocardium (blue-purple). There was no increased native T1 found in this patient.

Response to Breathing Maneuvers in Healthy Subjects

Myocardial oxygenation response in healthy subjects was characterized by a reduction of myocardial SI after 60 s of hyperventilation (-10.2 ± 8.3%) and an increase (+9.1 ± 5.3%) after 30 s of apnea. At the end of hyperventilation, PS was significantly augmented compared to baseline (**Figure 2**). This was accompanied by a shortening of TTP and acceleration of dSR. These changes returned to baseline during apnea (**Figure 3A**, **Supplementary Figures 1A, 2**). The findings for when TTP was additionally corrected for heart-rate are shown in **Supplementary Figure 3**, **Figure 3A** shows a homogenous oxygenation and strain response of a healthy subject.

Global Response in CAD Patients

In response to hyperventilation, CAD patients showed a global myocardial OS-SI response of −5.8 ± 9.6 % (p = 0.085 vs. controls), and in response to apnea a smaller global OS-SI increase (+2.7 ± 4.8 %, p < 0.001 vs. controls), when compared to healthy controls. Moreover, this attenuated global response was correlated with increasing T1 (r = −0.45, p = 0.002, **Supplementary Table 3**). Strain analysis of CAD patients demonstrated an attenuated hyperventilation-induced change of global PS (**Figure 2**) in comparison to healthy controls (Δ-1.3 ± 1.6 vs.−3.3 ± 1.6 %, p = 0.008). By 30 s of subsequent apnea, PS had significantly worsened beyond values at rest (p < 0.001). This peak strain response during apnea was also significantly attenuated in comparison to controls (**Figure 2**, p = 0.025). Global TTP of patients did not respond significantly to hyperventilation, in contrast to TTP of healthy controls. Apnea however prolonged global TTP in patients (p = 0.002). Global early dSR was attenuated both during hyperventilation and during apnea in CAD patients (p = 0.014 and p = 0.012, respectively). Radial strain data are given in **Supplementary Figure 2**, **Supplementary Table 2**. With the breathing maneuver stimulus patients reported the onset of minor adverse effects such as dizziness, dry mouth and tingling in the digits that dissipated upon termination of the maneuver. No patients reported any angina or significant discomfort.

Regional Myocardial Oxygenation and Function in CAD Patients

Hyperventilation did not induce oxygenation differences between post-stenotic (-5.5 ± 10.5 %), remote myocardium (-7.1 ± 11.3%) and reperfused territories (-3.3 ± 8.4%, p = 0.350). The subsequent apnea consistently provoked regional oxygenation heterogeneities in post-stenotic (+1.6 ± 3.9%, p = 0.004) and reperfused territories 1.3 ± 6.0%; p = 0.024) compared to the response in remote territories (+4.9 ± 5.7%). Strain and myocardial oxygenation responses of territories and provocation maneuvers steps are detailed in **Supplementary Table 2** and depicted in **Figures 2–5**. All territories exhibited attenuated PS during apnea when compared to post-hyperventilation (**Figure 1**, p < 0.05), while post-stenotic myocardium was the only territory to have a further reduction in strain with apnea beyond baseline (p = 0.004). Similarly, post-stenotic myocardium was the only territory to have a significantly prolonged TTP (rest: 319 ± 46, hyperventilation: 324 ± 59, apnea: 343 ± 58, p = 0.022 vs. rest). This can also be seen in **Supplementary Table 2**. Remote myocardium showed significantly shortened TTP after hyperventilation (p = 0.008) with recovery to baseline during apnea (p < 0.001), which was comparable to the respective global response of healthy controls, while no response in TTP was observed in reperfused myocardium. There were no significant territorial changes or differences in dSR. Medications taken by the patients such as beta-blockers did not have a statistical impact on the post-stenotic myocardial oxygenation response or on the strain parameters measured during hyperventilation or apnea (**Supplementary Figure 4**).

Resting vs. Post-stimulatory Discrimination of Post-stenotic Territory

The ROC analysis in **Figure 6** shows, that both tissue characterization and functional CMR measurements acquired in

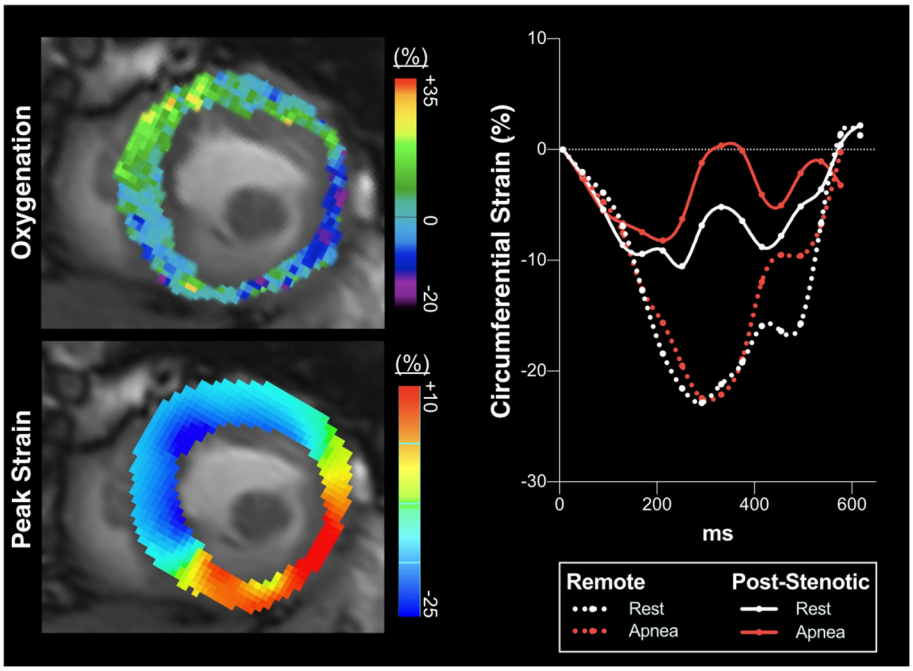

FIGURE 5 | Circumferential strain over the cardiac cycle. In a patient with a full occlusion of the right coronary artery partially compensated for by collaterals, deoxygenation occurs in the inferoseptal, inferior and lateral myocardial segments in response to brief intentional apnea seen with OS-CMR (upper left panel, mid-ventricular short axis slice, blue indicating oxygenation deficits, while green shows a normal response). This is accompanied by impaired peak strain (PS, yellow-orange) of the very same segments during apnea (lower left panel, circumferential strain CMR-FT analysis), while remote healthy myocardial segments display a normal physiologic response. The right panel shows strain over the cardiac cycle averaged for the post-stenotic and remote territories defined by the angiography analysis. While remote myocardium at apnea slightly increased (PS) beyond the resting baseline, the angiographically defined post-stenotic myocardium in the inferoseptal and inferior wall showed an averaged pronounced attenuation of PS represented by less negative strain values indicating aggravating severe hypokinesia to regional dyskinesia (seen also in the left lower panel) of these segments triggered by myocardial deoxygenation during apnea. This patient did not have any reperfused territory. Both native T1 (1381 ms) and T2 (44.2 ms) mapping were elevated in the post-stenotic territory.

normal resting conditions were not able to discriminate post-stenotic territory ($p > 0.05$). For CMR measures obtained with the breathing maneuver stimulus, both OS-CMR (AUC: 0.88, SE: 0.06, $p < 0.001$) and PS measured from the OS-cine (AUC: 0.73, SE: 0.09, $p = 0.023$) were able to individually detect post-stenotic territories at the end of apnea. The combination of the two measures of OS-CMR and PS yielded an AUC of 0.91 (SE: 0.04, $p < 0.001$) and was significantly better at defining post-stenotic territories than the post-apneic PS measurement alone ($p = 0.036$).

DISCUSSION

The major finding of this study is that in patients with chronic coronary syndromes and primarily intermediate coronary stenoses, regional impairment of myocardial kinetics provoked by voluntary breathing maneuvers is detected by feature tracking strain analysis on oxygenation-sensitive (OS) cine acquisitions. Moreover, myocardial oxygenation is compromised in these same territories, with the combined analysis of tissue and wall function improving the detection of post-stenotic myocardium. In fact, this could only be differentiated with the breathing maneuver as traditional contrast-free tissue and functional measures at rest were unable to discriminate post-stenotic myocardium of primarily intermediate-grade stenoses from healthy controls with similar age. These measurements of myocardial oxygenation and strain can be simultaneously obtained from the same set of OS cines, ensuring both measurements are of the same territory and represent the same timepoint during the breathing maneuver provocation stimulus.

Oxygenation and Strain Response to Hyperventilation

As previously reported, healthy participants respond to hyperventilation with decreasing myocardial oxygenation, and to apnea with increased tissue oxygenation (16, 17, 21). Although not completely understood, multiple mechanisms can simultaneously occur during breathing maneuvers that lead to this physiologic response with a key pathway likely driven by hypocapnic vasoconstriction and hypercapnic vasodilation of coronary vasculature (13, 16). The increase in heart rate which accompanies hypocapnic vasoconstriction can further increase oxygen consumption and promote deoxygenation (12, 22, 23). Enhanced contractility and heart rate acceleration from sympathetic stimulation can lead

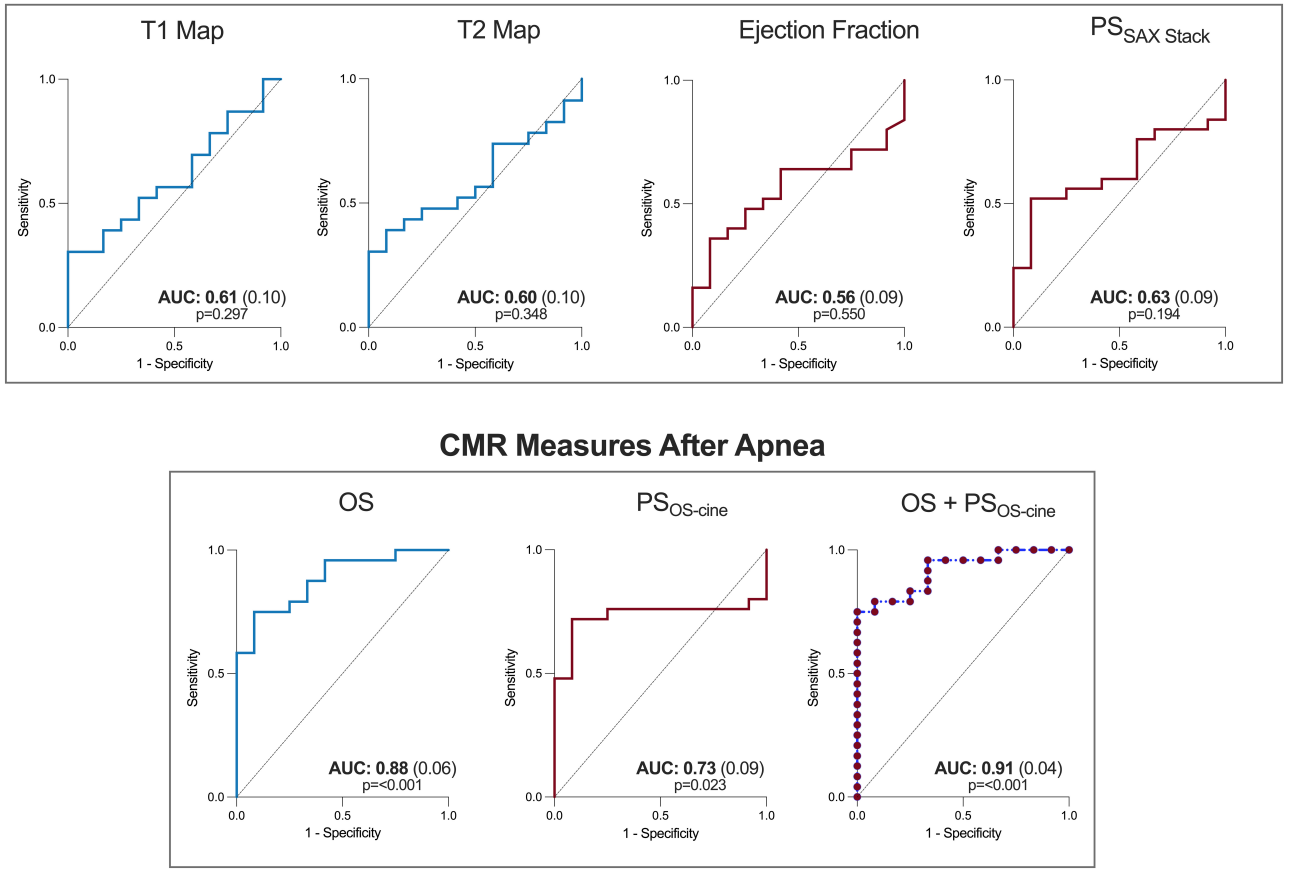

FIGURE 6 | Combined oxygenation-sensitive and feature tracking analysis improves determination of post-stenotic myocardium. Receiver operating characteristic curves are shown for the CMR parameters at resting conditions (top) for both tissue characterization sequences (blue) and functional measurements (red). The bottom row depicts the oxygenation-sensitive (OS) response after 30s of apnea, and the feature tracking peak strain (OS) measurements acquired from the same image, along with a combined predicted curve combining both tissue and functional measures. AUC, Area under the curve (standard error).

to the increase of PS and shortening of TTP observed in healthy subjects (24). For this combined breathing maneuver technique, hyperventilation primarily serves as the preparatory phase to induce a state of hypocapnia, which will result in a greater range of CO_2 manipulation to be observed with the apnea and also allow the patient to maintain a longer breath-hold. The second phase of the combined breathing maneuver, the apnea component, is the focus of the analysis where oxygenation and functional deficits are more consistently revealed.

Oxygenation and Strain Response to Apnea

During apnea arterial carbon dioxide partial pressure rises and heart rate slows, promoting vasodilation and enhancing myocardial oxygenation in healthy myocardium (12, 16). As even breath-holds as short as 10–15 s have been reported to lead to a detectible myocardial and cerebral hyperemic response (17, 25). A combined function of the respiratory, cardiac parasympathetic and vasomotor centers likely play a supporting role in improving myocardial perfusion (26). In healthy participants post-hyperventilation apnea was accompanied by luxury myocardial oxygenation and return of all strain parameters to resting values. However, in our patient group, a detailed regional analysis showed that these patients exhibited heterogenous territorial responses of both myocardial oxygenation and strain indicating that respiratory provocation maneuvers act differently on remote, reperfused and post-stenotic myocardium. Specifically, myocardial deoxygenation developed in the post-stenotic segments during apnea. Coronary arteries affected by a fixed epicardial stenosis exhibit a post-stenotic compensatory vasodilation, exploiting the vasodilatory range. Post-stenotic blood flow becomes pressure dependent and vasodilating stimuli such adenosine or apnea cannot increase blood flow further, which results in an attenuated or blunted increase in SI in OS-CMR sequences (5). In the presence of compensatory post-stenotic dilation and high reported post-stenotic pCO_2 levels in CAD patients, the post-stenotic vasculature cannot

dilate further and the observed regional heterogeneity may be further explained by redistribution of blood flow and possibly inter-coronary steal away from territory distal to a fixed stenosis, which may lead to a net decrease in OS-SI (12, 17, 27).

Importantly, myocardial deoxygenation does not reflect ischemia *per se*. As long as oxygen supply exceeds myocardial demand, the observed deoxygenation only delineates myocardium at risk for ischemia (28). If the oxygen demand is not matched by the supply, ischemia and myocardial dysfunction are the consequence. The worsened myocardial kinetics in post-stenotic myocardium in the CAD group occurred in the same myocardial tissue that desaturated during the breathing maneuver, hinting to early ischemic sequelae. Post-stenotic myocardium showed an increase of mean TTP along with attenuated peak strain from baseline to apnea, which may be explained by an increasingly compromised myocardial oxygenation. This was not seen in remote or reperfused territories. During isovolumetric contraction, pressure in the LV cavity increases when segments with sufficient oxygen supply contract in synchronized fashion (24, 29). Segments with compromised myocardial oxygenation are prone to delayed contraction after opening of the aortic valve compared to unaffected segments. This is known as post-systolic shortening, indicated by heterogenous TTP between segments, which has a high sensitivity to ischemia (30, 31).

Diastolic Function

Strain assessments can also provide details on diastolic dysfunction, which is an early harbinger of ischemia, preceding systolic dysfunction, electrocardiogram abnormalities and other ischemic sequelae (32). Early peak diastolic strain rate (dSR) at CMR-FT reports the deformation rate during the active, energy dependent part of ventricular relaxation (33). Accordingly, step-wise global deceleration of early diastolic strain across the breathing maneuvers was observed, and this was associated with increased T2 burden. Edema is also linked with ventricular stiffness and when myocardial edema aggravates, the rise of interstitial pressure reduces ventricular chamber compliance (34, 35). While T2 is not often chronically elevated, edema at the time of CO_2 challenges may predispose cardiac patients to diastolic dysfunction. However, the use of regional diastolic strain rate by FT is limited and still developing, as observed by the variation observed in **Figure 2**.

Imaging the Different Features of the Ischemic Sequalae

The onset of acute cardiac ischemia is a well described progression of abnormal cardiovascular features (2). The order of these features has often been described as a constellation or cascade, in which after the onset of a negative imbalance in myocardial oxygen supply and demand, myocardial perfusion abnormalities are observed early in the cascade, followed by ventricular diastolic and systolic dysfunction, before culminating in electrocardiogram abnormalities and symptoms of myocardial ischemia (3, 36). In an animal study, the spatiotemporal difference observed between perfusion deficits and ventricular dysfunction varied between the subjects based on the degree of disease (37). This variation highlights the importance of using imaging to target multiple stages of this cascade to detect the onset of ischemia in the early stages. In our findings, the presence of diastolic and systolic dysfunction as early sequelae of flow maldistributions in relation to our measured decreases in myocardial oxygenation is suggestive that our breathing maneuver may have triggered inducible ischemia. The fact that short breathing maneuver challenges can trigger this ischemic sequelae may be of concern to situations where the heart is under stress. This may occur if these patients undergo exertion, or during other medical procedures that expose a patient to multiple stimuli. An example may be during general anesthesia, which is an environment where fluctuations in blood gases and respiratory rates frequently occur in combination with other stimuli. Consequently, these CCS patients could be at risk of peri-operative induced ischemia, despite normal resting function.

Diagnostic Potential

While in echocardiography myocardial strain analysis is already firmly established, studies reporting diagnostic and prognostic potential of resting strain measurements from CMR imaging are emerging (38–41). Strain analysis from either modality is useful to identify subtle deficiencies in regional contractile function prior to decreases in left ventricular stroke volume. Reduced myocardial strain emerged as a superior predictor of adverse outcome from myocardial infarction when compared to cardiac output data (39). Strain can be an early marker as impaired contractility in small regions may not necessarily result in globally reduced ejection fraction as long as a sufficient mass of unaffected myocardium can compensate. However, in this cohort with CCS and often intermediate angiographically defined lesions, there was no difference between groups in CMR-FT acquired from the typical short-axis stack at resting conditions, nor could it discriminate post-stenotic territory. In line with strain, other contrast-free CMR measures acquired at rest including ejection fraction and the tissue characterization sequences of T1 and T2 also did not differentiate post-stenotic territory in this small sample.

In particular for investigating ischemia, stress exams are implemented to provoke inducible ischemia. This has been performed frequently with echocardiography based strain measurements, commonly using pharmacological stimuli such as dobutamine or dipyridamole (42). CMR-FT has already demonstrated its usefulness in the detection of CAD during dobutamine stress (43). More recently, Romano et al. (44) used blunted responses of feature tracking longitudinal strain to a vasodilator stress as an independent predictor of major adverse cardiac events in patients with CAD incremental to traditional clinical risk factors or imaging results such as ejection fraction and late gadolinium enhancement. CMR is beneficial as it also investigates myocardial tissue features and vascular function. First pass perfusion scans (5) and native T1 stress mapping both show perfusion deficits under vasodilator stress (45). However, there is a significant proportion of patients with contraindications against contrast agents and vasodilating agents. Similar to native T1 mapping and strain imaging, OS-CMR does

not rely on contrast agents. Previous studies have used OS-CMR together with adenosine as a vasodilator stress (5, 46), but non-pharmacological approaches such as inhalation of CO_2 and breathing maneuvers have been proposed as alternative vasodilator stimuli (14–16).

Provocation testing of strain parameters with simple breathing maneuvers may be another perspective for early non-invasive diagnostics, even by employing echocardiography as the more widely available imaging modality. As shown by Ochs et al. (47) by implementing strain encoded MR imaging after the same combined breathing maneuver, this group was able to detect coronary stenosis with an even higher diagnostic accuracy than adenosine-based perfusion imaging. This supports our findings about the functional impact of hyperventilation and apnea in a coronary artery disease population. Each approach has its advantages. Although strain encoded imaging is an acquisition-based technique requiring special images to be acquired during the exam, it can have a higher reproducibility than feature tracking based measurements (48). Recent publications have demonstrated that CMR-FT has a high reproducibility between readers in a patient cohort, especially for circumferential parameters in comparison to longitudinal markers (49). As mentioned above, the key advantage of our technique is the ability to use CMR-FT post-processing software to simultaneously acquire myocardial oxygenation and deformation information. In **Figure 6**, it can be observed that the combination of oxygenation-sensitive imaging on top of CMR-FT, increased the area under the curve for detecting post-stenotic territory over CMR-FT alone. However, to image this dynamic change in myocardial function rapid acquisition was required and consequently only two short-axis views were acquired, and long-axis views were not available. In the future it would be wise to apply this technique to investigate longitudinal strain as well, as ischemia is likely to first arise in the subendocardium. Since this myocardial layer is composed primarily of longitudinal fibers, longitudinal strain may have the potential to detect inducible ischemia even earlier. Future work needs to confirm the diagnostic utility of these techniques for non-pharmacologic and endogenous stress testing. Further work can investigate the comparison between strain response of orientations. Importantly, the circumferential strain analysis allows a better matching to the tissue characterization sequences often acquired in a short-axis view.

Limitations

As this was a contrast-free exam, our study is limited by the lack of late gadolinium enhancement (LGE) and extracellular volume mapping (ECV). Thus, the presence or absence of scar cannot be confirmed in this cohort, nor can the impact of scar on the strain response to breathing maneuvers be determined at this point. In patients with myocardial infarction, resting strain has been reported to be related to the extent of LGE (39). However, in a heart failure cohort without infarct patients, there was no association of resting strain with LGE, rather a correlation to T2 mapping and the OS response with apnea (50). This will have to be investigated in the future to determine if infarcted territory impacts both resting strain, and the dynamic response to a stimulus. Of note, there was no significant difference in native T1 or T2 between the allocated territories in our cohort. The role of native T1 and CMR-FT may help in the development of contrast free protocols (45, 47, 51). Our model did not take the hemodynamic significance of a stenosis and its possible collateralization into account. Our enrolment procedures were based on anatomical measures, as it was a marker available for all patients and is a measurement that is not limited by complex and serial lesions. FFR measurements to address this issue were not available for this study, and it would be important in the future to investigate the heterogeneity in strain responses in relation to the hemodynamic significance of the stenosis. This study had a small sample size, and utility of this technique needs to be validated in larger cohorts, in single and multi-vessel disease, and with a greater range of degrees of stenoses.

The fact that majority of the enrolled CAD patients were under chronic medication with beta-blockers and ACE inhibitors could confound the heart rate increase, oxygenation and strain response observed in the patient group. In this population, patient medications were not statistically associated with the oxygenation or strain results during hyperventilation or apnea. Pharmacological beta-blockade would not explain or confound the inter-territorial differences seen within our CAD patient cohort. Similar to our findings, it has been demonstrated that beta-blocker therapy did not impact myocardial perfusion imaging with adenosine (52), or the heart rate response to hyperventilation (23). Nevertheless, little is known about the effect of beta-blockers and breathing maneuvers on myocardial strain and oxygenation in larger samples.

CONCLUSION

In myocardium subtended to an anatomically defined intermediate-grade coronary stenosis of patients with chronic coronary syndromes, an oxygenation-sensitive (OS)-CMR cine acquisition during a breathing maneuver can simultaneously unmask an impaired vascular and functional response. The detection of post-stenotic myocardium was improved with a combined approach of measuring an attenuated myocardial oxygenation reserve along with CMR feature-tracking. Furthermore, peak strain is attenuated and time to peak strain is prolonged exclusively in post-stenotic segments at apnea. These findings may be indicative of inducible early myocardial ischemia.

DATA AVAILABILITY STATEMENT

The raw data supporting the conclusions of this article will be made available by the authors, without undue reservation.

ETHICS STATEMENT

The study protocol was approved by the Ethics Board of the Canton of Bern. The patients/participants provided their written informed consent to participate in this study.

AUTHOR CONTRIBUTIONS

DG, KF, BE, and BJ: conceptualization and methodology. DG, KF, BS, KY, YU, ZZ, CB, TO, MB, CG, and LR: investigation and analysis. BS, KF, and DG: original manuscript draft. KY, YU, BJ, TO, MB, CG, HvT-K, LR, BE, and DG: manuscript revision and editing. KF: visualization. DG, BE, HvT-K, and LR: supervision. DG and BE: project administration. All authors contributed to the article and approved the submitted version.

FUNDING

This work was supported by institutional research funds of the Department of Anaesthesiology and Pain Medicine at Inselspital, Bern University Hospital, Switzerland, and by the European Society of Anaesthesiology Research Project Grant.

ACKNOWLEDGMENTS

This study was made possible by the superb work of the study nurses Silvia Luescher, Monika Stucki, Céline Riecker, Sarah Overney and of imaging technician Leonie Scheuner.

SUPPLEMENTARY MATERIAL

The Supplementary Material for this article can be found online at: https://www.frontiersin.org/articles/10.3389/fcvm.2022.800720/full#supplementary-material

REFERENCES

1. Knuuti J, Wijns W, Saraste A, Capodanno D, Barbato E, Funck-Brentano C, et al. 2019 ESC Guidelines for the diagnosis and management of chronic coronary syndromes: the task force for the diagnosis and management of chronic coronary syndromes of the European society of cardiology (ESC). *Eur Heart J.* (2020) 41:407–77. doi: 10.1093/eurheartj/ehz425
2. Nesto RW, Kowalchuk GJ. The ischemic cascade: temporal sequence of hemodynamic, electrocardiographic and symptomatic expressions of ischemia. *Am J Cardiol.* (1987) 59:C23–30. doi: 10.1016/0002-9149(87)90192-5
3. Maznyczka A, Sen S, Cook C, Francis DP. The ischaemic constellation: an alternative to the ischaemic cascade-implications for the validation of new ischaemic tests. *Open Heart.* (2015) 2:e000178. doi: 10.1136/openhrt-2014-000178
4. Stillman AE, Oudkerk M, Bluemke DA, de Boer MJ, Bremerich J, Garcia EV, et al. Imaging the myocardial ischemic cascade. *Int J Cardiovasc Imaging.* (2018) 34:1249–63. doi: 10.1007/s10554-018-1330-4
5. Luu JM, Friedrich MG, Harker J, Dwyer N, Guensch D, Mikami Y, et al. Relationship of vasodilator-induced changes in myocardial oxygenation with the severity of coronary artery stenosis: a study using oxygenation-sensitive cardiovascular magnetic resonance. *Eur Heart J Cardiovasc Imaging.* (2014) 15:1358–67. doi: 10.1093/ehjci/jeu138
6. Pauling L, Coryell CD. The magnetic properties and structure of hemoglobin, oxyhemoglobin and carbonmonoxyhemoglobin. *Proc Natl Acad Sci U S A.* (1936) 22:210–6. doi: 10.1073/pnas.22.4.210
7. Ogawa S, Lee TM, Kay AR, Tank DW. Brain magnetic resonance imaging with contrast dependent on blood oxygenation. *Proc Natl Acad Sci USA.* (1990) 87:9868–72. doi: 10.1073/pnas.87.24.9868
8. Kim S-G, Ogawa S. Biophysical and physiological origins of blood oxygenation level-dependent fMRI signals. *J Cereb Blood Flow Metab.* (2012) 32:1188–206. doi: 10.1038/jcbfm.2012.23
9. Wacker CM, Bock M, Hartlep AW, Beck G, van Kaick G, Ertl G, et al. Changes in myocardial oxygenation and perfusion under pharmacological stress with dipyridamole: assessment using T*2 and T1 measurements. *Magn Reson Med.* (1999) 41:686–95. doi: 10.1002/(sici)1522-2594(199904)41:4<686::aid-mrm6>3.0.co;2-9
10. Guensch DP, Michel MC, Huettenmoser SP, Jung B, Gulac P, Segiser A, et al. The blood oxygen level dependent (BOLD) effect of in-vitro myoglobin and hemoglobin. *Sci Rep.* (2021) 11:11464. doi: 10.1038/s41598-021-90908-x
11. Fischer K, Neuenschwander MD, Jung C, Hurni S, Winkler BM, Huettenmoser SP, et al. Assessment of myocardial function during blood pressure manipulations using feature tracking cardiovascular magnetic resonance. *Front Cardiovas Med.* (2021) 8:1353. doi: 10.3389/fcvm.2021.743849
12. Fischer K, Guensch DP, Shie N, Lebel J, Friedrich MG. Breathing maneuvers as a vasoactive stimulus for detecting inducible myocardial ischemia - an experimental cardiovascular magnetic resonance study. *PLoS ONE.* (2016) 11:e0164524. doi: 10.1371/journal.pone.0164524
13. Crystal GJ. Carbon dioxide and the heart: physiology and clinical implications. *Anesth Analg.* (2015) 121:610–23. doi: 10.1213/ANE.0000000000000820
14. Beaudin AE, Brugniaux JV, Vöhringer M, Flewitt J, Green JD, Friedrich MG, et al. Cerebral and myocardial blood flow responses to hypercapnia and hypoxia in humans. *Am J Physiol Heart Circ Physiol.* (2011) 301:H1678–1686. doi: 10.1152/ajpheart.00281.2011
15. Yang H-J, Yumul R, Tang R, Cokic I, Klein M, Kali A, et al. Assessment of myocardial reactivity to controlled hypercapnia with free-breathing T2-prepared cardiac blood oxygen level-dependent MR imaging. *Radiology.* (2014) 272:397–406. doi: 10.1148/radiol.14132549
16. Guensch DP, Fischer K, Flewitt JA, Yu J, Lukic R, Friedrich JA, et al. Breathing manoeuvre-dependent changes in myocardial oxygenation in healthy humans. *Eur Heart J Cardiovasc Imaging.* (2014) 15:409–14. doi: 10.1093/ehjci/jet171
17. Fischer K, Yamaji K, Luescher S, Ueki Y, Jung B, von Tengg-Kobligk H, et al. Feasibility of cardiovascular magnetic resonance to detect oxygenation deficits in patients with multi-vessel coronary artery disease triggered by breathing maneuvers. *J Cardiovasc Magn Reson.* (2018) 20:31. doi: 10.1186/s12968-018-0446-y
18. Guensch DP, Fischer K, Yamaji K, Luescher S, Ueki Y, Jung B, et al. Effect of hyperoxia on myocardial oxygenation and function in patients with stable multivessel coronary artery disease. *J Am Heart Assoc.* (2020) 9:e014739. doi: 10.1161/JAHA.119.014739
19. Donato P, Coelho P, Santos C, Bernardes A, Caseiro-Alves F. Correspondence between left ventricular 17 myocardial segments and coronary anatomy obtained by multi-detector computed tomography: an ex vivo contribution. *Surg Radiol Anat.* (2012) 34:805–10. doi: 10.1007/s00276-012-0976-1
20. Fischer K, Ranjan R, Friess J-O, Erdoes G, Mikasi J, Baumann R, et al. Study design for a randomized crossover study investigating myocardial strain analysis in patients with coronary artery disease at hyperoxia and normoxemia prior to coronary artery bypass graft surgery (StrECHO-O2). *Contemp Clin Trials.* (2021) 110:106567. doi: 10.1016/j.cct.2021.106567
21. Fischer K, Guensch DP, Friedrich MG. Response of myocardial oxygenation to breathing manoeuvres and adenosine infusion. *Eur Heart J Cardiovasc Imaging.* (2015) 16:395–401. doi: 10.1093/ehjci/jeu202
22. Burton DA, Stokes K, Hall GM. Physiological effects of exercise. *Cont Educ Anaesth Crit Care Pain.* (2004) 4:185–8. doi: 10.1093/bjaceaccp/mkh050
23. Hawkins SM, Guensch DP, Friedrich MG, Vinco G, Nadeshalingham G, White M, et al. Hyperventilation-induced heart rate response as a potential marker for cardiovascular disease. *Sci Rep.* (2019) 9:1–10. doi: 10.1038/s41598-019-54375-9
24. Alexopoulos D, Christodoulou J, Toulgaridis T, Sitafidis G, Klinaki A, Vagenakis AG. Hemodynamic response to hyperventilation test in healthy volunteers. *Clin Cardiol.* (1995) 18:636–41. doi: 10.1002/clc.4960181109

25. Liu H-L, Huang J-C, Wu C-T, Hsu Y-Y. Detectability of blood oxygenation level-dependent signal changes during short breath hold duration. *Magn Reson Imaging.* (2002) 20:643–8. doi: 10.1016/S0730-725X(02)00595-7
26. Foster GE, Sheel AW. The human diving response, its function, and its control. *Scand J Med Sci Sports.* (2005) 15:3–12. doi: 10.1111/j.1600-0838.2005.00440.x
27. Becker LC. Conditions for vasodilator-induced coronary steal in experimental myocardial ischemia. *Circulation.* (1978) 57:1103–10. doi: 10.1161/01.CIR.57.6.1103
28. Guensch DP, Fischer K, Jung C, Hurni S, Winkler BM, Jung B, et al. Relationship between myocardial oxygenation and blood pressure: experimental validation using oxygenation-sensitive cardiovascular magnetic resonance. *PLoS ONE.* (2019) 14:e0210098. doi: 10.1371/journal.pone.0210098
29. Fukuta H, Little WC. The cardiac cycle and the physiologic basis of left ventricular contraction, ejection, relaxation, and filling. *Heart Fail Clin.* (2008) 4:1–11. doi: 10.1016/j.hfc.2007.10.004
30. Brainin P, Biering-Sørensen SR, Møgelvang R, de Knegt MC, Olsen FJ, Galatius S, et al. Post-systolic shortening: normal values and association with validated echocardiographic and invasive measures of cardiac function. *Int J Cardiovasc Imaging.* (2019) 35:327–37. doi: 10.1007/s10554-018-1474-2
31. Voigt J-U, Lindenmeier G, Exner B, Regenfus M, Werner D, Reulbach U, et al. Incidence and characteristics of segmental postsystolic longitudinal shortening in normal, acutely ischemic, and scarred myocardium. *J Am Soc Echocardiogr.* (2003) 16:415–23. doi: 10.1016/S0894-7317(03)00111-1
32. Schuijf JD, Shaw LJ, Wijns W, Lamb HJ, Poldermans D, de Roos A, et al. Cardiac imaging in coronary artery disease: differing modalities. *Heart.* (2005) 91:1110–7. doi: 10.1136/hrt.2005.061408
33. Westenberg JJM. CMR for assessment of diastolic function. *Curr Cardiovasc Imaging Rep.* (2011) 4:149–58. doi: 10.1007/s12410-011-9070-z
34. Dongaonkar RM, Stewart RH, Geissler HJ, Laine GA. Myocardial microvascular permeability, interstitial oedema, and compromised cardiac function. *Cardiovasc Res.* (2010) 87:331–9. doi: 10.1093/cvr/cvq145
35. Guensch DP, Yu J, Nadeshalingam G, Fischer K, Shearer J, Friedrich MG. Evidence for acute myocardial and skeletal muscle injury after serial transthoracic shocks in healthy swine. *PLoS ONE.* (2016) 11:e0162245. doi: 10.1371/journal.pone.0162245
36. Schinkel AFL, Bax JJ, Geleijnse ML, Boersma E, Elhendy A, Roelandt JRTC, et al. Noninvasive evaluation of ischaemic heart disease: myocardial perfusion imaging or stress echocardiography? *Eur Heart J.* (2003) 24:789–800. doi: 10.1016/S0195-668X(02)00634-6
37. Leong-Poi H, Rim S-J, Le DE, Fisher NG, Wei K, Kaul S. Perfusion versus function: the ischemic cascade in demand ischemia. *Circulation.* (2002) 105:987–92. doi: 10.1161/hc0802.104326
38. Gavara J, Rodriguez-Palomares JF, Valente F, Monmeneu JV, Lopez-Lereu MP, Bonanad C, et al. Prognostic value of strain by tissue tracking cardiac magnetic resonance after ST-segment elevation myocardial infarction. *JACC Cardiovasc Imaging.* (2018) 11:1448–57. doi: 10.1016/j.jcmg.2017.09.017
39. Eitel I, Stiermaier T, Lange T, Rommel K-P, Koschalka A, Kowallick JT, et al. Cardiac magnetic resonance myocardial feature tracking for optimized prediction of cardiovascular events following myocardial infarction. *JACC Cardiovasc Imaging.* (2018) 11:1433–44. doi: 10.1016/j.jcmg.2017.11.034
40. Fischer K, Obrist SJ, Erne SA, Stark AW, Marggraf M, Kaneko K, et al. Feature tracking myocardial strain incrementally improves prognostication in myocarditis beyond traditional CMR imaging features. *JACC Cardiovasc Imaging.* (2020) 13:1891–901. doi: 10.1016/j.jcmg.2020.04.025
41. Riffel JH, Siry D, Salatzki J, Andre F, Ochs M, Weberling LD, et al. Feasibility of fast cardiovascular magnetic resonance strain imaging in patients presenting with acute chest pain. *PLoS ONE.* (2021) 16:e0251040. doi: 10.1371/journal.pone.0251040
42. Argyle RA, Ray SG. Stress and strain: double trouble or useful tool? *Eur J Echocardiogr.* (2009) 10:716–22. doi: 10.1093/ejechocard/jep066
43. Schneeweis C, Qiu J, Schnackenburg B, Berger A, Kelle S, Fleck E, et al. Value of additional strain analysis with feature tracking in dobutamine stress cardiovascular magnetic resonance for detecting coronary artery disease. *J Cardiovasc Magn Reson.* (2014) 16:72. doi: 10.1186/s12968-014-0072-2
44. Romano S, Romer B, Evans K, Trybula M, Shenoy C, Kwong RY, et al. Prognostic implications of blunted feature-tracking global longitudinal strain during vasodilator cardiovascular magnetic resonance stress imaging. *JACC Cardiovasc Imaging.* (2020) 13:58–65. doi: 10.1016/j.jcmg.2019.03.002
45. Yimcharoen S, Zhang S, Kaolawanich Y, Tanapibunpon P, Krittayaphong R. Clinical assessment of adenosine stress and rest cardiac magnetic resonance T1 mapping for detecting ischemic and infarcted myocardium. *Sci Rep.* (2020) 10:14727. doi: 10.1038/s41598-020-71722-3
46. Walcher T, Manzke R, Hombach V, Rottbauer W, Wöhrle J, Bernhardt P. Myocardial perfusion reserve assessed by T2-prepared steady-state free precession blood oxygen level-dependent magnetic resonance imaging in comparison to fractional flow reserve. *Circ Cardiovasc Imaging.* (2012) 5:580–6. doi: 10.1161/CIRCIMAGING.111.971507
47. Ochs MM, Kajzar I, Salatzki J, Ochs AT, Riffel J, Osman N, et al. Hyperventilation/Breath-hold maneuver to detect myocardial ischemia by strain-encoded CMR: diagnostic accuracy of a needle-free stress protocol. *JACC Cardiovasc Imaging.* (2021) 14:1932–44. doi: 10.1016/j.jcmg.2021.02.022
48. Bucius P, Erley J, Tanacli R, Zieschang V, Giusca S, Korosoglou G, et al. Comparison of feature tracking, fast-SENC, and myocardial tagging for global and segmental left ventricular strain. *ESC Heart Fail.* (2019) 7:523–32. doi: 10.1002/ehf2.12576
49. Fischer K, Linder OL, Erne SA, Stark AW, Obrist SJ, Bernhard B, et al. Reproducibility and its confounders of CMR feature tracking myocardial strain analysis in patients with suspected myocarditis. *Eur Radiol.* (2021). doi: 10.1007/s00330-021-08416-5. [Epub ahead of print].
50. Fischer K, Guensch DP, Jung B, King I, Von Tengg-Kobligk H, Giannetti N, et al. Insights Into Myocardial Oxygenation and Cardiovascular Magnetic Resonance Tissue Biomarkers in Heart Failure With Preserved Ejection Fraction. *Circ Heart Fail.* (2022). doi: 10.1161/CIRCHEARTFAILURE.121.008903. [Epub ahead of print].
51. Zhang Q, Burrage MK, Lukaschuk E, Shanmuganathan M, Popescu IA, Nikolaidou C, et al. Toward replacing late gadolinium enhancement with artificial intelligence virtual native enhancement for gadolinium-free cardiovascular magnetic resonance tissue characterization in hypertrophic cardiomyopathy. *Circulation.* (2021) 144:589–99. doi: 10.1161/CIRCULATIONAHA.121.054432
52. Lakkireddy D, Aronow WS, Bateman T, McGhee I, Nair C, Khan IA. Does beta blocker therapy affect the diagnostic accuracy of adenosine single-photon-emission computed tomographic myocardial perfusion imaging? *Am J Ther.* (2008) 15:19–23. doi: 10.1097/MJT.0b013e31804c71a7

Conflict of Interest: The authors declare that the research was conducted in the absence of any commercial or financial relationships that could be construed as a potential conflict of interest.

Publisher's Note: All claims expressed in this article are solely those of the authors and do not necessarily represent those of their affiliated organizations, or those of the publisher, the editors and the reviewers. Any product that may be evaluated in this article, or claim that may be made by its manufacturer, is not guaranteed or endorsed by the publisher.

frontiers in Cardiovascular Medicine

ORIGINAL RESEARCH
published: 25 February 2022
doi: 10.3389/fcvm.2022.804442

Myocardial Segmentation of Cardiac MRI Sequences With Temporal Consistency for Coronary Artery Disease Diagnosis

Yutian Chen[1,2,3†], Wen Xie[1,2†], Jiawei Zhang[1,2,4,5†], Hailong Qiu[1,2†], Dewen Zeng[6], Yiyu Shi[6], Haiyun Yuan[1,2], Jian Zhuang[1,2], Qianjun Jia[1,7], Yanchun Zhang[5], Yuhao Dong[1,2,7], Meiping Huang[1,2,7*] and Xiaowei Xu[1,2*]*

[1] Guangdong Provincial People's Hospital, Guangdong Academy of Medical Sciences, Guangzhou, China, [2] Guangdong Provincial Key Laboratory of South China Structural Heart Disease, Guangdong Cardiovascular Institute, Guangzhou, China, [3] Department of Computer Science, Carnegie Mellon University, Pittsburgh, PA, United States, [4] Shanghai Key Laboratory of Data Science, School of Computer Science, Fudan University, Shanghai, China, [5] Cyberspace Institute of Advanced Technology, Guangzhou University, Guangzhou, China, [6] Department of Computer Science and Engineering, University of Notre Dame, Notre Dame, IN, United States, [7] Department of Catheterization Lab, Guangdong Provincial People's Hospital, Guangdong Academy of Medical Sciences, Guangzhou, China

OPEN ACCESS

Edited by:
Nay Aung,
Queen Mary University of London,
United Kingdom

Reviewed by:
Joris Fournel,
UMR7373 Institut de Mathématiques de Marseille (I2M), France
Musa Abdulkareem,
Barts Health NHS Trust,
United Kingdom

***Correspondence:**
Yuhao Dong
barbaradong1@outlook.com
Meiping Huang
huangmeiping@126.com
Xiaowei Xu
xiao.wei.xu@foxmail.com

[†] These authors have contributed equally to this work

Specialty section:
This article was submitted to Cardiovascular Imaging, a section of the journal Frontiers in Cardiovascular Medicine

Received: 02 November 2021
Accepted: 07 January 2022
Published: 25 February 2022

Citation:
Chen Y, Xie W, Zhang J, Qiu H, Zeng D, Shi Y, Yuan H, Zhuang J, Jia Q, Zhang Y, Dong Y, Huang M and Xu X (2022) Myocardial Segmentation of Cardiac MRI Sequences With Temporal Consistency for Coronary Artery Disease Diagnosis. Front. Cardiovasc. Med. 9:804442. doi: 10.3389/fcvm.2022.804442

Coronary artery disease (CAD) is the most common cause of death globally, and its diagnosis is usually based on manual myocardial (MYO) segmentation of MRI sequences. As manual segmentation is tedious, time-consuming, and with low replicability, automatic MYO segmentation using machine learning techniques has been widely explored recently. However, almost all the existing methods treat the input MRI sequences independently, which fails to capture the temporal information between sequences, e.g., the shape and location information of the myocardium in sequences along time. In this article, we propose a MYO segmentation framework for sequence of cardiac MRI (CMR) scanning images of the left ventricular (LV) cavity, right ventricular (RV) cavity, and myocardium. Specifically, we propose to combine conventional neural networks and recurrent neural networks to incorporate temporal information between sequences to ensure temporal consistency. We evaluated our framework on the automated cardiac diagnosis challenge (ACDC) dataset. The experiment results demonstrate that our framework can improve the segmentation accuracy by up to 2% in the Dice coefficient.

Keywords: myocardial segmentation, MRI, cardiac sequences, temporal consistency, coronary artery disease, diagnosis

1. INTRODUCTION

Coronary artery disease (CAD) is the most common cause of death globally. It affects more than 100 million people, and results in about 10 million death each year (1). In the United States, about 20% of those over 65 have CAD (2). MRI is a common tool for CAD diagnosis. With cardiac magnetic resonance (CMR), the myocardial structure and functionality can be assessed and analyzed. Particularly, experienced radiologists manually perform MYO segmentation on the CMR image sequences and measure several parameters to finally determine the diagnosis. For instance, the left and right ventricular (RV) ejection fractions (EF) and stroke volumes (SV) are widely used for cardiac function analysis (3).

Recently, automatic MYO segmentation of CMR image sequences has attracted considerable attention in the community (4, 5). On the one hand, with the aging society, the number of patients with CAD has been increasing for decades (6). On the other hand, manual MYO segmentation is tedious, time-consuming, and with low replicability. Considering the medical cost and quality, automatic MYO segmentation is highly desirable. However, it is a challenging task. First, there exist large shape variations in the images. Second, the labels of the noisy images are with low uniformity, which degrades the training efficiency and effectiveness.

Currently, there exist two approaches for automatic MYO segmentation. In the traditional MYO segmentation approach (7, 8), a manually defined contour or boundary is needed for initialization. Although an automatic initialization might be achieved by some algorithms (9, 10), the segmentation performance highly relies on the initialization quality, which makes the framework lack stability. Another approach (11, 12) uses deep learning for MYO segmentation, which does not need any initialization and the whole process can run without manual inter-action. However, these methods treat each CMR frame independently, which does not exploit the temporal consistency among sequences.

On the other hand, temporal consistency has been extensively used to improve segmentation accuracy in a variety of applications. Yan et al. (13) added temporal consistency in the left ventricle segmentation from cine MRI. Punithakumar et al. (14) investigated automatic segmentation of the RV endocardial borders in 3D+ time magnetic resonance sequences acquired from patients with hypoplastic left heart syndrome (HLHS). Qin et al. (15) proposed a novel deep learning method for joint estimation of motion and segmentation from cardiac MR image sequences. Guo et al. (16) focused on automated segmentation of left ventricular (LV) in temporal cardiac image sequences. Recently, temporal consistency has been explored in other cardiac imaging modalities including MRI, CT, and ultrasound (US), which is detailed in Hernandez et al. (17). As far as we know, the effectiveness of temporal consistency has not been explored currently for MYO segmentation of CMR sequences.

In this article, we propose to exploit temporal consistency for MYO segmentation of CMR sequences for automatic CAD diagnosis. Particularly, we propose to combine conventional neural networks and recurrent neural networks to perform segmentation in two stages. The first stage contains an initial segmentation network (ISN) to get the initial segmentation without temporal information, while the second includes a temporal consistency based network (TCN) for refinement considering temporal consistency. The contributions of our study are:

- We proposed to use temporal consistency for accurate MYO segmentation of CMR sequence, and our framework is able to incorporate temporal information between CMR frames.
- To further exploit the temporal consistency among frames, we adopted a bi-directional training approach that can reduce segmentation error introduced by the first few frames in the training process.
- We conducted comprehensive experiments on the ACDC dataset. Compared with the residual 3D U-net model of Yang et al. (18), our framework achieves an improvement of 1–2% of segmentation accuracy in the Dice coefficient.

2. BACKGROUND

2.1. MYO Segmentation of CMR Image

Cardiac MRI image is a widely used imaging tool for the assessment of MYO micro-circulation. It utilizes the electromagnetic signal with characteristic frequency produced by the hydrogen nuclei under a strong contrasting magnetic field and weak oscillating near field as the imaging agent.

Due to the high capacity for discriminating different types of tissues, CMR image is one of the most prominent standards for cardiac diagnosis through the assessment of the left and right ventricular EF and SV, the left ventricle mass and the myocardium thickness. For example, Bernard et al. (3) obtained these parameters from CMR images using an accurate segmentation of CMR image for the LV cavity, RV cavity, and the myocardium at end-diastolic (ED) frame and end-systolic (ES) frame can give out an accurate diagnostic of cardiac function.

In order to evaluate the MYO function, accurate segmentation of the LV cavity, RV cavity, and MYO need to be acquired from the framework. **Figure 1** shows the slices of typical CMR images of a patient at ED frame with and without ground truth mask along each axis, respectively. The label shows the ground truth of segment results for different parts of the CMR image.

2.2. Related Study

Medical image segmentation has attracted much attention recently (19–26). MYO segmentation of CMR sequences has the following challenges. First, the contrast between the myocardium and surrounding structures is low as shown in **Figure 1**. Second, the brightness heterogeneity in the left and RV cavities is due to blood flow (3). Third, misleading structures such as papillary muscle have the same intensity and grayscale information as myocardium, which makes it hard to extract the accurate boundary. There are two approaches among existing works toward myocardium segmentation.

The first approach is based on point distribution models (PDMs) (27). A good example is the active shape model (ASM) (28) or active appearance model (AAM) (29). The main idea of ASM is to learn patterns of variability from a training set of correctly annotated images. ASM uses principal component analysis (PCA) to build a statistical shape model from a set of training shapes and then fits an image in a way that is most similar to the statistical shape in the training set. Ordas et al. (30) proposed an algorithm for MYO and LV cavity segmentation in CMR images based on invariant optimal feature 3-D ASM (IOF-ASM). van Assen et al. (31) improved the ASM such that the method can work for sparse and arbitrary oriented CMR images. Tobon-Gomez et al. (32) proposed a new ASM model that includes the measurement of reliability during the matching process to increase the robustness of the model. Santiago et al. (33) proposed a method of applying ASM on CMR images with the varying number of slices to perform segmentation on arbitrary slices of CMR images with a new re-sampling strategy.

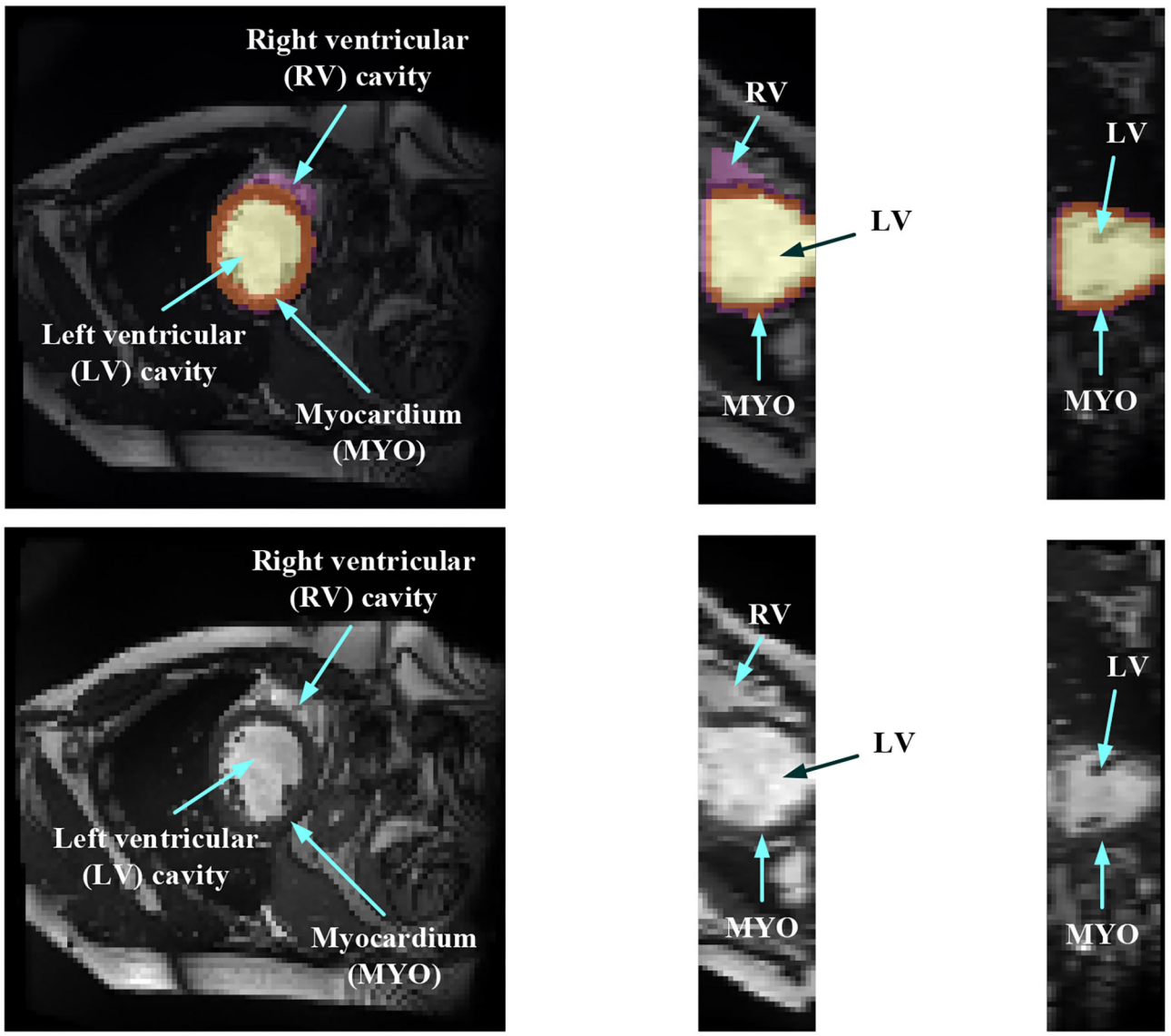

FIGURE 1 | Structure illustration of a typical CMR image. The images are the slices on the *z*-axis, *y*-axis, and *x*-axis, respectively, from Patient 001 in the automated cardiac diagnosis challenge (ACDC) dataset at end-diastolic (ED) frame with mask, and the second row of the figure is the raw CMR slices of Patient 001.

The prediction results of ASM must be constrained into certain shape variations so that the shape of the segmentation result does not go too far from the regular myocardium shape. Note that this is very important when artifacts and defects in the CMR image make the myocardium boundary unclear and hard to recognize. However, ASM is based on linear intensity information in the image, which is insufficient to model the appearance of CMR data with huge intensity variations and large artifacts. In addition, ASM requires a manual initialization shape and the final segmentation result is very sensitive to the shape and position of this initialization. Thus, a fully automatic and non-linear model is needed.

The second approach adopts machine learning techniques to perform image segmentation. For example, Zhang et al. (34) used a simple implementation of a fully connected neural network for the quality assessment of CMR images. Poudel et al. (35) used a recurrent fully connect network (RFCN) on the stack of 2D images for the segmentation of CMR images. The recurrent network is applied on the short axis so that the continuous spatial information on the short axis can be utilized. Simantiris et al. (36) proposed to use Dilation CNN, where each layer has the same resolution so that the localized information in the input image would not be lost. Isensee et al. (37) proposed a multi-structure segmentation for each time step of MRI sequences and extracted the domain-specific features. Simantiris et al. (38) used a simple network composed of cascaded modules of dilated convolutions with increasing dilation rate without using concatenation or operations like pooling that will lead to the decrease of resolution. Zotti et al. (39) introduced the shape prior obtained from the training dataset in the 3D Grid-net and employed the contour

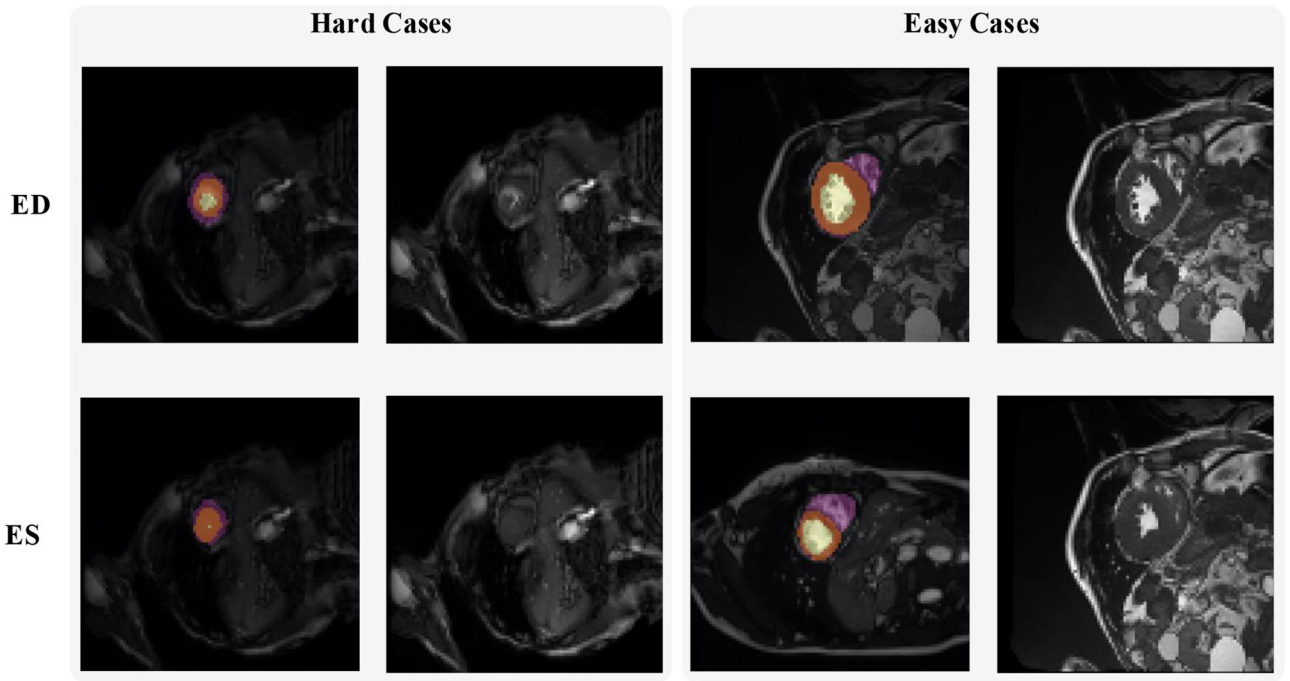

FIGURE 2 | Examples of hard and easy cases of CMR image (slices taken on short-axis). The first and second columns refer to hard cases and the third and fourth columns refer to easy cases.

loss as loss function to improve the performance on the border of segmentation result. Painchaud et al. (40) presented a method to guarantee the anatomical plausibility of segmentation results such that the anatomical invalid segmentation result of the model will be reduced to zero. Khened et al. (41) proposed a neural network with a dense block that contains dense connections between layers inspired by the Dense Net. Baumgartner et al. (42) compared the performance of 2D and 3D fully convolution network (FCN) and U-net. Calisto and Lai-Yuen (43) used a multi-objective evolutionary-based algorithm to incorporate 2D FCN and 3D FCN to search for an efficient and high-performing architecture automatically. Wolterink et al. (44) used six different types of model's average probability maps and cyclic learning rate schedule to improve the segmentation performance. Rohé et al. (45) proposed a combination of rigid alignment, non-rigid diffeomorphism registration, and label fusion to increase the performance of 3D U-net. Zotti et al. (46) used the shape prior that is embedded in the GridNet to reduce the anatomical impossible segmentation result. Patravali et al. (47) used the combination of 2D and 3D U-net and proposed a new class-balanced Dice loss to make the optimization easier.

Although these above methods showed great improvements in the segmentation performance compared to ASM or AAM. They treat each frame independently, which makes the segmentation results of some specific sequences inaccurate or the overall results lack coherence.

On the other hand, temporal consistency has been extensively used to improve the segmentation accuracy in various applications in multiple image modalities, which includes US, computerized tomography (CT) and CMR. Painchaud et al. (40) proposed a framework to deeply study the temporal consistency of 2D+ time segmentation methods in the US. Wei et al. (48) presented a co-learning model for temporal-consistent heart segmentation of echocardiographic sequences with sparsely labeled data. Guo et al. (16) leveraged to aggregate the characteristics of the spatial sequential network (SS-Net) to improve the LV segmentation during cardiac systole, and associated with excellent performance for temporal left ventricle segmentation on 4D cardiac CT sequence by sequential consistency (cardiac motion), achieving higher accuracy compared to the state-of-the-art methods on 4D cardiac CT dataset. Yan et al. (13) added temporal consistency in the left ventricle segmentation from cine MRI. Punithakumar et al. (14) investigated automatic segmentation of the RV endocardial borders in 3D+ time magnetic resonance sequences acquired from patients with HLHS. Zhang et al. (49) proposed a method to improve the segmentation of the left atrium (LA) by using a classification neural net to detect results with low accuracy and utilizing an unscented Kalman filter to improve temporal consistency. As far as we know, the effectiveness of temporal consistency has not been explored currently for MYO segmentation of CMR sequences.

2.3. Dataset

The automatic cardiac diagnostic challenge (ACDC) dataset consists of both patients with CAD and healthy individuals, whose diagnosis results are extracted from clinical medical cases. There are 150 patients in total and are evenly divided into five subgroups based on their diagnosis results. The five subgroups of patients have systolic heart failure with an infraction, dilated cardiomyopathy, hypertrophic cardiomyopathy, abnormal right ventricle, and no abnormality, respectively. A total of 50 of

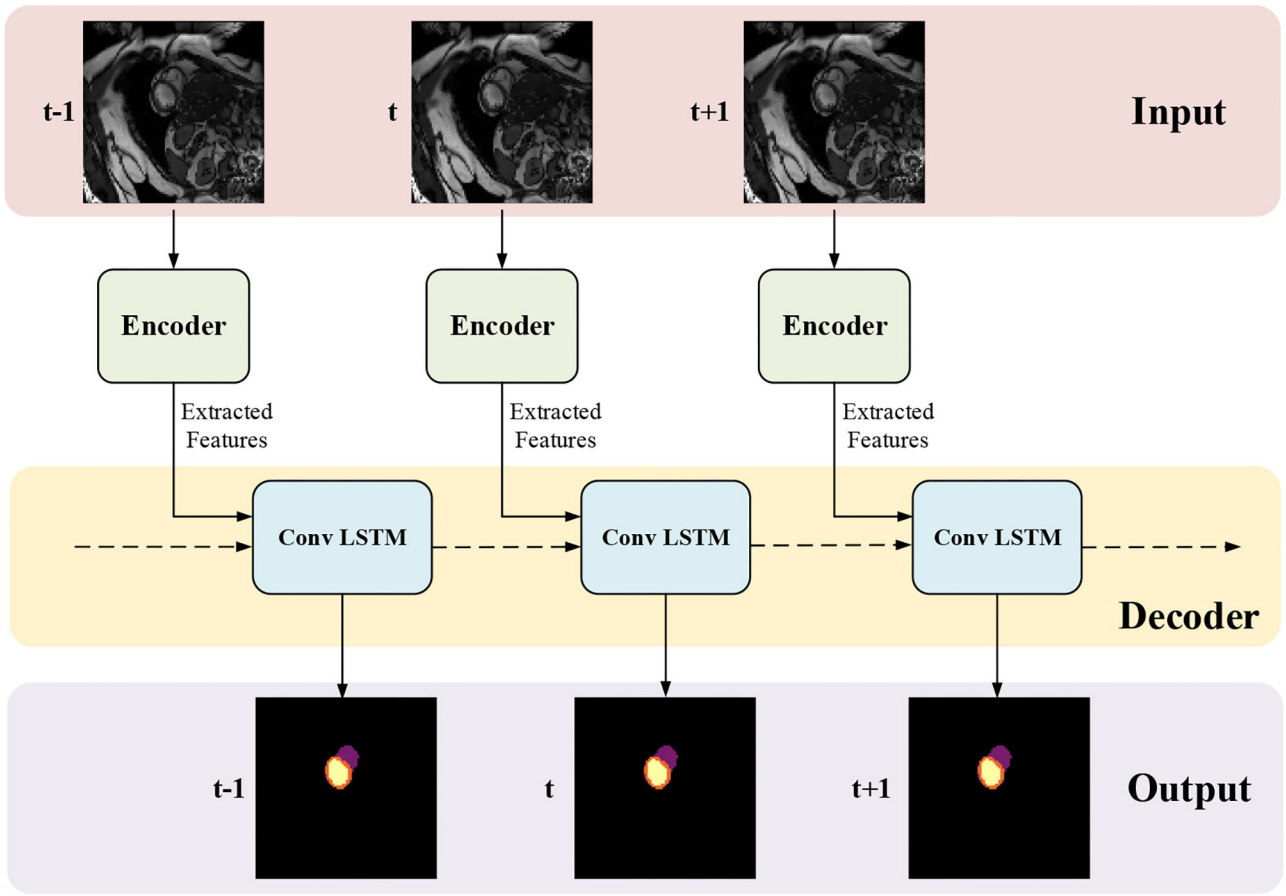

FIGURE 3 | The proposed myocardial (MYO) segmentation architecture, which contains an initial segmentation network (ISN) and a temporal consistency based network (TCN). TSN is based on residual U-net (Res U-Net) (50), while TCN is based on ConvLSTM (51).

the patients made up the test dataset on the ACDC website, and the other patients are released as the training dataset. CMR sequences of all patients are collected by two MRI systems with different magnetic strengths (1.5T-Siemens Area, Siemens Medical Solutions, Germany and 3.0T-Siemens Trio Tim, Siemens Medical Solutions, Germany). For each frame in the patient's CMR sequence, there contains a series of short-axis slices covering the LV from base to apex (3). For most patients, the dataset collected 28–40 consecutive frames to cover the whole cardiac cycle. Some of the patients in the dataset may have 5–10% of the cardiac cycle being omitted.

Figure 2 shows some hard and easy cases in both ED and ES phases of CMR image in the ACDC dataset. The hard cases usually have various characteristics such as low contrast blur image, or extreme anatomical structure. While the easy cases have a high contrast, and less misleading structure with the similar features as LV, RV, and MYO have.

3. METHODS

The proposed framework for MYO segmentation of CMR image sequences is shown in **Figure 3**. The input consists of a set of CMR frames from a CMR sequence. The output is the MYO segmentation at the ED and ES phases of the input. Note that the proposed method can accept input sequences with variable lengths by its structural design. Such a feature is designed and ensured in ISN and TCN separately. In ISN, the network will treat each frame of the CMR image sequence as an individual input. In TCN, the nature of RNN allows us to handle the sequence of variable lengths. Therefore, our framework can process input sequences of various lengths.

3.1. Initial Segmentation Network

Initial Segmentation Network is based on the U-net (50), which is an effective method for a broad range of medical image segmentation tasks. The network structure of ISN is shown in **Figure 4**. The input of ISN is a single-channel image corresponding to one frame in an MCE sequence. Based on the U-net, we add one residual block between each level of Res-UNet. Also, the results from each layer are combined using pointwise addition instead of concatenation. We expect the addition of residual blocks in the U-net can extract features from the input CMR image without suffering from serious gradient explosion or gradient vanishing problems.

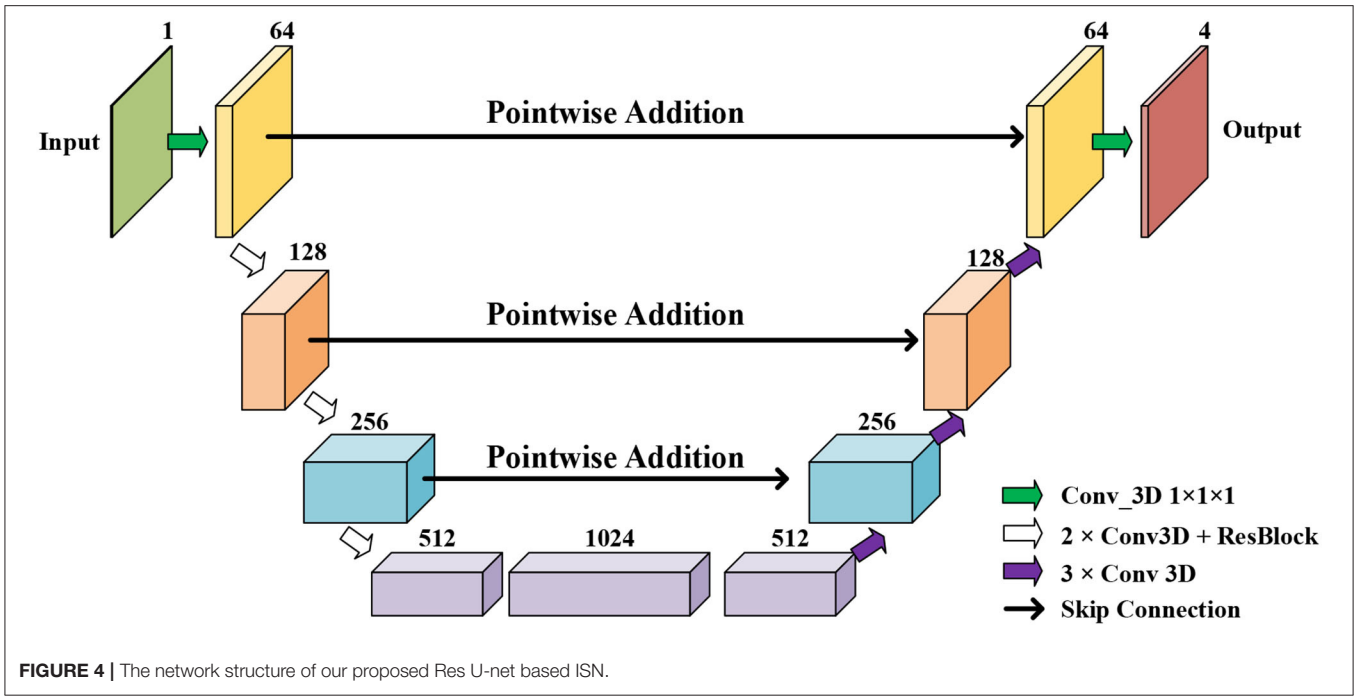

FIGURE 4 | The network structure of our proposed Res U-net based ISN.

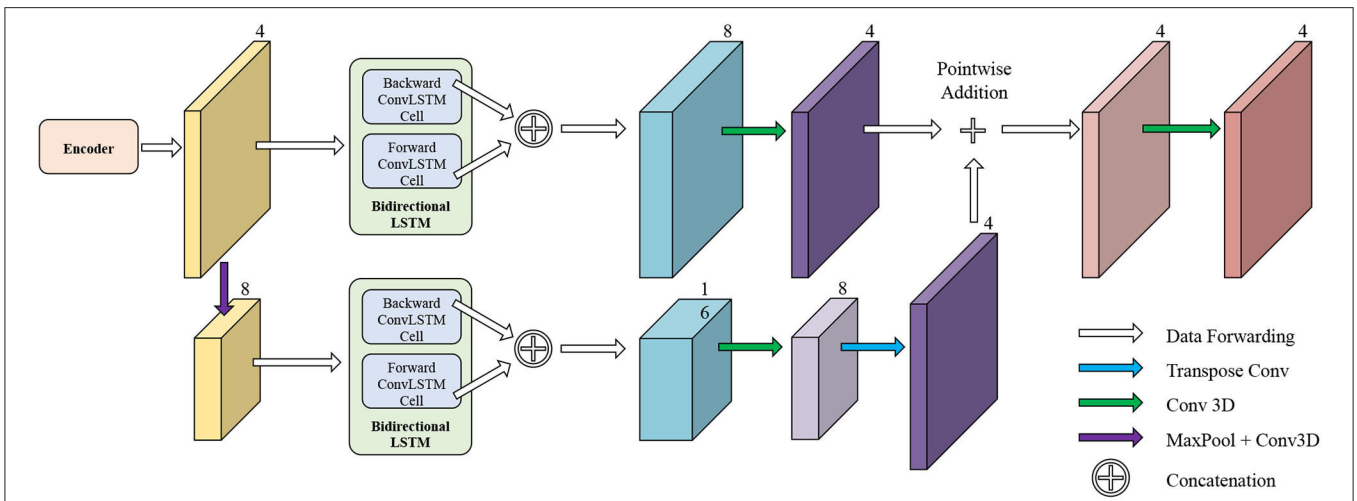

FIGURE 5 | The network structure of TCN. The input of TCN is the features extracted from ISN. TCN consists of hierarchical ConvLSTMs and is able to incorporate temporal information between CMR frames.

We extract four feature maps from U-net as the output of ISN. Four feature maps obtained from ISN represents the probability that one voxel belongs to the background, LV, RV, and MYO, respectively.

3.2. Temporal Consistency Based Network

The network structure of TCN is shown in **Figure 5**. It contains a hierarchical recurrent network of ConvLSTMs (52) which acts like a recurrent U-net. The output of TCN is the segmentation result of the myocardium of this frame. The dash arrows in **Figure 3** depict the temporal recurrence in TCN. We depict the features extracted by ISN for frame t as f_t, and $g_{t,k}$ as the feature for frame t in the kth level of hierarchical Conv LSTM network and the output of the k-th ConvLSTM layer for frame t as $y_{t,k}$. As shown in Equations (1–3), $y_{t,k}$ depends on three variables: (1) the output of the previous ConvLSTM layer $y_{t,k-1}$; (2) the extracted features in hierarchical ConvLSTM from ISN $g_{t,k}$; and (3) the hidden state of the same ConvLSTM layer for the previous frame $y_{t-1,k}$. Note that there is no direct connection between two levels of bi-directional ConvLSTMs in TCN's hierarchical LSTM model. The input of TCN (with 4 channels) will be copied into two copies. The one for level 2 bi-directional ConvLSTM will have 8 channels as the result of an extra 3D Convolution and Max Pooling operations. The one for level 1 bi-directional

ConvLSTM will have 4 channels. The outputs from two bi-directional ConvLSTM will be combined by pointwise addition.

$$h_{input} = [g_{t,k} \mid y_{t,k-1}] \quad (1)$$

$$h_{state} = y_{t-1,k} \quad (2)$$

$$y_{t,k} = ConvLSTM_k(h_{input}, h_{state}) \quad (3)$$

In Equation (3), h_{input} is the input of ConvLSTM, and h_{state} is the hidden state input of ConvLSTM. $[A|B]$ is the concatenate operation for tensors A and B on the feature axis. For the first

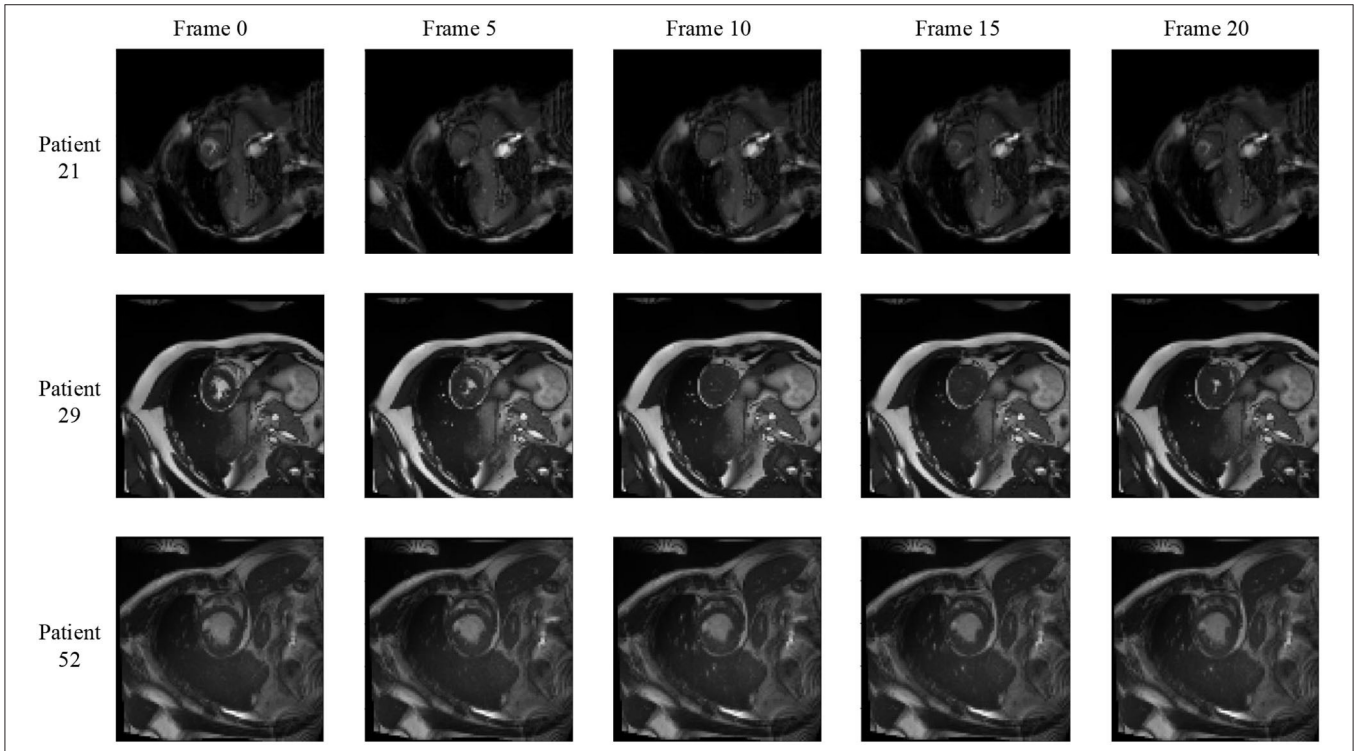

FIGURE 6 | Frames of CMR sequence from three patients. Note the brightness heterogeneity in left ventricular (LV) and right ventricular (RV) on the first few frames. Using LSTM in TCN, the model can get more temporal information from the previous and future frames and result in more accurate segmentation.

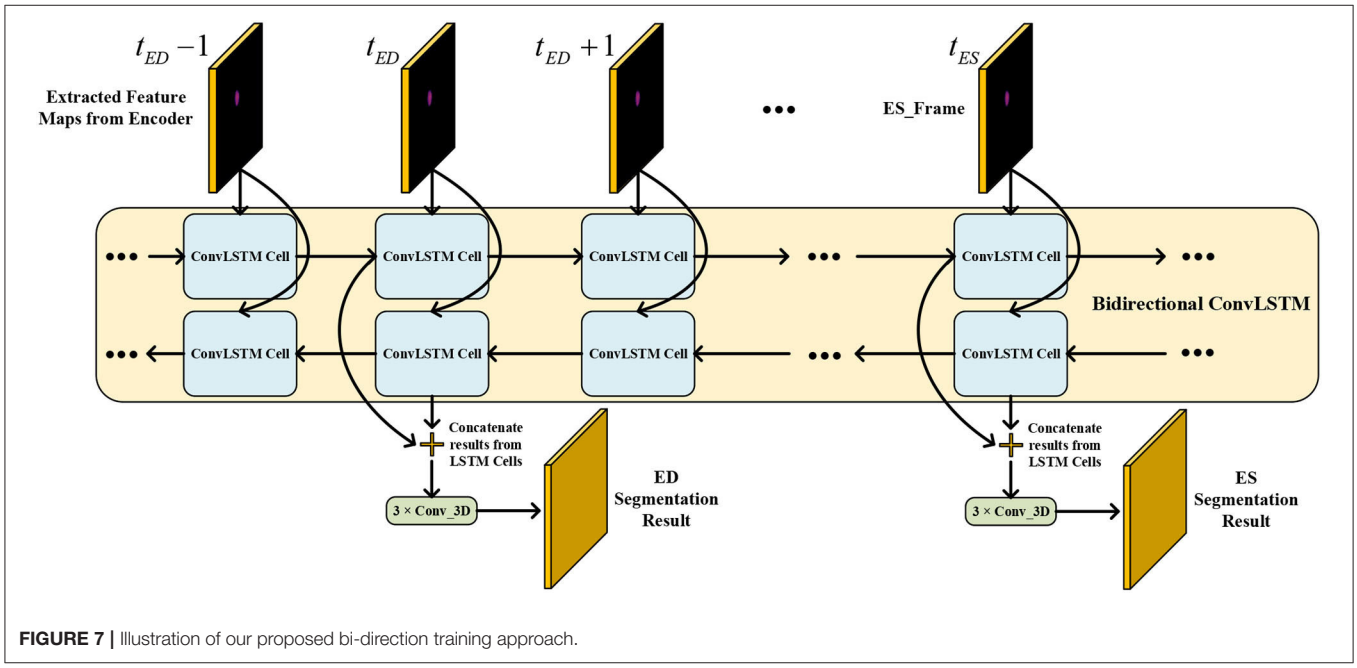

FIGURE 7 | Illustration of our proposed bi-direction training approach.

frame of a CMR sequence, h_{state} is a matrix of ones, which means no prior information is known.

3.3. Bi-Directional Training

We notice that the prediction results of myocardium segmentation in the CMR image are highly related to the segmentation result of frames either behind or after it. The first frame of the CMR sequence will not receive enough information if we only use forward Conv LSTM. **Figure 6** shows some frames of the CMR images of different patients in the ACDC dataset. We can see that the frames of CMR image of the last frame are highly related to the image of the next frame. Consequently, the prediction error of the first frame due to the brightness heterogeneity may propagate to the rest of the CMR frames.

Therefore, we adopted a bi-directional training approach to alleviate this problem. Specifically, we used two Conv LSTMs in our TCN model. One will propagate forward, from frame 1 to frame T, while the other will propagate backward, from frame T to frame 1. T is the total number of frames in one CMR sequence. **Figure 7** presents the workflow of the proposed bi-directional training approach. The Forward ConvLSTM cell at time t takes in two inputs: the cell state at time $t-1$ and the ISN's output for a frame of CMR image at time t. The Backward ConvLSTM cell at time t also takes in two inputs: the cell state at time $t+1$ and ISN's output for a frame of CMR image at time t. When the ConvLSTM cell is initialized, the cell's hidden state is initialized as a zero vector. Such an approach can better exploit the temporal information along with the frames, thus, improving the segmentation accuracy.

Note that our method is trained in two phases. In the first phase, ISN is trained. ISN's parameters are updated using the ground truth label from ACDC dataset frames at ED and ES. In the second phase, ISN and TCN are trained together. The supervision signal will only enter the framework from the output of TCN. The computation graph of ISN and TCN are connected, and the gradient can flow from TCN to ISN properly. TCN will give out segmentation result for each frame of the CMR sequence. Among all results, we will only take out the frame at ED and ES time for lost function calculation.

4. EXPERIMENTS

4.1. Experiment Setup

In this section, we evaluated the performance of our proposed framework in the MYO segmentation task of CMR sequences. The residual U-net (Res U-net) implementation is used as our baseline. We compared the proposed framework (Res U-net+ConvLSTM) and Res U-net. Res U-net and ConvLSTM are implemented using PyTorch based on Xingjian et al. (52) and Isensee et al. (53) separately. The CMR images are resampled into $96 \times 96 \times 24$ using the linear resample method. For data augmentation during training, we scaled all images by 0.8 and 1.2 and flipped them on the x-axis and y-axis, respectively. During testing and validation, we did not employ any augmentations. For each iteration, a complete CMR sequence containing 28–40 frames of a patient was used for training. Due to the limited GPU memory, the batch size is set to 1, which means in each iteration, 1 CMR sequence containing 28–40 frames is fed for training. We trained ISN for 10 epochs with a learning rate of 0.0001. Then, we trained ISN and TCN together with a learning rate of 0.0001 and a learning rate decay of 0.7 per epoch for another 10 epochs. Three loss functions including soft Dice loss, cross-entropy loss, and contour loss (54) are used for training. The adaptive momentum estimation (ADAM) optimizer is adopted to update the parameters.

We split the ACDC dataset into the training set, validation set, and testing set by a ratio of 7:2:1 based on the patient number. Therefore, there are 70 patients in the training set, 20 patients in the validation set, and 10 patients in the testing set. Dice coefficient and Inter-section over Union (IoU) are used to evaluate the segmentation performance, which is defined as:

$$Dice(P,T) = 2 \times \frac{\sum_{n=1}^{N}(P_n \times T_n)}{\sum_{n=1}^{N}(P_n + T_n)} \tag{4}$$

$$IoU(P,T) = \frac{\sum_{n=1}^{N}(P_n \times T_n)}{\sum_{n=1}^{N}(P_n + T_n - P_n \times T_n)} \tag{5}$$

in which P and T refer to the prediction and ground truth mask, respectively. n is the index of all voxels (totally N voxels).

4.2. Results and Discussion

Table 1 shows the results of MYO segmentation for LV, RV, and MYO at the ED phase and ES phase. Dice coefficient on

TABLE 1 | Comparison of our proposed framework against residual U-net (Res U-net).

	ED					ES				
	Dice			Overall		Dice			Overall	
	LV	RV	MYO	IoU	p-value	LV	RV	MYO	IoU	p-value
Res U-net	0.8856	0.8073	0.7178	0.5583±0.0045	<0.0001	0.8050	0.6841	0.7554	0.4053±0.0379	<0.0001
Res U-net + f-ConvLSTM	0.8857	0.8082	0.7097	0.5586±0.0044	<0.0001	0.8056	0.6896	0.7588	0.4186±0.0038	<0.0001
Our framework	**0.8967**	**0.8146**	**0.7260**	**0.5587±0.0045**	–	**0.8133**	**0.7080**	**0.7656**	**0.4231±0.0038**	–

Res U-net+f-ConvLSTM refers to forward ConvLSTM that is trained forwardly from frame 1 to frame T. Res U-net+bi-ConvLSTM (our framework) refers to training both forward ConvLSTM and backward ConvLSTM, where backward ConvLSTM processes input CMR images from frame T to frame 1. Two-sided t-test with 95% CI is used for statistic analysis. The bold values correspond to the optimal performance.

FIGURE 8 | Visualization of CMR image segmentation results of three different patients in both end-diastolic (ED) phase and end-systolic (ES) phase. Yellow, orange, and purple areas refer to the LV, myocardial (MYO), and RV, respectively. Each row refers to the segmentation result of Res U-net, our framework, Res U-net + *(Continued)*

FIGURE 8 | f-ConvLSTM, and ground truth from left to right, respectively. The white arrows in the image specifically point out the segmentation result that is inconsistent. We can see the f-ConvLSTM and bi-ConvLSTM model, which incorporates the temporal information between frames can greatly decrease the existence of such inconsistent segmentation results. Also, most errors in Res U-net + fConvLSTM and our framework are in hard cases like Patient 39, where the input CMR image has low contrast and vague contour between labeled tissue and background tissue.

TABLE 2 | Quantitative segmentation results of different models for frames in **Figure 8**.

Patient ID		Res U-net		Res U-net+f-ConvLSTM		Our framework	
		IoU	Dice	IoU	Dice	IoU	Dice
Patient 16	ED	0.5417	0.8245	0.5417	0.8433	0.5417	0.8499
	ES	0.5729	0.8168	0.5729	0.8196	0.5729	0.8234
Patient 39	ED	0.6771	0.8132	0.6771	0.8364	0.6771	0.8348
	ES	0.7396	0.7556	0.7396	0.7688	0.7396	0.7587
Patient 64	ED	0.6666	0.8537	0.6667	0.8653	0.6667	0.8616
	ES	0.6875	0.8334	0.6875	0.8368	0.6875	0.8347
Patient 90	ED	0.6563	0.8099	0.6563	0.8027	0.6563	0.8043
	ES	0.6563	0.7476	0.6563	0.7482	0.6563	0.7623

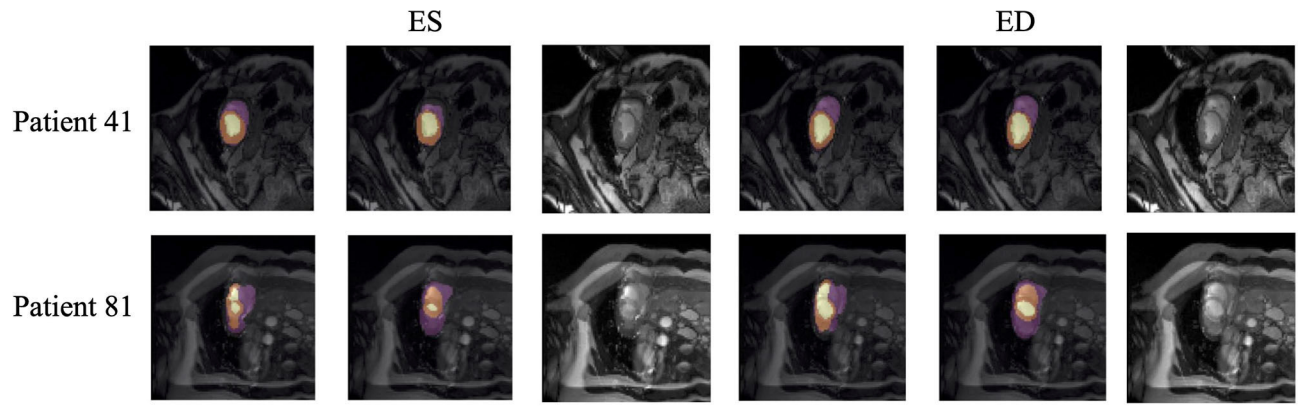

FIGURE 9 | Typical segmentation error of our framework. The image on Columns 1 and 4 are the segmentation results and images on Columns 2 and 5 are the corresponding ground truth. The segmentation error is usually caused by brightness heterogeneity, lack of contrast, or the improper input image due to faulty setup of magnetic resonance system or the misoperations of operators. The white arrows in the image specifically point out the segmentation result that is inconsistent.

each label class and IoU are reported. Res U-net+f-ConvLSTM refers to training the proposed framework forwardly from frame 0 to frame T while our framework (Res U-net+bi-ConvLSTM) refers to training in bi-direction. We noticed that our framework outperforms baseline implementation in all metrics for both ED and ES frames. Specifically, our Res U-net+f-ConvLSTM implementation has an improvement of 0.01, 0.10, −0.81, 0.61, 0.55, and 0.30% on the Dice coefficient of LV, RV, and MYO at ED frame and ES frame, respectively. The experiment results of Res U-net+f-ConvLSTM and our framework show that by adding a backward training step, we can further increase the segmentation performance. Our framework's implementation has an improvement of 1.11, 0.64, 0.82, 0.83, 2.39, and 1.02% on the Dice coefficient of LV, RV, and MYO at ED frame and ES frame, respectively.

Figure 8 shows the visualization of segmentation results of four different patients (Patient 16, Patient 39, Patient 64, and Patient 90) in both ED phase and ES phase by Res U-net, our framework, and Res U-net+f-ConvLSTM. Each row refers to the result of Res U-net, our framework, Res U-net+f-ConvLSTM, ground truth, and raw CMR slice, respectively. From **Figure 8**, we can see the f-ConvLSTM and bi-ConvLSTM, which has temporal consistency between frames, have less inconsistent segmentation result as marked by the white arrow in the figure. However, for few cases, the temporal consistency may not eliminate the inconsistency in the segmentation result completely. This happens when a stable feature on the CMR image is recognized as an incorrect label in the framework. Since the misleading structure will remain on all the CMR frames in the sequence, the temporal consistency provided by LSTM will not be able to remove such an inconsistency. **Table 2** demonstrates the quantitative results for the ED phase and ES phase of Patients 16, 39, 64, and 90 corresponding to **Figure 8**. We can see that our proposed framework tends to predict more consistently and accurately than the baseline, especially in the first few frames such as the ES phase of Patient 16, where the obvious defect exists

in the segmentation result. Comparing Res U-net+f-ConvLSTM and our framework on segmentation boundaries, we can observe that the bi-directional training can help our framework to produce more consistent results in most cases. Although in some cases the segmentation of Res U-net+f-ConvLSTM is better than that of our framework, this might be caused by the constraint from backward temporal information that makes the segmentation lack flexibility. The overall performance of our framework is superior in terms of all the metrics. It can be seen that the Dice coefficients of the ED phase are usually higher than the ES phase. However, our framework can achieve higher performance on both phases compared with Res U-net implementation.

Note that the work (18) used the class-balanced loss and transfer learning to improve the performance of Res 3D U-net on the ACDC dataset. They achieved Dice coefficients of 0.864, 0.789, 0.775, and 0.770 on segmentation of LV and RV in the ED phase and ES phase, respectively, while our framework achieves higher Dice coefficients of 0.897, 0.815, 0.813, and 0.708, respectively.

5. DISCUSSION

Quantitative segmentation results and grading results demonstrate the superiority of our framework compared with the Res U-net baseline implementation. However, there are still some cases where our framework cannot predict reasonable boundaries. For example, **Figure 9A** shows the segmentation results of Patient 41 in ES and ED phases by our framework. We can notice that there exists deviation between the ground truth boundary (images on Columns 2 and 4) and the prediction boundary (images on Columns 1 and 3). This is because the flow of blood in the RV cavity leads to the brightness heterogeneity in the RV area of the CMR image, which makes the image intensity of the ground truth RV region similar to the surrounding cardiac structures (e.g., heart chambers), and finally leads to segmentation failure.

There are some cases as shown in **Figure 9B** in which CMR sequences have serious defects and ghosting. This may be caused by the improper setup of the magnetic resonance system or the mistake of operators. Therefore, it is hard for our framework to find a plausible MYO boundary even though our framework is able to correct some segmentation errors based on temporal information between frames.

Note that compared with existing works for MYO segmentation of CMR sequences, our main contribution is to adopt temporal consistency for coronary artery disease (CAD) diagnosis which has not been extensively explored before. The results show that temporal consistency is important in the MYO segmentation of CMR sequences. Compared with existing works making use of temporal consistency, our methodology differs from the others as follows. Yan et al. (13) incorporated an optical flow field to capture the temporal consistency, while (14) adopted a moving mesh correspondence algorithm to refine segmentation using temporal consistency. Qin et al. (15) and Guo et al. (16) both proposed a motion estimation branch to assist the segmentation. Ours proposed a two-stage segmentation framework in which conventional neural networks and recurrent neural networks are combined to incorporate temporal information between sequences to ensure temporal consistency. In addition, ours additionally adopt contour loss (54) to facilitate the learning process.

6. CONCLUSION

In this article, we proposed an MYO segmentation framework of CMR sequences for CAD diagnosis. Specifically, we proposed to combine conventional neural networks and recurrent neural networks to incorporate temporal information between sequences to ensure temporal consistency. Extensive experiments showed that compared with Res U-net, our proposed framework can achieve an improvement of 1 to 2% in Dice coefficient. In addition, we introduced a bi-directional training approach to further reduce segmentation error introduced by the first few frames in the forward training process. Experiment results demonstrate that our bi-directional training approach can further improve the segmentation performance.

DATA AVAILABILITY STATEMENT

The original contributions presented in the study are included in the article/supplementary material, further inquiries can be directed to the corresponding author/s.

AUTHOR CONTRIBUTIONS

YC, WX, JZha, and HQ contributed to data collection, analysis, and experiment. DZ, YS, HY, JZhu, YD, and QJ contributed to discussion and writing. YZ, MH, and XX contributed to project planning, development, discussion, and writing. All authors contributed to the article and approved the submitted version.

FUNDING

This study was supported by the National Key Research and Development Program of China (No. 2018YFC1002600), the Science and Technology Planning Project of Guangdong Province, China (Nos. 2017B090904034, 2017B030314109, 2018B090944002, and 2019B020230003), Guangdong Peak Project (No. DFJH201802), and the National Natural Science Foundation of China (No. 62006050).

REFERENCES

1. Vos T, Allen C, Arora M, Barber RM, Bhutta ZA, Brown A, et al. Global, regional, and national incidence, prevalence, and years lived with disability for 310 diseases and injuries, 1990–2015: a systematic analysis for the global burden of disease study 2015. *Lancet.* (2016) 388:1545–602. doi: 10.1016/S0140-6736(16)31678-6

2. Malakar AK, Choudhury D, Halder B, Paul P, Uddin A, Chakraborty S. A review on coronary artery disease, its risk factors, and therapeutics. *J Cell Physiol.* (2019) 234:16812–23. doi: 10.1002/jcp.28350
3. Bernard O, Lalande A, Zotti C, Cervenansky F, Yang X, Heng P, et al. Deep learning techniques for automatic MRI cardiac multi-structures segmentation and diagnosis: is the problem solved? *IEEE Trans Med Imag.* (2018) 37:2514–25. doi: 10.1109/TMI.2018.2837502
4. Wang T, Xiong J, Xu X, Jiang M, Yuan H, Huang M, et al. MSU-Net: Multiscale statistical U-net for real-time 3D cardiac MRI video segmentation. In: *International Conference on Medical Image Computing and Computer-Assisted Intervention.* Springer; 2019. p. 614–622.
5. Wang T, Xu X, Xiong J, Jia Q, Yuan H, Huang M, et al. Ica-unet: Ica inspired statistical unet for real-time 3d cardiac cine mri segmentation. In: *International Conference on Medical Image Computing and Computer-Assisted Intervention.* Lima: Springer (2020). p. 447–57.
6. Odden MC, Coxson PG, Moran A, Lightwood JM, Goldman L, Bibbins-Domingo K. The impact of the aging population on coronary heart disease in the United States. *Am J Med.* (2011) 124:827–33. doi: 10.1016/j.amjmed.2011.04.010
7. Li Y, Ho CP, Chahal N, Senior R, Tang MX. Myocardial segmentation of contrast echocardiograms using random forests guided by shape model. In: *International Conference on Medical Image Computing and Computer-Assisted Intervention.* Athens: Springer (2016). p. 158–65.
8. Guo Y, Du GQ, Xue JY, Xia R, Wang Yh. A novel myocardium segmentation approach based on neutrosophic active contour model. *Comput Methods Prog Biomed.* (2017) 142:109–16. doi: 10.1016/j.cmpb.2017.02.020
9. Barbosa D, Dietenbeck T, Heyde B, Houle H, Friboulet D, D'hooge J, et al. Fast and fully automatic 3-d echocardiographic segmentation using B-spline explicit active surfaces: feasibility study and validation in a clinical setting. *Ultrasound Med Biol.* (2013) 39:89–101. doi: 10.1016/j.ultrasmedbio.2012.08.008
10. van Stralen M, Leung K, Voormolen MM, de Jong N, van der Steen AF, Reiber JH, et al. Time continuous detection of the left ventricular long axis and the mitral valve plane in 3-D echocardiography. *Ultrasound Med Biol.* (2008) 34:196–207. doi: 10.1016/j.ultrasmedbio.2007.07.016
11. Leclerc S, Grenier T, Espinosa F, Bernard O. A fully automatic and multi-structural segmentation of the left ventricle and the myocardium on highly heterogeneous 2D echocardiographic data. In: *2017 IEEE International Ultrasonics Symposium (IUS).* Washington, DC: IEEE (2017). p. 1–4.
12. Chen H, Zheng Y, Park JH, Heng PA, Zhou SK. Iterative multi-domain regularized deep learning for anatomical structure detection and segmentation from ultrasound images. In: *International Conference on Medical Image Computing and Computer-Assisted Intervention.* Athens: Springer (2016). p. 487–95.
13. Yan W, Wang Y, van der Geest RJ, Tao Q. Cine MRI analysis by deep learning of optical flow: adding the temporal dimension. *Comput. Biol. Med.* (2019) 111:103356. doi: 10.1016/j.compbiomed.2019.103356
14. Punithakumar K, Tahmasebi N, Boulanger P, Noga M. Convolutional neural network based automated RV segmentation for hypoplastic left heart syndrome MRI. In: *8th International Conference of Pattern Recognition Systems (ICPRS 2017).* IET (2017). p. 1–6.
15. Qin C, Bai W, Schlemper J, Petersen SE, Piechnik SK, Neubauer S, et al. Joint learning of motion estimation and segmentation for cardiac MR image sequences. In: *International Conference on Medical Image Computing and Computer-Assisted Intervention.* Springer (2018). p. 472–80.
16. Guo Y, Bi L, Zhu Z, Feng DD, Zhang R, Wang Q, et al. Automatic left ventricular cavity segmentation via deep spatial sequential network in 4D computed tomography. *Comput Med Imag Graph.* (2021) 91:101952. doi: 10.1016/j.compmedimag.2021.101952
17. Hernandez KAL, Rienmüller T, Baumgartner D, Baumgartner C. Deep learning in spatiotemporal cardiac imaging: a review of methodologies and clinical usability. *Comput Biol Med.* (2021) 130:104200. doi: 10.1016/j.compbiomed.2020.104200
18. Yang X, Bian C, Yu L, Ni D, Heng PA. Class-balanced deep neural network for automatic ventricular structure segmentation. In: *Lecture Notes in Computer Science.* Cham: Springer International Publishing (2018). p. 152–160.
19. Xu X, Lu Q, Yang L, Hu S, Chen D, Hu Y, et al. Quantization of fully convolutional networks for accurate biomedical image segmentation. In: *Proceedings of the IEEE Conference on Computer Vision and Pattern Recognition.* Salt Lake City, UT (2018). p. 8300–8.
20. Xu X, Ding Y, Hu SX, Niemier M, Cong J, Hu Y, et al. Scaling for edge inference of deep neural networks. *Nat Electron.* (2018) 1:216–22. doi: 10.1038/s41928-018-0059-3
21. Xu X, Wang T, Shi Y, Yuan H, Jia Q, Huang M, et al. Whole heart and great vessel segmentation in congenital heart disease using deep neural networks and graph matching. In: *International Conference on Medical Image Computing and Computer-Assisted Intervention.* Shenzhen: Springer (2019). p. 477–85.
22. Xu X, Wang T, Zhuang J, Yuan H, Huang M, Cen J, et al. Imagechd: a 3d computed tomography image dataset for classification of congenital heart disease. In: *International Conference on Medical Image Computing and Computer-Assisted Intervention.* Lima: Springer (2020). p. 77–87.
23. Xu X, Qiu H, Jia Q, Dong Y, Yao Z, Xie W, et al. AI-CHD: an AI-based framework for cost-effective surgical telementoring of congenital heart disease. *Commun ACM.* (2021) 64:66–74. doi: 10.1145/3450409
24. Zhang J, Zhang Y, Zhu S, Xu X. Constrained multi-scale dense connections for accurate biomedical image segmentation. In: *2020 IEEE International Conference on Bioinformatics and Biomedicine (BIBM).* Seoul: IEEE (2020). p. 877–84.
25. Liu Z, Xu X, Liu T, Liu Q, Wang Y, Shi Y, et al. Machine vision guided 3d medical image compression for efficient transmission and accurate segmentation in the clouds. In: *Proceedings of the IEEE/CVF Conference on Computer Vision and Pattern Recognition.* Long Beach, CA (2019). p. 12687–96.
26. Zhang J, Zhang Y, Xu X. Pyramid U-Net for retinal vessel segmentation. In: *ICASSP 2021-2021 IEEE International Conference on Acoustics, Speech and Signal Processing (ICASSP).* Toronto, ON: IEEE (2021). p. 1125–9.
27. Tobon-Gomez C, Butakoff C, Aguade S, Sukno F, Moragas G, Frangi AF. Automatic construction of 3D-ASM intensity models by simulating image acquisition: Application to myocardial gated SPECT studies. *IEEE Trans Med Imag.* (2008) 27:1655–67. doi: 10.1109/TMI.2008.2004819
28. Cootes TF, Taylor CJ, Cooper DH, Graham J. Active shape models-their training and application. *Comput Vis Image Understand.* (1995) 61:38–59. doi: 10.1006/cviu.1995.1004
29. Cootes TF, Edwards GJ, Taylor CJ. Active appearance models. *IEEE Trans Pattern Anal Mach Intell.* (2001) 23:681–685. doi: 10.1109/34.927467
30. Ordas S, Boisrobert L, Huguet M, Frangi A. Active shape models with invariant optimal features (IOF-ASM) application to cardiac MRI segmentation. In: *Comput Cardiol Volume 30.* Thessaloniki (2003) p. 633–6.
31. van Assen HC, Danilouchkine MG, Frangi AF, Ordás S, Westenberg JJM, Reiber JHC, et al. SPASM: a 3D-ASM for segmentation of sparse and arbitrarily oriented cardiac MRI data. *Med Image Anal.* (2006) 10:286–303. doi: 10.1016/j.media.2005.12.001
32. Tobon-Gomez C, Sukno FM, Butakoff C, Huguet M, Frangi AF. Automatic training and reliability estimation for 3D ASM applied to cardiac MRI segmentation. *Phys Med Biol.* (2012) 57:4155–74. doi: 10.1088/0031-9155/57/13/4155
33. Santiago C, Nascimento JC, Marques JS. A new ASM framework for left ventricle segmentation exploring slice variability in cardiac MRI volumes. *Neural Comput Appl.* (2016) 28:2489–500. doi: 10.1007/s00521-016-2337-1
34. Zhang L, Gooya A, Dong B, Hua R, Petersen SE, Medrano-Gracia P, et al. Automated quality assessment of cardiac MR images using convolutional neural networks. In: *Simulation and Synthesis in Medical Imaging.* Athens: Springer International Publishing (2016). p. 138–45.
35. Poudel RPK, Lamata P, Montana G. Recurrent fully convolutional neural networks for multi-slice MRI cardiac segmentation. In: *Reconstruction, Segmentation, and Analysis of Medical Images*. Springer (2016). p. 83–94.
36. Simantiris G, Tziritas G. Cardiac MRI segmentation with a dilated CNN incorporating domain-specific constraints. *IEEE J Sel Top Signal Process.* (2020) 14:1235–43. doi: 10.1109/JSTSP.2020.3013351
37. Isensee F, Jaeger PF, Full PM, Wolf I, Engelhardt S, Maier-Hein KH. Automatic cardiac disease assessment on cine-MRI via time-series segmentation and domain specific features. In: *Lecture Notes in Computer Science.* Cham: Springer International Publishing (2018). p. 120–9.

38. Simantiris G, Tziritas G. Cardiac MRI segmentation with a dilated CNN incorporating domain-specific constraints. *IEEE J Sel Top Signal Process.* (2020) 14:1235–43.
39. Zotti C, Luo Z, Lalande A, Jodoin PM. Convolutional neural network with shape prior applied to cardiac MRI segmentation. *IEEE J Biomed Health Inf.* (2019) 23:1119–28. doi: 10.1109/JBHI.2018.2865450
40. Painchaud N, Skandarani Y, Judge T, Bernard O, Lalande A, Jodoin PM. Cardiac MRI segmentation with strong anatomical guarantees. In: *Lecture Notes in Computer Science.* Shenzhen: Springer International Publishing (2019). p. 632–40.
41. Khened M, Alex V, Krishnamurthi G. Densely connected fully convolutional network for short-axis cardiac cine MR image segmentation and heart diagnosis using random forest. In: *Lecture Notes in Computer Science.* Cham: Springer International Publishing (2018). p. 140–51.
42. Baumgartner CF, Koch LM, Pollefeys M, Konukoglu E. An exploration of 2D and 3D deep learning techniques for cardiac MR image segmentation. In: *Lecture Notes in Computer Science.* Cham: Springer International Publishing (2018). p. 111–19.
43. Calisto MB, Lai-Yuen SK. AdaEn-Net: an ensemble of adaptive 2D–3D Fully Convolutional Networks for medical image segmentation. *Neural Netw.* (2020) 126:76–94. doi: 10.1016/j.neunet.2020.03.007
44. Wolterink JM, Leiner T, Viergever MA, Išgum I. Automatic segmentation and disease classification using cardiac cine MR images. In: *Lecture Notes in Computer Science.* Springer International Publishing (2018). p. 101–10.
45. Rohé MM, Sermesant M, Pennec X. Automatic multi-atlas segmentation of myocardium with SVF-net. In: *Lecture Notes in Computer Science.* Québec: Springer International Publishing (2018). p. 170–77.
46. Zotti C, Luo Z, Humbert O, Lalande A, Jodoin PM. GridNet with automatic shape prior registration for automatic MRI cardiac segmentation. In: *Lecture Notes in Computer Science.* Québec: Springer International Publishing (2018). p. 73–81.
47. Patravali J, Jain S, Chilamkurthy S. 2D-3D fully convolutional neural networks for cardiac MR segmentation. In: *Lecture Notes in Computer Science.* Québec: Springer International Publishing (2018). p. 130–9.
48. Wei H, Cao H, Cao Y, Zhou Y, Xue W, Ni D, et al. Temporal-consistent segmentation of echocardiography with co-learning from appearance and shape. In: *International Conference on Medical Image Computing and Computer-Assisted Intervention.* Lima: Springer (2020). p. 623–32.
49. Zhang X, Noga M, Martin DG, Punithakumar K. Fully automated left atrium segmentation from anatomical cine long-axis MRI sequences using deep convolutional neural network with unscented Kalman filter. *Med Image Anal.* (2021) 68:101916. doi: 10.1016/j.media.2020.101916
50. Ronneberger O, Fischer P, Brox T. U-net: convolutional networks for biomedical image segmentation. In: *International Conference on Medical image computing and computer-assisted intervention.* Munich: Springer (2015). p. 234–41.
51. Salvador A, Bellver M, Campos V, Baradad M, Marques F, Torres J, et al. Recurrent neural networks for semantic instance segmentation. *preprint* arXiv:171200617. (2017).
52. Xingjian S, Chen Z, Wang H, Yeung DY, Wong WK, Woo Wc. Convolutional LSTM network: a machine learning approach for precipitation nowcasting. In: *Advances in Neural Information Processing Systems.* Montreal, QC: MIT Press (2015). p. 802–810.
53. Isensee F, Petersen J, Klein A, Zimmerer D, Jaeger PF, Kohl S, et al. nnu-net: Self-adapting framework for u-net-based medical image segmentation. *arXiv preprint* arXiv:180910486. (2018).
54. Chen Z, Zhou H, Xie X, Lai J. Contour loss: Boundary-aware learning for salient object segmentation. *arXiv preprint* arXiv:190801975. (2019).

Conflict of Interest: The authors declare that the research was conducted in the absence of any commercial or financial relationships that could be construed as a potential conflict of interest.

frontiers in Cardiovascular Medicine

ORIGINAL RESEARCH
published: 07 March 2022
doi: 10.3389/fcvm.2022.772466

Renal Venous Stasis Index Reflects Renal Congestion and Predicts Adverse Outcomes in Patients With Heart Failure

Himika Ohara[1], Akiomi Yoshihisa[1,2], Yuko Horikoshi[2,3], Shinji Ishibashi[3], Mitsuko Matsuda[3], Yukio Yamadera[3], Yukiko Sugawara[1], Yasuhiro Ichijo[1], Yu Hotsuki[1], Koichiro Watanabe[1], Yu Sato[1], Tomofumi Misaka[1], Takashi Kaneshiro[1], Masayoshi Oikawa[1], Atsushi Kobayashi[1] and Yasuchika Takeishi[1]*

[1] Department of Cardiovascular Medicine, Fukushima Medical University, Fukushima, Japan, [2] Department of Clinical Laboratory Sciences, Fukushima Medical University School of Health Science, Fukushima, Japan, [3] Department of Clinical Laboratory Medicine, Fukushima Medical University, Fukushima, Japan

OPEN ACCESS

Edited by:
Christos Bourantas, University College London, United Kingdom

Reviewed by:
Bertram Pitt, University of Michigan, United States
Manuel Richter, Universitätsklinikum Gießen, Germany

***Correspondence:**
Akiomi Yoshihisa
yoshihis@fmu.ac.jp

Specialty section:
This article was submitted to Cardiovascular Imaging, a section of the journal Frontiers in Cardiovascular Medicine

Received: *08 September 2021*
Accepted: *10 February 2022*
Published: *07 March 2022*

Citation:
Ohara H, Yoshihisa A, Horikoshi Y, Ishibashi S, Matsuda M, Yamadera Y, Sugawara Y, Ichijo Y, Hotsuki Y, Watanabe K, Sato Y, Misaka T, Kaneshiro T, Oikawa M, Kobayashi A and Takeishi Y (2022) Renal Venous Stasis Index Reflects Renal Congestion and Predicts Adverse Outcomes in Patients With Heart Failure. Front. Cardiovasc. Med. 9:772466. doi: 10.3389/fcvm.2022.772466

Background: It has been recently reported that the renal venous stasis index (RVSI) assessed by renal Doppler ultrasonography provides information to stratify pulmonary hypertension that can lead to right-sided heart failure (HF). However, the clinical significance of RVSI in HF patients has not been sufficiently examined. We aimed to examine the associations of RVSI with parameters of cardiac function and right heart catheterization (RHC), as well as with prognosis, in patients with HF.

Methods: We performed renal Doppler ultrasonography, echocardiography and RHC in hospitalized patients with HF ($n = 388$). RVSI was calculated as follows: RVSI = (cardiac cycle time-venous flow time)/cardiac cycle time. The patients were classified to three groups based on RVSI: control group (RVSI = 0, $n = 260$, 67%), low RVSI group ($0 < \text{RVSI} \leq 0.21$, $n = 63$, 16%) and high RVSI group (RVSI > 0.21, $n = 65$, 17%). We examined associations of RVSI with parameters of cardiac function and RHC, and followed up for cardiac events defined as cardiac death or worsening HF.

Results: There were significant correlations of RVSI with mean right atrial pressure (mRAP; $R = 0.253$, $P < 0.001$), right atrial area ($R = 0.327$, $P < 0.001$) and inferior vena cava diameter ($R = 0.327$, $P < 0.001$), but not with cardiac index ($R = -0.019$, $P = 0.769$). During the follow-up period (median 412 days), cardiac events occurred in 60 patients. In the Kaplan–Meier analysis, the cumulative cardiac event rate increased with increasing RVSI (log-rank, $P = 0.001$). In the multivariate Cox proportional hazard analysis, the cardiac event rate was independently associated with RVSI (high RVSI group vs. control group: hazard ratio, 1.908; 95% confidence interval, 1.046–3.479, $P = 0.035$).

Conclusion: RVSI assessed by renal Doppler ultrasonography reflects right-sided overload and is associated with adverse prognosis in HF patients.

Keywords: heart failure, renal circulation, hemodynamics, kidney, prognosis

INTRODUCTION

Heart failure (HF) is a refractory clinical syndrome that originates from various types of structural or functional heart diseases. The number of patients with HF has been rapidly increasing, and HF is becoming a major public health concern worldwide (1, 2). Congestion is a key feature in HF, and its presence is associated with poor prognosis. However, congestion can go unrecognized, as it is sometimes not clinically evident. To evaluate the degree of congestion objectively, non-invasive image testing is required in patients with HF (3–5).

It has already been reported that the intrarenal venous flow (IRVF) patterns assessed by renal Doppler ultrasonography were associated with congestion and prognosis in patients with HF. Specifically, the most adverse prognosis was present in HF patients with monophasic IRVF pattern, followed in order by biphasic IRVF pattern and continuous IRVF pattern (6–9). However, the classification of IRVF patterns is not necessarily clear. There are patterns for which classification is difficult or classification itself may miss important changes in the pattern. Renal venous stasis index (RVSI) is a novel indicator of cardiac cycle-dependent stasis of renal venous flow. RVSI indicates the proportion of the cardiac cycle during which there is no renal venous outlet flow. RVSI can quantify IRVF patterns and completement the weaknesses of the IRVF pattern classification. According to a past study, RVSI provided information to stratify prognosis in patients with pulmonary hypertension (PH) in terms of propensity to develop right-sided HF. Namely, PH patients with high RVSI experienced more adverse events such as worsening PH or all-cause mortality (10). However, the clinical significance of RVSI in HF patients has not been sufficiently examined. We aimed to elucidate the associations of RVSI with parameters of cardiac function and right heart catheterization (RHC), as well as with cardiac events defined as cardiac death and worsening HF, in patients with HF.

METHODS

Subjects and Protocol

This was a prospective observational study of 402 patients who were classified as either stage C or stage D of heart failure stage classification in the American College of Cardiology Foundation/American Heart Association guideline and were hospitalized to Fukushima Medical University Hospital between April 2018 and September 2020 (11). Treatment of decompensated HF was provided by each patient's attending cardiologist based on the established HF guidelines (11, 12). Blood samples, renal Doppler ultrasonography and echocardiography were obtained during hospitalization in the patients in a stable condition before discharge. We subsequently excluded patients with who were undergoing dialysis ($n = 14$). At last, 388 patients were enrolled in this study. Two hundred and forty five of them had undergone RHC within 3 days of renal Doppler ultrasonography. Of these 388 patients, patients with RVSI of 0 were defined as the control group ($n = 260$, 67%). Patients with RVSI above 0 were divided into two groups on the basis of the median value of RVSI (0.21): the low RVSI group ($0 < \text{RVSI} \leq 0.21$, $n = 63$, 16%) and the high RVSI group ($\text{RVSI} > 0.21$, $n = 65$, 17%).

First, we compared the clinical features as well as the results from laboratory tests, echocardiography and RHC between the three groups. Second, the patients were followed up until November 2020 for cardiac events defined as cardiac death or worsening HF. Cardiac death was defined as death from acute coronary syndrome, ventricular fibrillation and HF, and worsening HF was defined as unplanned re-hospitalization for HF treatment. For patients who experienced ≥ two events, only the first event was included in the analysis. These patients visited hospital monthly or every other month. Therefore, we could follow up on all patients. Disease status and dates of death were gained from the patient's medical records. The results of the analysis were hidden from those conducting the survey, and written informed consent was gained from all enrolled patients. The protocol for this study was approved by the Ethics Committee of Fukushima Medical University and was conducted in accordance with the principles described in the Declaration of Helsinki. We reported this study in conformity to Strengthening the Reporting of Observational Studies in Epidemiology and the Enhancing the Quality and Transparency of Health Research guidelines.

Ischemic coronary artery disease was confirmed by either myocardial scintigraphy or coronary computed tomography angiography and/or coronary angiography (13). Atrial fibrillation (AF) was confirmed by electrocardiogram performed during hospitalization or from medical records including past medical history. Hypertension was defined as systolic blood pressure of ≥ 140 mmHg, diastolic blood pressure of ≥ 90 mmHg, or taking antihypertensive drugs. Dyslipidemia was defined as levels of triglyceride ≥ 150 mg/dL, levels of low-density lipoprotein cholesterol ≥ 140 mg/dL, levels of high-density lipoprotein cholesterol < 40 mg/dL, or taking cholesterol-lowering drugs. Diabetes mellitus was defined as recent use of antidiabetic drugs, levels of fasting glucose ≥ 126 mg/dL, levels of casual glucose ≥ 200 mg/dL and/or levels of HbA1c ≥ 6.5% (National Glycohemoglobin Standardization Program) (14). Chronic kidney disease (CKD) was defined as estimated glomerular filtration rate (eGFR) of <60 mL/min per 1.73 m^2 (15–17). Anemia was defined as levels of hemoglobin <12.0 g/dL in female and <13.0 g/dL in male (18, 19).

Renal Doppler Ultrasonography

The actual methods of acquisition were as follows. The patients were performed renal Doppler ultrasonography in a stable condition after treatment. Two experienced sonographers (M.M, with 27 years of experience in abdominal ultrasonography, and S.I, with 19 years of experience) performed renal Doppler ultrasonography, using an Aplio i800 system (Canon Medical Systems Corporation, Tochigi, Japan) with a convex transducer frequency range of 2.5–5.0 MHz. The velocity range of the color Doppler was set to approximately 10–20 cm/s. The two examiners were blinded to all clinical data. The patients fasted for at least 12 h before the renal Doppler ultrasonography and were placed in the lateral position. All renal Doppler ultrasonography examinations were performed in the right renal vein. This

was because left renal vein is entrapped in the fork between the abdominal aorta and the superior mesenteric artery, thus attenuating its phasicity. Furthermore, although this is a rare event in cases of ovarian or testicular varicose veins, the left ovarian or testicular veins draining into the left renal vein may have affected renal venous flow. The transducer was placed in the lateral abdominal region, and the patient's arms were raised above the chest to obtain a proper acoustic window. The patients were holding their breath while measurements. As shown in **Figure 1**, we used color Doppler images to record pulsed Doppler waveforms of the interlobar arteries and veins simultaneously. Transducer was placed with an angle of <60 degrees. The upward Doppler signal indicates the intrarenal arterial flow, and the downward Doppler signal indicates the venous flow. We used the interlobar vein flow to calculate RVSI. In patients with sinus rhythm, we selected the most stable value among five cardiac cycles. In patients with AF, an index beat (the beat following two preceding cardiac cycles of equal duration) was used for each measurement. We calculated RVSI, which indicates the proportion of the cardiac cycle during which there was no renal venous outlet flow, as follows: (cardiac cycle time - venous flow time)/cardiac cycle time (10). IRVF patterns were broadly categorized into continuous (RVSI = 0, non-congestive) and discontinuous (RVSI > 0, nadir velocity = 0) flow patterns. We further classified the discontinuous IRVF patterns into two stages: biphasic (with venous peaks during systole and diastole), and monophasic (with venous peak during diastole) (7). **Figure 1** shows representative RVSI along with IRVF patterns. **Figure 1a**, RVSI = 0 (control) with continuous pattern; **Figure 1b**, low RVSI with biphasic pattern; **Figure 1c**, high RVSI with biphasic pattern; and **Figure 1d**, high RVSI with monophasic pattern. Although both **Figures 1b,c** are classified into biphasic IRVF pattern, these patterns could be distinguished by RVSI (i.e., **Figure 1b:** Low RVSI and **Figure 1c:** High RVSI). On the contrary, both **Figures 1c,d** belonged to high RVSI, but classified into different IRVF patterns (i.e., **Figure 1c:** Biphasic pattern and **Figure 1d:** Monophasic pattern).

Echocardiography

Echocardiography was performed by experienced echocardiographers based on current recommendations (20, 21). The echocardiographic parameters included left ventricular ejection fraction (LVEF), left ventricular outflow tract velocity-time integral (LVOT VTI), left atrial volume, early transmitral flow velocity to mitral annular velocity ratio (mitral valve E/e'), right atrium area, right ventricular areas, right ventricular fractional area change (RV-FAC), inferior vena cava (IVC) diameter, severity of tricuspid regurgitation (TR), tricuspid regurgitation pressure gradient (TRPG), tricuspid annular plane systolic excursion (TAPSE), TAPSE/systolic pulmonary artery pressure ratio (TAPSE/sPAP ratio), and tissue Doppler-derived tricuspid lateral annular systolic velocity (tricuspid valve S') (21). The LVEF was calculated by Simpson's method. The RV-FAC, defined as (end diastolic area - end systolic area)/end diastolic area × 100, is a measure of right ventricular systolic function. The TAPSE/sPAP ratio is an indicator of right ventricle–to–pulmonary circulation coupling (22–27). All measurements were performed using ultrasound systems (ACUSON Sequoia, Siemens Medical Solutions USA, Inc., Mountain View, CA, USA).

Right Heart Catheterizations and Hemodynamic Measurements

Of the total of 388 patients, 245 underwent RHC based on remedial judgment of the attending physician. RHC was performed within 3 days of renal Doppler ultrasonography during hospitalization in the patients in a stable condition without changes in medications, including doses, similar to the setting for renal Doppler ultrasonography. All RHCs were performed under fluoroscopic guidance with the patients in the resting supine position breathing room air and at rest after more than 30 min of catheter placement. Cardiac output and mean right atrial pressure (mRAP) were measured using a 7F Swan-Ganz catheter (Edwards Lifesciences, Irvine, CA, USA). Cardiac output was calculated using the direct Fick method (28).

Measurement of Laboratory Data

We measured B-type natriuretic peptide (BNP) levels using a specific immunoradiometric assay (Shionoria BNP kit, Shionogi, Osaka, Japan). This assay was performed by experienced laboratory technicians in blind.

Statistical Analysis

Normally distributed data were presented as mean ± standard deviation, and non-normally distributed data were presented as median and interquartile range. Categorical variables were expressed as numbers and percentages, and the chi-square test was used for their comparisons. Among the three groups, parametric variables were compared using one-way analysis of variance, and non-parametric variables were compared using Kruskal-Wallis test. Kaplan-Meier analysis with log-rank test was used to evaluate the cardiac event rate. RVSI was assessed as a predictor of post-discharge cardiac events by the Cox proportional hazard analysis. In the univariate Cox proportional hazard analysis, to prepare for potential confounding, we considered the following clinical factors: age, sex and other confounding factors which differed statistically among the groups. Univariate factors with $P < 0.05$ were entered into the multivariate Cox proportional hazard analyses. A value of $P < 0.05$ was defined statistically significant for all comparisons. These analyses were performed using a statistical software package (SPSS ver. 27.0, IBM, Armonk, NY, USA).

RESULTS

Table 1 shows the clinical and demographic characteristics of the study population. Of the 388 patients included in the study, the median age was 71 (63.0–79.8) years and 225 (58.0%) were male. There were some unclassified IRVF patterns in our study. The prevalence of AF, hypertension, CKD and anemia increased in proportion to RVSI. In contrast, age, sex, body mass index, blood pressure, heart rate, coronary artery disease and diabetes mellitus, did not differ among the groups. There was not significant correlation between RVSI and heart rate

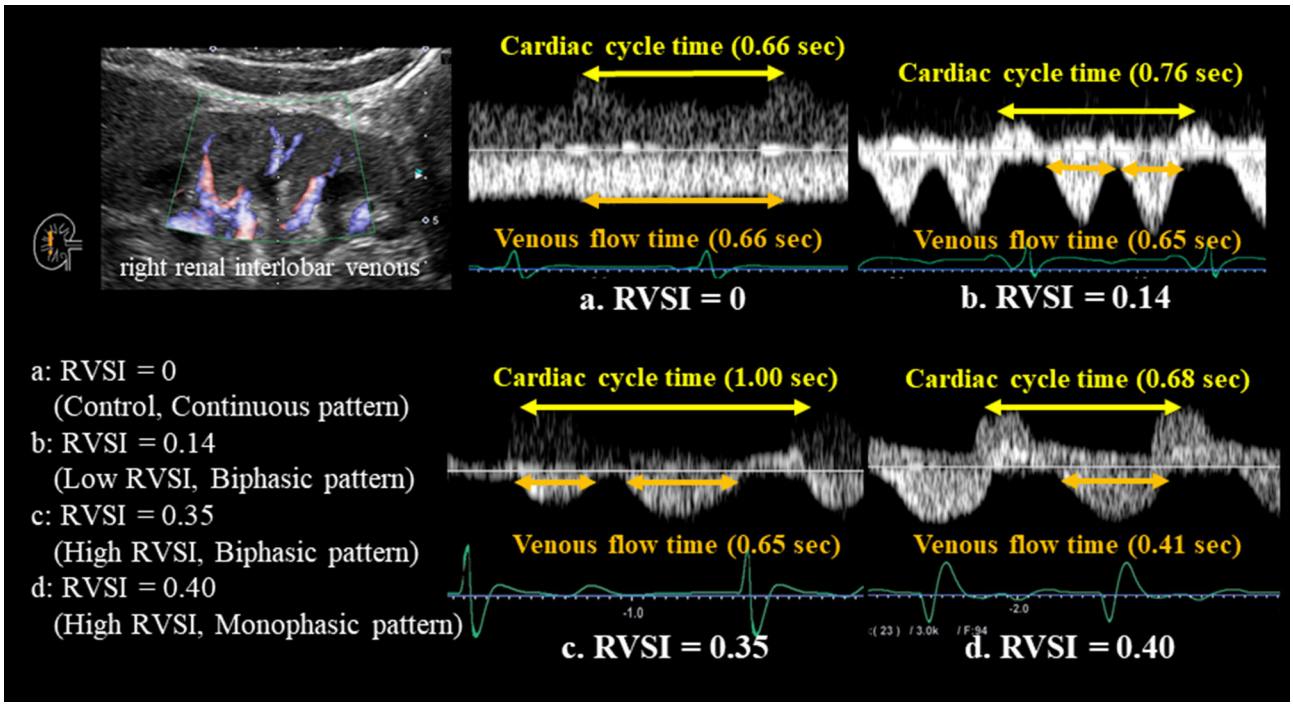

FIGURE 1 | All renal Doppler ultrasonography studies were performed in the right kidney. Color Doppler images were used to record pulsed Doppler waveforms of the interlobar arteries and veins simultaneously. The upward Doppler signal indicated the intrarenal arterial flow, and the downward Doppler signal indicated the venous flow. We measured venous flow time and calculated RVSI as follows: (cardiac cycle time-venous flow time)/cardiac cycle time. RVSI of 0 was defined as the control. RVSI above 0 were divided based on the median value of RVSI (0.21): the low RVSI ($0 < \text{RVSI} \leq 0.21$) and the high RVSI ($\text{RVSI} > 0.21$). RVSI increased with increasing severity of renal congestion. This figure shows representative IRVF patterns with RVSI in a patient with HF. IRVF patterns were broadly categorized into continuous (RVSI = 0, non-congestive) and discontinuous (RVSI > 0, nadir velocity = 0) flow patterns. We further classified the discontinuous IRVF patterns into two stages: biphasic (with venous peaks during systole and diastole), and monophasic (with venous peak during diastole). **(a)** RVSI = 0 (control) with continuous pattern; **(b)** low RVSI with biphasic pattern; **(c)** high RVSI with biphasic pattern; and **(d)** high RVSI with monophasic pattern. RVSI, renal venous stasis index; IRVF, intrarenal venous flow.

($R = 0.009$, $P = 0.852$). Regarding laboratory data, levels of BNP, C-reactive protein and urine albumin-to-creatinine ratio became higher, and levels of eGFR and hemoglobin became lower with increasing RVSI. However, sodium and proteinuria did not differ among the groups. With regard to the parameters of echocardiography, there was a significant increase in left atrial volume, mitral valve E/e', right atrial area, IVC diameter, severity of TR and TRPG, and a significant decrease in TAPSE and TAPSE/sPAP ratio with increasing RVSI. In contrast, LVEF and LVOT VTI were similar among the groups. Cardiopulmonary hemodynamics evaluated by RHC worsened with increasing RVSI. There was a gradual increase in mRAP (**Figure 2A**), mean pulmonary artery pressure (mPAP) and mean pulmonary artery wedge pressure (mPAWP) with increasing RVSI, whereas, there was no significant change in cardiac index (CI). As regards medications, the use of diuretic increased in proportion to RVSI. In contrast, angiotensin converting enzyme inhibitor, angiotensin II receptor blocker, angiotensin receptor-neprilysin inhibitor, mineralocorticoid receptor antagonist and sodium glucose cotransporter 2 inhibitor did not differ among the groups. Mean RAP showed a significant stepwise increase along the RVSI groups (**Figure 2A**, control, low RVSI and high RVSI groups) and IRVF patterns (**Figure 2B**, continuous, biphasic and monophasic patterns). Both RVSI and IRVF patterns showed similar associations with elevated mRAP (**Figure 2A**; $P < 0.001$ and **Figure 2B**; $P = 0.001$). In addition, RVSI showed a significant stepwise increase along the IRVF patterns (**Figure 2C**; $P < 0.001$). RVSI also showed a significant stepwise increase along the severity of TR (**Figure 2D**; $P < 0.001$). TAPSE/sPAP ratio showed a significant stepwise decrease along the RVSI groups (**Figure 2E**; $P < 0.001$). Furthermore, there were significant correlations of RVSI with right atrial area ($R = 0.327$, $P < 0.001$), IVC ($R = 0.327$, $P < 0.001$), TR severity ($R = 0.197$, $P < 0.001$), TAPSE ($R = -0.173$, $P = 0.002$), TAPSE/sPAP ratio ($R = -0.330$, $P < 0.001$), mRAP ($R = 0.253$, $P < 0.001$), mPAP ($R = 0.288$, $P < 0.001$) and mPAWP ($R = 0.279$, $P < 0.001$), but not with LVEF ($R = -0.063$, $P = 0.215$), LVOT VTI ($R = -0.031$, $P = 0.553$) and CI ($R = -0.019$, $P = 0.769$). These results suggest that elevated RVSI indicates right-sided overload rather than left-sided overload.

During the follow-up period (median 412 days; range 4–991 days), cardiac events occurred in 60 patients (16 cardiac deaths and 52 worsening HF). Sixteen cardiac deaths included 14 deaths from HF and 2 deaths from ventricular fibrillation.

TABLE 1 | Clinical and demographic characteristics of the study population.

	Total (*N* = 388)	**Control (RVSI = 0, *N* = 260)**	**Low RVSI (0 < RVSI ≤ 0.21, *N* = 63)**	**High RVSI (RVSI > 0.21, *N* = 65)**	***P*-value***
Renal Doppler ultrasonography IRVF pattern (n, %) continuous/ biphasic/ monophasic/ unclassified	260 (67.0)/ 78 (20.1)/ 48 (12.4)/ 2 (0.5)	260 (100)/ 0 (0)/ 0 (0)/ 0 (0)	0 (0)/ 38 (60.3)/ 23 (36.5)/ 2 (3.2)	0 (0)/ 40 (61.5)/ 25 (38.5)/ 0 (0)	<0.001
Demographics					
Age (years)	71 (63.0–79.8)	71.0 (63.0–78.0)	69.0 (58.0–80.0)	75.0 (66.0–82.0)	0.295
Male sex (*n*, %)	225 (58.0)	155 (59.6)	36 (57.1)	34 (52.3)	0.559
Body mass index (kg/m^2)	22.6 (20.3–25.4)	22.5 (20.4–25.4)	23.3 (20.1–24.8)	21.9 (20.2–25.8)	0.921
Systolic BP (mmHg)	116.0 (105.0–130.0)	117.0 (106.0–130.0)	113.0 (101.8–127.3)	116.0 (103.5–132.0)	0.453
Heart rate (bpm)	69.0 (60.0–80.0)	69.0 (60.0–81.8)	69.0 (60.0–77.0)	70.0 (60.5–79.5)	0.632
NYHA class III or IV (*n*, %)	111 (28.6)	67 (27.8)	16 (26.2)	28 (43.8)	0.036
Etiology (*n*, %) ischemic/ myopathy/ valvular/ arrhythmia/ pulmonary/ congenital/ others	77 (19.8)/ 92 (23.7)/ 126 (32.5)/ 40 (10.3)/ 37 (9.5)/ 7 (1.8)/ 9 (2.3)	53 (20.4)/ 65 (25.0)/ 84 (32.3)/ 25 (9.6)/ 23 (8.8)/ 5 (1.9)/ 5 (1.9)	10 (15.9)/ 16 (25.4)/ 19 (30.2)/ 7 (11.1)/ 8 (12.7)/ 1 (1.6)/ 2 (3.2)	14 (21.5)/ 11 (16.9)/ 23 (35.4)/ 8 (12.3)/ 6 (9.2)/ 1 (1.5)/ 2 (3.1)	0.979
Comorbidities					
CAD (*n*, %)	111 (28.6)	76 (29.2)	16 (25.4)	19 (29.2)	0.827
Atrial fibrillation (*n*, %)	139 (35.8)	79 (30.4)	25 (39.7)	35 (53.8)	0.002
Hypertension (*n*, %)	249 (64.2)	156 (60.0)	44 (69.8)	49 (75.4)	0.041
Dyslipidemia (*n*, %)	255 (65.7)	180 (69.2)	41 (65.1)	34 (52.3)	0.036
Diabetes mellitus (*n*, %)	139 (35.8)	93 (35.9)	20 (31.7)	26 (40.0)	0.623
CKD (*n*, %)	251 (64.7)	158 (60.8)	42 (66.7)	51 (78.5)	0.027
Anemia (*n*, %)	175 (45.1)	105 (40.4)	26 (41.3)	44 (67.7)	<0.001
Laboratory data					
BNP (pg/mL)	183.8 (77.8–396.2)	157.0 (67.3–334.5)	209.8 (76.8–501.4)	305.2 (158.2–582.6)	<0.001
Log BNP	2.26 (1.89–2.60)	2.20 (1.83–2.52)	2.32 (1.89–2.70)	2.49 (2.20–2.77)	<0.001
BUN (mg/dL)	19.0 (15.0–25.0)	19.0 (15.0–25.0)	19.0 (15.0–25.0)	21.0 (16.0–26.5)	0.285
Creatinine (mg/dL)	1.00 (0.82–1.24)	0.97 (0.79–1.19)	0.98 (0.82–1.30)	1.07 (0.86–1.32)	0.129
eGFR (mL/min/1.73 m^2)	52.5 (40.0–64.0)	54.0 (41.3–65.0)	51.0 (42.0–64.0)	45.0 (36.0–59.0)	0.017
Sodium (mEq/L)	140.0 (138.0–141.0)	140.0 (138.0–141.0)	140.0 (139.0–142.0)	140.0 (139.0–141.0)	0.186
CRP (mg/dL)	0.20 (0.08–0.70)	0.17 (0.07–0.66)	0.24 (0.06–0.68)	0.33 (0.13–1.07)	0.035
Hemoglobin (g/dL)	12.9 (11.3–14.4)	13.2 (11.6–14.7)	12.8 (11.6–14.5)	11.7 (10.3–13.5)	<0.001
Proteinuria (-)/ (±)/ (1+)/ (2+)/ missing (n, %)	205 (52.8)/ 90 (23.2)/ 52 (13.4)/ 35 (9.0)/ 6 (1.5)	152 (59.1)/ 55 (21.4)/ 28 (10.9)/ 22 (8.6)/ 3 (1.1)	26 (41.9)/ 18 (29.0)/ 13 (21.0)/ 5 (8.1)/ 1 (1.6)	27 (42.9)/ 17 (27.0)/ 11 (17.5)/ 8 (12.7)/ 2 (3.1)	0.072
UACR	22.0 (9.0–74.3)	19.0 (9.0–59.8)	22.5 (6.8–81.0)	56.0 (14.0–149.3)	0.008
Echocardiography					
LV ejection fraction (%)	53.0 (34.0–63.0)	54.0 (35.0–63.0)	57.0 (32.2–63.5)	46.0 (30.1–62.0)	0.201
LVOT VTI (cm)	16.1 (13.0–20.3)	16.2 (13.0–20.2)	17.5 (13.0–22.0)	15.5 (11.6–19.2)	0.219
Left atrial volume (mL)	86.0 (65.0–120.0)	82.4 (61.1–109.3)	87.5 (68.0–117.1)	119.1 (81.8–159.9)	<0.001
Mitral valve E/e'	13.7 (9.5–19.7)	12.9 (9.1–17.6)	14.5 (10.7–20.4)	15.6 (11.2–26.4)	0.006
RA area (cm^2)	19.0 (14.0–25.0)	15.8 (13.0–23.0)	20.0 (15.4–26.0)	23.0 (17.7–30.0)	<0.001
RV diastolic area (cm^2)	19.4 (15.0–25.6)	17.1 (12.8–23.5)	21.2 (16.9–34.2)	20.8 (18.4–27.9)	0.032
RV systolic area (cm^2)	11.5 (8.9–17.9)	10.2 (7.8–14.6)	13.7 (10.4–24.9)	12.4 (10.3–20.1)	0.025
RV–FAC (%)	36.0 (28.0–44.0)	38.0 (32.0–44.5)	31.2 (23.0–40.5)	34.5 (23.9–44.3)	0.039
IVC (mm)	15.0 (12.7–18.6)	14.0 (12.0–17.6)	15.7 (13.0–19.3)	18.8 (15.0–22.0)	<0.001
TR (*n*, %) none-trivial/ mild/ moderate/ severe	238 (61.3)/ 90 (23.2)/ 45 (11.6)/ 15 (3.9)	170 (65.4)/ 62 (23.8)/ 25 (9.6)/ 3 (1.2)	40 (63.5)/ 14 (22.2)/ 6 (9.5)/ 3 (4.8)	28 (43.1)/ 14 (21.5)/ 14 (21.5)/ 9 (13.8)	<0.001

(Continued)

TABLE 1 | Continued

	Total ($N = 388$)	Control (RVSI = 0, $N = 260$)	Low RVSI (0 < RVSI ≤ 0.21, $N = 63$)	High RVSI (RVSI > 0.21, $N = 65$)	*P*-value*
TRPG (mmHg)	24.9 (20.0–33.0)	23.0 (20.0–30.0)	27.0 (21.8–35.3)	29.0 (23.0–37.0)	0.003
TAPSE (mm)	17.3 (14.5–20.4)	17.7 (15.2–21.1)	17.7 (13.7–20.1)	15.0 (12.0–18.9)	0.008
TAPSE/systolic PAP ratio (mm/mmHg)	0.50 (0.36–0.68)	0.54 (0.40–0.78)	0.45 (0.29–0.55)	0.37 (0.28–0.52)	<0.001
S' (cm/s)	9.1 (7.3–10.7)	9.7 (7.9–11.2)	7.8 (6.2–10.2)	8.7 (6.9–9.8)	0.089
Right heart catherization					
Cardiac index (L/min/m^2)	2.4 (2.1–2.8)	2.4 (2.1–2.9)	2.5 (2.2–2.9)	2.2 (2.0–2.7)	0.200
Mean RAP (mmHg)	7.0 (4.0–10.0)	6.0 (3.8–9.0)	7.5 (5.3–10.0)	9.0 (6.0–11.0)	<0.001
Mean PAP (mmHg)	23.0 (18.0–31.0)	21.0 (16.3–28.8)	26.0 (20.0–34.8)	28.0 (22.0–35.5)	<0.001
Mean PAWP (mmHg)	14.0 (9.0–19.0)	13.0 (8.0–17.0)	14.0 (11.3–19.8)	19.0 (14.0–22.5)	<0.001
PVR (WoodU)	2.0 (1.3–3.2)	1.9 (1.3–2.8)	2.0 (1.5–6.2)	2.8 (1.6–5.0)	0.057
Medications					
β-Blocker (*n*, %)	270 (69.6)	191 (73.5)	33 (52.4)	46 (70.8)	0.005
ACE-I (*n*, %)	157 (40.5)	108 (41.5)	24 (38.1)	25 (38.5)	0.827
ARB (*n*, %)	95 (24.5)	63 (24.2)	12 (19.0)	20 (30.8)	0.300
ARNI (*n*, %)	0 (0)	0 (0)	0 (0)	0 (0)	-
MRA (*n*, %)	146 (37.6)	92 (35.4)	25 (39.7)	29 (44.6)	0.364
SGLT2 inhibitor (*n*, %)	1 (0.3)	0 (0)	1 (1.6)	0 (0)	0.075
Diuretic (*n*, %)	253 (65.2)	157 (60.4)	44 (69.8)	52 (80.0)	0.009

*RVSI, renal venous stasis index; IRVF, intrarenal venous flow; BP, blood pressure; NYHA, New York Heart Association; CAD, coronary artery disease; CKD, chronic kidney disease; BNP, B-type natriuretic peptide; BUN, blood urea nitrogen; eGFR, estimated glomerular filtration rate; CRP, C-reactive protein; UACR, urine albumin-to-creatinine ratio; LV, left ventricle; LVOT VTI, left ventricular outflow tract velocity-time integral; mitral valve E/e', early transmitral flow velocity to mitral annular velocity ratio; RA, right atrial; RV, right ventricle; RV-FAC, right ventricle fractional area change; IVC, inferior vena cava diameter; TR, tricuspid regurgitation; TRPG, tricuspid regurgitation pressure gradient; TAPSE, tricuspid annular plane systolic excursion; S', tissue Doppler-derived tricuspid lateral annular systolic velocity (tricuspid valve S'); RAP, right atrium pressure; PAP, pulmonary artery pressure; PAWP, pulmonary artery wedge pressure; PVR, pulmonary vascular resistance; ACE-I, angiotensin converting enzyme inhibitor; ARB, angiotensin II receptor blocker; ARNI, angiotensin receptor-neprilysin inhibitor; MRA, mineralocorticoid receptor antagonist; SGLT2 inhibitor, sodium glucose cotransporter 2 inhibitor. *A p-value indicates statistically significance in comparison across all groups.*

In the Kaplan–Meier analysis, the cumulative cardiac event rate significantly increased with increasing RVSI (**Figure 3**, log-rank, $P = 0.001$). In the univariate Cox proportional hazard analysis (**Table 2**), high RVSI was associated with high cardiac event rate (high RVSI group vs. control group, hazard ratio, 2.849; 95% confidence interval, 1.596–5.087, $P < 0.001$). In the multivariate Cox proportional hazard analyses, due to the limited number of cardiac events (60 events) and to avoid overfitting, we selected univariate factors with $P < 0.05$ (i.e., age, CKD, anemia, BNP and high RVSI). After adjusting for these confounding factors, high RVSI was an independent prognostic factor (**Table 2**; high RVSI group vs. control group: hazard ratio, 1.908; 95% confidence interval, 1.046–3.479, $P = 0.035$). In the subgroup analysis regarding LVEF, there was no significant interactions between prognostic impact of RVSI and LVEF ($P = 0.759$), and high RVSI was associated with high cardiac event rate both in the heart failure with reduced ejection fraction group and the heart failure with preserved ejection fraction group. In the Kaplan–Meier analysis stratified by IRVF patterns, the cumulative cardiac event rate significantly increased with worsening IRVF patterns (**Figure 4**, log-rank, $P = 0.002$). There were overlap and inversion between the groups with biphasic and monophasic IRVF patterns.

DISCUSSION

In this study, we investigated the relationship of RVSI assessed by renal Doppler ultrasonography with laboratory tests, echocardiography and RHC, as well as its prognostic impact in HF patients. According to a past study, PH patients with high RVSI experienced more adverse events such as worsening PH or all-cause mortality (10). However, the clinical significance of RVSI in HF patients has not been sufficiently examined.

Right ventricular function is the main determinant of symptomatology and outcome in patients with HF (23, 25, 26). Right ventricle adapts to increased afterload by increasing contractility to preserve the right ventricle–to–pulmonary circulation coupling. When this adaptation is unsustainable, the right ventricle increases preload (in other words, right ventricular end-diastolic volume) relying on Frank-Starling law (26). In normal subjects without right ventricular diastolic failure, the forward flow from the right atrium to the right ventricle is normal, because the right ventricular end-diastolic pressure remains low. However, in patients with right ventricular diastolic failure, the forward flow is impaired, because the right ventricle is stiff and right ventricular end-diastolic pressure is elevated. When the pressure in the vena cava (IVC and superior vena cava) becomes lower than that in the right ventricle, blood flow will

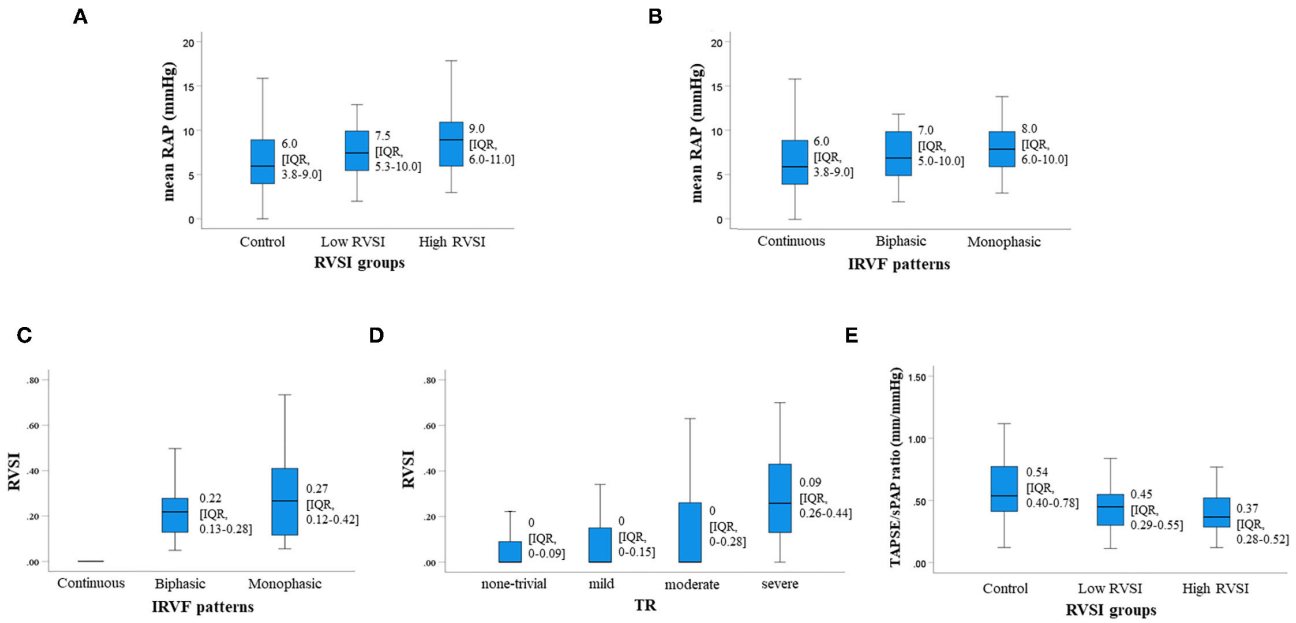

FIGURE 2 | The severity of renal congestion can be assessed by measuring RVSI using renal Doppler ultrasonography. **(A,C–E)** show the relationship between RVSI and mRAP **(A)** IRVF patterns **(C)** severity of TR **(D)** and TAPSE/sPAP ratio **(E)**. RVSI showed a significant stepwise increase along the IRVF patterns (**C**; $P < 0.001$) and severity of tricuspid regurgitation (**D**; $P < 0.001$). TAPSE/sPAP ratio showed a significant stepwise decrease along the RVSI groups (**E**; $P < 0.001$). In addition, both RVSI and IRVF patterns showed similar associations with elevated mRAP (**A**; $P < 0.001$ and **B**; $P = 0.001$). RVSI, renal venous stasis index; mRAP, mean right atrial pressure; IRVF, intrarenal venous flow; TR, tricuspid regurgitation; TAPSE/sPAP, tricuspid annular plane systolic excursion/systolic pulmonary artery pressure; IQR, interquartile range.

be partially directed backward into the vena cava. This leads to elevation of RAP (29). Namely, RAP is a surrogate marker of both right ventricular diastolic function and right ventricular diastolic stiffness (30–33). Furthermore, these series of processes lead to reduction of venous return to the right ventricle, and result in loss of right ventricular stroke volume and right ventricular dysfunction. In the present study, there was a positive correlation between RVSI and mPAP ($R = 0.253$, $P < 0.001$). RVSI also showed a positive correlation with TR severity ($R = 0.197$, $P < 0.001$) and a negative correlation with TAPSE/sPAP ratio ($R = -0.330$, $P < 0.001$). With advancing right-sided heart failure, TR generally becomes more severe (34). TAPSE/sPAP ratio is a surrogate of the right ventricle–to–pulmonary circulation coupling and is affected by right ventricular diastolic stiffness (26). We consider that RVSI was mainly affected by RAP, and was also affected by right heart diastolic failure, backflow, forward flow impairment and etc. Concordant with our results, it has been reported that RAP, right ventricular dysfunction, severity of TR and TAPSE/sPAP ratio are associated with worse prognosis in HF patients (25–27, 29–32, 35–43). To the best of our knowledge, this study is the first to report that the RVSI, as a marker of right-sided overload, is associated with cardiac events in HF patients.

Cardiorenal syndrome commonly refers to the collective dysfunction of heart and kidney resulting in a cascade of feedback mechanism that damages both organs (44). Renal dysfunction is associated with adverse prognosis in HF patients (45). Given the aging population, patients with HF and CKD are likely to continue to increase due to longer cumulative exposure to common risk factors including hypertension, obesity, diabetes and vascular disorders (46). Thus, we have to understand the various mechanisms of this syndrome. Renal congestion due to elevation of RAP is one of the main conditions of cardiorenal syndrome. Renal congestion may increase interstitial pressure and reduce vessel compliance in the renal parenchymal regions due to direct compression (47–49). Intrarenal venous flow depends on interstitial pressure, intra-abdominal pressure and intravenous pressure, and shows superimposed biphasic forward velocities that peak during systole and diastole (48, 50, 51). Under physiological conditions, intrarenal veins exhibit continuous flow independent of renal function (continuous pattern). With increasing RAP, renal veins become less compliant, continuous flow becomes discontinuous flow and increasing prominence of the superimposed biphasic forward velocities (biphasic pattern). Further increases in RAP finally lead to a diastolic-only flow (monophasic pattern) (52, 53). The classification of IRVF patterns has a weakness; some patterns may be difficult to be classified. According to **Table 1**, there were no differences in distribution of IRVF patterns between the high and low RVSI groups. RVSI can complement the weaknesses by quantifying IRVF. We consider that quantifying RVSI can detect renal congestion more sensitively than IRVF patterns.

We considered both RVSI and IRVF pattern might be useful as markers of right sided heart failure and prognostic indicators. Regarding comparison of RVSI with IRVF patterns

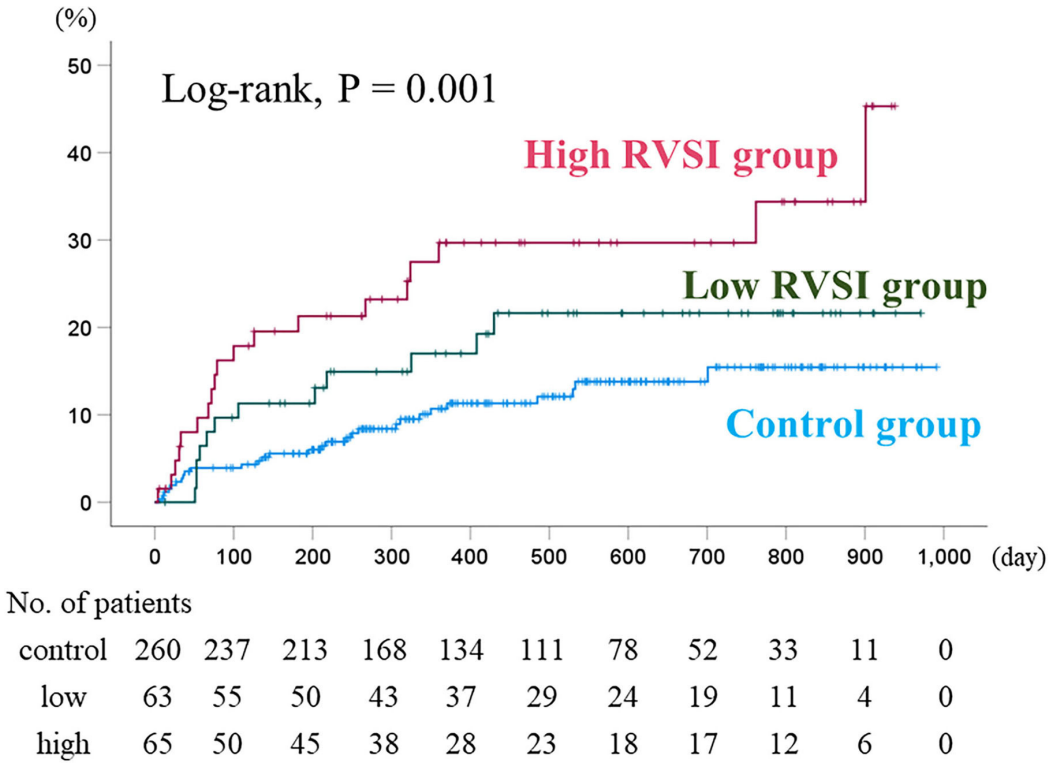

FIGURE 3 | Kaplan–Meier analysis for cardiac event rates stratified by RVSI. The cumulative cardiac event rate significantly increased with increasing RVSI (log-rank, *P* = 0.001). RVSI, renal venous stasis index.

TABLE 2 | Cox proportional hazard model for predicting cardiac events.

Cardiac events	Univariate			Multivariate		
	HR	95% CI	*P*-value	HR	95% CI	*P*-value
Age	1.038	1.015–1.063	0.001	1.016	0.990–1.042	0.232
Sex (male)	0.994	0.595–1.661	0.981			
atrial fibrillation	1.225	0.731–2.055	0.441			
hypertension	1.216	0.706–2.096	0.481			
dyslipidemia	1.198	0.689–2.084	0.522			
CKD	3.345	1.693–6.608	0.001	2.174	1.056–4.476	0.035
Anemia	2.113	1.260–3.544	0.005	1.313	0.755–2.286	0.335
BNP	1.002	1.001–1.002	<0.001	1.001	1.001–1.002	<0.001
RVSI						
Low RVSI vs. control	1.648	0.841–3.231	0.146			
High RVSI vs. control	2.849	1.596–5.087	<0.001	1.908	1.046–3.479	0.035

RVSI, renal venous stasis index; CKD, chronic kidney disease; BNP, B-type natriuretic peptide; HR, hazard ratio; CI, confidence interval.

for predicting prognosis, our data suggest that the RVSI may be superior to IRVF patterns. Namely, although Kaplan–Meier analysis of IRVF patterns (**Figure 4**) showed basically similar to those of RVSI classification (**Figure 3**), there were overlap and inversion between the biphasic and monophasic IRVF patterns (**Figure 4**). Additionally, to compare the high and low RVSI groups with the same IRVF patterns about cardiac event rates, in patients with biphasic pattern, we could find that the cardiac event rate was significantly higher in the high RVSI group than in the low RVSI group in the Kaplan–Meier analysis (log-rank, p = 0.004, data not shown in the manuscript). Moreover, RVSI was reported to be more sensitive and specific predictor of the outcome than IRVF patterns in the previous study (20). Taken together, RVSI can predict outcome more sensitive than IRVF patterns, even in cases of same IRVF pattern.

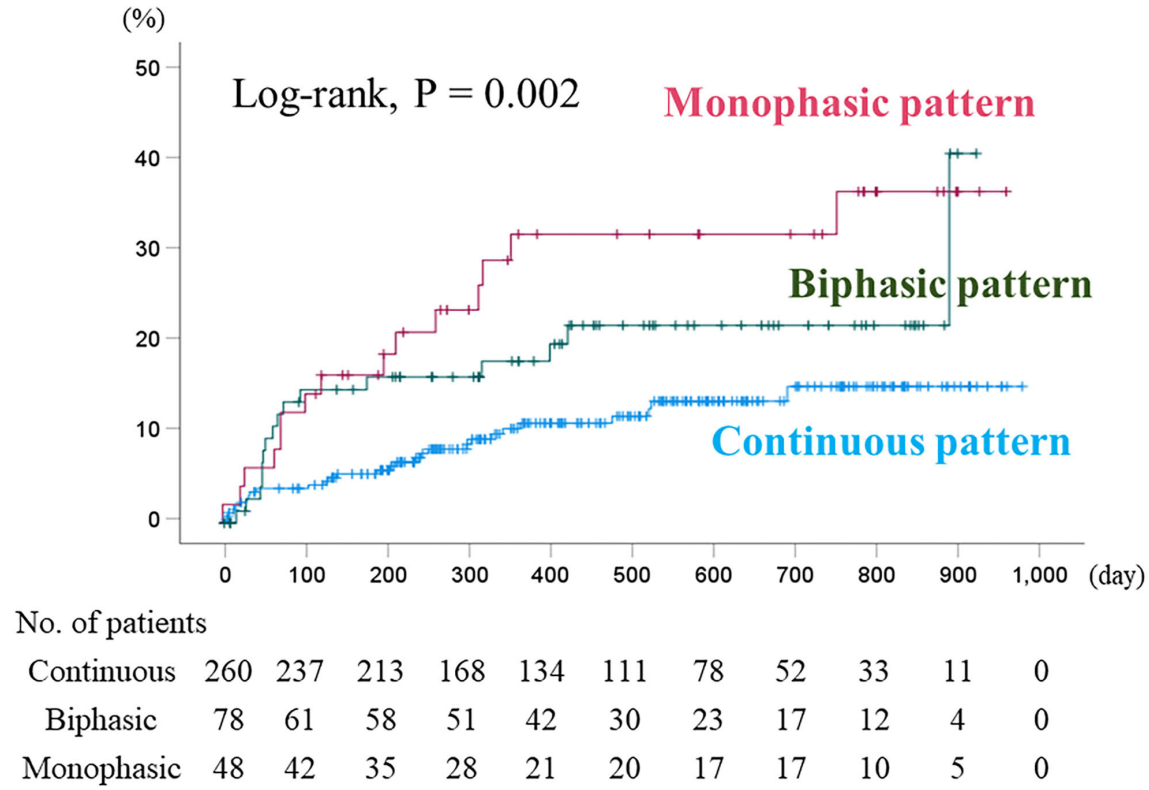

FIGURE 4 | Kaplan–Meier analysis for cardiac event rate stratified by IRVF patterns. The cumulative cardiac event rate significantly increased with worsening IRVF patterns (log-rank, $P = 0.002$). Although it showed basically similar to those of RVSI classification, there were overlap and inversion between the groups with biphasic and monophasic IRVF patterns. IRVF, intrarenal venous flow.

STUDY LIMITATIONS

There are some limitations in the present study. First, the study may be somewhat underpowered because of a single center prospective cohort study with a relatively small number of patients and a short follow-up period. Second, the present study used only variables during hospitalization and did not take into consideration changes in medical parameters or treatments after discharge. The hemodynamics of HF patients changes dynamically. Thus, future studies need to assess alterations of RVSI in response to hemodynamic changes. Third, since the attending physicians made decisions to perform RHC, there might be a potential selection bias. Therefore, the present results need to be viewed as preliminary, and further studies with a larger number of patients are needed.

CONCLUSION

RVSI assessed by renal Doppler ultrasonography reflects right-sided overload and is associated with adverse prognosis in HF patients.

DATA AVAILABILITY STATEMENT

The raw data supporting the conclusions of this article will be made available by the authors, without undue reservation.

ETHICS STATEMENT

The studies involving human participants were reviewed and approved by Ethics Committee of Fukushima Medical University. The patients/participants provided their written informed consent to participate in this study. Written informed consent was obtained from the individual(s) for the publication of any potentially identifiable images or data included in this article.

AUTHOR CONTRIBUTIONS

HO, KW, and YSa: conceptualization, methodology, formal analysis, investigation, writing–original draft, and visualization. AY: conceptualization, methodology, formal analysis, investigation, resources, data curation, writing–original draft, visualization, supervision, project administration, and funding acquisition. YHor, SI, MM, and YY: methodology, investigation, writing–original draft, and visualization. YSu, YI, YHot, TM, TK, MO, and AK: conceptualization, methodology, formal analysis, investigation, and writing–review and editing. YT: conceptualization, methodology, formal analysis, investigation, writing–original draft, supervision, and project administration. All authors contributed to the article and approved the submitted version.

FUNDING

This study was supported in part by a grant-in-aid for Scientific Research (Nos. 20K07828 and MO20K16529) from the Japan Society for the Promotion of Science.

SUPPLEMENTARY MATERIAL

The Supplementary Material for this article can be found online at: https://www.frontiersin.org/articles/10.3389/fcvm.2022.772466/full#supplementary-material

REFERENCES

1. Ho KK, Pinsky JL, Kannel WB, Levy D. The epidemiology of heart failure: the Framingham Study. *J Am Coll Cardiol.* (1993) 22:6A−13. doi: 10.1016/0735-1097(93)90455-A
2. Nakane E, Kato T, Tanaka N, Kuriyama T, Kimura K, Nishiwaki S, et al. Association of the induction of a self-care management system with 1-year outcomes in patients hospitalized for heart failure. *J Cardiol.* (2021) 77:48–56. doi: 10.1016/j.jjcc.2020.07.015
3. Girerd N, Seronde MF, Coiro S, Chouihed T, Bilbault P, Braun F, et al. Integrative assessment of congestion in heart failure throughout the patient journey. *JACC Heart Fail.* (2018) 6:273–85. doi: 10.1016/j.jchf.2017.09.023
4. Pellicori P, Kaur K, Clark AL. Fluid management in patients with chronic heart failure. *Card Fail Rev.* (2015) 1:90–5. doi: 10.15420/cfr.2015.1.2.90
5. Massari F, Scicchitano P, Iacoviello M, Passantino A, Guida P, Sanasi M, et al. Multiparametric approach to congestion for predicting long-term survival in heart failure. *J Cardiol.* (2020) 75:47–52. doi: 10.1016/j.jjcc.2019.05.017
6. Yoshihisa A, Watanabe K, Sato Y, Ishibashi S, Matsuda M, Yamadera Y, et al. Intrarenal doppler ultrasonography reflects hemodynamics and predicts prognosis in patients with heart failure. *Sci Rep.* (2020) 10:22257. doi: 10.1038/s41598-020-79351-6
7. Iida N, Seo Y, Sai S, Machino-Ohtsuka T, Yamamoto M, Ishizu T, et al. Clinical implications of intrarenal hemodynamic evaluation by doppler ultrasonography in heart failure. *JACC Heart Fail.* (2016) 4:674–82. doi: 10.1016/j.jchf.2016.03.016
8. Nijst P, Martens P, Dupont M, Tang WHW, Mullens W. Intrarenal flow alterations during transition from euvolemia to intravascular volume expansion in heart failure patients. *JACC Heart Fail.* (2017) 5:672–81. doi: 10.1016/j.jchf.2017.05.006
9. Puzzovivo A, Monitillo F, Guida P, Leone M, Rizzo C, Grande D, et al. Renal venous pattern: a new parameter for predicting prognosis in heart failure outpatients. *J Cardiovasc Dev Dis.* (2018) 5:52. doi: 10.3390/jcdd5040052
10. Husain-Syed F, Birk HW, Ronco C, Schormann T, Tello K, Richter MJ, et al. Doppler-derived renal venous stasis index in the prognosis of right heart failure. *J Am Heart Assoc.* (2019) 8:e013584. doi: 10.1161/JAHA.119.013584
11. Writing Committee M, Yancy CW, Jessup M, Bozkurt B, Butler J, Casey DE, et al. 2013 ACCF/AHA guideline for the management of heart failure: a report of the American college of cardiology foundation/American heart association task force on practice guidelines. *Circulation.* (2013) 128:e240–327. doi: 10.1161/CIR.0b013e31829e8776
12. Ponikowski P, Voors AA, Anker SD, Bueno H, Cleland JGF, Coats AJS, et al. 2016 ESC Guidelines for the diagnosis and treatment of acute and chronic heart failure: the task force for the diagnosis and treatment of acute and chronic heart failure of the European society of cardiology (ESC) developed with the special contribution of the heart failure association (HFA) of the ESC. *Eur Heart J.* (2016) 37:2129–200. doi: 10.1093/eurheartj/ehw128
13. Yoshihisa A, Sato Y, Watanabe S, Yokokawa T, Sato T, Suzuki S, et al. Decreased cardiac mortality with nicorandil in patients with ischemic heart failure. *BMC Cardiovasc Disord.* (2017) 17:141. doi: 10.1186/s12872-017-0577-3
14. American Diabetes A. Diagnosis and classification of diabetes mellitus. *Diabetes Care.* (2011) 34:S62–9. doi: 10.2337/dc11-S062
15. Stevens PE, Levin A, Kidney disease: improving global outcomes chronic kidney disease guideline development work group M. evaluation and management of chronic kidney disease: synopsis of the kidney disease: improving global outcomes 2012 clinical practice guideline. *Ann Intern Med.* (2013) 158:825–30. doi: 10.7326/0003-4819-158-11-201306040-00007
16. Miura S, Yoshihisa A, Takiguchi M, Shimizu T, Nakamura Y, Yamauchi H, et al. Association of hypocalcemia with mortality in hospitalized patients with heart failure and chronic kidney disease. *J Card Fail.* (2015) 21:621–7. doi: 10.1016/j.cardfail.2015.04.015
17. Sato Y, Yoshihisa A, Oikawa M, Nagai T, Yoshikawa T, Saito Y, et al. Prognostic impact of worsening renal function in hospitalized heart failure patients with preserved ejection fraction: a report from the JASPER registry. *J Card Fail.* (2019) 25:631–42. doi: 10.1016/j.cardfail.2019.04.009
18. Yancy CW, Jessup M, Bozkurt B, Butler J, Casey DE, Drazner MH, et al. 2013 ACCF/AHA guideline for the management of heart failure: a report of the American college of cardiology foundation/American heart association task force on practice guidelines. *J Am Coll Cardiol.* (2013) 62:e147–239. doi: 10.1016/j.jacc.2013.05.019
19. Yoshihisa A, Ichijo Y, Watanabe K, Sato Y, Kanno Y, Takiguchi M, et al. Prior history and incidence of cancer impacts on cardiac prognosis in hospitalized patients with heart failure. *Circ J.* (2019) 83:1709–17. doi: 10.1253/circj.CJ-19-0279
20. Kiely DG, Levin D, Hassoun P, Ivy DD, Jone PN, Bwika J, et al. EXPRESS: statement on imaging and pulmonary hypertension from the pulmonary vascular research institute (PVRI). *Pulm Circ.* (2019) 9:2045894019841990. doi: 10.1177/2045894019841990
21. Rudski LG, Lai WW, Afilalo J, Hua L, Handschumacher MD, Chandrasekaran K, et al. Guidelines for the echocardiographic assessment of the right heart in adults: a report from the American Society of Echocardiography endorsed by the European association of echocardiography, a registered branch of the European society of cardiology, and the canadian society of echocardiography. *J Am Soc Echocardiogr.* (2010) 23:685–713. doi: 10.1016/j.echo.2010.05.010
22. Guazzi M, Bandera F, Pelissero G, Castelvecchio S, Menicanti L, Ghio S, et al. Tricuspid annular plane systolic excursion and pulmonary arterial systolic pressure relationship in heart failure: an index of right ventricular contractile function and prognosis. *Am J Physiol Heart Circ Physiol.* (2013) 305:H1373–81. doi: 10.1152/ajpheart.00157.2013
23. Guazzi M, Naeije R. Pulmonary hypertension in heart failure: pathophysiology, pathobiology, and emerging clinical perspectives. *J Am Coll Cardiol.* (2017) 69:1718–34. doi: 10.1016/j.jacc.2017.01.051
24. Guazzi M, Naeije R. Right heart phenotype in heart failure with preserved ejection fraction. *Circ Heart Fail.* (2021) 14:e007840. doi: 10.1161/CIRCHEARTFAILURE.120.007840
25. Guazzi M. Use of TAPSE/PASP ratio in pulmonary arterial hypertension: an easy shortcut in a congested road. *Int J Cardiol.* (2018) 266:242–4. doi: 10.1016/j.ijcard.2018.04.053
26. Tello K, Wan J, Dalmer A, Vanderpool R, Ghofrani HA, Naeije R, et al. Validation of the tricuspid annular plane systolic excursion/systolic pulmonary artery pressure ratio for the assessment of right ventricular-arterial coupling in severe pulmonary hypertension. *Circ Cardiovasc Imaging.* (2019) 12:e009047. doi: 10.1161/CIRCIMAGING.119.009047
27. Guazzi M, Dixon D, Labate V, Beussink-Nelson L, Bandera F, Cuttica MJ, et al. RV Contractile function and its coupling to pulmonary circulation in heart failure with preserved ejection fraction: stratification of clinical phenotypes and outcomes. *JACC Cardiovasc Imaging.* (2017) 10:1211–21. doi: 10.1016/j.jcmg.2016.12.024
28. Galie N, Humbert M, Vachiery JL, Gibbs S, Lang I, Torbicki A, et al. 2015 ESC/ERS Guidelines for the diagnosis and treatment of pulmonary hypertension: the joint task force for the diagnosis and treatment of pulmonary hypertension of the European society of cardiology (ESC) and the European respiratory society (ERS): endorsed by: association for European paediatric and congenital cardiology (AEPC), international society for heart and lung transplantation (ISHLT). *Eur Heart J.* (2016) 37:67–119. doi: 10.1093/eurheartj/ehv317
29. Marcus JT, Westerhof BE, Groeneveldt JA, Bogaard HJ, de Man FS, Vonk Noordegraaf A. Vena cava backflow and right ventricular

stiffness in pulmonary arterial hypertension. *Eur Respir J.* (2019) 54:1900625. doi: 10.1183/13993003.00625-2019
30. D'Alonzo GE, Barst RJ, Ayres SM, Bergofsky EH, Brundage BH, Detre KM, et al. Survival in patients with primary pulmonary hypertension. results from a national prospective registry. *Ann Intern Med.* (1991) 115:343–9. doi: 10.7326/0003-4819-115-5-343
31. Benza RL, Miller DP, Gomberg-Maitland M, Frantz RP, Foreman AJ, Coffey CS, et al. Predicting survival in pulmonary arterial hypertension: insights from the registry to evaluate early and long-term pulmonary arterial hypertension disease management (REVEAL). *Circulation.* (2010) 122:164–72. doi: 10.1161/CIRCULATIONAHA.109.898122
32. Weatherald J, Boucly A, Chemla D, Savale L, Peng M, Jevnikar M, et al. Prognostic value of follow-up hemodynamic variables after initial management in pulmonary arterial hypertension. *Circulation.* (2018) 137:693–704. doi: 10.1161/CIRCULATIONAHA.117.029254
33. Wessels JN, Mouratoglou SA, van Wezenbeek J, Handoko ML, Marcus JT, Meijboom LJ, et al. Right atrial function is associated with RV diastolic stiffness: RA-RV interaction in pulmonary arterial hypertension. *Eur Respir J.* (2021). doi: 10.1183/13993003.01454-2021
34. Prihadi EA, Delgado V, Leon MB, Enriquez-Sarano M, Topilsky Y, Bax JJ. Morphologic types of tricuspid regurgitation: characteristics and prognostic implications. *JACC Cardiovasc Imaging.* (2019) 12:491–9. doi: 10.1016/j.jcmg.2018.09.027
35. Benfari G, Antoine C, Miller WL, Thapa P, Topilsky Y, Rossi A, et al. Excess mortality associated with functional tricuspid regurgitation complicating heart failure with reduced ejection fraction. *Circulation.* (2019) 140:196–206. doi: 10.1161/CIRCULATIONAHA.118.038946
36. De la Espriella R, Santas E, Chorro FJ, Minana G, Soler M, Bodi V, et al. Functional tricuspid regurgitation and recurrent admissions in patients with acute heart failure. *Int J Cardiol.* (2019) 291:83–8. doi: 10.1016/j.ijcard.2019.03.051
37. Wang N, Fulcher J, Abeysuriya N, McGrady M, Wilcox I, Celermajer D, et al. Tricuspid regurgitation is associated with increased mortality independent of pulmonary pressures and right heart failure: a systematic review and meta-analysis. *Eur Heart J.* (2019) 40:476–84. doi: 10.1093/eurheartj/ehy641
38. Richter MJ, Zedler D, Berliner D, Douschan P, Gall H, Ghofrani HA, et al. Clinical relevance of right atrial functional response to treatment in pulmonary arterial hypertension. *Front Cardiovasc Med.* (2021) 8:775039. doi: 10.3389/fcvm.2021.775039
39. Guazzi M. The alarming association between right ventricular dysfunction and outcome: aetiology matters. *Eur Heart J.* (2020) 41:1283–5. doi: 10.1093/eurheartj/ehaa080
40. Dietz MF, Prihadi EA, van der Bijl P, Goedemans L, Mertens BJA, Gursoy E, et al. Prognostic implications of right ventricular remodeling and function in patients with significant secondary tricuspid regurgitation. *Circulation.* (2019) 140:836–45. doi: 10.1161/CIRCULATIONAHA.119.039630
41. Naksuk N, Tan N, Padmanabhan D, Kancharla K, Makkar N, Yogeswaran V, et al. Right ventricular dysfunction and long-term risk of sudden cardiac death in patients with and without severe left ventricular dysfunction. *Circ Arrhythm Electrophysiol.* (2018) 11:e006091. doi: 10.1161/CIRCEP.117.006091
42. Kawut SM, Barr RG, Lima JA, Praestgaard A, Johnson WC, Chahal H, et al. Right ventricular structure is associated with the risk of heart failure and cardiovascular death: the multi-ethnic study of atherosclerosis (MESA)–right ventricle study. *Circulation.* (2012) 126:1681–8. doi: 10.1161/CIRCULATIONAHA.112.095216
43. Nochioka K, Querejeta Roca G, Claggett B, Biering-Sorensen T, Matsushita K, Hung CL, et al. Right ventricular function, right ventricular-pulmonary artery coupling, and heart failure risk in 4 US communities: the atherosclerosis risk in communities (ARIC) study. *JAMA Cardiol.* (2018) 3:939–48. doi: 10.1001/jamacardio.2018.2454
44. Kumar U, Wettersten N, Garimella PS. Cardiorenal syndrome: pathophysiology. *Cardiol Clin.* (2019) 37:251–65. doi: 10.1016/j.ccl.2019.04.001
45. Smith GL, Lichtman JH, Bracken MB, Shlipak MG, Phillips CO, DiCapua P, et al. Renal impairment and outcomes in heart failure: systematic review and meta-analysis. *J Am Coll Cardiol.* (2006) 47:1987–96. doi: 10.1016/j.jacc.2005.11.084
46. Damman K, Tang WH, Testani JM, McMurray JJ. Terminology and definition of changes renal function in heart failure. *Eur Heart J.* (2014) 35:3413–6. doi: 10.1093/eurheartj/ehu320
47. Mullens W, Abrahams Z, Francis GS, Sokos G, Taylor DO, Starling RC, et al. Importance of venous congestion for worsening of renal function in advanced decompensated heart failure. *J Am Coll Cardiol.* (2009) 53:589–96. doi: 10.1016/j.jacc.2008.05.068
48. Burnett JC, Knox FG. Renal interstitial pressure and sodium excretion during renal vein constriction. *Am J Physiol.* (1980) 238:F279–82. doi: 10.1152/ajprenal.1980.238.4.F279
49. Damman K, van Deursen VM, Navis G, Voors AA, van Veldhuisen DJ, Hillege HL. Increased central venous pressure is associated with impaired renal function and mortality in a broad spectrum of patients with cardiovascular disease. *J Am Coll Cardiol.* (2009) 53:582–8. doi: 10.1016/j.jacc.2008.08.080
50. Winton FR. The influence of venous pressure on the isolated mammalian kidney. *J Physiol.* (1931) 72:49–61. doi: 10.1113/jphysiol.1931.sp002761
51. Winton FR. Arterial, venous, intrarenal, and extrarenal pressure effects on renal blood flow. *Circ Res.* (1964) 15:103–9.
52. Avasthi PS, Greene ER, Scholler C, Fowler CR. Noninvasive diagnosis of renal vein thrombosis by ultrasonic echo-Doppler flowmetry. *Kidney Int.* (1983) 23:882–7. doi: 10.1038/ki.1983.111
53. Jeong SH, Jung DC, Kim SH, Kim SH. Renal venous doppler ultrasonography in normal subjects and patients with diabetic nephropathy: value of venous impedance index measurements. *J Clin Ultrasound.* (2011) 39:512–8. doi: 10.1002/jcu.20835

Conflict of Interest: The authors declare that the research was conducted in the absence of any commercial or financial relationships that could be construed as a potential conflict of interest.

frontiers in Cardiovascular Medicine

ORIGINAL RESEARCH
published: 08 March 2022
doi: 10.3389/fcvm.2022.797283

Analysis of Vascular Architecture and Parenchymal Damage Generated by Reduced Blood Perfusion in Decellularized Porcine Kidneys Using a Gray Level Co-occurrence Matrix

Igor V. Pantic[1,2], *Adeeba Shakeel*[3], *Georg A. Petroianu*[4] *and Peter R. Corridon*[3,5,6,7]*

[1] Department of Medical Physiology, Faculty of Medicine, University of Belgrade, Belgrade, Serbia, [2] University of Haifa, Haifa, Israel, [3] Department of Pharmacology, College of Medicine and Health Sciences, Khalifa University of Science and Technology, Abu Dhabi, United Arab Emirates, [4] Department of Immunology and Physiology, College of Medicine and Health Sciences, Khalifa University of Science and Technology, Abu Dhabi, United Arab Emirates, [5] Wake Forest Institute for Regenerative Medicine, Medical Center Boulevard, Winston-Salem, NC, United States, [6] Biomedical Engineering, Healthcare Engineering Innovation Center, Khalifa University of Science and Technology, Abu Dhabi, United Arab Emirates, [7] Center for Biotechnology, Khalifa University of Science and Technology, Abu Dhabi, United Arab Emirates

OPEN ACCESS

Edited by:
Diego Gallo,
Politecnico di Torino, Italy

Reviewed by:
Breno Valentim Nogueira,
Federal University of Espirito Santo, Brazil
Maria Aurora Morales,
National Research Council (CNR), Italy

***Correspondence:**
Peter R. Corridon
peter.corridon@ku.ac.ae

Specialty section:
This article was submitted to Cardiovascular Imaging, a section of the journal Frontiers in Cardiovascular Medicine

Received: *19 October 2021*
Accepted: *07 February 2022*
Published: *08 March 2022*

Citation:
Pantic IV, Shakeel A, Petroianu GA and Corridon PR (2022) Analysis of Vascular Architecture and Parenchymal Damage Generated by Reduced Blood Perfusion in Decellularized Porcine Kidneys Using a Gray Level Co-occurrence Matrix. Front. Cardiovasc. Med. 9:797283. doi: 10.3389/fcvm.2022.797283

There is no cure for kidney failure, but a bioartificial kidney may help address this global problem. Decellularization provides a promising platform to generate transplantable organs. However, maintaining a viable vasculature is a significant challenge to this technology. Even though angiography offers a valuable way to assess scaffold structure/function, subtle changes are overlooked by specialists. In recent years, various image analysis methods in radiology have been suggested to detect and identify subtle changes in tissue architecture. The aim of our research was to apply one of these methods based on a gray level co-occurrence matrix (Topalovic et al.) computational algorithm in the analysis of vascular architecture and parenchymal damage generated by hypoperfusion in decellularized porcine. Perfusion decellularization of the whole porcine kidneys was performed using previously established protocols. We analyzed and compared angiograms of kidneys subjected to pathophysiological arterial perfusion of whole blood. For regions of interest Santos et al. covering kidney medulla and the main elements of the vascular network, five major GLCM features were calculated: angular second moment as an indicator of textural uniformity, inverse difference moment as an indicator of textural homogeneity, GLCM contrast, GLCM correlation, and sum variance of the co-occurrence matrix. In addition to GLCM, we also performed discrete wavelet transform analysis of angiogram ROIs by calculating the respective wavelet coefficient energies using high and low-pass filtering. We report statistically significant changes in GLCM and wavelet features, including the reduction of the angular second moment and inverse difference moment, indicating a substantial rise in angiogram textural heterogeneity. Our findings suggest that the GLCM method can be successfully used as

an addition to conventional fluoroscopic angiography analyses of micro/macrovascular integrity following *in vitro* blood perfusion to investigate scaffold integrity. This approach is the first step toward developing an automated network that can detect changes in the decellularized vasculature.

Keywords: decellularized porcine kidney, vascular architecture, parenchymal damage, gray level co-occurrence matrix algorithm, angiography, bioengineering, bioartificial kidney, decellularized kidney

INTRODUCTION

The incidence of kidney failure, otherwise known as end-stage renal disease Zambon et al. is rising globally (1, 2). Unfortunately, there is no cure for this condition, which can develop form the progression of acute and chronic injuries (3–5). Currently, transplantation is the best option to treat ESRD. Nevertheless, very few patients receive a timely transplant due to the complexity of the procedure, lack of donors, low viability of organs, and prevailing immunological incompatibilities (6–8). As a result, there is a definite need for alternatives to address this worldwide problem. Whole organ bioengineering has been proposed as one such alternative. Major advancements in this field have been developed using three-dimensional bioprinting, advanced stem cell technologies, and organ decellularization. Among these advancements, decellularization techniques currently hold the most promise for creating a bioartificial kidney (9, 10).

Decellularization is a better alternative to porous scaffold fabrication systems, additive manufacturing procedures, and hydrogels, as it provides the necessary physical and biochemical environments to facilitate cell and tissue growth. This technology has garnered much attention within the past decade, as acellular scaffolds have been generated using bovine, equine, leporine, murine, and porcine models. However, substantial compromises to the scaffold architecture, observed under physiological conditions, inhibit their long-term viability and clinical utility (11, 12). Thus, further research is needed to overcome problems related to vascularization and help realize the promise of a bioartificial kidney (13). Using this assertion, it is necessary to devise methods to better evaluate vascular patency in post-transplantation settings. Imaging modalities like X-ray/computed tomography, magnetic resonance imaging, ultrasonography and positron emission tomography have been applied to investigate the decellularized vascular architecture (14).

Recently, our group reported the damage caused to decellularized porcine kidney scaffold vascular architecture and functionality by subjecting them to blood perfusion at pathophysiological rates using fluoroscopic angiography. We noticed substantial alterations to normal arterial branching patterns and patency, parenchymal damage, and glomerular microarchitecture disruption (12). These techniques provide useful information on the scaffold structure and function, as well as insight on the deformation that can arise after transplantation. Yet, the low spatial resolution, artifacts, and unwanted morphological alterations have always proved to be challenging to detect subtle defects (15). Such challenges have paved the way for radiomic approaches that can extract features far beyond the capability of the human eye or brain to appreciate (16).

Computer-automated mathematical image analysis methods have emerged to give potentially wide applications in radiology. In recent years, many different techniques, and algorithms have been proposed and tested, often with limited success regarding their potential for integration in current diagnostic and research protocols. Future developments in information technology ensure that many of these techniques will significantly improve diagnostic and prognostic accuracies in X-ray computed tomography, fluoroscopy, and angiography (17–19). Computational methods that use statistical analyses in evaluating image texture are potentially instrumental in X-ray imaging since they may enable fast, objective, and accurate detection of subtle changes in tissue architecture that are occasionally hard to notice during the conventional assessment. One such method is based on the gray level co-occurrence matrix Topalovic et al. algorithm, which has attracted much attention in computational medicine. The technique uses second-order statistics to determine indicators that reflect image features such as textural homogeneity, uniformity, and level of disorder. Previously, some of these indicators, such as angular second moment and inverse difference moment, have proven to be sensitive in assessing data obtained as the result of various X-ray digital image transformations (18, 20, 21).

In angiography, GLCM was successfully used as an addition to volumetric and radiomic metrics and image reconstruction of coronary lesions (22). Also, some authors have previously demonstrated the potential of this method to evaluate endoleaks in aneurysmatic thrombus CT images of abdominal aorta (23). Endovascular aortic aneurysm repair evolution might also be indirectly assessed with the help of GLCM and other textural algorithms (24). Finally, in some experimental animal models, this form of textural analysis may be used to research pulmonary parenchymatous changes associated with pulmonary thromboembolism (25). To the best of our knowledge, no such applications of GLCM have been used in evaluating kidney vascular architecture.

The aim of our work was to apply a gray level co-occurrence matrix GLCM computational algorithm to collectively assess vascular architecture and parenchymal damage generated from hypoperfusion in decellularized porcine kidneys using fluoroscopic angiography. We present evidence that GLCM may be highly applicable in the evaluation of normal and pathological kidney angiograms indicating its potential for inclusion in contemporary research practices in this area of radiology. Also, this is the first study to quantify textural changes in vascular

architecture in decellularized kidney scaffolds, serving as the useful basis for future research on this organ model. Overall, this approach is the initial step toward developing an automated network that can detect changes in the decellularized vasculature.

MATERIALS AND METHODS

Experimental Animals

Adult Yorkshire pigs were euthanized, and whole kidneys were harvested under the guidelines provided by the Institutional Animal Care and Use Committee (IACUC) at the School of Medicine, Wake Forest University. All experimental protocols followed the ethical guidelines and regulations approved by Wake Forest University and the Animal Research Oversight Committee (AROC) at Khalifa University of Science and Technology, Protocol # A20-001. Moreover, all methods were performed in accordance with the Animal Research: Reporting of *In Vivo* Experiments (ARRIVE) guidelines.

Porcine Kidney Perfusion Decellularization and Sterilization

Whole porcine kidneys were extracted with intact renal arteries, veins, and ureters. The kidneys were then decellularized and sterilized using previously established protocols (11, 12, 26). Briefly, the arteries were cannulated using PE-50 polyethylene catheter tubing (Clay Adams-Becton Dickson, Parsippany, NJ, USA) and a 14-guage cannula and then secured with a 4/0 silk suture (**Figure 1**). Kidneys were flushed with 0.5–1 ml of heparinized PBS and then attached to a peristaltic pump (Cole-Palmer, Vernon Hills, IL, USA). Triton X-100, SDS, and phosphate-buffered saline (PBS) were slowly infused into cannulated renal arteries at a constant rate of 5 ml/min. Initially, 1% Triton X-100 was perfused through the renal artery for 36 h followed by 0.5% SDS dissolved in PBS for another 36 h. Finally, to remove the residual traces of detergents and cellular components, PBS was perfused through the kidneys for 72 h. The decellularized scaffolds were then submerged in PBS and sterilized with 10.0 kGy gamma irradiation.

Blood Perfusion Studies

Blood perfusion studies were carried out as previously reported (12). Prior to perfusion, the bioreactor components, namely, suction pump heads (Ismatec, Cole-Palmer, Wertheim, Germany), standard pump tubing female and male luer x1/8" hose barb adapters, barbed fittings, reducing connectors, three-way stop cocks, and Kynar adapters (Cole-Palmer, Vernon Hills, IL, USA) were sterilized using a 60 Co Gamma Ray Irradiator. While the bioreactor tubing, chambers, and 2,000 ml round wide mouth media storage bottles with screw caps assemblies (Sigma-Aldrich, St. Louis, MO, USA) were autoclaved.

Once sterilized, the bioreactor systems were assembled within a biosafety cabinet as described earlier (12). Concisely, the chamber was assembled in a way that ensured the two outer blood flow lines were attached on either side of the suction pump head. This aided arterial outflow from the Ismatec MCP-Z Process or MCP-Z Standard programmable dispensing pump (Cole-Palmer, Vernon Hills, IL, USA) into the chamber's arterial line while the venous returns to the pump via the venous line. The scaffold was suspended in a reservoir of roughly 500 ml of heparinized pig whole blood in the bioreactor chamber (BioIVT, Westbury, NY, USA). The renal artery was attached to the arterial line inside the chamber. In comparison, the renal vein cannula remained detached to allow venous outflow from the scaffold into the reservoir. The venous line was freely suspended into the reservoir to support unreplenished and unfiltered blood recirculation through the dispensing pumps. The entire assembled bioreactor system was then placed in a cell culture incubator, and scaffolds were subjected to continuous hypoperfusion (at a rate of 200 ml/min) for 24 h.

The pumps were set to produce pulsatile blood perfusion with 1-second fluctuations, and the model was calibrated to ensure the rotational speeds (measured in RPM) produced the desired volume flow rate of 200 ml/min. This flow rate corresponded to a perfusion pressure of 25.46 mmHg. Perfusion pressures were recorded with a digital differential pressure manometer (Dwyer Instruments, Michigan City, IN, USA) by attaching the arterial line to the manometer. At the 24-h time point, perfusion was ceased, and the scaffolds were removed from the chambers and placed in 60 × 15 mm sterilized polystyrene Petri dishes (Sigma-Aldrich, St. Louis, MO, USA) for fluoroscopic angiography.

At the 24-h time point, perfusion was ceased, and the scaffolds were removed from the chambers and placed in 60 × 15 mm sterilized polystyrene Petri dishes (Sigma-Aldrich, St. Louis, MO, USA) for fluoroscopic angiography.

Fluoroscopic Angiography Analysis

Non-perfused ($n = 25$) and hypoperfused ($n = 25$) decellularized kidneys were first infused with 100 ml PBS via the renal artery. The contrast agent was infusion of Iothalamate meglumine contrast agent (60% Angio-Conray, Mallinckrodt Inc., St Louis, MO, USA). Once a sturdy flow of exiting contrast agent was achieved, the renal vein, renal artery, and ureter were occluded to prevent the contrast agent from leaking out of the organ. Angiograms were collected at ambient temperature in a sterilized suite with a Siemens C-arm Fluoroscope (Siemens AG, Munich, Germany). We measured the diameters of each major arterial branch of the renal vasculature (renal artery, segmental artery, lobar artery, interlobar artery, and arcuate artery) using ImageJ software [ImageJ 1.53 k (64-bit), US National Institutes of Health, Bethesda, MD, USA]. Specifically, three portions of each branch were randomly selected to estimate the mean diameter. Moreover, we tracked changes in the branching patterns that occurred with hypoperfusion by using the following criteria: 1° = only the renal artery was left intact; 2° = only the renal and segmental arteries were left intact; 3° = only the renal, segmental, and lobar arteries were left intact; 4° = only the renal, segmental, lobar, interlobar arteries were left intact; and 5° = all five vascular branches were left intact.

GLCM Analysis

We performed GLCM analysis of selected regions of interest in angiograms using Mazda computational platform. This software was created by Michal Strzelecki and Piotr Szczypinski of the Institute of Electronics, Technical University of Lodz (27–29),

Poland as a part of COST B21 European project "Physiological modeling of MR Image formation," and COST B11 AQ6 European project "Quantitative Analysis of Magnetic Resonance Image Texture" (1998–2002). The software, originally made using C++ and Delphi© programming languages can accurately calculate GLCM features on multiple regions of interest (ROIs) of high-resolution BMP images making it an ideal candidate for textural analysis of angiograms.

In our angiograms in 8-bit BMP format (bit depth equaled 24), we formed ROIs covering kidney medulla and the main elements of the vascular network, with the area of ∼80,000 resolution units (width of 200 and height of 400 resolution units) as shown in **Figure 2B**. For each ROI, five major GLCM features were calculated: angular second moment, inverse difference moment, GLCLM contrast, GLCM Correlation and Sum variance of the co-occurrence matrix. GLCM method assigns values to resolution units depending on their gray intensity, after which a series of complex second-order statistical calculations are performed on resolution unit pairs considering their distance and orientation. Values of individual GLCM features depend on the distribution patterns of the gray intensity pairs and the numerical organization of the resulting co-occurrence matrix.

In GLCM analysis, angular second moment (ASM) represents the level of textural uniformity in two-dimensional signal. It can be calculated as:

$$\mathrm{ASM} = \sum_{\mathrm{i}} \sum_{\mathrm{j}} \left\{ \mathrm{p}\left(\mathrm{i},\ \mathrm{j}\right) \right\}^2$$

In this formula, p (i, j) is the (i, j) th entry of the gray-level co-occurrence matrix, after the normalization. In this work, angular second moment was in essence a tool for quantification of textural orderliness of the angiogram ROIs.

A relatively similar feature to angular second moment that can also be calculated during GLCM analysis is inverse difference moment. Inverse difference moment Maidman et al. (30) is often used to quantify the level of textural smoothness, sometimes also referred to as "homogeneity." It can be calculated as:

$$IDM \ = \sum_{i} \sum_{j} \frac{1}{1 + \left(i - j\right)^2} \, p(i,j)$$

Some textural features take into account the mean (μ) and the standard deviation (σ) of normalized GLCM rows (i.e., x or y). Such is the GLCM Correlation parameter which is determined as:

$$\mathrm{COR} = \frac{\sum_{\mathrm{i}} \sum_{\mathrm{j}} \left(\mathrm{ij}\right) \mathrm{p}\left(\mathrm{i},\ \mathrm{j}\right) - \ \mu_{\mathrm{x}} \mu_{\mathrm{y}}}{\sigma_{\mathrm{x}} \sigma_{\mathrm{y}}}$$

Textural sum variance feature is also a useful measure that can indirectly measure the level of dispersion around the mean of the matrix:

$$\mathrm{SVAR} = \sum \left[\mathrm{i} - \sum \mathrm{ip}_{\mathrm{x-y}}(\mathrm{i}) \right]^2$$

Finally, in our study, we also quantified the textural contrast feature as:

$$\mathrm{CON} = \sum_{\mathrm{i}} \sum_{\mathrm{j}} \left(\mathrm{i} - \mathrm{j}\right)^{\mathrm{k}} \mathrm{P_d}[\mathrm{i},\mathrm{j}]^{\mathrm{n}}$$

Textual contrast was used to quantify the difference between the neighboring resolution units considering their respective gray intensities.

All GLCM parameters were calculated for 4 specific pixel directions [(d,0), (0,d), (d,d), (0,-d)] at 4 different inter-pixel distances (d = 1–4). For details on GLCM algorithm and the calculation of features, the reader is referred to previous works that deal on the application of this method in medical and other sciences (31–33).

Discrete Wavelet Transform Features

Discrete wavelet transform (DWT) analysis of angiogram ROIs was performed as an addition to calculation of GLCM features. The DWT algorithm in Mazda software includes linear transformation of data vectors to numerical vectors taking into account their lengths (in case of data vectors, the length of an integer power of two). The analysis is performed separately on rows and columns of data with the application of high (H) and low-pass (L) filtering (34). The final output of DWT includes energies (En) of wavelet coefficients (d) in different subbands (for a respective subband location x and y) at different scales for a ROI resolution unit number (n):

$$E = \frac{\sum_{x,y \in ROI} \left(d_{x,y}^{subband}\right)^2}{n}$$

Previous research on application of DWT in microscopy has indicated that textural heterogeneity may influence the values of coefficient energies in subbands. In this work, we focused on the quantification of 3 such energies depending on the use of high (H) and low-pass (L) filtering: EnLH, EnHL and EnHH. Additional details on DWT algorithm can be found in previous publications (34, 35).

Statistical Analysis

Non-parametric statistics were applied to analyze the data using SPSS v.25.0 (IBM Corporation, Chicago, IL). We used the Kruskal–Wallis one-way analysis of variance Ucci et al. (36) with the *post hoc* Dunn's test to compare the arterial diameters of the renal artery (RA), segmental artery (SA), lobar artery (LA), interlobar artery (IA), and arcuate artery Periayah et al. in both non-perfused and hypoperfused scaffolds. The comparison between the diameters of non-perfused and hypoperfused scaffolds was done using the Mann-Whitney U-test. Difference in GLCM and DWT values between non-perfused and hypoperfused decellularized kidneys were also evaluated using Mann-Whitney U and Kruskal-Wallis tests. A two-tailed p-value < 0.05 was considered to be statistically significant.

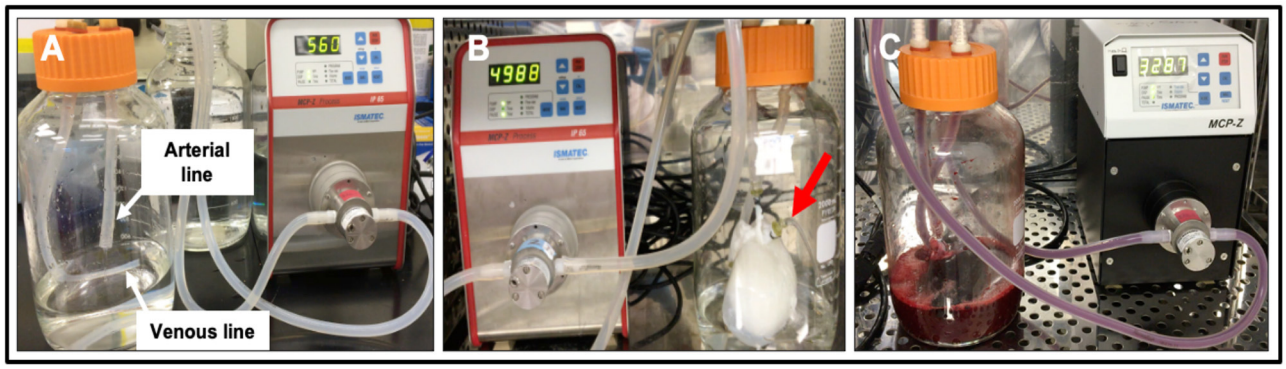

FIGURE 1 | Photographs of the bioreactor used to perfuse decellularized scaffolds with whole blood. **(A)** Image outlining the arterial line (which was then attached to the cannulated renal artery) and venous lines (which was left open to act as a venous reservoir to facilitate fluid recirculation) before the addition of the scaffold. **(B)** Image of an acellular kidney perfused with PBS illustrates how the scaffold recirculated fluid that emanated from its renal vein (red arrow) and open-ended venous line. **(C)** Image of a scaffold being perfused with whole pig blood.

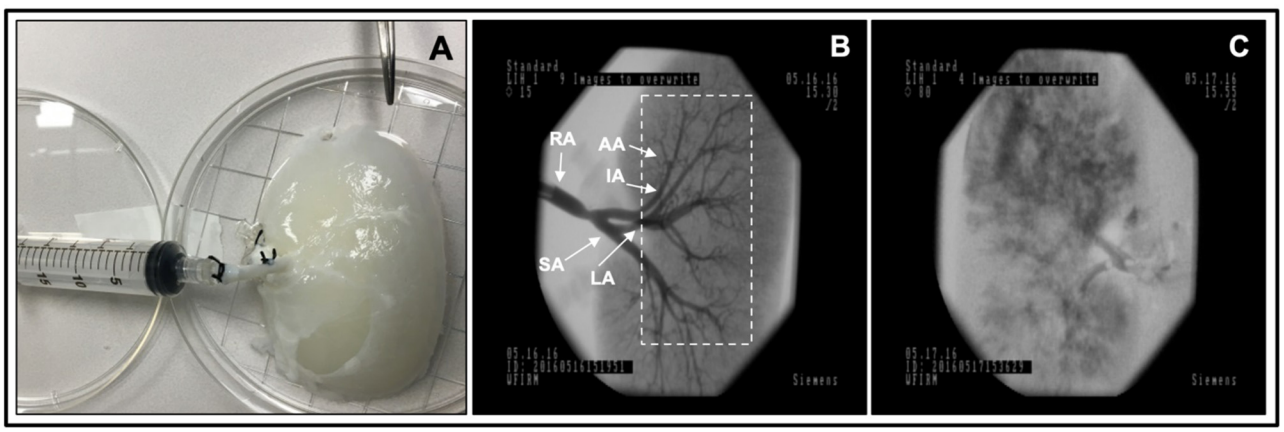

FIGURE 2 | Fluoroscopic angiography. **(A)** Photograph of a decellularized scaffold that was set to be infused with contrast agent. **(B)** An angiogram of the scaffold before it was perfused with blood displaying the decellularized vascular network and region of interest Davidovic et al., dashed rectangular region, covering kidney medulla and the main elements of this network. **(C)** An angiogram of the scaffold after 24 h of hypoperfusion (arterial infusion rate 20 ml/min). The major arterial branches of the renal vasculature are defined as follows, RA, renal artery; SA, segmental artery; LA, lobar artery; IA, interlobar artery; and AA, arcuate artery.

RESULTS

Scaffold Perfusion Analyzed Using Fluoroscopic Angiography and Venous Outflow

Fluoroscopic angiography showed that the vascular network was well-preserved post decellularization in non-perfused kidneys (**Figure 2B**). Angiograms taken from decellularized kidneys post-perfusion with unreplenished and unfiltered blood for 24 h revealed alterations in the decellularized vascular architecture and parenchyma (**Figure 2C**). Substantial levels of contrast agent extravasation were also observed throughout the cortical and medulla regions highlighting deleterious modifications to the integrity of decellularized renal parenchyma. Moreover, the hypoperfused acellular kidneys were unable to perfuse blood throughout their vascular networks and showed notable signs of thrombosis and cessation of venous outflow.

Furthermore, we observed considerable reductions in the diameter of each vascular segment (**Figure 3**), apart from the arcuate arterial track, within hypoperfused scaffolds. Angiographic analyses also revealed substantial disruptions to the branching patterns observed within these hypoperfused kidneys. The typical branching pattern (5°) was maintained in non-perfused kidneys, whereas hypoperfused kidneys displayed patterns that ranged from 5° to 1° (**Figure 4**). Specifically, the standard arterial branching patterns were noticeably disrupted by the end of perfusion, making it difficult to detect and differentiate the various branches of the arterial tree.

Kruskal–Wallis one-way analysis of variance Ucci et al. identified differences in the mean diameters of arterial branches, namely, renal artery (RA), segmental artery (SA), lobar artery (LA), interlobar artery (IA), and arcuate artery Periayah et al. in both non-perfused ($p < 0.001$) and hypoperfused ($p < 0.001$) scaffolds, individually. The *post hoc* Dunn's test applied to the

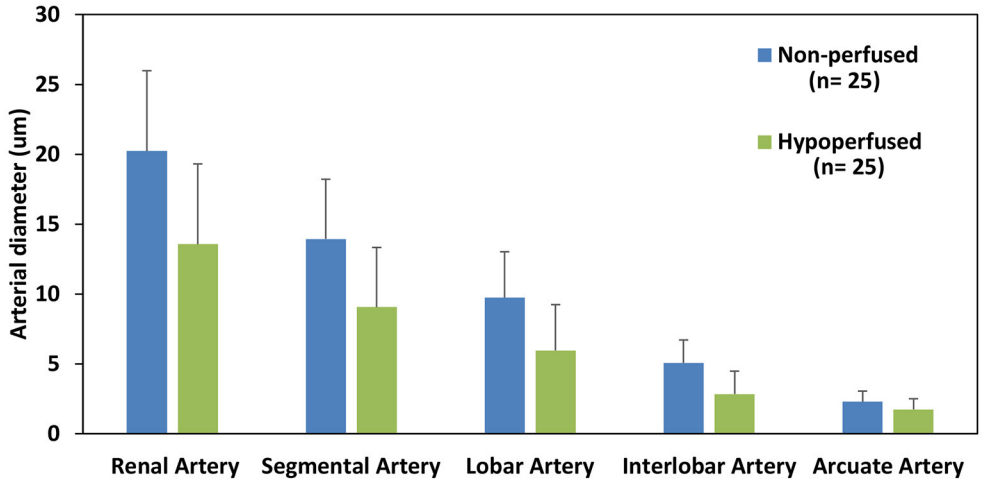

FIGURE 3 | Estimated diameters of each major arterial branch of the renal vasculature. A comparison of the diameters of the major arterial branch of the renal vasculature in non-perfused and hypoperfused decellularized kidneys.

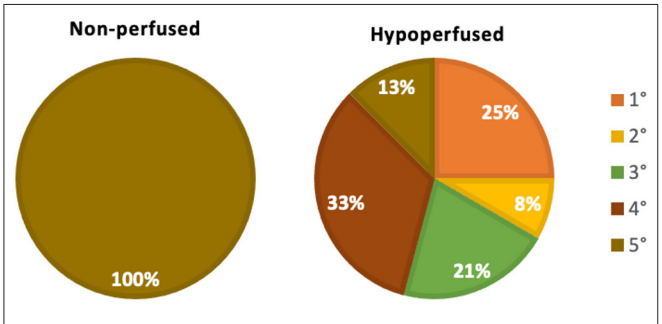

FIGURE 4 | Renal arterial branching patterns. A comparison of changes to the innate (non-perfused) branching patterns that occurred with hypoperfusion using the following criteria: 1°, only the renal artery was left intact; 2°, only the renal and segmental arteries were left intact; 3°, only the renal, segmental, and lobar arteries were left intact; 4°, only the renal, segmental, lobar, interlobar arteries were left intact; and 5°, all five vascular branches were left intact.

non-perfused decellularized data showed significant differences ($p < 0.05$) among the mean diameters of almost all pairs of branches except for SA-RA ($p = 0.63$) and AA-IA ($p = 0.13$). For the hypoperfused decellularized samples, the *post hoc* Dunn's pairwise test also revealed significant differences in the mean diameters for almost all the major arterial branches except for AA-IA ($p = 0.5$), IA-LA ($p = 0.065$), and LA-SA ($p = 0.05$).

Moreover, the Mann-Whitney *U*-test was used to compare the diameters of the various arterial branches of non-perfused and hypoperfused scaffolds. There were significant decreases ($p < 0.05$) in the diameter of the arterial branches in hypoperfused scaffolds as compared to non-perfused scaffolds, except for reductions observed between arcuate arteries of the two groups ($p = 0.342$).

GLCM Analysis

For the inter-pixel distance of 1 and direction (1,0), the average angular second moment of the ROIs was 0.053 ± 0.022 for decellularized kidneys before perfusion (pre-perfusion) and 0.030 ± 0.018 for after perfusion (post post-perfusion) angiograms (**Figure 5A**). Statistically highly significant difference was observed ($p < 0.01$). This result implied a substantial reduction of textural uniformity in post-perfusion vascular architecture. Similar reduction was observed with the mean values of inverse difference moment (0.781 ± 0.046 in post-perfusion compared to 0.805 ± 0.026 in controls) (**Figure 5B**). The difference was highly significant ($p < 0.05$) which implied that the textural homogeneity of ROIs decreased.

On the other hand, there was a substantial rise in the average values of GLCM Contrast (**Figure 5C**), GLCM Correlation feature (**Figure 5D**) and Sum variance (**Figure 5E**). The largest increase was observed in Sum variance (127.99 ± 91.53 in post-perfusion vs. 52.48 ± 43.36 in pre-perfusion angiograms, $p < 0.01$) followed by the Correlation (0.989 ± 0.007 vs. 0.978 ± 0.008, $p < 0.01$), and lastly GLCM Contrast (0.51 ± 0.15 vs. 0.44 ± 0.09, $p < 0.05$). This is in line with the results of the values of angular second moment and inverse difference moment, and imply the rise of the overall textural heterogeneity of vascular architecture. Average values and standard deviations (SD) of GLCM parameters before and after perfusion (per) for specific interpixel distances (d) and directions (dir) are presented in **Table 1**.

We also observed some changes in wavelet coefficient energies of the ROIs, however these changes were not as drastic as the ones exhibited by GLCM features. The average value of EnLH rose from 1.17 ± 0.45 in controls to 1.54 ± 0.70 in post-perfusion angiograms ($p < 0.05$). Similar rise and level of significance was observed for EnHL means (1.07 ± 0.36 compared to 1.37 ± 0.53 in controls, $p < 0.05$). Regarding EnHH, the average value in

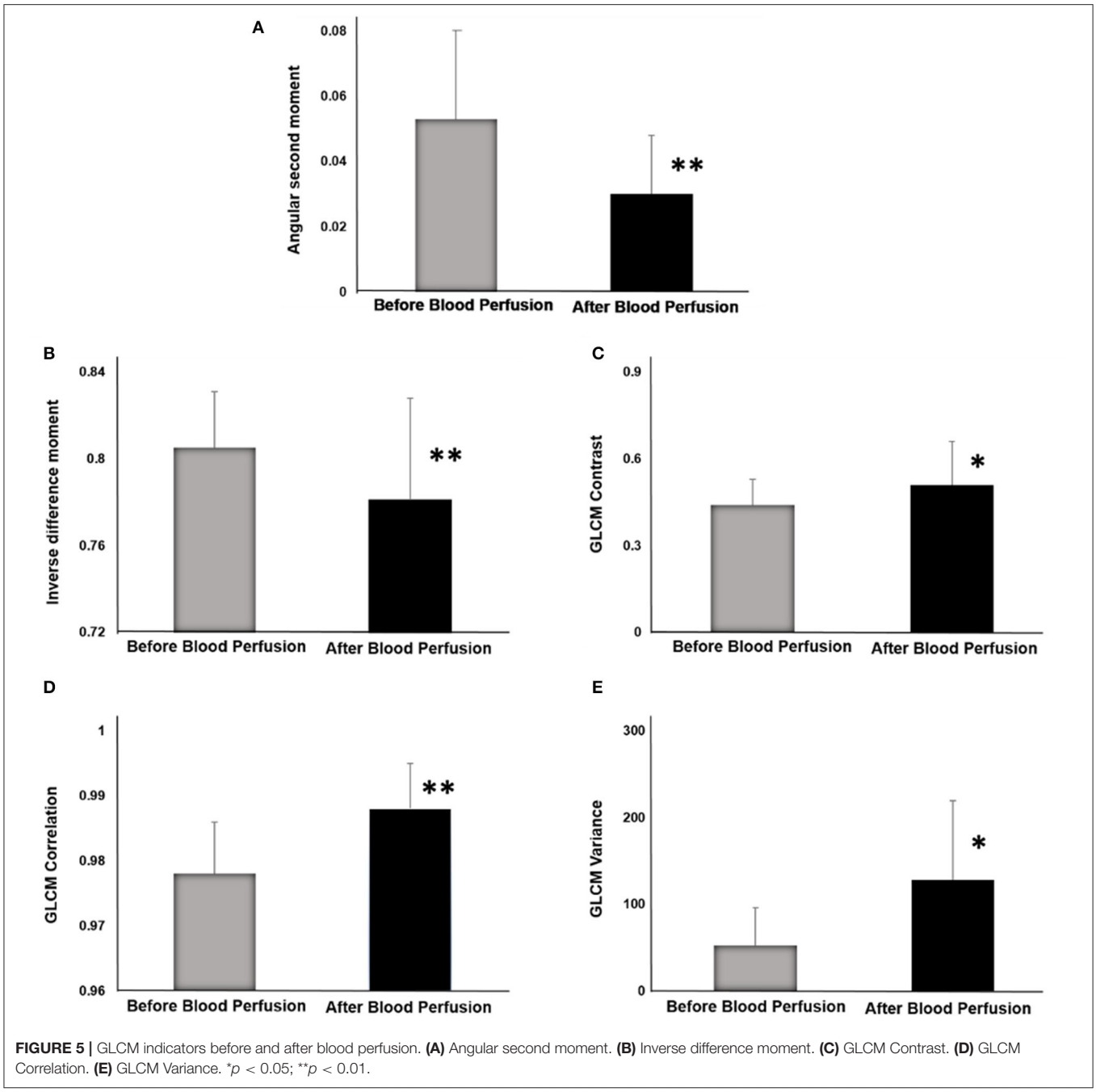

FIGURE 5 | GLCM indicators before and after blood perfusion. **(A)** Angular second moment. **(B)** Inverse difference moment. **(C)** GLCM Contrast. **(D)** GLCM Correlation. **(E)** GLCM Variance. *$p < 0.05$; **$p < 0.01$.

pre-perfusion angiograms was 0.08 ± 0.01 and in post-perfusion angiograms it rose to 0.09 ± 0.02 ($p > 0.05$).

Significant correlations were detected between GLCM and DWT parameters in both groups of angiograms. For example, statistically highly significant negative correlation ($p < 0.01$) existed between the DWT EnHL feature and the values of inverse difference moment. Similar statistically highly significant negative correlation ($p < 0.01$) was observed between EnHH feature and the values of angular second moment. These associations are expected, they are partly the result of the methodological similarities during the implementation of GLCM and DWT algorithms, and confirm the validity of the obtained dataset.

DISCUSSION

Time and again, emphasis has been given to the importance of maintaining the integrity of vascular networks in decellularized organs for transplantation. These vascular tracks support the homogenous recellularization process in complex organs like the kidney. It is vital to consider the infusion rate, volume, and cell

TABLE 1 | Average values and standard deviations (SD) of GLCM indicators before and after perfusion (per) for specific interpixel distances (d) and directions (dir).

d	dir	per	ASM	ASM SD	CON	CON SD	COR	COR SD	IDM	IDM SD	SVAR	SVAR SD
1	(1,0)	before	0.053	0.022	0.44	0.09	0.978	0.008	0.805	0.026	52.5	43.3
		after	0.030**	0.018	0.51*	0.15	0.99	0.007	0.781**	0.047	128.0**	91.5
	(0,1)	before	0.056	0.023	0.46	0.12	0.978	0.009	0.816	0.027	52.6	43.5
		after	0.031**	0.018	0.54*	0.18	0.988**	0.006	0.796*	0.044	128.4**	91.9
	(1,1)	before	0.043	0.018	0.71	0.21	0.965	0.013	0.742	0.032	52.1	43.1
		after	0.024**	0.016	0.85*	0.29	0.982**	0.010	0.714**	0.058	127.4**	91.2
	(1,-1)	before	0.043	0.018	0.72	0.20	0.965	0.013	0.741	0.033	52.1	43.1
		after	0.024**	0.016	0.87*	0.31	0.981**	0.010	0.712**	0.059	127.4**	91.2
2	(2,0)	before	0.036	0.016	1.05	0.36	0.950	0.017	0.680	0.042	51.6	42.8
		after	0.020**	0.014	1.33*	0.50	0.972**	0.014	0.641**	0.070	126.5**	90.6
	(0,2)	before	0.038	0.017	1.16	0.44	0.945	0.019	0.689	0.040	51.8	43.1
		after	0.020**	0.014	1.39	0.57	0.972**	0.013	0.654*	0.066	127.3**	91.4
	(2,2)	before	0.030	0.014	1.81	0.79	0.916	0.028	0.610	0.046	50.7	42.2
		after	0.016**	0.012	2.28*	0.96	0.954**	0.020	0.565**	0.077	125.1**	89.9
	(2,-2)	before	0.030	0.014	1.85	0.73	0.913	0.027	0.609	0.047	50.7	42.3
		after	0.016**	0.011	2.35	1.03	0.953**	0.021	0.562**	0.077	125.1**	89.9
3	(3,0)	before	0.031	0.015	1.77	0.78	0.919	0.024	0.611	0.054	50.7	42.2
		after	0.016**	0.012	2.35*	1.01	0.953**	0.021	0.557**	0.080	124.8**	89.6
	(0,3)	before	0.030	0.014	2.02	0.93	0.907	0.031	0.608	0.049	50.9	42.5
		after	0.016**	0.011	2.45	1.11	0.952**	0.020	0.562**	0.076	126.1**	90.8
	(3,3)	before	0.026	0.013	3.03	1.63	0.864	0.041	0.546	0.056	49.2	41.1
		after	0.013**	0.010	3.93*	1.82	0.923**	0.029**	0.485**	0.082	122.7**	88.4
	(3,-3)	before	0.025	0.013	3.08	1.45	0.860	0.041	0.544	0.057	49.2	41.3
		after	0.012**	0.009	4.06*	1.95	0.921**	0.031**	0.483**	0.083	122.5**	88.4
4	(4,0)	before	0.027	0.014	2.53	1.29	0.887	0.031	0.567	0.063	49.7	41.5
		after	0.013**	0.010	3.50*	1.62	0.932**	0.027**	0.501**	0.085	123.1**	88.5
	(0,4)	before	0.026	0.013	2.96	1.52	0.867	0.043	0.558	0.056	49.9	41.9
		after	0.013**	0.009	3.66	1.74	0.930**	0.027**	0.502**	0.080	124.7**	90.1
	(4,4)	before	0.023	0.012	4.22	2.54	0.814	0.054	0.509	0.063	47.8	39.9
		after	0.011**	0.008	5.66*	2.77	0.891**	0.038**	0.435**	0.084	120.1**	86.9
	(4,-4)	before	0.023	0.012	4.26	2.20	0.810	0.052	0.508	0.064	47.8	40.2
		after	0.011**	0.008	5.84*	2.94	0.888**	0.040**	0.433**	0.084	120.0**	86.9

*$p < 0.05$; **$p < 0.01$.

type to ensure that the repopulation process does not constrict vascular ducts. Another consideration is the effective removal of the detergents after decellularization. Ineffective removal would prolong the decellularization process and favor disruption of the ECM, and previous studies have shown that SDS and Triton X-100 can denature the triple-helical collagen structure (37, 38). Thus, it is crucial to understand the various conditions that lead to scaffold damage entirely. Such an improved understanding will help us develop enhanced scaffolds that may be able to withstand the recellularization process better and support the development of bioartificial organs.

To better understand these processes, we subjected decellularized scaffolds to hypoperfused infusion rates. Hypoperfusion substantially affected the vascular architecture of the decellularized kidney. For instance, platelet activation and coagulation usually do not occur within the intact vasculature. However, without an intact endothelium and a reduced perfusion rate, the whole blood would have been in direct contact with collagen for substantial periods. As a result, platelets would have been in direct contact with collagen fibers within the scaffold and enabled their adhesion and aggregation (39). This highly thrombogenic environment generated within the decellularized vasculature would have thus supported the development of vascular occlusions throughout the scaffold. Such occlusions would have increased blood viscosity, reduced flow rates, and facilitated the accumulation of viscous blood in the kidney over time, resulting in hemostasis and swelling. These events could explain the substantial disruptions to the scaffold parenchyma observed in the decellularized kidneys (12).

From our analyses, we observed significant decreases in the diameters of the major arterial branches in hypoperfused scaffolds compared to the non-perfused scaffolds. We then applied textural analysis algorithms based on gray level co-occurrence matrix and discrete wavelet transform to investigate

the pathologically changes in the vascular architecture of the decellularized kidneys subjected to conditions that mimic renal artery stenosis (12). This form of stenosis is a well-recognized disorder that compromises transplantation and has been shown to denature the acellular vascular tracks. Such deformation also leads to aberrant changes in the decellularized parenchyma. The images obtained using fluoroscopic angiography showed that significant differences in both GLCM and DWT features could be detected using this approach.

With respect to textural analysis, as reported in the previously published studies, we can assume that GLCM parameters are potentially useful indicators of discrete changes in tissue architecture (40). In tissue micrographs, this has been shown to be the case in both physiological and pathological conditions (41, 42).The reduction of angular second moment (textural uniformity) and inverse difference moment (textural homogeneity) might be related to parenchymal structural degradation and deterioration as suggested earlier (40). In general, previous research has shown that in parenchymatous organs, these GLCM parameters decrease as the level of entropy (degree of structural chaos and disorder) increases (43). As for the GLCM contrast and GLCM correlation, in micrographs, these parameters showed relatively good discriminatory power in differetiating between haelthy kidney medular tissue and the tissue following reperfusion injury (40). In our current research, since the analysis was done following the process of decellularization, we can speculate that the ASM and IDM reductions were associated with the changes in vascular network patterns, possibly due to the structural damage of blood vessels. Also, hypoperfusion-related clotting, as well as structural deterioration of extracellular and extravascular matrix might also have significantly contributed to the observed changes in GLCM parameters. Nevertheless, it should be noted that GLCM analysis is a relatively new method in both biology and radiology and additional research is needed to draw definite conclusions on the relationship between specific structural changes in kidney tissue and changes in GLCM parameters. Our findings imply that textural analysis, as a set of contemporary computer-based methods, has a great potential to be used as an addition to the conventional angiographic evaluation of the renal vascular network.

Perhaps the most important finding was the observed significant change of inverse difference moment of angiogram ROIs. This GLCM feature indicates textural homogeneity and is often used to quantify smoothness in the distribution of resolution units in grayscale images. Previous research articles in digital micrographs have shown the potential value of inverse difference moment in detecting structural alterations that are not visible to a professional pathologist (35, 44).

Along with angular second moment and GLCM contrast, this is probably also one of radiology's most frequently calculated textural features.

Generally, in the past, the most frequent application of textural computational algorithms in radiology was to assess images obtained through nuclear magnetic resonance, computerized tomography, and other tomography techniques. Probably the most common approach is to compare the images of tissue lesions or other pathological changes in tissue architecture with controls. After that, one of the possibilities is to determine the sensitivity of individual GLCM features for lesion detection or to test the discriminatory power of the method regarding the separation of post- and pre- perfusion radiographs or parts of a radiograph (20). Another strategy would be to use GLCM features as prediction tools for disease prognosis (45), or to test their ability to determine boundaries of the lesion in the same radiograph. Finally, it may be possible to develop a scoring system that considers GLCM (and other) indicators of texture and test its sensitivity and specificity (46).

In angiography, the GLCM method is much less frequently applied, and so far, only a handful of studies have been published on this topic. These mainly include the use of GLCM features for assessment of low attenuation non-calcified (LANCP), non-calcified and calcified coronary plaques (18, 22), or for computer-aided diagnosis-specific cases of endovascular aortic aneurysms (24). In optical coherence tomography angiography, as demonstrated earlier, some GLCM indicators can also be applied to quantify choriocapillaris in healthy and diseased eyes (47). To the best of our knowledge, there hasn't been a similar study trying to apply texture analysis for the assessment of vascular changes in kidney tissue. Therefore, our research is probably the first to demonstrate the applicability of these computational algorithms (GLCM and DWT techniques on an experimental model of decellularized kidney) in this rapidly developing area of radiology and also provides a potentially useful foundation for future research.

In the future, probably the most important application of both GLCM and DWT analyses will be to provide inputs for various artificial intelligence-based methods for image analysis in radiology. This application would include training and testing different machine learning models, some of which have already been suggested as suitable for GLCM data (44). The examples would be conventional decision tree algorithms such as CHAID (Chi-square Automatic Interaction Detector) or CART (classification and regression tree) or some more modern approaches such as random forests. Support vector machines, naive Bayes, linear discriminant analysis, and similarity learning are potential alternative strategies. The most considerable potential regarding the use of GLCM and DWT raw data may lie in designing various types of neural networks. This process includes simple concepts such as a multilayer perceptron or more complex ones such as recurrent and convolutional neural networks. Convolutional neural networks are a fascinating approach since they are already widely used in medicine and other disciplines of computer vision. Despite the promises that such a computer algorithm makes, many loopholes still need to be addressed that will require extensive quality assurance of these methods, including testing inter- and intra-observer reliability, for their effective application in the clinics.

As mentioned, the limitations of our study include the relatively small sample, which is not sufficient for the implementation of the more complex approaches such as machine learning or the creation of other artificial intelligence-based models. Also, another important aspect to consider is that the results of GLCM and DWT generally depend on various

factors associated with image creation. Brightness, contrast, hue, saturation, and many other image parameters which can vary in angiograms can substantially impact GLCM features such as angular second moment or inversed difference moment.

Another important limitation is that the fact that the results of GLCM and DWT analyses in certain circumstances may greatly vary and depend on the positioning of the region of interest within the image. In our study we positioned the ROI to always cover the same area of the kidney, with the left boundary in the proximate vicinity to the area where the branches of the renal artery appear to enter the hilum. Although in our study we successfully applied this approach in all angiograms, in the future it may not be always feasible due to radiological and other factors. Future studies will have to additionally validate this strategy and perform a comprehensive quality assurance of both GLCM and DWT techniques and their applications in renal angiography.

Finally, to our knowledge, the results of the textural analysis are not always the same across different computational platforms. Such variations can arise from the fact that existing software algorithms may use images in different formats (8-bit, 16-bit, BMP, JPG, etc.) or because of many other technical issues and solutions the developers tried to include into the programming code. All of these issues may in the future hinder the potential of successful integration of textural analysis methods in contemporary diagnostic protocols. For this to happen, extensive quality assurance of the processes, including testing inter- and intra-observer reliability, will have to be performed.

CONCLUSION

Our results designate that certain discrete changes in vascular architecture and renal parenchyma in the decellularized kidney can be successfully detected using well-known contemporary computational algorithms for texture analysis, thereby overcoming the limitations of conventional imaging modalities. We report statistically significant changes in GLCM and wavelet features, including reducing angular second moment and inverse difference moment, indicating a substantial rise in angiogram textural heterogeneity in pathological conditions. Our findings suggest that the GLCM method may be used as an addition to the conventional fluoroscopic angiography analysis of micro-/macrovascular integrity for a more accurate diagnosis. To the best of our knowledge, this is the first study to use GLCM and DWT based approach in decellularized kidney experimental model, augmenting appropriate evaluation of the decellularized kidneys vasculature, to accomplish lasting vascular patency post-transplantation, thereby giving hope to impede a looming epidemic of morbidity or mortality due to kidney diseases. This approach is the first step toward developing an automated network that can detect debilitating changes in the decellularized vasculature and supporting tissue network.

DATA AVAILABILITY STATEMENT

The raw data supporting the conclusions of this article will be made available by the authors, without undue reservation.

ETHICS STATEMENT

The animal study was reviewed and approved by Institutional Animal Care and Use Committee (IACUC) at the School of Medicine, Wake Forest University; Animal Research Oversight Committee (AROC) at Khalifa University of Science and Technology.

AUTHOR CONTRIBUTIONS

PC and IP conceived and designed project. PC performed all experiments, analyzed the associated data, and interpreted results of experiments. IP performed all computation analyses. IP, AS, GP, and PC drafted, edited, and approved final version of manuscript. All authors contributed to the article and approved the submitted version.

FUNDING

This study was supported in part by an Institutional Research and Academic Career Development Award (IRACDA), Grant No. NIH/NIGMS K12-GM102773, and funds from Khalifa University of Science and Technology, Grant Nos. FSU-2020-25 and RC2-2018-022 (HEIC).

ACKNOWLEDGMENTS

The author would like to acknowledge Dr. Zambon for help with decellularization. The authors would also like to thank Ms. Anousha Khan, Ms. Xinyu Wang, and Nnamdi Ugwuoke for reviewing the manuscript.

REFERENCES

1. Arikan H, Ozturk S, Tokgoz B, Dursun B, Seyahi N, Trabulus S, et al. Characteristics and outcomes of acute kidney injury in hospitalized COVID-19 patients: a multicenter study by the Turkish society of nephrology. *PLoS ONE.* (2021) 16:e0256023. doi: 10.1371/journal.pone.0256023
2. Kari JA, Shalaby MA, Albanna AS, Alahmadi TS, Alherbish A, Alhasan KA. Acute kidney injury in children with COVID-19: a retrospective study. *BMC Nephrol.* (2021) 22:202. doi: 10.1186/s12882-021-02389-9
3. Hsu RK, Hsu CY. The role of acute kidney injury in chronic kidney disease. *Semin Nephrol.* (2016) 36:283–92. doi: 10.1016/j.semnephrol.2016.05.005
4. Kolb AL, Corridon PR, Zhang S, Xu W, Witzmann FA, Collett JA, et al. Exogenous gene transmission of isocitrate dehydrogenase 2 mimics ischemic preconditioning protection. *J Am Soc Nephrol.* (2018) 29:1154–64. doi: 10.1681/ASN.2017060675
5. Corridon PR, Karam SH, Khraibi AA, Khan AA, Alhashmi MA. Intravital imaging of real-time endogenous actin dysregulation in proximal and distal tubules at the onset of severe ischemia-reperfusion injury. *Sci Rep.* (2021) 11:8280. doi: 10.1038/s41598-021-87807-6
6. Saidi RF, Hejazii Kenari SK. Challenges of organ shortage for transplantation: solutions and opportunities. *Int J Organ Transplant Med.* (2014) 5:87–96.
7. Job K, Antony A. *Organ Donation and Transplantation: "Life after Death"* London: IntechOpen (2018).

8. Wu H, Lau ESH, Yang A, Szeto CC, Ma RCW, Kong APS, et al. Trends in kidney failure and kidney replacement therapy in people with diabetes in Hong Kong, 2002-2015: a retrospective cohort study. *Lancet Reg Health West Pac.* (2021) 11:100165. doi: 10.1016/j.lanwpc.2021.100165
9. Corridon PR, Ko IK, Yoo JJ, Atala A. Bioartificial kidneys. *Curr Stem Cell Rep.* (2017) 3:68–76. doi: 10.1007/s40778-017-0079-3
10. Sohn S, Buskirk M, Buckenmeyer M, Londono R, Faulk D. Whole organ engineering: approaches, challenges, future directions. *Appl Sci.* (2020) 10:4277. doi: 10.3390/app10124277
11. Zambon JP, Ko IK, Abolbashari M, Huling J, Clouse C, Kim TH, et al. Comparative analysis of two porcine kidney decellularization methods for maintenance of functional vascular architectures. *Acta Biomater.* (2018) 75:226–34. doi: 10.1016/j.actbio.2018.06.004
12. Corridon PR. In vitro investigation of the impact of pulsatile blood flow on the vascular architecture of decellularized porcine kidneys. *Sci Rep.* (2021) 11:16965. doi: 10.1038/s41598-021-95924-5
13. Feng H, Xu Y, Luo S, Dang H, Liu K, Sun WQ. Evaluation and preservation of vascular architectures in decellularized whole rat kidneys. *Cryobiology.* (2020) 95:72–79. doi: 10.1016/j.cryobiol.2020.06.003
14. Huling JC, Atala A, Yoo JJ. Chapter 42 - decellularized whole organ scaffolds for the regeneration of kidneys. In: Little MH, editors. *Kidney Development, Disease, Repair and Regeneration.* San Diego: Academic Press (2016). p. 569–78.
15. Mostaco-Guidolin LB, Ko AC, Wang F, Xiang B, Hewko M, Tian G, et al. Collagen morphology and texture analysis: from statistics to classification. *Sci Rep.* (2013) 3:2190. doi: 10.1038/srep02190
16. Neri E, de Souza N, Brady A, Bayarri AA, Becker CD, Coppola F, et al. What the radiologist should know about artificial intelligence – an ESR white paper. *Insights Imag.* (2019) 10:44. doi: 10.1186/s13244-019-0738-2
17. Cao W, Pomeroy MJ, Gao Y, Barish MA, Abbasi AF, Pickhardt PJ, et al. Multi-scale characterizations of colon polyps via computed tomographic colonography. *Vis Comput Ind Biomed Art.* (2019) 2:25. doi: 10.1186/s42492-019-0032-7
18. Kolossvary M, Javorszky N, Karady J, Vecsey-Nagy M, David TZ, Simon J, et al. Effect of vessel wall segmentation on volumetric and radiomic parameters of coronary plaques with adverse characteristics. *J Cardiovasc Comput Tomogr.* (2021) 15:137–45. doi: 10.1016/j.jcct.2020.08.001
19. Gudigar A, Raghavendra U, Hegde A, Menon GR, Molinari F, Ciaccio EJ, et al. Automated detection and screening of traumatic brain injury (TBI) using computed tomography images: a comprehensive review and future perspectives. *Int J Environ Res Public Health.* (2021) 18:6499. doi: 10.3390/ijerph18126499
20. Chen H, Li W, Zhu Y. Improved window adaptive gray level co-occurrence matrix for extraction and analysis of texture characteristics of pulmonary nodules. *Comput Methods Programs Biomed.* (2021) 208:106263. doi: 10.1016/j.cmpb.2021.106263
21. Shankar K, Perumal E, Tiwari P, Shorfuzzaman M, Gupta D. Deep learning and evolutionary intelligence with fusion-based feature extraction for detection of COVID-19 from chest X-ray images. *Multimed Syst.* (2021) doi: 10.1007/s00530-021-00800-x. [Epub ahead of print].
22. Kolossvary M, Szilveszter B, Karady J, Drobni ZD, Merkely B, Maurovich-Horvat P. Effect of image reconstruction algorithms on volumetric and radiomic parameters of coronary plaques. *J Cardiovasc Comput Tomogr.* (2019) 13:325–30. doi: 10.1016/j.jcct.2018.11.004
23. Garcia G, Maiora J, Tapia A, De Blas M. Evaluation of texture for classification of abdominal aortic aneurysm after endovascular repair. *J Digit Imag.* (2012) 25:369–76. doi: 10.1007/s10278-011-9417-7
24. Garcia G, Tapia A, De Blas M. Computer-supported diagnosis for endotension cases in endovascular aortic aneurysm repair evolution. *Comput Methods Programs Biomed.* (2014) 115:11–9. doi: 10.1016/j.cmpb.2014.03.004
25. Marschner CB, Kokla M, Amigo JM, Rozanski EA, Wiinberg B, McEvoy FJ. Texture analysis of pulmonary parenchymateous changes related to pulmonary thromboembolism in dogs - a novel approach using quantitative methods. *BMC Vet Res.* (2017) 13:219. doi: 10.1186/s12917-017-1117-1
26. Sullivan DC, Mirmalek-Sani SH, Deegan DB, Baptista PM, Aboushwareb T, Atala A, et al. Decellularization methods of porcine kidneys for whole organ engineering using a high-throughput system. *Biomaterials.* (2012) 33:7756–64. doi: 10.1016/j.biomaterials.2012.07.023
27. Szczypinski PM, Strzelecki M, Materka A. Mazda - a software for texture analysis. In: *Proceedings of the 2007 International Symposium on Information Technology Convergence (ISITC 2007)* (IEEE Computer Society) (2007). p. 245–9.
28. Szczypinski PM, Strzelecki M, Materka A, Klepaczko A. MaZda–a software package for image texture analysis. *Comput Methods Programs Biomed.* (2009) 94:66–76. doi: 10.1016/j.cmpb.2008.08.005
29. Strzelecki M, Szczypinski P, Materka A, Klepaczko A. A software tool for automatic classification and segmentation of 2D/3D medical images. *Nucl Instrum Methods Phys Res Sect A.* (2013) 702:137–40. doi: 10.1016/j.nima.2012.09.006
30. Maidman SD, Eberly LM, Greenbaum AB, Guyton RA, Wells BJ. Postinfarction ventricular septal rupture and hemopericardium with tamponade physiology. *CASE.* (2021) 5:48–50. doi: 10.1016/j.case.2020.10.010
31. Haralick RM, Shanmugam K, Dinstein I. Textural features for image classification. *IEEE Transact Syst Man.* (1973) 610–21. doi: 10.1109/TSMC.1973.4309314
32. Santos TA, Maistro CE, Silva CB, Oliveira MS, Franca Jr MC, et al. MRI texture analysis reveals bulbar abnormalities in friedreich ataxia. *AJNR Am J Neuroradiol.* (2015) 36:2214–8. doi: 10.3174/ajnr.A4455
33. Topalovic N, Mazic S, Nesic D, Vukovic O, Cumic J, Laketic D, et al. Association between chromatin structural organization of peripheral blood neutrophils and self-perceived mental stress: gray-level co-occurrence matrix analysis. *Microsc Microanal.* (2021) doi: 10.1017/S143192762101240X. [Epub ahead of print].
34. Kociolek M, Materka A, Strzelecki M, Szczypiński P. Discrete wavelet transform-derived features for digital image texture analysis. (2001).
35. Paunovic J, Vucevic D, Radosavljevic T, Vukomanovic Djurdjevic B, Stankovic S, Pantic I. Effects of iron oxide nanoparticles on structural organization of hepatocyte chromatin: gray level co-occurrence matrix analysis. *Microsc Microanal.* (2021) 27:889–96. doi: 10.1017/S1431927621000532
36. Ucci G, Danova M, Riccardi A, Brugnatelli S, Girino M, Corridoni S, et al. Abnormalities of T cell subsets in a patient with cyclic neutropenia. *Acta Haematol.* (1987) 77:177–9.doi: 10.1159/000205986
37. Hwang J, San BH, Turner NJ, White LJ, Faulk DM, Badylak SF, et al. Molecular assessment of collagen denaturation in decellularized tissues using a collagen hybridizing peptide. *Acta Biomaterialia.* (2017) 53:268–78. doi: 10.1016/j.actbio.2017.01.079
38. Schmitt A, Csiki R, Tron A, Saldamli B, Tubel J, Florian K, et al. Optimized protocol for whole organ decellularization. *Eur J Med Res.* (2017) 22:31. doi: 10.1186/s40001-017-0272-y
39. Periayah MH, Halim AS, Mat Saad AZ. Mechanism action of platelets and crucial blood coagulation pathways in hemostasis. *Int J Hematol Oncol Stem Cell Res.* (2017) 11:319–27.
40. Pantic I, Nesic Z, Paunovic Pantic J, Radojevic-Skodric S, Cetkovic M, Basta Jovanovic, G. Fractal analysis and gray level co-occurrence matrix method for evaluation of reperfusion injury in kidney medulla. *J Theor Biol.* (2016) 397:61–7. doi: 10.1016/j.jtbi.2016.02.038
41. Pantic I, Dacic S, Brkic P, Lavrnja I, Jovanovic T, Pantic S, et al. Discriminatory ability of fractal and grey level co-occurrence matrix methods in structural analysis of hippocampus layers. *J Theor Biol.* (2015) 370:151–6. doi: 10.1016/j.jtbi.2015.01.035
42. Zaletel I, Milutinovi,ć K, Bajčeti,ć M, Nowakowski RS. Differentiation of amyloid plaques between Alzheimer's disease and non-alzheimer's disease individuals based on gray-level co-occurrence matrix texture analysis. *Microscopy Microanal.* (2021) 27:1146–53. doi: 10.1017/S1431927621012095
43. Pantic I, Pantic S. Germinal center texture entropy as possible indicator of humoral immune response: immunophysiology viewpoint. *Mol Imag Biol.* (2012) 14:534–40. doi: 10.1007/s11307-011-0531-1
44. Davidovic LM, Cumic J, Dugalic S, Vicentic S, Sevarac Z, Petroianu G, et al. Gray-level co-occurrence matrix analysis for the detection of discrete, ethanol-induced, structural changes in cell nuclei: an artificial intelligence approach. *Microsc Microanal.* (2022) 28:265–71. doi: 10.1017/s1431927621013878
45. Huang L, Feng B, Li Y, Liu Y, Chen Y, Chen Q, et al. Computed tomography-based radiomics nomogram: potential to predict local recurrence of gastric cancer after radical resection. *Front Oncol.* (2021) 11:638362. doi: 10.3389/fonc.2021.638362

46. Thuillier P, Bourhis D, Schick U, Alavi Z, Guezennec C, Robin P, et al. Diagnostic value of positron-emission tomography textural indices for malignancy of 18F-fluorodeoxyglucose-avid adrenal lesions. *Q J Nucl Med Mol Imag.* (2021) 65:79–87. doi: 10.23736/S1824-4785.19.03138-8
47. Khan HA, Shahzad MA, Iqbal F, Awan MA, Sharjeel M, Khan QA, et al. A novel method of quantifying the choriocapillaris in normal and post-inflammatory eyes. *Ocul Immunol Inflamm*. (2020) doi: 10.1080/09273948.2020.1800047. [Epub ahead of print].

Conflict of Interest: The authors declare that the research was conducted in the absence of any commercial or financial relationships that could be construed as a potential conflict of interest.

Publisher's Note: All claims expressed in this article are solely those of the authors and do not necessarily represent those of their affiliated organizations, or those of the publisher, the editors and the reviewers. Any product that may be evaluated in this article, or claim that may be made by its manufacturer, is not guaranteed or endorsed by the publisher.

frontiers in Cardiovascular Medicine

ORIGINAL RESEARCH
published: 09 March 2022
doi: 10.3389/fcvm.2022.830055

Left Atrial Function Post Radiofrequency and Cryoballoon Ablation Assessed by Volume-Pressure Loops

*Antonios Karanasos[1], Konstantinos Tyrovolas[2], Dimitrios Tsiachris[3], Michalis Efremidis[2], Athanasios Kordalis[1,3], Maria Karmpalioti[1], Efstathia Prappa[2], Stefanos Karagiannis[3], Constantina Aggeli[1], Konstantinos Gatzoulis[1], Dimitrios Tousoulis[1], Costas Tsioufis[1] and Konstantinos P. Toutouzas[1]**

[1] 1st Department of Cardiology, Athens Medical School, Hippokration Hospital, Athens, Greece, [2] Second Department of Cardiology, "Evangelismos" General Hospital of Athens, Athens, Greece, [3] Athens Heart Centre, Athens Medical Centre, Athens, Greece

OPEN ACCESS

Edited by:
Grigorios Korosoglou,
GRN Klinik Weinheim, Germany

Reviewed by:
Harilaos Bogossian,
Evangelisches Krankenhaus Hagen-Haspe, Germany
Kleopatra Kouraki,
Klinikum Ludwigshafen, Germany
Dimitrios Mouselimis,
Aristotle University of Thessaloniki, Greece

***Correspondence:**
Konstantinos P. Toutouzas
ktoutouz@gmail.com

Specialty section:
This article was submitted to Cardiovascular Imaging, a section of the journal Frontiers in Cardiovascular Medicine

Received: 06 December 2021
Accepted: 28 January 2022
Published: 09 March 2022

Citation:
Karanasos A, Tyrovolas K, Tsiachris D, Efremidis M, Kordalis A, Karmpalioti M, Prappa E, Karagiannis S, Aggeli C, Gatzoulis K, Tousoulis D, Tsioufis C and Toutouzas KP (2022) Left Atrial Function Post Radiofrequency and Cryoballoon Ablation Assessed by Volume-Pressure Loops. Front. Cardiovasc. Med. 9:830055. doi: 10.3389/fcvm.2022.830055

Background: Left atrial (LA) function is linked to atrial fibrillation (AF) pathogenesis. AF catheter ablation decreases disease burden with potentially favorable effects on cardiac function. Atrial volume-pressure loops can optimally assess the LA function.

Objective: To investigate changes in LA function by volume-pressure loops after paroxysmal AF ablation and explored potential differences between the radiofrequency and cryoballoon ablation.

Methods: We analyzed 44 patients undergoing paroxysmal AF ablation from 2 centers, 22 treated with radiofrequency and 22 with cryoablation. Pre- and post-procedure, all patients underwent a real-time three-dimensional transthoracic ECG to evaluate LA volume, while simultaneously recording LA pressure following transseptal puncture. Volume-pressure loops pre- and post-procedure were created by paired data. Areas of A-loop (LA booster pump function) and V-loop (LA reservoir function), and the stiffness constant determining the slope of the exponential curve during LA filling were calculated.

Results: Average LA pressure, A-wave amplitude, and V-wave amplitude were increased post-procedurally ($p < 0.001$). Overall, A-loop area decreased ($p = 0.001$) and V-loop area tended to increase ($p = 0.07$). The change in both A-loop and V-loop areas was similar between radiofrequency- and cryoballoon-treated patients ($p = 0.18$ and $p = 0.52$, respectively). However, compared with cryoballoon-treated patients, radiofrequency-treated patients had higher increase in the stiffness constant ($b = 0.059$; 95% CI: 0.022–0.096; $p = 0.006$).

Conclusion: AF catheter ablation by the radiofrequency or cryoballoon is associated with the decrease of the booster pump function and increase of the reservoir function. Moreover, there is a post-procedural increase of LA pressure which is associated with an acute increase in LA stiffness in radiofrequency ablation, but not in cryoablation.

Keywords: catheter ablation—atrial fibrillation, atrial fibrillation, left atrium, real-time three-dimensional echocardiography, volume pressure loops

INTRODUCTION

Atrial fibrillation (AF) is associated with significant patient morbidity and mortality (1). Recent research has led to the consideration of AF as a manifestation of atrial cardiomyopathy (2). This is supported by observations linking left atrial (LA) anatomy and physiology to pathogenesis of AF, with a prominent role of LA remodeling and fibrosis, while increased LA pressures play important roles in the initiation and recurrence of this arrhythmia (3). Catheter ablation of AF by pulmonary vein (PV) antral isolation and PV-LA junction ablation is an established therapy that decreases the disease burden, thus leading to reverse remodeling, decreasing LA size, and improving left ventricular (LV) function (4, 5). Yet, the mechanisms by which these actions are mediated have not been completely elucidated, while several studies have demonstrated controversial results regarding its impact on LA function, with stiff LA syndrome described in a small percentage of patients following LA ablation (6).

Atrial volume-pressure loops are the optimal method to assess LA function, based on the classic Newtonian mechanics (2, 7, 8). The loops allow physiological assessment of atrial systolic function, by providing information on LA work during reservoir and contraction phases, as well as on LA stiffness (8). Changes in atrial function induced by catheter ablation of AF have not been documented thus far using this approach.

The aim of this prospective study was (1) to investigate potential changes in LA function by volume-pressure loop assessment after catheter ablation of AF by PV antral isolation and PV-LA junction ablation in patients with paroxysmal atrial fibrillation (PAF), and (2) to explore a potential difference in this response between the radiofrequency catheter and cryoballoon ablation.

MATERIALS AND METHODS

Study Population

This is a prospective observational study of patients undergoing catheter ablation of PAF. Consecutive patients over 18 years old with PAF undergoing for the first time catheter ablation of PAF by PV antral isolation and PV-LA junction ablation, either with a radiofrequency or a cryoballoon catheter, as per clinical indication, were enrolled from 2 high-volume centers from 1 December 2017 to 31 October 2018. Each center enrolled consecutive patients undergoing PV antral isolation using the same method; i.e., radiofrequency ablation for "Evangelismos" General Hospital and cryoablation for Athens Medical Center. All patients included were required to have $\geq$2 paroxysms of PAF defined as self-terminating AF paroxysms or cardioverted within 7 days, were on sinus rhythm at the time of the ablation, and maintained sinus rhythm immediately after the procedure. Patients with severe mitral stenosis or regurgitation, previous cardiac surgery, any prosthetic valve, evidence of ischemia, LA thrombus, or severe LV systolic or diastolic dysfunction were excluded. Additionally, patients with echocardiographic images of suboptimal quality (i.e., inability to image the left atrium during the entire cardiac cycle, or very low frame rate not allowing a real-time 3D echocardiography analysis) or poor quality ECG recordings were excluded from the *post-hoc* analysis.

Study Protocol

Patients underwent PV isolation either by a radiofrequency or a cryoballoon catheter, according to the institutional practice and local standards, as described in the "Ablation Procedure" section. Before and after the procedure, all patients underwent a real-time 3D transthoracic ECG to evaluate LA volume changes during an entire cardiac cycle, while simultaneously recording LA pressure following the transseptal puncture. After the procedure, LA volume and pressure recordings were gated offline by ECG, and recorded values were used to plot the LA pressure as a function of LA volume. Demographic, clinical, and 2d-echocardiographic variables were prospectively obtained. All patients gave written informed consent. The protocol was approved by the institutional ethics committees and complied with the Declaration of Helsinki.

Ablation Procedure

All procedures were performed under conscious sedation according to institutional practices, either by radiofrequency ablation or cryoablation (9, 10). Conscious sedation for both methods included administration of intravenous boli of midazolam, while intravenous fentanyl was administered as bolus for analgesia. Heparin was administered before the transseptal puncture and maintained at activated clotting time levels >300. Briefly, for radiofrequency ablation, following a single transseptal puncture, LA was reconstructed by the CARTO 3 navigation system (Biosense Webster, CA, USA) and wide circumferential lesions around both ipsilateral PVs were performed by a 3.5 mm-tip ablation catheter (Thermo Cool Navi-Star and Smart Touch, Biosense Webster) and a power setting of 30–40 W. The endpoint of the ablation was the absence or dissociation of potentials in the isolated area as documented by the circular mapping catheter (Lasso, Biosense Webster) (10).

Cryoablation was performed without the 3D mapping. A 15-F steerable sheath (FlexCath, Medtronic, Minneapolis, Minnesota) was used to introduce the cryoballoon catheter system into the LA. A 28 mm cryoballoon (Arctic Front Advance, Medtronic) was then advanced through the FlexCath sheath, and positioned at the antrum of each PV guided by the circular mapping catheter (Achieve, Medtronic). The ablation strategy was wide antral isolation and additional LA lesions were not allowed. The protocol recommended the use of 240 s cryoapplications using a freeze-thaw-freeze technique. An additional freeze was delivered in the case of failure to isolate the PV, if time to isolation was >60 s, and in cases where a mapping catheter was unable to monitor the real-time isolation. To minimize the risk of phrenic nerve injury, right phrenic nerve pacing was performed by an electrode catheter in the superior vena cava and capture was confirmed by palpation and intermittent fluoroscopy. Application of cryoenergy was terminated immediately upon attenuation or loss of phrenic nerve capture.

For both procedures, entrance and exit block of the PVs were evaluated 30 min after the initial isolation. The procedure was considered complete once all PVs with conduction recovery were re-isolated. In cases where AF occurred during the procedure,

when not terminated by ablation, sinus rhythm was restored by cardioversion.

Transthoracic ECG

The studies were performed by two experienced echocardiographers (EP, SK) using a Vivid-E9 system with a 4 V probe (GE Healthcare, Chicago, US) at two time points: pre- and post-ablation. By real-time 3D echocardiography, apical full-volume datasets, taking care to avoid foreshortening, were recorded during end-expiratory apnoea. After the procedure, images were analyzed offline at the independent echocardiographic laboratory of Hippokration Hospital, blinded to the ablation method and timing of acquisition. Images were analyzed by two observers (AKa, MK) with a consensus approach, and images were re-evaluated by a third reviewer (CA) to ensure contingency of the analysis, with disagreements resolved by consensus. The LA borders were traced at multiple planes during the cardiac cycle using a semiautomated contour tracing algorithm (4DQ analysis) of the Echopac software (GE healthcare), excluding the PVs and the LA appendage from the volume measurement (11, 12). Thereby, LA volume within a cardiac cycle was calculated and plotted as a function of time with a simultaneous ECG recording (**Figure 1**). In the case of suboptimal images to reliably calculate LA volume during the systole, the patient was excluded from the study. Moreover, end-diastolic LA volume (LAEDV), end-systolic LA volume (LAESV), and LA volume pre-contraction were recorded, while *total atrial emptying volume* was calculated as LAESV minus LAEDV and *active atrial emptying volume* as LA volume pre-contraction minus LAEDV (12). *Atrial ejection* fraction was calculated as total atrial emptying volume divided by LAESV and multiplied by 100, while *LA active ejection fraction* as active atrial emptying volume divided by LAESV and multiplied by 100 (12).

LA Pressure Measurement

Following the transseptal puncture, LA pressure was measured by an oscillometric device (Truwave; Edwards Lifesciences) connected to a fluid-filled 6F multipurpose angiographic catheter or to the cryoballoon catheter after removing the Achieve circular mapping catheter. This measurement was performed after transseptal puncture and LA catheterization, just before the ablation procedure, and repeated before the sheath withdrawal. No chronotropic or inotropic agents were administered during measurements. Measurements from a single beat were used for each volume-pressure loop pre- and post-ablation, at an end-expiratory phase and with stable sinus rhythm for at least three beats. All pressure, electrogram, and surface ECG measurements were recorded by the Labsystem Pro software (Boston Scientific), and exported to digital format, containing synchronous values of ECG amplitude and instantaneous pressure at 1 ms intervals.

Calculation of Indices of LA Systolic Function

Recorded values of volume and pressure were gated offline using the ECG recordings, after adjusting for ultrasound signal delay due to the imaging depth (8). Thereby, paired values of volume and pressure were available. Since the sampling ratio of LA volume values is lower than the pressure sampling, and dependent on the sampling rate of the echocardiographic recording, the number of pairs was defined by the number of LA volume measurements, with a minimum of 12 pairs used. These paired values were used to graphically plot LA pressure as a function of LA volume, thus creating a volume-pressure loop (**Figure 1**) (8). The A-loop area or LA stroke work index, is a measure of the LA booster pump function. The V-loop area expresses the LA reservoir function. Pressure and volume data during the period of the clockwise ascending limb of the volume-pressure loop were fitted to the exponential function $P = \boldsymbol{b} \times e^{\boldsymbol{a}} \cdot V$, where P = instantaneous LA pressure and V = LA volume (2, 13). The least squares method was used for calculation of $\boldsymbol{a}$ and $\boldsymbol{b}$, where $\boldsymbol{a}$ is the passive elastic chamber stiffness constant (ml^{-1}) that determines the slope of the exponential curve and quantifies LA stiffness, while $\boldsymbol{b}$ is the elastic constant (mmHg) representing baseline LA pressure conditions.

Statistical Methods

All analyses were performed with SPSS 25.0. As this is a pilot study, no official study sample was calculated *ad hoc*. Continuous variables are presented as mean ± SD or as median [interquartile range, IQR], as appropriate, and nominal variables as *n* (%). Normality was assessed by the Shapiro–Wilk test. Between-patient normally distributed variables were compared by *t*-test, while non-normally distributed variables by Mann–Whitney test. Nominal variables were compared by Fisher's exact test. As most echocardiographic, haemodynamic, and volume-pressure loop variables were non-normally distributed, a Generalized Estimating Equation with repeated effects was used to assess the impact of the ablation procedure and of the applied method on these variables. The value of $p < 0.05$ indicated statistical significance.

RESULTS

We enrolled 59 patients with PAF. The study flow diagram is presented in **Figure 2**. Fifteen patients were excluded, eight due to suboptimal echocardiographic images, six due to poor-quality pressure recordings, and one because of failure to convert to sinus rhythm after the end of the procedure. Eventually, 44 patients were used for the analysis, 22 treated with radiofrequency ablation and 22 with cryoablation. The procedure was uneventful in all cases.

Baseline Characteristics

The mean age was 62.2 ± 10.7 years and 31 patients (70.5%) were men. There were no significant differences in baseline characteristics between patients treated with radiofrequency or cryoballoon (**Table 1**).

Echocardiographic Analysis

Table 2 summarizes differences before and after the procedure in LA morphometry by real-time 3D echocardiography. There were no significant differences in LAEDV or LA ejection fraction pre- and post-procedure. Conversely, LAESV, total atrial emptying volume, LA volume pre-atrial contraction, active atrial emptying

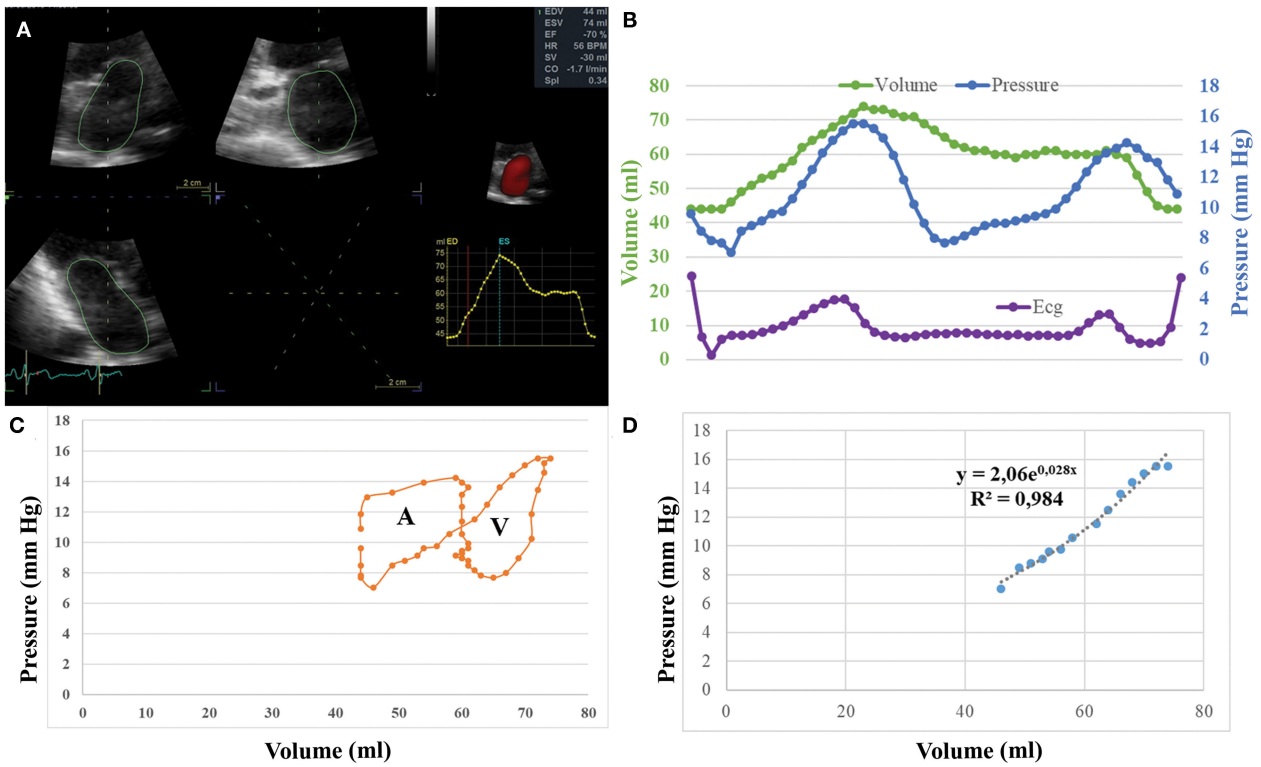

FIGURE 1 | (A) Methodology of echocardiographic analysis for left atrial (LA) volume calculation. **(B)** Simultaneous recording of LA pressure and LA volume during a cardiac cycle gated by ECG. **(C)** Graphical plotting of LA volume vs. LA pressure and creation of volume pressure loops. **(D)** Calculation of the passive elastic chamber stiffness constant (cm^{-3}) and of the elastic constant (mmHg).

volume, and LA active ejection fraction were significantly lower post-procedurally.

Table 3 demonstrates differences in echocardiographic variables between radiofrequency and cryoablation. There were no significant differences between the two groups, except for post-procedural active atrial emptying volume that was higher in patients treated with cryoballoon. Similarly, only active atrial emptying volume and LA volume pre-atrial contraction trended toward higher increase in patients treated with cryoballoon ($p = 0.05$ and $p = 0.10$, respectively), while all other changes pre- and post-procedure in real-time 3D-echocardiographic variables were not significantly different between patients treated with radiofrequency or cryoballoon.

Haemodynamic and Volume-Pressure Loop Analysis

Table 2 summarizes procedure-induced changes in LA pressure and volume-pressure loop variables. Average LA pressure, A-wave amplitude, and V-wave amplitude were all significantly increased post-procedurally ($p < 0.001$ for all). A-loop area decreased ($p = 0.001$), whereas V-loop area tended to increase ($p = 0.07$). Although the elastic constant increased ($p < 0.001$), there was no significant difference in the passive chamber elastic constant overall ($p = 0.63$).

Differences in haemodynamic and volume-pressure loop variables between radiofrequency- and cryoballoon-treated patients are demonstrated in **Table 4**. Post-procedurally, V-wave amplitude was similar in the two groups (24.3 mmHg [19.1–32.2] vs. 28.1 mmHg [19.9–43.2]; $p = 0.35$), but A-wave amplitude tended to be lower in radiofrequency-treated patients (19.0 mmHg [12.4–22.4] vs. 20.7 mmHg [17.2–37.9], $p = 0.06$), and average pressure was lower (16.6 mmHg [10.4–20.4] vs. 18.7 mmHg [16.5–30.6], $p = 0.03$). There were no significant differences in A-loop or V-loop area between the two groups, although both tended to be higher in radiofrequency-treated patients (A-loop: 40.3 ml*mmHg [28.0–70.6] vs. 22.7 ml*mmHg [9.5–56.1], $p = 0.10$; V-loop: 112.9 ml*mmHg [69.8-198.8] vs. 66.0 ml*mmHg [31.4–176.4], $p = 0.14$]. Change in V-wave amplitude was not significantly different between the two groups ($p = 0.24$), whereas increase in A-wave amplitude was lower in radiofrequency-treated patients compared with cryoballoon-treated patients (b = −7.87; 95% *CI*: −14.42 to −1.33; $p = 0.044$) and so was the change in average pressure (b = −8.51; 95% *CI*: −15.00 to −2.02; $p = 0.021$). The extent of change in both A-loop and V-loop areas was similar between radiofrequency- and cryoballoon-treated patients ($p = 0.18$ and $p = 0.52$, respectively). However, compared with cryoballoon-treated patients, radiofrequency-treated patients had lower increase in the elastic constant (b = −6.60; 95%

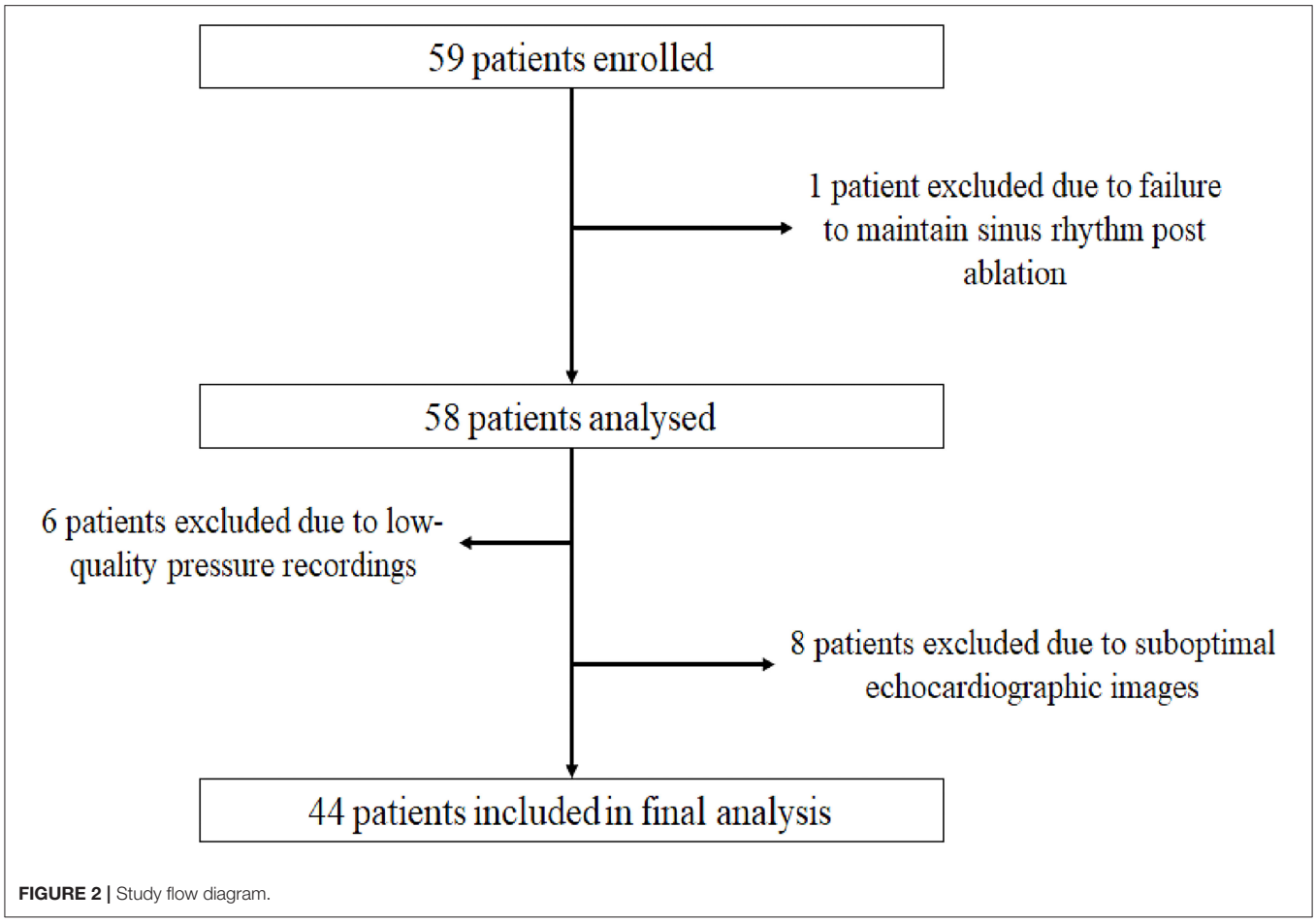

FIGURE 2 | Study flow diagram.

CI: −10.56 to −2.64; $p = 0.005$), and higher increase in the passive elastic chamber stiffness constant (b = 0.059; 95% *CI*: 0.022–0.096; $p = 0.006$). To assess a potential impact of peri-procedural fluid administration, especially with the irrigated radiofrequency catheter, we investigated the potential association of total fluid volume, procedural duration, and radiofrequency duration with all post-procedural volume-pressure variables (A- and V-loop area, elastic constant, and passive elastic stiffness constant; **Supplementary Table**). However, there was no significant correlation for any variable (all $p > 0.15$). Representative examples of volume-pressure loops in patients with radiofrequency and cryoballoon ablation are presented in **Figure 3**.

DISCUSSION

In this prospective pilot study, we thoroughly investigated the acute impact of PV antral isolation and LA-PV junction ablation on morphometric and haemodynamic metrics of LA function, as well as on metrics derived by volume-pressure loops which can quantify the work of the LA, during both the reservoir and active contraction phases, and the LA stiffness. Moreover, we investigated a possible effect of the applied energy source (i.e., radiofrequency versus cryoballoon) on these changes. The main findings of the present study are that: (1) there is a significant increase of average pressure, A-wave amplitude and V-wave amplitude after the procedure observed in both radiofrequency- and cryoballoon-treated patients; (2) although the total volume emptied from LA to LV does not change post-procedurally, the volume ejected during atrial systole is reduced; (3) both in radiofrequency- and cryoballoon-treated patients, there is a decrease in the LA booster pump function and trend for increase in the reservoir function; and (4) in radiofrequency-treated patients, the increase in LA pressure is mainly due to acute increase in LA stiffness, whereas in cryoballoon-treated patients, this increase is observed without such change in LA stiffness.

AF ablation by PV antral isolation and PV-LA junction ablation is a procedure that decreases the disease burden and improves AF-free survival (1). Several approaches, such as echocardiography including LA strain assessment, haemodynamic measurements, and volume-pressure relationships have studied the interaction of LA function with catheter ablation of AF. A decreased reservoir function that recovers following successful AF ablation has been demonstrated by atrial strain measurement (14). Similarly, an increase of the LA ejection fraction by the 3D echocardiography after 3 months has been observed after catheter ablation,

due to increase of the volume emptied to LV during the reservoir phase. This effect was more pronounced with cryoablation, as compared with radiofrequency ablation (15). This might be explained by our study, where radiofrequency but not cryoballoon ablation was associated with increased LA stiffness post-procedurally.

TABLE 1 | Patient and ECG characteristics by ablation method.

	Radiofrequency ablation ($n = 22$)	Cryoballoon ablation ($n = 22$)	*P*-value
Age (years)	61.1 ± 9.7	62.3 ± 12.3	0.75
Male gender, n (%)	18(91.7)	13(59.1)	0.19
Hypertension, n (%)	10(45.5)	10(45.5)	0.72
Dyslipidaemia, n (%)	6(27.3)	4(18.2)	0.68
Diabetes mellitus, n (%)	2(9.1)	1(4.5)	0.99
Thyroid disorders, n (%)	2(9.1)	2(9.1)	0.99
Medications			
B-blockers, n (%)	10(45.5)	11(50.0)	0.99
Sotalol, n (%)	1(4.5)	0	0.99
Amiodarone, n (%)	3(13.6)	3(13.6)	0.54
ACE† inhibitors, n (%)	8(36.4)	10(45.5)	0.76
Statins, n (%)	6(27.3)	5(22.7)	0.99
P wave duration pre (msec)	101 ± 15	105 ± 17	0.41
PR interval pre (msec)	173 ± 22	186 ± 29	0.09
QRS interval pre (msec)	88 [80–115]	89[79–106]	0.76
P wave duration post (msec)	103 ± 17	94 ± 21	0.14
PR interval post (msec)	177 ± 27	179 ± 34	0.84
QRS interval post (msec)	93[78–115]	93[79–106]	0.67

†*ACE, Angiotensin-converting enzyme.*

Moreover, LA hemodynamics have a potential impact on ablation procedure outcome. The increased pre-procedural LA pressure has been associated with adverse LA remodeling and AF recurrence post radiofrequency catheter ablation (3), while vice-versa the procedure itself has been associated with increase of LA pressure over time in patients undergoing redo procedures (16). Additionally, increased LA stiffness (assessed by the pressure difference within a cardiac cycle) was associated with the reduced diastolic function at follow-up of the same patients (16). This has further been corroborated by a study combining MRI imaging of the LA with subsequent invasive LA pressure measurements pre-ablation to generate volume-pressure loops. This study assessed the stiffness by calculating the linear slope of $\Delta P/\Delta V$ during the diastolic LA filling phase—albeit not taking into account the non-linear correlation between these variables—and found that increased pre-procedural LA stiffness was independently associated with AF recurrence after LA ablation (16). Finally, pre-existing LA fibrosis has been associated with recurrences after PV isolation, further supporting a potential adverse impact of LA stiffness (17).

Nevertheless, no study has used an integrated approach to characterize the acute impact of the ablation procedure on LA function. While the main determinants of the LA reservoir function are the LA myocardial compliance and the LV longitudinal displacement, LA contraction is to a greater extent dependent on ventricular filling pressures (18). In our study, despite a higher A-wave amplitude post-ablation, total LA work during active contraction (A-loop area) was reduced due to a lower active emptying volume, lending evidence to a hypothesis of a "stunned" LA unable to forward the blood into the LV despite a higher filling pressure.

TABLE 2 | Procedure-induced changes in echocardiographic, haemodynamic, and volume-pressure variables.

	Pre	Post	*P*-value[#]
LA† volume measurements			
LAEDV‡ (ml)	26.5 [22–38.8]	25.5 [20.3–37.5]	0.68
LAESV§ (ml)	59.6 ± 14.9	56.6 ± 15.0	0.04
LAV¶ pre-contraction (ml)	41.0 [33.0–50.0]	36.0 [28.0–50.0]	0.006
Total atrial emptying volume (ml)	29.0 [22.0-34.8]	27.0 [22.0–31.0]	0.04
Active atrial emptying volume (ml)	13.0 [8.0–17.0]	8.0 [5.0–10.0]	<0.001
LA ejection fraction (%)	50.2 ± 12.4	48.6 ± 10.4	0.34
LA active ejection fraction (%)	20.5 [16.4–24.6]	14.6 [11.0–18.9]	0.001
Pressure measurements			
V-wave (mmHg)	19.4 [15.0–28.6]	24.6 [19.8–34.4]	<0.001
A-wave (mmHg)	16.8 [13.0–23.3]	20.0 [14.3–25.6]	0.001
Average pressure (mmHg)	12.2 [10.0–19.3]	17.3 [12.9–23.8]	<0.001
Volume-pressure analysis			
A-loop area (ml*mmHg)	65.7 [32.7–93.7]	39.0 [15.4–67.5]	<0.001
V-loop area (ml*mmHg)	79.5 [32.7–150.2]	92.6 [48.0–181.5]	0.072
Passive elastic chamber stiffness constant (ml^{-1})	0.047 [0.028–0.073]	0.040 [0.021–0.068]	0.63
Elastic constant (mmHg)	1.91 [0.48–4.64]	4.15 [1.75–10.88]	<0.001

†*LA: left atrial.* ‡*LAEDV: left atrial end-diastolic volume.* §*LAESV: left atrial end-systolic volume.* ¶*LAV: left atrial volume.* #*Derived from Generalized Estimating Equation.*

TABLE 3 | Echocardiographic characteristics by ablation method.

	Radiofrequency ablation ($n = 22$)	Cryoballoon ablation ($n = 22$)	*P*-value
Baseline TTE findings			
LVEDD† (mm)	48 ± 3	49 ± 4	0.47
E-wave velocity (cm/s)	80 [60–90]	82 [75–91]	0.37
A-wave velocity (cm/s)	62 ± 16	61 ± 0	0.88
E/A ratio	1.33 [1.13–1.31]	1.28 [1.19–1.62]	0.86
E' Velocity (cm/s)	9 [7–10]	10 [9–11]	0.08
E/E' ratio	9.2 ± 1.6	8.9 ± 3	0.75
Real-time 3D-echocardiography measurements pre ablation			
LAEDV‡ pre (ml)	26.0 [19.0–39.0]	27.0 [22.0–39.0]	0.61
LAESV§ pre (ml)	58.9 ± 14.4	60.2 ± 15.8	0.78
LAV¶ pre-contraction pre (ml)	37.5 [32.0–49.3]	44.0 [35.0–54.5]	0.40
Total atrial emptying volume pre (ml)	29.5 [23.8–33.0]	29 [21.8–39.0]	0.97
Active atrial emptying volume pre (ml)	12.5 [7.8–16.0]	14.0 [8.0–17.0]	0.51
LA# ejection fraction pre (%)	51.4 ± 12.4	49.0 ± 12.5	0.53
LA# active ejection fraction pre (%)	21.2 [14.3–24.5]	20.5 [16.5–25.7]	0.88
Real-time 3D-echocardiography measurements post ablation			
LAEDV‡ post (ml)	24.5 [20.0–35.3]	29.5 [20.5–40.3]	0.47
LAESV§ post (ml)	55.9 ± 13.7	57.2 ± 16.5	0.78
LAV¶ pre-contraction post (ml)	32.5 [27.8–41.0]	40.0 [30.5–54.0]	0.06
Total atrial emptying volume post (ml)	27.0 [22.0–31.0]	25.5 [20.0–31.8]	0.44
Active atrial emptying volume post (ml)	7.0 [5.0–8.3]	10.0 [7.0–12.5]	0.02
LA# ejection fraction post (%)	50.4 ± 10.2	46.8 ± 10.5	0.25
LA# active ejection fraction post (%)	13.6 [8.9–16.4]	14.7 [11.8–22.5]	0.14

†*LVEDD: left ventricular end-diastolic diameter.*
‡*LAEDV: left atrial end-diastolic volume.*
§*LAESV: left atrial end-systolic volume.*
¶*LAV: left atrial volume.*
#*LA: left atrial.*

However, this acute adverse impact of the ablation procedure is counteracted by a compensatory increase of the reservoir function that manages to maintain an unchanged total emptying volume and atrial ejection fraction due to the increase in LA filling pressures.

In our study, both radiofrequency and cryoablation resulted in similar changes in LA function and hemodynamics: reservoir function was increased and booster pump function was decreased in the same extent, while average LA pressure was similarly increased in both methods. This increase in pressure might share common mechanisms in the two groups, such as change of preload with periprocedural fluid administration, or a potential impact of increased vagal stimulation, given the increased passive emptying and reduction of booster function. However, the increase in LA pressure for patients treated with radiofrequency ablation was clearly associated with a higher increase in LA stiffness, as assessed by the passive elastic chamber stiffness constant, which determines the slope in the exponential equation that expresses the changes in LA pressure as a function of volume (2, 13). A similar increase in LA stiffness has been described in an experimental model of the Cox maze procedure (19). It is unclear whether this differential response in LA stiffness in our study might be explained by differences in myocardial injury between the methods. In radiofrequency ablation, effective lesions are transmural and characterized by permanent electrical changes ensuring PV isolation, whereas cryo-lesions are characterized by preserved tissue architecture and cause less damage to the endocardium (20). These histologically well-demarcated and homogeneous lesions might be associated with a subtler response which does not increase LA stiffness to the same extent.

Perspectives

Using an integrated approach, we documented several important changes underlying catheter ablation of AF. Namely, we observed an acute decrease in active atrial emptying volume with a preservation of the total volume, an acute decrease of the LA booster pump function and an increase of the reservoir

TABLE 4 | Pressure data and volume-pressure variables by ablation method.

	Radiofrequency ablation ($n = 22$)	Cryoballoon ablation ($n = 22$)	*P*-value
Pressure measurements pre			
V-wave pre (mmHg)	19.8 [16.2–25.9]	18.9 [13.4–32.9]	0.93
A-wave pre (mmHg)	16.8 [14.0–21.0]	16.8 [11.1–28.8]	0.61
Average pressure pre (mmHg)	12.0 [10.6–15.9]	12.4 [8.5–22.4]	0.41
Pressure measurements post			
V-wave post (mmHg)	24.3 [19.1–32.2]	28.1 [19.9–43.2]	0.35
A-wave post (mmHg)	19.0 [12.4–22.4]	20.7 [17.2–37.9]	0.06
Average pressure post (mmHg)	16.6 [10.4–20.4]	18.7 [16.5–30.6]	0.03
Volume-pressure analysis pre			
A-loop area pre (ml*mmHg)	71.2 [55.6–114.7]	46.2 [26.9–86.2]	0.08
V-loop area pre (ml*mmHg)	87.1 [61.2–141.0]	73.1 [25.7–152.3]	0.29
Passive elastic chamber stiffness constant pre (ml^{-1})	0.053 [0.038–0.073]	0.031 [0.023–0.081]	0.02
Elastic constant pre (mmHg)	1.07 [0.47–2.40]	3.59 [0.46–5.37]	0.06
Volume-pressure analysis post			
A-loop area post (ml*mmHg)	40.3 [28.0–70.6]	22.7 [9.5–56.1]	0.10
V-loop area post (ml*mmHg)	112.9 [69.8–198.8]	66.0 [31.4–176.4]	0.14
Passive elastic chamber stiffness constant post (ml^{-1})	0.063 [0.037–0.100]	0.027 [0.015–0.042]	<0.001
Elastic constant post (mmHg)	2.46 [0.59–4.54]	6.79 [2.74–13.95]	0.001

function, increase in LA pressures, and in radiofrequency ablation increased LA stiffness. These changes were observed in varying extents among individual patients, and future studies need to examine whether these changes can be used as surrogate markers for assessing the long-term success of the procedure, and whether they might translate to changes in diastolic function over long term, given the well-defined relationship between LA physiology and diastolic filling of the LV (7).

Limitations

Although the study was not randomized, we included consecutive patients from two different hospitals with each hospital performing a single AF ablation method. Thus, there were no significant baseline differences between the groups. Moreover, the analysis was blinded to the method applied. An *ad-hoc* study sample was not predefined, and thus our study might be underpowered for endpoints with high variability, such as echocardiographic measurements. However, we used a real-time three-dimensional echocardiographic approach which improves reproducibility of the measurements and thus reduces bias (11). As we excluded patients with severe systolic or diastolic dysfunction or severe mitral valve dysfunction, our findings do not necessarily apply to such populations. The exclusion of patients with poor quality echocardiographic or pressure data limited our study sample, but enhanced the robustness of our data. Although micromanometers are the golden standard for invasive pressure measurements, fluid-filled systems remain the mainstay of invasive pressure measurement, as they also have high reproducibility and sampling rate, clearly superior to the sampling rate of echocardiographic measurements. Moreover, the same method was used pre- and post- procedurally, while poor quality tracings were excluded. Additional imaging modalities could have further corroborated the results of our study. Cardiac magnetic resonance is the standard for morphometric evaluation of left atrium with fast strain-encoded sequence allowing the evaluation of strain, while it may delineate myocardial scar within the left atrium, a surrogate marker of reduced compliance and atrial cardiomyopathy (4, 21). Additionally, a 3D echocardiography derived LA strain could have assisted in a more comprehensive evaluation of LA function (22). Nevertheless, the pressure-volume assessment remains an ideal tool for the acute assessment of physiological changes in a research setting, although not easily applicable in everyday practice (2). Non-invasive follow-up by the above mentioned methods will help investigate the long-term implications of the findings of the current study.

CONCLUSIONS

Catheter ablation of AF either by radiofrequency or cryoballoon is associated with functional changes of the left atrium, with a decrease of the booster pump function and an increase in the reservoir function. Moreover, there is a post-procedural increase in LA pressures which in radiofrequency ablation is associated with an

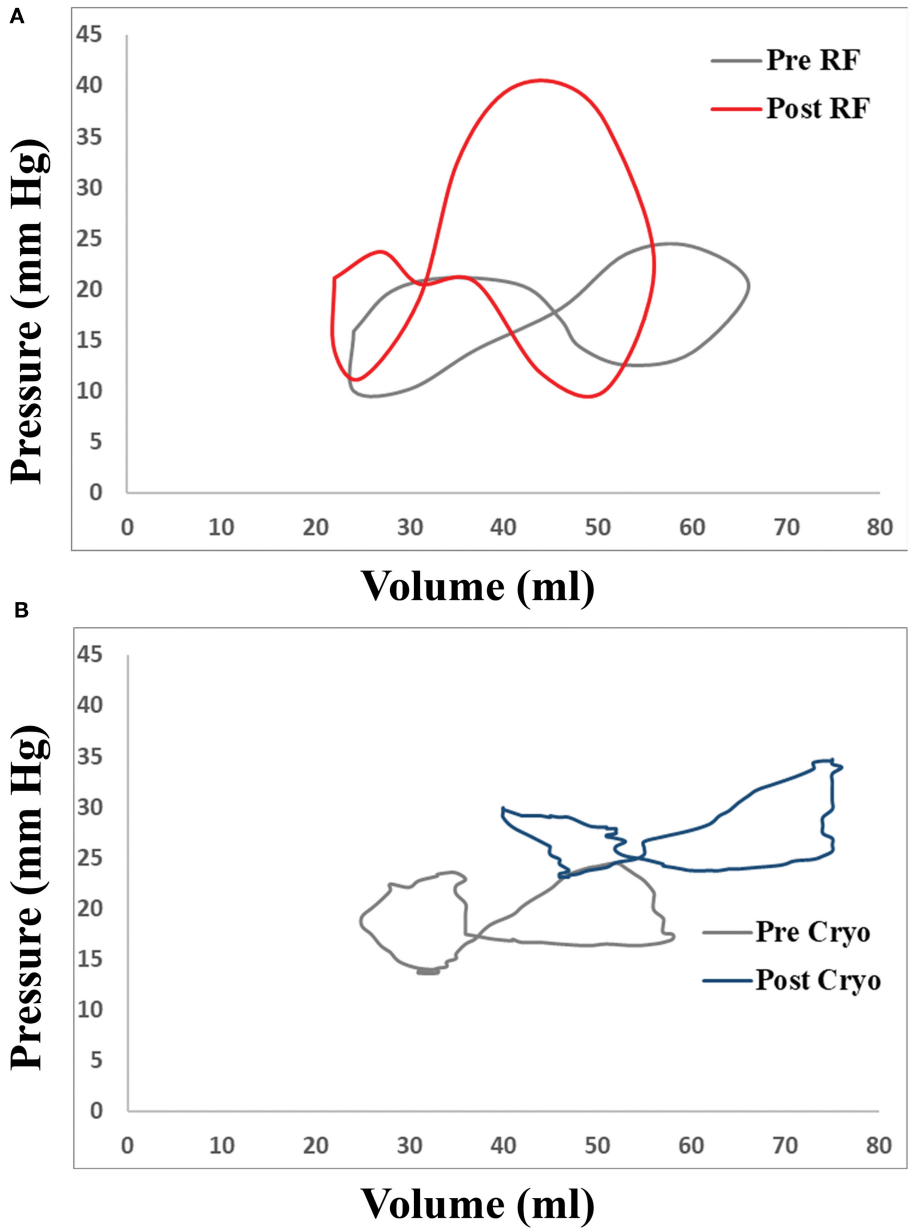

FIGURE 3 | Representative examples of changes in LA volume-pressure loops in patients undergoing transcatheter atrial fibrillation (AF) ablation with **(A)** radiofrequency catheter and **(B)** cryoballoon.

acute increase in LA stiffness, but not in cryoablation. Further studies are needed to elucidate the significance of this change on the patient outcome and the long-term diastolic function.

DATA AVAILABILITY STATEMENT

The raw data supporting the conclusions of this article will be made available by the authors, without undue reservation.

ETHICS STATEMENT

The studies involving human participants were reviewed and approved by Ethics Committee of Hippokration Hospital. The patients/participants provided their written informed consent to participate in this study.

AUTHOR CONTRIBUTIONS

AKa: conception of the design, drafting of the manuscript, and data analysis. KT, DTs, ME, and AKo: data analysis and revising

the manuscript. MK, EP, SK, and CA: data analysis. DTo, KG, and CT: revising the manuscript. KPT: conception of the idea and design, revising the manuscript, and final approval. All authors contributed to the article and approved the submitted version.

ACKNOWLEDGMENTS

We would like to thank the staff of the echocardiographic departments of Evangelismos General Hospital and Athens Medical Center for their assistance in echocardiographic data collection.

SUPPLEMENTARY MATERIAL

The Supplementary Material for this article can be found online at: https://www.frontiersin.org/articles/10.3389/fcvm.2022.830055/full#supplementary-material

REFERENCES

1. Hindricks G, Potpara T, Dagres N, Arbelo E, Bax JJ, Blomstrom-Lundqvist C, et al. 2020 ESC Guidelines for the diagnosis and management of atrial fibrillation developed in collaboration with the European Association of Cardio-Thoracic Surgery (EACTS). *Eur Heart J.* (2021) 42:373–98. doi: 10.1093/eurheartj/ehaa612
2. Goette A, Kalman JM, Aguinaga L, Akar J, Cabrera JA, Chen SA, et al. EHRA/HRS/APHRS/SOLAECE expert consensus on atrial cardiomyopathies: Definition, characterization, and clinical implication. *Heart rhythm.* (2017) 14:e3–e40. doi: 10.1016/j.hrthm.2016.05.028
3. Park J, Joung B, Uhm JS, Young Shim C, Hwang C, Hyoung Lee M, et al. High left atrial pressures are associated with advanced electroanatomical remodeling of left atrium and independent predictors for clinical recurrence of atrial fibrillation after catheter ablation. *Heart rhythm.* (2014) 11:953–60. doi: 10.1016/j.hrthm.2014.03.009
4. Jahnke C, Fischer J, Gerds-Li JH, Gebker R, Manka R, Fleck E, et al. Serial monitoring of reverse left-atrial remodeling after pulmonary vein isolation in patients with atrial fibrillation: a magnetic resonance imaging study. *Int J Cardiol.* (2011) 153:42–6. doi: 10.1016/j.ijcard.2010.08.034
5. Sugumar H, Prabhu S, Voskoboinik A, Young S, Gutman SJ, Wong GR, et al. Atrial remodeling following catheter ablation for atrial fibrillation-mediated cardiomyopathy: long-term follow-up of CAMERA-MRI study. *JACC Clinical Electrophysiol.* (2019) 5:681–8. doi: 10.1016/j.jacep.2019.03.009
6. Gibson DN, Di Biase L, Mohanty P, Patel JD, Bai R, Sanchez J, et al. Stiff left atrial syndrome after catheter ablation for atrial fibrillation: clinical characterization, prevalence, and predictors. *Heart rhythm.* (2011) 8:1364–71. doi: 10.1016/j.hrthm.2011.02.026
7. Thomas L, Marwick TH, Popescu BA, Donal E, Badano LP. Left atrial structure and function, and left ventricular diastolic dysfunction: JACC state-of-the-art review. *J Am Coll Cardiol.* (2019) 73:1961–77. doi: 10.1016/j.jacc.2019.01.059
8. Stefanadis C, Dernellis J, Stratos C, Tsiamis E, Tsioufis C, Toutouzas K, et al. Assessment of left atrial pressure-area relation in humans by means of retrograde left atrial catheterization and echocardiographic automatic boundary detection: effects of dobutamine. *J Am Coll Cardiol.* (1998) 31:426–36. doi: 10.1016/S0735-1097(97)00517-2
9. Su W, Aryana A, Passman R, Singh G, Hokanson R, Kowalski M, et al. Cryoballoon Best Practices II: Practical guide to procedural monitoring and dosing during atrial fibrillation ablation from the perspective of experienced users. *Heart rhythm.* (2018) 15:1348–55. doi: 10.1016/j.hrthm.2018.04.021
10. Efremidis M, Letsas K, Giannopoulos G, Lioni L, Vlachos K, Asvestas D, et al. Early pulmonary vein reconnection as a predictor of left atrial ablation outcomes for paroxysmal atrial fibrillation. *Europace.* (2015) 17:741–6. doi: 10.1093/europace/euu216
11. Badano LP, Miglioranza MH, Mihaila S, Peluso D, Xhaxho J, Marra MP, et al. Left atrial volumes and function by three-dimensional echocardiography: reference values, accuracy, reproducibility, and comparison with two-dimensional echocardiographic measurements. *Circ Cardiovasc Imaging.* (2016) 9:e004229. doi: 10.1161/CIRCIMAGING.115.004229
12. Olsen FJ, Bertelsen L, de Knegt MC, Christensen TE, Vejlstrup N, Svendsen JH, et al. Multimodality cardiac imaging for the assessment of left atrial function and the association with atrial arrhythmias. *Circ Cardiovasc Imaging.* (2016) 9:e004947. doi: 10.1161/CIRCIMAGING.116.004947
13. Kihara Y, Sasayama S, Miyazaki S, Onodera T, Susawa T, Nakamura Y, et al. Role of the left atrium in adaptation of the heart to chronic mitral regurgitation in conscious dogs. *Circ Res.* (1988) 62:543–53. doi: 10.1161/01.RES.62.3.543
14. Spethmann S, Stuer K, Diaz I, Althoff T, Hewing B, Baumann G, et al. Left atrial mechanics predict the success of pulmonary vein isolation in patients with atrial fibrillation. *J Interv Card Electrophysiol.* (2014) 40:53–62. doi: 10.1007/s10840-014-9876-0
15. Giannopoulos G, Kossyvakis C, Vrachatis D, Aggeli C, Tsitsinakis G, Letsas K, et al. Effect of cryoballoon and radiofrequency ablation for pulmonary vein isolation on left atrial function in patients with nonvalvular paroxysmal atrial fibrillation: A prospective randomized study (Cryo-LAEF study). *J Cardiovasc Electrophysiol.* (2019) 30:991–8. doi: 10.1111/jce.13933
16. Park JW, Yu HT, Kim TH, Uhm JS, Joung B, Lee MH, et al. Atrial fibrillation catheter ablation increases the left atrial pressure. *Circ Arrhythm Electrophysiol.* (2019) 12:e007073. doi: 10.1161/CIRCEP.118.007073
17. Marrouche NF, Wilber D, Hindricks G, Jais P, Akoum N, Marchlinski F, et al. Association of atrial tissue fibrosis identified by delayed enhancement MRI and atrial fibrillation catheter ablation: the DECAAF study. *JAMA.* (2014) 311:498–506. doi: 10.1001/jama.2014.3
18. Donal E, Behagel A, Feneon D. Value of left atrial strain: a highly promising field of investigation. *Eur Heart J Cardiovasc Imaging.* (2015) 16:356–7. doi: 10.1093/ehjci/jeu230
19. Voeller RK, Zierer A, Lall SC, Sakamoto S, Chang NL, Schuessler RB, et al. The effects of the Cox maze procedure on atrial function. *J Thorac Cardiovasc Surg.* (2008) 136:1257–64. doi: 10.1016/j.jtcvs.2008.01.053
20. Khairy P, Chauvet P, Lehmann J, Lambert J, Macle L, Tanguay JF, et al. Lower incidence of thrombus formation with cryoenergy vs. radiofrequency catheter ablation. *Circulation.* (2003) 107:2045–50. doi: 10.1161/01.CIR.0000058706.82623.A1
21. Korosoglou G, Giusca S, Montenbruck M, Patel AR, Lapinskas T, Gotze C, et al. Fast strain-encoded cardiac magnetic resonance for diagnostic classification and risk stratification of heart failure patients. *JACC Cardiovasc Imaging.* (2021) 14:1177–88. doi: 10.1016/j.jcmg.2020.10.024
22. Nabeshima Y, Kitano T, Takeuchi M. Reliability of left atrial strain reference values: A 3D echocardiographic study. *PLoS ONE.* (2021) 16:e0250089. doi: 10.1371/journal.pone.0250089

Conflict of Interest: The authors declare that the research was conducted in the absence of any commercial or financial relationships that could be construed as a potential conflict of interest.

frontiers in Cardiovascular Medicine

ORIGINAL RESEARCH
published: 22 March 2022
doi: 10.3389/fcvm.2022.828556

CT-Based Simulation of Left Ventricular Hemodynamics: A Pilot Study in Mitral Regurgitation and Left Ventricle Aneurysm Patients

Lukas Obermeier[1], Katharina Vellguth[1], Adriano Schlief[1], Lennart Tautz[1,2], Jan Bruening[1], Christoph Knosalla[3,4,5], Titus Kuehne[1,4,6], Natalia Solowjowa[3†] and Leonid Goubergrits[1,7†]*

[1] Institute of Computer-Assisted Cardiovascular Medicine, Charité - Universitätsmedizin Berlin, Berlin, Germany, [2] Fraunhofer Institute for Digital Medicine MEVIS, Bremen, Germany, [3] Department of Cardiothoracic and Vascular Surgery, German Heart Center Berlin, Berlin, Germany, [4] DZHK (German Centre for Cardiovascular Research), Partner Site Berlin, Berlin, Germany, [5] Charité - Universitätsmedizin Berlin, Corporate Member of Freie Universität Berlin, Humboldt - Universität zu Berlin and Berlin Institute of Health, Berlin, Germany, [6] Department of Congenital Heart Disease, German Heart Center Berlin, Berlin, Germany, [7] Einstein Center Digital Future, Berlin, Germany

OPEN ACCESS

Edited by:
Muralidhar Padala, Emory University, United States

Reviewed by:
Brooks Lane, Emory University, United States
Gediminas Gaidulis, Emory University, United States
Milan Toma, New York Institute of Technology College of Osteopathic Medicine, United States

***Correspondence:**
Lukas Obermeier
lukas.obermeier@charite.de

[†] *These authors share last authorship*

Specialty section:
This article was submitted to Cardiovascular Imaging, a section of the journal Frontiers in Cardiovascular Medicine

Received: *03 December 2021*
Accepted: *03 February 2022*
Published: *22 March 2022*

Citation:
Obermeier L, Vellguth K, Schlief A, Tautz L, Bruening J, Knosalla C, Kuehne T, Solowjowa N and Goubergrits L (2022) CT-Based Simulation of Left Ventricular Hemodynamics: A Pilot Study in Mitral Regurgitation and Left Ventricle Aneurysm Patients. Front. Cardiovasc. Med. 9:828556. doi: 10.3389/fcvm.2022.828556

Background: Cardiac CT (CCT) is well suited for a detailed analysis of heart structures due to its high spatial resolution, but in contrast to MRI and echocardiography, CCT does not allow an assessment of intracardiac flow. Computational fluid dynamics (CFD) can complement this shortcoming. It enables the computation of hemodynamics at a high spatio-temporal resolution based on medical images. The aim of this proposed study is to establish a CCT-based CFD methodology for the analysis of left ventricle (LV) hemodynamics and to assess the usability of the computational framework for clinical practice.

Materials and Methods: The methodology is demonstrated by means of four cases selected from a cohort of 125 multiphase CCT examinations of heart failure patients. These cases represent subcohorts of patients with and without LV aneurysm and with severe and no mitral regurgitation (MR). All selected LVs are dilated and characterized by a reduced ejection fraction (EF). End-diastolic and end-systolic image data was used to reconstruct LV geometries with 2D valves as well as the ventricular movement. The intraventricular hemodynamics were computed with a prescribed-motion CFD approach and evaluated in terms of large-scale flow patterns, energetic behavior, and intraventricular washout.

Results: In the MR patients, a disrupted E-wave jet, a fragmentary diastolic vortex formation and an increased specific energy dissipation in systole are observed. In all cases, regions with an impaired washout are visible. The results furthermore indicate that considering several cycles might provide a more detailed view of the washout process. The pre-processing times and computational expenses are in reach of clinical feasibility.

Conclusion: The proposed CCT-based CFD method allows to compute patient-specific intraventricular hemodynamics and thus complements the informative value of CCT. The method can be applied to any CCT data of common quality and represents a fair balance

between model accuracy and overall expenses. With further model enhancements, the computational framework has the potential to be embedded in clinical routine workflows, to support clinical decision making and treatment planning.

Keywords: cardiac computed tomography, intraventricular hemodynamics, image-based modeling, left ventricle aneurysm, mitral regurgitation, fluid-structure interaction, computational fluid dynamics

1. INTRODUCTION

Cardiac CT (CCT) is a preferred imaging modality for the treatment of various cardiovascular diseases and is for example used in the investigation of coronary artery disease, for the measurement of myocardial perfusion, or in the planning of interventions in valvular heart diseases (1, 2). For surgical or transcatheter aortic valve (AV) implantation, CCT is currently state of the art imaging technique (3–5). Due to a superior spatial resolution (0.5–0.625 mm), if compared to MRI (1–2 mm), or echocardiography (0.5–2 mm) (6), CCT allows for assessment and quantification of anatomical structures necessary for decision making and treatment planning (5). However, in clinical practice, intracardiac blood flow analysis is based on MRI or Doppler echocardiography, as CCT cannot capture flow quantities like blood velocity and pressure. Recently, Lantz et al. (7) demonstrated the potential of coupling CCT with computational fluid dynamics (CFD) for so-called 4D flow CCT that allows the computation of intraventricular hemodynamics based on CCT. Despite being more time-consuming in post-processing and in general, less investigated and established, the methodology potentially enables investigations at higher spatial resolutions as well as a reduction of acquisition time, and may thus be a promising alternative to 4D flow MRI (8).

Intraventricular blood flow behavior is believed to potentially serve as an early predictor for the manifestation of diseases (9) and is used to investigate pathological states (10, 11) or the success assessment of interventional procedures for heart diseases (12). It is furthermore used for the analysis of post-operative states like intraventricular flow with prosthetic mitral valves (MVs) (13) or the influence of annuloplasty rings (14). The *in vivo* analysis of intraventricular blood flow *via* medical images includes, for example, the quantification of blood flow kinetic energy (15, 16), the characterization of the LV hemodynamics *via* the analysis of large-scale flow patterns (17–22), intraventricular pressure gradient analysis (23) or diastolic vortex analysis in terms of formation time in early diastole (10), vortex strength (11) or rotational vortex direction (16). Techniques and quantities for intracardiac flow analysis were recently overviewed by Mele et al. (24).

Due to advancements in medical image acquisition and numerical modeling, as well as growing computational resources, the use of image-based patient-specific models for the analysis of intraventricular hemodynamics increased in recent years. Image-based CFD approaches are for example used to investigate intraventricular flow patterns and diastolic vortex formation (25–28) as well as loss of kinetic energy and pressure gradients in LVs (29). In contrast to medical imaging techniques, CFD allows to analyze wall shear stress at high spatio-temporal resolutions (30) and to model post-operative states, e.g., after MV treatment (12, 31) or surgical ventricular restoration (32). CFD furthermore enables the creation of synthetic cases, for example, LVs *via* statistical shape models (33) or different incorporated MV shapes in mitral regurgitation (MR) (34). Proposed modeling approaches vary significantly regarding complexity, ranging from 0D Lumped Element Models, where the cardiovascular system is described as an electro-mechanical circuit (35, 36), *via* image-based CFD approaches where the LV motion is prescribed as boundary condition (BC) (25, 26), to complex models coupling electro-, structural and fluid mechanics, as for example used in the Living Heart Project (37, 38). Doost et al. (39) gave a detailed review of heart blood flow simulation approaches and attributed the image-based, prescribed-motion CFD models the greatest popularity due to lower computational costs and their convenience in comparison to coupled fluid-structure-interaction (FSI) frameworks. An overview of different modeling approaches of FSI and a review on the current state of the art FSI modeling in cardiovascular medicine was recently given by Quarteroni et al. (40) and Hirschhorn et al. (41).

The balancing between model accuracy and complexity marks a central trade-off in the CFD-based investigation of LV hemodynamics. Modeling approaches need to incorporate the most important features to accurately reproduce the intraventricular hemodynamics. At the same time, data requirements, required working hours, computational expenses, and model uncertainties need to be minimized to enable a usability in the clinical routine. Finding an adequate compromise is the subject of this study. We propose a moderate complexity computational framework to compute LV hemodynamics by using CCT image-based, prescribed-motion CFD that requires pre-processing times and computational expenses that are within reach of clinical feasibility. The workflow is largely automated and applicable to arbitrary CCT data of common quality. The technical feasibility is demonstrated by means of four cases, each representing a subcohort with a respective pathological configuration: patients with and without LV aneurysm as well as with severe and no MR.

2. MATERIALS AND METHODS

The central workflow of the computational framework is illustrated in **Figure 1**. Following the image acquisition *via* CCT, the image data is used to segment end-diastolic and end-systolic LV geometries as well as both annuli. In the next step, the segmented data are used to set up LV geometries with 2D valves and to derive the ventricular movement. For the intracardiac flow simulations, adequate physics models and BCs are furthermore

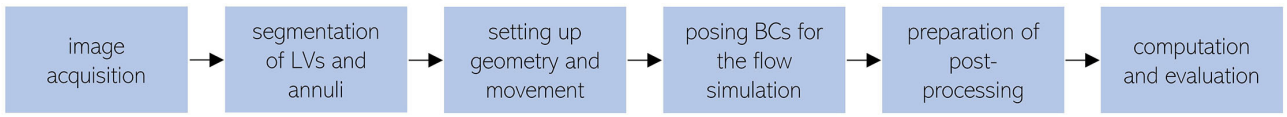

FIGURE 1 | Illustration of the central workflow of the computational framework.

posed. As the last step, valuable hemodynamic markers for the analysis of intraventricular flow features are selected before each of the four patient-specific cases is computed and evaluated. The individual steps are addressed in detail in the following.

2.1. Study Cohort

A cohort of heart failure patients after myocardial infarction (n = 125, mean age of 60.6 ± 10.0 years, 16.8 % women) was retrospectively analyzed. Data were collected in the German Heart Center Berlin between November 2005 and January 2016. The patients are grouped into two cohorts: patients without (Cohort I) and with (Cohort II) anterior LV aneurysm. The LV aneurysm was diagnosed by echocardiography and confirmed by CCT. The MR grade was defined echocardiographically. For each cohort, one case without MR and one with severe MR (grade III) were selected. The different cases are denominated *via* M{MR: 0 = no MR; 1, 2, 3 = grade I, II, III}A{aneurysm: 0 = no; 1 = yes}, resulting in the four cases: M3A1, M3A0, M0A1, and M0A0. The hemodynamics of all cases are investigated, each being representative for its subcohort. The four LVs were chosen such that the end-diastolic volumes (226 to 256 ml) and the reduced ejection fractions (EFs) (23 to 29 %) are comparable. **Table 1** summarizes the clinical and demographic data of the two cohorts and the four representative cases. Statistical analysis was performed with SPSS (version 27, IBM, Armonk, NY, USA), whereat a p-value below 0.05 was considered statistically significant.

2.2. Computed Tomography

Cardiac CT examinations were performed following injection of intravenous contrast agent. The scans were performed in a spiral modus with retrospective electrocardiogram-gating, using a dual-source multi-slice spiral CT scanner (Somatom Definition Flash, Siemens Healthcare GmbH, Erlangen, Germany). All scans were conducted at a tube voltage of 100 kV and an individually adapted tube current, using the scanners exposure control software. A multiphase data set of the whole heart cycle was reconstructed that allows identification of the diastolic phase with the largest left ventricular end-diastolic volume (LVEDV) and the systolic phase with the smallest left ventricular end-systolic volume (LVESV). All images were reconstructed using a standard soft-tissue convolution kernel and a dedicated noise reduction software. The spatial and temporal resolution of the CT images varied. Spatial resolutions of (0.39–0.648 mm) x (0.39–0.648 mm) in-plane resolution and (0.5–1.85 mm) slice thickness were used for segmentation. The temporal resolution ranged from 70 to 140 ms depending on the patient's heart rate. One heart cycle was always resolved by 10 phases.

TABLE 1 | Clinical and demographic data of the two study cohorts and the four representative cases.

Parameters	Cohort I (A0)	Cohort II (A1)	M3A1	M3A0	M0A1	M0A0
Nr. of cases	72	53	-	-	-	-
LV aneurysm	no	yes	yes	no	yes	no
Age (years)	60 [54 - 69]	59 [54 - 68]	60	60	49	62
Sex (m/w)	62/10	42/11	m	m	m	m
BSA (m^2)	1.98 ± 0.19	1.91 ± 0.23	2.18	2.02	1.76	2.36
MR (grade)	I [I - II/III]	I [I - II]	III	III	-	-
NYHA class	III [III - III]	III [III - III]	III	IV	III	III

Cohort p-values range from 0.143 to 0.676 and are not considered significant. If a parameter is not normally distributed in either cohort, values are shown as median [interquartile range (IQR)] for both cohorts, whereas values are shown as mean ± standard deviation (SD) otherwise. Normality was proved by the Shapiro-Wilk test. The BSA was calculated according to the Dubois formula (42). LV, left ventricle; BSA: body surface area; MR, mitral regurgitation; NYHA, New York Heart Association.

2.3. Segmentation

To analyze the LV anatomy as well as to prepare geometric and dynamic boundary conditions for the flow simulations, the LVs were segmented. The segmentations were created using a prototypical software developed earlier on the basis of the MeVisLab platform (43). A detailed description of the segmentation procedure can be found in Tautz et al. (44). In a first step, segmentations of the end-diastolic and end-systolic LVs were done automatically. The automated procedure is based on an adaptive 3D region growing approach, detection of the axial view of the ascending aorta (AO), and taking into account contextual information of the heart topology. Nevertheless, a manual correction was required to fix problems associated with artifacts due to implanted metal parts or uneven distribution of contrast agents. The segmentation of the end-diastolic myocardial wall was done manually based on the previously segmented LV. Subsequently, the mitral and aortic annuli were segmented manually by defining 36 landmarks in altogether 18 2D image planes, rotated around the estimated valvular axis. These landmarks were used to interpolate the aortic annulus onto an ellipse and the mitral annulus onto a cardioid. As the last step, three landmarks were set manually to define the right coronary artery ostium as well as the tips of the anterior and posterior papillary muscles. The right coronary artery was used for the registration of the end-diastolic and end-systolic geometry, necessary to implement 17-segment visualizations of the LV. The 17-segment visualizations of the myocardial wall movement and wall thickness are shown in **Figures 2A,B** for both cohorts

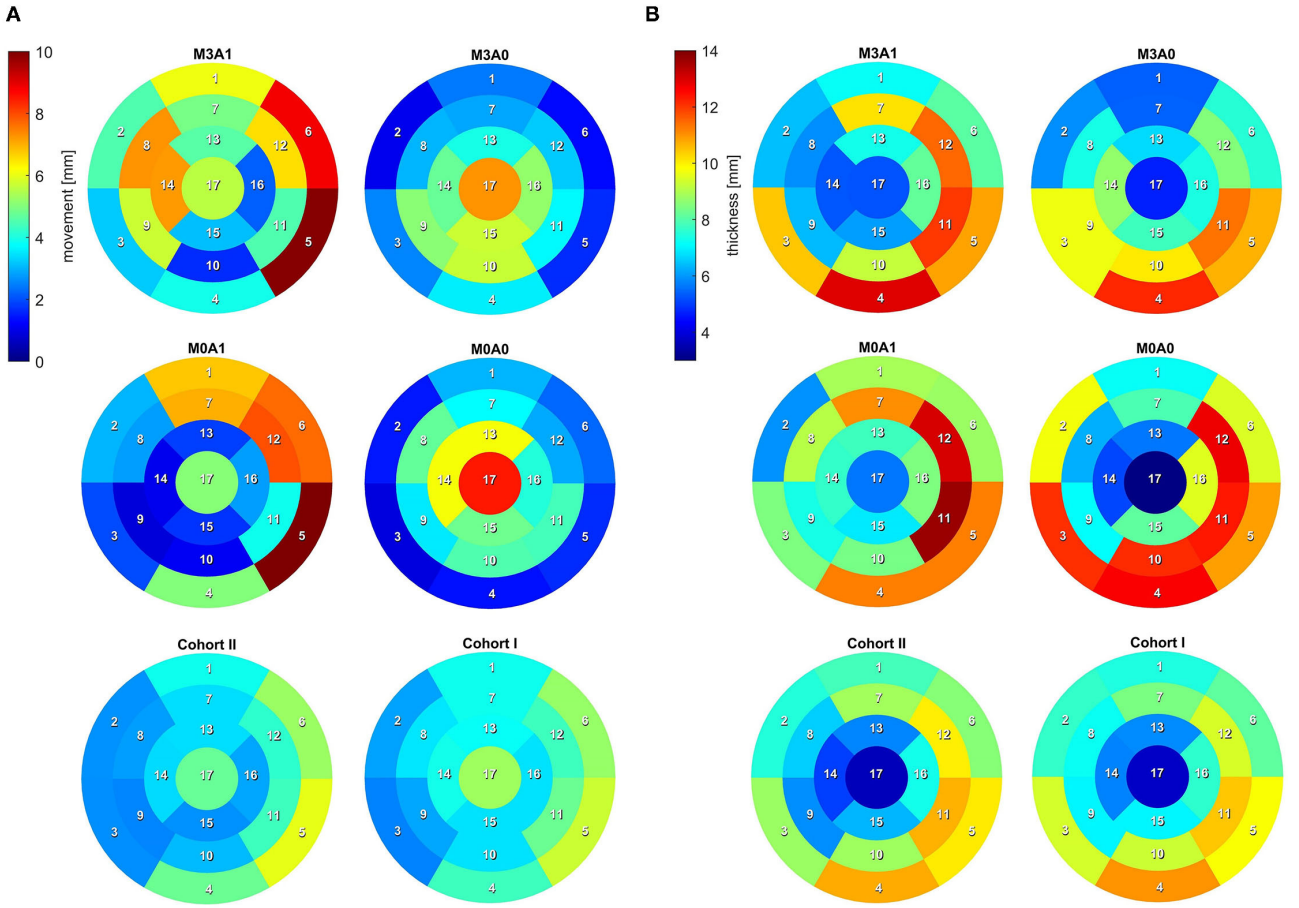

FIGURE 2 | 17-segment representation of **(A)** the myocardial wall movement (averaged wall distance from LVEDV to LVESV per segment) and **(B)** the myocardial wall thickness (segmented for the LVEDV). Data are shown averaged for Cohort I and II as well as for the four representative cases.

and the four representative cases. For details on the 17-segment visualizations, the reader is referred to Cerqueira et al. (45). The segmented lumina were saved as DICOM files and used to generate triangulated surfaces required for the computation of hemodynamics and the measurement of selected geometric parameters including LVEDV and LVESV, LV sphericity index, stroke volume (SV), EF, and the areas of both annuli. It is to note, that LVEDV, LVESV, and SV slightly increase when reconstructing the LV annuli area, while the EF is kept constant (see section 2.4). The sphericity index is calculated based on the LV volume and the LV long axis length according to the empiric formula in Equation (1) (46).

$$\mathrm{SI} = \frac{6 \cdot \mathrm{volume}}{(\mathrm{long\ axis})^3 \cdot \pi} \tag{1}$$

Table 2 summarizes the geometric parameters of both cohorts and the four representative cases. **Figure 3** displays a 3D wire-frame representation of the four investigated cases for visual comparison of the LV sphericity, annuli sizes, and positioning, as well as the location of the papillary muscle tips. Therein, the LVs are simplified by a half-ellipsoid of the case-respective LV volume and sphericity index.

2.4. Modeling Geometry and Motion

The segmentations are used to create well-defined surface meshes of the LVs and to derive the ventricular movement. For the sake of generalization that enables automation, the LVs are aligned *via* the MV centers. End-diastolic and end-systolic geometries are cut 1 cm below the most apical points of the AV and MV in the end-diastolic state and are slightly smoothed, preserving the LV volumes. The boundary points of that cutting plane as well as the segmented annuli are used to reconstruct a well-defined LV surface mesh of the end-diastolic geometry as follows and as schematically shown in **Figure 4A**. First, local coordinate axes are placed into the point clouds of the LV boundary points and both annuli *via* a best-fit plane for point clouds (47). All data is moved to the global Euclidean coordinate system, such that the LV boundary points are centered in the global origin, aligned in the x-y plane, and the vector

connecting the aortic annulus center to the mitral annulus center points in the positive x-direction. Subsequently, points are fitted in between the annuli and the LV boundary points using a cubic polynomial function. A Poisson surface reconstruction algorithm (48) available in the open-source software Meshlab (version 2021.05, ISTI-CNR, Pisa/Rome, Italy) is applied onto the resulting point cloud to retrieve a 3D triangulation of the entire LV with interpolated annuli. To obtain well-defined 2D planes for valve modeling, the annuli are stamped into the LV. Available non-case-specific high-quality segmentations of an LA and an AO were adapted to fit the size and shape of the annuli and are attached at the respective annulus.

TABLE 2 | Geometric parameters of the two investigated cohorts and the four representative cases.

Parameters	Cohort I (A0)	Cohort II (A1)	M3A1	M3A0	M0A1	M0A0
LVEDV (ml)	287 [228 - 349]	284 [233 - 356]	256	248	251	226
LVESV (ml)	208 [167 - 269]	218 [177 - 285]	181	191	181	170
SV (ml)	71 [59 - 84]	66 [54 - 89]	75	57	70	56
EF (%)	24.6 [20.6 - 29.7]	22.8 [19.2 - 27.7]	29.3	23.1	27.7	24.7
EDSI	0.83 ± 0.18	0.83 ± 0.19	0.88	0.76	0.67	0.56
ESSI	0.73 [0.62 - 0.88]	0.77 [0.62 - 0.91]	0.78	0.81	0.64	0.55
MWT (mm)	8.22 [7.21 - 9.28]	8.11 [7.02 - 8.55]	8.57	8.53	9.16	9.27
WM (mm)	3.72 [3.24 - 4.55]	3.63 [2.76 - 4.37]	5.22	3.59	3.95	3.50
ED AAA (cm^2)	5.80 ± 0.98	5.56 ± 0.96	6.30	6.45	5.30	5.32
ED MAA (cm^2)	10.73 ± 2.23	10.63 ± 2.64	12.13	11.91	10.20	8.28

Cohort p-values range from 0.124 to 0.834 and are not considered significant. If a parameter is not normally distributed in either cohort, values are shown as median [IQR] for both cohorts, whereas values are shown as mean ± SD otherwise. Normality was proved by the Shapiro-Wilk test. LVEDV, left ventricular end-diastolic volume; LVESV, left ventricular end-systolic volume; SV, stroke volume; EF, ejection fraction; EDSI, end-diastolic sphericity index; ESSI, end-systolic sphericity index; MWT, mean myocardial wall thickness; WM, mean wall movement; ED AAA, end-diastolic aortic annulus area; ED MAA, end-diastolic mitral annulus area.

The ventricular motion is derived from the cut end-diastolic and end-systolic geometries (**Figure 4B**). With two available states, a deformation field $\mathbf{d}(\mathbf{x})$ constant in time t and dependent on the position $\mathbf{x} = (x, y, z)$ in Euclidean coordinates, can be derived. It is scaled by a time-dependent factor $\alpha(t)$ to obtain a grid velocity vector $\mathbf{v}(\mathbf{x}, t)$ that allows the ventricular volume to follow any specified volume curve at a given EF (Equation 2).

$$\mathbf{v}(\mathbf{x}, t) = \alpha(t) \cdot \mathbf{d}(\mathbf{x}) \tag{2}$$

The deformation field $\mathbf{d}(\mathbf{x})$ is computed as follows. During geometry creation, the cut LVs were positioned in the global origin with the negative z-axis pointing toward the apex. From the highest z-coordinate to 1 cm above the lowest z-coordinate, 100 equidistantly distributed planes, being parallel to the x-y plane, are placed into the LV (as shown in **Figure 4B**, left, blue planes). The center of each plane is calculated, resulting in a centerline (**Figure 4B**, left, black line). Subsequently, the plane-LV intersection lines (**Figure 4B**, left, yellow line) are interpolated onto 180 points, being equidistantly distributed every 2° in azimuthal direction. Likewise, spherical plane cuts are placed in the apex region of the LV every 2° in the azimuthal direction (shown in **Figure 4B**, left, red planes). Again, at the intersection line of each plane with the LV, 25 points are interpolated, being equidistantly distributed in polar angle direction. The LV results to be resampled on a structured grid at 180 points in circumferential direction and 125 points in

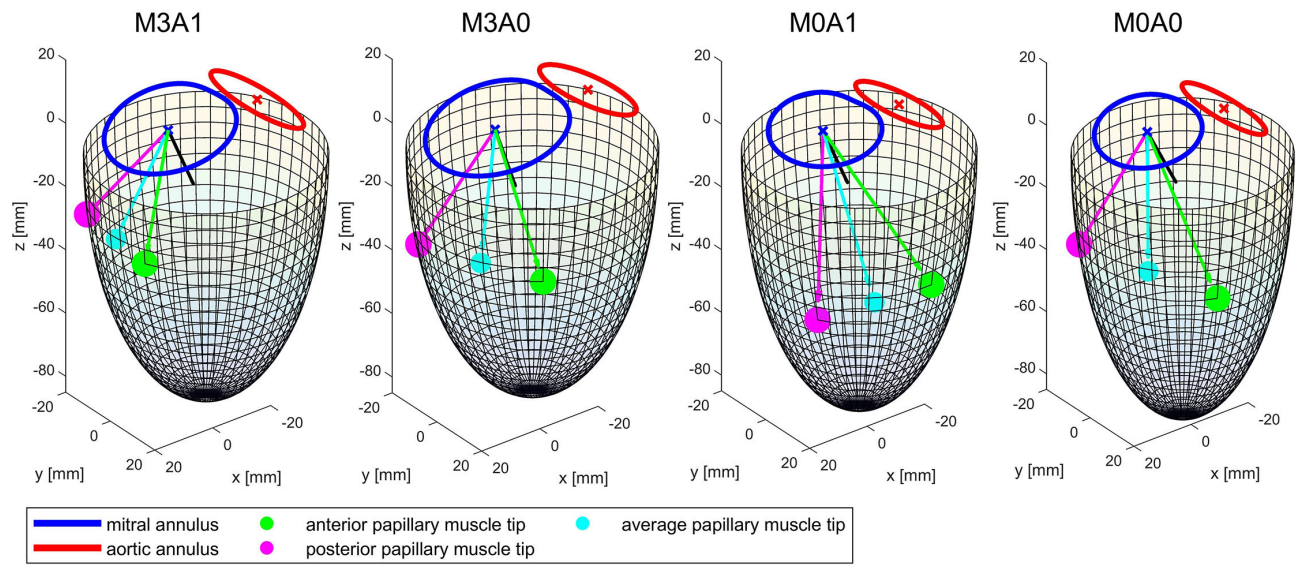

FIGURE 3 | Wireframe visualizations of the four representative cases at the end of systole. The papillary muscle tips are projected on the surface of the half-ellipsoid. The black line shows the vector normal on the mitral annulus plane. The cyan line and dot mark the average of the vectors connecting the papillary muscle tips with the center of the mitral annulus. It represents the direction of an averaged force of the chordae tendineae acting on the MV leaflets.

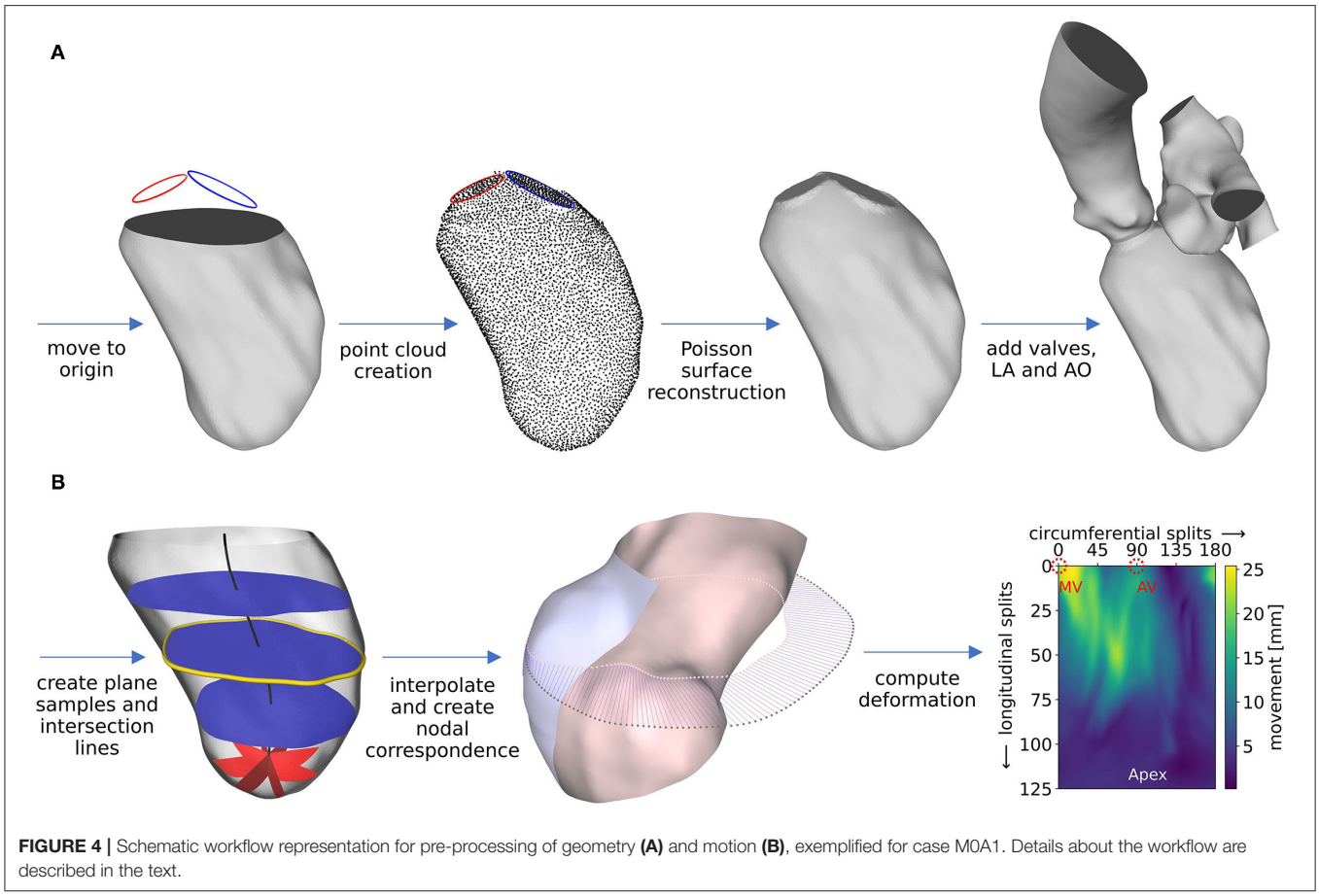

FIGURE 4 | Schematic workflow representation for pre-processing of geometry **(A)** and motion **(B)**, exemplified for case M0A1. Details about the workflow are described in the text.

longitudinal direction, leading to a total of 22,500 sampling points at clearly defined positions. This procedure is applied to the end-diastolic and the end-systolic geometry. **Figure 4B**, mid, shows the LV in the end-systolic state, displayed in a half-section without the annuli region for visualization purposes (inner surface: pink, outer surface: blue). The pink dots mark the interpolated points on an exemplary plane in mid region of the LV that lie on the end-systolic surface. The gray dots mark the corresponding points in the end-diastolic state of the LV. Under the simplifying assumptions of a homogeneous longitudinal deformation and negligence of the torsional LV motion, a point correspondence between the geometries can be deduced by assigning the respective points (as shown in **Figure 4B**, mid, blue lines). Thereby, the deformation field of the cut LVs can be computed (**Figure 4B**, right). It is smoothed making use of a 3x3 Gaussian convolution kernel. The annuli, LA, and AO are simplified to be stiff. The region between the annuli and the LV boundary points is set to move in response to the deformation field at the annuli and the cut LV parts, as calculated by the STAR-CCM+ (version 2020.1, Siemens PLM Software, Plano, TX, USA) internal cubic BSpline morpher.

As the last step, the scaling factor $\alpha(t)$ is derived. It is based on a multiplicative approach and realized by forcing the volume flux of the simulation to follow the volume flux BC and results in Equation (3).

$$\alpha(t) = \frac{V(t + \Delta t) - V(t)}{\Delta t \xi(V^{sim}(t), \Delta t, \mathbf{d}(\mathbf{x}))} \tag{3}$$

where t is time, V is the relative volume as specified in the BC, $V^{sim}(t)$ is the relative volume of the simulated LV, and $\xi(V^{sim}(t), \Delta t, \mathbf{d}(\mathbf{x}))$ is the differential relative volume flux that a deformation along $\mathbf{d}(\mathbf{x})$ over Δt at a specific volume $V^{sim}(t)$ induces. $\xi(V^{sim}(t), \Delta t, \mathbf{d}(\mathbf{x}))$ can be obtained by computing the deformation once for $\alpha(t) = 1$ and equating $\xi(V^{sim}(t), \Delta t, \mathbf{d}(\mathbf{x}))$ to the resulting volume flux $\dot{V}^{sim}(t)$ (Equation 4).

$$\xi(V^{sim}(t), \Delta t, \mathbf{d}(\mathbf{x})) = \dot{V}^{sim}(t) \tag{4}$$

Having obtained $\mathbf{d}(\mathbf{x})$ and $\alpha(t)$, the grid velocity vector (Equation 2) can be computed.

2.5. Governing Equations

An arbitrary Lagrangian-Eulerian method available within the STAR-CCM+ software package is utilized as discretization method. The governing equations consist of the 3*D* incompressible Navier-Stokes equations with moving mesh

for unsteady flow. No body-forces and source terms are added. Therefore, the governing equations for mass (Equation 5) and momentum (Equation 6) conservation in tensor notation read as follows (49).

$$\frac{\partial}{\partial t}\int_V \rho \mathrm{d}V + \int_\Omega \rho(\mathbf{v}-\mathbf{v}_g)\cdot\mathbf{n}\mathrm{d}\Omega = 0 \tag{5}$$

$$\frac{\partial}{\partial t}\int_V \rho\mathbf{v}\mathrm{d}V + \int_\Omega [\rho\mathbf{v}(\mathbf{v}-\mathbf{v}_g)+p\mathbf{I}-\mathbf{T}]\cdot\mathbf{n}\mathrm{d}\Omega = \mathbf{0} \tag{6}$$

Therein, t is time, V is the control volume, Ω is the boundary of the control volume, $\mathbf{n}$ is the outwardly directed vector normal to $d\Omega$, ρ is density, $\mathbf{v}$ is velocity, $\mathbf{v}_g$ is the grid velocity, p is pressure, $\mathbf{T}$ is the viscous stress tensor, and $\mathbf{I}$ is the unit tensor of second order. The viscous stress tensor $\mathbf{T}$ for an incompressible Newtonian fluid with μ being the dynamic viscosity is shown in Equation (7).

$$\mathbf{T} = \mu(\nabla\mathbf{v} + (\nabla\mathbf{v})^T) \tag{7}$$

Blood is modeled as Newtonian fluid with a density of 1,050 kgm^{-3} and a dynamic viscosity of 0.0035 Pas. The Star-CCM+ internal mesher is used to create a polyhedral volume mesh at a base size of 1 mm with a refinement to 0.25 mm in the valve region. Detailed information about the mesh can be found in the **Supplementary Material**.

2.6. Boundary Conditions and Valve Modeling

The ventricular motion is prescribed as BC at the walls. No-slip BCs are furthermore posed at the walls in terms of the relative movement of the fluid to the wall. For the non-MR cases, physiological pressure BCs are extracted from circadapt (35) and posed at the aortic outlet and the atrial inlet (**Figure 5B**). In the MR cases, a mass flux BC is applied at the aortic outlet instead of the pressure BC. It is set to zero in diastole and to the respective proportion of the stroke volume that does not regurgitate, in systole. The regurgitation fraction is calculated based on the MR grade by correlating MR grades of I, II, and III to regurgitation fractions of 15, 30, and 50% (50). To enable comparability, the same pressure BCs and the same qualitative volume curve are utilized for all cases. The volume curve (**Figure 5A**) was obtained from a representative cohort by mapping all individual volume curves onto the same cyclic time, computing the first five Fourier coefficients, and averaging these. The resulting curve is then scaled onto a cyclic time of 0.8 s (75 bpm) and the case-specific EF.

The valves are implemented in a 2D-planar modeling approach (25, 51). Therein, the valve is embodied as a 2D plane, incorporating the projected orifice area of the respective valve. The valve planes are modeled as porous baffle interface, where passing fluid experiences a pressure drop according to Darcy's law (49). Advantages of this 2D-planar model are the comparably easy implementation as well as low computational costs while being able to reproduce large-scale intraventricular flow patterns (51). For the MV, a projected orifice area from the work of Schenkel et al. (25) along with its halfway opened state for opening and closing is depicted. For the AV, the orifice is assumed to be elliptical, as the aortic flow is not of particular interest in this work. Subsequently, 19 intermediate valve shapes are placed in both valve planes (**Figure 5E**). For the AV, they are elliptical with the same aspect-ratios and rising areas. For the MV, they are interpolated *via* a quadratic sine function between the halfway opened and the final projected orifices. By varying the pressure drop at these intermediate valve shapes, valve opening and closing as well as the general valve function is mimicked. Common areas of the MV orifice range between 4.0 and 6.0 cm^2 (52). As all the considered LVs are dilated, a projected orifice area of 5.65 cm^2 for the MV is chosen. This value was obtained by measuring the projected orifice area of 10 segmented MVs of patients with MR and taking the median value. For the AV, an orifice area of 4 cm^2 is chosen, which lies at the upper end of the common range (53). The time intervals of AV opening and closing are set to 57 ms, and 39 ms, respectively, based on measured valve characteristics (54). For the MV, data availability concerning opening and closing times based on medical images is rather poor. Mao et al. (55) measured 50 ms for opening and 94 ms for closing *via* M-mode echo for one patient. In other investigations, porcine MVs (56, 57) or MVs in the ovine heart (58) were regarded. The authors reported opening times between 50 to 100 ms and closing times ranging from 50 to 150 ms. We visually inspected three MRI data sets of our own. Therein, the opening times ranged from 40 to 60 ms and the closing times from 50 to 80 ms at heart rates of 60 to 75 bpm and a temporal resolution of 40 frames per cycle. An opening time of 48 ms and a closing time of 60 ms lead to reasonable valve velocities and transvalvular pressure drops and were thus chosen. The resulting relative areas during valve opening and closing are shown in **Figures 5C,D**.

2.7. Post-processing of the LV Hemodynamics

Beside the large-scale flow patterns and the common clinical measures as transvalvular pressure differences, valve velocities, and E/A ratio, the focus is laid on the intraventricular washout and energetic efficiency. In the first cycle, a passive scalar (passive tracer that does not influence the fluid motion) is placed in the LA fluid to track the path of blood that flows into the LV in the first cycle. Therewith, a contrast agent washout can be mimicked. For the passive scalar, only convective transport is considered. To extrapolate the washout, an exponential function is used (Equation 8).

$$f(t) = e^{-B\cdot t} \tag{8}$$

Therein, t is time and B is the coefficient quantifying the washout. In terms of energetic efficiency, the cycle-averaged kinetic energy is regarded. To get a hold of the energetic loss, the dissipation function Φ is used. It is defined as the double-dot product of the stress tensor σ and the gradient of the velocity vector $\nabla\mathbf{v}$ (30, 59) as shown in Equation 9.

$$\Phi = \sigma \cdot\cdot \nabla\mathbf{v} \tag{9}$$

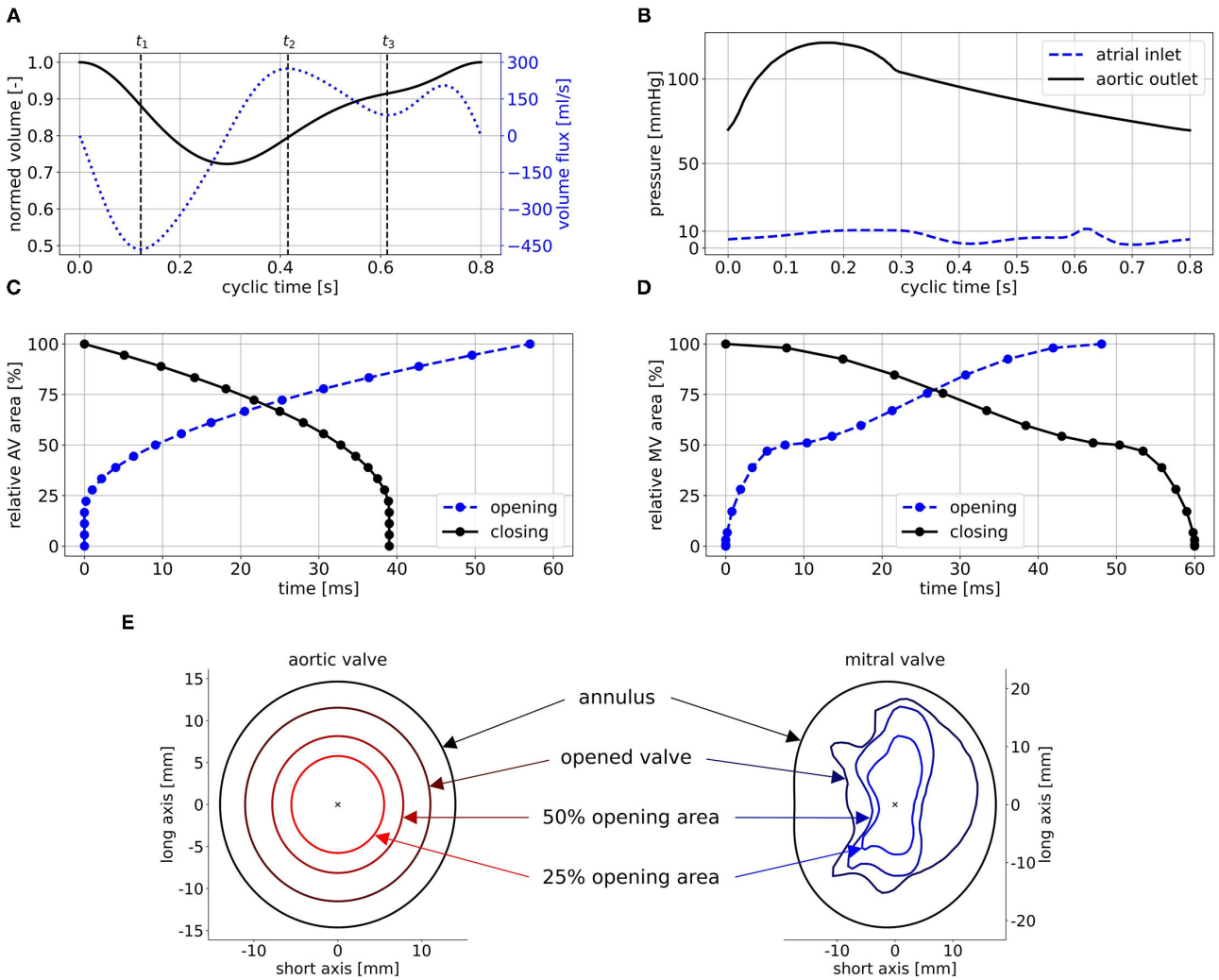

FIGURE 5 | Posed BCs exemplified for case M0A1: **(A)** shows the normed volume curve and the volume flux, **(B)** the physiological pressure BCs, **(C)** and **(D)** the opening and closing times of AV and MV, and **(E)** some intermediate valve shapes of the AV (left) and the MV (right) used to realize opening and closing. Time points t_1, t_2, and t_3 in **(A)** mark peak systole, peak E-wave, and diastasis.

To visualize vortex structures, isosurfaces of the Q-criterion are used. The Q-criterion is computed *via* the second invariant of the velocity gradient tensor (60).

3. RESULTS

For an experienced user, pre-processing from segmentation to a ready to process setup takes 6 - 8 h, depending on the image quality and necessity for manual rework. Computing the deformation requires 2 - 12 h, depending on the desired accuracy. By experience, a spatio-temporal resolution resulting in a 4 h computation is sufficient. The blood flow computations took 25 to 30 h per cycle on 4 nodes at 40 cores (Intel Skylake 6148) at 2.3 GHz on the Emmy system of the North-German Supercomputing Alliance. Concerning the accuracy of the deformation, the mean difference between the imposed and the computed volume curve is below 0.02 ml for all cases. The mean distances between the segmented and the computed end-systolic geometries of the four cases (when creating a nodal correspondence as described in section 2.4) are between 0.14 and 0.52 mm. The mesh quality shows no degeneration, and a mesh independence study was performed (see **Supplementary Material**). As the fluid is initialized in an unphysiological resting state, five cycles were computed in advance to receive a swung in the state. The consecutive eight cycles were then used for the analysis of large-scale flow patterns, energetic performance, and washout.

3.1. Large-Scale Flow Patterns

The intraventricular large-scale flow patterns are qualitatively evaluated by means of streamlines, first cycle diastolic inflowing blood (FCDIB), and Q-criterion. Latter two are provided in

TABLE 3 | Quantitative valve measures of the four representative cases averaged over cycles one to eight.

Parameters	M3A1	M3A0	M0A1	M0A0
v MV peak E-wave (m/s)	0.75 ± 0.10	0.63 ± 0.04	0.61 ± 0.01	0.53 ± 0.01
v MV peak A-wave (m/s)	0.44 ± 0.02	0.36 ± 0.03	0.44 ± 0.01	0.35 ± 0.01
v MV peak sys (m/s)	4.58 ± 0.01	4.46 ± 0.01	-	-
v AV peak sys (m/s)	0.70 ± 0.03	0.56 ± 0.02	1.38 ± 0.04	1.10 ± 0.03
mean E/A ratio (-)	1.72 ± 0.28	1.75 ± 0.16	1.39 ± 0.04	1.49 ± 0.04
Δp MV peak E-wave (mmHg)	0.69 ± 0.25	0.40 ± 0.28	0.67 ± 0.01	0.58 ± 0.01
Δp MV peak sys (mmHg)	77.96 ± 0.56	72.96 ± 0.36	-	-
Δp AV peak sys (mmHg)	0.93 ± 0.04	0.68 ± 0.02	3.91 ± 0.13	2.59 ± 0.01
Δp_B MV peak E-wave (mmHg)	2.30 ± 0.58	1.61 ± 0.19	1.48 ± 0.03	1.11 ± 0.02
Δp_B MV peak sys (mmHg)	84.06 ± 0.35	79.56 ± 0.18	-	-
Δp_B AV peak sys (mmHg)	1.95 ± 0.18	1.25 ± 0.07	7.66 ± 0.42	4.85 ± 0.28

Values are given in mean ± SD. The valve velocities are measured 5 mm downstream of the respective valve center. The transvalvular pressure difference is calculated via the static pressure of two point probes positioned 5 mm upstream and downstream of the respective valve center. MV, mitral valve; AV, aortic valve; Δp_B, pressure loss calculated from Bernoulli via $4v^2$ with the respective valve velocity as specified in this table.

video format in the **Supplementary Material** (videos M3A1-FCDIB, M3A0-FCDIB, M0A1-FCDIB, M0A0-FCDIB, M3A1-Q-criterion, M3A0-Q-criterion, M0A1-Q-criterion, and M0A0-Q-criterion). Quantitative valve measures are displayed in **Table 3**.

During systole, blood is accelerated toward the basal LV regions (**Figure 6** at t_1). In the non-MR cases, all blood is ejected through the LV outflow tract, whereas in the MR cases blood from the posterior-sided regions regurgitates into the LA. The regurgitating jet impinges on the upper LA wall and causes a chaotic, swirling blood motion in the LA. At the onset of diastole, a jet of blood is accelerated from the LA into the LV (**Figure 6** at t_2). In the MR cases, the jet transports vortex tubes, which are leftovers of the chaotic systolic flow field inside the LA caused by the regurgitation (videos M3A1-Q-criterion, M3A0-Q-criterion). Vortices are rolled up along a shear layer that forms between the resting and the inflowing blood. Whereas in the non-MR cases, a distinct ring vortex structure is visible at peak diastole, the ring structure does not entirely evolve in the MR cases (videos M3A1-Q-criterion, M3A0-Q-criterion, M0A1-Q-criterion, and M0A0-Q-criterion). Concerning the E-wave jet, its structure is being disrupted in the MR cases, such that by diastasis, it is split into several parts (**Figure 6** at t_3). In cases M0A1, M0A0, and partially M3A1, the jet impinges on the septal wall in mid region of the LVs in diastasis and is partially redirected toward the apex. In case M3A0, the E-wave jet moves along the posterior wall towards the apex. It is decelerated and decomposes without impinging on any wall. At late diastole (A-wave), a second jet at lower velocities rushes into all LVs. Again, vortices are rolled up along the shear layer, being weaker than the E-wave vortices. At the end of diastole, an unstructured flow field is present in all LVs.

The peak systolic LV volume change rates range from 342 to 465 ml/s (**Figure 7A**). In the non-MR cases, all systolic flow leaves *via* the AV, whereas in the MR-cases, 50 % regurgitates back into the LA. The regurgitating blood exceeds velocities of 4.5 m/s in cases M3A1 and M3A0 (**Table 3**). The systolic AV velocities in the MR cases are lower than those in the non-MR cases (**Figure 7B**). In diastole, flow rates between 201 and 275 ml/s in E-wave and flow rates between 151 and 206 ml/s in A-wave, are present. The MV velocities of the non-MR cases are smooth, peaking at E-wave, and a second time at lower magnitude at A-wave. In the MR cases, the MV velocities follow the same trend, being accompanied by oscillating behavior, especially in early diastole.

3.2. Energetic Performance

The cycle-averaged specific kinetic energy takes a qualitative similar course for all cases (**Figure 8A**). Local maxima are visible in peak systole, early diastole, and late diastole. In between, as the blood decelerates, local minima appear. In the non-MR cases, the global maximum is present at peak systole, whereas in the MR cases it appears at the end of early diastole when most of the vortex tubes were transported into the LV (videos M3A1-Q-criterion, M3A0-Q-criterion). The cycle-averaged specific kinetic energy magnitude is highest for cases M3A1 and M0A1, which are characterized by larger SVs.

Figure 8B displays the cycle-averaged specific energy dissipation. In the MR cases, higher specific energy dissipation is observable in systole. When comparing case M3A1 to M0A1 and case M3A0 to M0A0, where the SVs are very similar, the specific energy dissipation in peak systole is more than two times as high in the MR cases. In diastole, the maximum specific energy dissipation in the MR cases appears during early diastole, whereas in the non-MR cases, it is visible in diastasis. By taking the volume integral of the energy dissipation, a power loss can be calculated (30). The application of a time integral over the cardiac cycle can then reveal the cyclic power loss. Computing that cyclic power loss per case, it is revealed, that over a cardiac cycle, the MR cases dissipate approximately the same amount of energy as they have left at the end of that cycle, whereas the non-MR cases only dissipate around 60 % (cyclic power loss/end-diastolic kinetic energy in M3A1: 92.9; M3A0: 100.5; M0A1: 58.5; and M0A0: 64.1 %).

3.3. Intraventricular Washout

The blood in which the passive scalar was placed to track the fluid motion, the FCDIB, enters the LV in diastole of the first cycle and is ejected in the subsequent cycles (**Figure 9A**). The

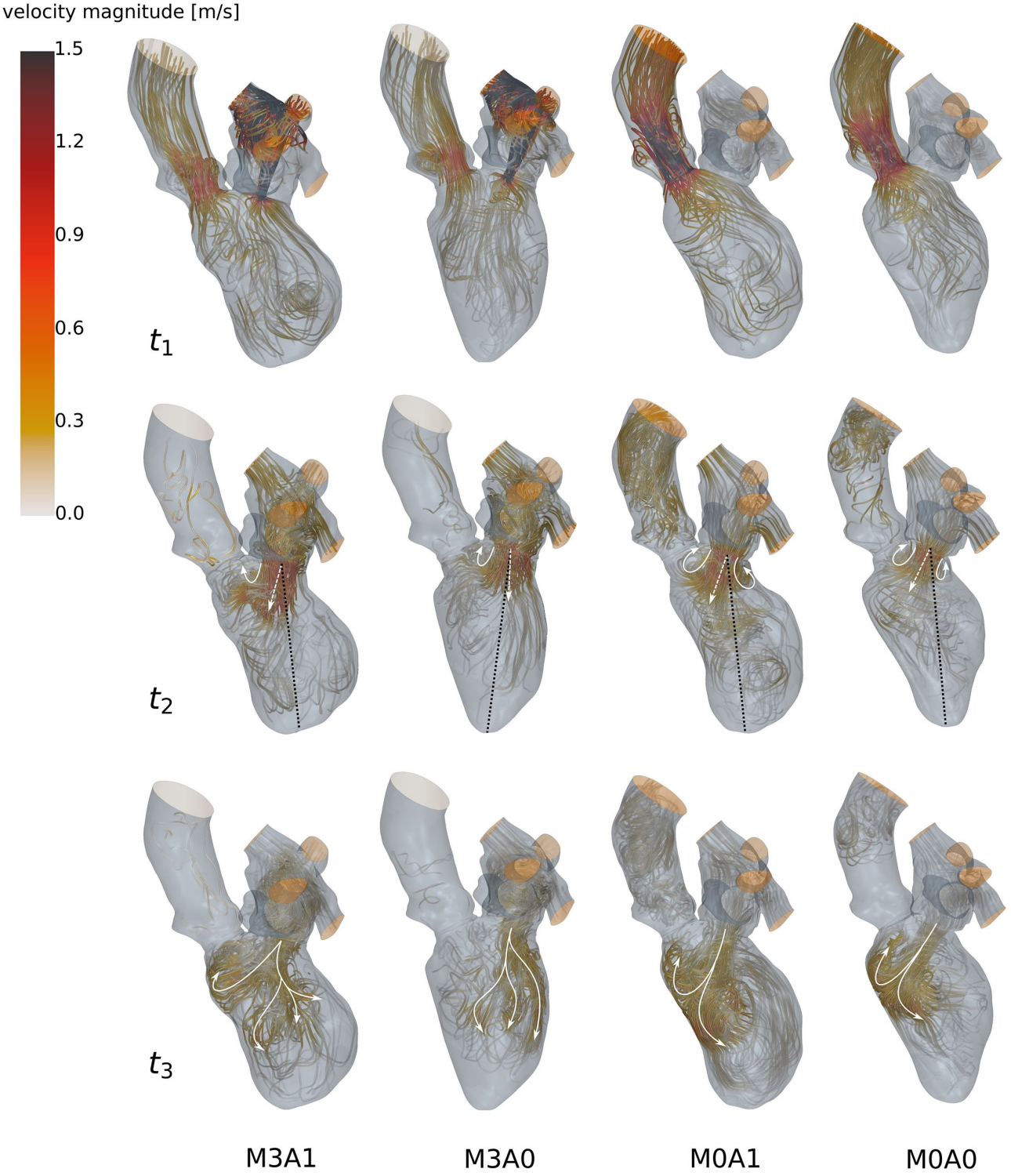

FIGURE 6 | Streamlines of all four cases (left to right: M3A1, M3A0, M0A1, and M0A0) at t_1: peak systole (top), t_2: peak E-wave (mid), and t_3: diastasis (bottom) of the seventh cycle. The white arrow, the dashed white arrow, and the dotted black line at t_2 qualitatively show the vortex formation, the orientation of the E-wave jet, and the ventricular axis from MV center to apex. The white arrows at t_3 schematically display the path of the E-wave jet. At low velocity regions, streamlines are made transparent and velocities above 1.5 m/s are clipped.

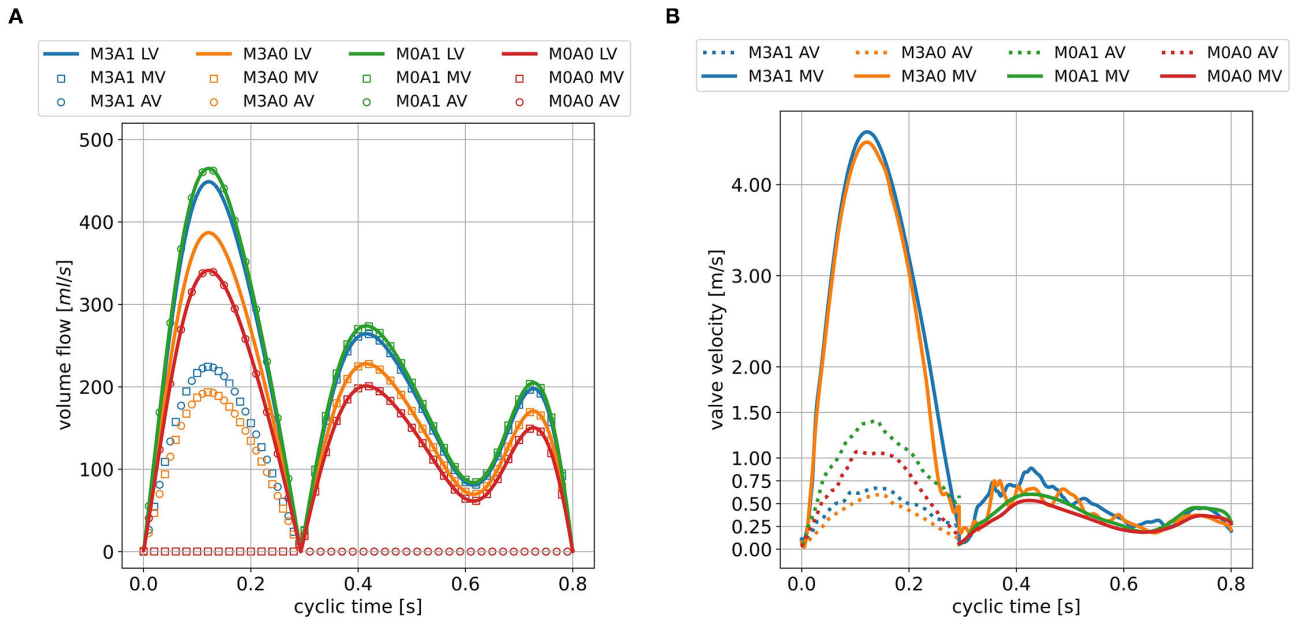

FIGURE 7 | LV volume change and valve volume flow rates **(A)** and valve velocities **(B)** in the seventh cycle for all cases. The valve velocities are measured 5mm downstream of the respective valve center and are only displayed at points in time when the respective valve is open.

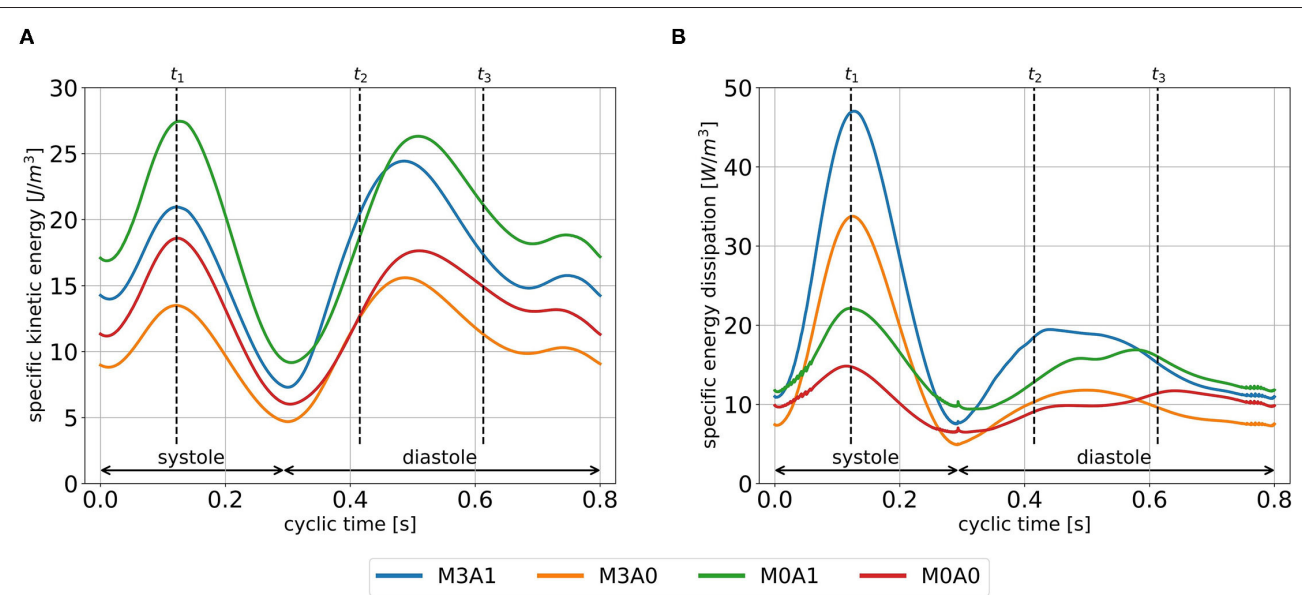

FIGURE 8 | Specific kinetic energy course **(A)**, and specific energy dissipation **(B)** averaged over cycles one to eight for all cases. Time points t_1, t_2, and t_3 mark peak systole, peak E-wave, and diastasis, respectively.

ejection evolutes in a staircase-like manner with reducing stair sizes. Characteristic washout measures are displayed in **Table 4**. The 99 % washout is computed *via* the exponential fit function in Equation (8). The R^2 values (quality criterion for regression models) for the exponential fits are above 97 % for all cases.

The ejected fractions of FCDIB per cycle are displayed in **Figure 9B**. Cases M3A1, M0A1, and M0A0 behave similar in a decreasing exponential shape, whereas the trend is linear in case M3A0. As a result, similar fractions of FCDIB inside the LVs are present at the end of cycle eight at 6.4 s (**Figure 9A**). A slightly worse washout is observed in the non-aneurysmatic cases M3A0 and M0A0. At the end of cycle eight, approximately 5 % more FCDIB are still present in the LVs in the non-aneurysmatic cases. They furthermore incorporate lower medium velocities in the

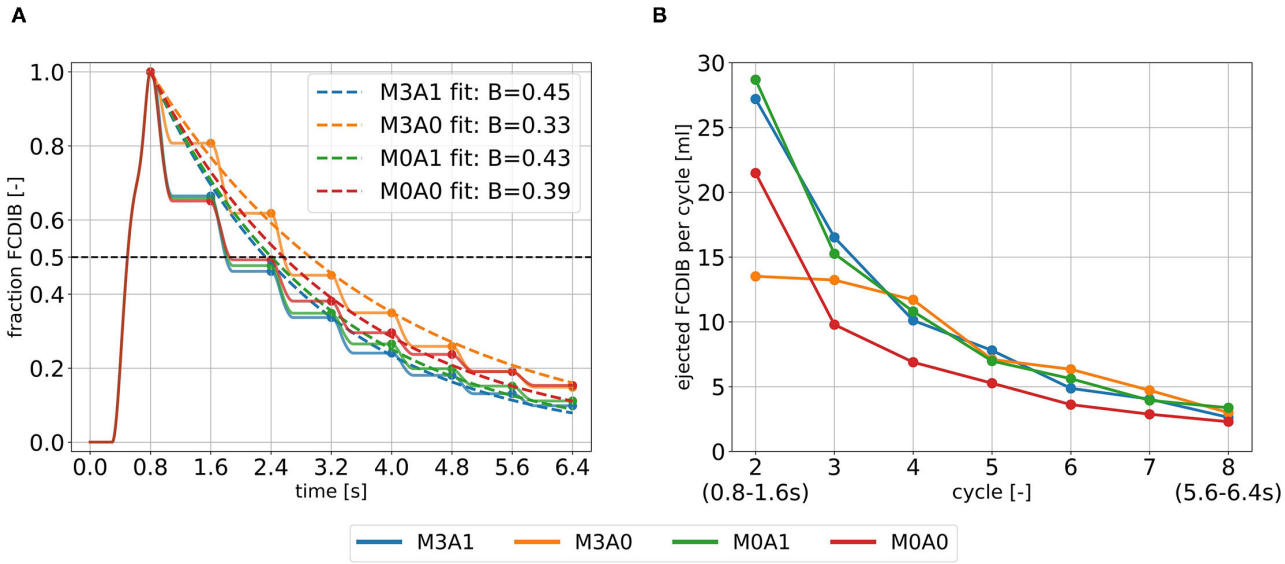

FIGURE 9 | Intraventricular washout of FCDIB until the end of cycle eight **(A)** and the respective ejected fractions of FCDIB per cycle **(B)**. To perform the exponential fit, the FCDIB fractions at the end of each cycle were used [marked as dots in **(A)**].

TABLE 4 | Intraventricular washout measures of the four representative cases.

Parameters	M3A1	M3A0	M0A1	M0A0
direct flow rate (%)	33.5	19.3	34.2	34.9
direct flow rate (ml)	27.2	13.5	28.7	21.5
half-life FCDIB (s)	1.80	2.57	1.82	1.85
99% washout FCDIB (s)	10.95	14.88	11.46	12.52

The half-life marks the time when 50% of FCDIB are ejected. The 99% washout marks the time when 99 % of FCDIB are ejected and is computed via an exponential fit function (Equation 8). FCDIB, first cycle diastolic inflowing blood.

apex region during systole and diastole and a slightly increased FCDIB accumulation in that region at the end of cycle eight (see **Supplementary Material**).

Figure 10 shows the FCDIB over several points in time of the first three cycles. At end systole of the first cycle (0.29 s), the entire LA is filled with the passive scalar. In peak E-wave of the first cycle (0.42 s), the FCDIB jet rushes into the LV. In the non-MR cases, the jet is coherent, whereas in the MR cases, it already starts disintegrating. By the end of the first cycle (0.8 s), regions the FCDIB did not reach are visible (see red marked contours in **Figure 10**). These regions differ from case to case (M3A1: concentrated lateral region; M3A0: septal and apical regions; M0A1: elongated lateral region; M0A0: lateral and apical regions) and are partially still visible in peak systole of the second cycle (0.92 s). It furthermore becomes visible, that the non-MR cases eject a larger fraction of FCDIB into the AO than the MR cases, in which some of the FCDIB regurgitates into the LA. At the end of the third cycle (2.4 s), the remaining FCDIB is distributed mostly homogeneous inside the LVs.

4. DISCUSSION

In this study, we propose a moderate complexity, generally applicable, and quick to preprocess modeling approach to calculate intraventricular hemodynamics with image-based CFD. The ventricular movement is derived from the segmented end-systolic and end-diastolic geometries and prescribed in an arbitrary Lagrangian-Eulerian formulation at the boundaries. The valves are modeled as 2D orifices, whereat the MV is represented by a projected orifice shape. LA and AO geometries are attached at the annuli and physiological pressure curves, respective mass flow rates are posed as inflow and outflow BCs. This methodology requires only end-diastolic and end-systolic geometries and is currently focused on CCT, which typically has a rather low temporal resolution due to the desired minimization of radiation dose and technical limitations. However, it is applicable in the same manner to MRI and echocardiographic data. To demonstrate the technical and clinical feasibility, the methodology was applied to four cases, each representing a subcohort of a pathological state of heart failure patients after myocardial infarction.

4.1. Intraventricular Hemodynamics

We evaluated the intraventricular hemodynamics of the four representative cases in terms of large-scale flow patterns, energetic behavior, and washout. The most noticeable observations were made in the MR cases. In these, no clear ring vortex structure evolves during the diastolic inflow. The E-wave jet is disrupted by the transported vortex tubes and the accompanying swirling motion supposedly prevents a distinct shear layer development, leading to fragmentary vortex formation. In the study of Le and Sotiropoulos (28), similar observations were made for wall-extracted secondary vortex

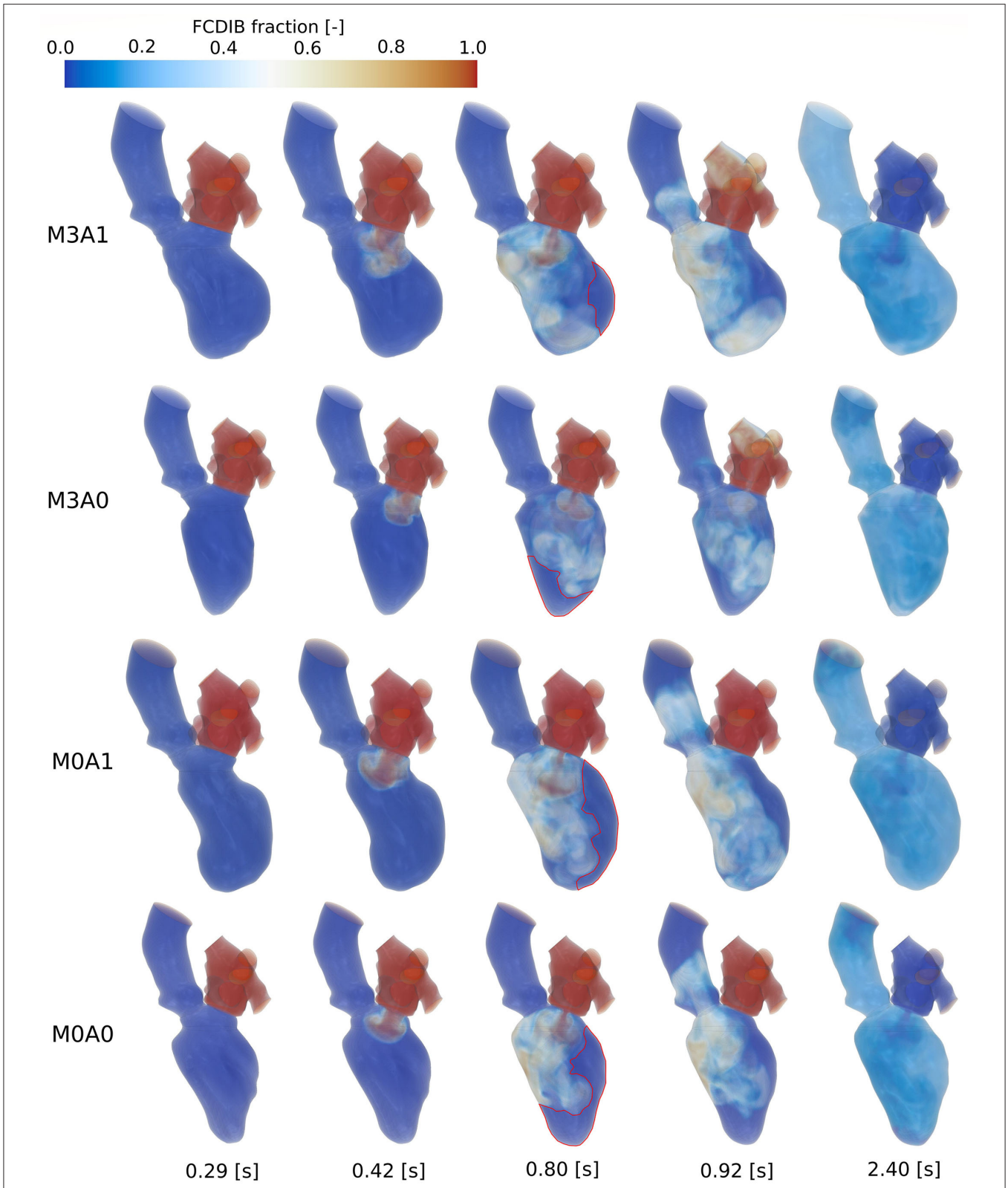

FIGURE 10 | FCDIB for all cases (top to bottom: M3A1, M3A0, M0A1, M0A0) from left to right at end systole of the first cycle (0.29 s), peak E-wave of the first cycle (0.42 s), end diastole of the first cycle (0.8 s), peak systole of the second cycle (0.92 s), and the end of the third cycle (2.4 s). Red contours at end diastole of the first cycle mark regions with poor washout, which are associated with a higher risk of thrombus formation.

tubes that cause instabilities in the circumferential direction of the vortex ring. Subsequently, the E-wave jet is decomposed in the temporal course of diastole in the MR cases, resulting in an unstructured, vortical flow. In terms of energetic behavior, the MR cases have their global specific kinetic energy maximum in early diastole, whereas it appears in systole in the non-MR cases. These observations correlate well with the findings of Al-Wakeel et al. (15), where MR patients were examined with 4D flow MRI. Therein, an unstructured diastolic LV flow field with several smaller vortex structures and an increased early diastolic kinetic energy state in MR patients that reduces after MV surgery were seen. The increased early diastolic kinetic energy state might be explained by the vortex tubes flowing from the LA into the LV during early diastole, storing kinetic energy. Regarding the temporal course of specific energy dissipation in diastole, the maximum values in the MR cases appear in early diastole, whereas it peaks in diastasis in the non-MR cases. Possible explanations can be found in the early diastolic decaying vortex structures and the jet impingement on the septal wall in diastasis. It furthermore strikes out, that the MR cases reveal a significantly increased specific energy dissipation in systole. To make estimates about the overall degree of abnormality of the energetic behavior in these pathological cases, a comparison to energetic states of a healthy LV analyzed in the same modeling approach seems promising.

In addition to the findings when comparing MR to non-MR cases, two further interesting aspects are to highlight. First concerns the intraventricular washout. Our results suggest that considering several cycles might provide a more detailed view of the washout process. When tracking the FCDIB over several cycles, it strikes out that case M3A0 has a significantly lower direct flow rate, but the fraction of FCDIB inside the LV catches up to the other cases by the end of the eighth cycle. We extrapolated the washout *via* a straightforward exponential fit function. The resulting fits overestimate FCDIB in the first cycles and underestimate FCDIB in the later ones or vice versa (**Figure 9A**). Such a discrepancy is likely to be transferred onto the extrapolation. However, this deviation can potentially be overcome by computing more cycles or applying enhanced fit functions (e.g., the sum of two time-weighted exponential functions), which might be interesting as a 99 % washout time could serve as a valuable metric for clinicians to quantify blood residence times, that CFD can provide.

In terms of tracking the FCDIB, it is also noticeable that the aneurysmatic LVs are characterized by a better washout. At first sight, this seems contra-intuitive. Yet, differences are small, and it must be taken into account that the non-aneurysmatic cases have higher EFs and SVs. Furthermore, all LVs suffered a myocardial infarction and are dilated with reduced EFs, thus being characterized by a pathological state.

The second aspect relates to the regions the FCDIB did not reach at the end of the first cycle, which are partially still present in the systole of the second cycle (**Figure 10**). These regions can be associated with a worsened washout. In cases M3A1, M0A1, and M0A0, mainly lateral regions are affected. In these cases, the E-wave jets are oriented away from the lateral regions toward the septal wall (**Figure 6** at t_2), suggesting a correlation between E-wave jet orientation and washout. Based on this, the question arises as to what determines the inflow orientation. We identify two potentially interesting relationships in this study. First concerns the deformation. In cases M3A1 and M0A1, the strongest deformation appears in septal and inferior regions, e.g., segments 5 and 6 (**Figure 2A**). As these regions expand strongest in diastole, they are prone to have a suction effect on the inflow. The second relates to the angle β between the normal on the MV plane and a vector connecting the MV center to the apex at LVEDV. This angle lies between 30° and 31° for cases M3A1, M0A1, and M0A0, whereas it is only 14.3° for case M3A0. The large angles indicate an inflow being oriented toward the septal walls. A link between the inflow angle and an abnormal LV flow field was also observed in the study of Witschey et al. (14). Such a causal chain from local deformation and angle β *via* the inflow orientation toward the intraventricular washout would be insofar interesting, as it links purely geometric metrics with the washout. This would allow clinical assessments without the need for actual flow measurements or CFD. However, for further investigations of such a relationship, a larger database needs to be considered and the influence of neglecting the 3D valve topology must be reviewed in this context.

It is to say, that this pilot study is based on a small number of investigated clinical cases and is thus not suited for statistical analysis and generalized statements of findings regarding intracardiac flow feature differences between the subcohorts. In general, the question arises whether intracardiac flow measures may, besides the usage to quantify and analyze the LV flow field, serve as biomarkers for an early prediction of LV diseases. This topic is currently discussed (9, 24, 61). As this study only covers snapshots of the LV states, the progression of the diseases cannot be assessed. However, we are aiming to make use of the low pre-processing time of the presented methodology to investigate the entire available LV cohort and search for patterns in different manifestations of the diseases, which might provide further insights.

4.2. Methodology

The proposed computational framework is set up at moderate complexity to obtain reasonable results for the intraventricular hemodynamics based on CCT in clinically realizable time frames. A modeling approach of this sort comes at the price of simplifications, which must be critically reviewed. In terms of the geometric level of detail, the negligence of papillary muscles and trabeculae must be noted. Lantz et al. (62) and Vedula et al. (63) simulated LV flow dynamics based on high-resolution CCT, including papillary muscles and trabeculae, and compared it to the same LVs excluding these features. In both publications, local flow differences become visible and, e.g., stagnant flow in the papillary muscle region (62) and an increased viscous dissipation rate in early diastole (63) are observed in the detailed LVs. Yet, for example, the specific kinetic energy course did not extensively differ between the cases in the study of Vedula et al. (63). Including papillary muscles and trabeculae and investigating their influence is planned in upcoming model development steps.

Validation of the 2D valves is currently ongoing. We incorporated 2D generic valves as adequate 3D patient-specific

valves could not be obtained for all cases from the available CCT data. We followed the approaches by Schenkel et al. (25) and Daub et al. (51) that implemented the 2D-planar valve model in previous studies. As the valves are simplified, not the entire MV apparatus, e.g. chordae tendineae, is modeled. The inclusion of the chordae into the MV model could however be necessary for biomechanical studies (64) or realization of a 3D MV movement using fully-coupled FSI (55). Yet, it is to note, that Morud et al. (65) found a negligible impact of chordae on the systolic intraventricular flow. Including chordae can furthermore be associated with time-consuming efforts in pre-processing. In case our ongoing studies indicate non-negligible differences between the valve models, the model will be adapted.

At the annuli, we attached available non-patient-specific high-quality segmentations of LA and AO. The aortic flow field and the patient-specific AO geometry are not of particular interest in this study. Concerning the LA, Mihalef et al. (66) compared vortex structures of the same configuration with and without including the LA. In their study, they observed that the main differences in terms of vortical flow come from the transported vorticity from the LA into the LV. Schenkel et al. (25) demonstrated a dependency of the LV flow field on the LA geometry by incorporating two different generic LA structures. The extent to which the LA geometry must be patient-specific and whether its motion must be represented to adequately model the LA-LV coupling remains to be clarified. The same applies to a representation of the arterial system at the AO outlet and the concomitant ventriculo-arterial coupling.

The ventricular motion is based on the end-diastolic and end-systolic geometries under the simplifying assumption of a longitudinal homogeneous contraction and negligence of the torsional motion. Including intermediate states would be desirable but was not adequately possible due to the temporal resolution of the CCT data. Yet, the imposed ventricular deformation is able to follow the specified volume curve at high precision. Additionally, the ventricular movement, with the simulation starting at the onset of systole at LVEDV, is able to closely match the respective segmented end-systolic geometry. Under these considerations, the prescribed motion can be verified. The mesh quality preservation and the results of the mesh independence study furthermore confirm an adequate computational mesh. It is left to point out, that in this pilot study we focused on establishing the workflow and performing a proof of concept. Further model enhancements and detail inclusion will be the subject of future developments.

In this study, we focused on the evaluation of the intraventricular flow field and investigated several hemodynamic parameters. The model allows the examination of further quantities like wall-shear-stress or blood residence times, such that in total, a broad range of hemodynamic markers is covered. Yet, to be able to investigate, for example, the pressure-volume loop, valve opening and closing times or tissue stresses and strains, complex modeling approaches that include tissue mechanics and potentially electrophysiology are required. Such modeling approaches are pursued, e.g., by Karabelas et al. (67), who introduced an electro-mechano-fluidic model or Mao et al. (55), who developed a fully-coupled FSI model including both valves. Despite having the potential to describe all aspects of cardiac physiology, these multi-physics models tend to have high requirements on data quality, introduce additional modeling uncertainties, and require additional resources for pre-processing, model parameterization, and computation, which might, however, impact clinical usability.

In comparison to *in vivo* measurements of hemodynamic quantities *via* flow MRI (16) or echocardiography (13, 23), the proposed computational framework introduces uncertainties due to model simplifications, especially in terms of anatomical shapes and resolution of fine structures (e.g., chordae tendineae, trabeculae, and valve leaflets). On the other hand, it allows for the computation of hemodynamics at considerably higher spatio-temporal resolution and enables a direct calculation of pressure fields and intraventricular washout over various cardiac cycles, whereas image-based *in vivo* measurements are unable to directly measure pressure fields. To make use of these advantages of the proposed CCT-based CFD framework, a validation with, e.g., 4D flow MRI is required to quantify the impact of the mentioned simplifications. Such a validation is planned in the near future, taking into consideration various hemodynamic parameters which are associated with pathological LVs.

4.3. Clinical Feasibility

The proposed computational framework is motivated by developing image-based CFD models toward a clinical feasibility. Beside data availability and model quality, the required working hours, computing time, and computational expenses affect the prospective clinical feasibility. Currently, pre-processing by an experienced user takes 6-8 h to get from medical images to a simulation setup, which is ready for computation. Further automation in the segmentation and pre-processing procedures offers the potential to reduce these working hours as well as to minimize possible impacts of operator-dependent manual interactions. Inter-user variability is known in the context of segmentation or surface preparation of geometric models, influencing the resulting cardiovascular structures and therewith the intraventricular flow (68, 69). The computation time per cycle at the specified CPU number results in computational costs of approximately 150 to 200 € per cycle at the North-German Supercomputing Alliance. In this study, we primarily focused on computational accuracy. An optimization toward low computational costs can significantly reduce these expenses.

Besides the costs per cycle, the investigated number of cycles is crucial for overall cost estimation. In this work, we computed five cycles in advance before assuming a swung in the state and considering the results for the evaluation. To review whether less than five cycles would be sufficient to receive a swung in state, we computed the mean cyclic energy for each of these in advance compute five cycles and compared it to the mean cyclic energy of the consecutive eight cycles that were used for the evaluation. The relative changes were 34.6–38.3% for the first cycle and ranged from 0.6–9.7% for cycles two to five. From an energetic perspective, it thus seems justifiable to only compute one cycle in advance for LVs at comparable volumes and EFs.

In the evaluated eight cycles, the specific kinetic energy, specific energy dissipation, and the averaged valve velocities

and transvalvular pressure drops show sufficiently small cyclic deviations to be evaluated in solely one cycle. The large-scale flow patterns behave qualitatively alike over all cycles, considering cyclic variations, which are also emphasized by Chnafa et al. (26). In terms of intraventricular washout, our results indicate that considering several cycles might provide a more detailed view of the washout process.

Taking these considerations into account, the here proposed computational framework yields orders of magnitude for pre-processing, solving, and post-processing, that are within range of clinical feasibility. Furthermore, there is still potential to minimize the need for manual interaction as well as pre-processing and computational times.

5. CONCLUSION

In this study, we propose a CCT-based CFD framework to compute intraventricular hemodynamics on a patient-specific level to complement the informative value of CCT. The computational framework enables pre-processing and computational times, respective expenses at an order of magnitude that is within reach of clinical feasibility. The technical feasibility was verified by means of four cases, each representing a subcohort with a respective pathology. Where possible, the plausibility of the results was confirmed by comparison with other publications. Comparing the four cases, the most noticeable observations were made in the LVs with MR. Developments toward the inclusion of geometric details and patient-specific valve geometries have the potential to provide further insights into the disease. We conclude the proposed computational framework to have a good potential of becoming clinically usable as it represents a fair balance between model accuracy and overall expenses. Further model refinement, workflow automation, computation acceleration, and a validation with 4D flow MRI are the next steps toward enabling a clinical translation and making image-based CFD usable to support clinical diagnosis and treatment planning in everyday routine.

DATA AVAILABILITY STATEMENT

The data sets (geometries and applied boundary conditions) presented in this study are provided as open data in an online repository. The name of the repository and accession number can be found at: https://doi.org/10.6084/m9.figshare.16964929.

ETHICS STATEMENT

The studies involving human participants were reviewed and approved by the Ethics Committee-Charité Universitätsmedizin Berlin (EA2/177/20). The study was performed according to the principles of the Declaration of Helsinki.

AUTHOR CONTRIBUTIONS

LG, NS, CK, and TK: conceptualization. LO, AS, NS, and CK: data curation. LO, LT, KV, JB, and LG: formal analysis and methodology. LG and TK: funding acquisition and supervision. LO and AS: visualization. LO, NS, CK, and LG: investigation. LO, KV, and LG: writing original draft. All authors review and editing. All authors contributed to the article and approved the submitted version.

FUNDING

This study was funded by the Einstein Center Digital Future and by the DFG grants for the project Nr. 465178743 in frames of the SPP2311.

ACKNOWLEDGMENTS

The work was supported by the North-German Supercomputing Alliance (HLRN).

SUPPLEMENTARY MATERIAL

The Supplementary Material for this article can be found online at: https://www.frontiersin.org/articles/10.3389/fcvm.2022.828556/full#supplementary-material

Supplemental Data

A mesh independence study and a regional ventricular analysis as well as the videos of the FCDIB (M3A1- FCDIB, M3A0-FCDIB, M0A1-FCDIB, and M0A0-FCDIB) and the Q-criterion (M3A1-Q-criterion, M3A0-Q-criterion, M0A1-Q-criterion, and M0A0-Q-criterion) are provided as supplemental data.

REFERENCES

1. Driessen RS, Danad I, Stuijfzand WJ, Raijmakers PG, Schumacher SP, van Diemen PA, et al. Comparison of coronary computed tomography angiography, fractional flow reserve, and perfusion imaging for ischemia diagnosis. *J Am Coll Cardiol.* (2019) 73, 161–173. doi: 10.1016/j.jacc.2018.10.056
2. Taron J, Foldyna B, Eslami P, Hoffmann U, Nikolaou K, Bamberg F. Cardiac computed tomography – more than coronary arteries? a clinical update. *RöFo – Fortschritte auf dem Gebiet der Röntgenstrahlen und der bildgebenden Verfahren.* (2019) 191:817–26. doi: 10.1055/a-0924-5883
3. Vahanian A, Beyersdorf F, Praz F, Milojevic M, Baldus S, Bauersachs J, et al. 2021 ESC/EACTS Guidelines for the management of valvular heart disease: developed by the Task Force for the management of valvular heart disease of the European Society of Cardiology (ESC) and the European Association for Cardio-Thoracic Surgery (EACTS). *Eur Heart J.* (2021) 43:Ehab395. doi: 10.1093/eurheartj/ehab395
4. Franke B, Brüning J, Yevtushenko P, Dreger H, Brand A, Juri B, et al. Computed tomography-based assessment of transvalvular pressure

gradient in aortic stenosis. *Front Cardiovasc Med.* (2021) 8:849. doi: 10.3389/fcvm.2021.706628
5. Chiocchi M, Ricci F, Pasqualetto M, D'Errico F, Benelli L, Pugliese L, et al. Role of computed tomography in transcatheter aortic valve implantation and valve-in-valve implantation: complete review of preprocedural and postprocedural imaging. *J Cardiovasc Med (Hagerstown).* (2020) 21, 182–91. doi: 10.2459/JCM.0000000000000899
6. Lin E, Alessio A. What are the basic concepts of temporal, contrast, and spatial resolution in cardiac CT? *J Cardiovasc Comput Tomography.* (2009) 3:403–8. doi: 10.1016/j.jcct.2009.07.003
7. Lantz J, Gupta V, Henriksson L, Karlsson M, Persson A, Carlhäll CJ, et al. Intracardiac flow at 4D CT: comparison with 4D flow MRI. *Radiology.* (2018) 289:51–8. doi: 10.1148/radiol.2018173017
8. Schoepf UJ, Varga-Szemes A. 4D flow meets CT: can it compete with 4D flow MRI? *Radiology.* (2018) 289:59–60. doi: 10.1148/radiol.2018181210
9. Pedrizzetti G, La Canna G, Alfieri O, Tonti G. The vortex – an early predictor of cardiovascular outcome? *Nat Rev Cardiol.* (2014) 11:545–53. doi: 10.1038/nrcardio.2014.75
10. Poh KK, Lee LC, Shen L, Chong E, Tan YL, Chai P, et al. Left ventricular fluid dynamics in heart failure: echocardiographic measurement and utilities of vortex formation time. *Eur Heart J Cardiovasc Imag.* (2011) 13:385–93. doi: 10.1093/ejechocard/jer288
11. Abe H, Caracciolo G, Kheradvar A, Pedrizzetti G, Khandheria BK, Narula J, et al. Contrast echocardiography for assessing left ventricular vortex strength in heart failure: a prospective cohort study . *Eur Heart J Cardiovasc Imag.* (2013) 14:1049–60. doi: 10.1093/ehjci/jet049
12. Vellguth K, Brüning J, Goubergrits L, Tautz L, Hennemuth A, Kertzscher U, et al. Development of a modeling pipeline for the prediction of hemodynamic outcome after virtual mitral valve repair using image-based CFD. *Int J Comput Assist Radiol Surg.* (2018) 13:1795–805. doi: 10.1007/s11548-018-1821-8
13. Faludi R, Szulik M, D'hooge J, Herijgers P, Rademakers F, Pedrizzetti G, et al. Left ventricular flow patterns in healthy subjects and patients with prosthetic mitral valves: an in vivo study using echocardiographic particle image velocimetry. *J Thoracic Cardiovasc Surg.* (2010) 139, 1501–10. doi: 10.1016/j.jtcvs.2009.07.060
14. Witschey WRT, Zhang D, Contijoch F, McGarvey JR, Lee M, Takebayashi S, et al. The influence of mitral annuloplasty on left ventricular flow dynamics. *Ann Thoracic Surg.* (2015) 100:114–21. doi: 10.1016/j.athoracsur.2015.02.028
15. Al-Wakeel N, Fernandes JF, Amiri A, Siniawski H, Goubergrits L, Berger F, et al. Hemodynamic and energetic aspects of the left ventricle in patients with mitral regurgitation before and after mitral valve surgery. *J Magn Resonan Imag.* (2015) 42:1705–12. doi: 10.1002/jmri.24926
16. Miyajima K, Urushida T, Ito K, Kin F, Okazaki A, Takashima Y, et al. Four-dimensional flow magnetic resonance imaging visualizes reverse vortex pattern and energy loss increase in left bundle branch block. *EP Europace.* (2021) 12:euab299. doi: 10.1093/europace/euab299
17. Carlhäll CJ, Bolger A. Passing strange: flow in the failing ventricle. *Circulat Heart Failure.* (2010) 3:326–31. doi: 10.1161/CIRCHEARTFAILURE.109.911867
18. Ebbers T, Wigström L, Bolger AF, Wranne B, Karlsson M. Noninvasive measurement of time-varying three-dimensional relative pressure fields within the human heart. *J Biomech Eng.* (2002) 124:288–93. doi: 10.1115/1.1468866
19. Kim WY, Walker PG, Pedersen EM, Poulsen JK, Oyre S, Houlind K, et al. Left ventricular blood flow patterns in normal subjects: A quantitative analysis by three-dimensional magnetic resonance velocity mapping. *J Am College Cardiol.* (1995) 26:224–38. doi: 10.1016/0735-1097%2895%2900141-L
20. Kilner PJ, Yang G, Wilkes AJ, Mohiaddin RH, Firmin DN, Yacoub MH. Asymmetric redirection of flow through the heart. *Nature.* (2000) 404:759–61. doi: 10.1038/35008075
21. Mohiaddin RH. Flow patterns in the dilated ischemic left ventricle studied by MR imaging with velocity vector mapping. *J Magn Resonan Imag.* (1995) 5:493–8. doi: 10.1002/jmri.1880050503
22. Walker PG, Cranney GB, Grimes RY, Delatore J, Rectenwald J, Pohost GM, et al. Three-dimensional reconstruction of the flow in a human left heart by using magnetic resonance phase velocity encoding. *Ann Biomed Eng.* (1995) 24:139–47. doi: 10.1007/BF02771002
23. Vallelonga F, Airale L, Tonti G, Argulian E, Milan A, Narula J, et al. Introduction to hemodynamic forces analysis: moving into the new frontier of cardiac deformation analysis. *J Am Heart Assoc.* (2021) 10:e023417. doi: 10.1161/JAHA.121.023417
24. Mele D, Smarrazzo V, Pedrizzetti G, Capasso F, Pepe M, Severino S, et al. Intracardiac flow analysis: techniques and potential clinical applications. *J Am Soc Echocardiography.* (2019) 32:319–32. doi: 10.1016/j.echo.2018.10.018
25. Schenkel T, Malve M, Reik M, Markl M, Jung B, Oertel H. MRI-based CFD analysis of flow in a human left ventricle: methodology and application to a healthy heart. *Ann Biomed Eng.* (2009) 37:503–15. doi: 10.1007/s10439-008-9627-4
26. Chnafa C, Mendez S, Nicoud F. Image-based large-eddy simulation in a realistic left heart. *Comput Fluids.* (2014) 94:173–87. doi: 10.1016/j.compfluid.2014.01.030
27. Zheng X, Seo JH, Vedula V, Abraham T, Mittal R. Computational modeling and analysis of intracardiac flows in simple models of the left ventricle. *Eur J Mech B/Fluids.* (2012) 35:31–9. doi: 10.1016/j.euromechflu.2012.03.002
28. Le TB, Sotiropoulos F. On the three-dimensional vortical structure of early diastolic flow in a patient-specific left ventricle. *Eur J Mech B/Fluids.* (2012) 35:20–4. doi: 10.1016/j.euromechflu.2012.01.013
29. Fumagalli I, Vitullo P, Vergara C, Fedele M, Corno AF, Ippolito S, et al. Image-based computational hemodynamics analysis of systolic obstruction in hypertrophic cardiomyopathy. *Front Physiol.* (2022) 12:787082. doi: 10.3389/fphys.2021.787082
30. Dimasi A, Cattarinuzzi E, Stevanella M, Conti CA, Votta E, Maffessanti F, et al. Influence of mitral valve anterior leaflet in vivo shape on left ventricular ejection. *Cardiovasc Eng Technol.* (2012) 3:388–401. doi: 10.1007/s13239-012-0105-7
31. Lantz J, Bäck S, Carlhäll CJ, Bolger A, Persson A, Karlsson M, et al. Impact of prosthetic mitral valve orientation on the ventricular flow field: comparison using patient-specific computational fluid dynamics. *J Biomech.* (2021) 116:110209. doi: 10.1016/j.jbiomech.2020.110209
32. Khalafvand SS, Zhong L, Ng EYK. Three-dimensional CFD/MRI modeling reveals that ventricular surgical restoration improves ventricular function by modifying intraventricular blood flow. *Int J Numer Method Biomed Eng.* (2014) 30:1044–56. doi: 10.1002/cnm.2643
33. Khalafvand SS, Voorneveld JD, Muralidharan A, Gijsen FJH, Bosch JG, van Walsum T, et al. Assessment of human left ventricle flow using statistical shape modelling and computational fluid dynamics. *J Biomech.* (2018) 74:116–25.
34. This A, Morales HG, Bonnefous O, Fernández MA, Gerbeau JF. A pipeline for image based intracardiac CFD modeling and application to the evaluation of the PISA method. *Comput Methods Appl Mech Eng.* (2020) 358:112627. doi: 10.1016/j.cma.2019.112627
35. Arts T, Delhaas T, Bovendeerd P, Verbeek X, Prinzen FW. Adaptation to mechanical load determines shape and properties of heart and circulation: the CircAdapt model. *Am J Physiol Heart Circul Physiol.* (2005) 288:H1943–H1954. doi: 10.1152/ajpheart.00444.2004
36. Heldt T, Mukkamala R, Moody G, Mark R. CVSim: an open-source cardiovascular simulator for teaching and research. *Open Pacing Electrophysiol Therapy J.* (2010) 3:45–54.
37. Baillargeon B, Rebelo N, Fox DD, Taylor RL, Kuhl E. The living heart project: a robust and integrative simulator for human heart function. *Eur J Mech A/Solids.* (2014) 48:38–47. doi: 10.1016/j.euromechsol.2014.04.001
38. Ghosh RP, Marom G, Bianchi M, D'souza K, Zietak W, Bluestein D. Numerical evaluation of transcatheter aortic valve performance during heart beating and its post-deployment fluid-structure interaction analysis. *Biomech Model Mechanobiol.* (2020) 19:1725–40. doi: 10.1007/s10237-020-01304-9
39. Doost SN, Ghista D, Su B, Zhong L, Morsi YS. Heart blood flow simulation: a perspective review. *BioMed Eng OnLine.* (2016) 15:101. doi: 10.1186/s12938-016-0224-8
40. Quarteroni A, Veneziani A, Vergara C. Geometric multiscale modeling of the cardiovascular system, between theory and practice. *Comput Methods Appl Mech Eng.* (2016) 302:193–252. doi: 10.1016/j.cma.2016.01.007
41. Hirschhorn M, Tchantchaleishvili V, Stevens R, Rossano J, Throckmorton A. Fluid-structure interaction modeling in cardiovascular medicine - A systematic review 2017-2019. *Med Eng Phys.* (2020) 78:1–13. doi: 10.1016/j.medengphy.2020.01.008

42. Du Bois D, Du Bois EF. Clinical calorimetry: tenth paper a formula to estimate the approximate surface area if height and weight be known. *Arch Internal Med.* (1916) XVII:863–71. doi: 10.1001/archinte.1916.00080130010002
43. Ritter F, Boskamp T, Homeyer A, Laue H, Schwier M, Link F, et al. Medical image analysis. *IEEE Pulse.* (2011) 2:60–70. doi: 10.1109/MPUL.2011.942929
44. Tautz L, Neugebauer M, Hüllebrand M, Vellguth K, Degener F, Sündermann S, et al. Extraction of open-state mitral valve geometry from CT volumes. *Int J Comput Assist Radiol Surg.* (2018) 13:1741–54. doi: 10.1007/s11548-018-1831-6
45. Cerqueira MD, Weissman NJ, Dilsizian V, Jacobs AK, Kaul S, Laskey WK, et al. Standardized myocardial segmentation and nomenclature for tomographic imaging of the heart. *J Cardiovasc Magn Resonan.* (2002) 4:203–10. doi: 10.1081/JCMR-120003946
46. Di Donato M, Dabic P, Castelvecchio S, Santambrogio C, Brankovic J, Collarini L, et al. Left ventricular geometry in normal and post-anterior myocardial infarction patients: sphericity index and "new" conicity index comparisons. *Eur J Cardio Thoracic Surg.* (2006) 29:S225–S230. doi: 10.1016/j.ejcts.2006.03.002
47. Gallo LC, Cristallini EO, Svarc M. A nonparametric approach for assessing precision in georeferenced point clouds best fit planes: toward more reliable thresholds. *J Geophys Res Solid Earth.* (2018) 123:10,297–308. doi: 10.1029/2018JB016319
48. Kazhdan M, Hoppe H. Screened poisson surface reconstruction. *ACM Trans Graph (TOG).* Plano, TX: Siemens (2013) 32:1–13. doi: 10.1145/2487228.2487237
49. Siemens Digital Industries Software. *Simcenter STAR-CCM+ User Guide v. 2020.1.* Siemens, (2020).
50. Ricciardi MJ, Beohar N, Davidson CJ. "Cardiac catheterization and coronary angiography," In: *Essential Cardiology: Principles and Practice*, ed C. Rosendorff. Totowa, NJ: Humana Press (2006). p. 197–219.
51. Daub A, Kriegseis J, Frohnapfel B. Replication of left ventricular haemodynamics with a simple planar mitral valve model. *Biomed Eng Biomedizinische Technik.* (2020) 65:595–603. doi: 10.1515/bmt-2019-0175
52. Omran AS, Arifi AA, Mohamed AA. Echocardiography in mitral stenosis. *J Saudi Heart Assoc.* (2011) 23:51–8. doi: 10.1016/j.jsha.2010.07.007
53. Garcia D. What do you mean by aortic valve area: geometric orifice area, effective orifice area, or Gorlin area? *J Heart Valve Dis.* (2006) 15:601–8.
54. Leyh RG, Schmidtke C, Sievers HH, Yacoub MH. Opening and closing characteristics of the aortic valve after different types of valve-preserving surgery. *Circulation.* (1999) 100:2153–0. doi: 10.1161/01.CIR.100.21.2153
55. Mao W, Caballero A, McKay R, Primiano C, Sun W. Fully-coupled fluid-structure interaction simulation of the aortic and mitral valves in a realistic 3D left ventricle model. *PLoS ONE.* (2017) 12:1–21. doi: 10.1371/journal.pone.0184729
56. He Z, Ritchie J, Grashow JS, Sacks MS, Yoganathan AP. In Vitro Dynamic Strain Behavior of the Mitral Valve Posterior Leaflet. *J Biomech Eng.* (2005) 127:504–11. doi: 10.1115/1.1894385
57. Saito S, Araki Y, Usui A, Akita T, Oshima H, Yokote J, et al. Mitral valve motion assessed by high-speed video camera in isolated swine heart. *Eur J Cardio Thoracic Surg.* (2006) 30:584–91. doi: 10.16/j.ejcts.2006.07.021
58. Karlsson MO, Glasson JR, Bolger AF, Daughters GT, Komeda M, Foppiano LE, et al. Mitral valve opening in the ovine heart. *Am J Physiol Heart Circul Physiol.* (1998) 274:H552–H563. doi: 10.1152/ajpheart.1998.274.2.H552
59. Durst F. *Grundlagen der Strömungsmechanik: eine Einführung in die Theorie der Strömungen von Fluiden.* Berlin: Springer (2006).
60. Hunt J, Wray A, Moin P. Eddies, streams, and convergence zones in turbulent flows. *Stud Turbulence Using Numer Simulat Databases.* (1988) 11:193–208.
61. Pierrakos O, Vlachos PP. The effect of vortex formation on left ventricular filling and mitral valve efficiency. *J Biomech Eng.* (2006) 128:527–39. doi: 10.1115/1.2205863
62. Lantz J, Henriksson L, Persson A, Karlsson M, Ebbers T. Patient-Specific Simulation of Cardiac Blood Flow From High-Resolution Computed Tomography. *J Biomech Eng.* (2016) 138:121004. doi: 10.1115/1.4034652
63. Vedula V, Seo J, Lardo AC, Mittal R. Effect of trabeculae and papillary muscles on the hemodynamics of the left ventricle. *Theor Comput Fluid Dyn.* (2016) 30:3–21. doi: 10.1007/s00162-015-0349-6
64. Panicheva D, Villard PF, Hammer PE, Perrin D, Berger MO. Automatic extraction of the mitral valve chordae geometry for biomechanical simulation. *Int J Comput Assist Radiol Surg.* (2021) 16:709–20. doi: 10.1007/s11548-021-02368-3
65. Morud JC, Skjetne P, Urheim S, Dahl SK. The effect of chordae tendineae on systolic flow. *Comput Biol Med.* (2019) 109:91–100. doi: 10.1016/j.compbiomed.2019.04.020
66. Mihalef V, Ionasec RI, Sharma P, Georgescu B, Voigt I, Suehling M, et al. Patient-specific modelling of whole heart anatomy, dynamics and haemodynamics from four-dimensional cardiac CT images. *Interface Focus.* (2011) 1:286–96. doi: 10.1098/rsfs.2010.0036
67. Karabelas E, Gsell MAF, Augustin CM, Marx L, Neic A, Prassl AJ, et al. Towards a computational framework for modeling the impact of aortic coarctations upon left ventricular load. *Front Physiol.* (2018) 9:538. doi: 10.3389/fphys.2018.00538
68. Celi S, Vignali E, Capellini K, Gasparotti E. On the Role and Effects of Uncertainties in Cardiovascular in silico Analyses. *Front Med Technol.* (2021) 3:748908. doi: 10.3389/fmedt.2021.748908
69. Vellguth K, Brüning J, Tautz L, Degener F, Wamala I, Sündermann S, et al. User-dependent variability in mitral valve segmentation and its impact on CFD-computed hemodynamic parameters. *Int J Comput Assist Radiol Surg.* (2019) 14:1687–96. doi: 10.1007/s11548-019-02012-1

Conflict of Interest: The authors declare that the research was conducted in the absence of any commercial or financial relationships that could be construed as a potential conflict of interest.

frontiers | Frontiers in Cardiovascular Medicine

ORIGINAL RESEARCH
published: 07 April 2022
doi: 10.3389/fcvm.2022.824470

Determinants of Non-calcified Low-Attenuation Coronary Plaque Burden in Patients Without Known Coronary Artery Disease: A Coronary CT Angiography Study

Hiroki Yamaura[1†], *Kenichiro Otsuka*[1,2*†], *Hirotoshi Ishikawa*[1,2], *Kuniyuki Shirasawa*[1], *Daiju Fukuda*[2] *and Noriaki Kasayuki*[1]

[1] Department of Cardiovascular Medicine, Kashibaseiki Hospital, Kashiba, Japan, [2] Department of Cardiovascular Medicine, Osaka City University Graduate School of Medicine, Osaka, Japan

OPEN ACCESS

Edited by:
Grigorios Korosoglou,
GRN Klinik Weinheim, Germany

Reviewed by:
Gitsios Gitsioudis,
Cardiology and Intensive Care Medicine, Germany
Christin Tesche,
Medical University of South Carolina, United States

***Correspondence:**
Kenichiro Otsuka
otsukakenichiro1@gmail.com

[†] These authors have contributed equally to this work

Specialty section:
This article was submitted to Cardiovascular Imaging, a section of the journal Frontiers in Cardiovascular Medicine

Received: 29 November 2021
Accepted: 28 February 2022
Published: 07 April 2022

Citation:
Yamaura H, Otsuka K, Ishikawa H, Shirasawa K, Fukuda D and Kasayuki N (2022) Determinants of Non-calcified Low-Attenuation Coronary Plaque Burden in Patients Without Known Coronary Artery Disease: A Coronary CT Angiography Study. Front. Cardiovasc. Med. 9:824470. doi: 10.3389/fcvm.2022.824470

Background: Although epicardial adipose tissue (EAT) is associated with coronary artery disease (CAD), it is unclear whether EAT volume (EAV) can be used to diagnose high-risk coronary plaque burden associated with coronary events. This study aimed to investigate (1) the prognostic impact of low-attenuation non-calcified coronary plaque (LAP) burden on patient level analysis, and (2) the association of EAV with LAP volume in patients without known CAD undergoing coronary computed tomography angiography (CCTA).

Materials and Methods: This retrospective study consisted of 376 patients (male, 57%; mean age, 65.2 ± 13 years) without known CAD undergoing CCTA. Percent LAP volume (%LAP, <30 HU) was calculated as the LAP volume divided by the vessel volume. EAT was defined as adipose tissue with a CT attenuation value ranging from −250 to −30 HU within the pericardial sac. The primary endpoint was a composite event of death, non-fatal myocardial infarction, and unstable angina and worsening symptoms requiring unplanned coronary revascularization >3 months after CCTA. The determinants of %LAP (Q4) were analyzed using a multivariable logistic regression model.

Results: During the follow-up period (mean, 2.2 ± 0.9 years), the primary endpoint was observed in 17 patients (4.5%). The independent predictors of the primary endpoint were %LAP (Q4) (hazard ratio [HR], 3.05; 95% confidence interval [CI], 1.09–8.54; $p = 0.033$] in the Cox proportional hazard model adjusted by CAD-RADS category. Cox proportional hazard ratio analysis demonstrated that %LAP (Q4) was a predictor of the primary endpoint, independnet of CAD severity, Suita score, EAV, or CACS. The independent determinants of %LAP (Q4) were CACS ≥218.3 ($p < 0.0001$) and EAV ≥125.3 ml ($p < 0.0001$). The addition of EAV to CACS significantly improved the area under the curve (AUC) to identify %LAP (Q4) than CACS alone (AUC, EAV + CACS *vs.* CACS alone: 0.728 *vs.* 0.637; $p = 0.013$).

Conclusions: CCTA-based assessment of EAV, CACS, and LAP could help improve personalized cardiac risk management by administering patient-suited therapy.

Keywords: chronic coronary syndrome (CCS), coronary CT angiography, high-risk plaque, coronary artery calcium score, epicardial adipose tissue, prognosis

INTRODUCTION

Coronary artery disease (CAD) is a progressive chronic disease that leads to acute coronary syndrome (ACS) often as the first manifestation (1). The assessment of myocardial ischemia is important for diagnosing patients who will benefit from coronary revascularization (2, 3). However, the ISCHEMIA trial (4) demonstrated that there was no significant differences in event-free survival between the invasive strategy (invasive coronary angiography and revascularization if necessary) plus optimized medical therapy (OMT) and conservative management with OMT alone. Therefore, it is important to identify high-risk patients treated with OMT who can develop subsequent coronary events.

Coronary plaque burden is a robust risk factor for plaque rupture, and it is the leading cause of ACS (3, 5, 6). There is a correlation between myocardial ischemia and coronary plaque burden; however, the disease progression of coronary atherosclerosis can be accelerated by the coexistence of distinct coronary risk factors such as metabolic activities (3, 7), which in turn account for the heterogeneity in the risk of developing unstable angina, myocardial infarction, and death among individuals. These findings suggest that there are potential mechanisms that accelerate the disease progression leading to ACS apart from myocardial ischemia (1, 3, 8). One of the mechanisms may involve an underlying high-risk coronary plaque composition in which earlier-stage plaques may have increased metabolic activities with a greater risk of plaque progression than advanced and more inert atherosclerotic lesions (3, 7, 9, 10). Coronary computed tomography angiography (CCTA) is a first-line, non-invasive diagnostic test to assess the presence, severity, and extent of CAD (11–13). It is mostly used in clinical practice because of its high negative predictive value for obstructive CAD. CCTA allows for fully quantitative assessment of coronary plaque burden, which has been shown to predict cardiovascular outcomes (7, 14, 15). A sub-analysis of the SCOT-HEART trial demonstrated that low-attenuation non-calcified coronary plaque (LAP) volume $\geq$4% was a robust predictor of the 5-year incidence of cardiac death or non-fatal myocardial infarction (16, 17). These observations indicate that quantifying high-risk coronary plaque burden is important to estimate the risk of future coronary events. Another mechanism that accelerates disease progression is inflammatory activity in the epicardial adipose tissue (EAT), a passive fat storage that functions as an endocrine organ (18). EAT volume (EAV) assessed using CCTA has been shown to play a pivotal role in coronary plaque progression (19–22). Even though EAV is associated with CAD extent, severity, and the presence of high-risk coronary plaque morphology (21, 23, 24), it is unclear whether EAV can be used to diagnose high-risk coronary plaque burden that progresses rapidly in patients without known CAD. In this CCTA study, we aimed to investigate (1) the prognostic impact of LAP burden on patient level analysis, as well as (2) the association of EAV with LAP volume in patients without known CAD.

MATERIALS AND METHODS

Study Population

This retrospective observational study protocol was approved by the ethics committee of Fujiikai Kashibaseiki Hospital (2021-E). The requirement of obtaining written informed consent from the participants was waived in accordance with the institutional requirements. The study was conducted in accordance with the Declaration of Helsinki. **Figure 1** shows the flow chart of the study population. The study population consisted of symptomatic patients with suspected CAD (n = 610) who visited the Fujiikai Kashibaseiki Hospital between April 2017 and January 2020 for CCTA examination. Patients meeting the following criteria were excluded from this study: (1) patients with a prior history of myocardial infarction (n = 10), percutaneous coronary intervention (n = 72), or coronary artery bypass grafting (n = 7); (2) patients with cardiogenic shock or ACS (n = 19); (3) patients with acute aortic dissection (n = 5); (4) patients with second follow-up CCTA imaging (n = 9); (5) patients with a poor CCTA image quality (n = 5), missing data to calculate clinical risk score (n = 60), (6) those less than 35 years old who did not meet the criteria to calculate the clinical risk score (n = 10); and (7) patients who were lost to follow-up (n = 37). A total of 376 patients without known CAD were included in the analysis (**Figure 1**).

To estimate the 10-year probability of CAD, the Suita score was calculated and reported for each patient. The Suita score is a risk score that predicts the probability of developing of coronary heart disease in 10 years in the Japanese population (25). The parameters used to calculate the Suita score were age, sex, smoking status, blood pressure, low-density lipoprotein (LDL)-cholesterol, high-density lipoprotein (HDL)-cholesterol, and chronic kidney disease (CKD, estimated glomerular filtration ratio, eGFR <60 ml/min/1.73 mm^2).

CCTA Image Acquisition

All the CCTA examinations were performed using a 320-row multidetector CT and an ECG-triggered prospective gating method during a single breath-hold (Aquilion ONE/NATURE Edition, Cannon Medical Systems, Inc., Japan). Patients with a heart rate of >60 bpm were pretreated with an oral beta-blocker. Coronary artery calcium score (CACS) was assessed using the Agatston scoring method at a fixed thickness of 3 mm (26). Following CACS scanning, the Bolus Tracking method was used for the image acquisition, where the non-ionic contrast medium of 270 mgI/kg (ranging from 33 ml to 74 ml, Iopamidol, 370 mg iodine per ml iopamilon; Bracco, Milan, Italy) was administrated with a power injector at a rate of 2.3–4.9 ml per second through a 20-gauge needle. After injecting the contrast medium, saline was injected through the same venous access at the same injection rate. A region of interest (ROI) was set in the ascending aorta at the bronchial bifurcation level. When the CT value exceeded 150 Hounsfield units (HU), ECG-synchronized scans were performed within a single breath-hold. The scan parameters were a detector collimation of 0.5 × 320 mm, gantry rotation time of 350 ms, tube voltage of 120 kV, and tube current of 130–600 mA. The images were reconstructed

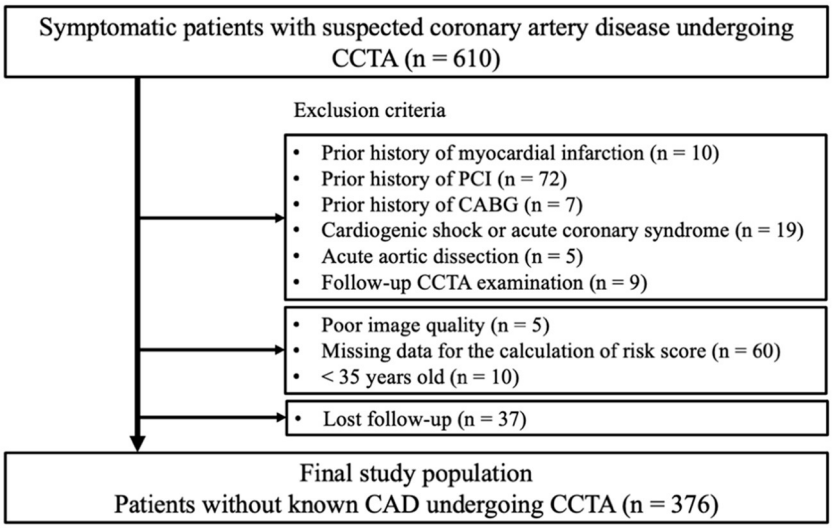

FIGURE 1 | Flow chart for the study population. ACS, acute coronary syndrome; CAD, coronary artery disease; CCTA, coronary computed tomography angiography; CABG, coronary artery bypass graft; PCI, percutaneous coronary intervention.

using a Forward-projected Model-based Iterative Reconstruction SoluTion (FIRST) for coronary artery analysis.

CCTA Image Analysis

Synapse Vincent software (Fujifilm Inc., Tokyo, Japan) was used to automatically generate three-dimensional volume-rendering images, straight and stretch curved planar reformation images, and cross-sectional multiplanar reconstruction (MPR) images. According to the Agatston scoring method, CACS was classified into five categories as follows: 0, 1–10, 11–100, 101–400 and >400. The diameter of the coronary artery stenosis was reported based on the SCCT guideline by two observers (K.O. and H.I.). According to the patient-level CAD-RADS classification (13), CAD was categorized into seven categories as follows: 0 (no plaque or no stenosis), 1 (1–24% stenosis), 2 (25–49% stenosis), 3 (50–69% stenosis), 4A (one or two vessels, 70–99% stenosis), 4B (left main artery >50% stenosis or three vessels ≥70% stenosis), and 5 (100%, total occlusion).

Regarding the vessel- and patient-level analysis of coronary plaque volume, we used the Synapse Vincent software (Fujifilm Inc.) to semiautomatically measure the lumen, vessel, and plaque volume of each major epicardial coronary artery. The luminal contour was automatically detected and manually corrected using cross-sectional MPR images. The vessel contour was automatically detected and manually corrected on the MPR images. The plaque components were categorized into either calcified plaque (CP, ≥150 HU), non-calcified plaque (NCP, <150 HU), or LAP <30 HU (17). The total coronary plaque burden and that for each plaque component was calculated using the following equation:

$$Coronary\ plaque\ burden\ (\%) = \frac{Vessel\ volume\ (ml) - Lumen\ volume\ (ml)}{Vessel\ volume\ (ml)} \times 100$$

In the patient-level analysis, each plaque volume for 3-vessel coronary arteries was categorized into quartiles. **Figure 2** illustrates the CCTA images (**Figures 2A–D**) of a patient with non-obstructive CAD and an increased LAP (Q4) who developed unstable angina requiring urgent coronary revascularization.

EAV was measured from contrast-enhanced CT images using the Synapse Vincent software (Fujifilm Inc.) as reported previously (27). To measure the EAV, several equidistant axial planes were extracted according to the size of each heart. The upper slice limit was at the bifurcation of the pulmonary artery trunk, and the lower slice limit was at the last slice that contained any structure of the heart. In each plane, the software automatically detected a smooth, closed pericardial contour as a region of interest, where the software automatically identifies adipose tissue as having CT attenuation values ranging from −250 to −30 HU within the pericardial sac (27). Finally, the EAV was calculated as the sum of the EAT areas.

Endpoints

Clinical follow-up was performed through interviews with the patients at each hospital visit. Interviews through telephone and mail were used to obtain the follow-up data. The primary endpoint was defined as a composite event of cardiovascular or non-cardiovascular death, non-fatal myocardial infarction, and unstable angina requiring coronary revascularization more than 90 days after CCTA examination, as well as worsening symptoms requiring unplanned coronary revascularization more than 90 days after CCTA examination. Myocardial infarction was defined as a typical persistent chest pain with elevation of cardiac enzymes (elevation of cardiac troponin I above the reference level), regardless of ST-segment elevation myocardial infarction or non-ST-segment elevation myocardial infarction. Unstable angina was defined as new-onset angina, exacerbated angina that

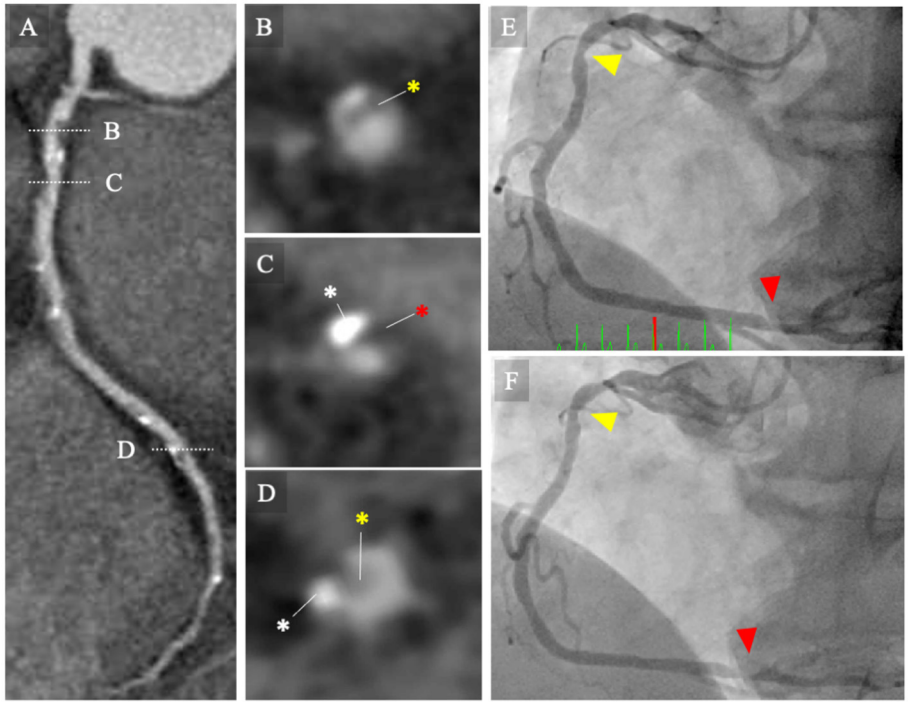

FIGURE 2 | CCTA images and invasive coronary angiography. **(A–D)** CCTA images of a patient with non-obstructive CAD and increased low-attenuation plaque (Q4) who developed to unstable angina requiring urgent coronary revascularization. The MPR image of the baseline CCTA image for right coronary artery (RCA) showing intermediate stenosis severity with low-attenuation coronary plaque (Q4). **(B–D)** Cross-sectional images of coronary lesions (white broken bars). **(B)** Mild stenosis with non-calcified plaque (yellow asterisk). **(C)** Intermediate stenosis with calcified plaque (white asterisk) and low-attenuation plaque (red asterisk). **(D)** Intermediate stenosis with calcified and non-calcified plaques. **(E)** Invasive coronary angiography performed at 12 days following the baseline CCTA examination. Invasive coronary angiography (ICA) image shows intermediate stenosis of the proximal (yellow arrowhead) and distal portions of the RCA (red arrowhead). The patient was managed with conservative strategy, including statins. **(F)** The patient presented with unstable angina and underwent emergency ICA at 1.5 years following the baseline CCTA examination. The ICA image revealed progression of the coronary lesions (red arrowheads). CCTA, coronary computed tomography angiography; ICA, invasive coronary angiography; MPR, multi-planar reconstruction; RCA, right coronary artery.

is symptomatic with light exertion, or angina that appears at rest, without elevated cardiac-deviated enzymes.

Statistical Analysis

Statistical analysis was performed using EZR (Saitama Medical Center, Jichi Medical University, Saitama, Japan), which is a modified version of the R commander. Categorical variables were reported as counts (percentage), and continuous variables as means (standard deviation, SD) or medians (interquartile range, IQR). The variables were compared using the chi-square test for categorical variables. One-way analysis of variance or the Kruskal-Wallis test was used to compare the %LAP quartiles for continuous variables. A Cox proportional hazard ratio analysis (forced entry method) was used to identify the predictors of the primary endpoint. The multivariable model using Cox hazard proportional ratio analysis included 4 models; LAP (Q4) was adjusted by CAD-RADS $\geq$3 for model 1, Suita score for model 2, EAV for model 3, and CACS >100 for model 4. Using the Kaplan-Meier curve analysis, a time-to-event analysis for patients with %LAP Q4 and those with %LAP Q1–3 was performed. The determinants of %LAP (Q4) were analyzed using logistic regression analysis. The model was adjusted for advanced age, body mass index, Suita score, and obstructive CAD. Suita scores of <56 and $\geq$56 points were classified as low risk (n = 274; <9 % for 10-year risk) or intermediate/high risk (n = 102; $\geq$9 % for 10-year risk), respectively. Spearman's correlation coefficient was used to analyze the association of %LAP with CACS and EAV. Receiver operating curve (ROC) analyses were performed to determine the best cutoff value of EAV and CACS in identifying patients with increased %LAP (Q4) and the areas under the curve (AUCs) as well as the sensitivities, specificities, and positive and negative predictive values of the diagnostic test. To test the hypothesis that EAV had additional diagnostic value than CACS, a multivariate ROC analysis adjusting for EAV and CACS was performed and compared with that of CACS alone. To report the reproducibility of coronary plaque burden, we performed an intraclass correlation (ICC) analysis for intra- and interobservers in 30 randomly selected patients. A p-value of <0.05 was considered as statistically significant.

RESULTS

Baseline Characteristics and CCTA Findings

All of the 376 patients who underwent CCTA examination had images of suitable quality as well as available clinical data for

analysis. **Table 1** shows the baseline characteristics of the patients. The patients had a mean age of 65.2 (13.1) years, and 56.6% (n = 213) were male with a range of cardiovascular risk factors. The mean Suita score was 48.4 (10.8) points, and 27.1% (n = 102) of the patients had Suita scores ≥56 (**Table 1**). **Table 1** shows that 5.0% (n = 19) and 25.5% (n = 96) of the patients were treated with aspirin and statins at study enrollment, respectively. Compared to patients without the primary endpoint, those with the primary endpoint tended to have greater prevalence of diabetes and were older (p = 0.011), as well as had a higher Suita scores (p = 0.003). There was no significant difference in serum CRP (p = 0.502) and eGFR (p = 0.161) levels between patients with and without the primary endpoint. **Table 2** shows patient-level CCTA findings at baseline and a comparison between patients with and without the primary endpoint. The median CACS was 17 (0–166). Accoridng to CAD-RADS category, CAD-RADS 1 (absence of CAD), CAD-RADS 1–2 (minimal-mild CAD), and CAD-RADS ≥3 (severe stenosis and total occlusion) were found in 20.2% (n = 76), 39.6% (n = 149), and 40.2% (n = 151) of the patients, respetively. The mean %LAP for all the patients was 1.35 (0.98) % and the mean EAV was 124.0 (52.0) ml. As expected, patients with the primary endpoint had higher prevalence of CAD-RADS ≥3, and a greater plaque volume for calcified plaque and low-attenuation non-calcified plaque (all p <0.05), but there were no statistically significant differences in EAV between the two groups (p = 0.40).

Excellent reproducibility was observed in %LAP volume (intraobserver ICC, 0.939; 95% CI, 0.887–0.96; interobserver ICC, 0.953; 95% CI, 0.900–0.978), %NCP volume (intraobserver ICC, 0.981; 95% CI, 0.966–0.991; interobserver ICC, 0.977; 95% CI, 0.952–0.989), and %CP volume (intraobserver ICC, 0.989; 95% CI, 0.979–0.994; interobserver ICC, 0.984; 95% CI, 0.966–0.992).

Predictors of the Primary Endpoint

During the mean follow-up period of 2.2 ± 0.9 years, the primary endpoint was observed in 15 patients (4.0%), including death (n = 2), ACS (n = 6), and unplanned coronary revascularization more than 90 days after CCTA examination (n = 7). **Table 3** shows the comparisons of the Suita score, CCTA findings, and the rates for the primary endpoints among the four groups stratified by %LAP (Q1-Q4). Further, %LAP in each quartile was 0.07–0.72% for Q1 (25 percentile), 0.72–1.06% for Q2 (25–50 percentile), 1.07%−1.66% for Q3 (50–75 percentile), and 1.67–7.09% for Q4 (75–100 percentile). Of the patients who developed the primary endpoints, 65% (n = 11) arose from %LAP (Q4), which was more frequent than the remaining groups of %LAP (Q1–Q3). Compared to patients with the %LAP (Q1–Q3), those

TABLE 1 | Baseline patient characteristics.

	Overall (n = 376)	Primary endpoint (+) (n = 15)	Primary endpoint (-) (n = 361)	p-value
Age, years	65.2 (13.1)	73.7 (9.8)	64.9 (13.1)	0.011
Male	213 (56.6 %)	10 (66.7%)	203 (56.2%)	0.424
Body mass index, kg/m^2	24.0 (4.1)	22.8 (3.0)	24.0 (4.1)	0.236
Smoking	58 (15.4 %)	2 (13.3%)	56 (15.5%)	0.819
Hypertension	269 (71.5 %)	10 (66.7%)	259 (71.7%)	0.669
Diabetes mellitus	84 (22.3 %)	6 (40.0%)	78 (21.6%)	0.094
Dyslipidemia	275 (73.1 %)	12 (80.0%)	263 (72.9%)	0.541
Atrial fibrillation	45 (12.0 %)	1 (6.7%)	44 (12.2%)	0.519
CKD	101 (26.9 %)	5 (33.3%)	96 (26.6%)	0.564
eGFR, ml/min/1.73 mm^2	67.9 (13.8)	63.0 (21.6)	68.2 (13.4)	0.161
LDL-Cholesterol, mg/dL	125 (35.1)	133.3 (25.2)	124.8 (35.4)	0.355
HDL-Cholesterol, mg/dL	63.7 (18.6)	61.4 (17.8)	63.8 (18.6)	0.615
Triglyceride, mg/dL	156 (216)	153.2 (87.4)	157.1 (219.8)	0.946
CRP, mg/dL	0.33 (0.84)	0.18 (0.29)	0.33 (0.86)	0.502
Hemoglobin A1c, %	6.0 (1.1)	6.1 (0.6)	6.0 (1.1)	0.897
Medication				
Aspirin	19 (5.0 %)	0 (0%)	19 (5.3%)	0.362
Beta blockers	22 (5.9 %)	0 (0%)	22 (6.1%)	0.324
RAS-inhibitors	86 (22.9 %)	4 (26.7%)	82 (22.7%)	0.581
Calcium channel blockers	102 (27.1 %)	5 (33.3%)	97 (26.9%)	0.182
Statins	96 (25.5 %)	5 (33.3%)	91 (25.2%)	0.479
Suita score	48.4 (10.8)	56.4 (9.8)	48.1 (10.7)	0.003

Variables were expressed as n (%) or mean (SD). eGFR, estimated glomerular filtration rate; CKD, chronic kidney disease; CRP, C-reactive protein; HDL, high-dense lipoprotein; LDL, low-dense lipoprotein; RAS, renin-angiotensin system.

with %LAP (Q4) had a greater Suita score, CACS, EAV, and frequent obstructive CAD (all $p < 0.05$) (**Table 3**).

In the Cox proportional hazard model adjusted by CAD-RADS ≥3 (model 1), %LAP (Q4) was independent predictors of the primary endpoint (hazard ratio [HR], 3.05; 95% confidence interval [CI], 1.09–8.54; $\boldsymbol{p} = 0.033$) (**Table 4**). Similarly, %LAP (Q4) remained as the predictor of the primary endpoint in model 2 adjusted by Suita score (LAP Q4; HR, 3.41; 95% CI, 1.23–9.45; $p = 0.018$), in model 3 adjusted by EAV (LAP Q4; HR, 3.15; 95% CI, 1.06–9.32; $p = 0.038$), and in model 4 adjusted by CACS ≥100 (LAP Q4; HR, 3.52; 95% CI, 1.28–9.71; $p = 0.015$) (**Table 4**). Kaplan-Meier curve analysis illustrated that patients with %LAP (Q4) had a worse prognosis than those with Q1–Q3 for both endpoints (both log rank $p < 0.001$) (**Figure 3**).

TABLE 2 | Baseline patient-level CCTA findings.

	Overall (*n* = 376)	Primary endpoint (+) (*n* = 15)	Primary endpoint (-) (*n* = 361)	*p*-value
CAD-RADS classification				
0	76 (20.2 %)	1 (6.7%)	75 (20.8%)	0.182
1	110 (29.3%)	1 (6.7%)	109 (30.2 %)	0.049
2	39 (10.3%)	3 (20.0%)	36 (10.0%)	0.212
3	74 (19.7%)	1 (6.7%)	73 (20.2%)	0.196
4A	44 (11.7%)	3 (20.0%)	41 (11.4%)	0.308
4B	21 (5.6%)	3 (20.0%)	18 (5.0%)	0.0131
5	12 (3.2%)	3 (20.0%)	9 (2.5%)	<0.001
≥3	151 (40.2 %)	10 (66.7%)	141 (39.1%)	0.033
Location of obstructive CAD				
LMCA	8 (2.1 %)	1 (6.7%)	7 (1.9%)	
LAD	105 (27.9 %)	9 (60.0%)	96 (26.6%)	
LCX	57 (15.2 %)	5 (33.3%)	52 (14.4%)	
RCA	59 (15.7 %)	6 (40.0%)	53 (14.7%)	
%NCP volume, %	21.7 (6.52)	23.4 (6.53)	21.7 (6.52)	0.302
%CP volume, %	1.03 (2.82)	6.22 (9.17)	0.82 (1.97)	<0.001
%LAP volume, %	1.35 (0.98)	1.92 (1.28)	1.33 (0.96)	0.023
CACS, Agatston unit	17 (0–166)	67 (0–390)	4.8 (0–108)	<0.001
EAV, ml	124.0 (52.0)	134.9 (51.0)	123.5 (51.2)	0.4
Abdominal visceral adipose tissue area, cm^2	101.3 (57.4)	110.4 (66.0)	100.9 (57.1)	0.53

Variables were expressed as n (%), mean (SD) or median (interquartile range, IQR). CACS = coronary artery calcium score, CAD, coronary artery disease; CCTA, coronary computed tomography angiography; EAV, epicardia adipose tissue volume; LAD, left anterior ascending artery; LCX, left circumflex artery; LMCA, left main coronary artery; RCA, right coronary artery; NCP, non-calcified plaque; CP, calcified plaque; LAP, low attenuation non-calcified plaque.

Predictors of Patients With %LAP (Q4)

We observed a weak but statistically significant positive correlation between CACS and %LAP ($\rho = 0.238$, $p < 0.001$) and between EAV and %LAP ($\rho = 0.386$, $p < 0.001$). To diagnose patients with %LAP (Q4), the ROC analysis demonstrated that the best cut-off value for CACS was 218.3 Agatston units (**Figure 4A**, AUC = 0.637, sensitivity of 38.3%, and specificity of 84.8%), and that for EAV was 125.3 ml (**Figure 4B**, AUC = 0.693, sensitivity of 69.1%, and specificity of 65.2%). In a logistic regression analysis after adjusting for age, body mass index, Suita score, and CAD-RADS category, the independent determinants

TABLE 4 | Multivariable Cox hazard model for the prediction of the primary and secondary endpoints during follow-up.

	Predictors of the primary endpoint			
	Hazard ratio	95% CI lower	95% CI upper	*p*-value
Model 1				
%LAP Q4	3.05	1.09	8.54	0.033
CAD-RADS ≥3	2.77	0.93	8.22	0.066
Model 2				
%LAP Q4	3.41	1.23	9.45	0.018
Suita score ≥56	2.37	0.86	6.55	0.096
Model 3				
%LAP Q4	3.15	1.06	9.32	0.038
EAT volume	1.45	0.48	4.37	0.511
Model 4				
%LAP Q4	3.52	1.28	9.71	0.015
CACS >100	1.45	0.41	5.65	0565

*Abbreviations as in **Tables 1**, **2**. A Cox proportional hazard model (forced entry method) was carried out to identify the predictors of the primary endpoint. The predictors included in the model were %LAP (Q4), CACS >300, EAV, obstructive CAD, and Suita score ≥56.*

TABLE 3 | Clinical risk score, CCTA findings, and event rates according to quartile of %LAP.

	%LAP Q1 *n* = 94	%LAP Q2 *n* = 94	%LAP Q3 *n* = 94	%LAP Q4 *n* = 94	*p*-value
%LAP, %	0.52 (0.15)	0.88 (0.10)	1.33 (0.16)	2.67 (1.08)	<0.001
Suita score	45.2 (11.3)	48.6 (9.6)	49.6 (11.2)	50.3 (10.3)	0.006
CACS	0 (0–64)	15 (0–93)	24 (0–169)	67 (0–390)	<0.001
EAV, mL	102.1 (44.0)	112.6 (43.7)	132.4 (51.0)	149.0 (53.0)	<0.001
Obstructive CAD	28 (29.8)	36 (38.3)	39 (41.5)	48 (51.1)	0.029
Number of patients with primary endpoints	2 (2.1%)	1 (1.1%)	4 (4.3%)	8 (8.5%)	0.046

Variables were expressed as n (%), mean (SD) or median (interquartile range, IQR).
*Abbreviations as in **Table 2**.*

of %LAP (Q4) were CACS ≥218.3 and EAV ≥125.3 ml (both $p < 0.001$, **Table 5**). For the identification of patients with %LAP (Q4), the addition of EAV to CACS significantly improved the AUC (**Figure 4C**, AUC, 0.728, $p = 0.013$) compared to that of CACS alone (**Figure 4A**, AUC, 0.637).

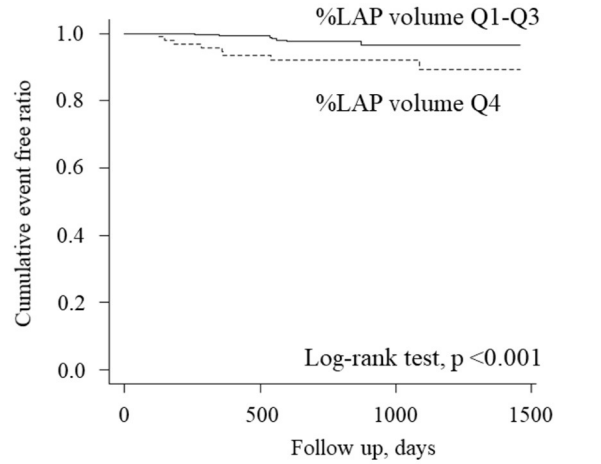

Patient number at risk

Follow-up, days	0	500	1000
%LAP Q1-3	282	237	87
%LAP Q4	94	70	36

FIGURE 3 | Kaplan-Meier curves analysis according to the LAP burden. Kaplan-Meier curve analysis illustrated that patients having %LAP (Q4) had a worse prognosis than those with Q1–Q3 ($p < 0.001$, log-rank test).

DISCUSSION

Our results show that in patients without overt known CAD, 3-vessel LAP volume is a significant predictor of the primary and secondary endpoints independent of CAD-RADS ≥3 (severe stenosis and total occlusion). The major findings of the present study are as follows: (1) Coronary high-risk plaque burden, assessed by LAP volume on CCTA, was a prognostic factor for mortality and coronary events; (2) EAV was independently associated with increased LAP volume; and (3) the combination of CACS and EAV provides a non-invasive method of identifying patients with increased LAP volume that can lead to coronary events. These findings suggest that the link between high-risk coronary plaque burden, death, and acute coronary events is potentially mediated by increased EAT volume.

Our understanding of the mechanisms of ACS largely stems from histopathological studies followed by investigations using imaging modalities (5, 28–32). The identification of patients at risk of developing ACS who will benefit from more intensive therapy is the focus of current clinical practice (11, 12, 31). Although the concept of rupture-prone "vulnerable plaque" was a driving motivation of the identification of patients at risk of ACS (5, 29), there are debates regarding how to diagnose patients who are most likely to develop coronary atherosclerotic disease burden leading to ACS (3).

Calcification plays a vital role in the natural history of coronary atherosclerosis and plaque rupture. Microcalcification (≥0.5 μm, and typically <15 μm) derived from dying macrophages and smooth muscle cells potentially causes stress-induced fibrous cap rupture (6, 33, 34). Several clinical studies using imaging modalities have demonstrated that spotty calcification is frequently found in the culprit lesion as compared

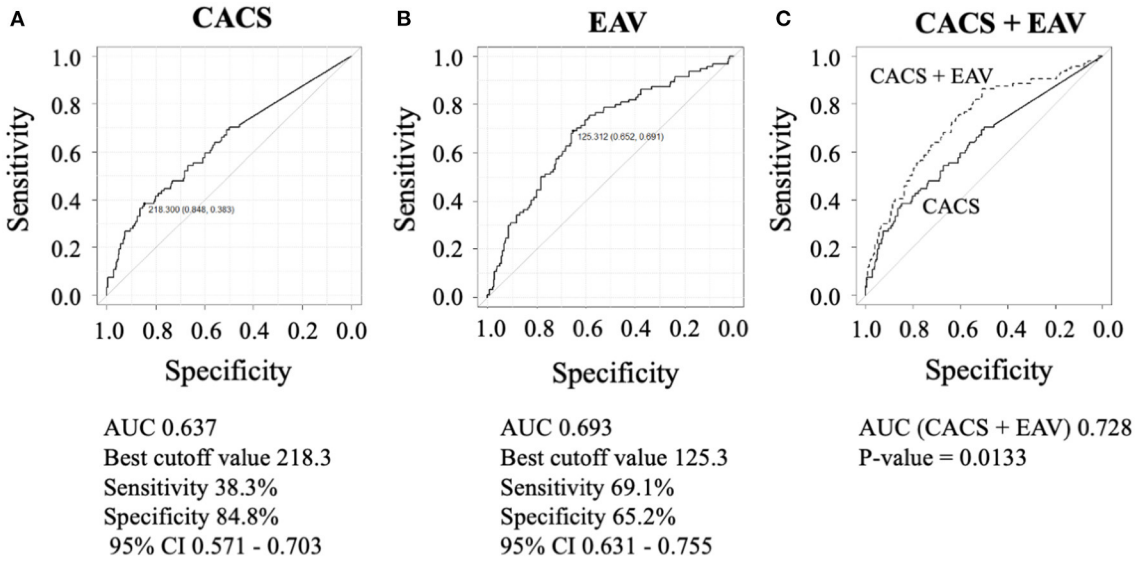

FIGURE 4 | To diagnose patients with %LAP (Q4), the ROC analysis demonstrated that the best cut-off value for CACS was 218.3 Agatston units **(A)**, and that for EAV was 125.3 ml **(B)**. **(C)** Addition of EAV on CACS significantly improved the AUC that is used to identify %LAP (Q4) than CACS alone (C, EAV + CACS versus CACS alone, 0.728 versus 0.637; p = 0.013).

TABLE 5 | Multivariable logistic regression analysis to predict %LAP (Q4).

	Odds ratio	95% CI lower	95% CI upper	*p*-value
Age >70 years	0.918	0.515	1.64	0.772
Body mass index, kg/m^2	1.06	0.990	1.14	0.093
Suita score ≥56	0.939	0.516	1.71	0.838
CACS ≥218.3 Agatston unit	3.38	1.84	6.20	<0.001
EAV ≥125.3 ml	3.14	1.73	5.69	<0.001
Obstructive CAD	1.29	0.751	2.23	0.353

Abbreviations as in ***Table 2****. Suita score ≥56: probability of coronary heart disease in 10 years ≥9%.*

to that of stable angina (28). It has been reported that high-density calcification on CCTA is a marker of plaque stability (10). Mortensen et al. recently demonstrated that CACS provides prognostic information regardless of the presence or absence of obstructive CAD (7), indicating the importance of assessing coronary plaque burden. These findings indicate that coronary lesions with mild-to-intermediate calcification exhibit a higher incidence of ACS (33). In lin with these findings, our results indicate that CACS ≥218.3 was independently associated with a greater high-risk plaque burden, as assessed by %LAP.

In recent years, atherosclerosis has been established as a chronic inflammatory disease (8). Adipose tissue is a passive fat storage and can function as an endocrine organ, releasing adipokines in response to extracellular stimuli or alterations in metabolic status (18). There is a link between local inflammation in EAT and lipid-rich coronary plaques and necrotic core, likely mediated by an increased density of vasa vasorum (35). Previous studies have reported an increased density of neovascularization from the adventitia into ruptured plaques (6, 36, 37), where increased expression of matrix metalloproteinases-2 and−9 by macrophages was observed in inflamed adventitia (38). As a result, more attention has been paid to assessing the inflammatory status of the pericoronary artery using non-invasive imaging modalities (39).

EAV has been independently associated with the extent and severity of obstructive CAD (21), hemodynamically significant stenosis (40), and the presence of high-risk coronary plaque detected on CCTA (24). Pericoronary fat volume has previously been reported to be significantly correlated with the presence of both calcified plaques and non-calcified plaques, indicating that perivascular fat depots play a pivotal role in the local process of atherosclerotic disease progression (19). Furthermore, Schlett et al. demonstrated that EAT volume is associated with high-risk coronary lesion morphology on CCTA independent of clinical characteristics and obesity (20). Hwang et al. (22) demonstrated that a greater amount of EAT at baseline CT was an independent predictor of NCP development in asymptomatic individuals. Taken together, these findings demonstrate the utility of measuring EAV to detect high-risk patients.

It remains controversial whether EAV enables the provision of prognostic information in patients with CAD (41, 42). Gitsioudis et al. (41) demonstrated that increased EAV (EAV ≥162.2 cm^3) is associated with coronary plaque burden and is a predictor of worse outcome independent of risk factors, although the increased EAV did not remain as an independent predictor when coronary artery luminal stenosis was included in the model. Brandt et al. demonstrated that EAT volume showed the improved prediction performance in addition to clinical risk score alone or its combination with CCTA findings (42). Contrastingly, CCTA-derived LAP has been validated by histopathology, demonstrating a close association between LAP and lipid core plaque (43) and outcomes, including mortality and non-fatal myocardial infarction (11, 17). While the detection of obstructive CAD is the central focus of CCTA in patients with symptomatic CAD, the identification of high-risk plaque burden may provide further information on risk stratification beyond luminal stenosis. Romijn et al. showed the importance of adding EAV to CACS in predicting functionally significant stenosis in patients with CAD who underwent CCTA and invasive coronary angiography (23). Our results indicate that the addition of EAV to CACS can be used for risk stratification of patients with a greater plaque burden requiring immediate coronary revascularization and at risk of developing future ACS event.

Study Limitations

This study has some limitations. First, this study had a small sample size with relatively high Suita scores (48.4 ± 10.8 points). This can be explained by the advanced age of the participants. Moreover, patients had a high prevalence of coronary risk factors, including hypertension (71.5%) and dyslipidemia (73.1%), whereas pharmacological therapeutic interventions were deemed to be insufficient at baseline. Second, to measure the CT attenuation values of coronary plaques, we used a tube voltage of 120 kV in all patients regardless of body weight. To reduce radiation exposure, however, we used the wide-volume scan method with a prospective gating method. Third, the event rate observed in this study was relatively high (4.5%), and this may be explained by the relatively high Suita scores of the participants. Another explanation is that the approximately half of the primary endpoint consisted of a soft endpoint, including unstable angina and coronary revascularization. Fourth, this study did not analyze pericoronary adipose tissue attenuation (PCATA) (39), which has been shown to be an independent predictor of prognosis in patients with CAD. Given that PCATA might be associated with inflammation around coronary arteries, analyzing PCATA will further help in risk stratification beyond the EAT burden. Fifth, although plaque rupture is a major leading cause of ACS and sudden cardiac death, attempts have been made in recent decades to identify patients at risk of ACS caused by plaque erosion, the second leading cause of ACS (8). ACS caused by plaque erosion has been reported to be more common in females. Plaque erosion has fewer inflammatory cells, and is a proteoglycan-rich lesion in contrast to plaque rupture (8). Further *in vivo* investigations are warranted to elucidate the mechanisms and plaque composition in patients with ACS caused by plaque erosion. Novel intracoronary imaging may provide new insights (30, 32). Sixth, cardiac troponin can be elevated even in patients with stable CAD, and has been shown to be associated with increased cardiovascular events

(44); however, this study did not include any biomarker analysis that may have provided mechanistic insights regarding the hypothesis of identifying patients at very high risk for developing a primary endpoint carrying both increased LAP volume and elevated CACS and EAT volume. Finally, due to the retrospective nature of the study, the effect of medical therapies on the outcomes was not included in the analysis. A recent CCTA study demonstrated that icosapent ethyl was effective for the reduction of coronary plaque volume assessed using CCTA (45). Accumulating evidence suggests potential therapeutic strategies for reducing EAT (46). These findings suggest that CCTA might be useful for identifying and monitoring patients at a higher risk of future ACS events in response to OMT.

CONCLUSIONS

In conclusion, CCTA-based assessment of EAV, CACS, and LAP could help improve personalized cardiac risk management by administering patient-suited therapy.

DATA AVAILABILITY STATEMENT

The data that support the findings of this study are available from the corresponding author, KO upon reasonable request.

ETHICS STATEMENT

This study was approved by the ethics committee of Fujiikai Kashibaseiki Hospital. The requirement of obtaining written informed consent from the participants was waived in accordance with the institutional requirements. The study was conducted in accordance with the Declaration of Helsinki.

AUTHOR CONTRIBUTIONS

KO and HY conceived this study design and contributed equally to this work. HY performed statistical analysis, interpreted the data, and prepared manuscript draft. KO and HI performed image analysis, interpreted the data, and prepared manuscript draft. KS performed data collection. NK and DF supervised this study and prepared manuscript draft. All authors contributed to the article and approved the submitted version.

ACKNOWLEDGMENTS

We would like to thank Editage (www.editage.com) for English language editing.

REFERENCES

1. Ahmadi A, Leipsic J, Blankstein R, Taylor C, Hecht H, Stone GW, et al. Do plaques rapidly progress prior to myocardial infarction?: the interplay between plaque vulnerability and progression. *Circ Res.* (2015) 117:99–104. doi: 10.1161/CIRCRESAHA.117.305637
2. Shaw LJ, Berman DS, Maron DJ, Mancini GBJ, Hayes SW, Hartigan PM, et al. Optimal medical therapy with or without percutaneous coronary intervention to reduce ischemic burden: results from the clinical outcomes utilizing revascularization and aggressive drug evaluation (COURAGE) trial nuclear substudy. *Circulation.* (2008) 117:1283–91. doi: 10.1161/CIRCULATIONAHA.107.743963
3. Arbab-Zadeh A, Fuster V. From detecting the vulnerable plaque to managing the vulnerable patient: JACC state-of-the-art review. *J Am Coll Cardiol.* (2019) 74:1582–93. doi: 10.1016/j.jacc.2019.07.062
4. Maron DJ, Hochman JS, Reynolds HR, Bangalore S, Oanaging the vulnera, et al. Initial invasive or conservative strategy for stable coronary disease. *N Engl J Med.* (2020) 382:1395–407. doi: 10.1056/nejmoa1915922
5. Tarkin JM, Dweck MR, Evans NR, Takx RAP, Brown AJ, Tawakol A, et al. Imaging atherosclerosis. *Circ Res.* (2016) 118:79–98. doi: 10.1161/CIRCRESAHA.115.306247
6. Yahagi K, Kolodgie FD, Otsuka F, Finn A V, Davis HR, Joner M, et al. Pathophysiology of native coronary, vein graft, and in-stent atherosclerosis. *Nat Rev Cardiol.* (2016) 13:79–98. doi: 10.1038/nrcardio.2015.164
7. Mortensen MB, Dzaye O, Steffensen FH, Bein graft, and in-stent atheroscler, et al. Impact of plaque burden vs. stenosis on ischemic events in patients with coronary atherosclerosis. *J Am Coll Cardiol.* (2020) 76:2803–13. doi: 10.1016/j.jacc.2020.10.021
8. Crea F, Libby P. Acute coronary syndromes: the way forward from mechanisms to precision treatment. *Circulation.* (2017) 136:1155–66. doi: 10.1161/CIRCULATIONAHA.117.029870
9. Otsuka K, Fukuda S, Tanaka A, Nakanishi K, Taguchi H, Yoshiyama M, et al. Prognosis of vulnerable plaque on computed tomographic coronary angiography with normal myocardial perfusion image. *Eur Heart J Cardiovasc Imaging.* (2014) 15:332–40. doi: 10.1093/ehjci/jet232
10. van Rosendael AR, Narula J, Lin FY, van den Hoogen IJ, Gianni U, Al Hussein Alawamlh O, et al. Association of high-density calcified 1K plaque with risk of acute coronary syndrome. *JAMA Cardiol.* (2020) 5:282–90. doi: 10.1001/jamacardio.2019.5315
11. Otsuka K, Fukuda S, Tanaka A, Nakanishi K, Taguchi H, Yoshikawa J, et al. Napkin-ring sign on coronary CT angiography for the prediction of acute coronary syndrome. *JACC Cardiovasc Imaging.* (2013) 6:44–57. doi: 10.1016/j.jcmg.2012.09.016
12. Knuuti J, Wijns W, Saraste A, Capodanno D, Barbato E, Funck-Brentano C, et al. 2019 ESC Guidelines for the diagnosis and management of chronic coronary syndromes. *Eur Heart J.* (2020) 41:407–77. doi: 10.1093/eurheartj/ehz425
13. Narula J, Chandrashekhar Y, Ahmadi A, Abbara S, Berman DS, Blankstein R, et al. SCCT 2021 expert consensus document on coronary computed tomographic angiography: a report of the society of cardiovascular computed tomography. *J Cardiovasc Comput Tomogr.* (2021) 15:192–217. doi: 10.1016/j.jcct.2020.11.001
14. Versteylen MO, Kietselaer BL, Dagnelie PC, Joosen IA, Dedic A, Raaijmakers RH, et al. Additive value of semiautomated quantification of coronary artery disease using cardiac computed tomographic angiography to predict future acute coronary syndrome. *J Am Coll Cardiol.* (2013) 61:2296–305. doi: 10.1016/j.jacc.2013.02.065
15. Gitsioudis G, Schof semiautomated quantification of coronary artery di, et al. Combined assessment of high-sensitivity troponin T and non-invasive coronary plaque composition for the prediction of cardiac outcomes. *Radiology.* (2015) 276:73–81. doi: 10.1148/radiol.15141110
16. Newby DE, Adamson PD, Berry C, Boon NA, Dweck MR, Flather M, et al. Coronary CT angiography and 5-year risk of myocardial Infarction. *N Engl J Med.* (2018) 379:924–33. doi: 10.1056/NEJMoa1805971
17. Williams MC, Kwiecinski J, Doris M, McElhinney P, D'Souza MS, Cadet S, et al. Low-attenuation noncalcified plaque on coronary computed tomography angiography predicts myocardial infarction: results from the multicenter SCOT-HEART Trial (Scottish computed tomography of the HEART). *Circulation.* (2020) 141:1452–62. doi: 10.1161/CIRCULATIONAHA.119.044720

18. Iacobellis G. Local and systemic effects of the multifaceted epicardial adipose tissue depot. *Nat Rev Endocrinol.* (2015) 11:363–71. doi: 10.1038/nrendo.2015.58
19. Mahabadi AA, Reinsch N, Lehmann N, Altenbernd J, Kltifaceted epicard, et al. Association of pericoronary fat volume with atherosclerotic plaque burden in the underlying coronary artery: a segment analysis. *Atherosclerosis.* (2010) 211:195–9. doi: 10.1016/j.atherosclerosis.2010.02.013
20. Schlett CL, Ferencik M, Kriegel MF, Bamberg F, Ghoshhajra BB, Joshi SB, et al. Association of pericardial fat and coronary high-risk lesions as determined by cardiac CT. *Atherosclerosis.* (2012) 222:129–34. doi: 10.1016/j.atherosclerosis.2012.02.029
21. Mahabadi AA, Berg MH, Lehmann N, Knd coronary high-risk le, et al. Association of epicardial fat with cardiovascular risk factors and incident myocardial infarction in the general population: the Heinz Nixdorf recall study. *J Am Coll Cardiol.* (2013) 61:1388–95. doi: 10.1016/j.jacc.2012.11.062
22. Hwang IC, Park HE, Choi SY. Epicardial adipose tissue contributes to the development of non-calcified coronary plaque: a 5-year computed tomography follow-up study. *J Atheroscler Thromb.* (2017) 24:262–74. doi: 10.5551/jat.36467
23. Romijn MA, Danad I, Bakkum MJ, Stuijfzand WJ, Tulevski II, Somsen GA, et al. Incremental diagnostic value of epicardial adipose tissue for the detection of functionally relevant coronary artery disease. *Atherosclerosis.* (2015) 242:161–6. doi: 10.1016/j.atherosclerosis.2015.07.005
24. Nerlekar N, Brown AJ, Muthalaly RG, Talman A, Hettige T, Cameron JD, et al. Association of epicardial adipose tissue and high-risk plaque characteristics: a systematic review and meta-analysis. *J Am Heart Assoc.* (2017) 6:6379. doi: 10.1161/JAHA.117.006379
25. Nishimura K, Okamura T, Watanabe M, Nakai M, Takegami M, Higashiyama A, et al. Predicting coronary heart disease using risk factor categories for a Japanese urban population, and comparison with the framingham risk score: the suita study. *J Atheroscler Thromb.* (2014) 21:784–98. doi: 10.5551/jat.19356
26. Detrano R, Guerci AD, Carr JJ, Bild DE, Burke G, Folsom AR, et al. Coronary calcium as a predictor of coronary events in four racial or ethnic groups. *N Engl J Med.* (2008) 358:1336–45. doi: 10.1056/NEJMoa072100
27. Nakanishi K, Fukuda S, Tanaka A, Otsuka K, Jissho S, Taguchi H, et al. Persistent epicardial adipose tissue accumulation is associated with coronary plaque vulnerability and future acute coronary syndrome in non-obese subjects with coronary artery disease. *Atherosclerosis.* (2014) 237:353–60. doi: 10.1016/j.atherosclerosis.2014.09.015
28. Ehara S, Kobayashi Y, Yoshiyama M, Shimada K, Shimada Y, Fukuda D, et al. Spotty calcification typifies the culprit plaque in patients with acute myocardial infarction: an intravascular ultrasound study. *Circulation.* (2004) 110:3424–9. doi: 10.1161/01.CIR.0000148131.41425.E9
29. Jang IK, Tearney GJ, MacNeill B, Takano M, Moselewski F, Iftima N, et al. *In vivo* characterization of coronary atherosclerotic plaque by use of optical coherence tomography. *Circulation.* (2005) 111:1551–5. doi: 10.1161/01.CIR.0000159354.43778.69
30. Bourantas CV, Jaffer FA, Gijsen FJ, Van Soest G, Madden SP, Courtney BK, et al. Hybrid intravascular imaging: recent advances, technical considerations, and current applications in the study of plaque pathophysiology. *Eur Heart J.* (2017) 38:400–12. doi: 10.1093/eurheartj/ehw097
31. Waksman R, Di Mario C, Torguson R, Ali ZA, Singh V, Skinner WH, et al. Identification of patients and plaques vulnerable to future coronary events with near-infrared spectroscopy intravascular ultrasound imaging: a prospective, cohort study. *Lancet.* (2019) 394:1629–37. doi: 10.1016/S0140-6736(19)31794-5
32. Otsuka K, Villiger M, Karanasos A, van Zandvoort LJC, Doradla P, Ren J, et al. Intravascular polarimetry in patients with coronary artery disease. *JACC Cardiovasc Imaging.* (2020) 13:790–801. doi: 10.1016/j.jcmg.2019.06.015
33. Kelly-Arnold A, Maldonado N, Laudier D, Aikawa E, Cardoso L, Weinbaum S. Revised microcalcification hypothesis for fibrous cap rupture in human coronary arteries. *Proc Natl Acad Sci.* (2013) 110:10741–6. doi: 10.1073/pnas.1308814110
34. Doradla P, Otsuka K, Nadkarni A, Villiger M, Karanasos A, Zandvoort LJC van, et al. Biomechanical stress profiling of coronary atherosclerosis: identifying a multifactorial metric to evaluate plaque rupture risk. *JACC Cardiovasc Imag.* (2019) 13:804–16. doi: 10.1016/j.jcmg.2019.01.033
35. Ito H, Wakatsuki T, Yamaguchi K, Fukuda D, Kawabata Y, Matsuura T, et al. Atherosclerotic coronary plaque is associated with adventitial vasa vasorum and local inflammation in adjacent epicardial adipose tissue in fresh cadavers. *Circ J.* (2020) 84:769–75. doi: 10.1253/circj.CJ-19-0914
36. Hasegawa T, Otsuka K, Iguchi T, Matsumoto K, Ehara S, Nakata S, et al. Serum n-3 to n-6 polyunsaturated fatty acids ratio correlates with coronary plaque vulnerability: an optical coherence tomography study. *Heart Vessels.* (2014) 29:596–602. doi: 10.1007/s00380-013-0404-4
37. Taruya A, Tanaka A, Nishiguchi T, Matsuo Y, Ozaki Y, Kashiwagi M, et al. Vasa vasorum restructuring in human atherosclerotic plaque vulnerability. *J Am Coll Cardiol.* (2015) 65:2469–469:2469–77. doi: 10.1016/j.jacc.2015.04.020
38. Moreno PR, Purushothaman KR, Fuster V, Echeverri D, Truszczynska H, Sharma SK, et al. Plaque neovascularization is increased in ruptured atherosclerotic lesions of human aorta: implications for plaque vulnerability. *Circulation.* (2004) 110:2032–8. doi: 10.1161/01.CIR.0000143233.87854.23
39. Antonopoulos AS, Sanna F, Sabharwal N, Thomas S, Oikonomou EK, Herdman L, et al. Detecting human coronary inflammation by imaging perivascular fat. *Sci Transl Med.* (2017) 9:12658. doi: 10.1126/scitranslmed.aal265810.1126/scitranslmed.aal2658
40. Brandt V, Decker J, Schoepf UJ, Varga-Szemes A, Emrich T, Aquino G, et al. Additive value of epicardial adipose tissue quantification to coronary CT angiography–derived plaque characterization and CT fractional flow reserve for the prediction of lesion-specific ischemia. *Eur Radiol.* (2022). doi: 10.1007/s00330-021-08481-w. [Epub ahead of print].
41. Gitsioudis G, Schmahl C, Missiou A, Voss A, Schuantification to coro, et al. Epicardial adipose tissue is associated with plaque burden and composition and provides incremental value for the prediction of cardiac outcome. A clinical cardiac computed tomography angiography study. *PLoS ONE.* (2016) 11:1–15. doi: 10.1371/journal.pone.0155120
42. Brandt V, Bekeredjian R, Schoepf UJ, Varga-Szemes A, Emrich T, Aquino GJ, et al. Prognostic value of epicardial adipose tissue volume in combination with coronary plaque and flow assessment for the prediction of major adverse cardiac events. *Eur J Radiol.* (2022) 148:110157. doi: 10.1016/j.ejrad.2022.110157
43. Han D, Torii S, Yahagi K, Lin FY, Lee JH, Rizvi A, et al. Quantitative measurement of lipid rich plaque by coronary computed tomography angiography: a correlation of histology in sudden cardiac death. *Atherosclerosis.* (2018) 275:426–33. doi: 10.1016/j.atherosclerosis.2018.05.024
44. Everett BM, Brooks MM, Vlachos HEA, Chaitman BR, Frye RL, Bhatt DL. Troponin and cardiac events in stable ischemic heart disease and diabetes. *N Engl J Med.* (2015) 373:610–20. doi: 10.1056/NEJMoa1415921
45. Budoff MJ, Bhatt DL, Kinninger A, Lakshmanan S, Muhlestein JB, Le VT, et al. Effect of icosapent ethyl on progression of coronary atherosclerosis in patients with elevated triglycerides on statin therapy: final results of the EVAPORATE trial. *Eur Heart J.* (2020) 41:3925–32. doi: 10.1093/eurheartj/ehaa652
46. Launbo N, Zobel EH, von Scholten BJ, Faerch K, Jronensen PG, Christensen RH. Targeting epicardial adipose tissue with exercise, diet, bariatric surgery or pharmaceutical interventions: a systematic review and meta-analysis. *Obes Rev an Off J Int Assoc Study Obes.* (2021) 22:e13136. doi: 10.1111/obr.13136

Conflict of Interest: The authors declare that the research was conducted in the absence of any commercial or financial relationships that could be construed as a potential conflict of interest.

Publisher's Note: All claims expressed in this article are solely those of the authors and do not necessarily represent those of their affiliated organizations, or those of the publisher, the editors and the reviewers. Any product that may be evaluated in this article, or claim that may be made by its manufacturer, is not guaranteed or endorsed by the publisher.

frontiers | Frontiers in Cardiovascular Medicine

CASE REPORT
published: 08 April 2022
doi: 10.3389/fcvm.2022.829392

Case Series of Potential Cardiac Inflammation Associated With Various SARS-CoV-2 Vaccinations Assessed by Cardiac MRI

Constantin Jahnke[1,2]*, *Patrick Doeblin*[1,2], *Radu Tanacli*[1,3], *Undine Witt*[1,2], *Matthias Schneider*[1,3], *Christian Stehning*[4], *Burkert Pieske*[1,2,3] and *Sebastian Kelle*[1,2,3]

[1] Department of Cardiology, German Heart Centre Berlin, Berlin, Germany, [2] German Centre for Cardiovascular Research DZHK, Partner Site Berlin, Berlin, Germany, [3] Department of Cardiology, Charité University Medicine Berlin, Berlin, Germany, [4] Philips Healthcare Systems, Hamburg, Germany

Serious adverse events associated with new vaccines targeting SARS-CoV-2 are of high interest to the public and to public health as a worldwide mass immunization campaign has been initiated to contain the ongoing COVID-19 pandemic. We describe a series of 4 individuals with signs of a myocarditis/pericarditis according to cardiac MRI results in temporal association with currently in the European Union authorized SARS-CoV-2 vaccines. We found mild abnormal MRI results independent of the type of SARS-CoV-2 vaccine. There is a need of continuing monitoring outcomes of myocarditis cases after COVID-19 vaccination as recently published cases suggest an uncomplicated short-term course whereas the long-term implications are not yet known but taking the available evidence into account the benefits of using COVID-19 vaccines still clearly outweigh the risks.

Keywords: CMR, COVID-19, SARS-CoV-2 vaccination, myocarditis, pericarditis

OPEN ACCESS

Edited by:
Grigorios Korosoglou, GRN Klinik Weinheim, Germany

Reviewed by:
Hafiz Naderi, Queen Mary University of London, United Kingdom
Alexandru Deaconu, Clinical Emergency Hospital Bucharest, Romania

***Correspondence:**
Constantin Jahnke
jahnke@dhzb.de

Specialty section:
This article was submitted to Cardiovascular Imaging, a section of the journal Frontiers in Cardiovascular Medicine

Received: *05 December 2021*
Accepted: *18 February 2022*
Published: *08 April 2022*

Citation:
Jahnke C, Doeblin P, Tanacli R, Witt U, Schneider M, Stehning C, Pieske B and Kelle S (2022) Case Series of Potential Cardiac Inflammation Associated With Various SARS-CoV-2 Vaccinations Assessed by Cardiac MRI. Front. Cardiovasc. Med. 9:829392. doi: 10.3389/fcvm.2022.829392

BACKGROUND

Before the COVID-19 pandemic, there have only been a few reports of myocarditis and pericarditis as an adverse event following immunization with the exception of cases following live-attenuated smallpox vaccine (1, 2).

Serious adverse events associated with new vaccines targeting SARS-CoV-2 are of high interest to the public and to public health as a worldwide mass immunization campaign has been initiated to contain the ongoing COVID-19 pandemic.

SARS-CoV-2 vaccines currently authorized for use in the European Union by the European Pharmacy Agency include the messenger RNA (mRNA) vaccine Comirnaty (Pfizer-BioNTech), Spikevax (Moderna) and the vector-based vaccines Vaxzevria (AstraZeneca), and Vaccine Janssen (Johnson and Johnson) (3).

We describe a series of 4 individuals with signs of a myocarditis/pericarditis according to cardiac MRI results in temporal association with SARS-CoV-2 vaccination to investigate any differences regarding the phenotype.

MATERIALS AND METHODS

For this report we retrospectively reviewed cardiac MRI exams performed at our institution between 07/01/2021-09/06/2021 for MRI findings of cardiac inflammation such as myocarditis or pericarditis associated with SARS-CoV-2 Vaccination. We reviewed the medical records

regarding the timing of COVID-19 or SARS-CoV-2 vaccination and the vaccine used. All available demographic, clinical or laboratory information were documented (**Table 1**).

The study complies with the declaration of Helsinki. Approval was obtained from the ethics committee of Charite – Unversitätsmedizin Berlin. All examinations have been clinically indicated.

Cardiac MRI was performed at 1.5T/3T [Philips Healthcare, Best, Netherlands] and evaluated using a standardized diagnostic protocol as described previously (4). The protocol included cine, T1 and T2 mapping, and late gadolinium enhancement (LGE) images. Cutoffs for elevated T1 values (normal 903 to 1,085 ms at 1.5 Tesla and 1,173 to 1,334 ms at 3 Tesla) and T2 values (normal 41 to 57 ms at 1.5 Tesla and 35 to 51 at 3 Tesla) were based on 2 standard deviations above the respective means in a healthy reference group examined on the same scanners. Clinical cardiac MRI reports were reviewed by three cardiologists experienced in cardiovascular imaging in consensus.

CASES

Patient 1

Patient 1, a healthy 21-year-old male, received his second vaccination dose of Spikevax (Moderna). The following day the patient complained about chest pain and discomfort, shortness of breath, limited physical capacity and malaise. At presentation to the hospital the electrocardiogram showed no pathological findings. The serum levels for C-reactive protein and NT-proBNP were normal. High-sensitive Troponin T was elevated up to 526 ng/l (normal <14 ng/l). A coronary angiography was performed with exclusion of a coronary artery disease. CT pulmonary angiography excluded a pulmonary embolism. Transthoracic echocardiography showed normal myocardial function without wall motion abnormalities or relevant valvular heart disease.

Cardiac MRI at 3 Tesla showed a normal left and right ventricular size with normal left and right ventricular ejection fraction and normal values for the global longitudinal strain. T2 weighted images indicated a regional edema anterolateral/inferolateral (basal) with corresponding elevated quantitative myocardial T2 mapping parameters up to 70 ms (normal 35 to 51 ms at 3 Tesla) (**Figure 1**). Corresponding patchy subepicardial LGE indicating inflammatory myocardial necrosis (**Figure 1**). Pericardial enhancement in the LGE and T2 weighted images in corresponding locations indicated a pericardial involvement (**Figure 1**). The global T1 relaxation time (1,227 ms, normal 1,173 to 1,334 ms at 3 Tesla) and global T2 relaxation time (43 ms, normal 35 to 51 ms at 3 Tesla) were normal. The patient was discharged after 6 days with stable cardiopulmonary parameter and improved symptoms with an anti-inflammatory therapy with ibuprofen and a supportive therapy with ACE-inhibitor and outpatient follow-up appointments.

Patient 2

Patient 2, a healthy 42-year-old male, received the second vaccination dose of Comirnaty (Pfizer-BioNTech). Two days later, the patient presented to the emergency room of a referring hospital with chest pain and discomfort, shortness of breath and a decreased physical capacity.

The electrocardiogram on admission showed no pathological findings. The serum levels for C-reactive protein (59 mg/l, normal <5.0 mg/l) and cardiac necrosis marker were elevated with a highsensitive Troponin-I level of 4,868 pg/ml (normal <34.1 pg/ml) and creatinin kinase of 581 U/l (normal 190 U/l). The levels for D-Dimer and BNP were normal. A coronary angiography was performed with exclusion of a coronary artery disease. CT pulmonary angiography excluded a pulmonary embolism. Transthoracic echocardiography showed normal myocardial function without wall motion abnormalities or relevant valvular heart disease.

Cardiac MRI at 3 Tesla showed a normal left and right ventricular size with normal left and right ventricular ejection fraction but reduced values for the global longitudinal strain with −17.8% (normal −28.5 to −20.5% according to local reference values). T2 weighted images indicated a regional edema inferior/inferolateral (basal) with corresponding elevated quantitative myocardial T2 mapping parameters up to 53 ms (normal 35 to 51 ms at 3 Tesla) and corresponding subepicardial LGE in this region (**Figure 1**). The global T1 relaxation time (989 ms, normal 903 to 1985 ms at 1.5 Tesla) was normal. In summary, this provided evidence for acute myocarditis without functional limitation. An anti-inflammatory therapy with ibuprofen was started. During hospitalization, the patient complained of left lower leg pain. Duplex sonography of the veins showed thrombosis of a collateral vein in the region of the posterior tibial artery. Compression therapy and oral anticoagulation were started. The patient was discharged after 6 days with improved symptoms with recommendation to continue the anti-inflammatory, compression and oral anticoagulation therapy.

Patient 3

Patient number 3 was an 18-year-old healthy and athletic young man. The patient reported that shortly after a vaccination with Janssen (Johnson and Johnson), he initially experienced an episode of fever and limb pain. The initial symptoms subsided significantly after 3 days. However, a marked limitation of physical capacity and a feeling of chestpain and discomfort at rest and under physical stress remained. After the complaints persisted even for 2 months after vaccination, an outpatient presentation was made for further diagnostics. The electrocardiogram showed no pathological findings. Transthoracic echocardiography showed normal myocardial function without wall motion abnormalities or relevant valvular heart disease. Cardiac MRI at 1.5 Tesla showed a normal left and right ventricular size with normal left and right ventricular ejection fraction and normal values for global longitudinal strain. The images showed a mild pericardial effusion in the area of the free RV wall and the basal posterior LV wall up to a maximum of 4 mm with evidence of inflammatory changes of the pericardium in the T2 weighted images and the LGE images in the area of the lateral LV wall. The global T2 relaxation time (49 ms, normal 35 to 51 ms at 1.5 Tesla) and T1 relaxation time (1,071 ms, normal 903 to 1,085 ms at 1.5 Tesla) were normal. Assuming a discrete pericarditis of the LV-lateral area, a native MRI follow-up after 3 months was recommended.

TABLE 1 | Four patients diagnosed with signs of myocarditis/pericarditis in temporal relation to a SARS-CoV-2 vaccination.

Clinical data	Patient 1	Patient 2	Patient 3	Patient 4
Demographic data	21 years old/male	42 years old/male	18 years old/male	18 years old/male
Type of vaccine	2nd dose Spikevax (Moderna)	2nd dose Comirnaty (Pfizer-BioNTech)	Janssen (Johnson and Johnson)	Vaxzevria (AstraZeneca)
Symptoms	Chest pain and discomfort, malaise, dyspnea, limited physical capacity	Chest pain and discomfort, dyspnea, limited physical capacity	Chest pain and discomfort, dyspnea, limited physical capacity	Chest pain and discomfort, limited physical capacity
Vaccination–symptoms (days)	1	2	1	12
Vaccination–Cardiac MRI (days)	6	8	57	68
Troponin (ng/ml)	Troponin-T-hs 526 (normal <14 ng/l)	Troponin-I-hs 4,868 (normal <34.1 ng/l)	NA	Troponin-I-hs <5.1 (normal<34.1 ng/l)
NT-pro-BNP (ng/l)	79 (normal <97 ng/l)	40 (normal <100 ng/l)	NA	NA
Coronary angiography	No pathological findings	No pathological findings	NA	No pathological findings
Pulmonary angiography	No pathological findings	NA	NA	NA
Cardiac MRI results				
LV-EF (%) (normal 57 to 77%)	58	64	60	60
RV-EF (%) (normal 52 to 72%)	59	NA	55	62
GLS (%) (normal −28.5 to −20.5%)	−21. 2	−17.8	−23.2	−24
ECV (%) (normal ≤ 30%)	21	25	26	25
Wall motion abnormalities	+	−	−	−
Local T2w signal abnormality	+	+	+	−
Elevated global T2 relaxation time	−	−	−	−
Elevated global T1 relaxation time	−	−	−	−
Pericardial effusion	−	+	+	+
Local LGE	+	−	+	−

LV-EF, Left ventricular ejection fraction; RV-EF, Right ventricular ejection fraction; GLS, Global longitudinal strain; ECV, Extracellular volume; LGE, Late gadolinium enhancement; NA, Not available; NT-pro-BNP, N-terminal pro-B-type natriuretic peptide.

Patient 4

Patient number 4, a healthy 18-year-old male received the first dose of Vaxzevria (AstraZeneca) at the end of June 2021. The patient reported new episodes of chestpain and discomfort and exercise limitation ∼10 days after the vaccination. Initially, no medical presentation was made in the expectation that the symptoms would disappear. After a clear increase of the symptoms in the course of time, the patient presented to the emergency department of a referring hospital. The electrocardiogram on admission showed ST segment elevation in the inferior leads (II, III, and aVF). A coronary angiography was performed with exclusion of a coronary artery disease. The serum levels for C-reactive Protein [<1.0 mg/l, normal < 5.0 mg/l)] and highsensitive Troponin-I [<5.1 pg/ml, normal<34.1 pg/ml)] were normal. Creatinin kinase was increased with a serum level of 255 U/l (normal <190 U/l). Transthoracic echocardiography showed normal myocardial function without wall motion abnormalities or relevant valvular heart disease.

Cardiac MRI at 1.5 Tesla showed a normal left and right ventricular size with normal left and right ventricular ejection fraction and normal values for global longitudinal strain. The examination showed a mild to moderate pericardial effusion up to 11 mm in the mid-posterior wall of the LV. There was no evidence of acute cardiac inflammation in the T2 weighted and LGE images. The global T2 relaxation time (52 ms, normal 35 to 51 ms at 1.5 Tesla) and T1 relaxation time (979 ms, normal 903 to 1,085 ms at 1.5 Tesla) were normal. In the absence of signs of acute cardiac inflammation in the T2 weighted images and the LGE images, the pericardial effusion was considered as a possible residual of an expired pericarditis/myocarditis.

DISCUSSION

Myocarditis is an inflammation of the heart muscle in the absence of ischemia (5). If it is accompanied by pericarditis, an inflammation of the pericardium, it is referred to as myopericarditis. Myocarditis is predominantly mediated by viral infection, but can also be induced by bacterial, protozoal or fungal infections as well as systemic immune-mediated diseases and a variety of toxic substances and certain drugs as well as vaccine exposures (5).

For vaccine associated myocarditis the underlying mechanisms are not fully understood either. Molecular mimicry between the spike protein of SARS-CoV-2 and self-antigens, trigger of preexisting dysregulated immune pathways, immune response to mRNA, and activation of immunologic pathways, and dysregulated cytokine expression have recently been proposed (6).

Vaccine associated myocarditis is still overall rare and more common in males and the young population (7). The

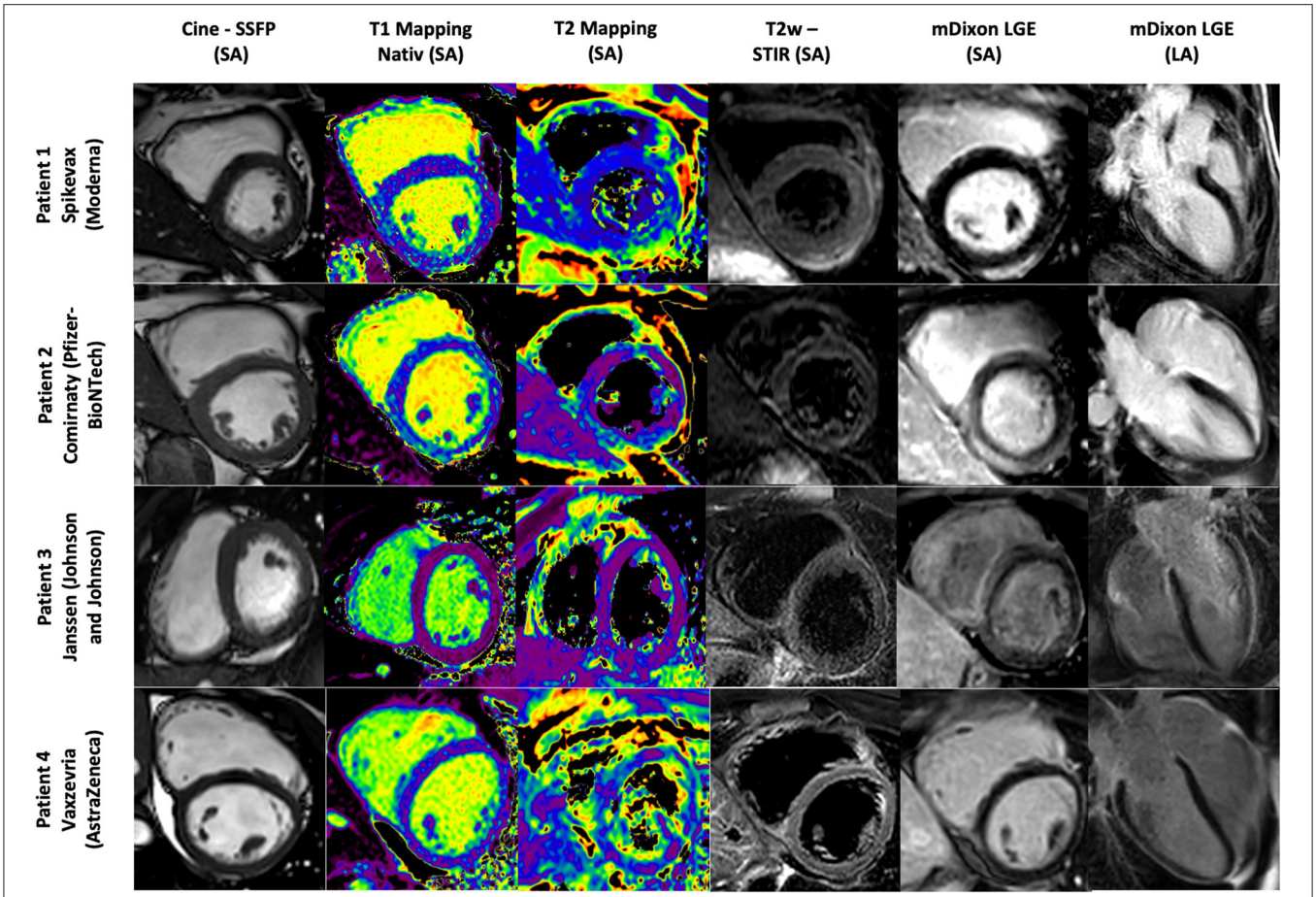

FIGURE 1 | Cardiac MR images of Patient 1–4. Patient 1 with signs of a myopericarditis after mRNA SARS-CoV-2 vaccination with Spikevax (Moderna). Patient 2 with signs of a myocarditis after mRNA SARS-CoV-2 vaccination with Comirnaty (Pfizer-BioNTech). Patient 3 with signs of a discrete pericarditis in the LV-lateral area after SARS-CoV-2 vaccination with Janssen (Johnson and Johnson). Patient 4 with a mild to moderate pericardial effusion up to 11 mm in the medial posterior wall of the LV as a possible residual of an expired pericarditis/myocarditis after SARS-CoV-2 vaccination with Vaxzevria (AstraZeneca). SSFP, Stady state free precession; T2w FSE, T2-weighted fast spin echo; mDixon, Single breath-hold three-dimensional (3D) ECG-gated multi-echo chemical shift-based sequence; T1 relaxation were calculated from single breath-hold two-dimensional (2D) modified Look-Locker inversion recovery (MOLLI) sequence LA, long axis; SA, short axis.

Advisory Committee on Immunization Practices (ACIP) recently published an incidence of 40.6 cases per million second doses of mRNA SARS-CoV-2 vaccinations in a population of males aged 12–29 years compared to 2.4 per million second doses administered to males aged ≥30 years (7).

The reasons for male predominance is unknown, but theories relate to sex hormone differences in immune response and myocarditis and underdiagnosis of cardiac disease in women (6).

Severity and clinical presentation of myocarditis or pericarditis vary among patients. Symptoms might include dyspnea, chest pain or palpitations, although especially in younger children other symptoms might be present (8). The clinical diagnostic evaluation might show elevated cardiac injury marker, pathological findings on electrocardiogram, echocardiogram, or as shown cardiac MRI results.

As also seen in our patients the clinical course of SARS-Cov2 vaccination associated myocarditis is typically mild and self-limited (2). Data published by the Israeli Ministry of Health showed 148 cases of myocarditis among 10.4 million vaccinated Israelis (9). Most cases occurred within 30 days after the second dose of a mRNA vaccination. Most cases required a hospitalization up to 4 days but were considered mild (9).

Regarding the guidelines for a mild and uncomplicated myocarditis/pericarditis a myocardial biopsy or viral serology was not performed in our patients. According to the guidelines the management depends on supportive therapy with targeted cardiac and anti-inflammatory medications and specific interventions if necessary (10, 11). Exercise restriction is recommended until the heart recovers (10, 11).

We found mild abnormal MRI results independent of the type of SARS-CoV-2 vaccine. We hypothesize, that abnormal findings might be present independent of vaccine and potentially might also be present when patients are flu-vaccinated. Future research work should also focus on this aspect. A more pragmatic approach might be to look first for cardiac abnormalities in cases of cardiac symptoms after vaccination, such as elevated lab values as troponin and NTproBNP or abnormalities at

echocardiography as previously described from our group post COVID-19 (12).

In conclusion clinicians should be aware of vaccine-induced myocarditis as a possible adverse event after SARS-CoV-2-vaccination.

There is a need of continuing monitoring outcomes of myocarditis cases after COVID-19 vaccination as recently published cases suggest an uncomplicated short-term course whereas the long-term implications are not yet known.

Taking into account the available evidence including the risks of myocarditis and pericarditis, it can be determined that the benefits of using COVID-19 vaccines still clearly outweigh the risks. There is a need for a continued educational campaign for the public regarding the risk of COVID-19 and the benefits and risks of a SARS-CoV-2 vaccination.

DATA AVAILABILITY STATEMENT

The original contributions presented in the study are included in the article/supplementary material, further inquiries can be directed to the corresponding author/s.

ETHICS STATEMENT

The studies involving human participants were reviewed and approved by Charite Unversitätsmedizin Berlin. The patients/participants provided their written informed consent to participate in this study. Written informed consent was obtained from the individual(s) for the publication of any potentially identifiable images or data included in this article.

AUTHOR CONTRIBUTIONS

The first draft of the manuscript was written by CJ and all authors commented on previous versions of the manuscript. All authors contributed to the study conception and design, read, and approved the final manuscript.

FUNDING

SK received funding from the DZHK (German Centre for Cardiovascular Research) and by the BMBF (German Ministry of Education and Research).

REFERENCES

1. Mei R, Raschi E, Forcesi E, Diemberger I, De Ponti F, Poluzzi E, et al. Myocarditis and pericarditis after immunization: gaining insights through the Vaccine Adverse Event Reporting System. *Int J Cardiol.* (2018) 273:183–6. doi: 10.1016/j.ijcard.2018.09.054
2. Gargano JW, Wallace M, Hadler SC, Langely G, Su JR, Oster ME, et al. Use of mRNA COVID-19 vaccine after reports of myocarditis among vaccine recipients: update from the advisory committee on immunization practices — United States, June 2021. *MMWR Morb Mortal Wkly Rep.* (2021) 70:977–82. doi: 10.15585/mmwr.mm7027e2
3. Paul-Ehrlich Institut. Paul-Ehrlich-Institut - COVID-19-Impfstoffe. In: *Covid 19 Vaccine*. (2021). Available online at: https://www.pei.de/DE/arzneimittel/impfstoffe/covid-19/covid-19-node.html (accessed August 15, 2021).
4. Kelle S, Bucciarelli-Ducci C, Judd RM, Kwong RY, Simonetti O, Plein S, et al. Society for Cardiovascular Magnetic Resonance (SCMR) recommended CMR protocols for scanning patients with active or convalescent phase COVID-19 infection. *J Cardiovasc Magn Reson.* (2020) 22:61. doi: 10.1186/s12968-020-00656-6
5. Tschöpe C, Ammirati E, Bozkurt B, Caforio ALP, Cooper LT, Felix SB, et al. Myocarditis and inflammatory cardiomyopathy: current evidence and future directions. *Nat Rev Cardiol.* (2021) 18:169–93. doi: 10.1038/s41569-020-00435-x
6. Bozkurt B, Kamat I, Hotez PJ. Myocarditis with COVID-19 mRNA vaccines. *Circulation.* (2021) 144:471–84. doi: 10.1161/circulationaha.121.056135
7. Montgomery J, Ryan M, Engler R, Hoffman D, McClenathan B, Collins L, et al. Myocarditis following Immunization with mRNA COVID-19 Vaccines in Members of the US Military. *JAMA Cardiol.* (2021) 92134:6–10. doi: 10.1001/jamacardio.2021.2833
8. Cooper LT Jr. Myocarditis. *N Engl J Med.* (2009) 360:1526–38. doi: 10.1056/NEJMra0800028
9. Israel Ministry of Health. *Surveillance of Myocarditis (Inflammation of the Heart Muscle) Cases Between December 2020 and May 2021 (Including) | Ministry of Health*. (2021). Available online at: https://www.gov.il/en/departments/news/01062021-03 (accessed August 18, 2021).
10. Adler Y, Charron P, Imazio M, Badano L, Barón-Esquivias G, Bogaert J, et al. 2015 ESC Guidelines for the diagnosis and management of pericardial diseases. *Eur Heart J.* (2015) 36:2921–64. doi: 10.1093/eurheartj/ehv318
11. Caforio ALP, Pankuweit S, Arbustini E, Basso C, Gimeno-Blanes J, Felix SB, et al. Current state of knowledge on aetiology, diagnosis, management, and therapy of myocarditis: a position statement of the European Society of Cardiology Working Group on Myocardial and Pericardial Diseases. *Eur Heart J.* (2013) 34:2636–48. doi: 10.1093/eurheartj/eht210
12. Doeblin P, Kelle S. Going after COVID-19 myocarditis. *Eur Hear J Cardiovasc Imaging.* (2021) 22:852–4. doi: 10.1093/ehjci/jeab097

Conflict of Interest: SK as a researcher is supported by a grant from Philips Healthcare. CS is an employee of Philips Healthcare. The following authors report financial activities outside the submitted work: BP reports having received consultancy and lecture honoraria from Bayer Daiichi Sankyo, MSD, Novartis, Sanofi-Aventis, Stealth Peptides and Vifor Pharma; and editor honoraria from the Journal of the American College of Cardiology.

The remaining authors declare that the research was conducted in the absence of any commercial or financial relationships that could be construed as a potential conflict of interest.

frontiers | Frontiers in Cardiovascular Medicine

ORIGINAL RESEARCH
published: 31 May 2022
doi: 10.3389/fcvm.2022.830165

Abnormal Right Ventricular Myocardial Performance Index Is Not Associated With Outcomes in Invasively Ventilated Intensive Care Unit Patients Without Acute Respiratory Distress Syndrome—*Post hoc* Analysis of Two RCTs

Charalampos Pierrakos[1,2], Anna Geke Algera[1], Fabienne Simonis[1], Thomas G. V. Cherpanath[1], Wim K. Lagrand[1], Frederique Paulus[1], Lieuwe D. J. Bos[1], Marcus J. Schultz [1,3,4] the PReVENT– and RELAx–Investigators*

[1] Laboratory of Experimental Intensive Care and Anesthesiology (L·E·I·C·A), Department of Intensive Care, Amsterdam University Medical Centers, Amsterdam, Netherlands, [2] Department of Intensive Care, Brugmann University Hospital, Université Libre de Bruxelles, Brussels, Belgium, [3] Mahidol–Oxford Tropical Medicine Research Unit (MORU), Mahidol University, Bangkok, Thailand, [4] Nuffield Department of Medicine, University of Oxford, Oxford, United Kingdom

OPEN ACCESS

Edited by:
Lucas Liaudet,
Centre Hospitalier Universitaire Vaudois (CHUV), Switzerland

Reviewed by:
Andrew Conway Morris,
University of Cambridge, United Kingdom
Annagrazia Cecere,
University of Padua, Italy

***Correspondence:**
Charalampos Pierrakos
charalampos_p@hotmail.com

Specialty section:
This article was submitted to Cardiovascular Imaging, a section of the journal Frontiers in Cardiovascular Medicine

Received: 06 December 2021
Accepted: 20 April 2022
Published: 31 May 2022

Citation:
Pierrakos C, Geke Algera A, Simonis F, Cherpanath TGV, Lagrand WK, Paulus F, Bos LDJ and Schultz MJ (2022) Abnormal Right Ventricular Myocardial Performance Index Is Not Associated With Outcomes in Invasively Ventilated Intensive Care Unit Patients Without Acute Respiratory Distress Syndrome—Post hoc Analysis of Two RCTs. Front. Cardiovasc. Med. 9:830165. doi: 10.3389/fcvm.2022.830165

Background: The objective of the study was to determine the association between right ventricular (RV) myocardial performance index (MPI) and successful liberation from the ventilator and death within 28 days.

Methods: *Post hoc* analysis of 2 ventilation studies in invasively ventilated patients not having ARDS. RV-MPI was collected through transthoracic echocardiography within 24–48 h from the start of invasive ventilation according to the study protocols. RV-MPI $\leq$ 0.54 was considered normal. The primary endpoint was successful liberation from the ventilator $<$ 28 days; the secondary endpoint was 28-day mortality.

Results: A total of 81 patients underwent transthoracic echocardiography at median 30 (24–42) h after the start of ventilation—in 73 (90%) patients, the RV-MPI could be collected. A total of 56 (77%) patients were successfully liberated from the ventilator $<$ 28 days; A total of 22 (30%) patients had died before or at day 28. A total of 18 (25%) patients had an abnormal RV-MPI. RV-MPI was neither associated with successful liberation from the ventilator within 28 days [HR, 2.2 (95% CI 0.47–10.6); $p = 0.31$] nor with 28-day mortality [HR, 1.56 (95% CI 0.07–34.27); $p = 0.7$].

Conclusion: In invasively ventilated critically ill patients without ARDS, an abnormal RV-MPI indicative of RV dysfunction was not associated with time to liberation from invasive ventilation.

Keywords: heart-lung interactions, echocardiography, hemodynamic monitoring, mechanical ventilation, mortality, successful extubation

INTRODUCTION

Acute right ventricular (RV) dysfunction is a common complication in critically ill patients and is associated with higher morbidity and mortality (1). RV function is affected by the change from negative to positive intrathoracic pressure in patients who receive invasive ventilation, by the decrease in venous return and increase in RV afterload (2). Acute RV failure in invasively ventilated patients can cause life-threatening hemodynamic instability and delay liberation from the ventilator (3, 4). Accordingly, monitoring RV function could be important for fluid optimization, vasopressor strategy, and respiratory support in these patients (3, 5).

The RV myocardial performance index (MPI) is an easy-to-obtain variable through transthoracic echocardiography (6). It is a measure for systolic and diastolic RV performance, and to a certain degree fluid status-independent (7). Right ventricular myocardial performance index (RV-MPI) has been shown to have predictive capacity for mortality in chronically ill patient, including patients with primary pulmonary hypertension (8) and patients with chronic heart failure (9). RV-MPI has also been shown to have predictive capacity for mortality in acutely ill patients, including patients after cardiac surgery (10), patients after myocardial infarction (11), patients with acute pulmonary embolism (12), and patients with sepsis (13). Whereas RV-MPI has been shown to have predictive capacity for liberation from the ventilator in critically ill ventilated patients with acute respiratory distress syndrome (ARDS) (14), it is uncertain whether it also holds prognostic capacity in critically ill ventilated patients without ARDS. To test the hypothesis that an abnormal RV function has associations with delayed extubation and higher mortality in these patients, we collected RV-MPI who underwent transthoracic echocardiography in two studies on invasive ventilation in patients without ARDS.

MATERIALS AND METHODS

Design

This is a *post hoc* analysis of patients included in two multicenter randomized clinical trials of invasive ventilation—in one study, ventilation with a low tidal volume (V_T) was compared with ventilation with an intermediate V_T (the "Protective Ventilation in Patients Without ARDS" (PReVENT) study) (15); in the other study, ventilation with lower positive end-expiratory pressure (PEEP) was compared to ventilation with higher PEEP (the "REstricted vs. Liberal positive end-expiratory pressure in patients without ARDS" (RELAx) study) (16). The results of the substudy with the PReVENT study have been published in part before (17). Echocardiography was performed as the part of two substudies that focused on the effects of the tested ventilation strategies on cardiac function and enrolled patients in only one center, the Amsterdam UMC, location "AMC," Amsterdam, the Netherlands, from 4 November 2014 to 20 August 2017 (in the PReVENT study) and from 26 October 2017 to 17 December 2019 (in the RELAx study).

Ethics

Ethical approval for the two parent studies (ethical committee number: 2014_075#B2014424ENG and ethical committee number 2017_074#C2017635) was provided by Medical Ethics Review Committee of AMC on 19 September 2014 and 28 June 2018. Ethical approval for the two substudies (ethical committee number W14_2992017_074 and ethical committee number #B2018435) was provided by Medical Ethics Review Committee of AMC on 4 November 2014 and 18 July 2018. Patients or relatives had to provide written informed consent before the participation in the parent study, as well as the substudy.

Study Registration

The studies were registered at clinicaltrials.gov (NCT02153294, 3 June 2014; NCT03167580, 13 May 2017).

Patients

The PReVENT and RELAx studies had identical inclusion and exclusion criteria and enrolled patients who received invasive ventilation shortly before and not longer than 1 h after admission to the intensive care unit (ICU) and who were expected not to be extubated within 24 h of randomization. The exclusion criteria were age $<$ 18 years, the presence of ARDS according to the current definition of ARDS (18) known chronic obstructive pulmonary disease (COPD), pregnancy, increased and uncontrollable intracranial pressure, history of pulmonary disease, and new pulmonary thromboembolism. Patients were excluded from participation in the substudies if known poor left ventricular function, with left ventricular ejection fraction less than or equal to 30%, and severe shock, requiring norepinephrine $\geq$ 0.5 μ g/kg/min.

Data Collected

Patient demographics, disease severity scores, and reasons for intubation and invasive ventilation were collected at baseline. Ventilator settings and parameters, fluid status, and inotropic and vasopressor use were collected at the time of transthoracic echocardiography.

Transthoracic Echocardiography

Transthoracic echocardiography was performed by physicians trained in cardiac ultrasound in critically ill patients using a Vivid 9 Dimension Ultrasound System (GE Healthcare, Hoevelaken, the Netherlands). Transthoracic echocardiography was performed in the supine position without any major mobilization 24–48 h after invasive ventilation initiation. A comprehensive transthoracic echocardiogram was performed, and the right and left heart were assessed using parasternal, apical, and subcostal sonographic windows. Continuous cardiac rhythm was recorded. Images and videos were stored digitally and analyzed blindly using automated function imaging software (EchoPAC®, GE Vingmed, Norway). For the analysis of echocardiographic variables, the median values of three or five cardiac cycles were calculated for sinus rhythm and atrial fibrillation, respectively.

Pulsatile and continuous wave Doppler was used to assess blood velocities. Tissue Doppler imaging (TDI) and motion mode (M–mode) synchronized with electrocardiogram readings were used to assess mitral and tricuspid valve annulus motion. Isovolumetric contraction time, isovolumetric relaxation time, and ejection time were calculated from the TDI trace. MPI was calculated as the ratio between the sum of the isovolumetric contraction and relaxation time to the ejection time. The two-dimensional speckle tracking for the right and left ventricles was calculated from the 4–chamber apical view after tracing the endocardial borders of the left and right ventricles. Regions of interest (ROIs) were automatically generated and manually corrected when necessary. The global longitudinal strain was calculated for the left ventricle. For the RV, the free wall was automatically divided into three segments, that is, basal, mid, and apical, and the means of the strain values were calculated for each segment.

Outcomes

The primary outcome of this *post hoc* analysis was successful liberation from invasive ventilation within 28 days, in which successful liberation was defined as no requirement for tracheal intubation within a 48-h period following extubation and alive. The secondary outcome was the 28-day mortality.

Statistical Analysis

The number of available patients in the substudies of the two randomized clinical trials served as the sample size for this analysis.

Demographic, clinical, echocardiographic, and outcome variables were presented as percentages for categorical variables and as medians with interquartile ranges (IQRs) for continuous variables and compared using the Mann–Whitney *U*-test or chi-square test, as appropriate. Patients were classified as having a normal or an abnormal RV–MPI based on a previously defined cutoff (RV-MPI $\leq$ 0.54, normal) (19).

The association of RV-MPI with outcomes was analyzed with multistate, competing risk proportional hazard models as described in the *survival* package *via* the *compete* function in R. Risks were estimated for successful extubation and mortality and compared to persistent intubation (reference category). We considered mortality and successful extubation as competing outcomes for persistent intubation. Follow-up was censored after 28 days. Patients who died and received a follow-up of less than 28 days with no events were not censored to eliminate bias through censoring by mortality. This analysis was repeated for other parameters of RV dysfunction.

Moderation of the association of RV-MPI with outcomes by V_T or PEEP was evaluated by adding an interaction term to the above-mentioned models. Hazard ratios (HR) with 95% confidence intervals (CI) were calculated for each outcome.

All analyses were performed in R using the R-Studio interface (R version 3.3.1)[1] (accessed on 08/05/2022). Statistical significance was set at $p < 0.05$.

[1]www.r-project.org

RESULTS

Patients

A total of 81 patients were enrolled in the two substudies. We excluded four patients from the cohort of patients enrolled in the substudy of the PReVENT study, because outcomes of interest were missing for these patients. Thus, we had 73 patients left for the current analysis (**Figure 1**). Patient characteristics are presented in **Table 1**. A total of eighteen patients (25%) had abnormal RV-MPI; a total of 2 patients were randomized to the high PEEP ventilation strategy, 1 patient to the low PEEP strategy, 12 patients to the high V_T strategy, and 3 patients to the low V_T strategy. A total of 55 patients (75%) had a normal RV–MPI; a total of 19 patients were randomized to the high PEEP strategy, 17 patients to the low PEEP strategy, 4 patients to the high V_T strategy, and 15 patients to the low V_T strategy. Differences in noradrenaline use or in the applied dosages did not achieve statistical significance. Echocardiography findings, including RV-MPI, are presented in **Table 2**.

Association of Right Ventricular Myocardial Performance Index With Liberation Form Invasive Ventilation

The RV-MPI, used as a continuous variable, was not associated with successful liberation from invasive ventilation before day 28 [HR, 2.2 (95% CI 0.47–10.6); $p = 0.31$]. RV-MPI > 0.54 was also not associated with a lower probability of successful liberation from mechanical ventilation [HR, 0.89 (95% CI 0.49–1.62); $p = 0.72$] (**Figure 2**).

Association of Right Ventricular Myocardial Performance Index With Mortality

The RV-MPI was not associated with 28-day mortality [HR, 1.56 (95% CI 0.07–34.27); $p = 0.78$]. An RV-MPI > 0.54 was also not associated with mortality [HR, 2.1 (95% CI 0.46–9.17); $p = 0.34$] (**Figure 2**).

Associations of Other Echocardiography-Derived Parameters for Right Ventricular Function With Outcomes

Other echocardiography-derived parameters for RV function were not associated with successful liberation from invasive ventilation before day 28 (**Table 3**).

Subgroup Analyses

PEEP levels were not different between patients with normal RV-MPI and those with abnormal RV-MPI (**Table 4**), and there was no evidence of moderation by PEEP of the associations of RV-MPI with outcome ($p = 0.81$). V_T was higher in patients with RV-MPI > 0.54 (**Table 4**), but there was no evidence of moderation by V_T of the association of RV-MPI with outcome ($p = 0.35$).

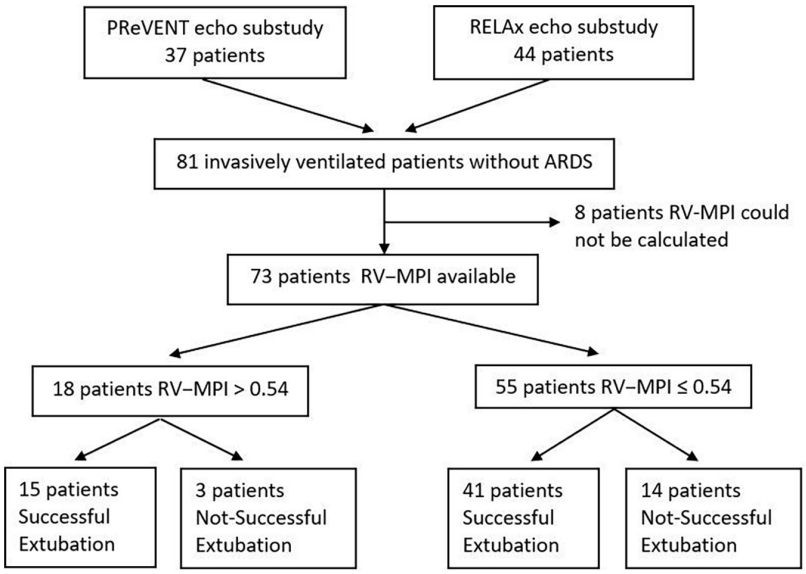

FIGURE 1 | Flow chart of the patients enrolled in the study.

TABLE 1 | Demographic and clinical characteristics according to normal or abnormal right ventricular myocardial performance index (RV-MPI).

Variables	Abnormal PI (*n* = 18)	Normal RV-MPI (*n* = 55)	*P*-value
Age, years, median (IQR)	68 (56–73)	64 (54–70)	0.29
Female gender, No. (%)	5 (27)	30 (54)	0.06
Height, cm, median (IQR)	175 (170–183)	173 (168–178)	0.27
Weight, kg, median (IQR)	79 (72–88)	75 (66–71)	0.81
SOFA score, median (IQR)*	9.5 (6.5–13)	9.0 (7.0–11.0)	0.47
APACHE II score, median (IQR)*	25 (23-29)	22 (17-27)	0.34
PaO_2/FiO_2, median (IQR)	354 (219–375)	284 (220–370)	0.53
Medical reasons for admission, No. (%)	14 (77)	40 (72)	0.76
Reason of intubation, No. (%)			
Respiratory failure	6 (33)	11 (20)	0.17
Cardiac arrest	2 (11)	8 (15)	0.99
Depressed level of consciousness	4 (22)	12 (22)	0.73
Planned postoperative ventilation	5 (28)	19 (34)	0.98
Airway protection	1 (6)	5 (9)	0.99
Ventilatory mode, No. (%)*			
Pressure controlled ventilation	3 (17)	23 (42)	0.08
Volume controlled ventilation	5 (27)	1 (2)	<0.01
Pressure support ventilation	10 (55)	31 (56)	0.98
Vasopressor use*			
Norepinephrine, No (%)	10 (55)	19 (34)	0.09
Norepinephrine dose, μ g/kg/min, median (IQR)	0.16 (0.10–0.27)	0.11 (0.09–0.17)	0.11
Sinus rhythm, No (%)*	16 (88)	49 (89)	0.99
ICU LOS, days	9.5 (5.0-15.5)	4.5 (3.0-13.5)	0.29
Successfully extubated 28 days, No. (%)	15 (83)	41 (74)	0.53
Ventilation free days	22.5 (12.6-25.3)	18.8 (0.0-26.3)	0.66
Mortality 28 days, No. (%)	3 (16)	13 (23)	0.23
Duration of invasive ventilation, days	5.1 (2.7-10.6)	5.3 (2.3-10.6)	0.77

** At time of echocardiography.*

IQR, interquartile range; SOFA, Sequential Organ Failure Assessment; APACHE, Acute Physiology and Chronic Health Evaluation; ICU LOS, intensive care length of stay.

TABLE 2 | Echocardiographic variables of left and right ventricle of invasively ventilated patients examined within 48 h after mechanical ventilation initiation according to normal or abnormal right ventricular myocardial performance index (RV-MPI).

Variables	Abnormal RV-MPI (*n* = 18)	Normal RV-MPI (*n* = 55)	*P*-value
Right ventricular function			
Systolic parameters			
Myocardial performance index [n]	0.71 (0.61–0.75) [18]	0.36 (0.29–0.41) [55]	NA
Tricuspid annular plane systolic excursion (mm) [n]	16 (15–19) [18]	22 (18–26) [55]	< 0.01
Global longitudinal strain,% [n]	−12 (−18—10) [17]	−19 (−24—16) [41]	< 0.01
Isovolumetric acceleration, m/sec [n]	2.1 (1.4–2.7) [16]	3.1 (2.1–4.7) [55]	< 0.01
Systolic maximal velocity, cm/sec [n]	11 (8–12) [18]	13 (11–16) [55]	0.02
Diastolic *parameters*			
Early (E)/Atrial velocity ratio [n]	1.1 (0.8–1.4) [14]	1.1 (0.8–1.2) [47]	0.29
Early maximal diastolic velocity (E'), cm/sec [n]	10 (8–12) [18]	12 (10–15) [54]	0.07
E/E' [n]	4.7 (3.1–5.4) [14]	4.1 (3.2–5.4) [47]	0.61
General parameters			
Pulmonary acceleration time (m/s^2) [n]	8.2 (7.1-8.8) [10]	10.5 (7.1-12.5) [39]	0.25
Right ventricle/left ventricle diameter* [n]	0.81 (0.73–0.87) [15]	0.79 (0.65–0.89) [46]	0.37
Left ventricular function			
Systolic parameters			
Myocardial performance index [n]	0.58 (0.44–0.68) [18]	0.42 (0.38–0.52) [55]	< 0.01
Ejection fraction,% [n]	43 (37–53) [18]	55 (47–61) [55]	< 0.01
Global longitudinal strain,% [n]	−12 (−14—10) [18]	−14 (−18—10) [55]	0.09
Isovolumetric acceleration, m/sec [n]	1.5 (1.1–2.8) [17]	2.5 (1.7–4.1) [55]	0.01
Systolic maximal velocity, cm/sec [n]	7.5 (6.0–10.0) [18]	8.7 (7.0–10.0) [55]	0.21
Diastolic parameters			
Early (E)/atrial velocity ratio [n]	0.9 (0.7–1.2) [14]	1.0 (0.7–1.2) [54]	0.91
Early maximal diastolic velocity (E'), cm/sec [n]	8.0 (7.0–10.0) [18]	8.5 (6.5–11.0) [55]	0.62
E/E' [n]	6.9 (5.7–10.1) [14]	8.2 (6.2–10.8) [54]	0.32
General parameters			
Cardiac index, $L/min/m^2$ [n]	2.00 (1.63–2.92) [13]	2.57 (1.93–3.36) [49]	0.06
Eccentricity index [n]	1.00 (0.85–1.26) [15]	0.92 (0.81–1.05) [46]	0.23

[n], number of patients for which this measure was available.
**Basal diameters (endocardial to endocardial surface) obtained in the four-chamber view at the end of diastole.*

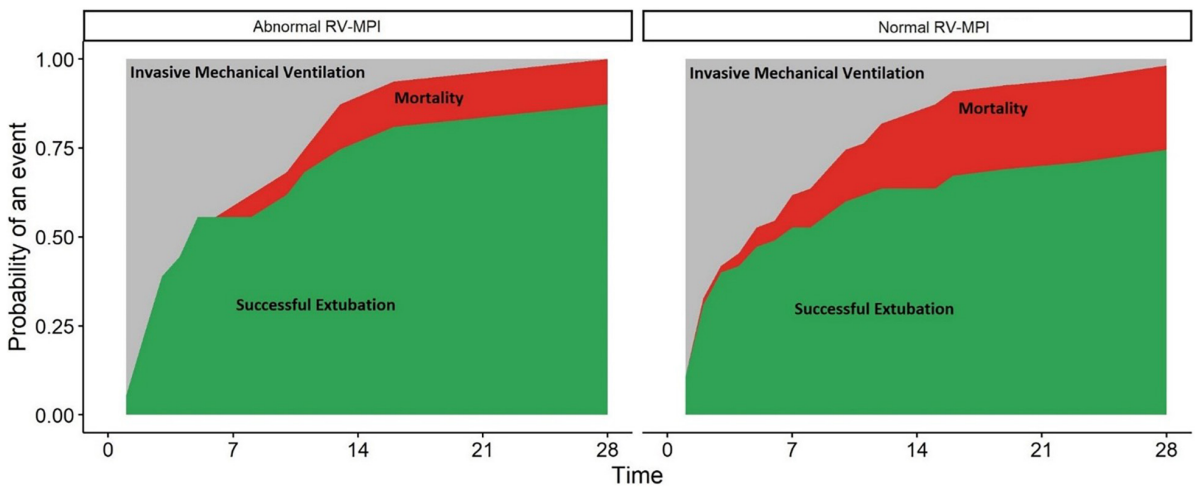

FIGURE 2 | Abnormal right ventricular myocardial performance index (RV-MPI > 0.54) and normal RV-MPI (≤0.54) and cumulative incidence of outcomes. *X*-axis: Days since intubations. *Y*-axis: probability of an event (extubation or death) in the population. The two facets show the risk for patients with an abnormal RV-MPI **(left)** and normal RV-MPI **(right)**. Red areas represent patients who died. Green areas represent patients who were successfully extubated. Gray areas represent patients who remained invasively ventilated.

TABLE 3 | The association of right ventricular parameters obtained with transthoracic echocardiography with the probability of successful liberation from invasive ventilation and death at 28 days.

Variables	Hazard ratio (95% CI)	*P*-value
Endpoint: Successful extubation		
Myocardial performance index	2.2 (0.47–10.63)	0.30
Tricuspid annular plane systolic excretion	0.9 (0.95-1.04)	0.93
Systolic maximal velocity	1.0 (0.94-1.06)	0.91
Global longitudinal strain	1.1 (0.99-1.08)	0.10
Right ventricle/left ventricle diameter	0.6 (0.21-2.11)	0.48
Endpoint: Mortality		
Myocardial performance index	1.6 (0.07–34.27)	0.77
Tricuspid annular plane systolic excretion	1.1 (0.93-1.12)	0.59
Systolic maximal velocity	1.1 (0.87-1.09)	0.67
Global longitudinal strain	0.9 (0.86-1.01)	0.09
Right ventricle/left ventricle diameter	0.5 (0.22-14.33)	0.58

DISCUSSION

The findings of this study can be summarized as follows: (1) RV-MPI is abnormal in a substantial number of patients who receive invasive ventilation for reasons other than ARDS; (2) in these patients, RV-MPI is neither associated with successful liberation from the ventilator within 28 days; (3) nor with 28-day mortality.

The findings of our study are in contrast to the results of one previous study (14). Indeed, in that study, RV-MPI was strongly associated with the duration of ventilation. Several difference between our study and that previous study should be mentioned, though. First, that study enrolled patients with ARDS, while we restricted the enrollment of patients not having ARDS. Second, and probably as a consequence of this, patients in the previous study were ventilated with higher PEEP than in our study. The results of this study add to our understanding of the association of RV-MPI with liberation of mechanical ventilation and mortality in critically ill patients, by showing that the prognostic value of RV-MPI may depend on the presence of ARDS and may be also the level of PEEP.

The findings of our study are in line with the results of several other studies (20–22) and one meta-analysis (23), Indeed, these investigations did not find an association of right ventricular dysfunction with successful liberation from invasive ventilation. Of note, associations of diastolic left ventricular function with successful liberation from invasive ventilation have been reported before (23). An abnormal right ventricular function could be associated with an abnormal systolic or diastolic left ventricular function (24–26). However, only left ventricular diastolic dysfunction, and not systolic dysfunction, has been found to have an association with successful extubation (23), and in our cohort, we did find only systolic, and not diastolic dysfunction of the left ventricle.

Right ventricular myocardial performance index is, at least in part, preload-dependent, and the size of V_T and level of PEEP could affect the preload of the right ventricle in invasively ventilated patients. In our cohort, patients were ventilated with higher or lower V_T (15), and with higher or lower PEEP (16), as per the study protocols of the two parent studies. Of note, several patients treated with V_T near to 10 ml/kg (PBW) which can cause significant instant preload variations (27) affecting, in theory, RV-MPI measurement reliability and, consequently, its association with the outcome. In this relatively small *post hoc* study, we could not clearly establish the relationship between V_T and RV dysfunction, and it cannot be excluded that V_T actually affects RV-MPI. One potential weakness of our approach is that there

TABLE 4 | Respiratory and hemodynamic variables at the time of transthoracic echocardiography according to normal or abnormal right ventricular myocardial performance index (RV-MPI).

Variables	Abnormal RV-MPI (*n* = 18)	Normal RV-MPI (*n* = 55)	*P*-value
Respiration			
Tidal volume, ml/kg PBW, median (IQR)	8.55 (7.47–9.72)	7.3 (5.7–8.6)	0.02
PEEP, cm H_2O, median (IQR)	5 (5–7)	8 (1–8)	0.56
FiO_2,%, median (IQR)	25 (22–33)	30 (25–35)	0.51
SpO_2, median (IQR)	95 (94–96)	97 (94–98)	0.39
RR, breaths/min, median (IQR)	17 (14–21)	19 (15–24)	0.27
Laboratory			
pH, median (IQR)	7.43 (7.40–7.48)	7.44 (7.40–7.46)	0.97
$PaCO_2$, kPa, median (IQR)	4.9 (4.21–5.75)	5.0 (4.5–5.4)	0.67
PaO_2, kPa, median (IQR)	10.8 (10.2–11.7)	10.6 (9.7–11.9)	0.81
Hemodynamics			
Heart rate, mmHg, median (IQR)	90 (79–103)	80 (67–99)	0.18
Systolic blood pressure, mmHg, median (IQR)	118 (104–141)	130 (109–163)	0.29
Diastolic blood pressure, mmHg, median (IQR)	67 (57–79)	65 (56–72)	0.48
Mean arterial pressure, mmHg, median (IQR)	86 (73–92)	85 (76–102)	0.82

PBW, per predicted body weight; PEEP, positive end expiratory pressure; FiO_2, fraction inspired oxygen; SpO_2, peripheral oxygen saturation; RR, respiratory rate; $PaCO_2$, partial pressure of carbon dioxide in the arterial blood; PaO_2, partial pressure of carbon dioxide in the arterial blood.

could be an interaction between the intervention being tested in the original trial(s) and the outcome of the secondary analysis. We cannot exclude that ventilation with high V_T does not affect the reliability of RV-MPI to evaluate right heart function.

The results of this study can be used to decide on whether RV-MPI should be monitored with transthoracic echocardiography in invasively ventilated patients without ARDS. One could hypothesize that right ventricular dysfunction is in part caused by higher intrathoracic pressures, as patients randomized to ventilation with higher V_T and patients randomized to ventilation with higher PEEP more often had an abnormal RV-MPI. While we show that RV-MPI has no predictive validity, we cannot exclude that RV-MPI may be useful in guiding fluid and inotrope therapy in these patients. While RV-MPI seems a relatively easy to collect index, in 8 out of 81 patients, we were not able to capture it. However, other parameters are usually more difficult to collect—-for instance, right ventricular global longitudinal strain, another parameter for right ventricular function could not be measured in more than a quarter of these patients.

The strength of this study was the systematic evaluation of the prognostic validity of RV function in a homogeneous population of critically ill patients without ARDS. Patients were examined soon after the start of invasive ventilation, thereby reducing the risk of the effects of other strategies, as well as bias by left truncation. We also excluded patients with pre-existing heart failure. Echocardiographic parameters were evaluated in a blind fashion, and only in a small portion of patients, the RV-MPI could not be collected.

This study also has limitations. First, although the sample size was larger than that in most other studies on this topic, the confidence intervals were wide and repeating this study in a larger cohort of patients would likely result in a more precise estimate of effect. Seen the lack of previous studies on associations of RV-MPI with outcome in this specific group of critically ill patients, we were not able to perform a proper sample size calculation. Nevertheless, given that the observed difference in mortality was opposite to the hypothesis, the likelihood that a larger sample size would provide an opposite result (a higher mortality in patients with a more abnormal RV function) is minimal. Second, we did not analyze inter-observer and intra-observer variability of MPI measurement; however, all measurements were taken blindly for the ventilator settings. Third, patients were evaluated only one time in the acute phase, and we cannot exclude the possibility that some patients developed right ventricular dysfunction at later timepoints in the course of their disease or in response to certain treatments, like the administration of fluid, or the use of inotropes and vasopressors.

CONCLUSION

In this *post hoc* analysis of two studies in invasively ventilated critically ill patients without ARDS, an abnormal RV-MPI indicative of RV dysfunction was prevalent, but was not associated with successful liberation from invasive ventilation or death. The association between RV function should be further studied in prospective investigations that have a larger sample size, possibly focusing on patients with a higher likelihood of extubation failure specifically.

DATA AVAILABILITY STATEMENT

The raw data supporting the conclusions of this article will be made available by the authors, without undue reservation.

ETHICS STATEMENT

The studies involving human participants were reviewed and approved by the AMC Review Board. The patients/participants provided their written informed consent to participate in this study.

AUTHOR CONTRIBUTIONS

CP, LB, and MS contributed to study conception and design, data analysis, and interpretation, drafted the manuscript, and approved the submitted version of the manuscript. AG, FS, TC, WL, and FP revised the manuscript for critical content and approved the submitted version of the manuscript. PReVENT– and the RELAx–investigators performed the parent studies and by that made it possible to design and to perform this study. All authors contributed to the article and approved the submitted version.

REFERENCES

1. Zochios V, Jones N. Acute right heart syndrome in the critically ill patient. *Heart Lung Vessel.* (2014) 6:157–70.
2. Grübler MR, Wigger O, Berger D, Blöchlinger S. Basic concepts of heart-lung interactions during mechanical ventilation. *Swiss Med Wkly.* (2017) 147:w14491. doi: 10.4414/smw.2017.14491
3. Vieillard-Baron A, Naeije R, Haddad F, Bogaard HJ, Bull TM, Fletcher N, et al. Diagnostic workup, etiologies and management of acute right ventricle failure : a state-of-the-art paper. *Intensive Care Med.* (2018) 44:774–90. doi: 10.1007/s00134-018-5172-2
4. Richard C, Teboul JL. Weaning failure from cardiovascular origin. *Intensive Care Med.* (2005) 31:1605–7. doi: 10.1007/s00134-005-2698-x
5. Vieillard-Baron A, Prigent A, Repessé X, Goudelin M, Prat G, Evrard B, et al. Right ventricular failure in septic shock: characterization, incidence and impact on fluid responsiveness. *Crit Care.* (2020) 24:630. doi: 10.1186/s13054-020-03345-z
6. Bahler RC, Mohyuddin T, Finkelhor RS, Jacobs IB. Contribution of Doppler tissue imaging and myocardial performance index to assessment of left ventricular function in patients with Duchenne's muscular dystrophy. *J Am Soc Echocardiogr.* (2005) 18:666–73. doi: 10.1016/j.echo.2004.10.003
7. Longobardo L, Suma V, Jain R, Carerj S, Zito C, Zwicke DL. Role of two-dimensional speckle-tracking echocardiography strain in the assessment of right ventricular systolic function and comparison with conventional parameters. *J Am Soc Echocardiogr.* (2017) 30:937–46.e6. doi: 10.1016/j.echo.2017.06.0162017

8. Tei C, Dujardin KS, Hodge DO, Bailey KR, McGoon MD, Taji AJ, et al. Doppler echocardiographic index for assessment of global right ventricular function. *J Am Soc Echocardiogr.* (1996) 9:838–47. doi: 10.1016/s0894-7317(96)90476-9
9. Vizzardi E, D'Aloia A, Bordonali T, Bugatti S, Piovanelli B, Bonadei I, et al. Long-term prognostic value of the right ventricular myocardial performance index compared to other indexes of right ventricular function in patients with moderate chronic heart failure. *Echocardiography.* (2012) 29:773–8. doi: 10.1111/j.1540-8175.2012.01703.x
10. Haddad F, Denault AY, Couture P, Cartier R, Pellerin M, Levesque S, et al. Right ventricular myocardial performance index predicts perioperative mortality or circulatory failure in high-risk valvular surgery. *J Am Soc Echocardiogr.* (2007) 20:1065–72. doi: 10.1016/j.echo.2007.02.017
11. Zamfir D, Pitic D, Tamaşescu G, Onciul S, Tăutu O, Angelescu C, et al. Prognostic value of right ventricular function assessed by echocardiography in patients presenting with a first acute ST elevation myocardial infarction treated by primary PCI. *Rev Med Chir Soc Med Nat Iasi.* (2016) 120:824–33.
12. Shmueli H, Steinvil A, Aviram G, Moaad S, Sharon A, Bendet A, et al. Re-appraisal of echocardiographic assessment in patients with pulmonary embolism: prospective blinded long-term follow-up. *Isr Med Assoc J.* (2020) 11:688–95.
13. Harmankaya A, Akilli H, Gul M, Akilli NB, Ergin M, Aribas A, et al. Assessment of right ventricular functions in patients with sepsis, severe sepsis and septic shock and its prognostic importance: a tissue Doppler study. *J Crit Care.* (2013) 28:1111.e7–11. doi: 10.1016/j.jcrc.2013.07.059
14. Taha A, Zaytoun T, Eid H, Baess A, Elreweny E. Echocardiographic assessment of the right ventricle and its correlation with patient outcome in acute respiratory distress syndrome. *Adv Respir Med.* (2020) 88:412–9. doi: 10.5603/ARM.a2020.0153
15. Simonis FD, Serpa Neto A, Binnekade JM, Braber A, Bruin K, Determann RM, et al. Effect of a low vs intermediate tidal volume strategy on ventilator-free days in intensive care unit patients without ARDS: a randomized clinical trial. *JAMA.* (2018) 320:1872–80. doi: 10.1001/jama.2018.14280
16. Algera AG, Pisani L, Serpa Neto A, den Boer SS, Bosch F, Bruin K, et al. Effect of a lower vs higher positive end-expiratory pressure strategy on ventilator-free days in ICU patients without ARDS: a randomized clinical trial. *JAMA.* (2020) 324:2509–20. doi: 10.1001/jama.2020.23517
17. Cherpanath T, Simonis FD, Bouma BJ, de Bruin-Bon RH, Determann RM, Juffermans NP, et al. Myocardial function during low versus intermediate tidal volume ventilation in patients without acute respiratory distress syndrome. *Anesthesiology.* (2020) 132:1102–13. doi: 10.1097/ALN.0000000000003175
18. Ranieri VM, Rubenfeld GD, Thompson BT, Ferguson ND, Caldwell E, Fan E, et al. Acute respiratory distress syndrome: the Berlin definition. *JAMA.* (2012) 307:2526–33. doi: 10.1001/jama.2012.5669
19. Lang RM, Badano LP, Mor-Avi V, Afilalo J, Armstrong A, Ernande L, et al. Recommendations for cardiac chamber quantification by echocardiography in adults: an update from the American society of echocardiography and the European association of cardiovascular imaging. *Eur Heart J Cardiovasc Imaging.* (2015) 16:233–70. doi: 10.1093/ehjci/jev014
20. Vieillard-Baron A, Schmitt JM, Augarde R, Fellahi JL, Prin S, Page B, et al. Acute cor pulmonale in acute respiratory distress syndrome submitted to protective ventilation: incidence, clinical implications, and prognosis. *Crit Care Med.* (2001) 29:1551–5. doi: 10.1097/00003246-200108000-00009
21. Lemarié J, Maigrat CH, Kimmoun A, Dumont N, Bollaert PE, Selton-Suty C, et al. Feasibility, reproducibility and diagnostic usefulness of right ventricular strain by 2-dimensional speckle-tracking echocardiography in ARDS patients: the ARD strain study. *Ann Intensive Care.* (2020) 10:24. doi: 10.1186/s13613-020-0636-2
22. Mekontso Dessap A, Boissier F, Charron C, Bégot E, Repessé X, Legras A, et al. Acute cor pulmonale during protective ventilation for acute respiratory distress syndrome: prevalence, predictors, and clinical impact. *Intensive Care Med.* (2016) 42:862–70. doi: 10.1007/s00134-015-4141-2
23. Sanfilippo F, Di Falco D, Noto A, Santonocito C, Morelli A, Bignami E, et al. Association of weaning failure from mechanical ventilation with transthoracic echocardiography parameters: a systematic review and meta-analysis. *Br J Anaesth.* (2021) 126:319–30. doi: 10.1016/j.bja.2020.07.059
24. Naeije R, Badagliacca R. The overloaded right heart and ventricular interdependence. *Cardiovasc Res.* (2017) 113:1474–85. doi: 10.1093/cvr/cvx160
25. Richard C, Teboul JL, Archambaud F, Hebert JL, Michaut P, Auzepy P. Left ventricular function during weaning of patients with chronic obstructive pulmonary disease. *Intensive Care Med.* (1994) 20:181–6. doi: 10.1007/BF01704697
26. Liu J, Shen F, Teboul JL, Anguel N, Beurton A, Bezaz N, et al. Cardiac dysfunction induced by weaning from mechanical ventilation: incidence, risk factors, and effects of fluid removal. *Crit Care.* (2016) 20:369. doi: 10.1186/s13054-016-1533-9
27. Renner J, Cavus E, Gruenewald M, Steinfath M, Scholz J, Lutter G, et al. Myocardial performance index during rapidly changing loading conditions: impact of different tidal ventilation. *Eur J Anaesthesiol.* (2008) 25:217–23. doi: 10.1017/S0265021507002967

Conflict of Interest: The authors declare that the research was conducted in the absence of any commercial or financial relationships that could be construed as a potential conflict of interest.

Advantages of publishing in Frontiers

OPEN ACCESS
Articles are free to read for greatest visibility and readership

FAST PUBLICATION
Around 90 days from submission to decision

HIGH QUALITY PEER-REVIEW
Rigorous, collaborative, and constructive peer-review

TRANSPARENT PEER-REVIEW
Editors and reviewers acknowledged by name on published articles

Frontiers
Avenue du Tribunal-Fédéral 34
1005 Lausanne | Switzerland

Visit us: www.frontiersin.org
Contact us: frontiersin.org/about/contact

REPRODUCIBILITY OF RESEARCH
Support open data and methods to enhance research reproducibility

DIGITAL PUBLISHING
Articles designed for optimal readership across devices

FOLLOW US
@frontiersin

IMPACT METRICS
Advanced article metrics track visibility across digital media

EXTENSIVE PROMOTION
Marketing and promotion of impactful research

LOOP RESEARCH NETWORK
Our network increases your article's readership